LEABHARLANN CHOLÁISTE NA TRÍONÓIDE, BAILE ÁTHA CLIATH | TRINITY COLLEGE LIBRARY DUBLIN
Ollscoil Átha Cliath | The University of Dublin

Terms and Conditions of Use of Digitised Theses from Trinity College Library Dublin

Copyright statement

All material supplied by Trinity College Library is protected by copyright (under the Copyright and Related Rights Act, 2000 as amended) and other relevant Intellectual Property Rights. By accessing and using a Digitised Thesis from Trinity College Library you acknowledge that all Intellectual Property Rights in any Works supplied are the sole and exclusive property of the copyright and/or other IPR holder. Specific copyright holders may not be explicitly identified. Use of materials from other sources within a thesis should not be construed as a claim over them.

A non-exclusive, non-transferable licence is hereby granted to those using or reproducing, in whole or in part, the material for valid purposes, providing the copyright owners are acknowledged using the normal conventions. Where specific permission to use material is required, this is identified and such permission must be sought from the copyright holder or agency cited.

Liability statement

By using a Digitised Thesis, I accept that Trinity College Dublin bears no legal responsibility for the accuracy, legality or comprehensiveness of materials contained within the thesis, and that Trinity College Dublin accepts no liability for indirect, consequential, or incidental, damages or losses arising from use of the thesis for whatever reason. Information located in a thesis may be subject to specific use constraints, details of which may not be explicitly described. It is the responsibility of potential and actual users to be aware of such constraints and to abide by them. By making use of material from a digitised thesis, you accept these copyright and disclaimer provisions. Where it is brought to the attention of Trinity College Library that there may be a breach of copyright or other restraint, it is the policy to withdraw or take down access to a thesis while the issue is being resolved.

Access Agreement

By using a Digitised Thesis from Trinity College Library you are bound by the following Terms & Conditions. Please read them carefully.

I have read and I understand the following statement: All material supplied via a Digitised Thesis from Trinity College Library is protected by copyright and other intellectual property rights, and duplication or sale of all or part of any of a thesis is not permitted, except that material may be duplicated by you for your research use or for educational purposes in electronic or print form providing the copyright owners are acknowledged using the normal conventions. You must obtain permission for any other use. Electronic or print copies may not be offered, whether for sale or otherwise to anyone. This copy has been supplied on the understanding that it is copyright material and that no quotation from the thesis may be published without proper acknowledgement.

Trinity College Dublin

The University of Dublin

An Integrated Water Resources, Climate and Land Use Changes Model for the Shannon River Catchment

Submitted by:

Salem S. Gharbia

Supervisors:

Ass. Prof. Francesco Pilla

Assistant Professor - Environmental Systems Modelling

Prof. Laurence Gill

Professor - Civil Structural & Environmental Engineering

Department of Civil, Structural and Environmental Engineering

Trinity College Dublin, Ireland

A PhD Thesis Submitted in Partial Fulfilment of Requirements for the Degree of Doctor in Philosophy in the Department of Civil, Structural and Environmental Engineering.

July 2017

P.hD

TRINITY COLLEGE DUBLIN

27 SEP 2017

ACADEMIC REGISTRY

School of Engineering

THESIS

11461

50763045

50763045

DEDICATION

This thesis is dedicated to my parents for their endless love, support, and encouragement.

TRINITY LIBRARY
05 APR 2018
DUBLIN

Thesis 11461

ACKNOWLEDGEMENT

First and foremost, I would like to express my sincere gratitude and my extreme appreciation to my supervisor, Dr Francesco Pilla. I would like to thank you for encouraging my research and providing insight and inspiration towards this PhD thesis, your great support, continuous guidance, valuable comments, encouragement, and the challenges that always bring me one step forward, Grazie mille.

I would like to thank my co-supervisor Prof. Laurence Gill, for his time, valuable comments and the guidance to assist me throughout the research.

I would like to thank my PhD project advisor, Prof. Paul Johnston, for his thoughts and comments throughout the project.

I would like to thank my external examiner Prof. Okke Batelaan of Flinders University for all his valuable comments and suggestions during my PhD defence.

I would especially like to thank my internal examiner Dr Niamh Harty for her comments, suggestions and efforts that helped in improving the final presentation of my thesis.

I would especially like to thank Gabor Makrai, a research staff member in the Department of Computer Science at the University of York, Gabor, your assistance and corporation in the machine learning techniques was greatly appreciated.

Also, I would like to thank Trevor Smullen and Sara Abd Alfatah, two master students at Trinity college, for their help in the testing process for some suggested algorithms.

I would also like to acknowledge Met Eireann for the metrological data OPW and ESB for the rivers gauging data. I would also like to acknowledge Teagasc and Irish EPA for the spatially distributed environmental data. I would like to thank Mairead Conlon of JACOBS Engineering for her help in getting the data from the different sources.

The whole department of civil, structural and environmental engineering group at Trinity College, who has resembled one family for the whole past three years. I will have fond memories of all of you 'guys'.

My heart felt deep gratitude to my parents, family and friends for their constant love, support, encouragement, and care during the past years. My Marwa, thanks for being there every moment.

Finally, all of you, including those whose names are not listed here, but contributed in one way or the other, I say thank you very much, all of you have been my extended hands, eyes, ears, legs...

Salem S. Gharbia

July 2017

DECLARATION

I declare that this thesis has not been previously submitted as an exercise for a degree at this or any other university and it is entirely my own work.

I agree that Trinity College library may lend or copy the thesis upon request. This permission covers only single copies made for study purposes, subject to normal conditions of acknow

Signed

Date

ABSTRACT

The main goal of this research is to create an innovative and integrated environmental modelling framework and tool by applying Machine Learning Techniques to a Geographic Information system (GIS). This will allow the scientific community, modellers, planners and decision makers to study the impact of climate and land use changes on water resources on the large catchment scale. The main simulation steps for this tool are:

- Climate change modelling and projection.
- Land use scenarios modelling and projection.
- Hydrological system simplifying algorithm and long-term variation analysis for historical data such as water level and streamflow.
- Future dynamical spatially distributed water balance projection.
- Using Machine Learning Techniques to model and predict water level and streamflow regime.

The developed tool uses as test and validation case the Shannon River catchment in Ireland.

In this research, climate change projections for the Shannon River are simulated and presented using a Geographical Spatially Distributed Water Balance Model (GEO-CWB) for several climate variables (temperature, precipitation, wind speed, solar radiation and relative humidity) from multi-GCM ensembles for three future time intervals (2020, 2050, and 2080) using a range of different Representative Concentration Pathways (RCPs). This research presents the innovative use of GIS as the climate change downscaling environment, which is unprecedented in literature. As part of the integrated environmental modelling approach, the future spatially distributed urban expansion scenarios for the Shannon river basin are simulated and presented based on realistic land cover change models and projected to several time intervals using a hybrid modelling technique combining a logistic regression and a cellular automata (CA) model. This GIS integrated approach improves the understanding of the application of urban expansion models to highly fragmented landscapes such as the Shannon River basin. This research provides an appropriate methodology for the long-term change analysis in the European river's water level and streamflow parameters after using a designed GIS-based algorithm to simplify the large and complicated hydrological system. The study uses the model to identify the long-term variations in multi-time scale water level and streamflow regime over a 30-year period from 1980 to 2010 for the Shannon River.

Potential evapotranspiration is the largest component of the terrestrial hydrological budget after precipitation, of decisive relevance for water resources evaluation and sustainable water management policies. GEO-CWB provides an integrated GIS tool for modelling potential evapotranspiration on the large catchment scale. This tool uses observed historical data of meteorological stations with daily time steps of precipitation, temperature, humidity, daytime and solar radiation. The effectiveness of water resources management and policies need to consider the dynamic nature of any catchment's water balance, particularly in the planning stage, to develop the best strategies for the future. Hence, future management planning scenarios and policies for a specific catchment have to integrate a dynamic water balance with future changes in climate variables and land use in a spatially distributed form. This integration allows decision makers and water resources modelers to predict climate change impacts and land use effects with more confidence in simulations for future scenarios or plans.

The GEO-CWB tool has been developed to simulate and predict future spatially distributed dynamic water balances using a GIS environment at a catchment scale in response to a future change in climate variables and land use. The tool allows researchers to test any assumed or planned future scenarios and to quantify their impacts and intrinsic uncertainties related to

different components making up the catchment water balance. In addition to the analysis of previous studies in the area of dynamic water balance simulation and management, this research illustrates the innovative approach adopted in GEO-CWB. This dynamic water balance simulation tool is completely integrated into a GIS platform, which is to the author's knowledge unprecedented in literature. GEO-CWB operates on a GIS platform. Thus its results can be used as inputs for other GIS related applications, such as drought and flood risk analysis and aquatic eco-system applications to target areas for enforcement of environmental regulations. The issues related to the identification of the appropriate dynamic water balance parameters related to a spatially distributed hydrological model are illustrated and discussed in relation to the test catchment. The research presents a first pass case study assessment of the impacts of climate and land-use changes using GEO-CWB with a wide range of input parameters and grids, including seasonally climate variables and changes, land use/land cover and its seasonal parameters and future changes, seasonal groundwater depth, soil properties, topography and slope. GEO-CWB gives a wide range of seasonally and yearly gridded output layers as surface runoff, subsurface water, interception, evapotranspiration, soil evaporation, transpiration including total change in storage/error in the water balance. In addition, the research provides and tests the performance of suitable data mining methods, as well as spatial and temporal downscaling methods to be used for the input and output data in order to fit the wide range of time steps and spatial resolutions for different modelling processes and purposes, which is highly valuable for ungauged catchments, where there is a lack of high-resolution data.

The Machine Learning Techniques Wavelet, Support Vector Machine (SVM), Artificial Neural Network (ANN) and the hybrid methods Wavelet-ANN and Wavelet-SVM are applied as transfer functions on the outcomes of the GEO-CWB model for the Shannon River in order to model and predict the water level and streamflow parameters for each station along the river for daily time steps. This research shows the novelty of using an integrated physical Computer Learning Technique to model the complicated hydrological systems. These innovative methods and tools developed as part of this project, and their integration with GIS represent an effective approach to study and predict the effects of climate and land use changes in a river basin because it can provide a solid ground for future daily hydrographs predictions, which lead to a well-known and planned future hydrological system.

LIST OF CONTENTS

DEDICATION ---- I

ACKNOWLEDGEMENT ---- II

DECLARATION ---- III

ABSTRACT ---- IV

LIST OF CONTENTS ---- VI

LIST OF ABBREVIATIONS ---- X

LIST OF FIGURES ---- XII

LIST OF TABLES ---- XIX

CHAPTER 1. INTRODUCTION ---- 1

1.1 INTRODUCTION ---- 1

1.2 THE PROJECT OVERVIEW, THE PROBLEM STATEMENT AND OBJECTIVES ---- 2

1.2.1 The aims and overview ---- 2

1.2.2 The research objectives ---- 4

1.3 THESIS LAYOUT ---- 4

CHAPTER 2. GENERAL BACKGROUND / LITERATURE REVIEW ---- 6

2.1 HYDROLOGICAL MODELLING OF LARGE CATCHMENTS ---- 6

2.1.1 Hydrological models classification ---- 6

2.1.2 Metric hydrological models ---- 7

2.1.3 Conceptual hydrological models ---- 7

2.1.4 Physical-based hydrological models ---- 8

2.1.5 Hybrid hydrological models ---- 9

2.2 SPATIALLY-DISTRIBUTED HYDROLOGICAL MODELLING ---- 9

2.3 ASPECTS OF CLIMATE CHANGE ---- 10

2.3.1 Representative Concentration Pathways (RCP) ---- 12

2.3.2 Global Climate Model (GCM) ---- 12

2.3.3 Climatic baseline period ---- 12

2.3.4 Climate change projections downscaling ---- 12

2.4 HYDROLOGICAL MODELING OF THE IMPACTS OF CLIMATE CHANGE AND URBAN DEVELOPMENT ON THE CATCHMENT SCALE ---- 15

2.4.1 Impacts of climate change on hydrology ---- 15

2.4.2 Impacts of urban development on hydrology ---- 18

2.4.3 Spatial and temporal hydrological impact model resolution ---- 18

2.4.4 GIS in impact hydrological modeling ---- 19

2.5 EVAPORATION AND POTENTIAL EVAPOTRANSPIRATION ---- 20

2.5.1 Role of evapotranspiration in hydrological cycle ---- 20

2.5.2 Evapotranspiration (ET) ---- 20

2.5.3 Potential Evapotranspiration (PET) ---- 21

2.5.4 Actual Evapotranspiration (AET) ---- 21

2.6 LAND USE/COVER MODELING AND SIMULATION ---- 22

2.6.1 Land use/cover Conceptual basis ---- 22

2.6.2 Urban expansion ---- 23

2.6.3 Analyzing of spatiotemporal dynamics of urbanization and land use/cover growth 24

CHAPTER 3. STUDY AREA DESCRIPTION ---------- 26

3.1 GENERAL DESCRIPTION OF THE STUDY AREA ---------- 26
3.2 WATER RESOURCES IN THE SHANNON CATCHMENT ---------- 28
3.2.1 Rivers ---------- 28
3.2.2 Lakes ---------- 29
3.2.3 Estuarine/Coastal ---------- 30
3.2.4 Groundwater ---------- 30
3.2.5 Canals ---------- 30
3.2.6 Hydrometric stations ---------- 30
3.2.7 Previous hydrological studies in Shannon River catchment ---------- 32
3.3 SHANNON PROTECTED AREAS ---------- 33

CHAPTER 4. MULTI-GCM ENSEMBLES PERFORMANCE FOR CLIMATE PROJECTION ON A GIS PLATFORM ---------- 35

4.1 INTRODUCTION ---------- 35
4.2 MATERIALS AND METHODS ---------- 37
4.2.1 Model data ---------- 39
4.2.2 Selecting Representative Concentration Pathways (RCPs) ---------- 40
4.2.3 Modeling procedures and downscaling ---------- 40
4.2.4 GIS-based Python algorithm ---------- 40
4.3 RESULTS AND DISCUSSIONS ---------- 43
4.3.1 Validation and performance evaluation ---------- 43
4.3.2 Climate change projections ---------- 48
4.4 CONCLUSIONS ---------- 59

CHAPTER 5. THE INTEGRATION OF GIS-BASED ALGORITHMS AND TIME SERIES STATISTICS FOR HYDROLOGICAL LONG-TERM VARIATION ANALYSIS 60

5.1 INTRODUCTION ---------- 60
5.2 MATERIALS AND METHODS ---------- 61
5.2.1 Data setup ---------- 61
5.2.2 GIS-based algorithm for simplifying the hydro-system ---------- 63
5.2.3 Statistical long-term variation analysis ---------- 69
5.3 RESULTS AND DISCUSSIONS ---------- 71
5.3.1 Simplified structure hydrological system ---------- 71
5.3.2 Validation and performance evaluation ---------- 73
5.3.3 Long-term changes and trends ---------- 78
5.4 CONCLUSIONS ---------- 83

CHAPTER 6. LAND COVER SCENARIOS AND PROJECTIONS SIMULATION USING AN INTEGRATED GIS CELLULAR AUTOMATA ALGORITHMS ---------- 84

6.1 INTRODUCTION ---------- 84
6.2 MATERIALS AND METHODS ---------- 85
6.2.1 Cellular Automata (CA) ---------- 85
6.2.2 Data setup ---------- 88
6.2.3 Model setup and integration with the GIS platform ---------- 91

6.3 Model validation and calibration ---- 113
6.4 Results and discussions ---- 116
6.5 Conclusions and limitations ---- 122

CHAPTER 7. GIS ALGORITHMS FOR SPATIALLY DISTRIBUTED POTENTIAL EVAPOTRANSPIRATION MODELING ---- 123

7.1 Introduction ---- 123
7.2 Materials and Methods ---- 124
7.2.1 Evaluating and choosing models to quantify PET ---- 124
7.2.2 Data Setup ---- 131
7.2.3 Design the PET GIS-based algorithms ---- 131
7.2.4 Validation and performance evaluation ---- 136
7.2.5 Climate change effects on PET ---- 137
7.3 Results and Discussions ---- 138
7.3.1 Baseline PET monthly simulation ---- 138
7.3.2 Validation and performance evaluation ---- 145
7.3.3 Future PET simulations ---- 148
7.3.4 Discussion ---- 153
7.4 Conclusions ---- 155

CHAPTER 8. GEO-CWB: GIS-BASED ALGORITHMS FOR PARAMETERIZING THE RESPONSES OF CATCHMENT DYNAMIC WATER BALANCE REGARDING CLIMATE AND LAND USE CHANGES ---- 157

8.1 Introduction ---- 157
8.2 Conceptualization of GEO-CWB framework ---- 158
8.3 GEO-CWB: The physical base and algorithm design ---- 161
8.3.1 GEO-CWB calculation stages ---- 163
8.4 GEO-CWB integration with GIS ---- 172

CHAPTER 9. GEO-CWB APPLICATION: CLIMATE AND LAND USE CHANGES EFFECTS ON THE SHANNON RIVER CATCHMENT ---- 173

9.1 GEO-CWB validation ---- 173
9.2 Water balance simulated parameters results ---- 174
9.2.1 Surface runoff ---- 174
9.2.2 Subsurface water component ---- 178
9.2.3 Interception ---- 182
9.2.4 Evapotranspiration ---- 185
9.2.5 Soil evaporation ---- 189
9.2.6 Transpiration ---- 192
9.2.7 Error in water balance/change in storage ---- 199
9.3 Simulated and projected water balance for Shannon catchment ---- 199
9.4 Vulnerability parameters results ---- 207
9.4.1 Accumulated surface runoff volume ---- 207
9.4.2 The safe yield groundwater abstraction ---- 207
9.4.3 The water deficit for ideal crop ---- 207

CHAPTER 10. HYBRID DATA-DRIVEN MODELS FOR HYDROLOGICAL PARAMETERS SIMULATION AND PROJECTION ON THE CATCHMENT SCALE 210

10.1 INTRODUCTION ---- 210
10.2 MATERIALS AND METHODS ---- 212
10.2.1 Data setup and hydrometric stations ---- *212*
10.2.2 Workflow and framework ---- *212*
10.2.3 Artificial Neural Network (ANN) ---- *216*
10.2.4 Support Vector Machine (SVM) ---- *216*
10.2.5 Wavelet transformation ---- *217*
10.2.6 Hybrid models ---- *217*
10.2.7 Validation and performance evaluation ---- *217*
10.2.8 Lag value ---- *218*
10.3 MODELS APPLICATION AND EVALUATION ---- 223
10.3.1 Flow evaluation ---- *223*
10.3.2 Water level evaluation ---- *224*
10.4 RESULTS AND DISCUSSION ---- 225
10.4.1 Flow simulation results ---- *225*
10.4.2 Water level simulation results ---- *229*
10.4.3 Projections based on climate change scenarios ---- *234*
10.5 CONCLUSIONS ---- 239

CHAPTER 11. CONCLUSIONS AND RECOMMENDATIONS ---- 240

11.1 CONCLUSIONS ---- 240
11.2 CONTRIBUTION TO KNOWLEDGE ---- 245
11.3 PUBLISHED PAPERS FROM THIS RESEARCH ---- 246
11.4 RECOMMENDATIONS FOR FUTURE RESEARCH ---- 247

REFERENCES ---- 249

APPENDICES ---- 285

APPENDIX A: KEY STUDIES ---- 285
APPENDIX B: SOIL DATA ---- 287
APPENDIX C: ADDITIONAL CLIMATE DOWNSCALING RESULTS ---- 294
APPENDIX D: GEO-CWB USER INTERFACES ---- 300
APPENDIX E: ADDITIONAL GEO-CWB RESULTS ---- 304
APPENDIX F: ADDITIONAL MACHINE LEARNING TECHNIQUES RESULTS ---- 320
APPENDIX G: LIST OF PUBLICATIONS ---- 328
APPENDIX H: DATASETS AND ALGORITHMS ---- 330
I THE CLIMATE CHANGE RESULTS AND TABLES. ---- 330
II HYDROMETRIC STATION TABLES AND OBSERVED DATA. ---- 330
III LAND USE FORCING FACTORS RASTER MAPS, TABLES AND THE RESULTED MAPS. ---- 330
IV POTENTIAL EVAPOTRANSPIRATION RESULTED MAPS. ---- 330
V GEO-CWB MODEL AND THE PYTHON CODE. ---- 330
VI SHANNON CATCHMENT WATER BALANCE MAPS. ---- 330
VII THE RESULTED TABLES FOR CHAPTER 10. ---- 330

LIST OF ABBREVIATIONS

A	Calibrated soil texture factor (Vandewiele et al., 1991)
AET	Actual Evapotranspiration (mm/t)
ANN	Artificial Neural Network
AR4	4th Assessment Report
AR5	5th Assessment Report
C	Vegetation coefficient
CA	Cellular Automata
CLUE	Conversion of Land Use and its Effects
CMIP5	Coupled Model Intercomparison Project
CORINE	Coordination of Information on the Environment
CSO	Central Statistics Office
DBM	Data Based Mechanistic
DEM	Digital Elevation Map
DLA	Diffusion Limited Aggregation
ECTS	European Credit Transfer and Accumulation System
ED	Electoral Division
E_o	Seasonal potential evapotranspiration (mm/year)
Eps	Penman evaporation for wet soil (mm/t)
ET	Evapotranspiration (mm/t)
F_{bs}	Bare soil fraction
F_{is}	Impervious surface fraction
F_{ow}	Open water
F_v	Vegetated fraction
GCM	Global Climate Model
GEO-CWB	Geographical Spatially Distributed Water Balance Model
GHG	Greenhouse Gas
GIS	Geographic Information Systems
Gwd	Groundwater depth
GPU	Graphics processing unit
H	Vegetation height (m)
h_t	Tension saturated height (m)
h_w	Wind measuring height (m)

I	Interception (mm/year)
IPCC	Intergovernmental Panel on Climate Change
LUCC	Land use Land Cover
MAD	Mean Absolute Deviation
MAPE	Mean Absolute Percentage Error
MLR	Multiple Linear Regression
MLT	Machine Learning Techniques
MSD	Mean Squared Deviation
NHA	National Heritage Area
NRA	National Roads Authority
P	Precipitation (mm/t)
PCBA	Pixelated Cubical Balance Approach
PET	Potential Evapotranspiration (mm/t)
PET	Potential Evapotranspiration (mm/t)
PWA	Plant available water content (%)
RBD	River Basin District
RCM	Regional Climate Models
RCP	Representative Concentration Pathways
R_d	Root depth (m)
R_o	Recharge of open water fraction
SAC	Special Area of Conservation
S_o	Runoff of open water fraction
SPA	Special Protected Area
S_r	Potential surface runoff (mm/t)
S_v	Surface runoff in the vegetated fraction (mm)
SVM	Support Vector Machine
T	Temperature ^oC
T_{rv}	Reference transpiration (mm/t)
T_v	Transpiration (mm/t)
U	Wind speed (Km/hr)
VIC	Variable Infiltration Capacity (mm/t)

LIST OF FIGURES

FIGURE 1.1: SHANNON RIVER CATCHMENT LOCATION MAP. 3
FIGURE 2.1: LUMPED AND DISTRIBUTED HYDROLOGICAL MODELS (ABDULLAH ET AL., 2015). 10
FIGURE 2.2: SCHEMATIC VIEW OF THE COMPONENTS OF THE CLIMATE SYSTEM, THEIR PROCESSES, AND INTERACTIONS (CHANGE, 2013). 11
FIGURE 2.3: THE CONCEPT OF SPATIAL DOWNSCALING (TRZASKA AND SCHNARR, 2014)..... 13
FIGURE 2.4: DEVELOPING A REGIONAL CLIMATE PROJECTION (ADAPTED AFTER (TRZASKA AND SCHNARR, 2014)) 14
FIGURE 2.5: FLOWCHART FOR CHOOSING THE MOST APPROPRIATE DOWNSCALING METHOD (TRZASKA AND SCHNARR, 2014). 14
FIGURE 2.6: THE 84 IDENTIFIED MODEL IMPLEMENTATIONS OF 43 ANALYZED MODELING APPROACHES ARE SEPARATED INTO (A) BLUE DOTS FOR MODELS APPLIED AT THE URBAN CATCHMENT SCALE ($\geqslant$10 KM^2) AND (B) RED CROSSES FOR MODELS APPLIED TO SMALL URBAN AREAS (<10 KM^2). THE MODELS SIMULATING THE CATCHMENT SCALE COVER THE FULL RANGE OF SPATIAL AND TEMPORAL RESOLUTION, WHILE MODELS APPLIED TO SMALLER STUDY SITES ARE CONCENTRATED IN TWO REGIONS: (1) NON-SPATIALLY EXPLICIT ZONE WITH TEMPORAL RESOLUTION RANGING FROM 1 MIN TO 1 DAY; AND (2) VERY FINE SPATIAL RESOLUTION WITH TEMPORAL RESOLUTION RANGING FROM 1 S TO 1 DAY (SALVADORE ET AL., 2015). 19
FIGURE 2.7: EVAPOTRANSPIRATION PROCESS (IRMAK AND HAMAN, 2003)..... 21
FIGURE 2.8: PROCESS OF CALCULATING CROP ET FROM PET (QASSIM AND ASHCROFT, 2002).22
FIGURE 3.1: MAP OF THE SHANNON CATCHMENT WITH THE SHANNON RIVER, SHANNON RIVER CATCHMENT UNITS OF MANAGEMENTS (ASSESSMENT 2013, OPW 2015). 27
FIGURE 3.2: LONGITUDINAL SECTION OF THE RIVER SHANNON SUMMER AND WINTER AVERAGE WATER LEVELS (OFFICE OF PUBLIC WORKS, 2011). 29
FIGURE 3.3: OBSERVED WATER FLOW (Q) M3/S FOR SOME SELECTED HYDROMETRIC STATIONS IN THE RIVER SHANNON CATCHMENT FOR THE YEAR 2014. 30
FIGURE 3.4: OBSERVED WATER LEVEL (WL) (M) FOR SOME SELECTED HYDROMETRIC STATIONS IN THE RIVER SHANNON CATCHMENT FOR THE YEAR 2014. 31
FIGURE 3.5: THE SELECTED HYDROMETRIC STATIONS LOCATIONS. 31
FIGURE 3.6: PROTECTED AREAS IN THE SHANNON CATCHMENT. 34
FIGURE 4.1: MAP OF THE SHANNON CATCHMENT WITH THE SHANNON RIVER, CLIMATE STATIONS, AND THE CATCHMENT SURFACE ELEVATION HIGHLIGHTED. 36
FIGURE 4.2: GENERAL FRAMEWORK FLOWCHART. 38
FIGURE 4.3: TAYLOR DIAGRAM FOR THE MEAN TEMPERATURE, PRECIPITATION, WIND SPEED, SOLAR RADIATION AND RELATIVE HUMIDITY OF EACH FORCED RCP FOR THE MEDIAN (50%) AND 3RD QUARTILE 75% ENSEMBLES. THE HORIZONTAL AND VERTICAL AXES REPRESENT THE RATIO OF THE STANDARD DEVIATIONS OF THE REFERENCE AND SIMULATED FIELDS. THE RADIAL AXIS INDICATES THE SPATIAL CORRELATION BETWEEN THE REFERENCE AND SIMULATED FIELDS. THE DISTANCE BETWEEN THE ORIGIN AND ANY POINT IS PROPORTIONAL TO THE RMSE. CONSIDER WIND SPEED GROUP OF MODELS, FOR EXAMPLE, ITS PATTERN CORRELATION WITH OBSERVATIONS IS ABOUT 0.88. THE CENTERED ROOT-MEAN-SQUARE (RMS) DIFFERENCE BETWEEN THE SIMULATED AND OBSERVED PATTERNS IS PROPORTIONAL TO THE DISTANCE TO THE POINT ON THE X-AXIS IDENTIFIED AS "OBSERVED, EQUAL TO 1" THE BROWN CONTOURS INDICATE THE RMS VALUES AND IT CAN BE SEEN THAT IN THE CASE OF WIND SPEED MODELS THE CENTERED RMS ERROR IS ABOUT 0.28. THE NORMALISED STANDARD DEVIATION OF THE SIMULATED PATTERN IS PROPORTIONAL TO

THE RADIAL DISTANCE FROM THE ORIGIN. FOR WIND SPEED MODELS THE NORMALISED STANDARD DEVIATION OF THE SIMULATED FIELD (ABOUT 3.3 MM/DAY) IS CLEARLY GREATER THAN THE OBSERVED STANDARD DEVIATION WHICH IS INDICATED BY THE DASHED ARC AT THE OBSERVED VALUE OF 0.88. 45
FIGURE 4.4: AVERAGE PRECIPITATION (MM/YEAR) CHANGES FROM THE BASELINE PERIOD FOR EACH SIMULATED SCENARIO OVER THE SHANNON CATCHMENT. 49
FIGURE 4.5: AVERAGE TEMPERATURE (^{o}C) CHANGES FROM THE BASELINE PERIOD FOR EACH SIMULATED SCENARIO OVER THE SHANNON CATCHMENT. 50
FIGURE 4.6: AVERAGE SOLAR RADIATION (J/CM^2) CHANGES FROM THE BASELINE PERIOD FOR EACH SIMULATED SCENARIO OVER THE SHANNON CATCHMENT. 50
FIGURE 4.7: PRECIPITATION LONG-TERM AVERAGE FOR THE BASELINE AND PROJECTION PERIODS ACCORDING TO DIFFERENT REPRESENTATIVE CONCENTRATION PATHWAYS. 53
FIGURE 4.8: TEMPERATURE LONG-TERM AVERAGE FOR THE BASELINE AND PROJECTION PERIODS ACCORDING TO DIFFERENT REPRESENTATIVE CONCENTRATION PATHWAYS. 54
FIGURE 4.9: SOLAR RADIATION LONG-TERM AVERAGE FOR THE BASELINE AND PROJECTION PERIODS ACCORDING TO DIFFERENT REPRESENTATIVE CONCENTRATION PATHWAYS..... 55
FIGURE 4.10: AVERAGE RELATIVE HUMIDITY (%) CHANGES FROM THE BASELINE PERIOD FOR EACH SIMULATED SCENARIO OVER THE SHANNON CATCHMENT. 56
FIGURE 4.11: AVERAGE WIND SPEED (KM/HR) CHANGES FROM THE BASELINE PERIOD FOR EACH SIMULATED SCENARIO OVER THE SHANNON CATCHMENT. 57
FIGURE 4.12: RELATIVE HUMIDITY LONG-TERM AVERAGE FOR BASELINE AND PROJECTION PERIODS ACCORDING TO DIFFERENT REPRESENTATIVE CONCENTRATION PATHWAYS... 298
FIGURE 4.13: WIND SPEED LONG-TERM AVERAGE FOR BASELINE AND PROJECTION PERIODS ACCORDING TO DIFFERENT REPRESENTATIVE CONCENTRATION PATHWAYS. 299
FIGURE 5.1: THE SHANNON HYDROMETRIC STATIONS AND MAIN RIVERS CENTERLINE..... 64
FIGURE 5.2: THE TO IDENTIFIED HYDROMETRIC STATIONS THAT INTERSECT THE MAIN RIVER BODIES. 65
FIGURE 5.3: THE MAIN POPULATED AREAS AND CITIES IN THE SHANNON CATCHMENT. 66
FIGURE 5.4: THE FINAL SELECTED HYDROMETRIC STATIONS AND THE RE-CALCULATED SUB-CATCHMENTS. 68
FIGURE 5.5: RESULTED SIMPLIFIED STRUCTURED HYDROLOGICAL SYSTEM. 72
FIGURE 5.6: VALIDATION CHART BETWEEN THE OBSERVED AND THE CALCULATED WATER FLOW (M^3/SEC) TIME SERIES FOR THE INNY HYDROMETRIC STATION. 74
FIGURE 5.7: VALIDATION CHART BETWEEN THE OBSERVED AND THE CALCULATED WATER FLOW (M3/SEC) TIME SERIES FOR THE SUCK HYDROMETRIC STATION. 75
FIGURE 5.8: VALIDATION CHART BETWEEN THE OBSERVED AND THE CALCULATED WATER FLOW (M3/SEC) TIME SERIES FOR THE BROSNA HYDROMETRIC STATION. 75
FIGURE 5.9: VALIDATION CHART BETWEEN THE OBSERVED AND THE CALCULATED WATER FLOW (M3/SEC) TIME SERIES FOR THE NENAGH HYDROMETRIC STATION. 76
FIGURE 5.10: THE CROSS CORRELATION BETWEEN THE OBSERVED AND THE CALCULATED WATER FLOW (M3/SEC) TIME SERIES FOR THE INNY HYDROMETRIC STATION. 76
FIGURE 5.11: THE CROSS CORRELATION BETWEEN THE OBSERVED AND THE CALCULATED WATER FLOW (M3/SEC) TIME SERIES FOR THE NENAGH HYDROMETRIC STATION. 77
FIGURE 5.12: THE CROSS CORRELATION BETWEEN THE OBSERVED AND THE CALCULATED WATER FLOW (M3/SEC) TIME SERIES FOR THE BROSNA HYDROMETRIC STATION. 77
FIGURE 5.13: THE CROSS CORRELATION BETWEEN THE OBSERVED AND THE CALCULATED WATER FLOW (M3/SEC) TIME SERIES FOR THE SUCK HYDROMETRIC STATION. 78

FIGURE 5.14: NORMALITY AND RESIDUAL PLOTS FOR THE LN ( ) TRANSFORMED WATER FLOW TIME SERIES OF LOWER-SHANNON HYDROMETRIC STATION. 79
FIGURE 5.15: TIME SERIES COMPONENT ANALYSIS FOR THE LN ( ) TRANSFORMED WATER FLOW TIME SERIES OF LOWER-SHANNON HYDROMETRIC STATION. 80
FIGURE 5.16: TIME SERIES DECOMPOSITION PLOT FOR THE LN ( ) TRANSFORMED WATER FLOW TIME SERIES OF LOWER-SHANNON HYDROMETRIC STATION. 80
FIGURE 5.17: NORMALITY AND RESIDUAL PLOTS FOR THE WATER LEVEL TIME SERIES OF LOWER-SHANNON HYDROMETRIC STATION. 81
FIGURE 5.18: TIME SERIES COMPONENT ANALYSIS FOR THE WATER LEVEL TIME SERIES OF LOWER-SHANNON HYDROMETRIC STATION. 82
FIGURE 5.19: TIME SERIES DECOMPOSITION PLOT FOR THE WATER LEVEL TIME SERIES OF LOWER-SHANNON HYDROMETRIC STATION. 82
FIGURE 6.1: RECLASSED LAND COVER MAP FOR 2000 (CORINE DATASET). 95
FIGURE 6.2: RECLASSED LAND COVER MAP FOR 2006 (CORINE DATASET). 96
FIGURE 6.3: RECLASSED LAND COVER MAP FOR 2012 (CORINE DATASET). 97
FIGURE 6.4: DRIVING FACTOR OF DISTANCE TO MAJOR ROADS. 98
FIGURE 6.5: DRIVING FACTOR OF DISTANCE TO MINOR ROADS. 99
FIGURE 6.6: DISTANCE TO SMALL POPULATED ELECTORAL DIVISIONS. 101
FIGURE 6.7: DISTANCE TO MEDIUM POPULATED ELECTORAL DIVISIONS (M). 102
FIGURE 6.8: DISTANCE TO HIGHLY POPULATED ELECTORAL DIVISIONS (M). 103
FIGURE 6.9: DISTANCE TO TOWNS/CITIES RASTER MAP (M) 104
FIGURE 6.10: DISTANCE TO EXISTING URBAN AREAS RASTER MAP (M) 105
FIGURE 6.11: CONSTRAINT MAP FOR SHANNON BASIN. 107
FIGURE 6.12: GENERAL MODEL FRAMEWORK (PRATOMOATMOJO, 2016). 113
FIGURE 6.13: THE MODEL'S SIMULATION ACCURACIES UNDER ALL TRANSITION RULES OVER TIME (2006-2012). 114
FIGURE 6.14: CELLULAR AUTOMATA (CA) PREDICTED LAND COVER FOR 2020 119
FIGURE 6.15: CELLULAR AUTOMATA (CA) PREDICTED LAND COVER FOR 2050 120
FIGURE 6.16: CELLULAR AUTOMATA (CA) PREDICTED LAND COVER FOR 2080 121
FIGURE 7.1: HARGREAVES AND SAMANI DESIGNED ALGORITHM FLOWCHART 132
FIGURE 7.2: THORNTHWAITE DESIGNED ALGORITHM FLOWCHART. 133
FIGURE 7.3: HAMON DESIGNED ALGORITHM FLOWCHART. 134
FIGURE 7.4: BLANEY-CRIDDLE AND KHARRUFA DESIGNED ALGORITHM FLOWCHART. 135
FIGURE 7.5: OUDIN DESIGNED ALGORITHM FLOWCHART. 136
FIGURE 7.6: PET PROJECTION DESIGNED ALGORITHM FLOWCHART 138
FIGURE 7.7: BLANEY-CRIDDLE BASELINE MONTHLY PET RASTER MAPS 139
FIGURE 7.8: KHARRUFA BASELINE MONTHLY PET RASTER MAPS 140
FIGURE 7.9: HARGREAVES AND SAMANI BASELINE MONTHLY PET RASTER MAPS 141
FIGURE 7.10: OUDIN BASELINE MONTHLY PET RASTER MAPS. 142
FIGURE 7.11: THORNTHWAITE BASELINE MONTHLY PET RASTER MAPS 143
FIGURE 7.12: HAMON BASELINE MONTHLY PET RASTER MAPS. 144
FIGURE 7.13: MET ÉIREANN AND MODELED MONTHLY PET AT FOUR SYNOPTIC STATIONS LOCATED IN THE SHANNON RBD. 147
FIGURE 7.14: SEASONAL PET BASELINE AND PROJECTIONS FOR 2020 ACCORDING TO DIFFERENT REPRESENTATIVE CONCENTRATION PATHWAYS. 149
FIGURE 7.15: SEASONAL PET BASELINE AND PROJECTIONS FOR 2050 ACCORDING TO DIFFERENT REPRESENTATIVE CONCENTRATION PATHWAYS. 150

FIGURE 7.16: SEASONAL PET BASELINE AND PROJECTIONS FOR 2080 ACCORDING TO DIFFERENT REPRESENTATIVE CONCENTRATION PATHWAYS. 152
FIGURE 7.17: THE SIX LYSIMETERS LOCATIONS 153
FIGURE 7.18: AVERAGE MONTHLY EVAPOTRANSPIRATION MEASURED AT SIX LYSIMETERS OVER THE PERIOD 1971-1990 (MILLS, 2000). 154
FIGURE 7.19: MEAN DEVIATION OF FUTURE SEASONAL PET FROM BASELINE RESULTS FOR FOUR CLIMATE CHANGE SCENARIOS. 155
FIGURE 8.1: GEO-CWB GENERAL FRAMEWORK. 159
FIGURE 8.2: GEO-CWB GENERAL FRAMEWORK POWERED BASED ON GIS PLATFORM. 160
FIGURE 8.3: PIXELATED CUBICAL BALANCE APPROACH (PCBA) SIMPLIFIED THE STRUCTURE FOR THE MODEL DOMAIN EXTENT. 162
FIGURE 8.4: GEO-CWB SINGLE CELL WATER BALANCE COMPONENTS. 163
FIGURE 8.5: GEO-CWB CELL-BY-CELL CALCULATIONS FLOW CHART. 171
FIGURE 8.6: GEO-CWB AS A TOOL IN THE ARC TOOLBOX 172
FIGURE 9.1: SIMULATED SURFACE RUNOFF CHANGES PERCENT FOR EACH CLIMATE CHANGE SCENARIO FROM THE BASELINE PERIOD. 175
FIGURE 9.2: GEO-CWB WINTER SURFACE RUNOFF (MM), SOIL AND LAND USE CATEGORIES INTERACTION PLOT. 176
FIGURE 9.3: GEO-CWB SUMMER SURFACE RUNOFF (MM), SOIL AND LAND USE CATEGORIES INTERACTION PLOT. 176
FIGURE 9.4: THE AVERAGE ANNUAL SURFACE RUNOFF FOR EACH CLIMATIC PERIOD AND LAND USE SCENARIO SIMULATED BY GEO-CWB. 177
FIGURE 9.5: SIMULATED SUBSURFACE WATER COMPONENT CHANGES PERCENT FOR EACH CLIMATE CHANGE SCENARIO FROM THE BASELINE PERIOD. 179
FIGURE 9.6: GEO-CWB WINTER SUBSURFACE WATER COMPONENT (MM), SOIL AND LAND USE CATEGORIES INTERACTION PLOT. 180
FIGURE 9.7GEO-CWB SUMMER SUBSURFACE WATER COMPONENT (MM), SOIL AND LAND USE CATEGORIES INTERACTION PLOT. 180
FIGURE 9.8: THE AVERAGE ANNUAL SUBSURFACE WATER COMPONENT FOR EACH CLIMATIC PERIOD AND LAND USE SCENARIO SIMULATED BY GEO-CWB. 181
FIGURE 9.9: SIMULATED INTERCEPTION CHANGES PERCENT FOR EACH CLIMATE CHANGE SCENARIO FROM THE BASELINE PERIOD. 182
FIGURE 9.10: GEO-CWB WINTER INTERCEPTION (MM), SOIL, AND LAND USE CATEGORIES INTERACTION PLOT. 183
FIGURE 9.11: GEO-CWB SUMMER INTERCEPTION (MM), SOIL AND LAND USE CATEGORIES INTERACTION PLOT. 183
FIGURE 9.12: THE AVERAGE ANNUAL INTERCEPTION FOR EACH CLIMATIC PERIOD AND LAND USE SCENARIO SIMULATED BY GEO-CWB. 184
FIGURE 9.13: SIMULATED EVAPOTRANSPIRATION CHANGES PERCENT FOR EACH CLIMATE CHANGE SCENARIO FROM THE BASELINE PERIOD. 186
FIGURE 9.14: AVERAGE ESTIMATED ACTUAL EVAPOTRANSPIRATION AS PERCENTAGE OF ANNUAL PRECIPITATION (MILLS, 2000). 186
FIGURE 9.15: GEO-CWB WINTER EVAPOTRANSPIRATION (MM), SOIL AND LAND USE CATEGORIES INTERACTION PLOT. 187
FIGURE 9.16: GEO-CWB SUMMER EVAPOTRANSPIRATION (MM), SOIL AND LAND USE CATEGORIES INTERACTION PLOT. 187
FIGURE 9.17: THE AVERAGE ANNUAL EVAPOTRANSPIRATION FOR EACH CLIMATIC PERIOD AND LAND USE SCENARIO SIMULATED BY GEO-CWB. 188

FIGURE 9.18: SIMULATED SOIL EVAPORATION CHANGES PERCENT FOR EACH CLIMATE CHANGE SCENARIO FROM THE BASELINE PERIOD. 189
FIGURE 9.19: GEO-CWB WINTER SOIL EVAPORATION (MM), SOIL AND LAND USE CATEGORIES INTERACTION PLOT. 190
FIGURE 9.20: GEO-CWB SUMMER SOIL EVAPORATION (MM), SOIL AND LAND USE CATEGORIES INTERACTION PLOT. 190
FIGURE 9.21: THE AVERAGE ANNUAL SOIL EVAPORATION FOR EACH CLIMATIC PERIOD AND LAND USE SCENARIO SIMULATED BY GEO-CWB. 191
FIGURE 9.22: SIMULATED TRANSPIRATION CHANGES PERCENT FOR EACH CLIMATE CHANGE SCENARIO FROM THE BASELINE PERIOD. 192
FIGURE 9.23: GEO-CWB WINTER TRANSPIRATION (MM), SOIL AND LAND USE CATEGORIES INTERACTION PLOT. 193
FIGURE 9.24: GEO-CWB SUMMER TRANSPIRATION (MM), SOIL AND LAND USE CATEGORIES INTERACTION PLOT. 193
FIGURE 9.25: THE AVERAGE ANNUAL TRANSPIRATION FOR EACH CLIMATIC PERIOD AND LAND USE SCENARIO SIMULATED BY GEO-CWB. 194
FIGURE 9.26: THE AVERAGE ERROR/CHANGE IN STORAGE IN WATER BALANCE (%) FOR EACH CLIMATIC PERIOD AND LAND USE SCENARIO SIMULATED BY GEO-CWB. 200
FIGURE 9.27: THE SPATIALLY DISTRIBUTED AVERAGE ANNUAL ERROR/CHANGE IN STORAGE IN WATER BALANCE (MM/YEAR) FOR EACH CLIMATIC PERIOD AND LAND USE SCENARIO SIMULATED BY GEO-CWB. 201
FIGURE 9.28: GEO-CEB SIMULATED WATER BALANCE (MM/YEAR). 202
FIGURE 9.29: THE GEO-CWB SIMULATED WATER BALANCE COMPONENTS FOR THE BASELINE AND THE PROJECTED PERIODS FORCED BY RCP 4.5 (50%) CLIMATIC SCENARIO. 203
FIGURE 9.30: THE GEO-CWB SIMULATED WATER BALANCE COMPONENTS FOR THE BASELINE AND THE PROJECTED PERIODS FORCED BY RCP 4.5 (75%) CLIMATIC SCENARIO. 204
FIGURE 9.31: THE GEO-CWB SIMULATED WATER BALANCE COMPONENTS FOR THE BASELINE AND THE PROJECTED PERIODS FORCED BY RCP 8.5 (50%) CLIMATIC SCENARIO. 205
FIGURE 9.32: THE GEO-CWB SIMULATED WATER BALANCE COMPONENTS FOR THE BASELINE AND THE PROJECTED PERIODS FORCED BY RCP 8.5 (75%) CLIMATIC SCENARIO. 206
FIGURE 9.33: THE ACCUMULATED SURFACE RUNOFF FOR EACH CLIMATIC PERIOD AND LAND USE SCENARIO SIMULATED BY GEO-CWB. 208
FIGURE 9.34: THE AVERAGE ANNUAL SAFE YIELD GROUNDWATER ABSTRACTION FOR EACH CLIMATIC PERIOD AND LAND USE SCENARIO SIMULATED BY GEO-CWB. 209
FIGURE 10.1: THE STRUCTURE AND FRAMEWORK OF THE PROPOSED HYBRID COMBINATION MODELS. 215
FIGURE 10.2: MEAN R-SQUARED INTERACTION DIAGRAM WITH THE SIMULATED LAG VALUES AND THE FOUR DIFFERENT WATER FLOW MODELS FOR THE SUCK STATION. 218
FIGURE 10.3: MEAN R-SQUARED INTERACTION DIAGRAM WITH THE SIMULATED LAG VALUES AND THE FOUR DIFFERENT WATER FLOW MODELS FOR THE LOWER-SHANNON STATION. 219
FIGURE 10.4: MEAN R-SQUARED INTERACTION DIAGRAM WITH THE SIMULATED LAG VALUES AND THE FOUR DIFFERENT WATER LEVEL MODELS FOR THE SUCK STATION. 221
FIGURE 10.5: MEAN R-SQUARED INTERACTION DIAGRAM WITH THE SIMULATED LAG VALUES AND THE FOUR DIFFERENT WATER LEVEL MODELS FOR THE LOWER-SHANNON STATION. 221
FIGURE 10.6: INTERACTION FLOW VALIDATION R^2 DIAGRAM FOR THE MODELS AND STATIONS. 224

FIGURE 10.7: INTERACTION WATER LEVEL VALIDATION R^2 DIAGRAM FOR THE MODELS AND STATIONS. 225
FIGURE 10.8: COMPARISONS BETWEEN THE MEASURED AND PREDICTED FLOW (M^3/S) BASED ON THE TESTING DATA FOR SUCK HYDROMETRIC STATION. 226
FIGURE 10.9: COMPARISONS BETWEEN THE MEASURED AND PREDICTED FLOW (M^3/S) BASED ON THE TESTING DATA FOR LOWER-SHANNON HYDROMETRIC STATION. 227
FIGURE 10.10: RESIDUALS OF BEST PERFORMING FLOW SVM MODEL FOR SUCK. 228
FIGURE 10.11: RESIDUALS OF BEST PERFORMING WATER FLOW SVM MODEL FOR LOWER-SHANNON. 228
FIGURE 10.12: COMPARISONS BETWEEN THE MEASURED AND PREDICTED WATER LEVEL (M) BASED ON THE TESTING DATA FOR SUCK HYDROMETRIC STATION. 230
FIGURE 10.13: COMPARISONS BETWEEN THE MEASURED AND PREDICTED WATER LEVEL (M) BASED ON THE TESTING DATA FOR BROSNA HYDROMETRIC STATION. 231
FIGURE 10.14: COMPARISONS BETWEEN THE MEASURED AND PREDICTED WATER LEVEL (M) BASED ON THE TESTING DATA FOR LOWER-SHANNON HYDROMETRIC STATION. 232
FIGURE 10.15: RESIDUALS OF BEST PERFORMING WATER LEVEL WANN MODEL FOR SUCK. . 233
FIGURE 10.16: RESIDUALS OF BEST PERFORMING WATER LEVEL WANN MODEL FOR BROSNA. 233
FIGURE 10.17: RESIDUALS OF BEST PERFORMING WATER LEVEL WANN MODEL FOR LOWER-SHANNON. 234
FIGURE 10.18: LOWER-SHANNON WATER FLOW (M^3/S) DAILY PROJECTIONS (2014-2080) FOR THE DIFFERENT FOUR CLIMATIC SCENARIOS USING THE DEVELOPED SVM MODEL. 237
FIGURE 10.19: LOWER-SHANNON WATER LEVEL (M) DAILY PROJECTIONS (2014-2080) FOR THE DIFFERENT FOUR CLIMATIC SCENARIOS USING THE DEVELOPED WANN MODEL. 238
FIGURE A.1: IRISH SOIL CLASSIFICATION (SOURCE: FAO). 287
FIGURE D.1: GEO-CWB STAGE (1) INTERFACE. 300
FIGURE D.2: GEO-CWB STAGE (2) INTERFACE. 301
FIGURE D.3: GEO-CWB STAGE (3) INTERFACE. 302
FIGURE D.4: GEO-CWB STAGE (4) INTERFACE. 303
FIGURE E.1: THE AVERAGE SUMMER SURFACE RUNOFF FOR EACH CLIMATIC PERIOD AND LAND USE SCENARIO SIMULATED BY GEO-CWB. 304
FIGURE E.2: THE AVERAGE WINTER SURFACE RUNOFF FOR EACH CLIMATIC PERIOD AND LAND USE SCENARIO SIMULATED BY GEO-CWB. 305
FIGURE E.3: THE AVERAGE SUMMER SUBSURFACE WATER COMPONENT FOR EACH CLIMATIC PERIOD AND LAND USE SCENARIO SIMULATED BY GEO-CWB. 306
FIGURE E.4: THE AVERAGE WINTER SUBSURFACE WATER COMPONENT FOR EACH CLIMATIC PERIOD AND LAND USE SCENARIO SIMULATED BY GEO-CWB. 307
FIGURE E.5: THE AVERAGE SUMMER INTERCEPTION FOR EACH CLIMATIC PERIOD AND LAND USE SCENARIO SIMULATED BY GEO-CWB. 308
FIGURE E.6: THE AVERAGE WINTER INTERCEPTION FOR EACH CLIMATIC PERIOD AND LAND USE SCENARIO SIMULATED BY GEO-CWB. 309
FIGURE E.7: THE AVERAGE SUMMER EVAPOTRANSPIRATION FOR EACH CLIMATIC PERIOD AND LAND USE SCENARIO SIMULATED BY GEO-CWB. 310
FIGURE E.8: THE AVERAGE WINTER EVAPOTRANSPIRATION FOR EACH CLIMATIC PERIOD AND LAND USE SCENARIO SIMULATED BY GEO-CWB. 311
FIGURE E.9: THE AVERAGE SUMMER SOIL EVAPORATION FOR EACH CLIMATIC PERIOD AND LAND USE SCENARIO SIMULATED BY GEO-CWB. 312

FIGURE E.10: THE AVERAGE WINTER SOIL EVAPORATION FOR EACH CLIMATIC PERIOD AND LAND USE SCENARIO SIMULATED BY GEO-CWB. 313
FIGURE E.11: THE AVERAGE SUMMER TRANSPIRATION FOR EACH CLIMATIC PERIOD AND LAND USE SCENARIO SIMULATED BY GEO-CWB. 314
FIGURE E.12: THE AVERAGE WINTER TRANSPIRATION FOR EACH CLIMATIC PERIOD AND LAND USE SCENARIO SIMULATED BY GEO-CWB. 315
FIGURE E.13: THE SPATIALLY DISTRIBUTED AVERAGE SUMMER ERROR/CHANGE IN STORAGE IN WATER BALANCE (MM/YEAR) FOR EACH CLIMATIC PERIOD AND LAND USE SCENARIO SIMULATED BY GEO-CWB. 316
FIGURE E.14: THE SPATIALLY DISTRIBUTED AVERAGE WINTER ERROR/CHANGE IN STORAGE IN WATER BALANCE (MM/YEAR) FOR EACH CLIMATIC PERIOD AND LAND USE SCENARIO SIMULATED BY GEO-CWB. 317
FIGURE E.15: THE AVERAGE SUMMER SAFE YIELD GROUNDWATER ABSTRACTION FOR EACH CLIMATIC PERIOD AND LAND USE SCENARIO SIMULATED BY GEO-CWB. 318
FIGURE E.16: THE AVERAGE WINTER SAFE YIELD GROUNDWATER ABSTRACTION FOR EACH CLIMATIC PERIOD AND LAND USE SCENARIO SIMULATED BY GEO-CWB. 319
FIGURE F.1: COMPARISONS BETWEEN THE MEASURED AND PREDICTED FLOW (M^3/S) BASED ON THE TESTING DATA FOR NENAGH HYDROMETRIC STATION. 320
FIGURE F.2: COMPARISONS BETWEEN THE MEASURED AND PREDICTED FLOW (M^3/S) BASED ON THE TESTING DATA FOR BROSNA HYDROMETRIC STATION. 321
FIGURE F.3: COMPARISONS BETWEEN THE MEASURED AND PREDICTED FLOW (M^3/S) BASED ON THE TESTING DATA FOR INNY HYDROMETRIC STATION. 322
FIGURE F.4: RESIDUALS OF BEST PERFORMING FLOW SVM MODEL FOR NENAGH. 323
FIGURE F.5: RESIDUALS OF BEST PERFORMING FLOW SVM MODEL FOR BROSNA. 323
FIGURE F.6: RESIDUALS OF BEST PERFORMING WATER FLOW SVM MODEL FOR INNY. 324
FIGURE F.7: COMPARISONS BETWEEN THE MEASURED AND PREDICTED WATER LEVEL (M) BASED ON THE TESTING DATA FOR NENAGH HYDROMETRIC STATION. 325
FIGURE F.8: COMPARISONS BETWEEN THE MEASURED AND PREDICTED WATER LEVEL (M) BASED ON THE TESTING DATA FOR INNY HYDROMETRIC STATION. 326
FIGURE F.9: RESIDUALS OF BEST PERFORMING WATER LEVEL WANN MODEL FOR NENAGH. 327
FIGURE F.10: RESIDUALS OF BEST PERFORMING WATER LEVEL WANN MODEL FOR INNY. 327

LIST OF TABLES

TABLE 4-1: MULTI-GCM ENSEMBLES MODELS DETAILS. 39
TABLE 4-2: CLIMATE MODELS VALIDATION STATISTICAL TESTS RESULTS. 43
TABLE 4-3: MONTHLY ABSOLUTE VALUES BOX-WHISKER PLOTS FOR EACH PREDICTED YEAR AND BASELINE VARIABLES. 46
TABLE 4-4: MONTHLY DIFFERENCES FROM BASELINE VALUES BOX-WHISKER PLOTS FOR EACH YEAR OF PREDICTED VARIABLES. 47
TABLE 4-5: RASTER MAPS STATISTICS FOR PRECIPITATION BASELINE AND PROJECTIONS FOR 2020, 2050 AND 2080 PERIODS ACCORDING TO DIFFERENT REPRESENTATIVE CONCENTRATION PATHWAYS. 51
TABLE 4-6: RASTER MAPS STATISTICS FOR TEMPERATURE BASELINE AND PROJECTIONS FOR 2020, 2050 AND 2080 PERIODS ACCORDING TO DIFFERENT REPRESENTATIVE CONCENTRATION PATHWAYS. 51
TABLE 4-7: RASTER MAPS STATISTICS FOR SOLAR RADIATION BASELINE AND PROJECTIONS FOR 2020, 2050 AND 2080 PERIODS ACCORDING TO DIFFERENT REPRESENTATIVE CONCENTRATION PATHWAYS. 52
TABLE 4-8: RASTER MAPS STATISTICS FOR RELATIVE HUMIDITY BASELINE AND PROJECTIONS FOR 2020, 2050 AND 2080 PERIODS ACCORDING TO DIFFERENT REPRESENTATIVE CONCENTRATION PATHWAYS. 58
TABLE 4-9: RASTER MAPS STATISTICS FOR WIND SPEED BASELINE AND PROJECTIONS FOR 2020, 2050 AND 2080 PERIODS ACCORDING TO DIFFERENT REPRESENTATIVE CONCENTRATION PATHWAYS. 58
TABLE 5-1: HYDROMETRIC DATA QUALITY CODES. 62
TABLE 5-2: THE CHARACTERISTICS OF THE HYDROMETRIC STATIONS IN THE SIMPLIFIED SYSTEM. 71
TABLE 6-1: LAND USE CLASSES USED IN THE STUDY (EPA, 2015). 88
TABLE 6-2: LIST OF THE USED DATASETS IN THIS STUDY. 91
TABLE 6-3: LAND COVER CLASSES USED IN THE SIMULATION. 92
TABLE 6-4: TRANSITION MATRIX FOR SHANNON CATCHMENT BASED ON LAND COVER DATA FOR 2000 AND 2006, UNITS IN KILOMETER SQUARE. 93
TABLE 6-5: TRANSITION MATRIX FOR SHANNON CATCHMENT BASED LAND COVER DATA FOR 2006 AND 2012, UNITS IN KILOMETER SQUARE. 93
TABLE 6-6: RASTER WEIGHTED VALUES USED FOR THE URBAN AREA LAND USE CLASS. 111
TABLE 6-7: TRANSITION MATRIX FOR SHANNON CATCHMENT BASED LAND COVER DATA FOR 2006 AND 2012, UNITS IN KILOMETER SQUARE. 112
TABLE 6-8: DEFINITIONS OF TERMS USED IN AN ERROR MATRIX AND THEIR COMPUTATIONS. 115
TABLE 6-9: LAND COVER TRANSITION MATRIX OF RIVER SHANNON BASIN AREA. 118
TABLE 7-1: PET MODELS. 127
TABLE 7-2: SYNOPTIC METEOROLOGICAL STATIONS WITHIN THE SHANNON RBD 137
TABLE 7-3: STATISTICAL PARAMETERS FOR PERFORMANCE EVALUATION PROCESS. 146
TABLE 7-4: SEASONAL PET BASELINE AND PROJECTIONS FOR 2020 AT FOUR SYNOPTIC STATIONS LOCATED IN THE SHANNON RBD. 148
TABLE 7-5: SEASONAL PET BASELINE AND PROJECTIONS FOR 2050 AT FOUR SYNOPTIC STATIONS LOCATED IN THE SHANNON RBD. 151
TABLE 7-6: SEASONAL PET BASELINE AND PROJECTIONS FOR 2080 AT FOUR SYNOPTIC STATIONS LOCATED IN THE SHANNON RBD. 151

TABLE 8-1: REFERENCES, COMMENTS AND LIMITATIONS BEHIND PHYSICAL AND EMPIRICAL METHODS THAT HAVE BEEN USED IN GEO-CWB. 164
TABLE 9-1: GEO-CWB EVALUATION TABLE BETWEEN THE SIMULATED AVERAGE DAILY FLOW AND THE OBSERVED AVERAGE DAILY FLOW FOR THE SIMPLIFIED SHANNON SYSTEM. ... 174
TABLE 9-2: ANNUAL, SUMMER AND WINTER RASTERS' AREAL STATISTICS FOR ALL SIMULATED WATER BALANCE COMPONENTS BY GEO-CWB FOR THE BASELINE PERIOD AND THE PROJECTED PERIODS WITH THE CALCULATED AVERAGE VALUES OF THE ERROR IN THE SIMULATED WATER BALANCE. 195
TABLE 10-1: DESCRIPTIVE STATISTICS FOR THE VARIABLES' TRAINING AND TESTING DATA SETS. 213
TABLE 10-2: DIFFERENT LAG VALUES EVALUATION AMONG THE DIFFERENT FOUR MACHINE LEARNING TECHNIQUES WATER FLOW MODELS. 219
TABLE 10-3: DIFFERENT LAG VALUES EVALUATION AMONG THE DIFFERENT FOUR MACHINE LEARNING TECHNIQUES WATER LEVEL MODELS. 222
TABLE 10-4: R2, MAE, AND RMSE VALUES FOR FLOW (M^3/S) BY ANN, SVM, WANN AND WSVM MODELS IN THE TESTING PERIOD. 223
TABLE 10-5: R2, MAE, AND RMSE VALUES FOR THE WATER LEVEL (M) BY ANN, SVM, WANN AND WSVM MODELS IN THE TESTING PERIOD. 224
TABLE 10-6: LOWER-SHANNON WATER FLOW (M^3/S) DAILY PROJECTIONS (2014-2080) STATISTICS BASED ON THE DIFFERENT FOUR CLIMATIC SCENARIOS USING THE DEVELOPED SVM MODEL. 235
TABLE 10-7: LOWER-SHANNON WATER LEVEL (M) DAILY PROJECTIONS (2014-2080) STATISTICS BASED ON THE DIFFERENT FOUR CLIMATIC SCENARIOS USING THE DEVELOPED WANN MODEL. 236
TABLE A-1: KEY STUDIES THAT DEMONSTRATE THE EFFECTS OF THE CATCHMENT'S GEOGRAPHY ON THE HYDROLOGICAL IMPACT STUDIES RESULTS. 285
TABLE B-1: SOIL CLASSIFICATION SCHEME USED IN IRELAND AND THE EQUIVALENT FAO CLASSIFICATION. 288
TABLE B-2: IRISH SOIL CLASSIFICATION AND DESCRIPTION. 288
TABLE C-1: RASTER MAPS STATISTICS FOR BASELINE AND PROJECTED SEASONAL SUMMER PRECIPITATION ACCORDING TO DIFFERENT REPRESENTATIVE CONCENTRATION PATHWAYS. 294
TABLE C-2: RASTER MAPS STATISTICS FOR BASELINE AND PROJECTED SEASONAL WINTER PRECIPITATION ACCORDING TO DIFFERENT REPRESENTATIVE CONCENTRATION PATHWAYS. 295
TABLE C-3: RASTER MAPS STATISTICS FOR BASELINE AND PROJECTED SEASONAL SUMMER TEMPERATURE ACCORDING TO DIFFERENT REPRESENTATIVE CONCENTRATION PATHWAYS. 296
TABLE C-4: RASTER MAPS STATISTICS FOR BASELINE AND PROJECTED SEASONAL WINTER TEMPERATURE ACCORDING TO DIFFERENT REPRESENTATIVE CONCENTRATION PATHWAYS. 297

Chapter 1. Introduction

1.1 Introduction

The climate is one of the key parameters in the earth's environment. Climate is usually defined as the average weather and, in a broad sense, it is the statistical description in terms of the mean and variability of relevant quantities over a period of time ranging from months to thousands or millions of years (Change, 2007b, Change, 2007a, Change, 2007c, Clarke et al., 2007, Kattenberg et al., 1996, Kulkarni et al., 2011, Riahi et al., 2011). During the last half century, the global climate has experienced warming because of the continuous increase in the concentration of greenhouse gasses in the atmosphere, which has been attributed to human activities (Stocker et al., 2013a).

In general and based on the people's beliefs and perceptions, global warming is a contentious issue. Research on climate change beliefs and concern consistently demonstrates the significant effect of political orientation in predicting environmental attitudes (Bohr, 2014).

Continued increases in greenhouse gas emissions at or above current rates will cause further warming during the 21st century which has been predicted to be greater than that observed during the 20th century (Solomon, 2007, Stocker et al., 2013a). Projections of future climate change under scenarios obtained using climate system models have important practical significance, particularly for climate impact assessment studies and future emission control strategies (Xiaoge et al., 2013, Stocker et al., 2013a).

Human activities that could possibly change the climate as a result of emission of gases to the atmosphere include, industrial activities, development of extensive cities, pollution of water ways and cities, creation of dams and lakes, conversion of grassland or forest to cropland, agricultural activities etc. (Garbrecht and Piechota, 2006, Riahi et al., 2007, Taylor et al., 2009b, van Vuuren et al., 2011b, Wilby and Harris, 2006). The Intergovernmental Panel on Climate Change (IPCC) 4th Assessment Report (AR4) (2007) provided a global context for climate change and included the outputs from a number of Global Climate Models (GCMs) under different greenhouse gas emission scenarios. Global climate change is interrupting the water circulation balance by changing rates of precipitation, recharge, discharge, and evapotranspiration.

The IPPC (Change, 2007b, Change, 2007a, Change, 2007c, Hay et al., 2000, Kattenberg et al., 1996, Riahi et al., 2011, Solomon, 2007, van Vuuren et al., 2011b) makes "changes in rainfall pattern due to climate changes and consequent shortage of available water resource" a high priority because it is the most affected part of the human-environment by future climate changes. Also, groundwater, which occupies a considerable portion of the world's freshwater resources, is related to climate change via surface water such as rivers, lakes, and marshes, and direct interactions, being indirectly affected through recharge (Lee et al., 2009, Nelson et al., 2009, Garbrecht and Piechota, 2006, Akhtar et al., 2008, Wilby et al., 2006).

Climate change is of most concern where water resources are either heavily allocated or particularly vulnerable to changes in rainfall. In these systems, the reduction in water availability due to climate change may impact on surface water and groundwater use and entitlements (Matilainen et al., 2011, Crosbie et al., 2011, White and Blum, 1995, Baron et al., 2002). Climate change is already beginning to transform life on earth. Around the globe, seasons are shifting, rainfall patterns are changing - decreasing in some areas and becoming more intense in others,

temperatures are climbing so water demands are increasing and sea levels are rising (Silver and DeFries, 1992, Dupont, 2008, Bergkamp et al., 2003, Change, 2007a, Pachauri and Reisinger, 2007a, Stocker et al., 2013a, Taylor et al., 2009b).

Modelling and assisting the impacts of climate change effects on water resources is a fragmented and multi-stage process, which can be processed through several methods and techniques such as physically based models, statistically based models and/or machine learning methods (Leavesley, 1994, Coppola Jr et al., 2003, Grotch and MacCracken, 1991, Kim and Valdés, 2003, Dibike et al., 2001, Berkhout et al., 2002, Sweeney et al., 2003, Change, 2007b, Tripathi et al., 2006, Chen et al., 2006).

Providing an integrated method by the application of these techniques through geo-referenced spatially distributed calculation using Geographic Information System (GIS) platform with the ability to validate and calibrate the results is a scientific need. This research project contributes to the scientific knowledge by addressing this need through an innovative and integrated tool and method. The designed method and the developed tool presented in this thesis has used the Shannon River basin, as shown in Figure 1.1, as a test and validation case. Surface freshwater, specifically lakes, reservoirs and rivers in addition to groundwater are the main water resources in Ireland. The water demands and threats to both surface water and groundwater resources have grown dramatically in recent years, fuelled by the competing interests of urbanisation, agriculture, industrial development and tourism, and compounding the threats now posed by climate change. Furthermore, the disparity between demand and supply in Ireland due to the abundant water resources in the west compared to the greatest demand along the eastern seaboard is likely to increase with climate change (Sweeney et al., 2003, Charlton et al., 2006, Steele-Dunne et al., 2008, Wilby et al., 2006, Akhtar et al., 2008, Kiely, 1999).

1.2 The project overview, the problem statement and objectives

1.2.1 The aims and overview

This research addresses gaps in the state of knowledge regarding the modelling and prediction of climate and land use changes and their impacts on water resources. This research, mainly, focuses on the large catchment scale. The main aim of this research project is to create an innovative and integrated environmental modelling tool (GEO-CWB) by applying Machine Learning Techniques to a Geographic Information system (GIS). The main contribution of this research is a model which can be used to predict the impacts of climate and land cover change in very large river catchments using high spatial and temporal resolutions because existing models can only deal with small catchments. This tool will allow the scientific community, modellers, planners and decision makers to study the impact of climate and land use changes on water resources based on an integrated multi-stage modelling approach.

This study uses the Shannon river basin as a test and validation case for the developed integrated environmental modelling tool, see Figure 1.1. Right now, Ireland is considered as relatively 'water rich', but in future, Ireland may have less water when and where it will be needed so the drinking water shortages problem might rise on the top.

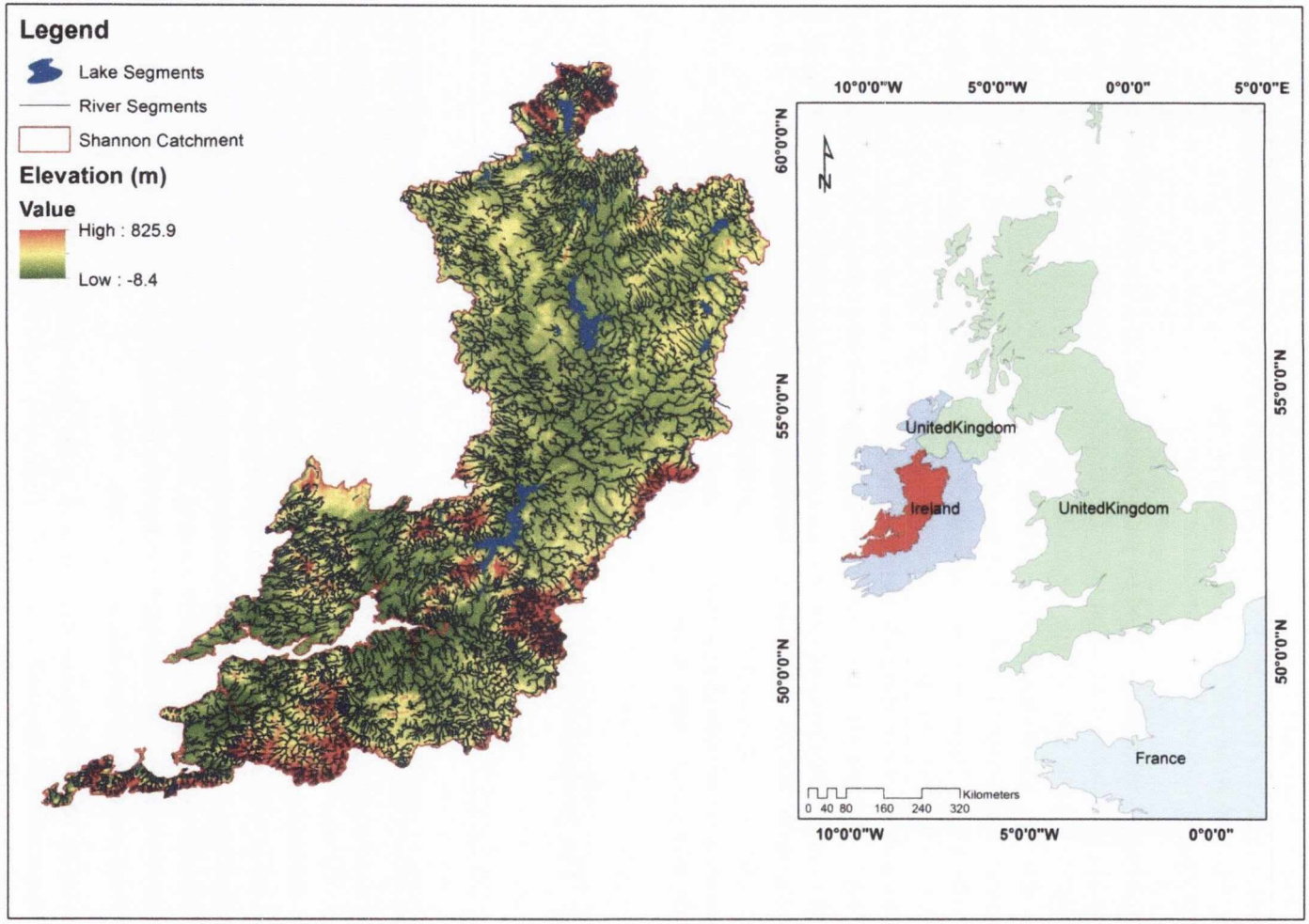

Figure 1.1: Shannon River catchment location map.

1.2.2 The research objectives

The primary objective of this research is to develop a framework and a model which can be used to predict climate and land use change impacts on very large river catchments.

To achieve the primary objective of this research six systematic steps are aimed to be developed as follows:

- Step (1): Develop a GIS algorithm to evaluate and downscale climate changes from multi GCMs ensembles and apply this algorithm to the River Shannon catchment.
- Step (2): Model and evaluate the long-term urban and land cover expansions and changes under GIS environment and provide the results to the River Shannon catchment scale.
- Step (3): Investigate the long-term variation in observed hydrological data for a simplified hydrological system using a designed GIS algorithm for the Shannon River catchment.
- Step (4): Develop a GIS-based tool to calculate potential evapotranspiration depending on different methods and time scales and apply it to the River Shannon catchment.
- Step (5): Develop a transferable GIS framework and algorithm for dynamical water balance determination taking into account the projected climate and land use changes and apply it to the River Shannon catchment.
- Step (6): Investigate and evaluate the integration of Machine Learning Techniques and physically based modelling under GIS environment on the hydrological modelling process of the Shannon River catchment.

1.3 Thesis Layout

This dissertation consists of 11 chapters, each chapter discussing one main part of the GEO-CWB. The chapters' descriptions are as follows:

I Chapter (2): General background / Literature Review

This chapter summarises the state of knowledge with regards to study key areas. The thesis provides a comprehensive discussion on:

- Climate change modelling, GCM downscaling and performance evaluation.
- Statistical long-term variation analysis for observed hydrological data.
- Urban expansion modelling: background and methods.
- Potential evapotranspiration modelling and projection.
- Spatially distributed water balance modelling.
- Machine learning techniques in water resources modelling.

II Chapter (3): Study area description

This chapter introduces the study area of Shannon River Basin District (RBD) in Ireland. This chapter includes an overview of the study area, spatial database collection and the River Shannon's measuring gauges and data.

Chapter (4): Climate change projection and GCM-Ensembles performance evaluation

This chapter addresses the climate change modelling and projection stage of GEO-CWB.

III Chapter (5): The integration of GIS-based systematic algorithms and time series statistical decomposition method for hydrological parameters' long-term variation analysis.

As part of GEO-CWB multi-stage framework, this chapter aims to provide an appropriate methodology for the analysis of long-term changes in the river's water level and streamflow parameters.

IV Chapter (6): Land cover scenarios and projections simulation using an integrated GIS cellular automata algorithms.

This chapter presents the land cover simulation and projection stage of GWO-CWB. The main objective of this chapter is to present a useful tool that can monitor and analyse the urban growth process, by application to the River Shannon Basin area using a GIS platform in order to understand urban expansion better and to support effective urban planning towards more sustainable urban development.

V Chapter (7): GIS algorithms based on physical and empirical formulas for spatially distributed potential evapotranspiration modeling and projection.

This chapter discusses and presents the potential evapotranspiration GEO-CWB tool.

VI Chapter (8): GEO-CWB: GIS-based algorithms for parameterizing the responses of catchment dynamic water balance regarding climate and land use changes.

This chapter presents the main simulation stage of GEO-CWB which is a GIS-based tool for spatially distributed water balance calculations.

VII Chapter (9): GEO-CWB application: Climate and land use change effects on water balance for the Shannon River catchment.

This chapter presents the application of GEO-CWB on the Shannon Catchment as a case study.

VIII Chapter (10): Hybrid data-driven models for hydrological parameter simulation and projection at a catchment scale.

This chapter contains the application of Machine Learning Techniques (MLT) such as Wavelet, Support Vector Machine (SVM), Artificial Neural Network (ANN) and the hybrid models between wavelet transform, SVM and ANN on the Shannon River.

IX Chapter (11): Conclusions and recommendations

This chapter includes, (i) a summary of the research carried out, (ii) a summary of the critical findings enhanced with critical reflections and (iii) recommendations for further studies.

Chapter 2. General background / Literature Review

This chapter provides an overview of the literature review for this thesis, more specific literature reviews are provided in each chapter's introduction.

2.1 Hydrological modelling of large catchments

Based on the problem that needs to be investigated hydrological models have many objectives. Singh and Woolhiser (2002) and later Pechlivanidis et al. (2011) summarised the different common aims of hydrological modelling, as following:

- Building new hydrological models or increase the ability of the old models in order to study the current and future management scenarios.
- Understanding the fundamentals of hydrological systems and build the hydrological impacts studies (e.g. climate and land cover change).
- Modelling and predicting certain location or point hydrological measurements in both spatial and time scales.

Many review studies addressing hydrological modelling techniques, classifications and recent developments have been published, e.g. (Wagener et al., 2004, Wagener et al., 2007, Beven, 2001, Wheater et al., 1993, Pechlivanidis et al., 2011, Singh and Woolhiser, 2002, Salvadore et al., 2015, Praskievicz and Chang, 2009). This section provides an extensive summary and review for the hydrological modelling on catchment scale.

2.1.1 Hydrological models classification

The widely used hydrological models classification system divides the models as metric, physically-based and conceptual (e.g. Pechlivanidis et al. (2011)).

Metric models are based on the fact that a great amount of information is held in measured data that the model can extract to run predictions and estimations. In general, metric hydrological models are described as black-box approaches, because they are mainly based on the data, and most of the used techniques are not based on hydrological sciences.

The main idea behind physically-based models is that they should be a true representation of the physical processes in the modelled systems, which make developing such models not fully possible as empiricism has to be introduced to the developed model (Beven, 2001). Physically-based models are developed following the downward approach (Sivapalan et al., 2003) The downward method is a data-based approach, learning and interpreting behaviour of a catchment from patterns of data obtained at catchment scale.

Conceptual models consider the most important processes in a simplified conceptualization, which are often by the means of reservoirs or buckets. Conceptual models are lumped or semi-distributed (Maréchal, 2004). Semi-distributed models are based on the concept that catchment

areas can have similar hydrological behaviour; these similar areas can be defined and grouped in order to simplify the modelling process, however, lumped models treat the catchment as a one homogenous area.

2.1.2 Metric hydrological models

Metric models consider the catchment as a single unit and relate its output (the flow $Q(t)$) to its input (the rainfall $I(t)$) where t is the time, through an operator Φ called a transfer function.

Essentially, metric models are based on observations and aim to measure and simulate the hydrological system response from the available data (Wheater et al., 1993), which indicates that metric models are empirical. Unit hydrograph (UH) theory for event-based catchment-scale simulation is one of the early examples of metric models (Sherman, 1932). Catchment-scale simulations means that the model simulation domain is equal to the catchment area, which is the area that has one discharge point according to the elevation and the slope. The degree of simplicity in the metric models has allowed them to be used easily in ungauged catchments. Examples of the most interesting and most used metric models are Data Based Mechanistic (DBM) modelling (Young and Beven, 1994, Lees, 2000, Ratto et al., 2007, Young, 2003) and Artificial Neural Networks (ANN) (Ebtehaj and Bonakdari, 2013, Aziz et al., 2014, Kenabatho et al., 2015, Wu et al., 2014b, Aziz et al., 2013, Chen et al., 2014, Kalteh, 2013, Valipour et al., 2013, Chattopadhyay and Rangarajan, 2014, Mekanik et al., 2013, Shamseldin et al., 2007), which is discussed in detail in chapter 10. DBM modelling contains a powerful series of approaches for time-series analysis, simulation and prediction. It is an empirical approach whereby the model structure is developed as an empirical transfer function model based on the available input-output data; hence parameters can be estimated from input-output data only (Pechlivanidis et al., 2011).

2.1.3 Conceptual hydrological models

The main difference between the conceptual models and metric models is that they are built from an *a priori* representation of the hydrological processes in the simulated system. Many conceptual models could be like the data-based mechanistic models described previously in metric approaches. However, the difference is that their structure and modelling steps have been designed according to the developer's perception of the important processes (Holmes et al., 2002, Young, 2002). Conceptual models can be distinguished from physically-based models in that they are built to be only a simplification of reality. The simplification can be achieved by one of the following approaches:

1. Through choosing the most important physical processes by deliberately accepting that some processes are not significant in some cases.
2. Through the mathematical representation of the processes, such as by representing an unconfined aquifer by a non-linear tank.

The number of available and developed conceptual models is very large, each one different from the others; and their application is very wide for both research and practical purposes. Conceptual models can be classified into two groups as following:

- The first group is composed of storage based models as Stanford (Crawford and Linsley, 1966) and HBV (Bergström and Forsman, 1973), they were mainly developed in the 1960's and 1970's and were adapted and reviewed in several studies.
- The second group is based on models which were developed in the 1980's and 1990's and are based on hydrological similarities as TOPMODEL (Beven and Kirkby, 1979) and SWAT (Winchell et al., 2007, Arnold et al., 1998). Hydrologically similar areas of the catchment are defined and grouped together. It is worth mentioning that these models vary in the definition and representation of the similar areas.

Conceptual models that are based on hydrological similarities can be described as reactions to the physically-based models as they have integrated the main criticisms made of the physically-based models (non-correctness of the equations at spatial scales and over-parameterisation) (Maréchal, 2004).

Two semi-distributed conceptual models based on hydrological similarities TOPMODEL (Beven and Kirkby, 1979) and SWAT (Winchell et al., 2007, Arnold et al., 1998) have shown success. SWAT is an integrated tool that incorporates sediment, nutrient and pesticide routines in addition to the hydrological processes. TOPMODEL is an innovative approach to using topography. TOPMODEL parameterises topography and soils data to predict the extent of areas contributing to the runoff.

2.1.4 Physical-based hydrological models

In the hope of getting the real and true physical representation of the simulated hydrological system, physically-based models were constructed. The aim of getting a true picture of the catchment was the basis of building such models (Freeze and Harlan, 1969), in order to build transferable models to be used in ungauged catchments as a benefit from addressing the physical meaning of their parameters (Todini, 1988).

Based on Freeze and Harlan (1969), physically-based models follow the developed blue-print and are based on the laws of the conservation of mass, momentum and energy. Physically-based models address a full range of physical processes including canopy interception and snow pack routines. In general, these models solve the differential equations for all the physical process occurs in the catchment as overland and channel flows, and unsaturated and saturated subsurface flows; and they link these subsystems to meet their boundary conditions.

At the beginning, physically-based models such as the Système Hydrologique Européen (SHE) (Abbott et al., 1986a, Abbott et al., 1986b) or IHDM (Rogers et al., 1985) were not completely 3-dimensional models because of the computing resources and time. However, the recent models are fully 3-dimentional models because of the great modern computer computational power.

However, building the physically-based models was accompanied with huge expectations. These models have not performed as the solution to all hydrological problems and understandings.

Physically-based models have been criticised regarding some main problems, which can be listed as follows:

- The hydrological parameters that were developed based on a physical meaning cannot be directly related to the measured values (Grayson et al., 1992) because of the difference

between the scale at which the parameters have been measured and the scale that the parameters need to be applied to the models.

- Because of a large number of the parameters that need to be calibrated in the physically-based models, these models were classified as overparameterized models (Perrin et al., 2001).
- The questions of the correctness of the equations at the single pixel size have been raised as the equations that produced in the laboratories and experiments cannot be proven to be valid to the catchment scale modelling (Beven, 1996).
- In general, physically-based models do not perform better than simpler conceptual models at the catchment scale (Perrin et al., 2001), so using the conceptual models instead makes more sense.

However, despite the problems that have been raised, physically-based models are still valuable methods and tools, essentially, when detailed and fine spatial information is needed (Maréchal, 2004).

2.1.5 Hybrid hydrological models

A lot of hydrological models are classified as one of the above types but in fact include elements of two or more types. Hybrid conceptual-metric models have been built to combine the strengths of both data-based and conceptual models (Pechlivanidis et al., 2011). They usually consist of a simple conceptual loss function as soil moisture accounting module to produce effective rainfall and a simple routing component such as a routing module to transfer the effective rainfall to streamflow (Pechlivanidis et al., 2011). These hybrid models provide a good solution to the problem of lack of parameters identification. In general, as stated by Pechlivanidis et al. (2011), hybrid models have the benefit of:

- The unique parameterization of metric models and their ability to characterise the observational and measured data in statistical terms.
- Other areas of knowledge to test hypotheses about the structure of a model's component.

A lot of named physically-based models are in fact hybrid physically-based-conceptual models such as SWAT (Winchell et al., 2007, Arnold et al., 1998). This type of hybrid model aims to simplify the model's structure by representing some of the mathematical-physics based processes in a conceptual way, especially in cases where physical parameters are difficult to measure or to observe. Such models, generally, have a very high dimensionality of the parameter space.

2.2 Spatially-distributed hydrological modelling

Figure 2.1 shows in a simplified way the difference between the lumped and the distributed models, in the distributed models the model domain is divided into pixels however the lumped model treat the model domain one unit. Nowadays, using spatially distributed models has been encouraged due to the increasing availability of spatially distributed datasets at relatively fine scales especially with the availability of GIS and remotely sensed data.

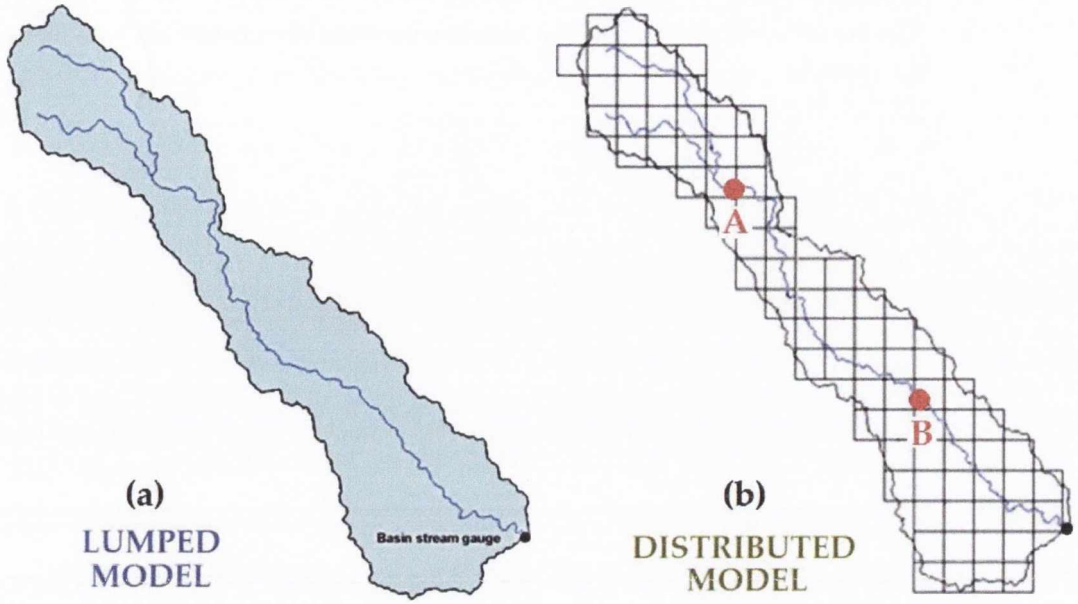

Figure 2.1: Lumped and distributed hydrological models (Abdullah et al., 2015).

In general, spatially distributed modelling has usually been driven by rain gauge data; however, remotely sensed data have significantly improved the spatially distributed modelling. However, the use of distributed models has been encouraged in hydrological applications for many different reasons such as availability of spatial data, and their potential to simulate flow at interior catchment points. There are still some major concerns regarding the scale of parameterization and the calibration issues (Pechlivanidis et al., 2010). Also, distributed models could be over-parameterised and subsequently provide over-fitted results with respect to the available input-output data (Pechlivanidis et al., 2011).

Ajami et al. (2004) proved that the cases when a hydrological distributed model is more efficient than a lumped model, were mainly because of the adequate spatial distribution of rainfall, model parameters and channel routing. However, in cases where a lumped model performs better than a distributed model, it has been stated that this is mainly due to poor spatial consistency of the model parameters.

2.3 Aspects of climate change

The climate is usually defined as the "mean weather", or more precisely, as the statistical description of the weather in terms of the means and variability of relevant quantities over periods of several decades (typically three decades as defined by the World Metrological Organization (WMO)). These quantities are most often surface variables such as temperature, precipitation, and the wind, but in a wider sense, the "climate" is the description of the state of the climate system (Houghton et al., 1997, Change, 2013, Pachauri and Reisinger, 2007b, Kroeze et al., 1999). According to Houghton et al. (1997), the climate system consists of the following major components:

1. The atmosphere
2. The oceans

3. The terrestrial
4. Marine biospheres
5. The cryosphere (sea ice, seasonal snow cover, mountain glaciers and continental-scale ice sheets)
6. The land surface

Figure 2.2 shows the interactions between the different climate and how, through this collective interaction, the Earth's surface climate is determined. These interactions occur through flows of energy in various forms, through exchanges of water, through flows of various other radioactively important trace gasses, including CO_2 (carbon dioxide) and CH_4 (methane), and through the cycling of nutrients. The climate system is powered by the input of solar energy, which is balanced by the emission of infrared ("heat") energy back to space. Solar energy is the ultimate driving force for the motion of the atmosphere and ocean, the fluxes of heat and water, and of biological activity (Kroeze et al., 1999, Houghton et al., 1997, Change, 2013, Pachauri and Reisinger, 2007b).

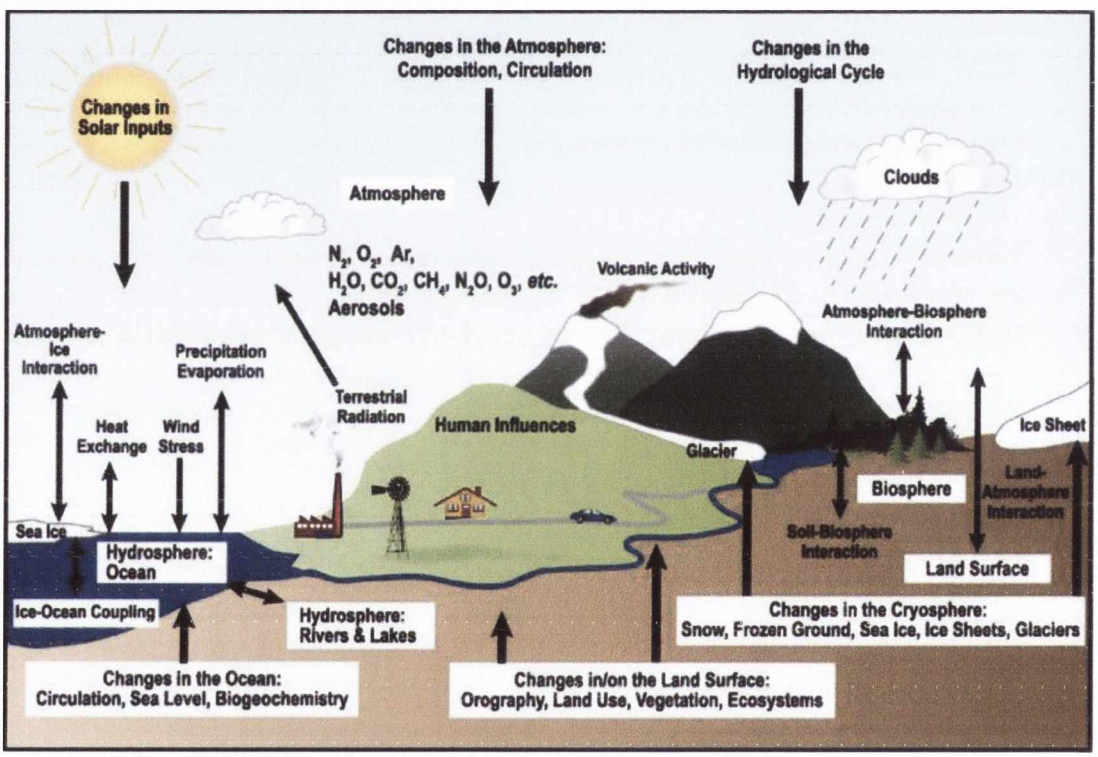

Figure 2.2: Schematic view of the components of the climate system, their processes, and interactions (Change, 2013).

The degree of climate change caused by human activities, such as the emission of greenhouse gasses or land-use change, may be partly predictable, particularly on the larger, continental and global, spatial scales. However, there are limitations on accurately predicting population change, economic change, technological development, and other relevant characteristics of future human activities. Thus, climate projections should be made based on carefully constructed human behavior scenarios. The climate is determined by the atmospheric circulation and by its interactions with the large-scale ocean currents and the land with its features such as albedo, vegetation, and soil moisture. To understand the climate of the Earth and its variations, and to understand and possibly predict the changes of the climate brought about by human activities, one

needs to consider all the factors that influence the radioactive balance, such as the atmospheric composition, solar radiation or volcanic eruptions (Change, 2013, Pachauri and Reisinger, 2007b, Kroeze et al., 1999, Houghton et al., 1997).

2.3.1 Representative Concentration Pathways (RCP)

The RCPs are four greenhouse gas concentration trajectories adopted by the IPCC for its Fifth Assessment Report (AR5) (Stocker et al., 2013b, Change, 2013). The four RCPs, RCP2.6, RCP4.5, RCP6.0, and RCP8.5, are named after a possible range of radiative forcing values in the year 2100 of 2.6, 4.5, 6.0, and 8.5 W/m^2, respectively. RCPs are defined as follows: peaks in radiative forcing at ~ 3 W/m^2 before 2100 and decline for RCP 2.6; stabilization without overshoot pathway to 4.5 W/m^2 at 2100 for RCP 4.5; stabilization without overshoot pathway to 6 W/m^2 at 2100 for RCP 6.0; and rising radiative forcing pathway leading to 8.5 W/m^2 in 2100 for RCP 8.5 (Riahi et al., 2007, Kurosawa, 2004, Clarke et al., 2007, Smith and Wigley, 2006, Whetton et al., 2006, Van Vuuren et al., 2007, Van Vuuren et al., 2011a).

2.3.2 Global Climate Model (GCM)

GCMs are numerical models that represent physical processes in the atmosphere, ocean, cryosphere and land surface, which are the most advanced tools currently available for simulating the response of the global climate system to the increasing in the greenhouse gas concentrations (Melillo et al., 1993, Pachauri and Reisinger, 2007b, Houghton et al., 1997). GCMs depict the climate using a three-dimensional grid over the globe, typically having a horizontal resolution of between 250 and 600 km, 10 to 20 vertical layers in the atmosphere and sometimes as many as 30 layers in the oceans. Their resolution is thus quite coarse in relation to the scale of exposure units in most impact assessments (Melillo et al., 1993, Pachauri and Reisinger, 2007b, Houghton et al., 1997).

2.3.3 Climatic baseline period

Changes in climate are calculated with reference to a baseline period and this reference baseline period is a necessity in developing climate scenarios. It serves to characterize the sensitivity of the exposure unit to present-day climate and usually serves as the base on which data sets that represent climate change are constructed. According to Houghton et al., (1997), the baseline period should be representative of the present-day or recent mean climate in the study region and of a sufficient duration to encompass a range of climatic variations, including several significant weather anomalies (e.g., severe droughts or cool seasons). The WMO defines a very popular climatological baseline period of 30 years that encompasses the period of 1961 – 1990 as a 'normal' period. This period provides a standard reference for many impact studies. However, observations during this period of time in some regions may exhibit anthropogenic climate changes relative to earlier periods. Sources of baseline data include a wide variety of observed data, a combination of observed and model-simulated data (reanalysis data), control runs of GCM simulations, and time series generated by stochastic weather generators (Pachauri and Reisinger, 2007b, Kroeze et al., 1999, Houghton et al., 1997).

2.3.4 Climate change projections downscaling

Although GCMs are very important climate predictive tools, they cannot work for fine-scale climate variability predictions due to their coarse resolution. Different landscape features such as mountains, water bodies, infrastructure, land-cover characteristics, and components of the climate system such as convective clouds and coastal breezes, have scales that are much finer than 100–

500 km (GCMs' spatial scale). Such heterogeneities are important for decision makers who require information on potential impacts on many environmental systems such as crop production, hydrology, species distribution, etc. at scales of 10–50 km. Many methods have been developed to fill the gap between what GCMs can provide and what researchers need for their work. The derivation of fine-scale climate information assumes that the local climate is conditioned by interactions between large-scale atmospheric characteristics (circulation, temperature, moisture, etc.) and local features (water bodies, mountain ranges, land surface properties, etc.). It is possible to model these interactions and establish relationships between present-day local climate and atmospheric conditions through the downscaling process. It is important to understand that the downscaling process adds information to the coarse GCM output so that information is more realistic at a finer scale, capturing sub-grid scale contrasts and inhomogeneities (Trzaska and Schnarr, 2014). Figures 2.3-2.5 show a visual representation of the concept of downscaling process and the different approaches. Figure 2.3 represents the difference of the spatial resection between the GCM and the hydrological area of interest for hydrological modelling. However, figure 2.4, represents the steps of developing climate projections through the downscaling process. Figure 3.5 shows how the most appropriate downscaling method can be chosen.

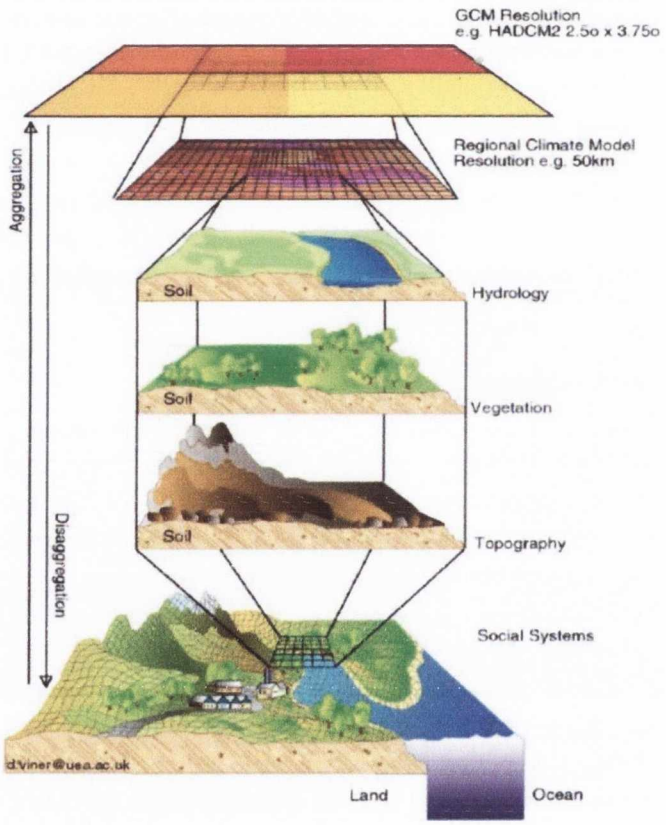

Figure 2.3: The concept of spatial downscaling (Trzaska and Schnarr, 2014).

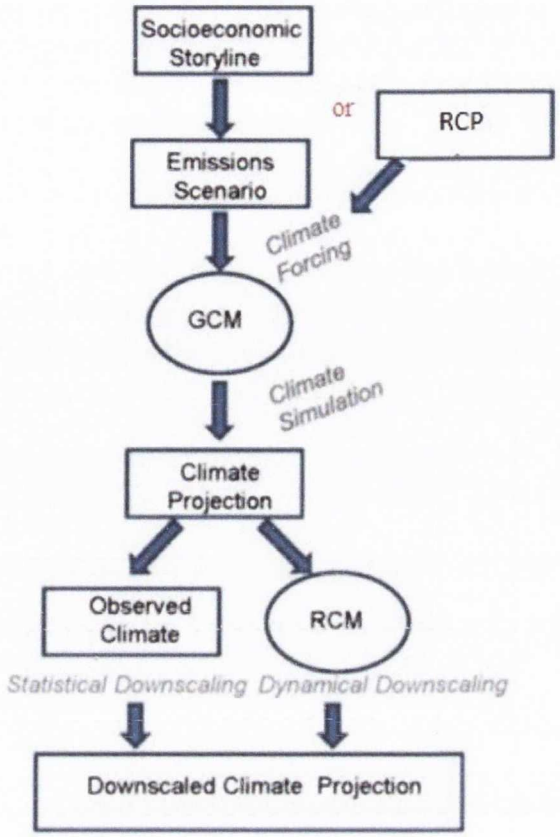

Figure 2.4: Developing a regional climate projection (adapted after (Trzaska and Schnarr, 2014)).

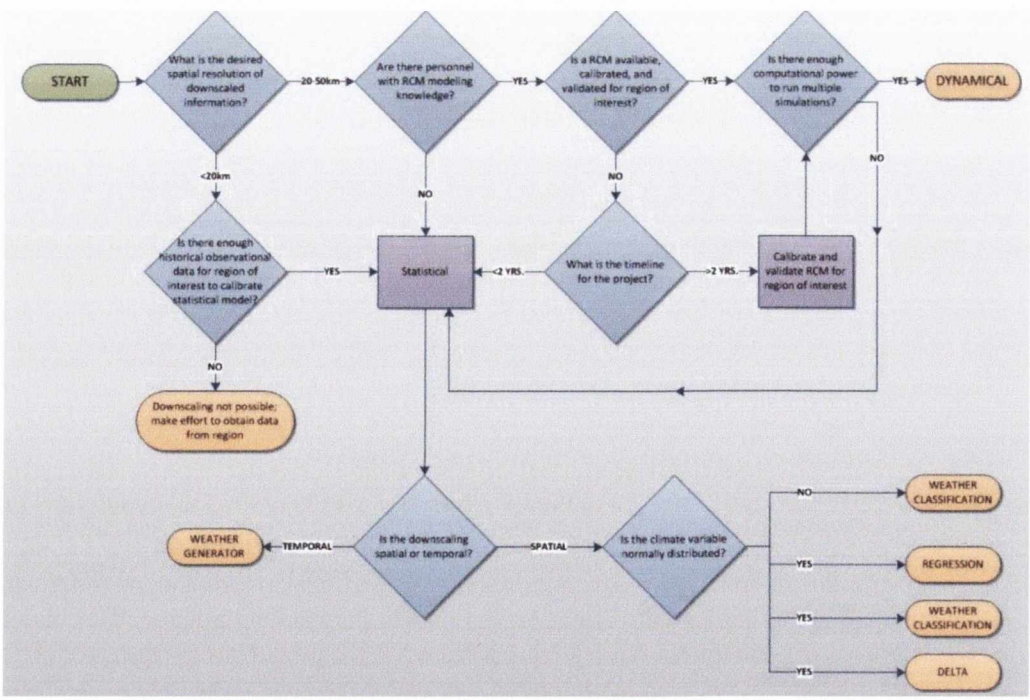

Figure 2.5: Flowchart for choosing the most appropriate downscaling method (Trzaska and Schnarr, 2014).

2.4 Hydrological modeling of the impacts of climate change and urban development on the catchment scale

2.4.1 Impacts of climate change on hydrology

2.4.1.1 Uncertainty in climate change impact modeling

Four different aspects of uncertainty in climate change impact evaluation in hydrology and water resources are documented (Salvadore et al., 2015, Praskievicz and Chang, 2009). These aspects can be listed as following:

- The choice of Global Climate Models (GCMs).
- Transferring large-scale climatology to regional-scale climatology appropriate for hydrological and water resource impact assessment - namely the downscaling processes.
- The parameters and structures of hydrological models used for impact assessment.
- The uncertainty related to water resources impact models employed for the study.

In general, there are two different general classes of climate change impact studies, which can be classified by the assumptions made about the direction and magnitude of climate change that may occur in the study area (Salvadore et al., 2015, Praskievicz and Chang, 2009).

2.4.1.1.1 Synthetic climate change scenarios approach

Synthetic climate change scenarios mean that historical average temperature and precipitation are changed by fixed amounts at annual, seasonal, or monthly scales. This avoids the uncertainty related to GCMs and allows for sensitivity analysis, an estimate of the amount of change in a hydrological variable resulting from a series of incremental changes in a climatic variable, which is a highly useful type of impact analysis for determining how much the climate must change for significant impacts to occur. This approach has many disadvantages, one of them being that the chosen amounts of change in climatic variables are not necessarily realistic consequences of increased atmospheric greenhouse gas concentrations.

The second disadvantage of the synthetic approach is that, when the changes are applied to raw historical climate data, the range of variability in the scenario remains unchanged, which is problematic because climate change is likely to alter variability, particularly in precipitation. As a method to address this problem, Chiew et al. (2003) developed the daily scaling method, in which change factors are applied to ranked historical precipitation data so that change factors are not constant across all years, seasons, or months in the simulated climatic period, but are dependent on the relative magnitude of the event.

2.4.1.1.2 Greenhouse gas (GHG) emissions scenarios approach or RCP

The Intergovernmental Panel on Climate Change's (IPCC) Special Report on Emissions Scenarios (SRES) and the new Representative Concentration Pathway (RCP) approach as illustrated in the subsections 2.3.1, are used to drive GCMs, which depend on large-scale simulations of the coupled ocean-atmosphere system to predict the response of the climate to the projected/predicted increase in GHG concentrations. As the outputs from these models are at too large scale to be useful for most hydrological applications, they must be downscaled using either a regional climate model (RCM), which simulates local topographic and other influences on climate, or a statistical downscaling technique, which alters historic climate records according to

the projected future change, (see Section 2.3.4). Studies indicate that the greatest source of uncertainty in the climate impact modelling chain is the GCM (Graham et al., 2007, Wilby and Harris, 2006, Salvadore et al., 2015, Praskievicz and Chang, 2009).

GCMs simulations differ widely in their projections, especially for precipitation, as they all model atmospheric conditions in different ways. The choice of emission scenario is less important for the near term, because most scenarios show very similar levels of emissions through the 2050s and it takes time for the atmosphere to respond (Wilby and Harris, 2006, Chiew et al., 2003, Salvadore et al., 2015, Praskievicz and Chang, 2009). In catchments where summer is the low flow period, the uncertainty in GCM-derived river flows is greatest in summer (Wilby and Harris, 2006), suggesting that changing precipitation and temperature signals and patterns alter seasonal water balance components in different ways.

Choosing the hydrological model is another source of uncertainty in the climate impact studies. Different hydrological models vary in their inputs, parameters, and assumptions and are suited for simulations at different spatial and temporal scales. Kay and Davies (2008), Kay et al., (2009) compared the temperature-based potential evaporation (PE) with the physically based Penman-Monteith PE. It was found that the temperature-based PE matched the observed PE better than did Penman-Monteith PE, for all climate models studied for three catchments spread across Britain. The main conclusion reported by Praskievicz and Chang (2009) was that different hydrological models tend to produce similar outcomes, given the same climatic inputs, but the same hydrological model run under different GCM simulations may give widely differing results.

Downscaling methods is another big source of uncertainty. Many papers compare different downscaling methods and try to relate the downscaling method selection with the uncertainty (Chen et al., 2011b, Prudhomme et al., 2003, Wilby and Harris, 2006, Fowler et al., 2007). Dibike and Coulibaly (2005) examined the output from a GCM to compare two downscaling methods regarding mainly temporal downscaling; regression analysis and a stochastic weather generator. Generally, the weather generator performed better when estimating the length of wet spells in the historical period. A comparison was performed between dynamical downscaling using RCM and statistical downscaling by Salathe et al. (2007), with the results finding significant differences in regional climate response in the Pacific Northwest using statistical downscaling versus an RCM. The RCM produced the historical climate most accurately. In comparing downscaling methods, RCMs and other dynamic techniques are generally more accurate because they simulate regional climate systems, but also require more data and time than the statistical techniques (Salvadore et al., 2015, Praskievicz and Chang, 2009). However, the dynamical downscaling needs more computational power and cost to run the simulations. Wood et al. (2004) compared three statistical downscaling methods, using the Variable Infiltration Capacity (VIC) macroscale hydrological model. In that comparison, bias correction and spatial disaggregation were found to be the most accurate downscaling methods.

2.4.1.2 Factors influencing catchment hydrological response to climate change

Catchments are natural hydrological units, each with its own water balance. Generally, catchments are ideal spatial units for hydrological modeling, and many climate change impact studies are at its scale (Salvadore et al., 2015, Praskievicz and Chang, 2009). A very important advantage of catchment-scale simulation is that many water resource management plans are made and evaluated at the catchment scale, which moves the application of modeling results to real-world decision-making. The many factors which affect the hydrological response for any simulated catchment climate impact study may be listed as follows:

- Catchment geology is a very important determining factor for hydrological response to climate change. Catchments with significant groundwater exchange may be less sensitive to changes in climate in the near term (Scibek et al., 2007, Hatch et al., 2006, Tucker and Slingerland, 1997, Salvadore et al., 2015, Praskievicz and Chang, 2009). An evaluation and comparison of Oregon's Western Cascades catchment, with a shallow active groundwater system, to one in the High Cascades, with deep aquifer reserves, was carried out by Tague et al. (2008). Surface flows in the High Cascades basin were predicted to be reduced more with respect to temperature increases resulting from climate change than in the Western Cascades basin, which indicates to the different responses of the two different systems according to their different geology.

- The projected impacts of climate change on catchment hydrology depend on the geography of the study area and its climatic zone. Many areas, especially in tropical regions and the higher latitudes, might get increased water resources as a result of more precipitation. This may have negative effects on flood risk in these regions. Other regions, particularly those which are experiencing high demand on water resources, such as Mediterranean and semi-arid climates, increased hydrological variability may decrease water availability (Salvadore et al., 2015, Praskievicz and Chang, 2009, Gharbia et al., 2015b, Gharbia et al., 2015d). Table A-1 in the appendix A summarises some key studies that demonstrate the effects of the geography of the catchments on the climate change impact studies.

- One important factor is a catchment's spatially distributed elevation and, especially, whether the catchments is dominated by rainfall or snowmelt. The University of British Columbia's conceptual Watershed Model was derived from different GCM scenarios to determine climate-driven changes in runoff in two British Columbia catchments (Loukas et al. 2002). In the rainfall dominated basin, the results indicated that total runoff increased in autumn and winter and decreased in spring and summer, while the snowmelt-dominated catchment was projected to experience an earlier spring peak and a nearly 18% increase in winter runoff. Generally, the hydrology of rainfall-dominated catchment is more controlled by changes in precipitation than temperature, while snowmelt-dominated catchments are highly sensitive to temperature changes (Salvadore et al., 2015, Praskievicz and Chang, 2009).

- Different climate models forced by different emissions scenarios or RCPs might result in different projections of hydrological change. The impacts of climate change on water in two catchments in New York's Catskill Mountains, which contribute to the municipal water supply of New York City were investigated by Frei et al. (2002). The results included potential changes in water supply in both catchments ranging from an increase of 10% to a decrease of 30% by 2080, because of differences in precipitation projections among the climate models and emission scenarios.

2.4.2 Impacts of urban development on hydrology

Many studies report that the increase in impervious surface area in the catchment accompanied by urban development severely alters hydrological response, in particular by increasing the 'flashiness' or quickness to and magnitude of peak flow from rainfall events (Dunne and Leopold, 1978, Salvadore et al., 2015, Poelmans et al., 2010). Generally, as urbanized areas increase in a catchment, the water balance of the catchment is affected, with increased surface runoff and decreased groundwater recharge and evapotranspiration (Salvadore et al., 2015, Poelmans et al., 2010). Many studies have modelled the hydrological response of catchments to historical or potential future urbanized areas (Zhou et al., 2013, Miller et al., 2014, Quilbé et al., 2008, De Roo et al., 2003, Choi and Deal, 2008, DeFries and Eshleman, 2004, Niehoff et al., 2002).

For example, Nirupama and Simonovic (2007) used data on land use, meteorology, and hydrology to estimate the increase in flood risk caused by urbanization in London, Ontario. This study illustrates that approximately 15% impervious surface area may be a threshold above which catchment hydrology exhibits the typical urban flashiness.

In general, catchment size dominates hydrological sensitivity to urbanization, with smaller catchments experiencing relatively greater effects than larger catchments. Runoff does not increase linearly with rainfall, and the amount and location of catchment impervious surfaces impact the relation between these variables (Dunne and Leopold, 1978, Salvadore et al., 2015).

2.4.3 Spatial and temporal hydrological impact model resolution

In general, hydrological models are often characterized based on their spatial and temporal resolutions. Salvadore et al. (2015) defined models that are applied to an area equal or larger than 10 km^2 as catchment scale applications; and models applied to smaller areas are city scale applications. Salvadore et al. (2015), figure 2.2, identified that 30 out of the 66 case studies are catchment scale applications, the remaining city scale applications that have more advanced algorithms or modeling concepts for urban applications.

Salvadore et al. (2015) defined the term of 'model implementation', which related to the modeling resolution concept, as the application of one of the 43 modeling approaches to a particular case study with a specific combination of at (time step) and dx (spatial resolution), see Figure 2.6, which summarises the previous studies' scale of application and it can be concluded that catchment scale size application in dynamic temporal scale is the most addressed by the scientific community because of its importance in providing the understanding of the hydrological system that been modelled. In this research, catchment scale size application in dynamic temporal scale are the size and scale of application.

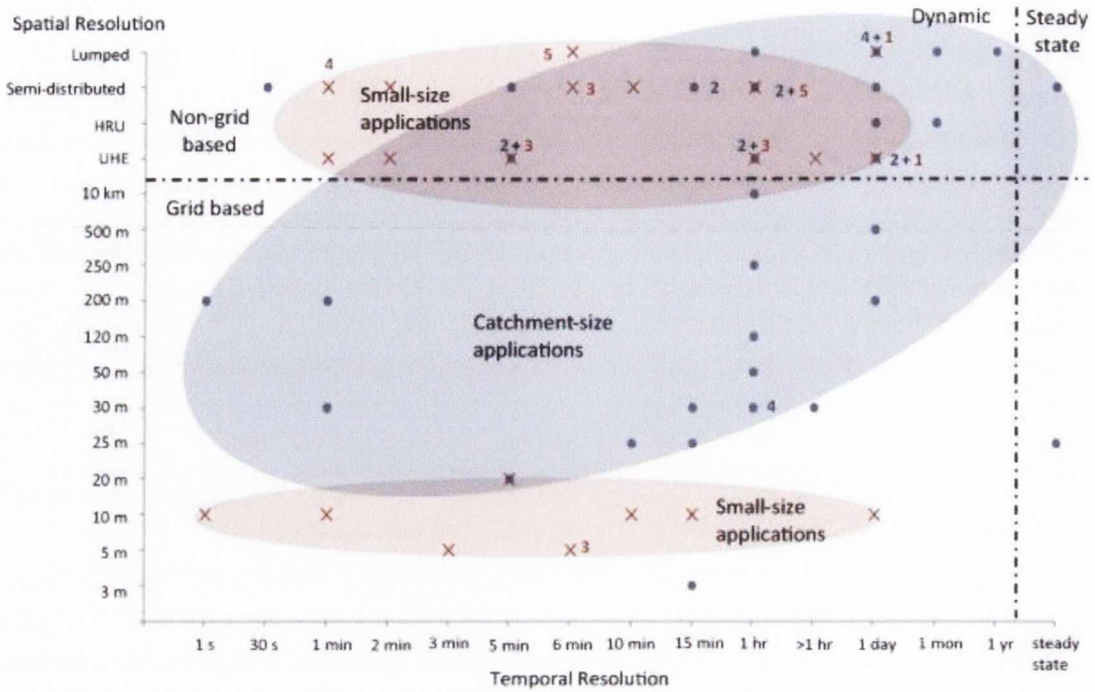

Figure 2.6: The 84 identified model implementations of 43 analyzed modeling approaches are separated into (a) blue dots for models applied at the urban catchment scale (≥10 km²) and (b) red crosses for models applied to small urban areas (<10 km²). The models simulating the catchment scale cover the full range of spatial and temporal resolution, while models applied to smaller study sites are concentrated in two regions: (1) Non-spatially explicit zone with temporal resolution ranging from 1 min to 1 day; and (2) very fine spatial resolution with temporal resolution ranging from 1 s to 1 day (Salvadore et al., 2015).

2.4.4 GIS in impact hydrological modeling

Recently, hydrological simulation tools have taken advantage of GIS functionalities. Most of the currently available hydrological models are either loosely or tightly coupled with a GIS platform. The spread of GIS tools certainly was one of the main drivers in the development of spatially distributed hydrological models, but nowadays nearly all types of models take benefit from spatial data management to drive (for example) average input parameter values (Salvadore et al., 2015, Poelmans et al., 2010).

GIS is well suited for urban hydrology because of the strong spatial variability and dynamics of urban lands. Urban databases, with detailed and up to date information, are a precious source of information for hydrological models. Salvadore et al. (2015) summarize that GIS platforms are used for:

- Pre- and post-processing of model parameters and inputs.
- Managing and displaying spatial data.
- Watershed surface representation, which includes topographic aspects and subwatershed delineation.
- Remote sensing data assimilation.

- Identification of hydrologic unit response or unit hydrological elements.
- Coupling model as a framework.

The most used GIS functionalities are data management and map algebra calculations to estimate hydrological model parameters.
For example, in the WetSpa model (Safari et al., 2012, Liu and De Smedt, 2004, Wang et al., 1996), which used GIS, overland, and channel flow are routed to the outlet using the diffusive wave approximation, a unit response function is derived for each grid cell of the catchment based on spatially-distributed morphological characteristics such as flow direction, slope, and roughness.

2.5 Evaporation and Potential evapotranspiration

2.5.1 Role of evapotranspiration in hydrological cycle

After precipitation, evapotranspiration (ET) is the largest component of the terrestrial hydrological budget (Espana et al., 2011). ET represents the most active of land-based hydrological processes, with approximately 65% of precipitation being evaporated and transpired globally (Federer et al., 1996). Thus, it is evident that ET will have a profound effect on numerous aspects of the hydrological cycle as well as other related processes. It is clear and widely identified in the literature (Chattopadhyay and Hulme, 1997, Federer et al., 1996, Espana et al., 2011, Qassim and Ashcroft, 2002, Jackson et al., 1981) that understanding Potential Evapotranspiration (PET) is of decisive importance in resource evaluation and sustainable water resource management policies.

PET is of paramount importance in numerous projects such as hydrological catchment studies, agricultural irrigation system design and management, water supply, flow forecasting, land resource planning ect. PET has been identified as a key factor in the water balance of land surface (Kumar et al., 2002), and must be accurately accounted for in hydrological modeling (Kay and Davies, 2008). This is because of the effect ET has on groundwater recharge, as recharge effectively can be calculated as precipitation minus Actual Evapotranspiration (AET) (Poelmans et al., 2010, Batelaan and De Smedt, 2007, Batelaan and De Smedt, 2001, Irmak and Haman, 2003). When precipitation is greater than Actual Evapotranspiration (AET), storage is increased, and if soils become saturated this surplus will eventually generate runoff. If precipitation is less than AET plants extract stored moisture creating a deficit. Chattopadhyay and Hulme, (1997) identified that long-term changes in PET can have a profound effect on hydrological processes as well as agricultural crop performance. All these principles are addressed in designing the spatially distributed water balance model GEO-CWB in Chapter 8.

2.5.2 Evapotranspiration (ET)

Evapotranspiration is a combined term for two hydrological processes that occur simultaneously in the soil-plant-atmosphere system. These processes are direct evaporation of moisture from the Earth's surface, and the exchange of water vapour which occurs within the leaves of plants (transpiration) because of the extraction of water from the soil by a plant's root system (Xu et al., 2006, Allen et al., 1998, Irmak and Haman, 2003). This process is presented in Figure 2.7.

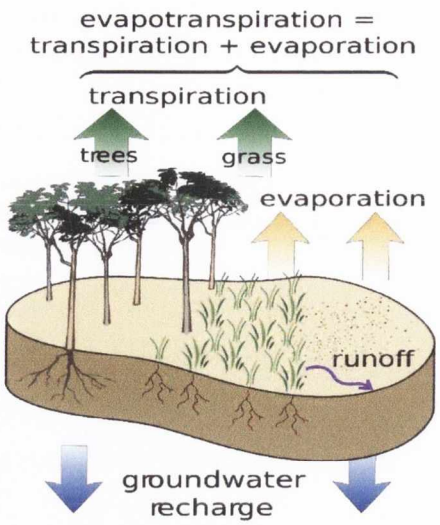

Figure 2.7: Evapotranspiration process (Irmak and Haman, 2003).

From a comprehensive review of relevant literature (Shukla and Mintz, 1982), three key requirements for ET have been identified:

1. There must be moisture available in the soil for both evaporation and transpiration processes.
2. Vegetation is required to transfer moisture from the soil to the interface with the atmosphere.
3. Energy is required to convert moisture to water vapour.

2.5.3 Potential Evapotranspiration (PET)

PET is a measure of the ability of the atmosphere to remove moisture through ET processes. It represents the theoretical volume of water which could be transferred to the atmosphere through ET if sufficient soil moisture was always available (Holdridge, 1959). PET has been a freely used hydrological term for over 60 years, first introduced by Thornwhite in 1948 in the context of the classification of climate (Granger, 1989).

One of the most widely recognized definitions is that introduced by the Food and Agricultural Organization of the United Nations (FAO) in which PET is defined as the ET of a reference crop under optimal conditions, having the characteristics of well-watered grass with an assumed height of 12 cm (Allen et al., 1998). Thus, PET would equal AET when water is readily available and the land surface is completely covered by vegetation.

2.5.4 Actual Evapotranspiration (AET)

PET estimates are widely used in the hydrological sector and are often used as a more accessible or predictable index from which AET values may be determined. Value for AET/PET will vary from 1 where ample water is available, to 0 for conditions where no water is available (Jackson et al., 1981). PET has now become a standard component in the development of new methods of determining AET, most methods currently in operation estimate AET as some fraction of PET depending on crop type, growth stage, water availability etc. An example of this would be crop coefficients which are published by the FAO, which are multiplied by PET to estimate

a given crop AET as shown in Figure 2.8. PET is generally estimated from empirical equations which use a variety of meteorological parameters. Chapter 7 presents the spatially distributed calculation for PET and Chapter 8 uses these calculated PET values in the dynamical spatially distributed water balance calculations in order to calculate actual transpiration, soil evaporation and AET, as part of GEO-CWB. GEO-CWB uses PET as an input to calculate AET.

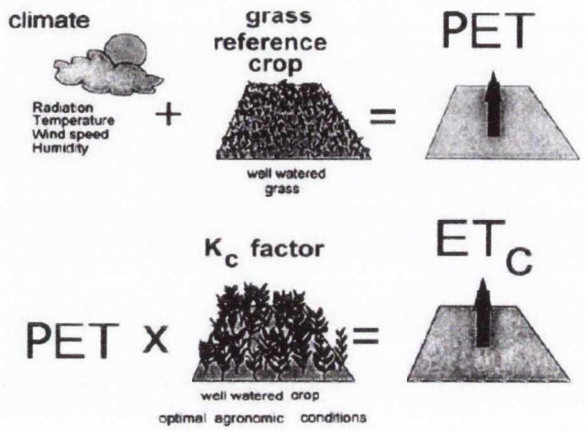

Figure 2.8: Process of calculating crop ET from PET (Qassim and Ashcroft, 2002).

2.6 Land use/cover modeling and simulation

2.6.1 Land use/cover Conceptual basis

2.6.1.1 Variations in Land use and land cover

Land use and land cover change (LULCC), is a term used for any modification made by the human of the Earth's terrestrial surface (Campbell et al., 2005, Turner Ii et al., 1990). It is a central component of global environmental change with direct impacts on climate, environment, and human societies. Changes in land use and land cover are among the most important drivers of global change (Turner Ii et al., 1990).

Land cover describes the land in terms of the vegetation or another biophysical surface types present on the land (Yang et al., 2012a, Liu et al., 2014, Liu et al., 2010). A typical land cover classification scheme will have varying levels of detail starting with the general land cover and then working its way down to more habitat specific descriptions. According to (Lambin et al., 2003), land cover refers to physical and biological cover over the earth's land surface and immediate subsurface. It includes water, vegetation, bare soil, and/or artificial structures. Foody (2002) stated that land cover is a fundamental variable that affects and links many parts of the human and physical environments.

Land use is a more complicated term to define as it is based solely on the human activity or usage of a land parcel, i.e. the intended human employment and management of a land cover: the ways and means of its exploitation to meet human demands (Meyer and Turner II, 1996) for example, industrial and commercial land. There is a strong relationship between land use and human activities in the environment (Turner Ii et al., 1990). The Food and Agriculture Organization (1995) stated: *"land use concerns the function or purpose for which the land is used for the local*

human population and can be defined as the human activities which are directly related to land, making use of its resources or having an impact on them". It comes out from the above definitions that land use and land cover are not equivalent although they may partially overlap.

2.6.2 Urban expansion

Urbanization is the physical growth of urban areas as a result of global change. It is also defined by the United Nations as "*the movement of people from rural to urban areas with population growth equating to urban migration*" (United Nations, 2012). This process, with no sign of slowing down, may be the most powerful and visible anthropogenic force that has brought about fundamental changes in land use and landscape pattern around the globe, which may cause crucial hydrological effects issues especially in the developing countries (Deng et al., 2009). Associated with the process of rapid urbanization, the spatial expansion of built-up areas has been accelerating as well. Although urban land cover occupied in 2009 only 2% or 3% of the earth surface (Poelmans and Van Rompaey, Poelmans et al., 2010), yet their rapid expansion has marked effects on the environment and socio-economy such as the displacement of agriculture and forest (Kueppers et al., 2004) , the decline in wetlands and wildlife habitats (Serneels and Lambin, 2001b), the local impact on hydrology, the degradation of ecosystem compositions and the global impact of changes in atmospheric compositions (Foley et al., 2005).

The process of urban growth can be described as either a change in the area of a town/city (a measure of extent) or the rate at which non-urban land is converted to urban uses (a measure of rate) (Seto and Fragkias, 2005). However, the extent and rate of urban growth cannot provide detailed information about spatial patterns of urbanization or the underlying processes. Therefore, the urban spatial pattern has been the other subject of interest for geographers and economists to study the changes in urban areas.

Regarding the urban growth pattern, urban sprawl has received much attention in the late 1950s; Urban sprawl is a type of urban growth characterized by a low-density, dispersed spatial pattern with both environmental and social impacts. It is currently one of the main challenges for spatial planners in the 21st century (Aguilera et al., 2011).

Engaging the sprawl and managing the growth of urbanization appear to be fundamental prerequisites for sustainable urban areas, which are well-documented to be the major sources of environmental degradation. The delicate balance between the demands of human consumption and the supply of naturally regenerating resources has to be moderated constantly, which predicates continual protection of open spaces, farmlands, natural wildlife habitats and ecosystems against the uncontrolled urbanization.

2.6.2.1 Characteristics of the urban systems and its complexity

Cities are among the most complex structures created by human societies. However, understanding the cities' complexity helps in modelling the future land use and urban expansion scenarios, which help in more accurate future hydrological studies. Complex systems are usually defined in terms of the strength of dynamic linkage between components. According to Batty, (2009b) the complex systems "*show surprising and unanticipated or 'emergent' behaviors as shown in patterns that arise at the aggregate level from the operation of system processes at the micro of agent level*". While Parker et al., (2003) defined that complex systems are regarded as dynamic systems that present recognizable patterns of organization across spatial and temporal scales.

On the other hand, modeling cities' growth may be a difficult or almost intractable task without tools that show their complexity. Cities can be defined as complex objects from the point of view of their intricate mix of urban activities (White and Engelen, 1993). Moreover, cities' complexity can be seen from two points of view: the complexity represents the information-rich nature of the system, and the complexity is necessary for the successful functioning of the city as a system (White et al., 1997).

From the first law of geography by Tobler, (1970) "*Everything is related to everything else, but near things are more related than distant things*", the basic understanding of urban dynamics can be drawn. The law explains the basis of spatial analysis applications in which the neighborhood space of a feature can influence the feature as a function of distance.

It is worth mentioning that the complexity of urban growth is mainly due to the complex way in which humans and the environment interact to each other, whereby these interactions are regulated by a wide range of factors influencing land-use decisions at different temporal and spatial scales (Torrens, 2000b, Torrens, 2000a). Therefore, cities are the spatial result in time of all these influences, which continuously contribute to shaping the city. If all the influences were considered acting simultaneously the chaotic expansion of cities would not surprising (Barredo et al., 2003).

2.6.3 Analyzing of spatiotemporal dynamics of urbanization and land use/cover growth

2.6.3.1 Land cover change

Mapping and monitoring land cover have been recognized as an important step to better understand and provide long-term solutions for social, economic, and environmental problems (Dewan and Yamaguchi, 2009) and (Foody, 2002). Therefore, for urban planning and future urban expansion prediction, the historical information of land cover and land cover change is very important (Ramankutty and Foley, 1999). With the wide requirement and application of land cover data, there has been an increasing interest in obtaining those data.

The first Earth resource satellite Landsat-1 was launched in 1972, and since then satellite remote sensing has become an increasingly powerful and effective tool for the monitoring and management of land cover (Zhang and Zhu, 2011). Compared with more traditional mapping methods such as field surveys and basic aerial photo interpretation, remote sensing has the advantages of low cost, large area coverage, repetitive data, digital format and accurate georeferencing procedures (Yuan et al., 2005). Therefore, the satellite image information provided for the land use have become a very necessary database for land cover management and urban planning. Specifically, in developing countries, where the land cover data are not available, remote sensing has the ability to provide that fundamental information in a cost effective way (Dewan and Yamaguchi, 2009, Li, 2014).

An example in defining and monitoring urban growth, expansion, and sprawl utilizing spatial analysis and remote sensing technologies can be found in the 2008 article by Jat et al. (2008). The article offers a review of software such as ERDAS (Leica) and ArcGIS (ESRI) *"used for the monitoring and planning purposes as these enable the reporting of overall sprawl at a detailed level"* (Jat et al., 2008). Using the images obtained from sources like Landsat MSS, TM, ETM+ and IRS LISSIII, the various features of these images are analyzed with extreme care for details as far as population growth, built-up area, and patchiness, which are used to establish the metrics, dynamics and modeling of urban growth. Based on these data, various scenarios of sprawl can be

constructed by utilizing statistical classification approaches. Urban sprawl, its spatial features, and temporal characteristics are derived from these classified satellite images (Li, 2014).

In other research, urban sprawl of the Ajmer City (Rajasthan, India) has focussed on data collected on the area of impervious surfaces and their spatial and temporal variations between the period of 1977 and 2002. The study employed multivariate statistical techniques to establish the relationship between the urban sprawl and its prominent factors. The results of the study suggest that the land development in Ajmer (160.8%) is more than three times the population growth (50.1%). The article clearly stated that *"Without remote sensing data, one may not be able to monitor and estimate the urban sprawl effectively over a time period, especially for elapsed time period"* (Jat et al., 2008).

2.6.3.2 Urban growth models

A model is a simplified representation of a physical system. By using models, the behavior and future evolution of the systems can be simulated. Therefore, they can be used as interpretative tools for analysing system dynamics, and providing hints for data collection and design of experiments (Giudici, 2002), Urban models are the representations of functions and processes which produce urban spatial structure in terms of land cover, population, and transportation, commonly embodied in computer programs.

Modeling of the urban growth process is an important technique to provide a better understanding of causes and mechanisms governing urban growth; to analyze alternative urban growth consequences, therefore, to support the appropriate urban planning and decision-making responses to urban growth (Berling-Wolff and Wu, 2004).This task, however, is challenging due to unpredictability in decision-making or social phenomena such as arbitrary zoning changes or population movement. At best, urban growth prediction models can provide a scenario-based approach, where abrupt changes are integrated into the modeling prediction as external constraints. Another factor contributing to model uncertainty is the high variability in model validation techniques (Li, 2014). The scientific community has developed numerous urban growth prediction models over the past decades to study urban land use dynamics and simulate urban growth. These models, even though they have a common goal, vary widely in underlying methodologies and theoretical assumptions, and spatial/temporal resolutions and extents. Examples of urban expansion models are as following:

- Cellular Automata Modelling (Santé et al., 2010, He et al., 2006, Clarke and Gaydos, 1998, Arsanjani et al., 2013, He et al., 2008, Batty, 2007, Jat et al., 2008).
- Artificial Neural Networks Modelling (Pijanowski et al., 2002, Mas et al., 2004, Almeida et al., 2008, Pijanowski et al., 2010).
- Fractal Modelling (Arsanjani et al., 2013, White and Engelen, 2000, White and Engelen, 1993).
- Linear/Logistic Regression (Chiang et al., 2006, Bai et al., 2011, Triantakonstantis and Mountrakis, 2012, Press and Wilson, 1978, Cheng and Masser, 2003).
- Agent-Based Modelling (Brown and Robinson, 2006, Brown et al., 2005, Batty, 2009a, Matthews et al., 2007, Heppenstall et al., 2011, Batty, 2007).
- Decision Trees Modelling (Jantz et al., 2004, Xian and Crane, 2005, Triantakonstantis and Mountrakis, 2012, Stevens et al., 2007).

Chapter 6 simulates the land use scenarios and projections using an integrated method between cellular automata and GIS systematic algorithms.

Chapter 3. Study area description

3.1 General description of the study area

The River Shannon, the focus of this study, is the largest transboundary river system and catchment on the island of Ireland and one of the most important waters and power resources in the Republic of Ireland. The Shannon river basin district (see Figure 3.1), defined according to the objectives of Water Framework Directive (Directive, 2000), includes an area of about 18,000 km^2 and covers around 20% of the island of Ireland, mostly in the lowland central area of the Republic of Ireland but with a small part (6 km^2) of the upper River Shannon basin extending across the border to Northern Ireland. It has been estimated that there are more than 1,600 lakes in the river basin district. The area includes about 73% agricultural land and 12% wetland, mostly peatland habitat (Engler and Werner, 2015, McCarthy et al., 2008).

The River Shannon (Figure 3.1) drains an area of approximately 11,700 km^2, before flowing into the sea at Limerick. The gradient is remarkably low, with the river rising at about 152 m above sea level and then flowing southwards with only a 12-m drop in altitude over 185 km, before finally descending more rapidly to sea level (Engler and Werner, 2015, McCarthy et al., 2008). The potential impacts of climate and land-use changes are of most concern where water resources are either heavily allocated or particularly vulnerable to changes in rainfall (Engler and Werner, 2015, Assessment, 2013), in addition to risks due to extreme events (Engler and Werner, 2015, Assessment, 2013). In the Shannon catchment, the possibility of a reduction in water availability or the possibility of future flooding scenarios as a result of higher intensity rainfall events (due to climate change) may affect surface water and groundwater use which can severely impact upon human life and livelihoods. This, therefore, gives a strong justification for choosing the Shannon as a study area.

Figure 3.1 shows the whole Shannon River Discrete Basin (RDB) as defined by the Office of Public Works (OPW) and the Irish Environmental Protection Agency (EPA), which includes the actual Shannon River hydrological system, see figure 3.6, and some other small management discrete areas. In this study, the whole Shannon River Discrete Basin (RDB) area, see Figure 3.1, is used as the actual domain of simulation for all stages except in chapter 5 when the simplified and structured hydrological system for the Shannon River catchment is represented, only at this stage the Shannon River basin area shown in figure 3.6 is used.

The Shannon River Basin District (RBD) stretches from the source of the River Shannon in the Cuilcagh Mountains in counties Cavan and Fermanagh to the tip of the Dingle peninsula in north Kerry. As well as the natural drainage basin of the Shannon River itself, which drains an extensive area of central Ireland, it also includes coastal parts of Kerry and Clare which drain to the sea. It drains eighteen local authority areas and is also an international River Basin District (RBD), as a small portion of County Fermanagh in Northern Ireland drains underground to the Shannon Pot.

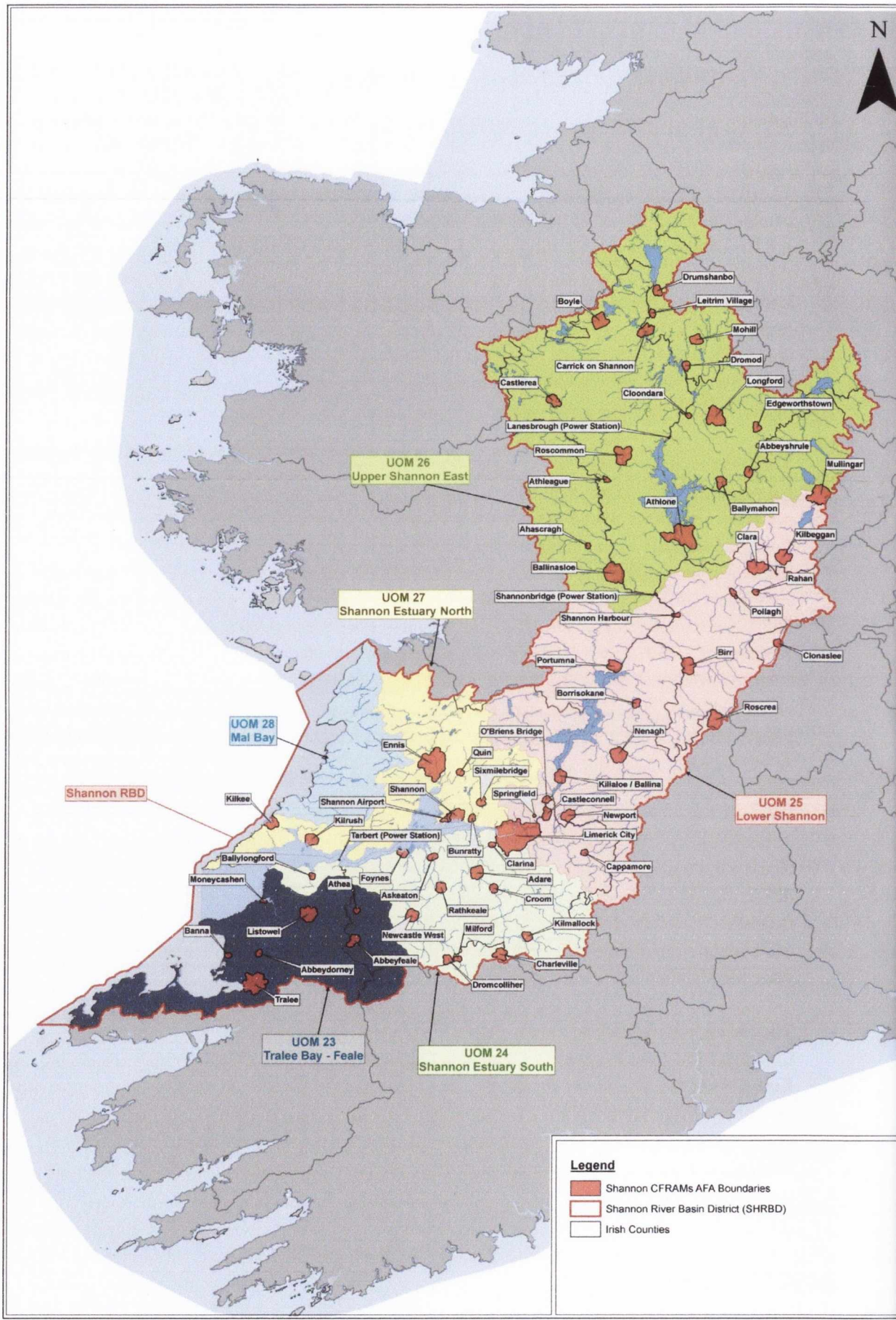

Figure 3.1: Map of the Shannon catchment with the Shannon River, Shannon River catchment units of managements (Assessment 2013, OPW 2015).

As defined under the Water Framework Directive (WFD) an RBD is divided further into Units of Management (UoM). The UoM constitute major catchments or river basins and their associated coastal areas, or conglomerations of smaller river basins and their associated coastal areas. In the Shannon RBD, there are five UoMs within the Study Area, see Figure 3.1:

- Tralee Bay – Feale (Hydrometric Area 23 – 'HA23') – UoM 23
- Shannon Estuary South - (Hydrometric Area 24 – 'HA24') – UoM 24
- Shannon Upper and Lower (Hydrometric Area 25 & 26 – 'HA25 & 26') – UoM 25/26
- Shannon Estuary North (Hydrometric Area 27 – 'HA27') – UoM 27
- Mal Bay (Hydrometric Area 28 – 'HA-28') – UoM 28

The Shannon District encompasses large areas of counties Limerick, Clare, North Tipperary, Offaly, Westmeath, Longford, and Roscommon as well as significant portions of counties Kerry, Galway, Leitrim and Cavan. Other countries that have smaller portions in the Shannon District include Sligo, South Tipperary, Mayo, Cork, Laois, Meath, and Fermanagh. All of Limerick City is located within the District.

The distribution of people and types of activities that take place vary throughout the District. Although around 793,037 people live in the Shannon District (OPW, 2015a, Assessment, 2013), the population density is lower than in eastern Ireland. The largest urban area is Limerick City (with a population of 57,106) but other sizable towns include Athlone (19,053), Ennis (22,324), Mullingar (19,770), Tralee (22,837) and Tullamore (14,376) (Office, 2011). Urban areas have a lot of industries and most of them are centered on rivers or the coastline. Many people live in small villages or one-off houses in rural areas (Engler and Werner, 2015, Assessment, 2013, McCarthy et al., 2008, Alfatah, 2015).

3.2 Water resources in the Shannon catchment

3.2.1 Rivers

The River Shannon is the largest in Ireland. It rises in County Cavan and flows for 260 km before flowing into the Shannon Estuary at Limerick City. An unusual feature of the Shannon River is that it is remarkably flat catchment.

Figure 3.2 presents a sampled longitudinal section of the 223 km length of the Shannon from Lough Allen to Parteen Weir near Limerick, see Figure 3.6. Figure 3.2 shows that the river falls only some 15m over this length with an average gradient of about 1 in 15,000. The figure also shows 2009 flood events for the Shannon which indicate that during significant flood events, there is a relatively steep hydraulic gradient in the 8 km reach between Victoria Lock and Banagher. The first hydro-electric power generation station in Ireland was constructed on this stretch, at Ardnacrusha, in the 1920s. In winter, seasonal flooding occurs and the flood plains on either side of the river, called "callows", are world famous for the plants and animals found there. The main tributaries of the Upper Shannon are the Rivers Suck, Inny and Brosna while the main tributaries of the Lower Shannon are the Rivers Fergus, Maigue, Deel and Mulkear.

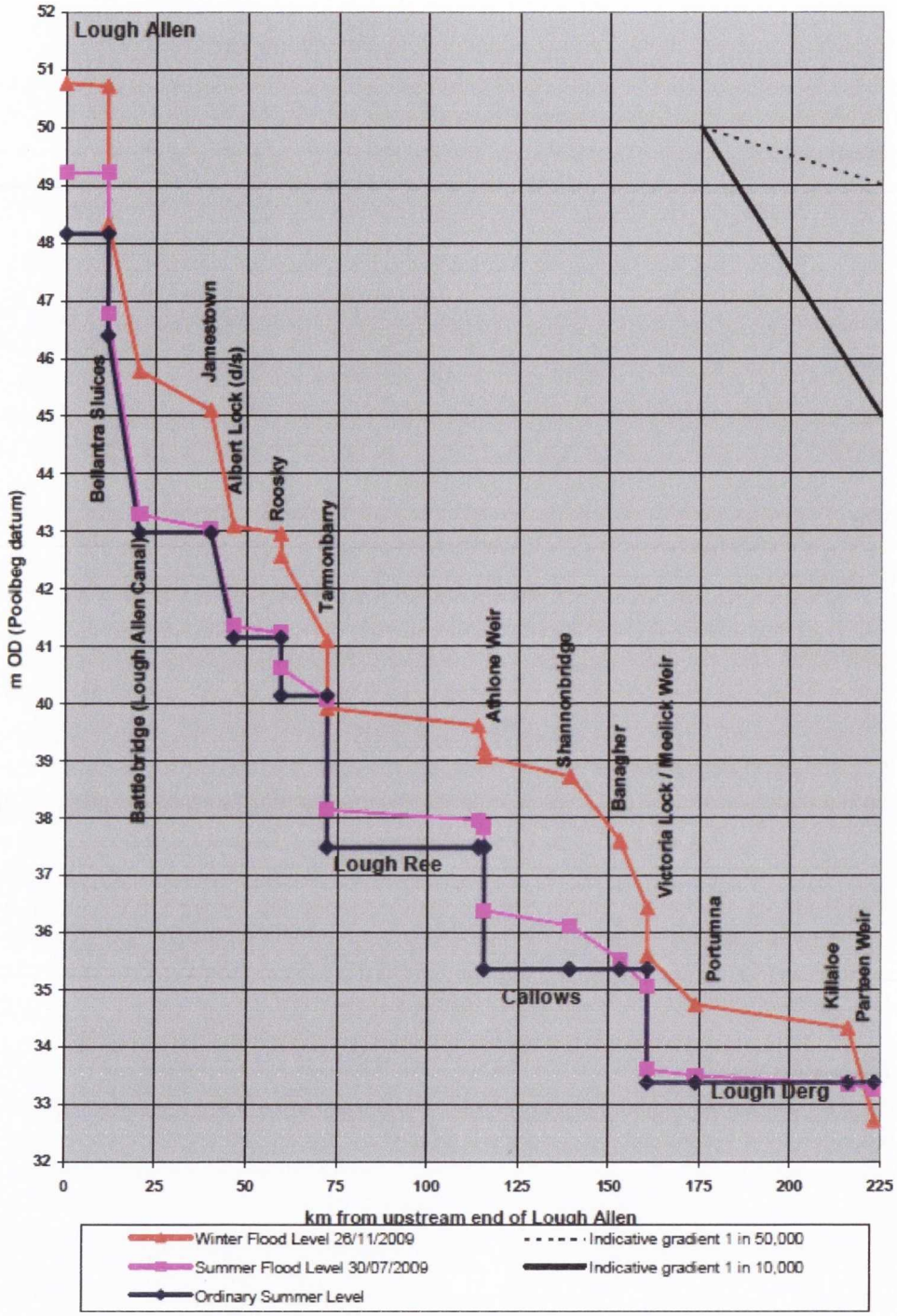

Figure 3.2: Longitudinal Section of the River Shannon summer and winter average water levels (Office of Public Works, 2011).

3.2.2 Lakes

There are more than 1,600 lakes in the Shannon District but less than 50 of them are over 1 km^2 in area. The largest lakes are Lough Derg (120 km^2), Lough Ree (100 km^2) and Lough Allen (30 km^2) - these large lakes are all on the River Shannon, see figure 3.2 for average summer and winter water levels on these lakes.

3.2.3 Estuarine/Coastal

The River Shannon flows into the Shannon Estuary and into the Atlantic Ocean. The Shannon estuary is the largest estuary in Ireland with an area of approximately 150 km^2. The Fergus, Deel and Maigue rivers all flow into the Shannon Estuary.

The District's coastline incorporates most of the coastline of County Clare and about one-third of the coastline of County Kerry. Also, there are a number of ports and harbors, the main ones are at Limerick and Foynes.

3.2.4 Groundwater

Limestone rocks dominate the geology of the Shannon District. The Burren in County Clare is probably one of the best-known landscapes internationally. The karstified limestone creates unique groundwater features including seasonal lakes (turloughs) and disappearing rivers during prolonged dry spells. Swallow holes form where the limestone bedrock is dissolved along fissures and cracks allowing the surface streams to disappear into the ground to emerge, possibly miles away, as springs. Different soil groups and textures for Ireland are presented in the appendix B.

3.2.5 Canals

The Shannon navigation is the longest navigable network in Ireland and Britain. There are several major canal systems that connect in the Shannon District, the main canals being the Grand and Royal Canals and the cross-border Shannon-Erne Waterway (OPW, 2015a, Assessment, 2013).

3.2.6 Hydrometric stations

The Shannon catchment hydrometric stations' locations and their measurements are discussed in detail in chapter 5. Figures 3.3 and 3.4 show water flow and water level, respectively, for some selected hydrometric stations in the Shannon River catchment in order to give the reader an idea about the values and the quantities in the catchment. The locations for the selected hydrometric stations are shown in Figure 3.5. As shown in Figure 3.3, the lower-Shannon hydrometric station has the highest water flow in the catchment, and that is because lower-Shannon contains the main Shannon river discharge point as it has the lowest elevation in the catchment which means that lower-Shannon sub-catchment collects the water from all the other sub-catchment that are higher in elevation.

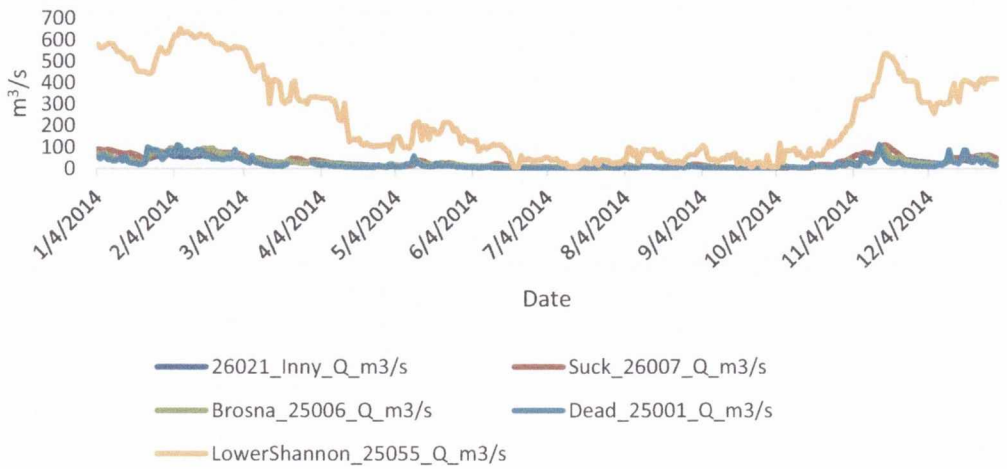

Figure 3.3: Observed water flow (Q) m3/s for some selected hydrometric stations in the River Shannon catchment for the year 2014.

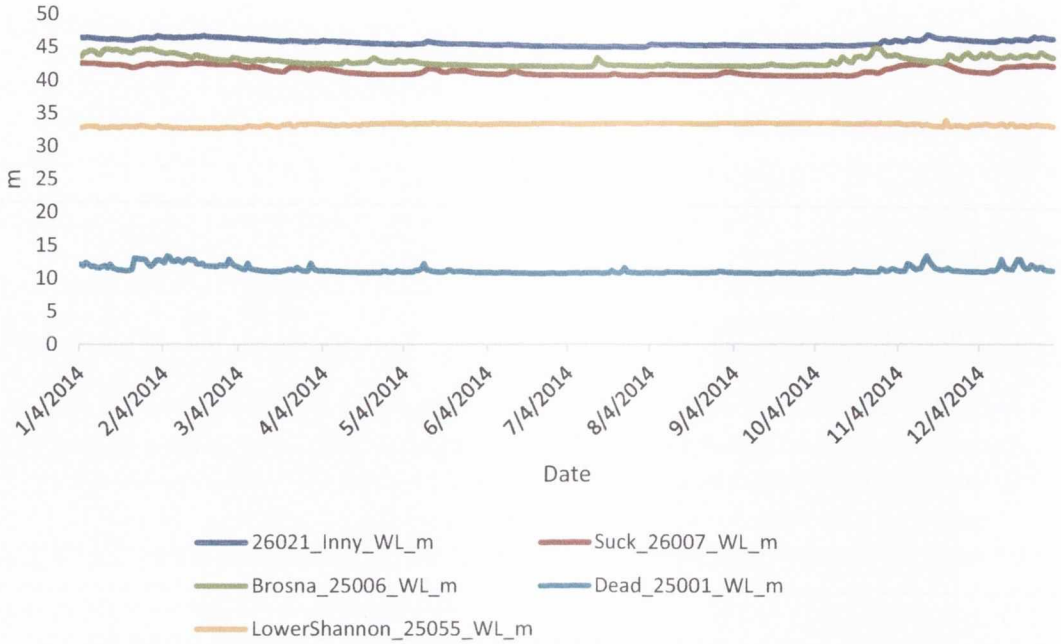

Figure 3.4: Observed Water level (WL) (m) for some selected hydrometric stations in the River Shannon catchment for the year 2014.

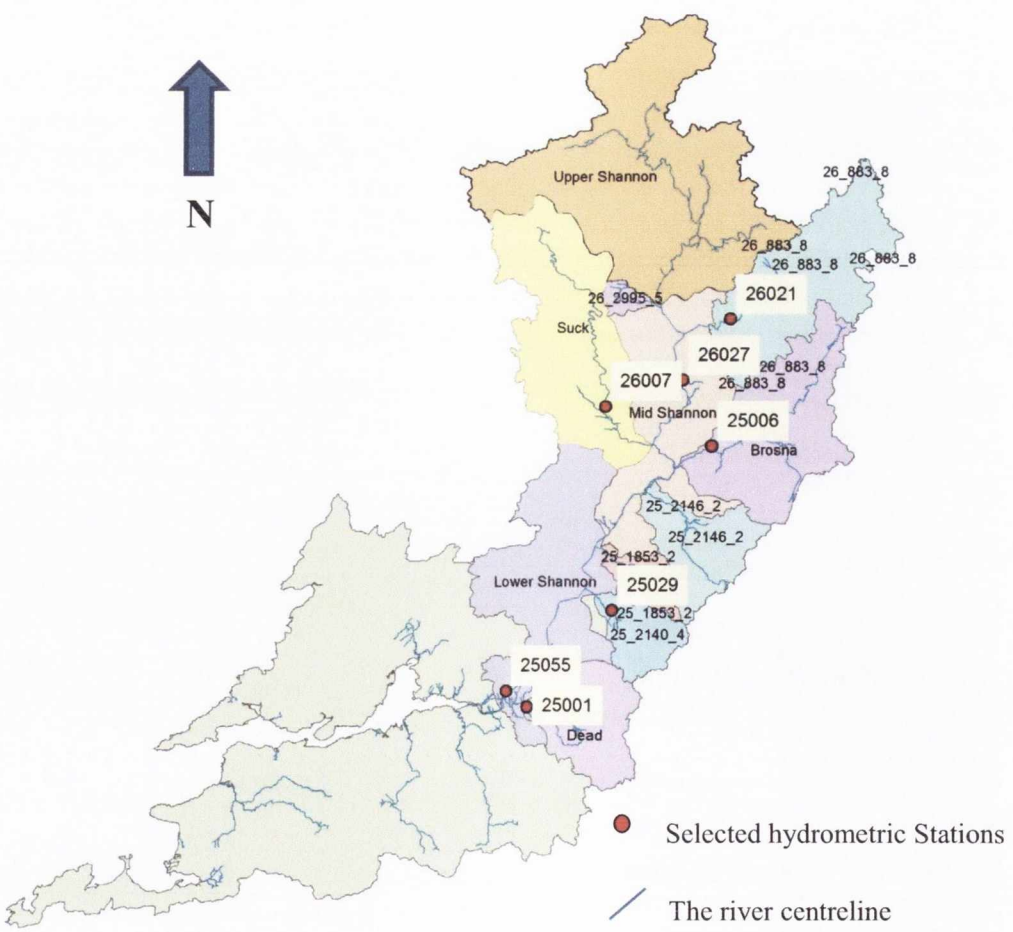

Figure 3.5: The selected hydrometric stations locations.

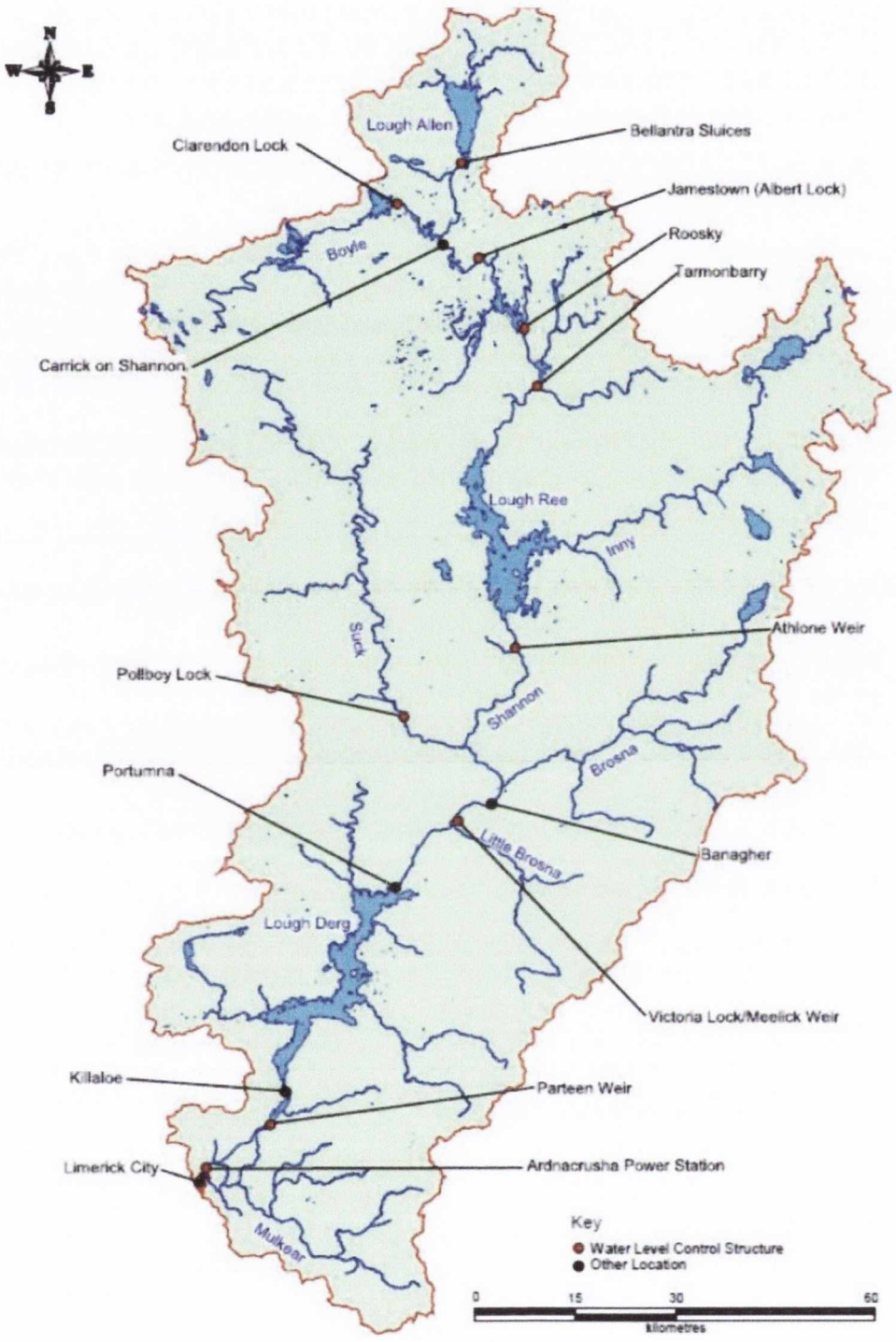

Figure 3.6: Shannon River as a hydrological system from the upstream to the discharge area (Office of Public Works, 2011).

3.2.7 Previous hydrological studies in Shannon River catchment

The first available hydrological study, which tried to address the flood risk issue for the Shannon River was published in 1956 (Rydellu, 1956). This study was based on a request from the Irish Government, through the American Ambassador to the United States Department of State. The

study discusses the possibility of dealing effectively and permanently with the periodic flooding in the Shannon Valley. The published report reviews the physical, hydraulic and flood characteristics of Shannon River and its tributaries; the potential for increased utilization of these water resources, including power; and the general economy of the area.

Mc Cumiskey (1976) published a paper to discuss the Shannon River as a water resource in terms of abstraction quantities and distributions.

The Irish government published the Shannon River Basin Management Plan (2009-2015). This plan covers the period 2009–2015 and it was prepared in consultation with all the stakeholders. It provided measures to be taken by all stakeholders and the tools to prioritise the application of available resources to those measures, with the aim of achieving the objectives of the Water Framework Directive (Directive, 2000).

Recently in 2011, the Office of Public Work (OPW) has started the Catchment Flood Risk Assessment and Management (CFRAM) project. This national CFRAM project comprises three phases:

- The Preliminary Flood Risk Assessment (PFRA): 2011
- The CFRAM Studies and parallel activities: 2011-2015
- Implementation and Review: 2016 onwards.

Shannon RBD is a main part of CFRAM project, and mainly flood risk reports and flood extent maps for each UoM in the Shannon RBD are provided through this study (Office of Public Works, 2011).

3.3 Shannon Protected areas

All areas requiring special protection in the Shannon River Basin District in this study were identified and obtained from the Irish Environmental Protection Agency (EPA), see Figure 3.7. Approximately, 158 areas in the Shannon River Basin have been designated as Special Areas of Conservation (SACs) under the EU Habitats Directive 1992 (Evans, 2006, Alfatah, 2015, EPA, 2012) because they contain selected habitat types or areas important for the continual well-being/survival of selected non-bird species.

Also, 94 areas were classified as Natural Heritage Areas (NHA) which were considered important for the habitats present or held species of plants and animals whose habitat needs protection under the Wildlife Amendment Act. They are legally protected from damage from the date they are formally proposed for designation (Evans, 2006, Alfatah, 2015, EPA, 2012).

Moreover, 58 areas were protected as Special Protection Areas (SPAs) under the EU Birds Directive due to their European importance in providing habitat for birds. The responsibility for implementing these EU Directives lies with Dúchas, the Heritage Service of the Department of Arts, Heritage, Gaeltacht and the Islands.

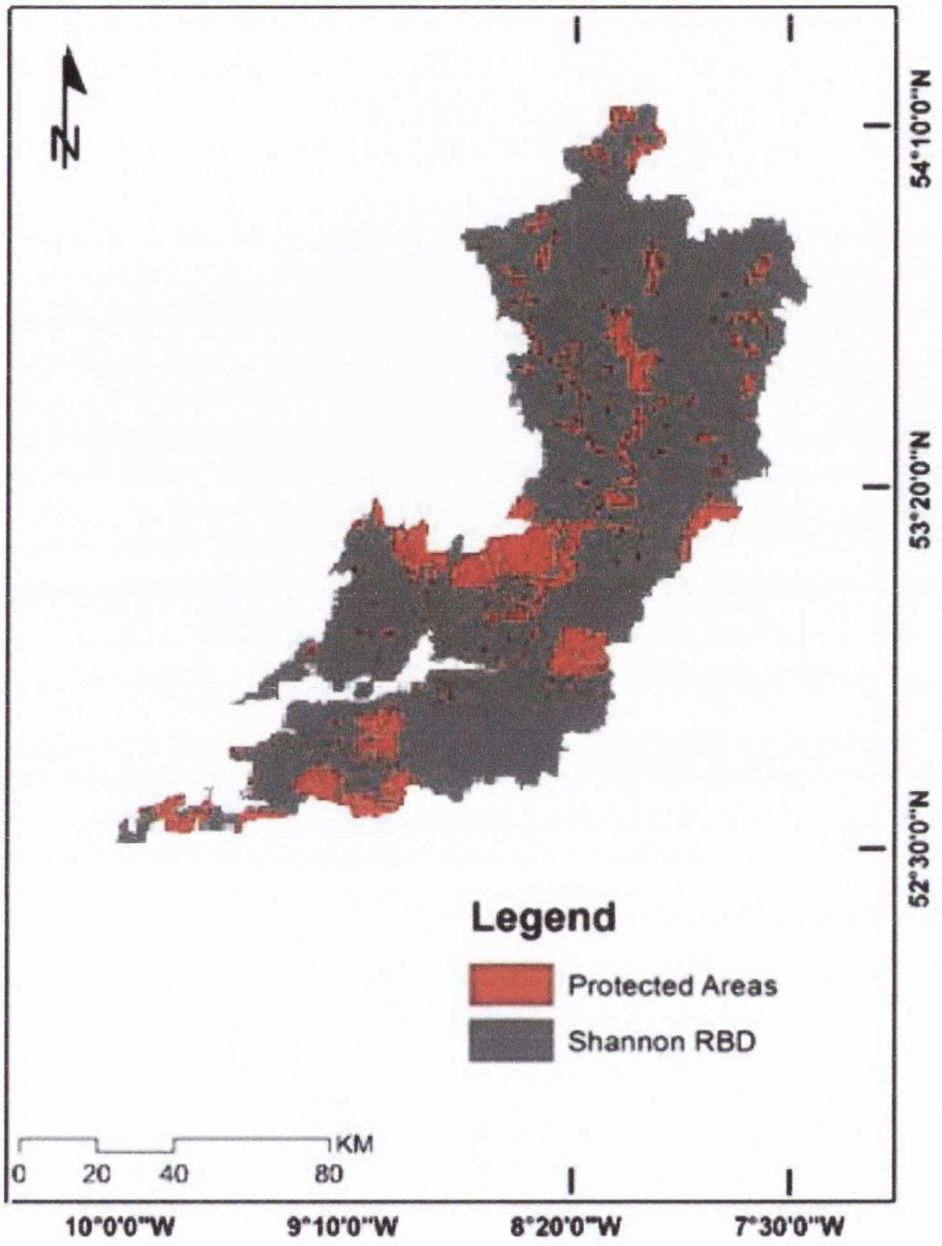

Figure 3.7: Protected areas in the Shannon catchment including SACs, NHAs and SPAs.

Chapter 4. Multi-GCM Ensembles performance for climate projection on a GIS platform

4.1 Introduction

During the last half century, the global climate has experienced warming because of the continuous increase of greenhouse gasses concentrations in the atmosphere, which has been attributed to human activities (Stocker et al., 2013b). Continued increases in greenhouse gas emissions at or above current rates will cause further warming during the 21st century which has been predicted to be greater than that observed during the 20th century (Stocker et al., 2013b, Solomon, 2007). Projections of future climate change under scenarios obtained using climate system models have important practical significance, particularly for climate impact assessment studies and future emission control strategies (Stocker et al., 2013b, Xiaoge et al., 2013).

Global Climate Model (GCMs) are an essential tool in order to help to understand and predict the impacts of climate change. These numerical coupled models combine several earth systems including the atmosphere, oceans, land surface and sea-ice and offer considerable potential for the study of climate change and variability (Fowler et al., 2007). These climate models have been evolving steadily over the past several decades and in addition, are the most adapted tools for studying the impact of climate change on a regional scale. Recently, fully coupled Atmosphere–Ocean GCMs, along with transient methods of forcing the concentration of greenhouse gasses, have brought considerable improvement in the results obtained from climate model (Tripathi et al., 2006).

Modeling the impacts of climate change on different environment systems requires high-resolution regional data for future scenarios of temperature and precipitation and other climatic factors (Salathe et al., 2007). The current resolution of the GCMs, on average, is more than two polar degrees on the earth's surface for both directions in each pixel, which is close to a few hundred kilometers between grid points. Hence, GCMs typically provide an output at grid boxes, which are tens of thousands of square kilometers in area, whereas the scale of interest with respect to most environmental system impact studies is of the order of a few hundred square kilometers, or even less.

Several downscaling methodologies have thus been developed to deal with this problem of mismatch of spatial scales (Tripathi et al., 2006), such as dynamical downscaling (Regional Climate Models (RCMs)) and statistical downscaling methods. RCMs are developed based on dynamic formulations using initial and time-dependent lateral boundary conditions of GCMs to achieve a higher spatial resolution at the expense of limited area modeling. The main problem of RCMs is the computational cost and so it is only available for limited regions. Moreover, despite improvements, outputs of RCMs are still too coarse for some practical applications, such as hydrological impact studies, which need local and site-specific climate scenarios. Hence, statistical downscaling techniques have been developed to overcome these challenges (Chen et al., 2011a, Quintana Segui et al., 2010, Seguí et al., 2010, Willems and Vrac, 2011). In such environmental system impact studies, the emission scenario and the GCM are the main sources of uncertainty (Maurer and Hidalgo, 2008, Boé et al., 2007). Unfortunately, each step of the

downscaling procedure also has associated uncertainties which all add up and constitute a cascade of uncertainty that must be taken into account (Seguí et al., 2010, Quintana Segui et al., 2010).

Recently, a set of scenarios known as Representative Concentration Pathways (RCPs) has been adopted by climate researchers to provide a range of possible futures for the evolution of atmospheric composition. These RCPs have started to replace earlier scenario-based projections of atmospheric composition. For example, the RCPs are being used to drive climate model simulations as part of the World Climate Research Programme's Fifth Coupled Model Intercomparison Project (CMIP5) and other comparison exercises (Meinshausen et al., 2011, Moss et al., 2008, Moss et al., 2010, Taylor et al., 2012, Taylor et al., 2009a). Since climate change projections obviously depend on the climate model results, the scientific community has set up an international project to compare these models. The various phases of the CMIP have grown steadily as testified both in terms of participants' number and scientific impacts (Dufresne et al., 2013).

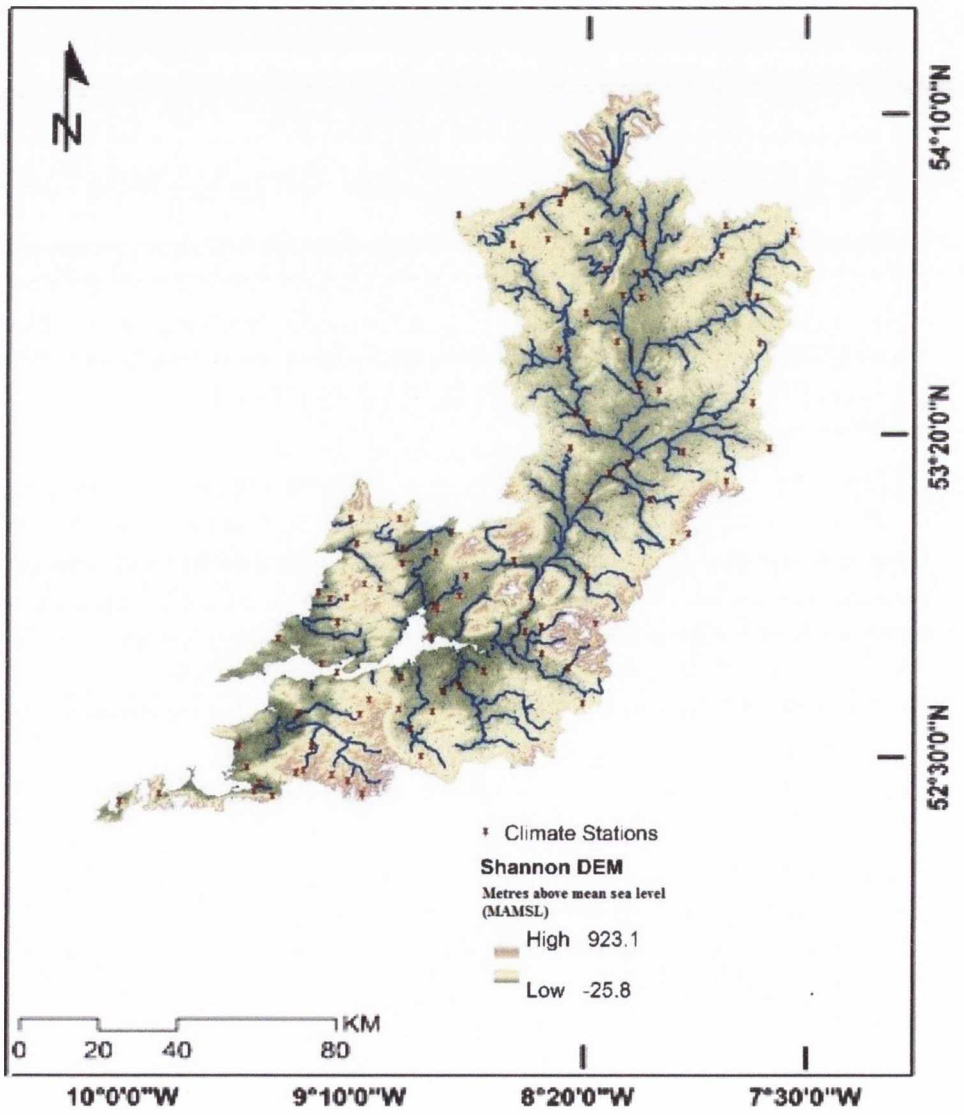

Figure 4.1: Map of the Shannon River Basin District (RBD) shows the climate stations that used in this chapter, and the surface elevation highlighted.

Figure 4.1 shows the study area with the climate stations and the topography of the catchment. In this study, climate change projections for the Shannon River catchment are presented for several climate variables (temperature, precipitation, wind speed, solar radiation and relative humidity) from multi-GCM ensembles for three future time intervals using a range of different Representative Concentration Pathways (RCPs) (Moss et al., 2010). This chapter presents the innovative use of a Geographical Information System (GIS) as a downscaling environment, which is presented for the first time in this research. The projection process used a statistical downscaling procedure based on statistical relationships linking a set of large-scale atmospheric variables to regional climate variables in an observational calibration period. After a particular verification and performance evaluation using several techniques (such as the Taylor diagram for each GCM-ensemble within independent sub-periods), the established statistical relationships have been used to predict the response of future regional climates from the simulated changes to the large-scale variables in the climate model. This chapter aims to present the GIS platform as a downscaling environment through a suggested algorithm, which applies statistical downscaling models to multidimensional GCM-Ensembles simulations. Applying such an algorithm on a GIS platform provides a wide range of output formats for the datasets, which can be used in most of the impact models without any extra effort in formatting the output datasets.

4.2 Materials and Methods

As shown in the general framework flowchart in Figure 4.2, multi-stage formulation modeling was carried out entirely within the GIS environment in order to evaluate the performance of climate model multi-GCM ensembles and thereby adequately describe the future climate over Shannon river basin. A GIS-based Python algorithm was developed to implement downscaling and the performance evaluation, which is described in this section.

A set of weather variables (temperature, precipitation, wind speed, solar radiation and relative humidity) were downscaled from climate change models at high-quality resolution (cell size 50 m*50 m) from the GIS model and projected to three future time periods, the 2020s, 2050s, and 2080s. Climate change models based on two different RCPs (using radiative forcing of 4.5 and 8.5 W/m^2 respectively) were produced from median and 3rd quartile simulation results of multi-GCM ensembles. These ensembles simulations were calculated from the overlay process for GCMs datasets after fixing the temporal scale for each GCM to a monthly time scale. The median and 3rd quartile simulation results were used because it was recommended in the literature that these simulations have the optimal minimum uncertainty in projections of risk from climate change (Araújo et al., 2005). The performance evaluation process for climate model results using the Taylor diagram and different statistical tests then lead to the development of high spatial resolution projected maps for temperature, precipitation, wind speed, solar radiation, and relative humidity.

This section presents the data, methods and the developed GIS-based Python algorithms used in the downscaling procedure.

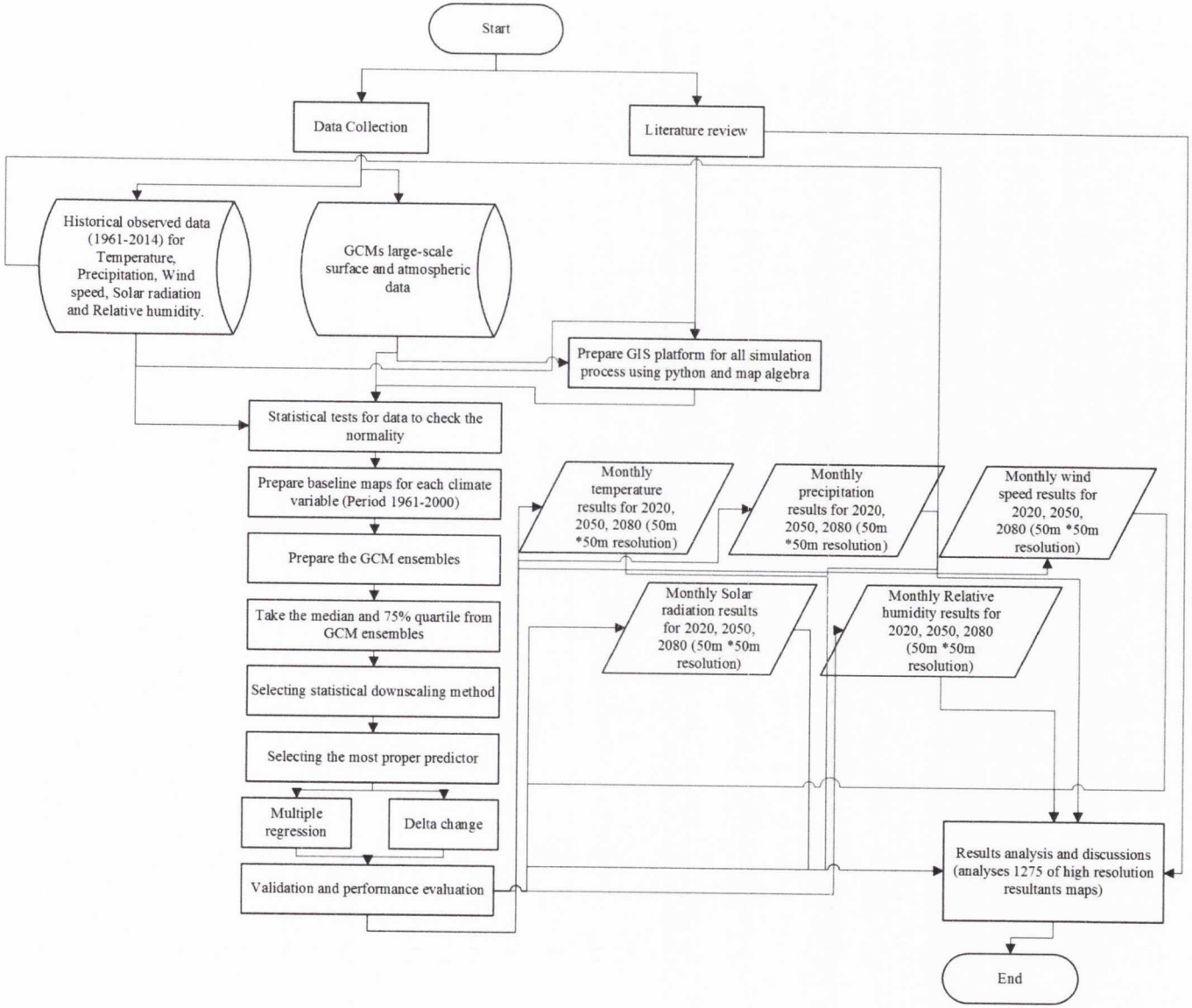

Figure 4.2: General framework flowchart.

4.2.1 Model data

Observed daily data for precipitation, temperature, wind speed, solar radiation, and relative humidity were obtained from all available stations (96 stations) in the Shannon Catchment from the national Irish meteorology organization (Met Éireann), for the period 1961-2014, see Figure 4.1. The selected stations are generally at low elevations and can be considered of high quality, data being collected by experienced meteorological officers. Although there were some missing readings in the data, their number was not so large as to be statistically significant and so they were excluded from the data set used. For baseline calculation purposes, data from 1961 to 2000 were used and the remaining data from 2000 to 2014 were used for the calibration and evaluation processes.

Large-scale surface and atmospheric data were obtained from the datasets of the International Centre for Tropical Agriculture (CIAT) and the CGIAR Research Program on Climate Change, Agriculture and Food Security (CCAFS) (Mitchell and Osborn, 2005, Ramirez and Jarvis, 2008, Wilby and Wigley, 1997). Standardized reanalysis variables were then used as candidate predictor variables to calibrate the transfer functions, linking the large-scale surface and atmospheric variables to the observed station's data. The large scale atmospheric data such as precipitation and temperature from all the GCMs in table 4-1 are resampled to one large-scale pixel size and then overlaid on top of each other to calculate an ensemble of the median and 75% quantile as will be shown later in this chapter. After formulating the ensembles, some atmospheric parameters will be downscaled to fine-scale spatial resolution to be used as climatic scenarios in this study.

GCM data were obtained, for five models from the Hadley Centre, Canadian Centre for Climate Modelling and Analysis, Centre for Climate Research in Japan, the Commonwealth Scientific and Industrial Research Organization and National Centre for Atmospheric Research, USA for both representative concentration pathways RCP 4.5 and RCP 8.5. The datasets exist on grid resolutions as illustrated in Table 4.1, and were obtained for the grid box representing Ireland in the GCM domain. These GCMs have been chosen because they have been used individually before in UK and Ireland and because they have the smaller spatial grid size among the available GCMs.

Table 4-1: Multi-GCM ensembles models details.

GCM	Institution	Resolution
CSIRO-MK3.0	CSIRO, Australia	175 km * 175 km
MIROC-H	Centre for Climate Research, Japan	100 km * 100 km
HADGEM1	Hadley Centre, UK	125 km * 125km
NCAR-CCSM	National Centre for Atmospheric Research, USA	125 km * 125km
CanESM2	Canadian Climate Centre, Canada	128 km * 128km

4.2.2 Selecting Representative Concentration Pathways (RCPs)

Modeling the response of any environmental system according to changes makes more sense if the worst case and the middle case were used as the forcing cases by applying their factors, parameters and boundary conditions in the modeling and evaluation process. Hence, RCP 4.5 and RCP 8.5 were used in this study as forcing scenarios for climate models (Stocker et al., 2013b, Solomon, 2007, Meinshausen et al., 2011, Taylor et al., 2009b, Kattenberg et al., 1996, Giorgi et al., 2001, New and Hulme, 2000).

4.2.3 Modeling procedures and downscaling

Although global simulations indicate coarse grid patterns of change associated with natural and anthropogenic climate forcing, they cannot capture the detailed effects of narrow mountain ranges, complicated land/water interactions, or variations in land-use. Statistical or empirical downscaling is an alternative approach for obtaining regional-scale climate information from large-scale simulations to bridge the gap between global climate models and local impacts. Statistical downscaling has an important advantage over a regional model/dynamical downscaling: it is computationally efficient and allows the consideration of a large set of climate scenarios. However, statistical downscaling of future climate scenarios must be based on predictors that can capture the effects of climate change, and not just of climate variability. The main idea behind statistical downscaling is to use statistical relationships to link resolved behaviors in GCMs with the climate in a study area. This approach encompasses a range of statistical techniques as simple linear regression, delta change method, multiple regression, weather generators, canonical correlation analysis and artificial neural networks (Salathe et al., 2007, Kattenberg et al., 1996, Giorgi et al., 2001, Hewitson and Crane, 2006, Joubert and Hewitson, 1997, von Storch et al., 1993, Crane and Hewitson, 1998).

The GIS-based approach used in this research employed statistical downscaling; specifically, two different techniques were used according to the suitability to the targeted climatic datasets:

1. The delta change method was used to downscale temperature and precipitation because of the high-quality data and continuous readings for these datasets.

2. Multiple regression models were used to predict wind speed, solar radiation and relative humidity using both the temperature and precipitation predictands for each model in order to prevent the uncertainty related to some missing readings in the same predictor's data. Using regression models in the statistical downscaling is a common technique, where there are some gaps in the bassline period for the predicted parameters.

4.2.4 GIS-based Python algorithm

This chapter presents a GIS-based Python algorithm for GCM-Ensembles downscaling and performance evaluation simulations. This algorithm uses GIS as the platform for the simulation process through spatial geo-processors. The algorithm loops through a process to downscale the climate variable and evaluate the performance of the designed GCM-ensemble experiment. The

observed weather data for the Shannon RBD, GCMs data, and the selected RCPs are employed as a case study for different experiments using this GIS-based algorithm.

The algorithm has been developed using an integration between ArcGIS built-in spatial analysis tool package and spatial-statistical tool that has been developed by the author using Python. The integration between all the tools has been done using Python.

The algorithm spatial simulation steps are as follow, which are presented in the general framework, figure 4.2:

1. Choose the GCMs that participated in the ensembles, as described in the previous sections.

2. Choose the forcing RCPs targeted for each experiment, as described in subsection 4.3.2.

3. Feed the multidimensional files for each global model experiment into the algorithm, as based on the GCMs simulation data.

4. Calculate the mean temporal scale for each simulated multidimensional file of each GCM experiment, in order to fix the temporal resolution between all the experiments that participated in the ensemble, (i.e. all GCMs were set to a common monthly temporal scale).

5. Resample the grid size for each gridded file result from each experiment to unify the large-scale resolutions, in order to have the same pixel size for each gridded file per experiment.

6. Overlay, a spatial operation in which two or more grids registered to a common coordinate system are superimposed for the purpose combine them in the same tabulated dataset, the simulated grids for all GCMs that participated in the experiments.

7. Run a sub-algorithm for the geostatistical simulation for each experiment in order to resample the two targeted grids weights (50% (median) and 75% ensembles). The geostatistical processor is used to produce values for each simulated parameter for each location that have no observed values in the domain of simulation using statistical interpolation between the two nearest observed locations.

8. Choose the downscaling method for each climatic variable in each experiment.

9. Run a sub-algorithm for the selected downscaling method for the specific experiment with the observed data as input.

10. Evaluate the results of each experiment through statistics and Taylor diagram.

Regarding step number 7, different GCMs produce several regional climate results even when run with the same emissions data (Stocker et al., 2013a, Solomon, 2007, Meinshausen et al., 2011,

Taylor et al., 2009b, Kattenberg et al., 1996, Giorgi et al., 2001, Hulme and Carter, 1999). However, many impact studies employ only one climate change scenario, based on one emissions scenario, derived by single GCM. From a risk assessment perspective, this could be considered unsound. Ensembles or weighting of the downscaled results were used in this GIS-based algorithm to overcome this risk in climate change projections. This ensembles or weighting was based on the individual GCM's ability to reproduce the properties of the observed climate. The modified impacts relevant climate prediction index is weighted based on the individual GCM's ability to reproduce the properties of the observed climate and is derived from the root-mean-square difference between modelled and observed climatological data (Hulme and Carter, 1999, Wilby and Harris, 2006), median and 75 percentile (3rd quartile), assessed over the baseline period. The median and 75 percentile ensembles, produced from the weighted median and 75 percentile results for multi-GCM described above, were developed for the Shannon catchment and assessed over the baseline using the developed GIS-based algorithm.

Regarding step number 8, in this case study, the GIS-based algorithm that was developed applies the delta change method and multiple regression models as selected statistical downscaling methods under the GIS platform. The delta method or change factor is the ratio between GCM simulations of future and current climate with respect to precipitation and it is the difference between GCM simulations of future and current climate with respect to temperature. It is used as a multiplicative factor to obtain future regional conditions so that the differences between the control and future GCM simulations are applied to baseline observations by adding or scaling the mean climatic to each time step. The method assumes that GCMs more accurately simulate relative change more than absolute values. In addition, the change factors only scale the mean, maximum and minimum of the climatic variables, ignoring changes in variability and assuming the spatial pattern of climate will remain constant. In the delta change method, the predictor is the currently observed value for the same predictand variables. The predictor multiplies with the change factor, which is the ratio between the simulated values from the GCM output for the current period and the future. More generally, the predictor and predictand need to be the same variable (Fowler et al., 2007, Prudhomme et al., 2002, Diaz-Nieto and Wilby, 2005, Hay et al., 2000). The transfer function is a term used to describe methods that directly quantify a relationship between the predictand and a set of predictor variables (Giorgi et al., 2001). Multiple regression models are constructed using grid cell values of atmospheric variables as predictors for the surface climatic variables. There have been a number of recent innovations in this type of downscaling methods such as the use of a logistic regression model for daily precipitation probability and a generalized linear model to predict the number of wet days in the Ebro Valley in Spain (Abaurrea and Asín, 2005). Multiple regression models exist when there are two or more predictor variables (such as coarse gridded rainfall and temperature), which act as the input signal for the regional climate. A method called forwarded selection is the most common method used to establish a multiple regression equations in which the predictor variable that explains the most variance is first identified. The remaining variables are then classified and the variable that most reduces the remaining variance is selected. This method has been used which has resulted in relative humidity, solar radiation and wind speed variables being eliminated from regression models and it has been concluded that the temperature and precipitation variables should be used in the regression models. This procedure is repeated in order to get the most appropriate variable until no further improvement is obtained. An essential assumption behind the regression models is that they are symmetrically distributed around the mean or normally distributed without any skew (Hay and Clark, 2003, Zorita and Von Storch, 1999).

4.3 Results and Discussions

4.3.1 Validation and performance evaluation

In order to validate the climate models results, observed data for each modeled climate variable for the 1961-2014 periods were used, specifically 1961-2000 data used for the training process and the 2001-2014 data used for the validation process. High correlations were obtained for climate models validation as shown in Table 4.2 which illustrated statistical tests results (R^2 values) for all modeled variables for the Shannon catchment. These statistics are for monthly time steps and averaged for all stations.

Table 4-2: climate models validation statistical tests results.

Predictands	Method	Predictors	R	R^2	Ad-R^2	SE
Temperature	Delta-change	Temperature	0.97	0.95	0.94	0.02
Precipitation	Delta-change	Precipitation	0.97	0.94	0.93	1.58
Wind speed	Multiple regression model	Temperature & Precipitation	0.96	0.93	0.92	0.71
Solar radiation	Multiple regression model	Temperature & Precipitation	0.95	0.91	0.89	5952.5
Relative Humidity	Multiple regression model	Temperature & Precipitation	0.87	0.78	0.73	1.75

For the climate models and ensembles performance evaluations, Taylor diagrams and box-whisker plots have been prepared for each modeled monthly climate variable. Taylor diagrams (Taylor, 2001) provide an efficient way of graphically summarizing how closely a model or ensemble fits observations. The similarity between two patterns is quantified in terms of their correlation, their root-mean-square difference and the amplitude of their variations. Hence, Taylor diagrams have been used to validate and evaluate the performance of climate models and their ensembles predictions. In the Taylor diagram, see Figure 4.3, statistics for 20 models were computed with a colored point assigned to each model. The position of each point appearing on the plot quantifies how closely the model's simulated results match the observations. The horizontal and vertical axes represent the ratio of the standard deviations of the reference and simulated fields. The radial axis indicates the spatial correlation between the reference and simulated fields. The distance between the origin and any point is proportional to the RMSE. Consider wind speed group of models, for example, its pattern correlation with observations is about 0.88. The centered root-mean-square (RMS) difference between the simulated and observed patterns is proportional to the distance to the point on the x-axis identified as "observed, equal to 1" The brown contours indicate the RMS values and it can be seen that in the case of wind speed models the centered RMS error is about 0.28. The normalised standard deviation of the simulated pattern is proportional to the radial distance from the origin. For wind speed models the normalised standard deviation of the simulated field (about 3.3 mm/day) is clearly greater than the observed standard deviation which is indicated by the dashed arc at the observed value of 0.88.

First of all, it can be seen that the pattern correlations are generally high (higher than 0.7 in all cases). Secondly, one can notice that the variance is generally underestimated by the models, whatever the climatic variable, RCP or ensemble. This was actually expected from the high values of R-square for the validation period. It is also interesting to note that there is high coherence between the models: i.e. they share similar qualities or deficiencies (see the clusters of color points for each climatic variable). Also for the multi-GCM ensembles performance evaluation, Tables 4.3&4.4 were developed for each projected climatic variable and for each climate scenario for both absolute values and changes from baseline values, respectively. Each table has 20 box-whisker diagrams in which the centre lines show the medians, the box limits indicate the 25th and 75th percentiles as determined by R software, the whiskers extend to 1.5 times the interquartile range from the 25th and 75th percentiles, outliers are represented by dots, crosses represent sample means, bars indicate 95% confidence intervals of the means and notches are defined as +/-1.58* interquartile range /sqrt(n) and represent the 95% confidence interval for each media. Non-overlapping notches give 95% confidence that two medians are different. It is clear that the absolute values and the changes from baseline values for each climate variable increase with increasing projected years and by moving from left to right in each table from RCP 4.5 (50%) to RCP 8.5 (75%). This is valid for all variables except wind speed.

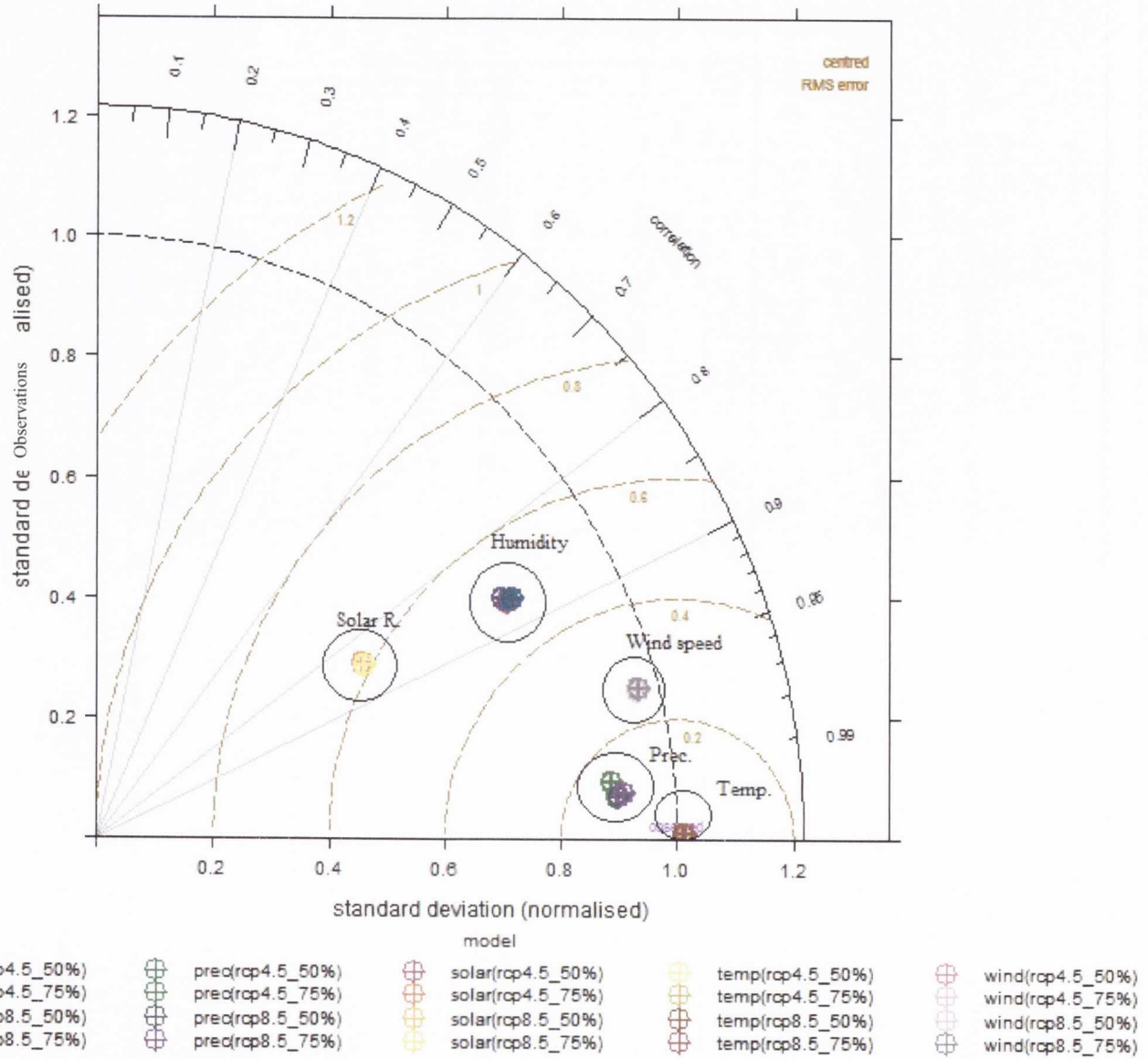

Figure 4.3: Taylor diagram for the mean temperature, precipitation, wind speed, solar radiation and relative humidity of each forced RCP for the median (50%) and 3rd quartile 75% ensembles.

Table 4-3: Monthly absolute values box-whisker plots for each predicted year and baseline variables.

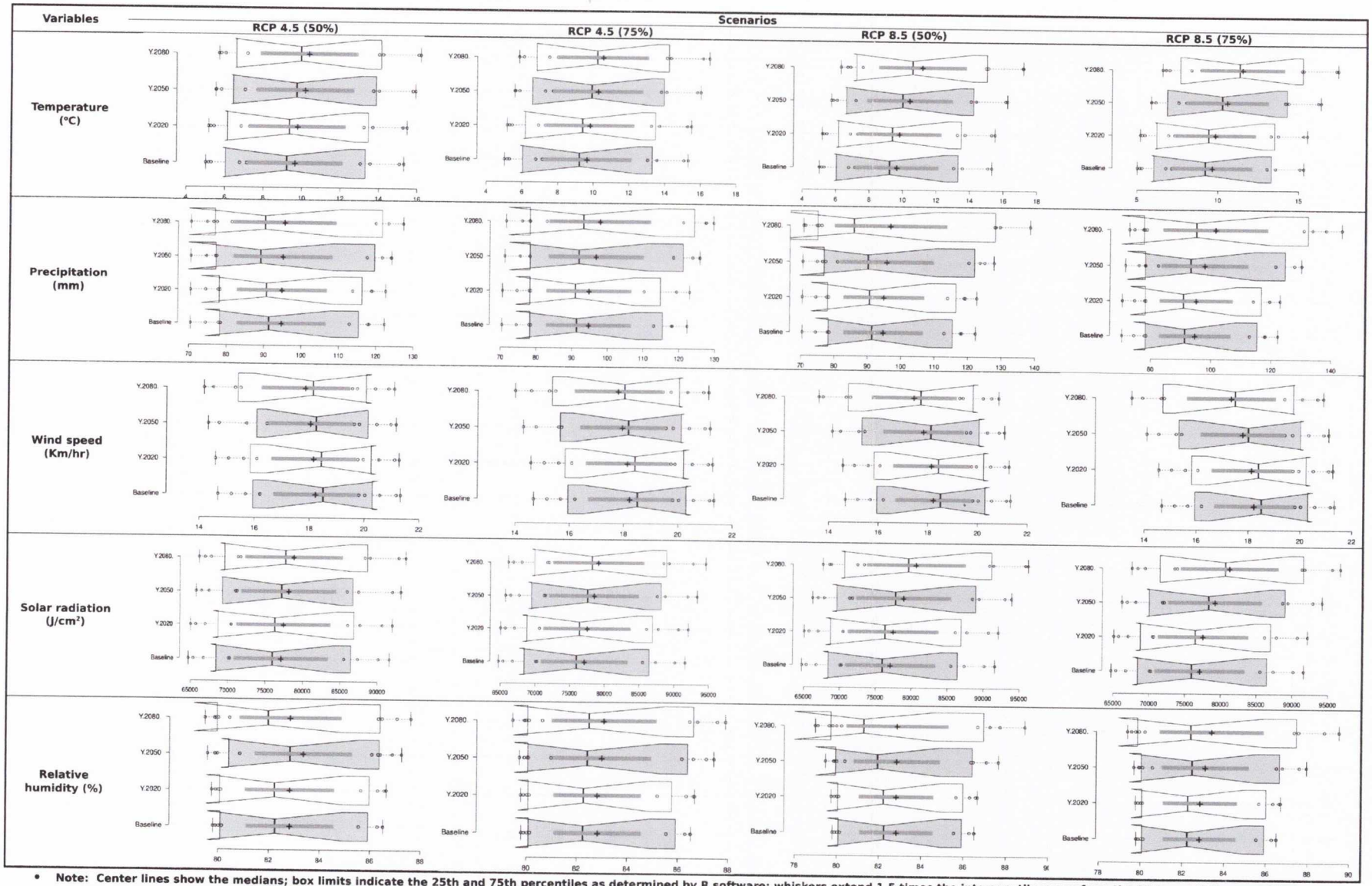

- **Note: Center lines show the medians; box limits indicate the 25th and 75th percentiles as determined by R software; whiskers extend 1.5 times the interquartile range from the 25th and 75th percentiles, outliers are represented by dots; crosses represent sample means; bars indicate 95% confidence intervals of the means; data points are plotted as open circles.**

Table 4-4: Monthly differences from baseline values box-whisker plots for each year of predicted variables.

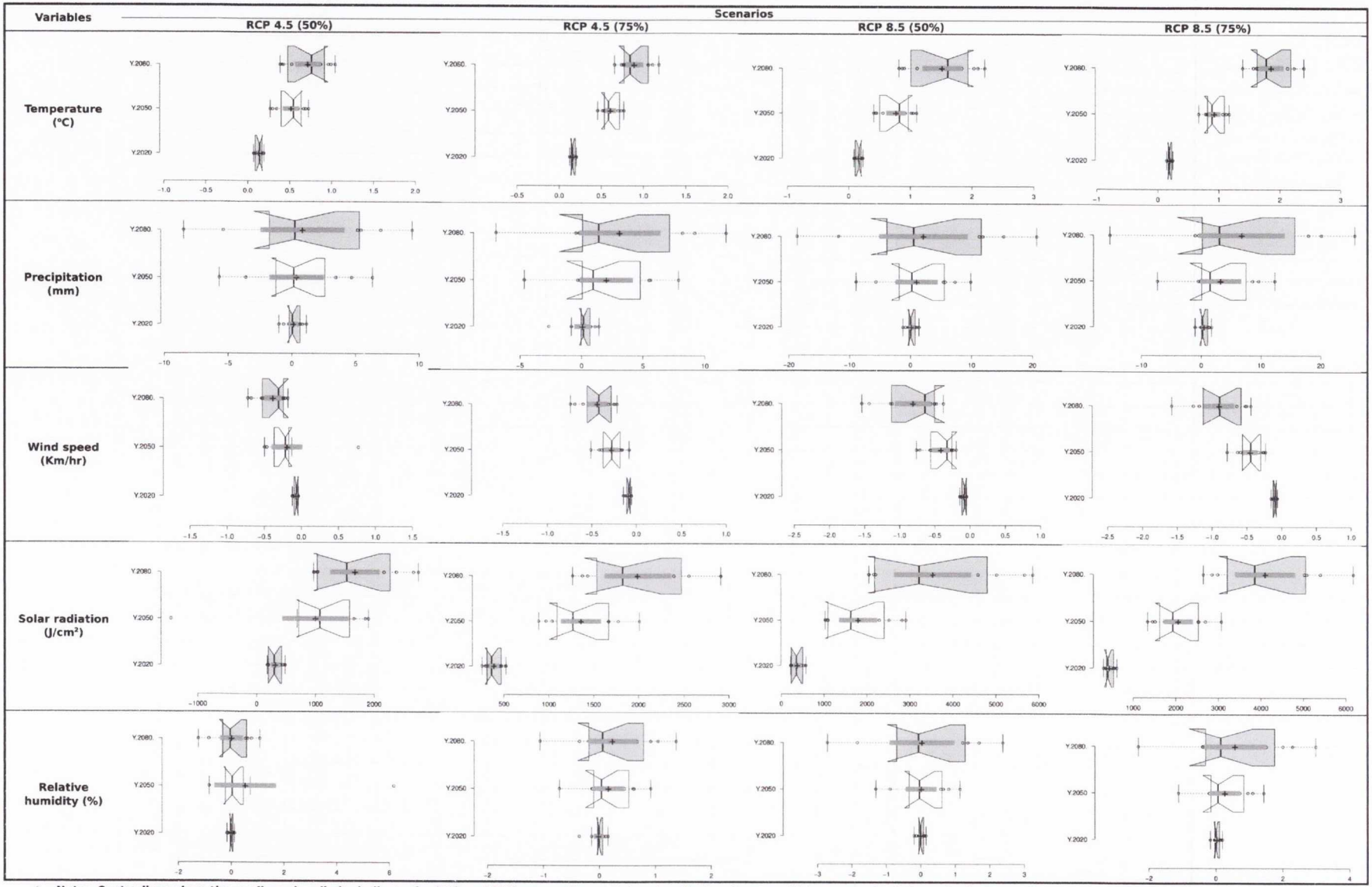

- **Note: Center lines show the medians; box limits indicate the 25th and 75th percentiles as determined by R software; whiskers extend 1.5 times the interquartile range from the 25th and 75th percentiles, outliers are represented by dots; crosses represent sample means; bars indicate 95% confidence intervals of the means; data points are plotted as open circles.**

4.3.2 Climate change projections

So far, the studies in literature addressing climate change downscaling in Ireland have used only one GCM (Ellis et al., 2007, Wang et al., 2006, Sweeney et al., 2003, Lindner et al., 2010, Bastola et al., 2011, Araújo et al., 2005, Berry et al., 2002) and the IPCC fourth assessment report (AR4) emission scenarios (Change, 2007a, Pachauri and Reisinger, 2007a). It also should be noted that these studies completed the downscaling using a coarse resolution and they did not address such a wide range of climate variables as presented in this research. Fealy and Sweeney (2008) illustrate one technique for downscaling GCM output for a selection of sites in Ireland using a weighted ensemble mean, derived from multiple GCMs for a high emissions scenario (A2). The study acknowledges inherent weaknesses due to lack of performance evaluation for the downscaling method. It also uses one AR4 emission scenario without any comparison with other scenarios and it ignores the need for a fine scale resolution results. In this research, in addition to a performance evaluation for the used methodologies and GIS platform, the obtained projections are presented for the future climate over the River Shannon catchment. In this section, climate projections for three time intervals 2020, 2050 and 2080, which refers to 12 months in each period, (a summary of 1275 high-resolution (50m * 50m) resultant maps, 255 for each climate variable including the predicted seasonal maps for each climate variable) were illustrated and compared with the baseline period (1961-2000), in order to assess the differences and changes in climate for temperature, precipitation, solar radiation, relative humidity and wind speed. Four different scenarios, RCP ensembles (RCP 4.5 (50%), RCP 4.5 (75%), RCP 8.5 (50%) and RCP 8.5 (75%) were used to force these results, as discussed previously.

4.3.2.1 Precipitation

The spatial variation of precipitation is influenced by many different natural aspects such as elevation. Precipitation time series grids were derived by averaging gridded data over the Shannon catchment according to different scenarios and ensembles, as previously discussed. Figure 4.7 shows a series of projected high-resolution precipitation maps for the Shannon catchment and Table 4.5 shows quantitative statistics for each map. Trends in precipitation show greater regional variation than temperatures, with occasional conflicting trends from stations which are geographically relatively close. However, there is evidence of an increase in the quantity of precipitation with time in general except for RCP 4.5 (50%) values they are higher in 2050 than 2080 and that because of the different adapted parameters in the downscaled GCMs in that particular climate scenario, as shown in Figure 4.4, which illustrates that RCP 8.5 (75%) would predict the highest future precipitation quantities over the catchment. By comparing the different precipitation spatial patterns presented in the maps of Figure 4.7, one can notice that there are significant changes in the spatial patterns among all the maps. An increase in the hotspot areas can be observed among all the simulated RCPs by moving from 2020, 2050 and 2080. Table 4.5 shows that there are significant changes in the standard deviation among all the projected raster maps, which indicates that the areal distribution of the precipitation is changing between the maps. Additional results regarding the expected seasonal changes and their statistics are presented in Appendix C.

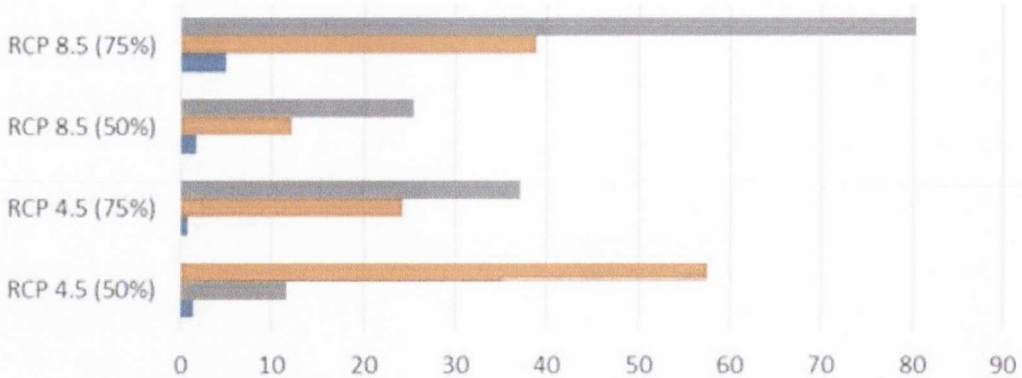

	RCP 4.5 (50%)	RCP 4.5 (75%)	RCP 8.5 (50%)	RCP 8.5 (75%)
Period 2080	11.59	37.062	25.42	80.5
Period 2050	57.27	24.264	12.13	38.863
Period 2020	1.401	0.818	1.7	4.9

Figure 4.4: Average precipitation (mm/year) changes from the baseline period for each simulated scenario over the Shannon catchment.

4.3.2.2 Temperature

Projected time series maps for temperature were compared with long-term observed temperature records (1961-2014) and the results of the projected maps are shown in Figure 4.8 and Table 4.6 with the mean changes in temperature from baseline period shown in Figure 4.5. In general, the results for all the ensembles simulations show that temperature will increase every year. Again RCP 8.5 (75%) has the highest increasing rate (1.85°C in 2080 as an average over Shannon catchment), which is consistent with the global rise in air temperatures. All seasons show an increase in temperature with the highest increases occurring in the spring and summer.

By comparing the different temperature spatial patterns presented in the maps of Figure 4.8, one can notice that there are smooth changes of the spatial patterns among all the maps. A noticeable increase in the hotspot areas can be observed among all the simulated RCPs by moving from 2020, 2050 and 2080. Table 4.6 shows that there are little changes in the standard deviation among the projected raster maps, which indicates that the areal distribution of the temperature does not change significantly in patterns but mostly in values between the projected maps. Additional results regarding the expected seasonal changes and their statistics are presented in Appendix C.

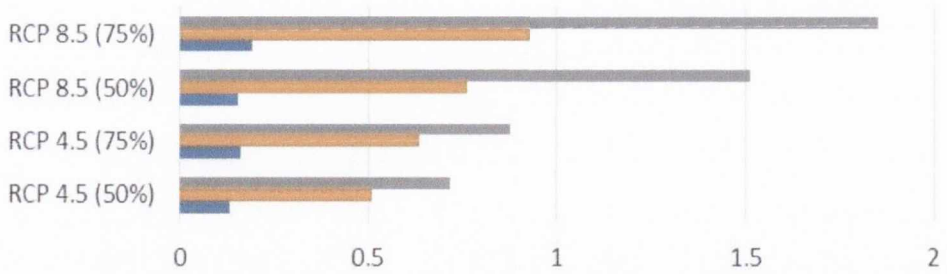

	RCP 4.5 (50%)	RCP 4.5 (75%)	RCP 8.5 (50%)	RCP 8.5 (75%)
Period 2080	0.716	0.876	1.513	1.85
Period 2050	0.511	0.635	0.761	0.925
Period 2020	0.134	0.163	0.158	0.193

Figure 4.5: Average temperature (°C) changes from the baseline period for each simulated scenario over the Shannon catchment.

4.3.2.3 Solar radiation

As shown in Figure 4.6, Table 4.7 and Figure 4.9 for solar radiation, all simulations indicate that there will be a significant increase in solar radiation over the Shannon catchment in the future, with such an incremental increase obvious when moving from RCP 4.5 (50%), RCP 4.5 (75%), RCP 8.5 (50%) to RCP 8.5 (75%), respectively.

By comparing the different solar radiation spatial patterns presented in the maps of Figure 4.8, one can notice that there are smooth changes of the spatial patterns among all the maps. There is no noticeable increase in the hotspot areas can be observed among all the simulated RCPs by moving from 2020, 2050 and 2080. Table 4.6 shows that there is little increase in the standard deviation among the projected raster maps, which indicates that the areal distribution of the solar radiation does not change significantly in patterns but mostly in values between the projected maps. Additional results regarding the expected seasonal changes and their statistics are presented in Appendix C.

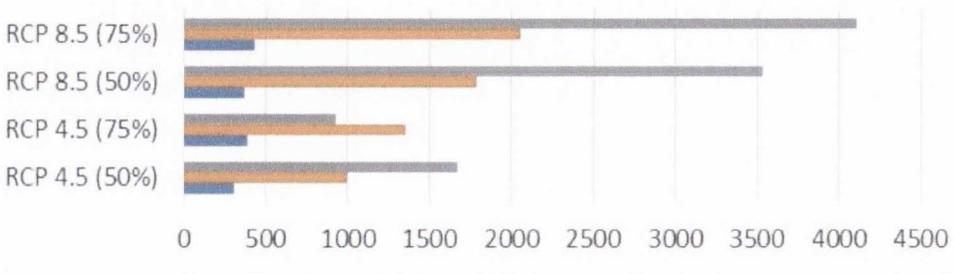

	RCP 4.5 (50%)	RCP 4.5 (75%)	RCP 8.5 (50%)	RCP 8.5 (75%)
Period 2080	1673.3	929.86	3532	4104.8
Period 2050	999.55	1358.87	1792.04	2056.64
Period 2020	314.9	388.95	372.19	440.54

Figure 4.6: Average solar radiation (j/cm^2) changes from the baseline period for each simulated scenario over the Shannon catchment.

Table 4-5: Raster maps statistics for precipitation baseline and projections for 2020, 2050 and 2080 periods according to different Representative Concentration Pathways.

Period																
Baseline				2020					2050				2080			
Min. (mm/y)	Max. (mm/y)	Mean (mm/y)	Standard Deviation (mm/y)	Scenarios	Min. (mm/y)	Max. (mm/y)	Mean (mm/y)	Standard Deviation (mm/y)	Min. (mm/y)	Max. (mm/y)	Mean (mm/y)	Standard Deviation (mm/y)	Min. (mm/y)	Max. (mm/y)	Mean (mm/y)	Standard Deviation (mm/y)
813.85	3013.25	1136.27	224.02	RCP 4.5 (50%)	815.28	3010.07	1137.67	223.67	845.138	3145.5	1193.54	239.25	825.76	2986.89	1147.86	221.16
				RCP 4.5 (75%)	813.08	3004.35	1137.08	223.94	834.75	3063.7	1160.53	226.42	841.67	3096.01	1173.33	229.49
				RCP 8.5 (50%)	815.61	3009.14	1137.97	223.58	826.32	2985.48	1148.40	221.01	840.05	2956.42	1161.69	218.05
				RCP 8.5 (75%)	817.93	3025.5	1141.17	224.82	843.02	3100.88	1175.13	229.75	875.07	3185.92	1216.77	235.33

Table 4-6: Raster maps statistics for temperature baseline and projections for 2020, 2050 and 2080 periods according to different representative concentration pathways.

Period																
Baseline				2020					2050				2080			
Min. (°c)	Max. (°c)	Mean (°c)	Standard Deviation (°c)	Scenarios	Min. (°c)	Max. (°c)	Mean (°c)	Standard Deviation (°c)	Min. (°c)	Max. (°c)	Mean (°c)	Standard Deviation (°c)	Min. (°c)	Max. (°c)	Mean (°c)	Standard Deviation (°c)
5.342	11.495	9.649	0.550	RCP 4.5 (50%)	5.397	11.624	9.783	0.552	5.558	11.99	10.16	0.56	5.637	12.186	10.365	0.565
				RCP 4.5 (75%)	5.418	5.418	5.418	5.418	5.418	5.418	5.418	5.418	5.418	5.418	5.418	5.418
				RCP 8.5 (50%)	815.619	3009.146	1137.97	11.673	11.673	11.673	11.673	11.673	11.673	11.673	11.673	11.673
				RCP 8.5 (75%)	817.931	3025.51	1141.17	9.812	9.812	9.812	9.812	9.812	9.812	9.812	9.812	9.812

Table 4-7: Raster maps statistics for solar radiation baseline and projections for 2020, 2050 and 2080 periods according to different Representative Concentration Pathways.

Period																
Baseline					2020				2050				2080			
Min. (J/cm^2)	Max. (J/cm^2)	Mean (J/cm^2)	Standard Deviation (J/cm^2)	Scenarios	Min. (J/cm^2)	Max. (J/cm^2)	Mean (J/cm^2)	Standard Deviation (J/cm^2)	Min. (J/cm^2)	Max. (J/cm^2)	Mean (J/cm^2)	Standard Deviation (J/cm^2)	Min. (J/cm^2)	Max. (J/cm^2)	Mean (J/cm^2)	Standard Deviation (J/cm^2)
58579.8	80791.4	77086.6	1889.03	RCP 4.5 (50%)	58725.6	81094.5	77401.5	1905.9	58523.35	81694.02	78086.15	1994.66	59403.08	82428.14	78759.9	1985.94
				RCP 4.5 (75%)	58802.07	81206.17	77475.55	1907.61	59045.93	82261.25	78445.47	1981.77	58886.78	81711.14	78016.46	2063.198
				RCP 8.5 (50%)	58753.7	81149.82	77458.79	1909.16	59444.40	82512.68	78878.64	1993.87	60324.55	84253.09	80618.60	2102.67
				RCP 8.5 (75%)	58743.86	81263	77527.14	1916.63	59241.3	83005.37	79143.24	2033.87	60030.632	84928.42	81191.40	2174.21

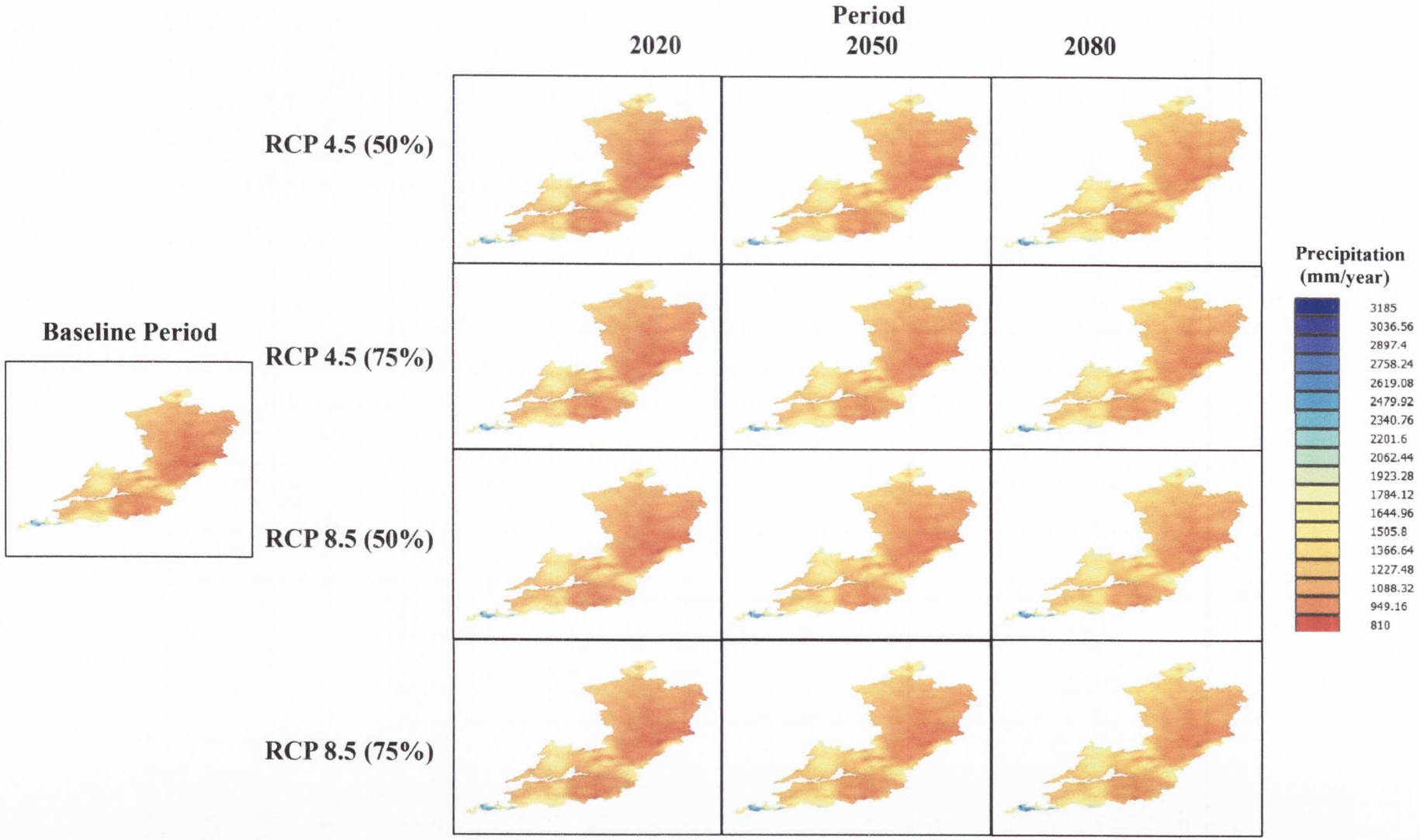

Figure 4.7: Precipitation long-term average for the baseline and projection periods according to different Representative Concentration Pathways.

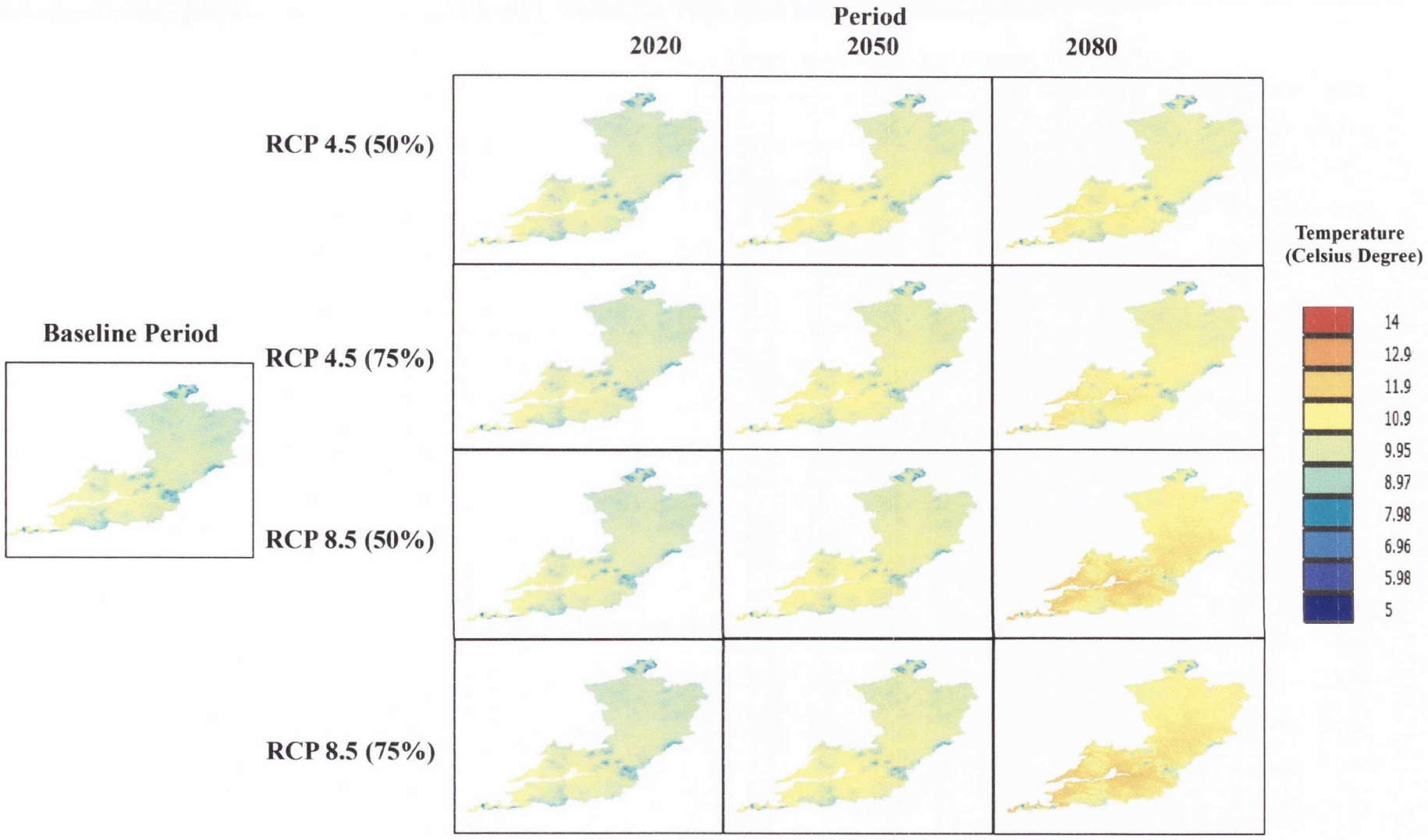

Figure 4.8: Temperature long-term average for the baseline and projection periods according to different Representative Concentration Pathways.

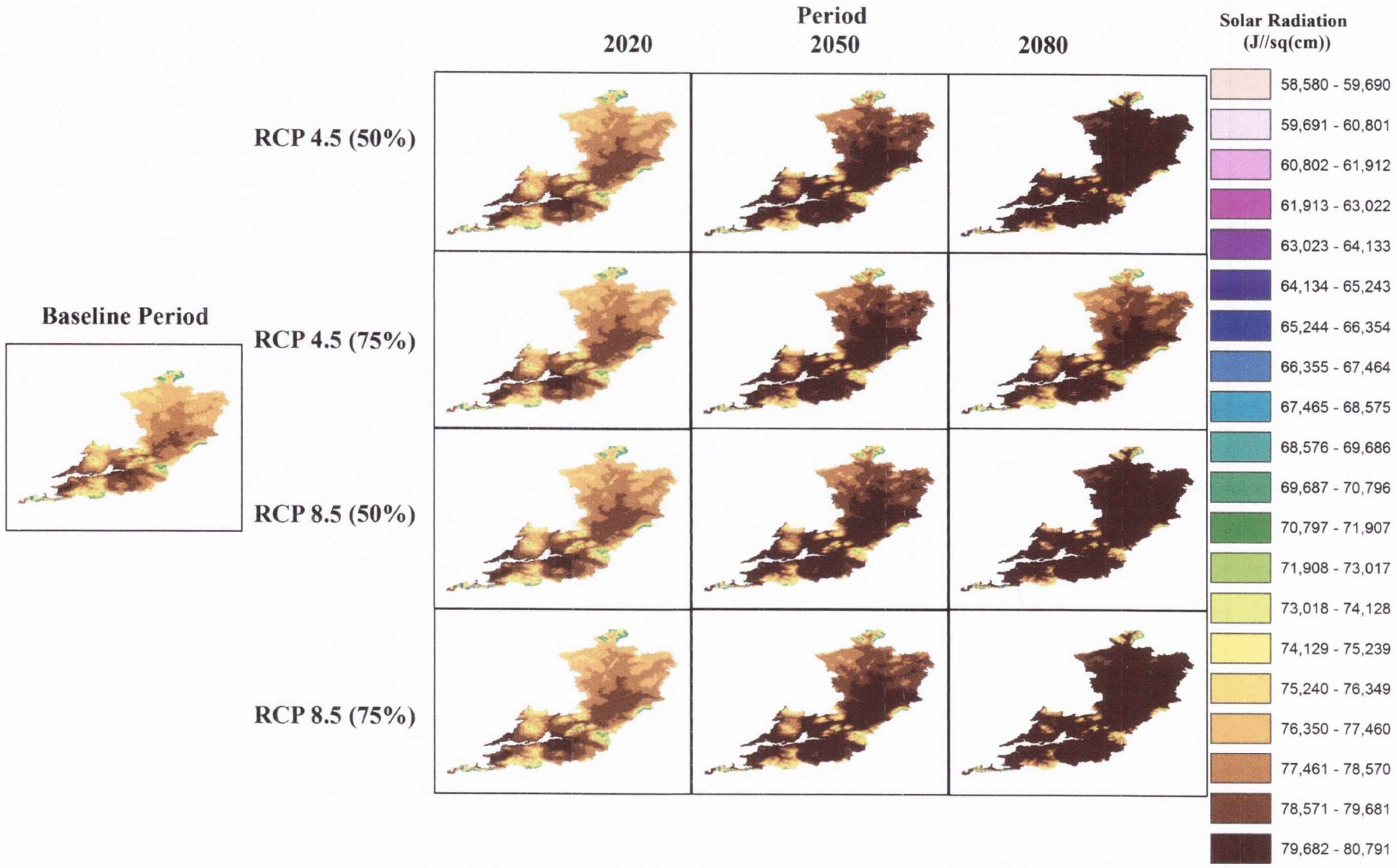

Figure 4.9: Solar radiation long-term average for the baseline and projection periods according to different Representative Concentration Pathways.

4.3.2.4 Relative humidity

The relative humidity simulation results are shown in Table 4.8, Figure 4.10, which all indicate a fluctuation in values but with slight increases dominant over the Shannon catchment. Again, predicted increases are clear when moving from RCP 4.5 (50%), RCP 4.5 (75%), RCP 8.5 (50%) to RCP 8.5 (75%), respectively. There are significant increases in the relative humidity for the 2050 and 2080 from the RCP4.5 (75%) and RCP8.5 (75%) projections, as shown in Table 4.8 and Figure 4.10. One can notice from Table 4.8 that there are almost no changes in the standard deviation between all the projected maps, which indicates that there are no changes in the spatial patterns of relative humidity.

Additional results regarding the projected maps and the spatially distributed results for relative humidity are presented in Appendix C.

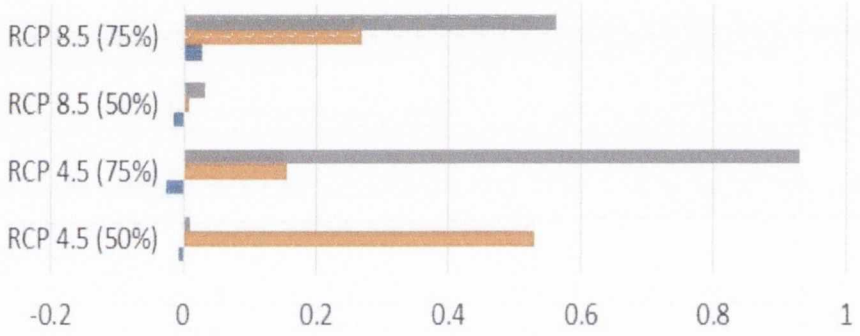

	RCP 4.5 (50%)	RCP 4.5 (75%)	RCP 8.5 (50%)	RCP 8.5 (75%)
Period 2080	0.011	0.931	0.032	0.563
Period 2050	0.529	0.155	0.008	0.268
Period 2020	-0.006	-0.025	-0.015	0.027

Figure 4.10: Average relative humidity (%) changes from the baseline period for each simulated scenario over the Shannon catchment.

4.3.2.5 Wind speed

The wind speed simulation results shown in Table 4.9, Figure 4.11, all indicate a fluctuation in values but with slight decreases in wind speed over the Shannon catchment in the future. Again, this incremental decrease is clear when moving from RCP 4.5 (50%) to RCP 4.5 (75%) to RCP 8.5 (50%) to RCP 8.5 (75%).

Also, one can notice from Table 4.8 that there are almost no changes in the standard deviation between all the projected maps, which indicates that there are no changes in the spatial patterns of wind speed.

Additional results regarding the projected maps and the spatially distributed results for relative humidity are presented in Appendix C.

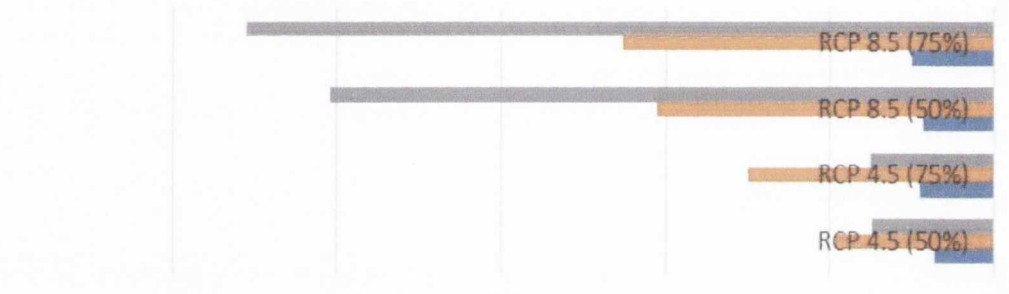

	RCP 4.5 (50%)	RCP 4.5 (75%)	RCP 8.5 (50%)	RCP 8.5 (75%)
Period 2080	-0.148	-0.15	-0.808	-0.91
Period 2050	-0.192	-0.3	-0.411	-0.453
Period 2020	-0.072	-0.09	-0.086	-0.099

Figure 4.11: Average wind speed (km/hr) changes from the baseline period for each simulated scenario over the Shannon catchment.

Table 4-8: Raster maps statistics for relative humidity baseline and projections for 2020, 2050 and 2080 periods according to different Representative Concentration Pathways.

Period																
Baseline					2020				2050				2080			
Min. (%)	Max. (%)	Mean (%)	Standard Deviation (%)	Scenarios	Min. (%)	Max. (%)	Mean (%)	Standard Deviation (%)	Min. (%)	Max. (%)	Mean (%)	Standard Deviation (%)	Min. (%)	Max. (%)	Mean (%)	Standard Deviation (%)
79.378	97.539	82.825	2.381	RCP 4.5 (50%)	79.370	97.5132	82.819	2.378	79.615	98.036	83.354	2.521	79.38	97.293	82.836	2.350
				RCP 4.5 (75%)	79.34	97.53	82.80	2.38	79.499	97.511	82.98	2.397	79.735	96.21	83.756	2.517
				RCP 8.5 (50%)	79.36	97.50	82.81	2.377	79.377	97.268	82.833	2.348	79.393	96.58	82.857	2.311
				RCP 8.5 (75%)	79.389	97.531	82.852	2.388	79.534	97.495	83.093	2.423	79.723	97.313	83.388	2.454

Table 4-9: Raster maps statistics for wind speed baseline and projections for 2020, 2050 and 2080 periods according to different Representative Concentration Pathways.

Period																
Baseline					2020				2050				2080			
Min. (Km/hr)	Max. (Km/hr)	Mean (Km/hr)	Standard Deviation (Km/hr)	Scenarios	Min. (Km/hr)	Max. (Km/hr)	Mean (Km/hr)	Standard Deviation (Km/hr)	Min. (Km/hr)	Max. (Km/hr)	Mean (Km/hr)	Standard Deviation (Km/hr)	Min. (Km/hr)	Max. (Km/hr)	Mean (Km/hr)	Standard Deviation (Km/hr)
17.302	23.927	18.22	0.575	RCP 4.5 (50%)	17.227	23.890	18.148	0.58	17.10	24.036	18.028	0.613	17.149	23.734	18.072	0.6054
				RCP 4.5 (75%)	17.209	23.868	18.13	0.580	16.975	23.854	17.92	0.601	17.135	23.883	18.07	0.628
				RCP 8.5 (50%)	17.21	23.88	18.134	0.581	16.873	23.7037	17.809	0.6034	16.456	23.476	17.412	0.6306
				RCP 8.5 (75%)	17.196	23.897	18.121	0.5833	16.810	23.835	17.767	0.6161	16.355	23.71	17.31	0.655

4.4 Conclusions

This chapter, in addition to performance evaluation for the methodologies and GIS platform used, presents the significant changes in temperature, precipitation, wind speed, solar radiation, and relative humidity, which are projected for three future time intervals 2020, 2050 and 2080 using a multi-model ensemble approach forced by AR5 RCPs.

This chapter aims to present the GIS platform as a suitable downscaling environment through a suggested algorithm, which applies statistical downscaling models to multidimensional GCM-Ensembles simulations. Applying such an algorithm on a GIS platform provides a wide range of output formats for the datasets, which can be used in most of the impact models without any extra effort in formatting the output datasets.

This chapter demonstrates the use of a GIS platform with raster data as a powerful multidimensional downscaling tool, which gives the ability to spatially link all the variables that participated in the downscaling process. The GIS platform also allows for the control of these links through the geostatistical processors, in order to derive very fine scale data for future projected changes in climate. The algorithm has been developed using an integration of the ArcGIS built-in spatial analysis tool package and a spatial-statistical tool that has been developed by the author using Python. The integration between all the tools has been done using Python.

There are many sources of uncertainty in climate projection studies. The main source is related to the GCM simulation and selection, which often needs to be taken into account. This study shows that the differences between ensembles mainly depend on the original GCMs that were used in the ensembles. In this study, the comparisons between ensembles forced by two different RCPs show that there are some agreements in the climate change signal simulation in the study area. However, it is not easy to locate the changes with spatial precision and accuracy especially for precipitation, which makes the use of such results for decision-making by relevant stakeholders and practitioners problematic.

This chapter suggests that multi-climate models should be applied as an ensemble under the GIS environment for climate change simulations, especially for hydrological impact studies, as the output results in formats from the GIS platform can be used directly in the hydrological models, as raster or vector data formats.

Using a GIS platform as a downscaling environment gives the ability to capture different seasonality and spatial patterns within climate variables. For example, the study of temperature in this chapter shows that there are important differences between the ensembles results, especially in summer months. These differences may be of interest because of how they affect the accuracy of simulations of hydrological models.

Generally, it can be concluded that the uncertainty related to the downscaling process is lower than the uncertainty related to the RCP selection. Further work is still needed in the area of climate projections using a GIS platform, especially in the context of linking climate change simulations with hydrological physical-based models.

Chapter 5. The integration of GIS-based algorithms and time series statistics for hydrological long-term variation analysis

5.1 Introduction

Analyzing and studying the long-term changes in a large and complicated hydrological system is essential for hydrological future adaptation studies and plans. Water levels and streamflow are a river basin's integrated reaction to rainfall, groundwater discharge and other relevant hydrological parameters under certain climatological conditions (Worrall and Burt, 2004, Tallaksen and Van Lanen, 2004). The identification of suitable models to simplify any complicated hydrological system for long-term change analysis and future forecasting is a significant precondition to minimize the uncertainty and make the computational process possible. The results for the simplified hydrological system, especially long-term prediction, are useful in many water resources applications such as environment protection, drought management, the operation of water supply utilities, optimal reservoir operation involving multiple objectives of irrigation, hydropower generation, and sustainable development of water resources. Because of the complexity of most hydrological systems and the normal lack of observed hydrological data, it is not always possible to get the observed time series for sub-catchments in hydrological basins. Hydrologic time series long-term changes and forecasting has always been of particular interest in operational hydrology (Hipel and McLeod, 1994, Wang et al., 2009). Hydrological time series analysis and prediction have received significant attention from researchers in the last few decades and many models for hydrologic time series forecasting have been proposed to improve the hydrology forecasting. In most of these efforts, the researchers have focused on each single hydrometric station and each single observed time series as an independent station and independent time series, which is not related to the other stations in the same sub-catchment or in the same hydrological basin.

Such extensive application and reviews of the hydrological time series were reported (Cheng et al., 2005, Jayawardena et al., 2002, Jayawardena and Lai, 1994, Nayak et al., 2004, Coulibaly and Baldwin, 2005, Nourani et al., 2014, Jain and Kumar, 2007, Khaliq et al., 2009, Hipel and McLeod, 1994, Wang et al., 2009, Worrall and Burt, 2004).

To fully understand the long-term streamflow and water level variations, related statistical analyses should be conducted using extensive records for a spatially representative hydrological system, which should be simplified for the complicated hydrological system in order to make the process computationally possible; trends quantified from short records may be part of climate fluctuations (Opitz-Stapleton and Gangopadhyay, 2011, Gautam and Acharya, 2012, Manton et al., 2001). Several reasons can be responsible for changes in streamflow and water level, such as climate variability, human activities, and geomorphic changes, all of which are related to the spatial location. Investigating the long-term variations and rates in a streamflow and water level is a key to understanding the influence of climatic variability and fluctuations on basin hydrologic systems.

Machiwal et al. (2016) analyzed 43-year (1965–2007) monthly and annual rainfall time series of ten rainfall stations in a semi-arid region of western India by adopting three tests for testing normality and by applying the autoregressive technique for exploring persistence. Machiwal et al. (2016) emphasized that the significantly increasing trend of rainfall may have linkages with climate change and/or variability. Finally, this study recommends the use of multiple statistical

tests for analyzing hydrologic time series in order to ensure reliable decisions. Seyam et al. (2015) identified the long-term variations in annual streamflow regime over a 50-year period from 1961 to 2010 in the Selangor River. The perceived changes validate the existence of long-term changes in the annual streamflow regime, which increase the probability of floods and droughts occurring in future. Chen et al. (2013) quantified the effects of climate variability and human activities on streamflow for Kaidu River basin in an arid region of northwest China over the period from 1960 to 2009 where unusual increases have been observed in annual streamflow.

These research works (and others) show the importance of gaining a better understanding of river's hydrological observed time series which is a fundamental tool for river systems and surface water resource planning, design, and management.

The main objective of this part of research is to provide the scientific community with a method to simplify a large and complicated hydrological system with a spatially representative simplified system, through a designed Python GIS-based algorithm in order to integrate the simplified system in the process of hydrological long-term statistical variation analysis.

5.2 Materials and Methods

5.2.1 Data setup

In this chapter, three main sources of data are used: The Office of Public Work (OPW), Irish Environmental Protection Agency (EPA) and Electricity Supply Board (ESB).

The following five types of data are used in this chapter:

- Hydrometric station locations and metadata (from the EPA).
- Hydrometric station measurements of water flow and level (from the OPW and ESB).
- River centre lines (from the EPA).
- Catchment and sub-catchment shapefiles and metadata (from the EPA).
- The urban area data.

The collected data can be divided into two types of data: GIS data (from the EPA) and hydrometric measurements (from the OPW and ESB). The EPA is the competent authority in Ireland for river basin management planning in Ireland under the Water Framework Directive (WFD). The EPA runs a national surface water and groundwater monitoring and assessment program in cooperation with some Irish governmental and nongovernmental bodies. The EPA GIS Team provides a number of national hydrological GIS layers, such as:

- 1:50,000 River network
- The WFD river water body
- 1:50,000 lake polygons and a selection of approximately 800 lakes that are designated as Lake Water Bodies under the WFD
- National transitional, coastal and groundwater bodies
- A suite of catchment layers generated to help with River Basin Management planning
- A suite of catchment layers pre-dating the WFD generated before 2005.

For the hydrometric station measurements that are collected from OPW and ESB, they have been provided with some quality codes, which have been used in the data cleaning process in this chapter in order to use a high quality observed database in the simulation process. Quality codes provide an indicative measure of the reliability and confidence placed on each item of data and

can appear numerically or as a symbol, depending on the format of the data. The majority of the codes are allocated following certain criteria but are subjective, and are not associated with any given confidence limits in terms of percentage, absolute value or standard error. Hence, the codes are used only as an indication of the reliability of the data, see Table 5-1.

Table 5-1: Hydrometric data quality codes.

Code	Symbol	Description
WATER LEVEL DATA		
1	*	Unchecked digitized water level data – Data is provisional only and must be used with caution
31		Inspected water level data – Data may contain some error, but has been approved for general use
32	C	As per Code 31, but where the digitized water level data has been corrected
41		Poor measured water level data
42		As per Code 41, but where the digitized water level data has been corrected.
99	*	Superseded quality code, see code 254.
145	<	Data is below prescribed data range and must only be used with caution
146	>	Data is above prescribed data range and must only be used with caution
150	I	Partial statistic – Data has been derived from records that are incomplete and do not necessarily represent the true value
101	!	Unreliable water level data – Data is suspected of being erroneous or is artificially affected (e.g., during drainage works) and must only be used with caution
>150	Various	Data is not available as it is missing, erroneous or of unacceptable quality
254	*	Unchecked imported water level data – Data is provisional only and must be used with caution
ESTIMATED FLOW DATA		
31		Flow data estimated using a rating curve that it is considered to be of **good** quality and inspected water level data – Data may contain some error, but is considered to be of acceptable quality for general use
32	C	As per Code 31, but using water level data of Code 32
36	F	Flow data estimated using a rating curve that it is considered to be of **fair** quality and inspected or corrected water level data – Data may contain a fair degree of error and should, therefore, be treated with some caution
46	B	Flow data estimated using a rating curve that it is considered to be of **poor** quality and inspected or corrected water level data – Data may contain a

		significant degree of error and should, therefore, be used for indicative purposes only
56	X	Flow data estimated using an extrapolated rating curve (see Section 3.2) and inspected or corrected water level data – Reliability of data is unknown and it should, therefore, be treated with caution
99	*	Superseded quality code, see code 254.
101	!	Flow data that has been estimated using unreliable water level data – Data is suspected of being erroneous and must only be used with caution
145	<	Data is below prescribed data range and must only be used with caution
146	>	Data is above prescribed data range and must only be used with caution
150	I	Partial statistic – Data has been derived from records that are incomplete and do not necessarily represent the true value
>150	Various	Data is not available as it is missing, erroneous or of unacceptable quality
254	*	Flow data that has been estimated using unchecked water level data – Data is provisional only and must be used with caution

5.2.2 GIS-based algorithm for simplifying the hydro-system

As shown in figure 5.1, the Shannon River catchment is a large system which has more than 500 hydrometric stations. Some of these stations have flow data and some have water level data and few of them have both, and they do not have the same observation period and time steps. These hydrometric stations are randomly distributed throughout the catchment area to serve local purposes. Using this system is not possible to study the hydrological long-term variation analysis, as the system is very random and not representative to the catchment. This chapter presents a GIS-based Python algorithm for simplifying large and complicated hydrological systems and performance evaluation simulations in order to use the simplified system for the long-term variations and trends analysis process. This designed algorithm is transferable to simplify other large hydrological systems in order to run the long-term variation analysis on them. This algorithm uses GIS as the platform for the simulation process through spatial geo-processors in the integration with geostatistical packages. The algorithm loops through a process to get the hydrological simplified system and validate the resulted system.

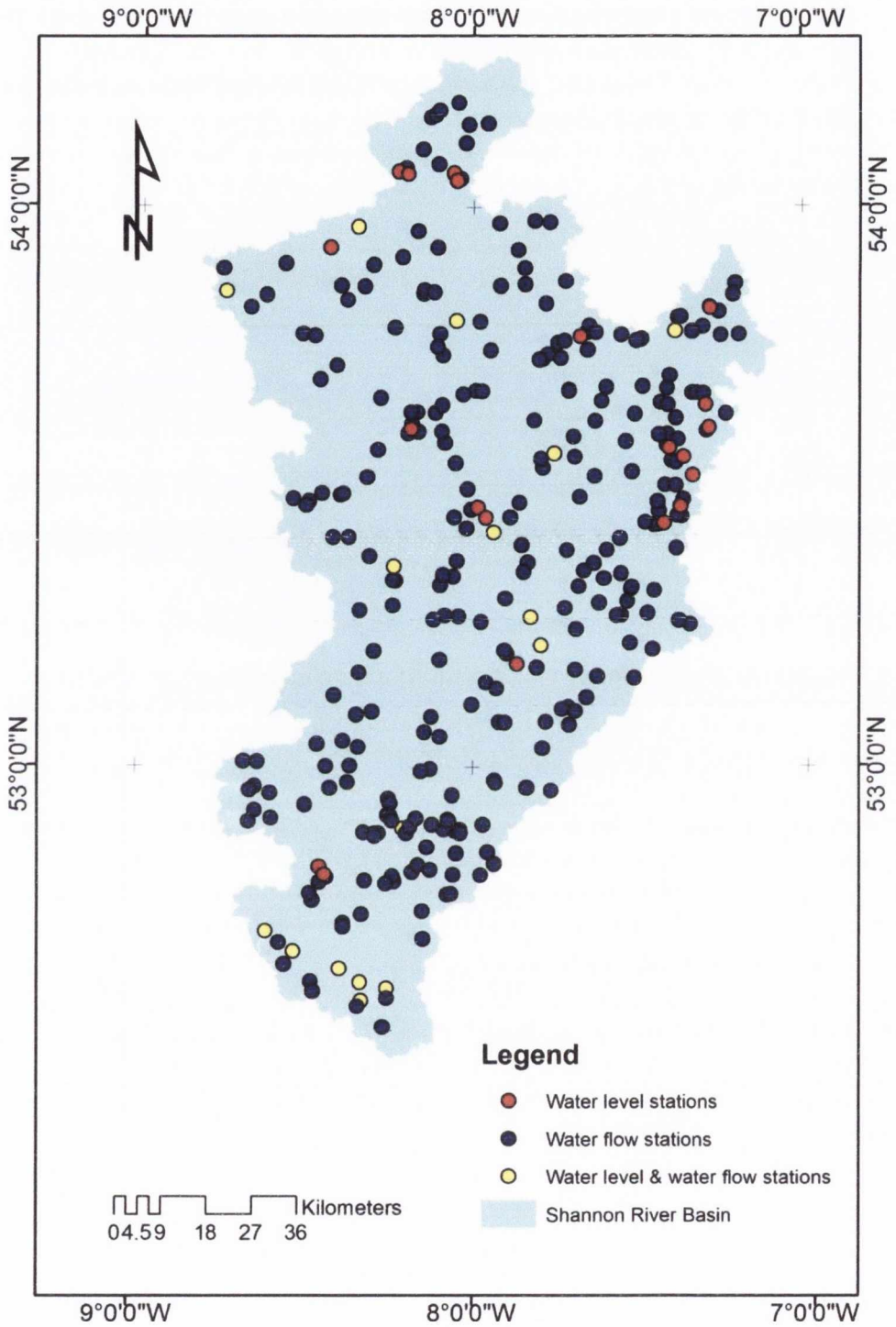

Figure 5.1: The Shannon hydrometric stations and main rivers centerline.

The algorithm spatial simulation steps are as follow:

1. The algorithm imports the hydrometric stations in the catchment, which are provided as a multi-feature class in a designed geo-database. The Shannon geodatabase contains 517 hydrometric stations, see Figure 5.1.

2. River centreline simulation using the provided Digital Elevation Model (DEM). This step aims to produce the surface water bodies' centreline based on the elevation map that used in the simulation. This means that this step produces the rivers' network in the catchment based on the elevation and slope.
3. Run a geospatial query to identify the hydrometric stations that intersect the main river body, see Figure 5.2.

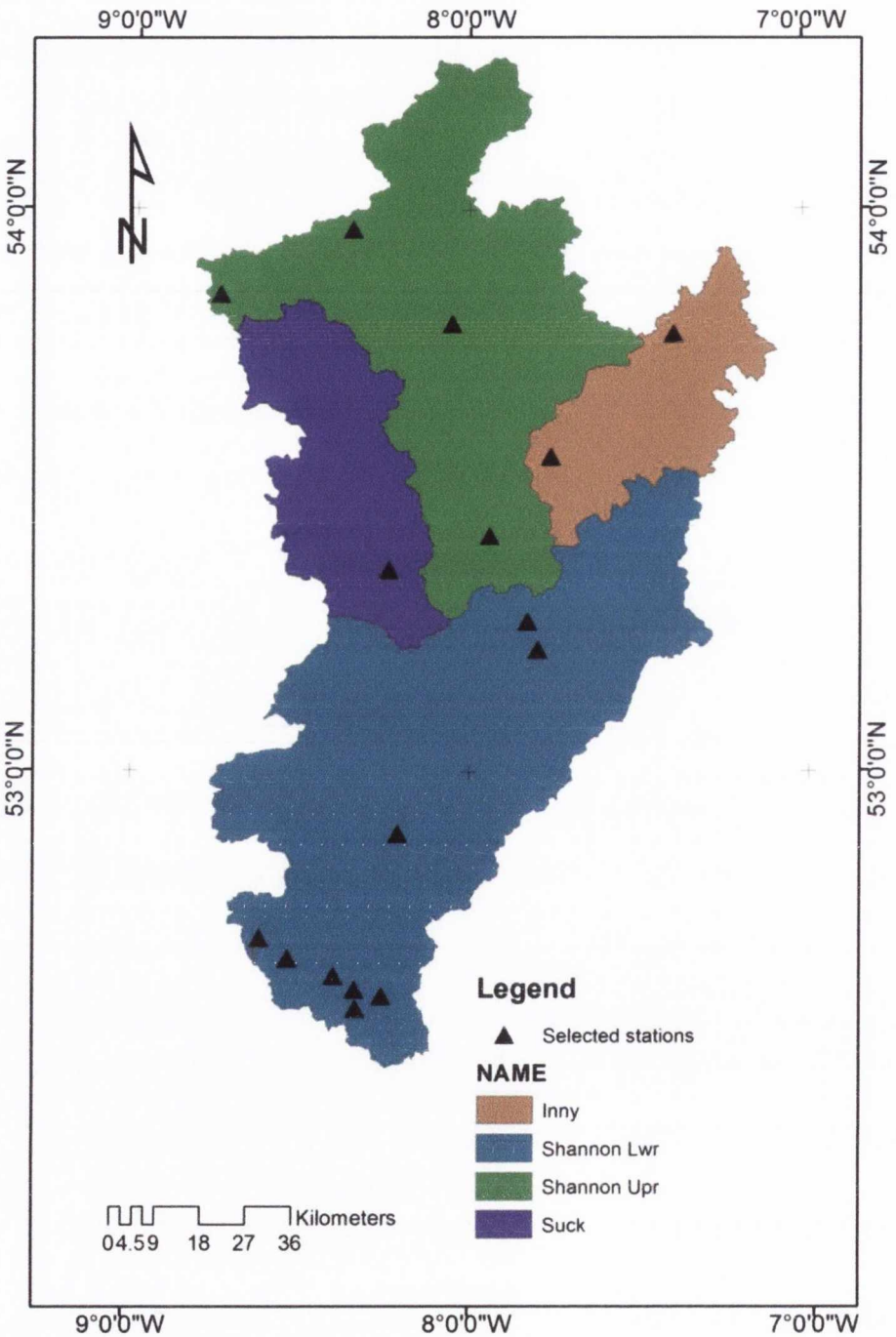

Figure 5.2: The identified hydrometric stations that intersect the main river bodies.

4. The algorithm imports the main populated areas and cities in the catchment: these areas are based on a polygon feature class in the main geodatabase, see Figure 5.3.

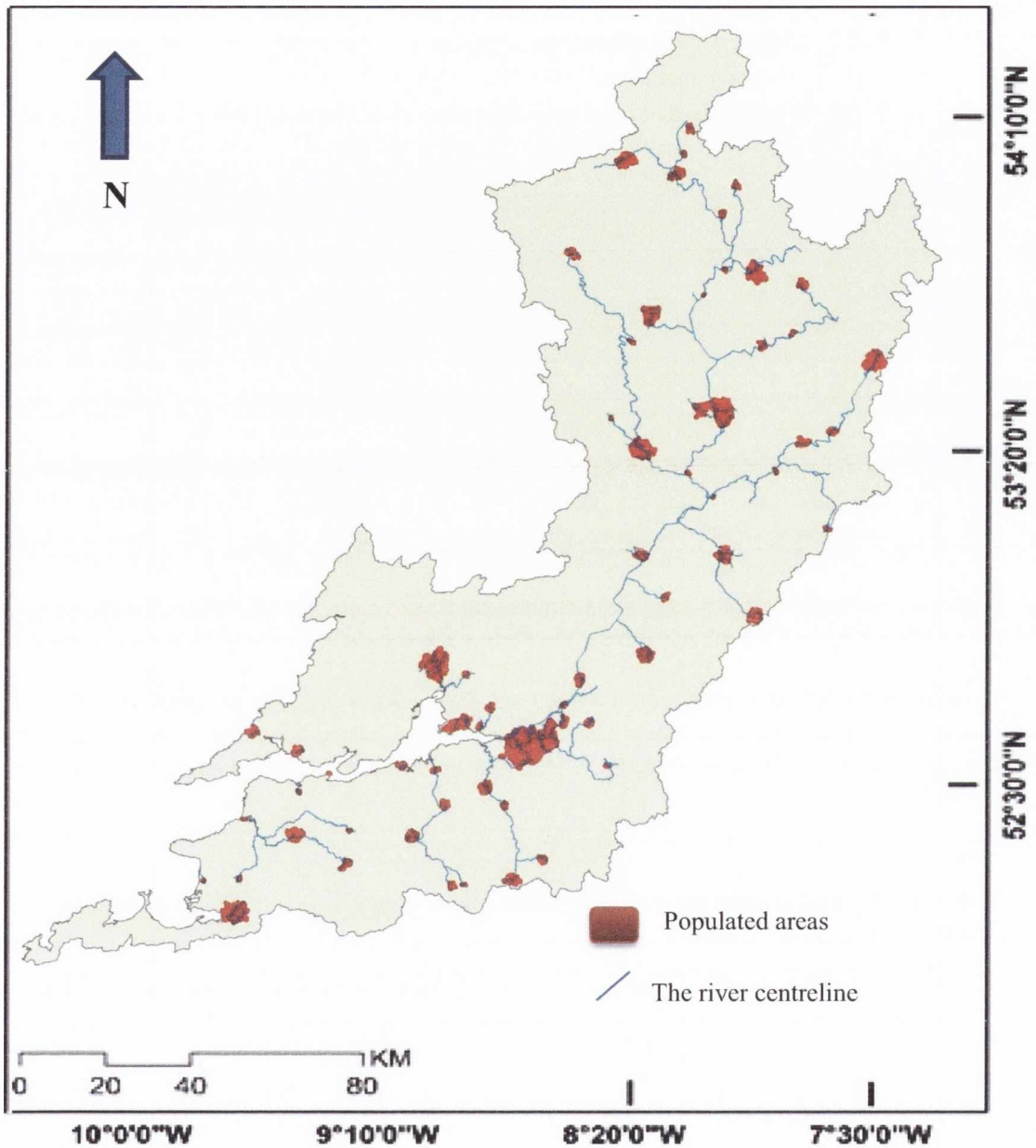

Figure 5.3: The main populated areas and cities in the Shannon catchment.

5. The algorithm generates the sub-catchments polygon feature class depending on the generated river centerline and the fine scale Digital Elevation Model (DEM), see Figure 5.2. These generated areas represent the theoretical sub-catchment area that each main river segment collects the water from. This step is done by integrating the Arc Hydro package in ArcMap with the designed algorithm.
6. The algorithm runs a query analysis written in Structured Query Language (SQL) to sub-select the hydrometric stations that have the following criteria:
    - Intersect at least one populated area.
    - Intersect a single sub-catchment.

- Has the lowest elevation among the hydrometric stations within a single populated area and simulated sub-catchment. Selecting the stations that are in the populated area helps the model later on to learn about the water levels and water flows in the urban areas, which are the most important areas in the risk assessment studies.
- Has both water level and water flow observed data for more than 30 years.

7. The resulted selected hydrometric stations from the previous steps are 7 stations out of 574 stations, which can be assumed as spatially representative hydrometric stations if they cover all the sub-catchment areas and therefore they can represent the whole catchment. In this step, the designed algorithm recalculates the sub-catchment polygons using the final selected hydrometric stations (7 stations) as discharge points for each sub-catchment's river or river branch, in addition to the high-resolution DEM and the main catchment/basin polygon feature class as inputs and restriction boundaries for the sub-catchments re-calculation process. In this step, and because of the random spatial location for each station from the selected ones, the re-calculated sub-catchments might not be representative and including all the area of the main basin. In this case, the designed algorithm connects the uncovered areas by an imaginary canal/pipe to the one of the nearest re-calculated sub-catchment, depending on the elevation differences and the relative sub-catchment areas, see Figure 5.4.

In figure 5.4, one can notice that Suck sub-catchment is presented in the simplified system by its area and one hydrometric station (26007) which is not near the boundary line of the Suck sub-catchment. This hydrometric station (26007) has been included to the system because there is no other hydrometric station in the Suck sub-catchment that has water level and water flow measurements. The uncovered area from the Suck sub-catchment by this selected hydrometric station (26007) is connected to the following hydrometric station in the system which takes into account the total amount of water flow coming from its area and from the uncovered areas by the previous hydrometric station.

The resulting system, which contains the selected hydrometric stations and the recalculated sub-catchments, can be considered as a simplified representative system. This system, after the validation process and performance evaluation, can be used to create the simplified and representative structured hydrological system in order to use it for trend and long-term variation analysis. The simplified and representative structured hydrological system, as seen in Section 5.2.4, represents each sub-catchment as a reservoir with a certain area, and each hydrometric station as a monitoring station for each reservoir; the reservoirs are connected using and imaginary canals/pipes in order to convey the water through the sub-catchments to the sea through the final discharge point.

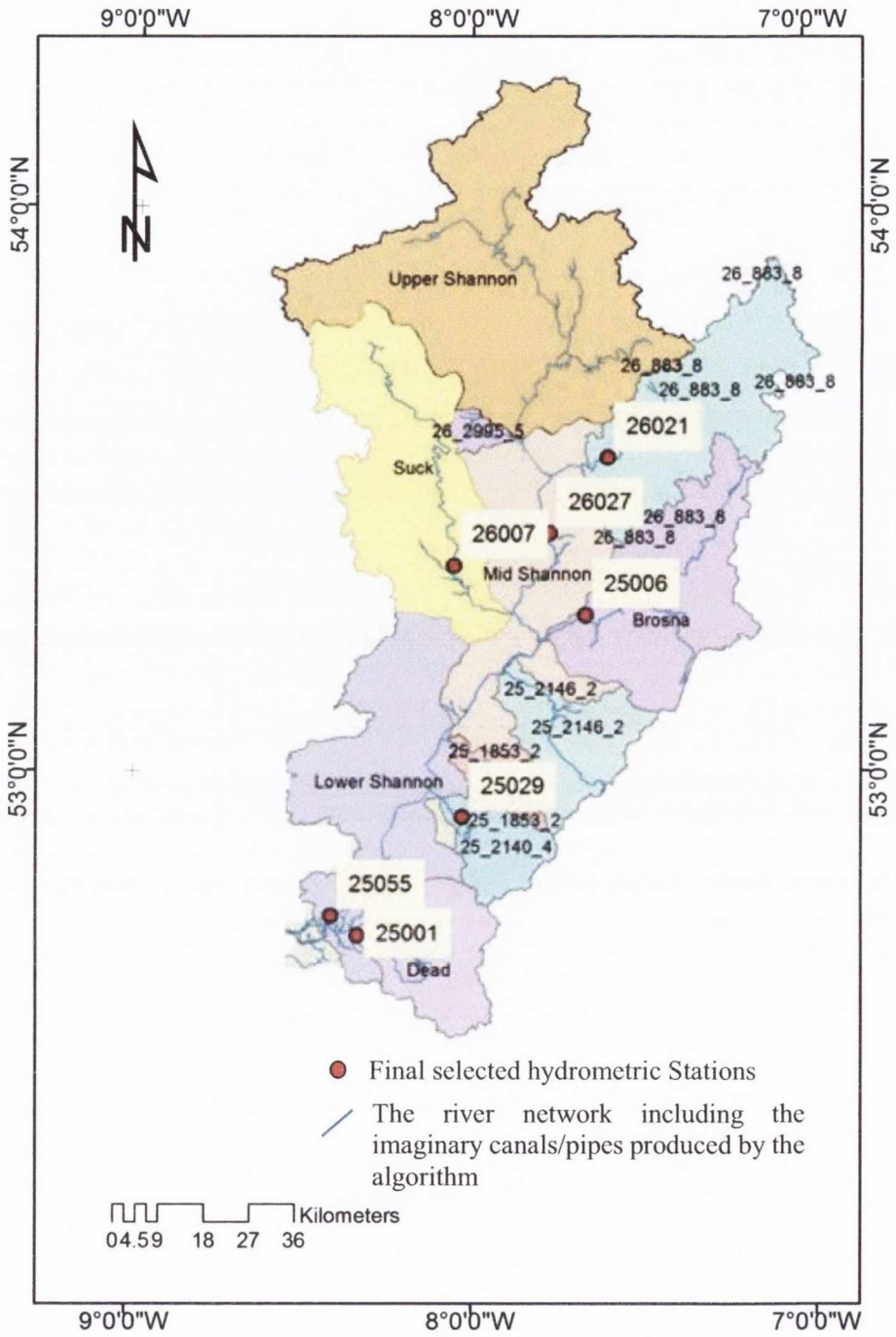

Figure 5.4: The final selected hydrometric stations and the re-calculated sub-catchments.

5.2.3 Statistical long-term variation analysis

The long-term trend analysis for the simplified system was completed through a set of systematic steps for both water flow and level parameters. The steps were as follows:

1. Normality and homogeneity check for each dataset. Some data transformation methods can be used to test the validity of the normality assumption.
2. Use the decomposition method (Box et al., 2015, Bowerman and O'Connell, 1993) to separate the time series into linear trend and seasonal components, as well as a statistical error, to give a full understanding of the time series components and variations.
3. Select whether the seasonal component is additive or multiplicative with the trend.
4. Smoothing the data using a centred moving average with a length equal to the length of the seasonal cycle, a two-step moving average is required to synchronize the moving average correctly. The temporal dimension for each time series for each hydrometric station is simplified using a seasonal and yearly moving average method. The method of moving average is a technique to get an overall idea of the time series in a subset of the period; it is an average of any subset of numbers of the whole dataset. The moving average is extremely useful for forecasting long-term trends. A moving average is a time series constructed by taking averages of several sequential values of the original time series. It is a type of mathematical convolution (Said and Dickey, 1984, Theiler et al., 1992, Box and Pierce, 1970).
5. Divide the moving average into (multiplicative model) or subtracting it from (additive model) the data to obtain what are often referred to as raw seasonal values.
6. Determine the median of the raw seasonal values.
7. Adjust the medians of the raw seasonal values so that their average is one (multiplicative model) or zero (additive model). These adjusted medians constitute the seasonal indices.
8. Use the seasonal indices to seasonally adjust the data.
9. Fit a trend line to the seasonally adjusted data using least-squares regression. Run the exponential or linear trend analysis for the temporarily simplified time series for each hydrometric station.
   The linear model is:
   $Y_t = \beta_0 + (\beta_1 * t) + e_t$ Eq 5.1
   In this model, Y_t is an observation at time t, β_1 represents the average change from one period to the next, β_0 represents the actual value, e_t is the exponential component of the equation. The exponential growth trend model explains exponential growth or decay. The model is:
   $Y_t = \beta_0 + (\beta_1^t) + e_t$ Eq 5.2
   In this model, Y_t is an observation at time t, β_1 represents the average change from one period to the next, β_0 represents the actual value.
10. The data can be detrended by either dividing the data by the trend component (multiplicative model) or subtracting the trend component from the data (additive model).

11. The trend and the seasonal component for the input time series can then be separated and investigated

12. Statistical parameters were calculated for assessing the quality of each statistical step. The parameters were the correlation (R), the coefficient of determination (R^2), the mean absolute percentage error (MAPE) and the median absolute deviation (MAD). MAPE, MAD, and the mean signed deviation (MSD) statistics were used to compare the fits of different forecasting and smoothing methods.

    Mean absolute percentage error (MAPE) expresses accuracy as a percentage of the error. Because this number is a percentage, it can be easier to understand than the other statistics. The equation is:

$$\frac{\sum|(y_t-\hat{y}_t)/y_t|}{n}\times 100\ (y_t \neq 0) \qquad \text{Eq5.3}$$

    Where y_t is the actual value, $\hat{y}_t$ is the fitted value, and n is the number of observations.

    Mean absolute deviation (MAD) expresses accuracy in the same units as the data, which helps conceptualize the amount of error. Outliers have less of an effect on MAD than on MSD. The equation is:

$$\frac{\sum_{t=1}^{n}|y_t-\hat{y}_t|}{n} \qquad \text{Eq5.4}$$

    Mean squared deviation (MSD) is commonly used a measure of the accuracy of fitted time series values. Outliers have a greater effect on MSD than on MAD. The equation is:

$$\frac{\sum_{t=1}^{n}|y_t-\hat{y}_t|^2}{n} \qquad \text{Eq5.5}$$

5.3 Results and Discussions

5.3.1 Simplified structure hydrological system

As shown in Figure 5.5, the resultant simplified system contains 10 sub-catchments, which includes the connected areas in order to cover the whole Shannon catchment area. The simplified hydrological system contains 7 hydrometric stations which have long-term observed data as discussed before. This structural hydrological system is validated in the next section and is used as a simplified system for the calculation in this project. In this system, each sub-catchment represents a reservoir; these reservoirs in the system vary by area and the distance from the main discharge point of the system. These reservoirs are connected by imaginary pipes/canals, which are monitored and controlled by the selected 7 hydrometric stations. For each main representative sub-catchment, there is an assigned related hydrometric station that acts as a discharge point which collects all the water from this sub-catchment by the water re-routing process that implemented by the added imaginary pipelines/canals. Table 5-2 shows the characteristics of the selected hydrometric stations in the simplified system. Table 5-2 shows the areal and the distance weight of each simplified sub-catchment in the system. These weighted areas calculated based on the original Shannon River Discrete total area which contains more sub-catchments than the selected in the simplified system that means the sums for the areal and distance weights presented in the Table 5-2 do not equal 1.

Table 5-2: The characteristics of the hydrometric stations in the simplified system.

Station	Inny 26021	Mid-Shannon 26027	Suck 26007	Brosna 25006	Nenagh 25029	Dead 25001	Lower Shannon 25055 + 25075
Areal weight from the original catchment area.	0.105	0.115	0.134	0.108	0.027	0.057	0.133
Distance weight	0.15	0.10	0.11	0.11	0.05	0.03	0.04
Centroid distance from the pouring point (km)	135.2	86.9	98.4	101.3	40.9	23.7	34.7
Area (Km^2)	1249.20	1376.50	1596.51	1284.84	317.80	679.47	1582.73

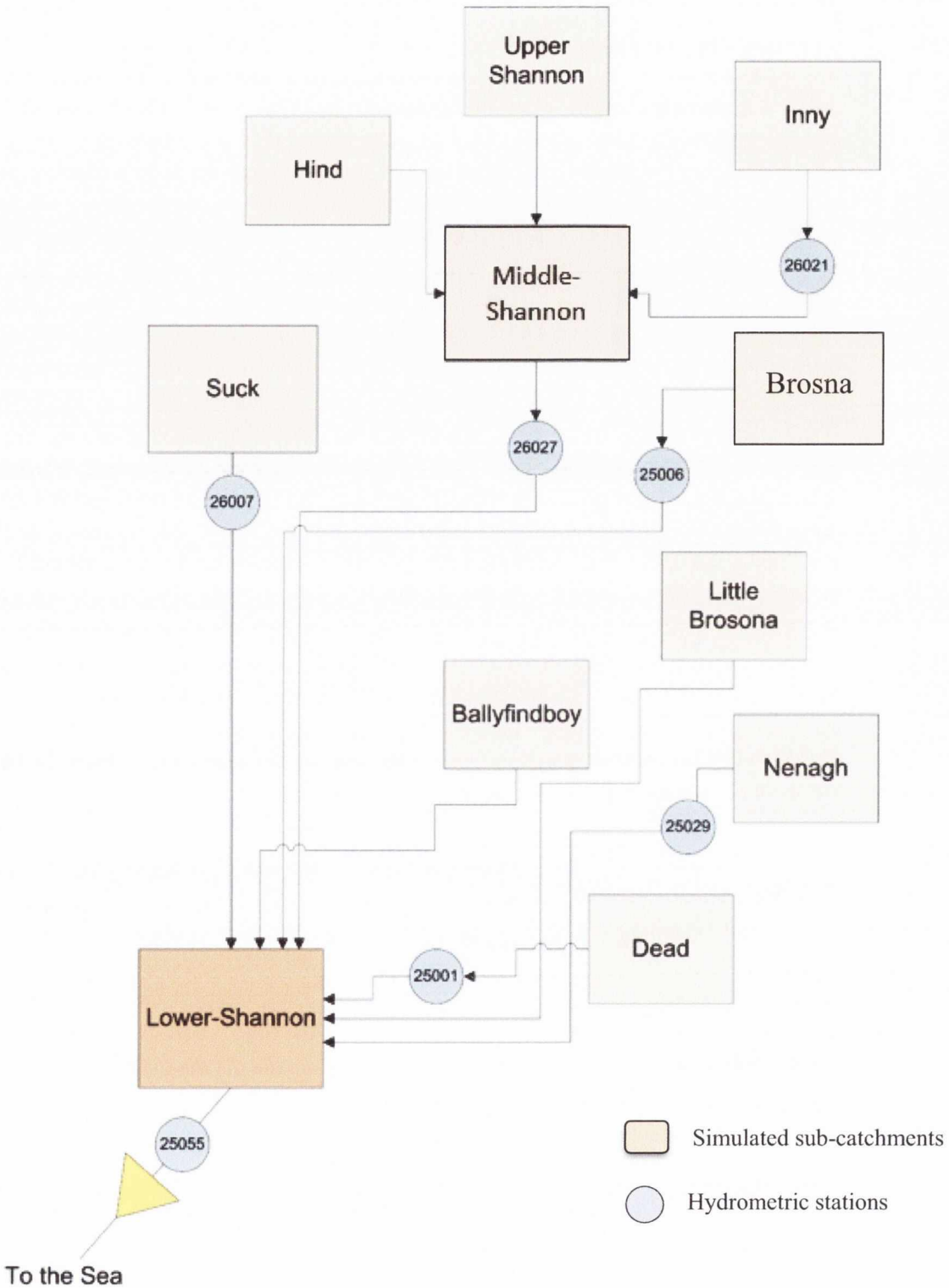

Figure 5.5: Resulted simplified structured hydrological system.

5.3.2 Validation and performance evaluation

The main idea behind the validation process is to reproduce the water flow time series (Q) in a selected hydrometric station using the produced simplified system. Flow continuity equation concept is applied to validate the system. The observed Q time series from all the stations in the simplified system is needed for the calculation process except the station that is used for the validation. The discharge point observes the total Q, and it is the summation of all the Q time series from all sub catchments in the simplified system. The missing Q time series for the selected hydrometric station for validation can be calculated by knowing all the other Q time series including the total Q at the discharge point. After calculating the Q time series for the selected hydrometric station, a comparison between the calculated time series and the observed one is performed to validate the simplified system and its performance in producing water flow time series. To validate the resulting simplified hydrological system, the flow continuity equation is applied to the system, where ε is the summation of the storage and the error.

$$Qin = Qout \pm \varepsilon \qquad \text{Eq5.6}$$

The water flow time series for each hydrometric station in the system has been calculated using the continuity equation concept by assuming its flow time series is missing and then a comparison between the calculated and the observed time series has been done in order to validate the simplified system. The continuity equation itself cannot be enough in order to complete the calculation; another two concepts have been used in the calculation process, which is the area and distance weights in order to get another two equations to help to solve the problem. To summarize the process the following equations represent the process.

$$Q_{\text{at discharge point}} = Q_{\text{validation station}} + Q_{\text{station 1}} + Q_{\text{station 2}} + \ldots + Q_{\text{station } n} \pm \varepsilon \qquad \text{Eq5.7}$$

$$A\,(Total) = A_{\text{validation station}} + A_{\text{station 1}} + A_{\text{station 2}} + \ldots + A_{\text{station } n} \qquad \text{Eq5.8}$$

$$Distance\ from\ discharge\ point(Total) = D_{\text{validation station}} + D_{\text{station 1}} + D_{\text{station 2}} + \ldots + D_{\text{station } n} \qquad \text{Eq5.9}$$

$$\text{Areal weight}_{\text{validation station}} = \frac{A_{\text{validation station}}}{A\,(Total)} \qquad \text{Eq5.10}$$

$$\text{Distance weight}_{\text{validation station}} = \frac{D_{\text{validation station}}}{Distance\ from\ discharge\ point(Total)} \qquad \text{Eq5.11}$$

$$Q_{\text{Nenagh(25029)}} = Q_{25055} - Q_{25006} - Q_{26027} - Q_{25001} - Q_{26007} \pm \varepsilon \qquad \text{Eq5.12}$$

For example, to validate the simplified hydrological system illustrated in Figure 5.5 using Nenagh station (25029) as a validation station, the Nenagh flow time series is assumed to be missing. Using the equations (Eq 5.7 – 5.12) the flow for Nenagh is calculated, and then compared statistically with the observed time series. Where a strong agreement is observed between the calculated time series and the observed one, then the simplified hydrological system is confirmed as a valid simplification for the more complicated hydrological system. The simplified system

developed in this chapter has thus been approved as a valid system for the Shannon catchment, see Figures 5.6 – 5.9. Four main hydrometric stations have been used to validate the structured simplified hydrological system for the whole Shannon catchment, which are Brosna, Nenagh, Inny, and Suck. The statistics from each validation process show very good agreements between observed and calculated flow time series, as shown in the Figures 5.6 – 5.9. The figures show the values for R^2, S (standard variation) and R^2 adjusted for each validation hydrometric station.

In addition to the validation charts, a cross-correlation between the observed and the calculated flow time series for each validation hydrometric station has been run using different lag values. From Figures 5.10-5.13, it can be concluded that the calculated water flow time series for all validation hydrometric station has a very high correlation with the observed water flow time series for the lag values close to zero. The high cross-correlation around the zero-lag value means that the observed time series and the calculated one are very close to being identical. The calculation process in this chapter was carried out using R software.

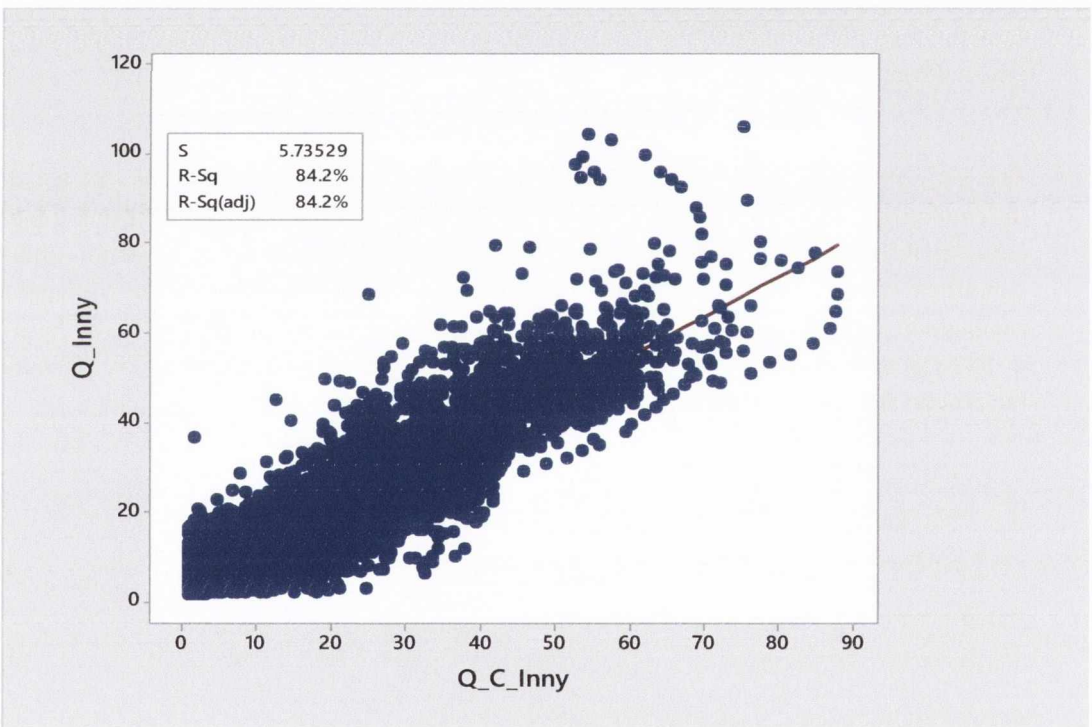

Figure 5.6: Validation chart between the observed and the calculated water flow (m^3/sec) time series for the Inny hydrometric station.

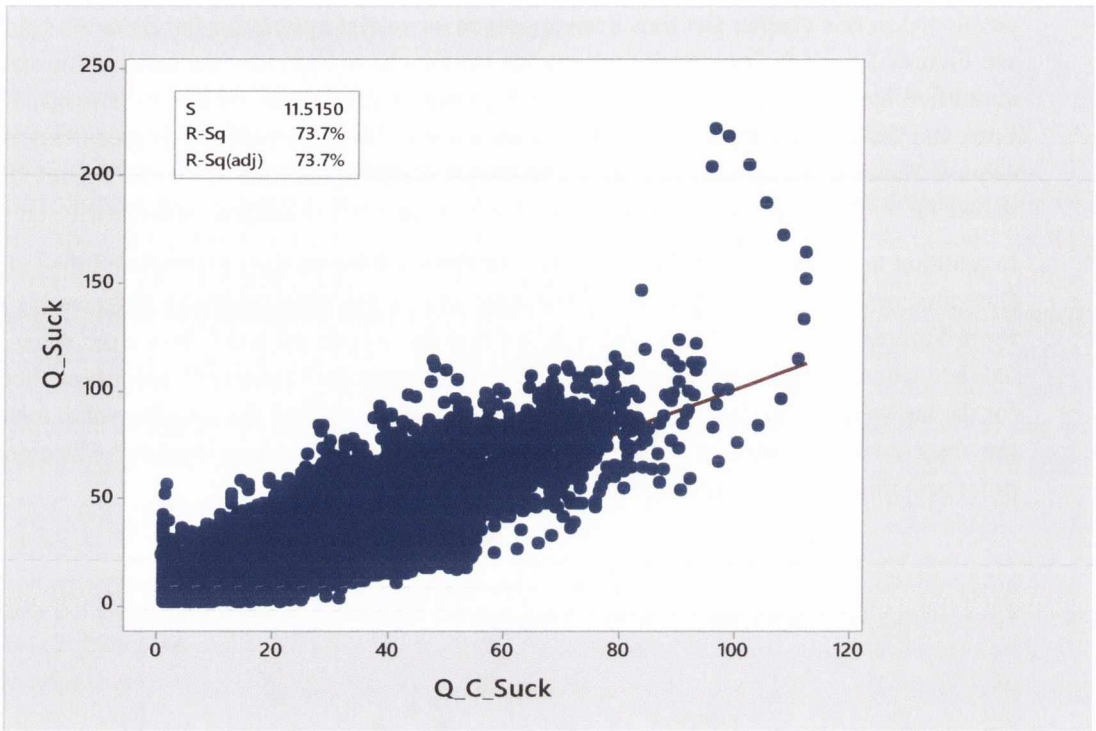

Figure 5.7: Validation chart between the observed and the calculated water flow (m3/sec) time series for the Suck hydrometric station.

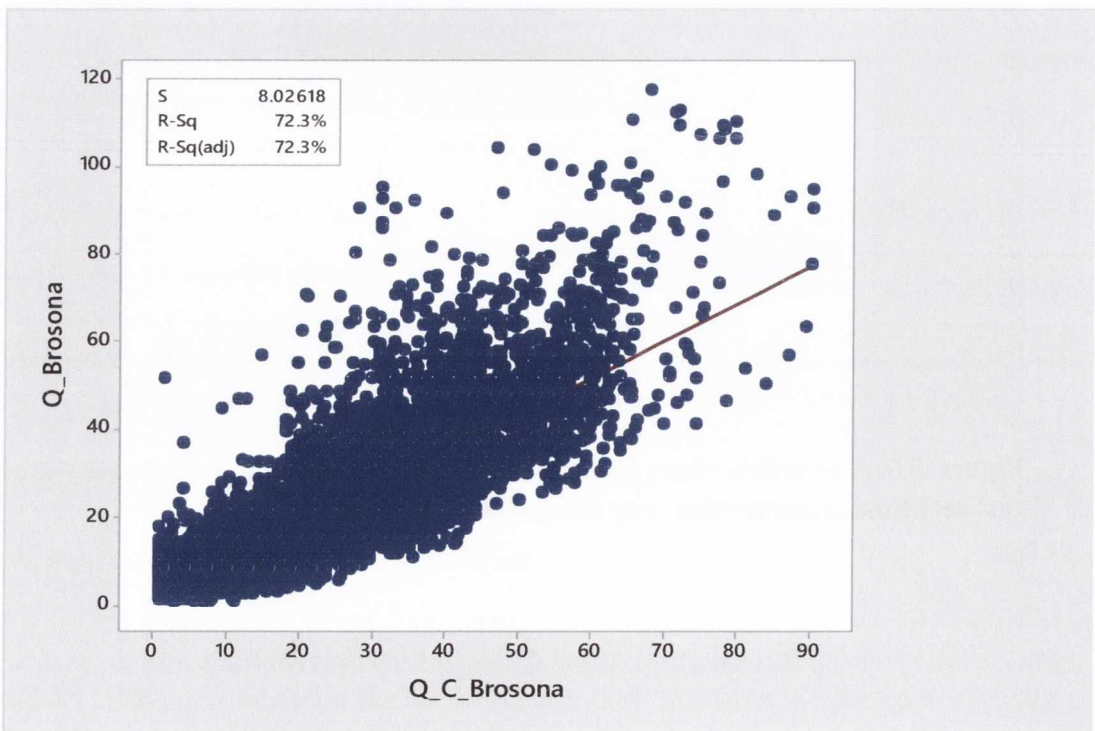

Figure 5.8: Validation chart between the observed and the calculated water flow (m3/sec) time series for the Brosna hydrometric station.

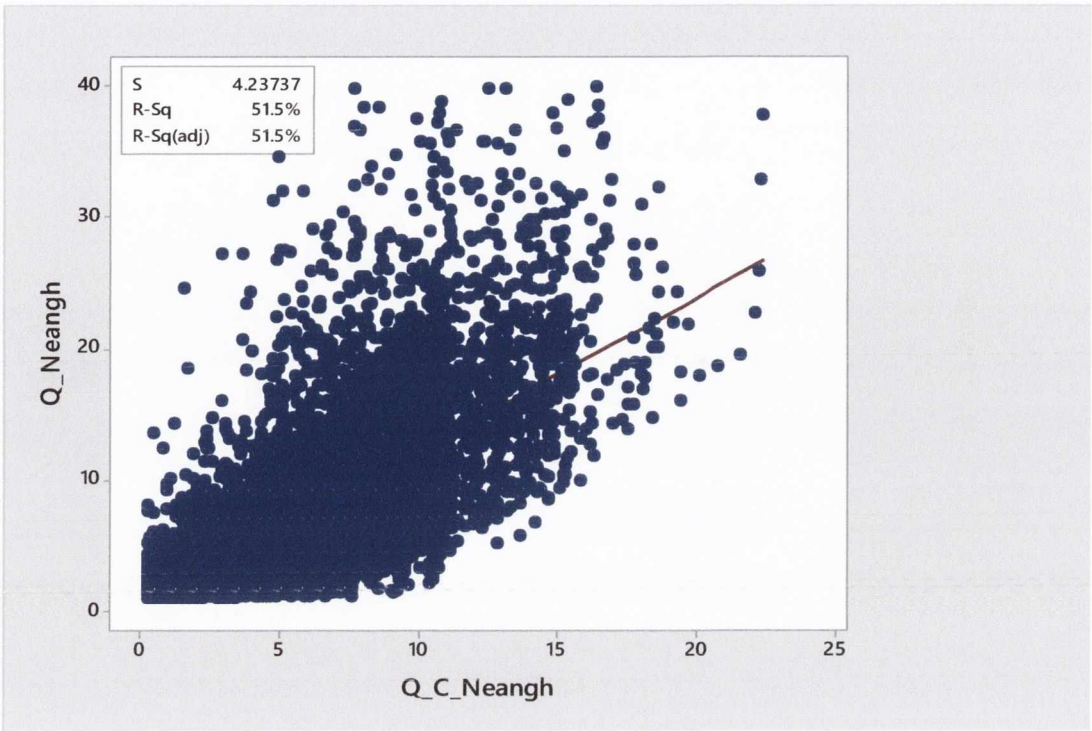

Figure 5.9: Validation chart between the observed and the calculated water flow (m3/sec) time series for the Nenagh hydrometric station.

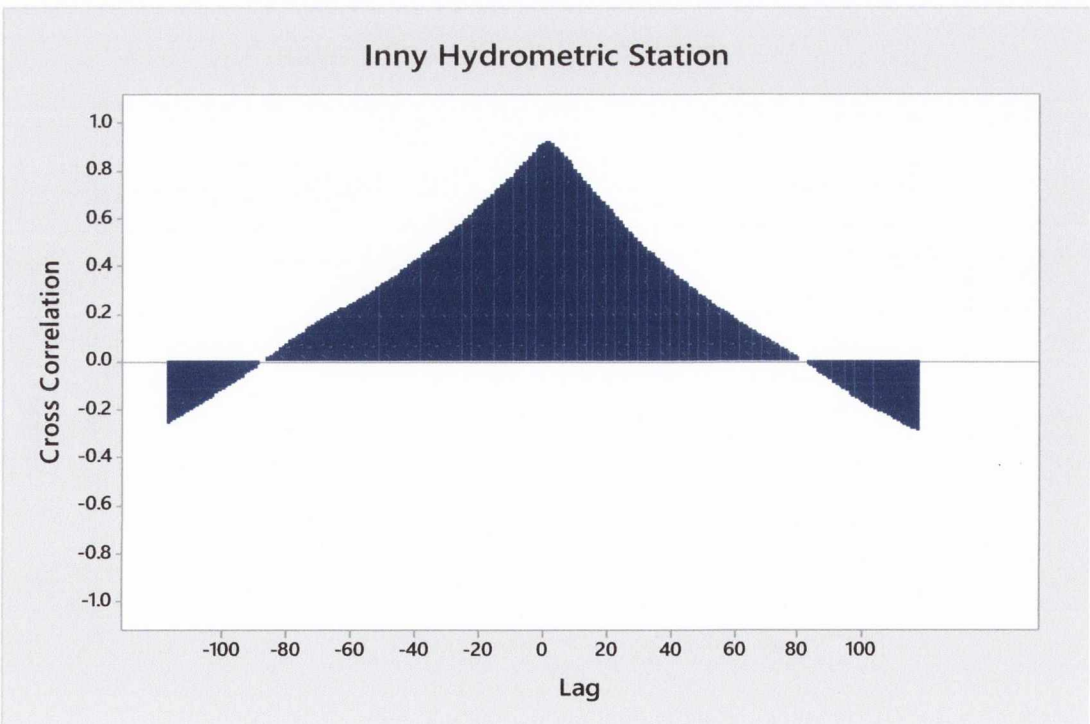

Figure 5.10: The cross correlation between the observed and the calculated water flow (m3/sec) time series for the Inny hydrometric station.

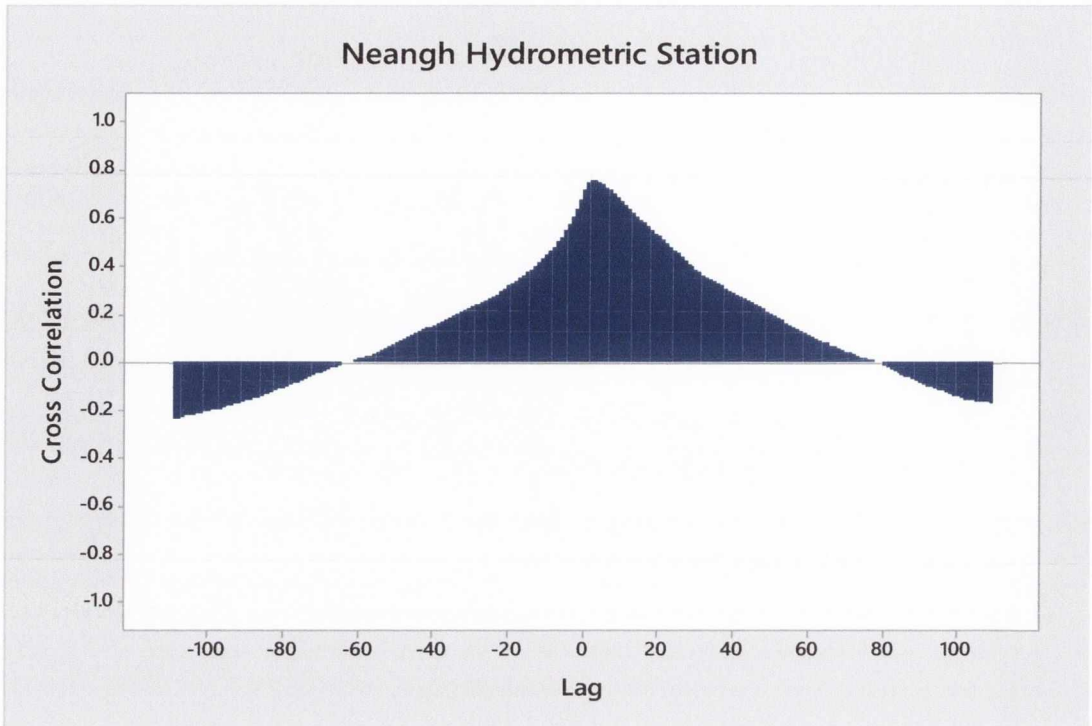

Figure 5.11: The cross correlation between the observed and the calculated water flow (m3/sec) time series for the Nenagh hydrometric station.

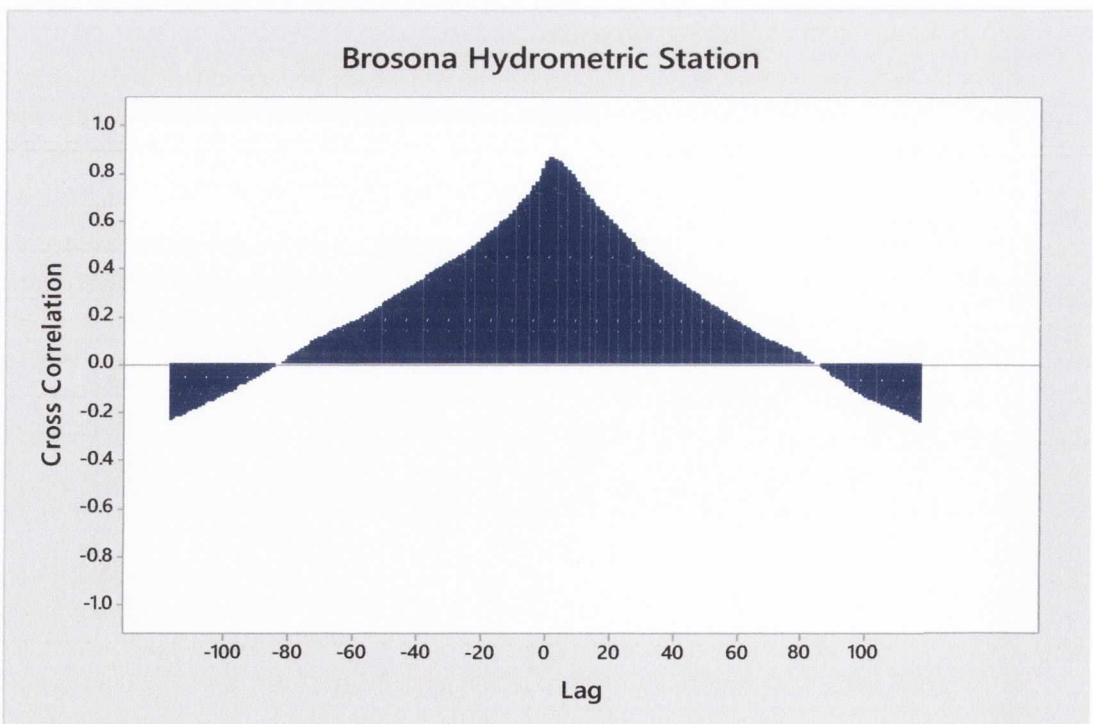

Figure 5.12: The cross correlation between the observed and the calculated water flow (m3/sec) time series for the Brosna hydrometric station.

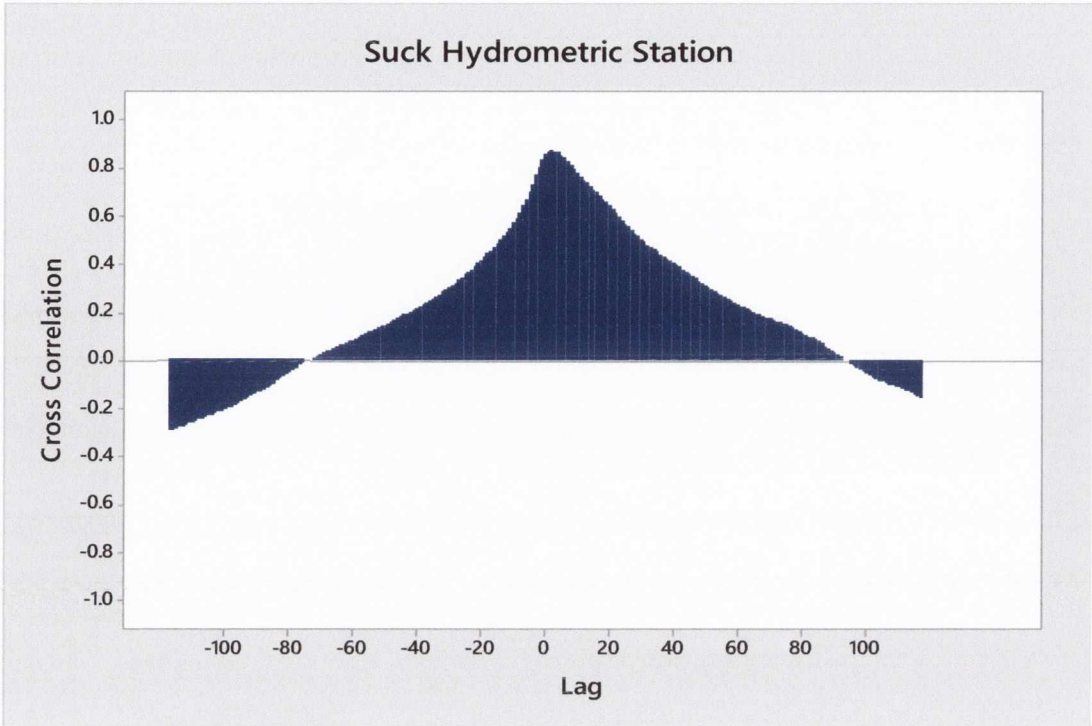

Figure 5.13: The cross correlation between the observed and the calculated water flow (m3/sec) time series for the Suck hydrometric station.

5.3.3 Long-term changes and trends

Since the previous sections of this chapter prove that the structured simplified hydrometric system works and can be used as representative of the complete hydrological system, this simplified system was then used for investigating the long-term changes and trends for the Shannon catchment.

The following equation (Eq5.13), developed from Figure 5.5, shows that the hydrometric station Lower-Shannon (25055) can capture the trends and the changes in the catchment, as the hydrological behaviour at this station is a result of the behaviours and reactions in all the other stations in the structured simplified hydrological system.

$$Q_{25055(\text{discharge point})} = Q_{25029} + Q_{25006} + Q_{26027} + Q_{25001} + Q_{26007} \pm \varepsilon \qquad \text{Eq5.13}$$

The Lower-Shannon hydrometric station contains the only discharge point for the system to the sea. By using Lower-Shannon hydrometric station, the total volumetric quantity of water flow in the catchment can be calculated by Equation 5.13. The total catchment volumetric change in the water flow can be captured at the Lower-Shannon hydrometric station by calculating the differences between the observed total flow at different time steps. These calculated differences in the total flow represent the summation of the water flow variations in all the sub-catchments. The calculated trend in the total flow at the Lower-Shannon is reflecting all the trends from all the sub-catchments in the system. Based on the previous argument, it can be concluded that

analysing the Lower-Shannon hydrometric station (25055) for long-term change and trends should give an understanding of the trends and changes for the whole Shannon catchment.

In this section, long-term trend analysis results for the water flow and water level parameters for the lower-Shannon station 25055 are presented.

5.3.3.1 Water flow parameter

Long-term variation and trend analysis for water flow related parameters have been addressed in many previous studies (Wang et al., 2015, Bhaduri et al., 2000, Esper et al., 2007, Li et al., 2007, Partal and Küçük, 2006). However, this study provides a systematic integrated GIS-statistical methodology that can analyse a large hydrological system taking into account the spatial variations in addition to the temporal variations and trends.

For the water flow parameter, an algorithmic transformation has been carried out on the original time series in order to obtain the normality condition, as seen in Figure 5.14.

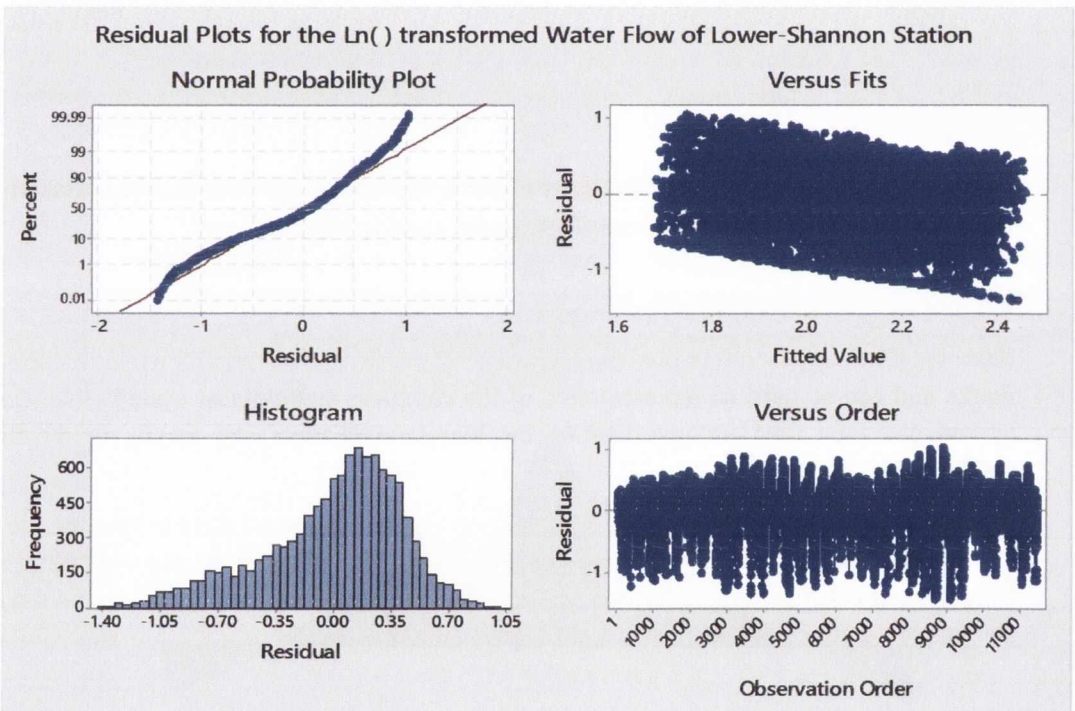

Figure 5.14: Normality and residual plots for the Ln ( ) transformed water flow time series of Lower-Shannon hydrometric station.

The flow time series component is decomposed and analyzed to get the seasonal signal and the trend. Figure 5.15 shows the detrended time series and the seasonally adjusted time series, showing a significant long-term variation and trend; the time series has a positive trend with respect to time. Figure 5.16 shows the flow time series decomposition plot, showing the smoothed (temporarily simplified time series) and trend analysis.

The decomposition plot shows the statistical quality parameters for the calculation (MAPE 18.7, MAD 0.33 and MSD 0.17) which shows a high-quality calculation.

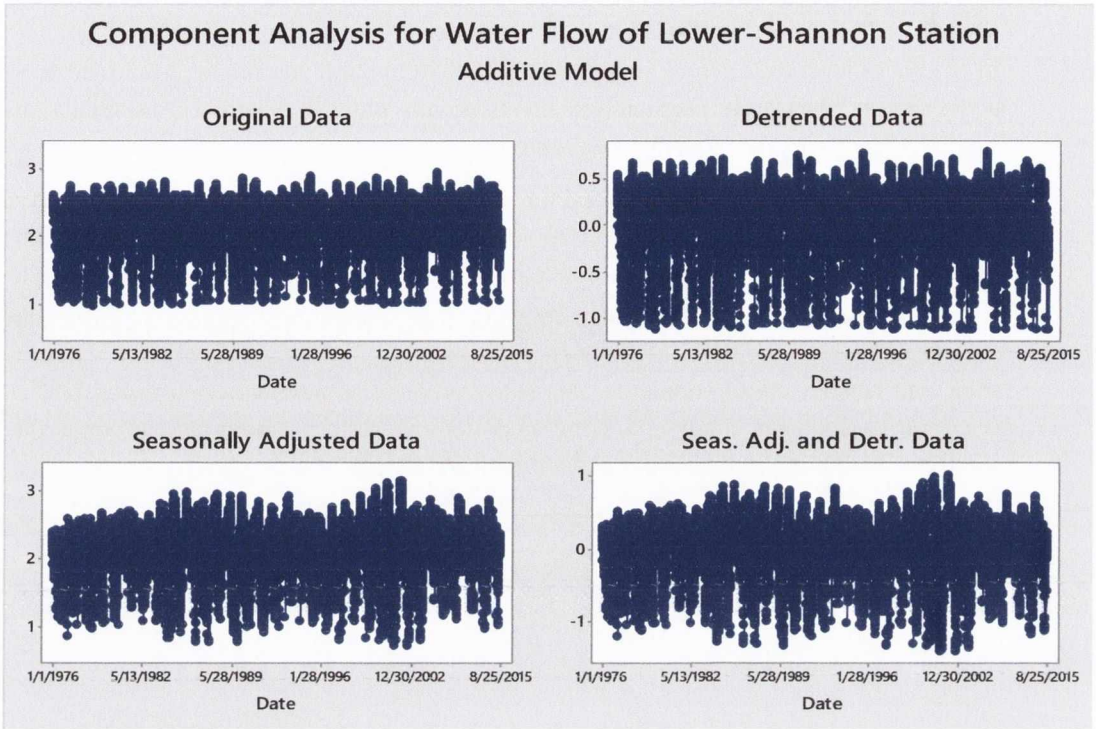

Figure 5.15: Time series component analysis for the Ln ( ) transformed water flow time series of Lower-Shannon hydrometric station.

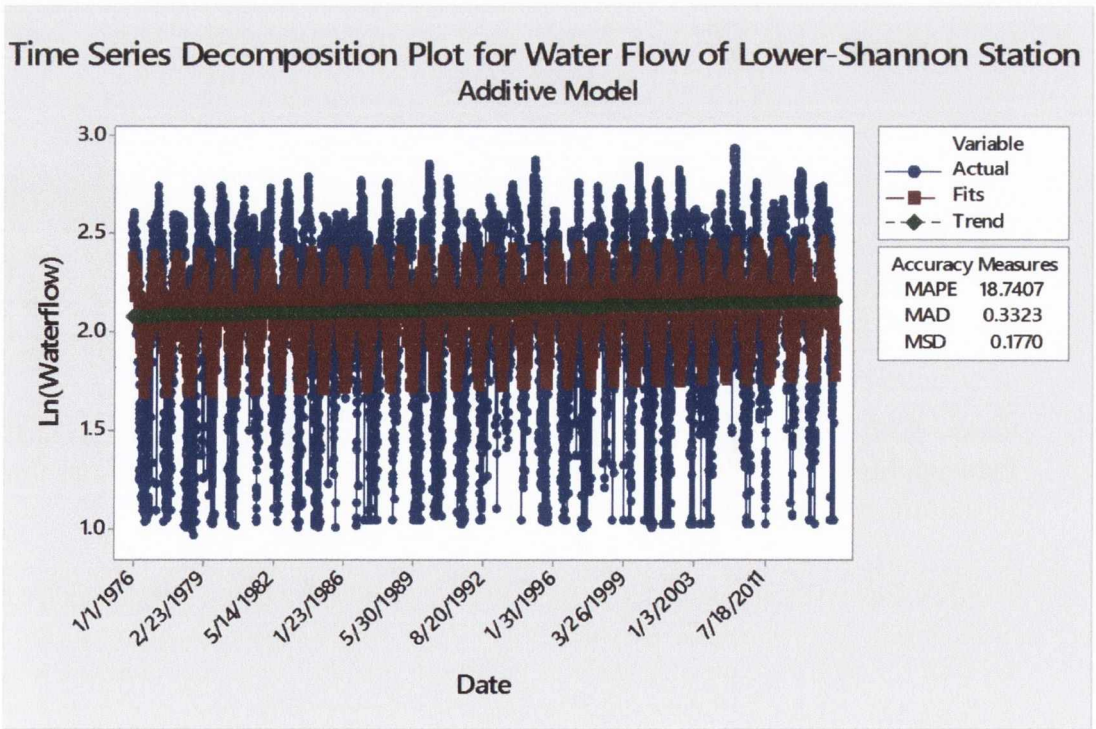

Figure 5.16: Time series decomposition plot for the Ln ( ) transformed water flow time series of Lower-Shannon hydrometric station.

5.3.3.2 Water level parameter

For the water level time series, no algorithmic transformation was required in order to obtain the normality condition as the original time series already showed evidence of normality, as seen in Figure 5.17.

The water level time series components are decomposed and analyzed to get the seasonal signal and the trend. Figure 5.18 shows the detrended time series and the seasonally adjusted time series, revealing a significant long-term variation and trend; with a positive trend with respect to time.

Figure 5.19 shows the water level time series decomposition plot; the plot shows the smoothed (temporarily simplified time series) and the trend analysis.

The decomposition plot shows the statistical quality parameters for the calculation (MAPE 0.40, MAD 0.134 and MSD 0.0328) which shows a high-quality results.

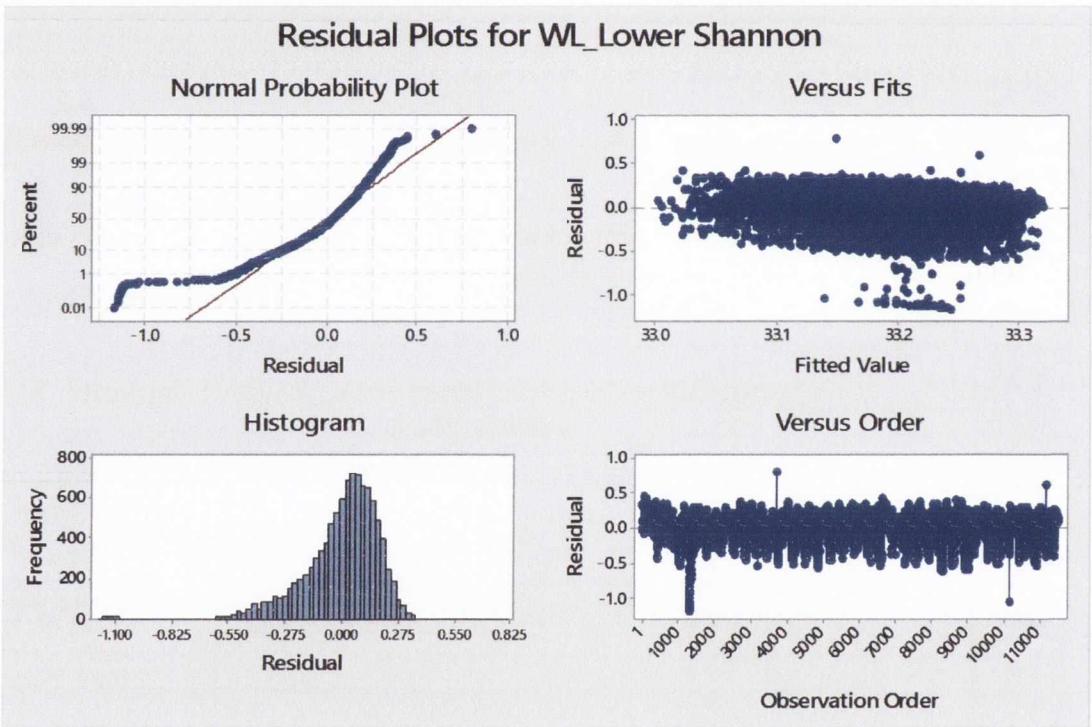

Figure 5.17: Normality and residual plots for the water level time series of Lower-Shannon hydrometric station.

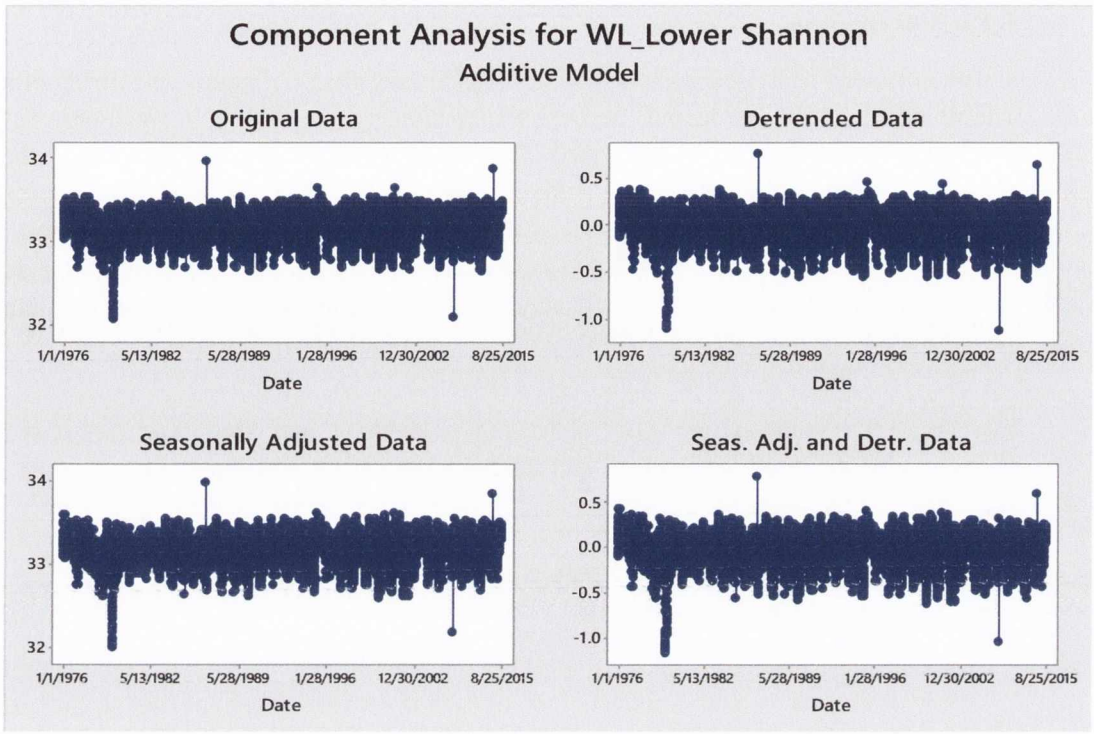

Figure 5.18: Time series component analysis for the water level time series of Lower-Shannon hydrometric station.

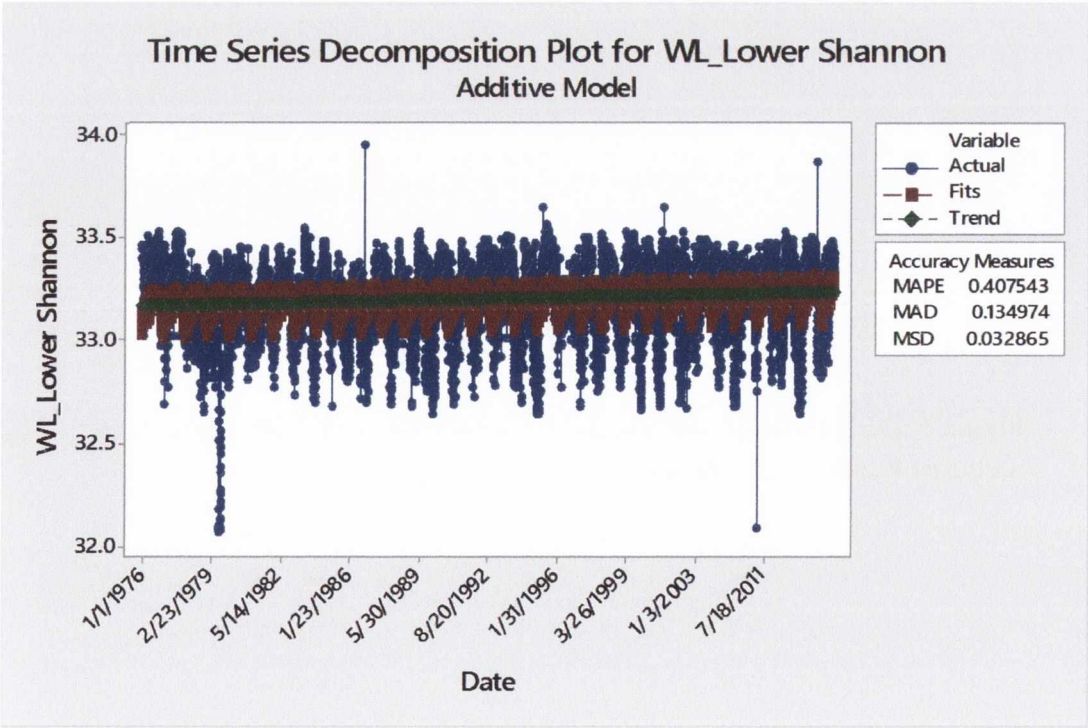

Figure 5.19: Time series decomposition plot for the water level time series of Lower-Shannon hydrometric station.

5.4 Conclusions

A new advanced analytical approach to investigate long-term variations and trends of a large hydrological system, taking into account the spatial and the temporal variations, has been developed in this chapter. An integrated GIS-based algorithm was used to simplify the large hydrological system to a structured system, which can be used for the long-term trend and variation analysis. The long-term change analysis included a study of the changes in water level and flow hydrological variables. Prior to conducting the long-term change analyses, the data was tested with the assumption of independence, normality, and homogeneity using subsequent data transformation methods (if required) in order to obtain a normal data set. The analysis shows changes in the flow over the study period (1976-2015).

This research combines the GIS geospatial algorithms and the time series statistical decomposition functions to analyze and evaluate the spatial and temporal variations of the Shannon River catchment in Ireland.

The conclusions are drawn as follows.

- The designed GIS-based algorithm for simplifying the large and complicated hydrological system is an efficient algorithm which can capture the spatial variation within the larger system.
- The long-term trend analysis showed a significant increase (at the 95% confidence level) of streamflow in the Shannon river for the period of 1976–2015. Seasonal and annual streamflow analyses showed consistency with the increasing trends.
- The algorithm is transferable to other river basins where there is a large catchment with a complicated hydrometric stations system.

Chapter 6. Land cover scenarios and projections simulation using an integrated GIS cellular automata algorithms

6.1 Introduction

Urbanization, land cover and land use transformation have been a universal and important socioeconomic phenomenon around the world. Urban growth has been accelerating with the significant increase in urban population (Cohen, 2004, DeFries et al., 2010, Preston, 1979). Urbanization is the most powerful and visible anthropogenic force that has caused the fundamental conversion from natural to artificial land cover in the cities around the world (Clarke et al., 1997, Cohen, 2004, DeFries et al., 2010, Preston, 1979).

Rapid urban expansion has marked effects on the environment and socio-economy, usually happening at the expense of prime agricultural land, with the destruction of the natural landscape and public open space such as the displacement of agriculture and forest (Kueppers et al., 2004, Sim and Balamurugan, 1991, Simmie and Martin, 2010, Chen et al., 2010), the decline in wetlands and wildlife habitats (Serneels and Lambin, 2001a), local impact on hydrology, the degradation of ecosystem compositions and the global impact of changes in atmospheric compositions (Foley et al., 2005). The spatiotemporal process of urban development and the social–environmental consequences of such development deserve serious study by urban geographers, planners, and policy makers because of the direct and profound impacts on human beings (Sim and Balamurugan, 1991, Simmie and Martin, 2010, Chen et al., 2010, Cohen, 2004, DeFries et al., 2010, Preston, 1979, Evans, 2006).

Hence, although urban areas cover a very small percentage of the world's land surface in comparison with other land use types, it becomes increasingly important to monitor and analyze the urban growth process, in addition to adopting appropriate sustainable land use plans. Continual, historical, and precise information about the urban land cover change is a prerequisite to the further analysis and sustainable development, which has been greatly emphasized. In order to obtain better understanding of the urban growth process, recent issues related to urban growth have attracted increasing attention, ranging from spatial and temporal land cover patterns, the factors affecting the urban growth, to urban growth scenarios by using Land Cover maps, GIS and different modelling techniques (Li, 2014, Pijanowski et al., 2002, Lambin, 1997, Liu et al., 2005, Herold et al., 2003, Herold et al., 2005).

Cities are characterized by an immense complexity and internal heterogeneity, but also display a certain degree of internal organization in terms of spatial patterns and temporal processes (Bourne, 1982, Grimm et al., 2000, Clarke et al., 1997, Turner, 1989). Understanding the spatial patterns and temporal processes of urban development has been the subject of numerous historical studies involving the application of models (Grimm et al., 2000, Clarke et al., 1997, Turner, 1989).

Land use/cover models have proven to be effective in describing and estimating urban development and have consequently been valuable for informed urban planning decision (Munshi et al., 2014, Herold et al., Herold et al., 2003, Sim and Balamurugan, 1991, Cohen, 2004). Cellular automata (CA) have gained popularity as modeling tools for urban process simulation. Since the pioneering work of Tobler (Tobler et al., 1979), several approaches have been proposed for modifying standard Cellular Automata (CA) in order to make them suitable for urban simulation (White et al., 1997, White et al., 1999, Itami, 1994, White and Engelen, 1993). Cellular Automata

based models are a powerful tool for representing and simulating spatial processes underlying the spatial decisions due to their accuracy, simplicity, flexibility and intuitiveness. This chapter investigates the implementation of an urban growth Cellular Automata (CA) model in the River Shannon Basin area in order to produce future land cover scenarios to be used in the dynamical water balance simulation for the Shannon catchment, helpful for hydrologists / water planners.

The main objective is to propose a useful tool that is able to monitor and capable of analyzing the urban growth process in the River Shannon Basin area. The focus is on the investigation of spatio-temporal dynamics of land cover patterns from land cover maps and simulation of the urban growth. The main objectives are: (i) extract and compare the historical land cover information for the investigation area through the interpretation of land cover maps and the using of quantitative measures, (ii) Identify any strategies currently formulated by the government to manage the extent and nature of urban growth in Ireland, (iii) Practically implement and evaluate the performance of the proposed integrated model between CA and GIS to predict future urban expansion, (iiii) quantify the future urban expansion in the River Shannon Basin area and investigate the spatio-temporal dynamics effects of the factors on urban growth to provide insights into how driving factors contribute to the urban growth.

6.2 Materials and methods

6.2.1 Cellular Automata (CA)

A cellular automaton can be defined as a self-operating machine that "*processes information, proceeding logically, inexorably performing its next action after applying data received from outside itself in light of instructions programmed within itself*" (Liu and He, 2009). Although Cellular Automata (CA) are models that simulate complex systems, CA have been defined as very simple dynamic spatial systems (Torrens, 2000a, Reinau, 2006, Liu and He, 2009). In Cellular Automata, the state of each cell in an array depends on the previous state of the cells within a neighborhood, according to a set of transition rules (White et al., 1999, White and Engelen, 1993, White et al., 1997). Despite their simplicity, some classes of CA are capable of "*universal computation*"(Wolfram, 1984), which means that some types of CA can have reproducing behaviours with a high level of complexity, such as of physical, biological or social complex systems. Cellular Automata has a remarkable potential for modelling complex spatiotemporal processes (Deutsch and Dormann, 2007, Barredo et al., 2003), and some simple CA have the ability to produce complex forms through simple set of rules (Deutsch and Dormann, 2007, Barredo et al., 2003). An understanding of CA leads to the conclusion that the description of complex systems need not be themselves complex (May, 1976, Couclelis, 1988).

Many processes in nature and in social systems are somehow too complicated to be able to be modeled through linear equations, therefore non-linear differential equations are needed in such cases. In these kinds of equations, a magnitude (X) at a time (t + 1) is the consequence of the magnitude in the preceding time (t). This configuration defines a basic non-linear differential equation (Barredo et al., 2003):

$$X_{(t+1)} = f(X_t) \qquad \text{Eq 6.1}$$

These equations, although fully deterministic, can produce a very dynamic behavior, from stable points and limit cycles to chaotic regimes (strange attractors) (Wolfram, 1984, May, 1976). Moreover, the behavior of non-linear differential equations may be indistinguishable from the one produced by a random process.

Wolfram (1984) stated that CA have been considered as spatial idealizations of partial differential equations with discrete space and time, thus it is not strange that CA shows behaviors analogous to non-linear ordinary differential equations. Therefore, it is not surprising that CA are capable of producing and simulating complex spatial processes showing non-linear dynamics such as some socio-spatial processes (i.e. spatial segregation of socio-economic groups). Moreover, CA produce spatial patterns that show chaotic behavior in the sense of irregular dynamics in a deterministic system. In these kinds of systems, the behavior depends on its own internal logic (Barredo et al., 2003).

In CA, cells are the basic and smallest spatial unit in a cellular space which must manifest some adjacency or proximity (Li and Yeh, 2000). They are typically represented by a regular grid of two dimensions usually composed of square cells, although some researchers have proposed hexagonal cells to obtain a more homogeneous neighborhood (Iovine et al., 2005). Moreover, the regular cell can be modified by using irregular tessellations such as Voronoi polygons (Shi and Pang, 2000). Santé et al. (2010) stated that irregular cells may provide a more realistic representation of the objects being modeled. The cell size is the area of the landscape each cell will cover. In the early applications of cellular automata in urban modeling, the resolution of cells seemed to be less an issue of concern. The use of cell resolution was either based on the availability of data or on the convenience for computation. Therefore, the resolution of cells varies significantly from one application to another. Li and Yeh (2000) in their study to simulate urban land use pattern for Dongguan city in China used 100 m cell size, however Clarke et al. (1997) used a cell size of 300 m for the San Francisco Bay area. Indeed, different researchers have used different cell sizes related to the different conditions of the study area (White and Engelen, 1993, Cho and Swartzlander, 2007, Chen and Mynett, 2003).

The cell state defines the attributes of the system. Each cell can take only one state from a set of states at any one time. The state can be a number that represents a property. In urban-based cellular automata models, the states of cells may represent the types of land use or land cover, such as urban or rural, or any specific type of land use; or it may be used to represent other features of the urban area, such as social categories of populations (immigrant vs. native population) as was proposed by Portugali and Benenson (1995).

A neighborhood is a set of one or more locations that are within a specific distance and/or have a relationship to the particular location (Verburg et al., 2004, Balzter et al., 1998, Wolfram, 1983). A cell's neighborhood is the region that serves as an input to assess the neighborhood effect in the transition rules. This effect is calculated as a function of a cell's own state and the state of the cells within its neighborhood. The neighborhood configuration determines the distribution and number of neighborhood cells that will affect the evolution of each central cell (Mnard and Marceau, 2005, Balzter et al., 1998, Wolfram, 1983). Barredo and Demicheli (2003) stated that neighborhood configuration in a CA is generally characterized by neighborhood size and shape. Mnard and Marceau (2005) carried out a sensitivity analysis which showed that neighborhood size and type significantly affect the performance of the CA model employed for land use change modeling.

The traditional neighborhood types for two-dimensional raster based CA models are Von Neumann neighborhood and rectangular (Moore) neighborhood (Flache and Hegselmann, 2001, Vezhnevets and Konouchine, 2005). The Von Neumann neighborhood consists of four cells which include the North, South, East, and West neighbors of a cell in question. The Moore neighborhood consists of eight cells which include the cells defined in the von Neumann

neighborhood as well as cells in the North-west, North-east, South-east, and South-west directions, which are commonly used in Cellular Automata model applications (Wu and Webster, 1998a, Lau and Kam, 2005, Flache and Hegselmann, 2001, Vezhnevets and Konouchine, 2005). In the research carried out by Li and Yeh (2000), it was proposed that the use of a rectangular neighborhood such as Moore might produce significant distortions between cells at different directions. While, the circular neighborhood has no bias in all directions, which was adopted by many studies in order to improve the model's performance (White and Engelen, 1997). Neighborhood size defines the extent of interactions between land use and the dynamics of the system (Caruso et al., 2005). In general, the effect of neighborhood cell decreases with the increasing distance to the central cell. Each cell in the neighborhood should receive a calibrated weight according to its state and the distance to the central cell. Some researchers proposed that neighborhood effect of different cells may be considered as an approximation of distance decay (Barredo et al., 2003). A distance decay function is usually introduced in defining a neighborhood, so that the effect of a neighborhood cell decreases with the increase in distance between both cells.

The definition of the transition rules of a CA model is the most important part to achieve realistic simulations of land use and land cover change (Verburg et al., 2004). This is the key component of CA because these rules represent the process of the system being modeled, and are thus essential to the success of a good modeling practice (White, 1998).

The traditional transition rules are dependent on the current cell state and its neighborhood effects (Jenerette and Wu, 2001, Li et al., 1990, Liu et al., 2008). In the context of urban growth, however, a variety of factors have significant impacts on urban growth, such as physical suitability for a specific land use, accessibility, socioeconomic factors, urban planning factors, and stochastic disturbance related to the complexity of the human system. Consequently, the CA model cannot generate an observed urban pattern by using a traditional transition rule without considering various factors. The transition rules involving the effects of different factors, allow for a more realistic simulation (Jokar Arsanjani et al., 2013, Li et al., 1990, Liu et al., 2008).

In addition, traditional CA models employ only one uniform transition rule for different periods and sub-regions, while the urban growth process may vary over time and space, so it is necessary to apply different transition rules to the specific characteristics of each period and area. Spatial and temporal varying transition rules can be obtained by calibration (Geertman et al., 2007, Li et al., 1990, Liu et al., 2008). According to the definition of cellular automata, the states of all cells are updated simultaneously every iteration. However, this restriction can be released by operating the CA model at different temporal speed for different cells, as was seen in the work carried out by Uljee, Engelen, and White (1996) as their model simulated the low-lying areas on a monthly basis and the upland areas on a yearly basis (Liu, 2008).

Urban development resembles the behavior of a cellular automaton in many aspects. The space of an urban area can be regarded as a combination of a number of cells, each cell taking a finite set of possible states representing the extent of its urban development. The state of each cell evolves in discrete time steps according to some local rules.

6.2.2 Data setup

The CORINE dataset (EPA, 2012, NPWS, 2015, EPA, 2015) is one of the main datasets that was used in this study. The CORINE Land Cover is a vector map with a scale of 1:100 000, a minimum cartographic unit (MCU) of 25 ha and a geometric accuracy better than 100 m. It maps homogeneous landscape patterns, i.e. more than 75% of the pattern has the characteristics of a given class from the nomenclature (2012). This nomenclature is a 3-level hierarchical classification system and has 34 classes at the third and most detailed level, see Table 6.1.

Table 6-1: Land use classes used in the study (EPA, 2015).

Level 1	Level 2	Level 3
1.Artificial surfaces	1.1 Urban fabric	Continuous urban fabric
		1.1.2 Discontinuous urban fabric
	1.2 Industrial, commercial and transport units	1.2.1 Industrial or commercial units
		1.2.2 Road and rail networks and associated land
		1.2.3 Sea ports
		1.2.4 Airports
	1.3 Mines, dumps and construction sites	1.3.1 Mineral extraction sites
		1.3.2 Dump
		1.3.3 Construction sites
	1.4 Artificial non-agricultural vegetated areas	1.4.1 Green urban areas
		1.4.2 Sport and leisure facilities
2. Agricultural areas	2.1 Arable land do whatever they did	2.1.1 Non-irrigated arable land
		2.1.2 Permanently irrigated land
		2.1.3 Rice fields
	2.2 Permanent crops	2.2.1 Vineyards
		2.2.2 Fruit trees and berries plantations
		2.2.3 Olive groves
	2.3 Pastures	2.3.1 Pastures
	2.4 Heterogeneous agricultural areas	2.4.1 Annual crops associated with permanent crops
		2.4.2 Complex cultivation patterns
		2.4.3 Land principally occupied by agriculture with significant areas of natural vegetation
		2.4.4 Agro-forestries
3.Forest and semi-natural areas	3.1 Forests (one category)	3.1.1 Broad-leafed forest
		3.1.2 Coniferous forests
		3.1.3 Mixed forest
	3.2 Scrub and/or herbaceous vegetation associations	3.2.1 Natural grassland
		3.2.2 Moors and heathlands
		3.2.3 Sclerophyllous vegetation
		3.2.4 Transitional woodland-scrub
	3.3 Open spaces with little or no vegetation	3.3.1 Beaches, dunes, sand
		3.3.2 Bare rocks
		3.3.3 Sparsely vegetated areas
		3.3.4 Burnt areas
		3.3.5 Glaciers and permanent snowfields
4.Wetlands	4.1 Inland wetlands	4.1.1 Inland marshes

		4.1.2 Peat bogs
	4.2 Coastal wetlands	4.2.1 Salt marshes
		4.2.2 Salines
		4.2.3 Intertidal flats
5. Water bodies	5.1 Continental waters	5.1.1 Stream courses
		5.1.2 Water bodies
	5.2 Marine waters	5.2.1 Coastal lagoons
		5.2.2 Estuaries
		5.2.3 Sea and ocean

The CORINE (Co-Ordinated Information on the Environment) data series was established by the European Community (EC) as a means of compiling geospatial environmental information in a standardized and comparable manner across the European continent. The first iteration of the data series covered the reference year of 1990 with subsequent releases covering the years 2000, 2006 and 2012. The first dataset in 1990 provided a 'snapshot' baseline of the geographical distribution of natural and built environments across Europe. Through this baseline and subsequent updating of changes, CORINE has become a key data source for informing environmental and planning policy on a national and European level. CORINE is coordinated and part-financed by the European Environment Agency under the Copernicus (formerly GMES) land monitoring program. On a national level in Ireland, the Environmental Protection Agency has been coordinating the CORINE project since 2000 under its role as the Irish National Focal Point (NFP) and National Reference Centre (NRC) for EIONET and GMES Land monitoring activities (EPA, 2012, OPW, 2015b, Office, 2011, NPWS, 2015, EPA, 2015).

Land-cover data sets for 2000, 2006 and 2012 constituted a principal source of data for this study. The data were used to examine spatial patterns and trends of urban expansion over time, using GIS techniques. Further analysis explored the conversion history of particular land-use classes. For input into the CA model, the 34 classes in the land use map bases on level 3 nomenclatures were reduced to 5 by aggregating related classes from the initial land use layer, see Table 6.1. This simplification to the land use classes has been done in order to make the computational process possible.

Land use modeling, especially urban growth, is a complex process which involves the interaction influence of various factors. According to data availability, the possible variables representing natural, socioeconomic, spatial policies and neighborhood factors were selected to design this study are listed in Table 6.2.

6.2.2.1 Modeling data classification

Table 6-2 summarises the different factors and datasets that used in this study. The table shows that the collected datasets have different year of collections, the only reason for this is the data availability. It was not possible to get all the datasets on the same year, but the closest datasets to each other have been selected for this study. The difference in the observation years for the datasets could have some impact on the results, but as the main aim of this study is to produce long-term predictions of the land cover maps, then the little differences in the observation time for the data sets should have limited effects on the results.

- **Physical factors**

A Digital Elevation Model (DEM) obtained from Eurostat at a spatial resolution of 25 m of the study areas was used to represent topography. Slope gradient was derived from the elevation surface using 3D analyst package toolbox in ArcMap (Minami, Booth, 2000, McCoy et al., 2001).

- **Socioeconomic factors**

The influence of the socioeconomic conditions in the region can be best characterized by the access of that location to a socioeconomic center, which has a significant effect on the urban growth pattern (Li et al., 2013, Verburg et al., 2004). In this study, the socioeconomic center can be represented by town/city centers, with the data obtained from the Central Statistics Office, Ireland (CSO). These centers can reflect the accessibility effect on land use development at different levels.

Transportation is an important factor in accelerating urban development and attracting new development. A good transportation network increases the accessibility of land (Miller, 1999, Couclelis, 2000). Consequently, areas with good accessibility are more easily selected for urban development. Major roads (motorways and national primary roads) and minor roads (national secondary roads and regional roads) were considered in this study. The data were obtained from Environmental Protection Agency (EPA), see Table 6.2. Because of the infrastructure construction, the traffic system changes all the time, therefore, in this study, it was assumed that the roads dataset remained unchanged during one period (2000-2012).

Population is one of the main drivers of urban growth: more urban land will be required to satisfy further growth of urban population in the future. The population variable was represented by the population density of Electoral Divisions (EDs) administrative units because the overall population for the whole study area is more related to the demand of urban land, and has less effect on urban growth allocation. The Electoral Divisions (EDs) unit are the smallest legally defined administrative areas in the State for which Small Area Population Statistics (SAPS) are published from the Census.

- **Spatial Policy factor**

Policy variables affect urban growth because they can be simulated as constraints or incentives to development (Buss, 2001, Jantz et al., 2004). Development Plans constitute the basic policy document of the land use and development system in Ireland. It is a statutory function of local government to produce a county development plan.

The development plan generally contains a written statement in addition to a number of maps. Land use development policy is primarily articulated through the designation of land use objectives specific to particular lands within the planning authority's jurisdiction. The approach taken to the zoning of land varies between planning authorities. However, in general, most of the land within urban areas is zoned for a particular objective, while in the case of many rural areas specific land use zoning objectives are not designated. The interpretation of each zoning objective may be further refined through the inclusion of a matrix where a large number of potential land uses are classified under each zoning objective as acceptable, open for consideration or not acceptable. In this study, initial attempts were made to apply direct translation of the development plans into zoning maps for the CA model. The spatial datasets used were registered to the same Irish Transverse Mercator (ITM) coordinate system and sampled to the same cell size of 100 m x 100 m, which was sufficient to capture the detailed information about urban dynamics while

keeping the volume of computation manageable. As spatial policy factors a combined dataset of the layout of special protected areas, special areas of conservation and natural heritage areas has been used.

Table 6-2: List of the used datasets in this study.

Variable	Year	Description	Sources
Physical factor			
Slope		It was derived from Digital Elevation map (DEM), resolution of 25 m	European statistics, Eurostat
Socioeconomic factor			
Dist2Majr	2010	Distance to Major Road	Environmental Protection agency (EPA)
Dist2Minr	2005	Distance to Minor Road	Environmental Protection agency (EPA)
Dist2Town	2006	Distance to Towns/Cities	Central Statistics Office Ireland (CSO)
PopDen	2002	Population Density collected using Electoral Divisions units	Central Statistics Office Ireland (CSO)
Spatial Policy factor			
Environmental	Published 2013 updated 2015	Layout of Special Protection Areas, Special Areas of Conservation and Natural Heritage Areas	The National Parks and Wildlife Service (NPWS)
Neighborhood factor			
Dist2Urban	2000	Distance to existing Urban area	Extracted from Land Cover Map Obtained from Environmental Protection agency

6.2.3 Model setup and integration with the GIS platform

Modelling geographical phenomena and processes using CA simulations are based on constructing regular spatial tessellation models. These models are naturally related to raster-based GIS, which gives the opportunity to use the geo-processors' advantages related to the integration of GIS and CA models (Wagner, 1997, Takeyama and Couclelis, 1997, Batty et al., 1999, Clarke and Gaydos, 1998, Li and Yeh, 2000).

Even using a loose coupling approach to integrating GIS and a CA model, GIS can provide spatial data that forms the initial configuration in a CA model, and the simulation results can be returned to a GIS for further processing, visualization, and storage (Wesselung et al., 1996, Clarke and Gaydos, 1998). The application of CA in modeling urban development is "*virtually impossible without the data management capabilities of GIS*" (Clarke and Gaydos, 1998). Therefore,

applications of CA in geography are mostly integrated within a GIS; consequently, they can work at a high spatial resolution with computational efficiency.

In this study, a CA GIS-based algorithm has been implemented in the GIS environment using raster data formats in order to simulate the urban expansion and land use trends in the Shannon River catchment. The calibrated model has then been used to produce future land use scenarios.

Cellular Automata models require all input maps to be strictly comparable; they must cover the same area and have the same resolution. Various spatial analysis techniques in ArcGIS were applied to process the raw data and verify the quality and consistency of data collected from different sources. Land use maps of 2000, 2006 and 2012 were used in this study (EPA, 2012, EPA, 2015). Table 6-3 shows the adopted main land cover class that used in the simulation for this study. The adapted classes have been aggregated based on the Table 6-1. This classification of the land cover class was adopted from (Li, 2014) in this study.

Table 6-3: Land cover classes used in the simulation.

Land Cover classes	Description
Water bodies	Stream courses, Water bodies, Coastal lagoons, Estuaries, Sea, and ocean.
Wetlands	Inland marshes, Peat bogs, Salt marshes , Salines, Intertidal flats
Urban area	Road and rail networks and associated land, Airports, Mineral extraction sites, Dump, Green urban areas, Sport and leisure facilities, Continuous urban fabric, Discontinuous urban fabric, sea port, Industrial and commercial, construction site.
Agricultural areas	Non-irrigated arable land, Pastures, Complex cultivation patterns, Land principally occupied by agriculture with significant areas of natural vegetation.
Forest	Broad-leafed forest, Coniferous forests, Mixed forest, Natural grassland, Moors and heathlands, Transitional woodland-scrub, Beaches, dunes, sand, Bare rocks, sparsely vegetated areas.

Using the ArcGIS 10.1 conversion tool, the Land Cover maps were converted from a vector to raster grid according to the maximum area principle.

Change detection analysis was used to analyse patterns of Land Cover change during the study period. Change detection can be defined as the process of identifying differences in the states of an object by observing it at different times (Singh, 1989).

Several methods can be used for change detection, such as image differencing, principal component analysis and post classification detection (Lu and Weng, 2004).In this study, post classification was selected as the change detection method to identify the changes in land cover

over different time intervals for the River Shannon Basin Area. The method involves independent classification results for each end of the time interval of interest, followed by a pixel by pixel comparison to detect land cover changes (Coppin et al., 2004). The post-classification method generated a two-way cross matrix, providing "from-to" land cover conversion information, as shown in Tables 6.4 & 6.5. The change detection analysis was conducted primarily through the use of ArcGIS by using the overlay tool. A new thematic map containing a different combination of "from-to" change information was also produced for each period. GIS has been applied widely to visualize the spatiotemporal process of physical changes (Batty, 1998, Clarke and Gaydos, 1998). The main advantage of this method lies in the fact that each land use map is classified separately; moreover, the Land Cover matrix produced was also used to get the conversion rate from one land use to another between two periods.

Table 6-4: Transition matrix for Shannon catchment based on land cover data for 2000 and 2006, units in kilometer square.

Land Cover categories 2006	Land Cover categories 2000						
	Water bodies	Wetlands	Urban area	Agricultural	Forest	Total 2006	% 2006
Water bodies	427.08	2.31	0.14	7.75	1.93	439.21	2.4%
Wetlands	9.43	1531.54	1.25	114.05	167.25	1823.52	9.9%
Urban area	0.6	0.92	229.84	48.3	5.95	285.61	1.6%
Agricultural	24.98	270.61	17.79	12838.66	429.82	13581.86	73.9%
Forest	4.44	306.69	0.65	363.98	1565.3	2241.06	12.2%
Total 2000	466.53	2112.07	249.67	13372.74	2170.3	18371.26	100.0%
% 2000	2.5%	11.5%	1.4%	72.8%	11.8%	100.0%	

Table 6-5: Transition matrix for Shannon catchment based land cover data for 2006 and 2012, units in kilometer square.

Land Cover categories 2012	Land Cover categories 2006						
	Water bodies	Wetlands	Urban area	Agricultural	Forest	Total 2012	% 2012
Water bodies	406.62	5.24	0.83	22.5	4.47	439.66	2.39%
Wetlands	5.22	1637.13	0.86	112.73	54.36	1810.3	9.85%
Urban area	0.83	1.15	243.1	45.62	2.04	292.74	1.59%
Agricultural	22.37	114.29	39.46	13202.12	178.71	13556.95	73.79%
Forest	4.17	65.71	1.36	198.89	2001.48	2271.61	12.37%
Total 2006	439.21	1823.52	285.61	13581.86	2241.06	18371.26	100%
% 2006	2.39%	9.93%	1.55%	73.93%	12.20%	100%	

The overall trend analysis and visualization of the data in ArcGIS demonstrates that the urban areas of River Shannon Basin had significantly increased from 1.4% in 2000 to 1.6% in 2006 - an

overall change percentage of 14.4 %, equating to 35.94 km^2 increase in the urban area. The analysis showed that urban area cover increased at the expense of agricultural and forest cover. Forest cover increased at the expense of wetlands and agricultural cover, as the trend toward forest regeneration on abandoned land continued. The analysis showed the forest cover had increased from 11.81% in 2000 to 12.20% in 2006 with an overall increase of 3.3%, equating to 70.81 km^2. Moreover, agricultural cover increased as well from 72.79% in 2000 to 73.93% in 2006 at the expense of wetlands, water bodies and forest cover mainly, with an overall increase of 209.12 km^2, i.e. 1.56%. The wetlands had been reduced severely with a percentage of 11.5% in 2000 to 9.93% in 2006 - a reduction of 288.55 km^2, – (13.7%).

On the other hand, urban area increased from 1.55% in 2006 to 1.59% in 2012 at the expense of agricultural and forest covers mainly, with an overall increase of 2.5% equating to 7.13 km^2. The recession from 2007 to 2012 highlighted the major impacts on the environment and society of a contraction in economic activities and development decisions. This might be one of the reasons that the urban expansion from 2006-2012 is less than urban expansion during 2000-2006. The forest area slightly increased from 12.20% in 2006% to 12.37% in 2012 at the expense of wetlands and agricultural area, with an overall increase of 1.36%, i.e. 30.55 km^2. The agricultural cover reduced slightly from 73.92% in 2006 to 73.79% in 2012; the overall reduction land was 24.91 km^2 which is -0.18%. Also, wetland area had witnessed a small reduction from 9.93% in 2006 to 9.85% in 2012 with an overall reduction of 13.22 km^2, equivalent to -0.72%. Figures 6-1, 6-2 and 6-3 show the Land Cover classification for the periods of 2000, 2006 and 2012, these maps show the reclassified land cover Corine data sets according to the adopted land cove class to be used for the CA simulations.

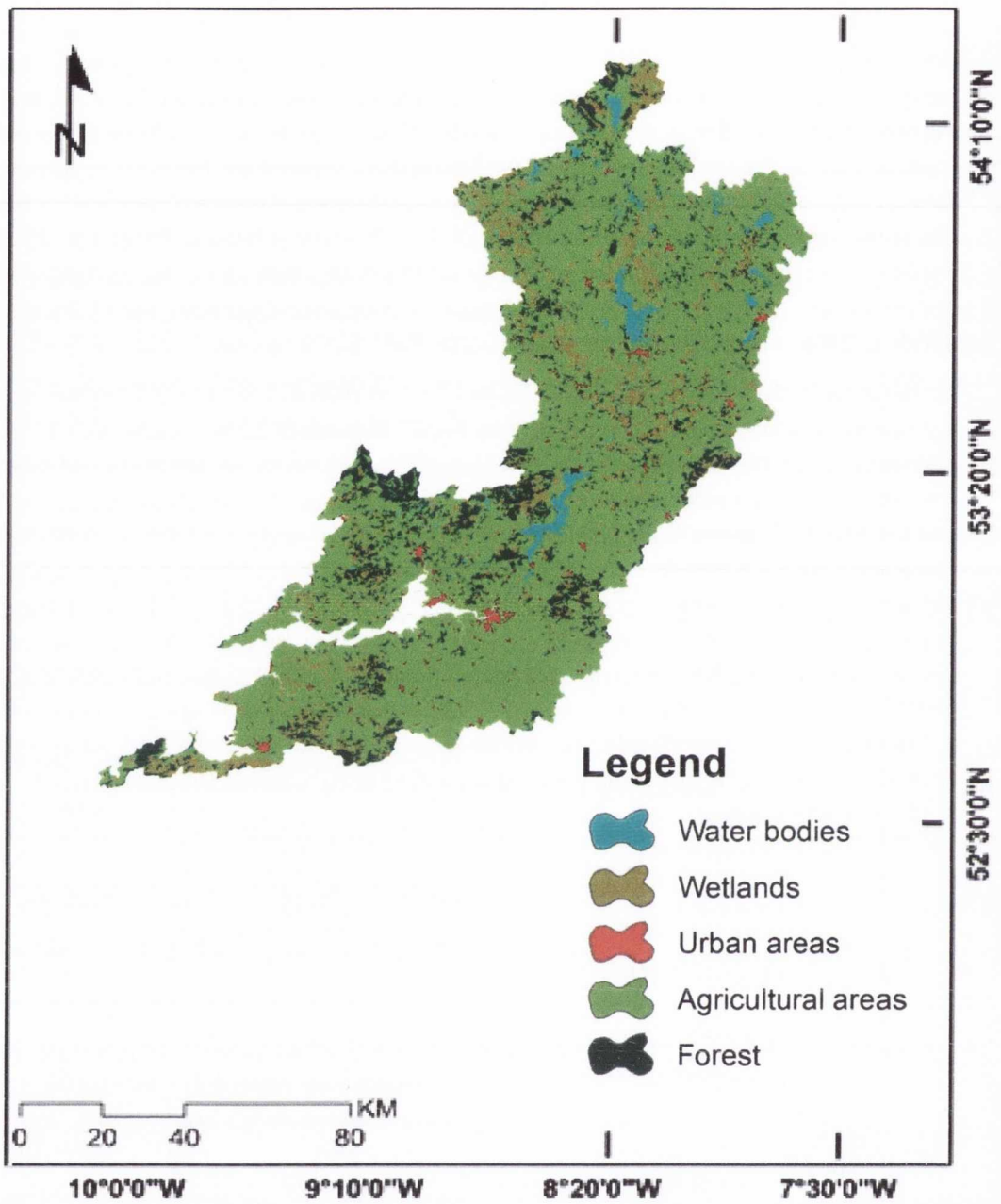

Figure 6.1: Reclassed land cover map for 2000 (Corine dataset).

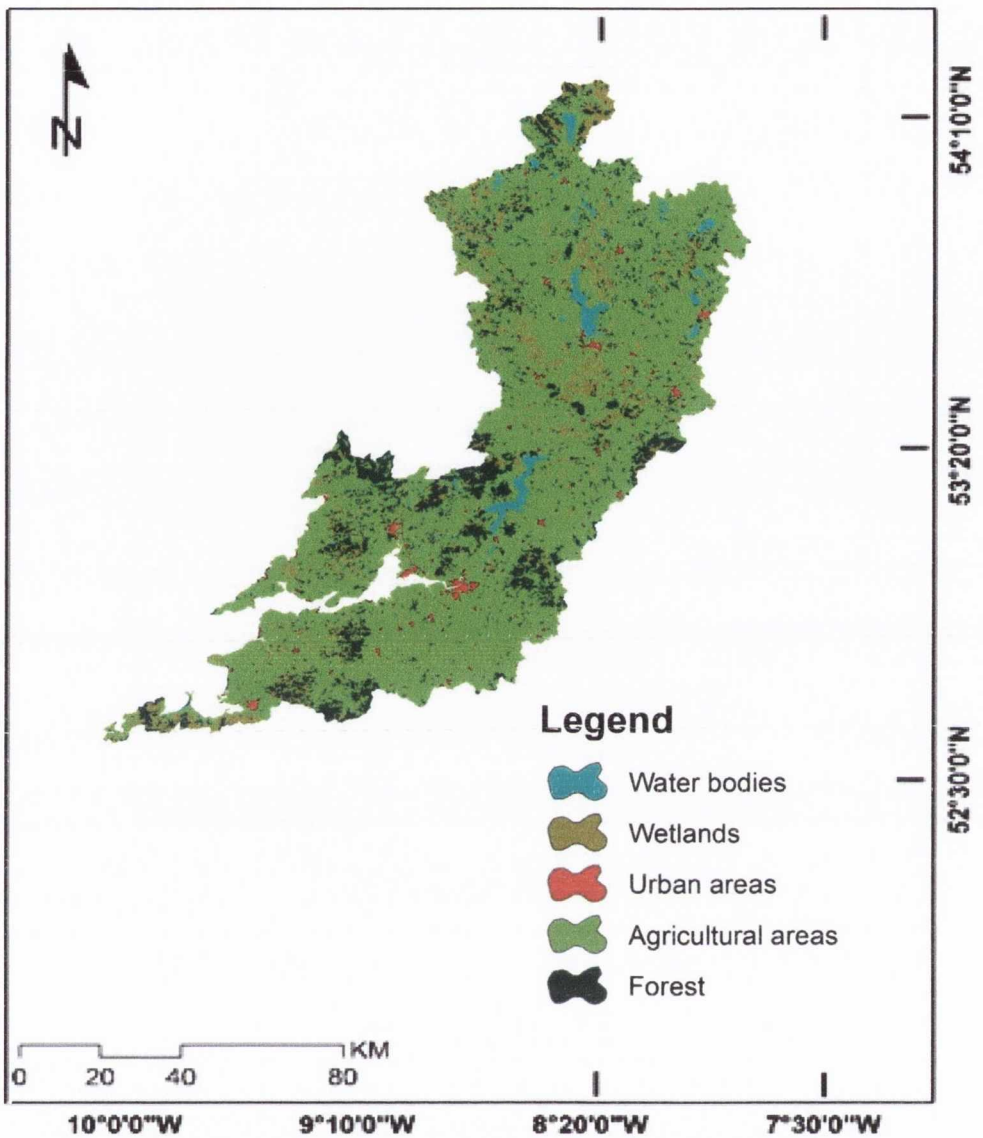

Figure 6.2: Reclassed land cover map for 2006 (Corine dataset).

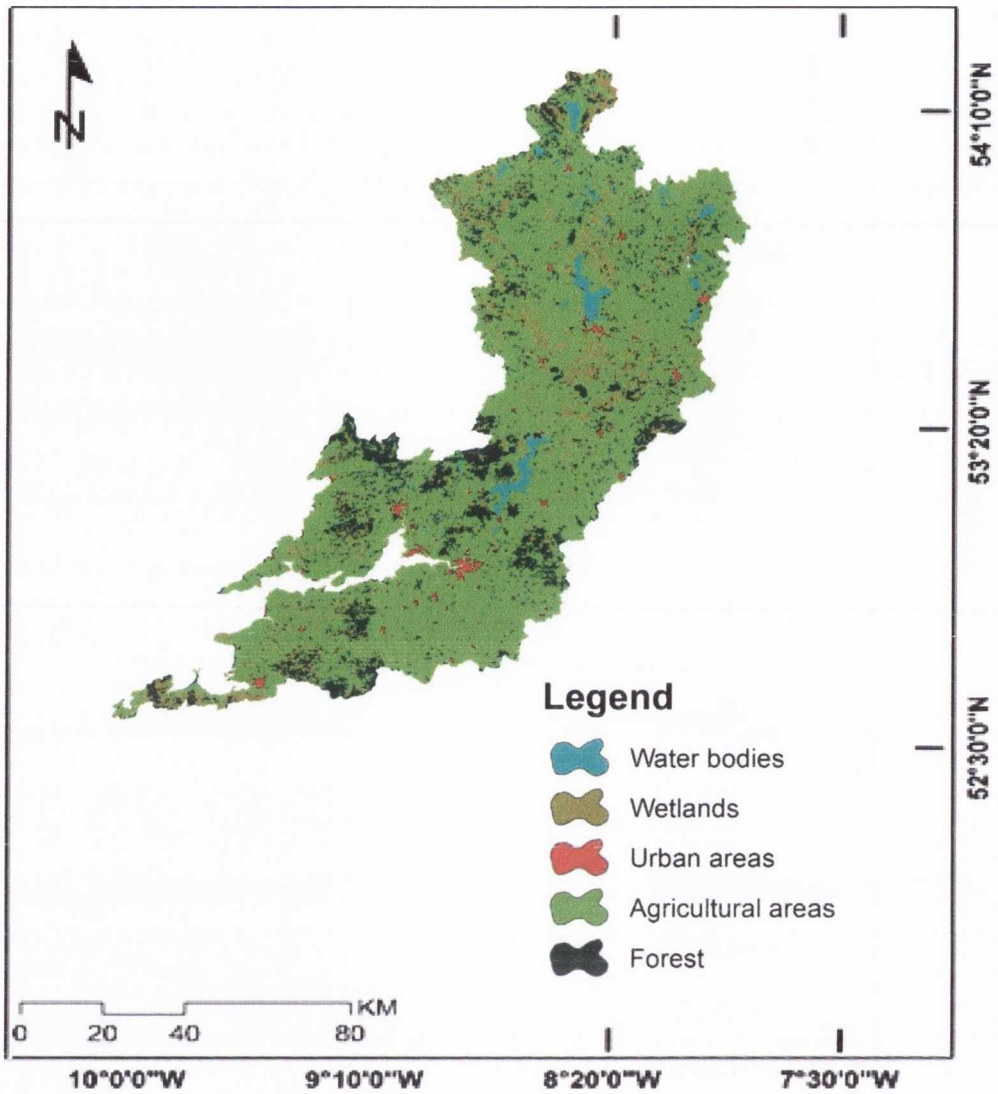

Figure 6.3: Reclassed land cover map for 2012 (Corine dataset).

6.2.3.1 Simulation driving factors, constraint, and suitability map

One of the main inputs for CA urban expansion simulation is the land suitability map. The land suitability map overlay is generated by the mechanism overlaying the driving factor maps as well as several restrictions, such as zoning, protected areas, slope, hazards, etc., so in other words it represents the suitability of each cell in the simulated area to the urban expansion.

In order to prepare the suitability map, driving factors maps which are the factors that drive a certain area to be converted to urban area, distance to major and minor roads, population density, distance to towns/cities and distance to existing urban area, need to be prepared first. Secondly, constraint maps need to be prepared which are the slope and protected areas in this study.

6.2.3.1.1 Transportation Network

Transportation plays an important part in urban growth because a good transportation increases the accessibility of land and decreases the cost of construction (Reilly et al., 2009, Du and Mulley, 2006, Rietveld and Bruinsma, 2012, Geurs and Van Wee, 2004). Consequently, areas with good accessibility are more easily selected for urban development. Major roads (motorways and

national primary roads) and minor roads (national secondary roads and regional roads) were considered in this study. The data map used for the major roads was for 2010 and for the minor roads was for 2005. Because of infrastructure construction, the traffic network continually changes. However, in this study, it was assumed that the roads dataset remained unchanged; therefore, these transportation maps were entered for Land Cover 2000 assuming the transportation network were similar during that period. The accessibilities were calculated as the Euclidean distance using the Spatial Analyst geo-processor. The Euclidean distance tools describe each cell's relationship to a source or a set of sources based on the straight-line distance. It gives the distance from each cell in the raster to the closest source, for example, it gives the closest distance to town. Figures 6.4 & 6.5 show the major and minor road Euclidean distance respectively.

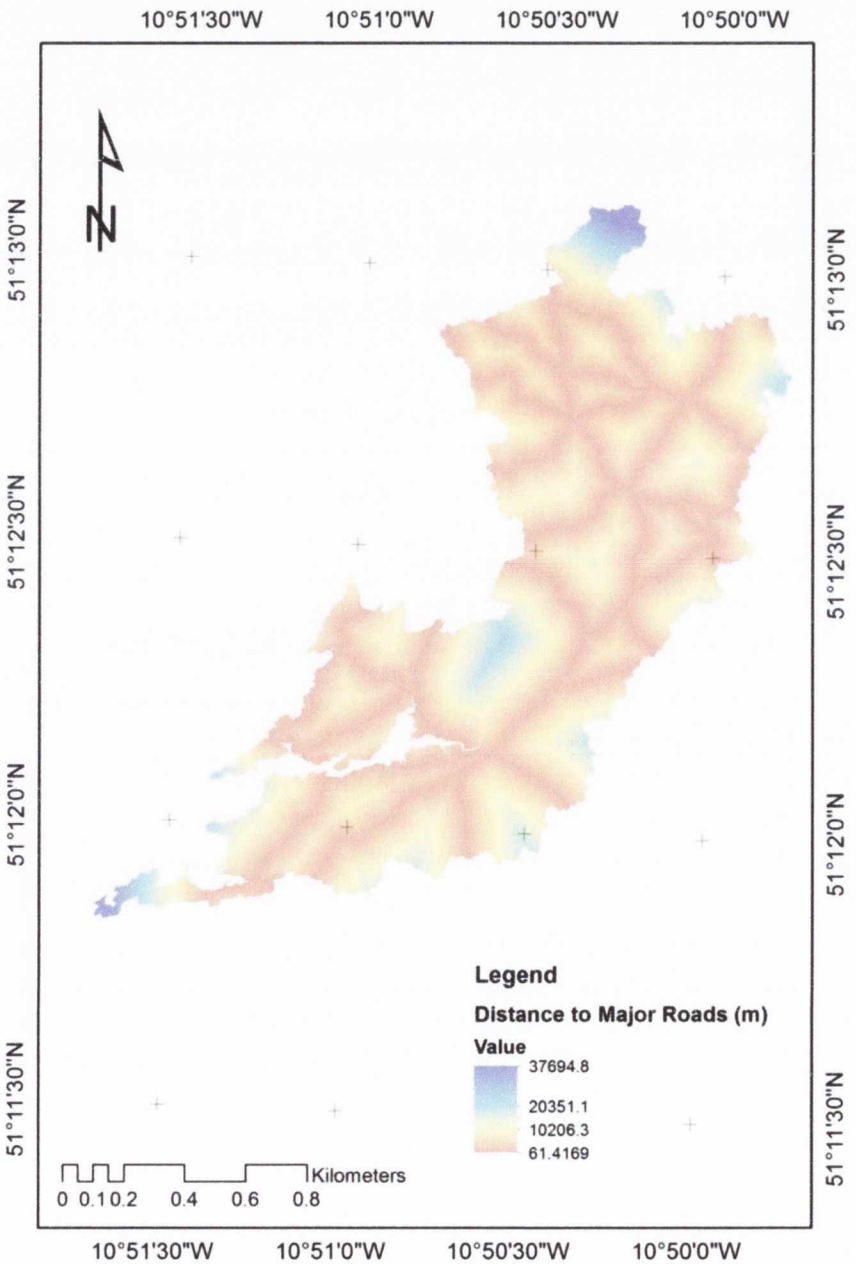

Figure 6.4: Driving factor of distance to major roads.

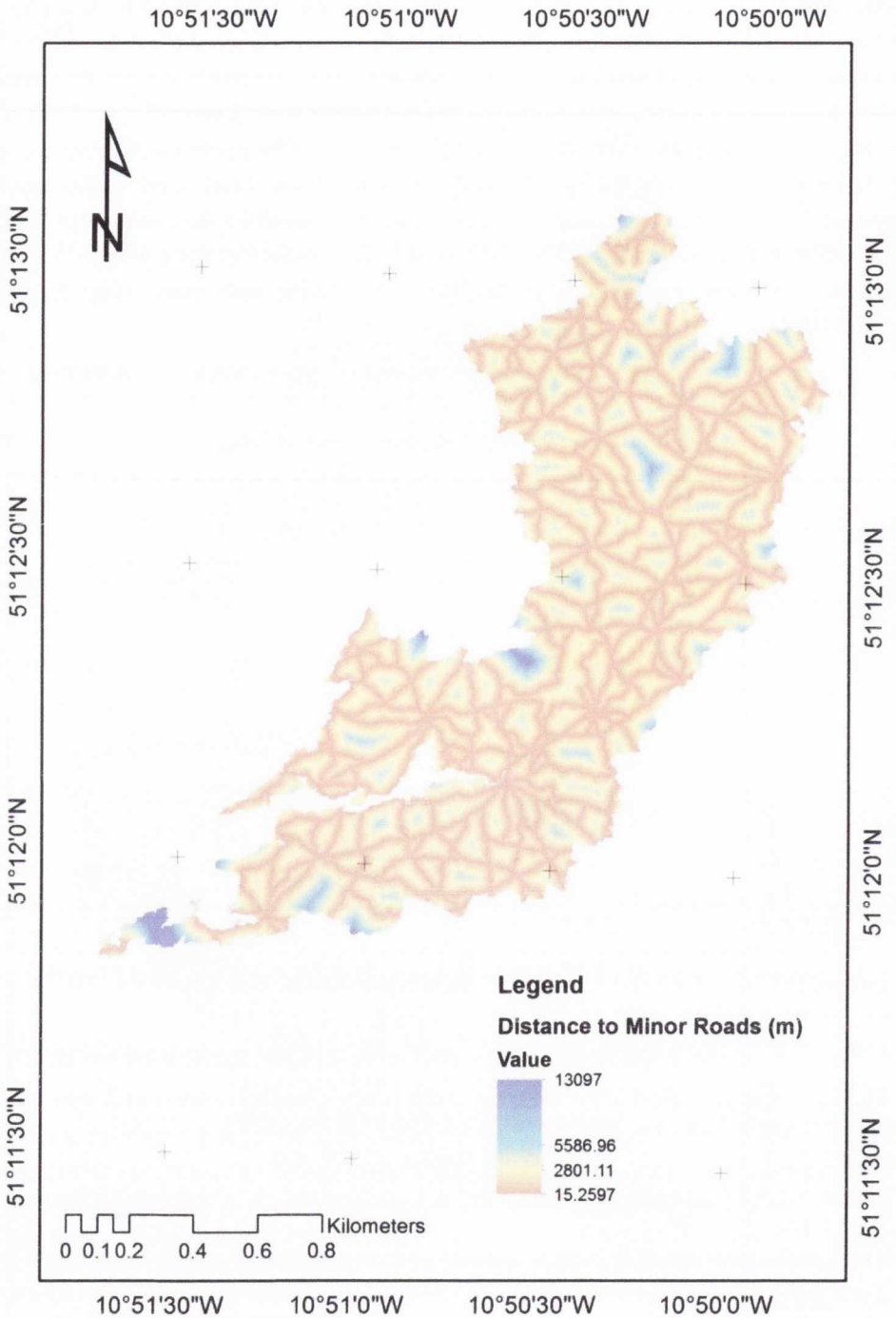

Figure 6.5: Driving factor of distance to minor roads.

6.2.3.1.2 Population density

The population is one of the main drivers of urban growth (Liu et al., 2005, Meyer and Turner, 1992). More urban land will be required to satisfy further growth of urban population in the future. The population variable was represented by the population density of Electoral Divisions (EDs)

administrative units. The Central Statistics Office Ireland (CSO) had implemented the last five censuses in the Republic of Ireland in 1986, 1991, 1996, 2002, 2006 and 2011.

$$Population\ density = \frac{Number\ of\ people}{The\ area\ they\ occupy} \qquad \text{Eq 6.2}$$

For the Shannon River Basin area model, population data for 2000 was required. A study carried out by Shahumyan et al. (2009) to stimulate the future urban growth for the Greater Dublin Region used the following equation to estimate the population for 2000

$$P_{2000} = P_{1996} + \frac{4}{6}(P_{2002} - P_{1996}) \qquad \text{Eq 6.3}$$

Where:

P_{2000}= Estimated population for the year 2000

P_{1996} =Population for the year 1996

P_{2002}= Population for the year 2002

Using equation (6.3), the average annual increase between 1996 and 2002 years can be applied for 2000 population estimation, but due to the fact that a map of Electoral Divisions was used in this study (only available for the 2002, 2006 and 2011 censuses), the above formula could not be applied to estimate the population for 2000, therefore, the population of the year 2002 was used for the year 2000 in this study.

To prepare the population density map to be input into the CA model, first the population density formula (6.2) was applied to all the Electoral divisions for the year 2002, and then the data were extracted into three maps (small population, medium population and high population). Using this method the weighting parameter for the high population map would be higher than the medium population map, and the medium population map will have higher weighting parameter than the small population map, which basically means that the probability of the urban land expansion is higher around the highly populated area than it is in the area with medium population, also the probability of the urban expansion around the area with medium population is higher than the area with small population. Figures 6.6, 6.7 & 6.8 show the distance to the different population categories.

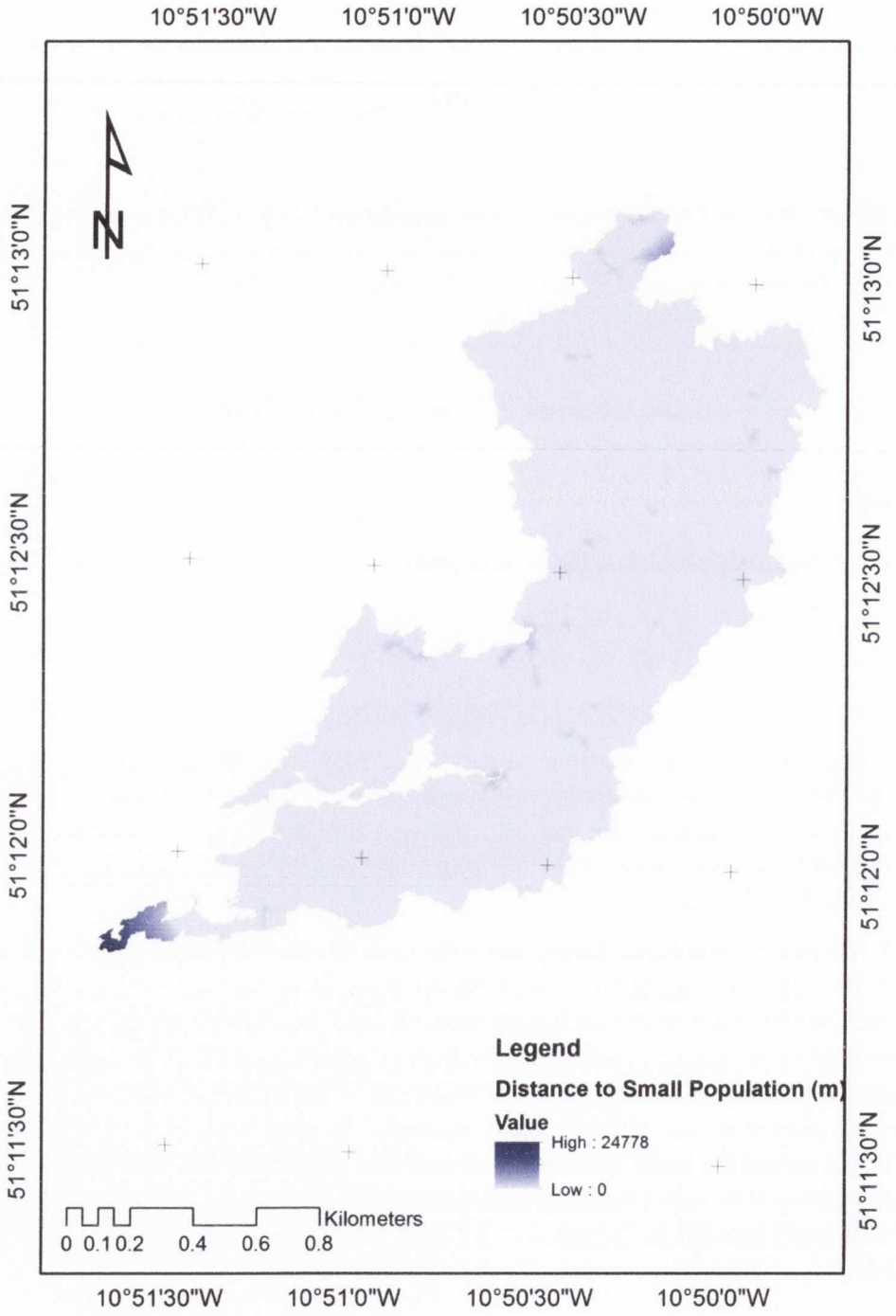

Figure 6.6: Distance to small populated Electoral Divisions.

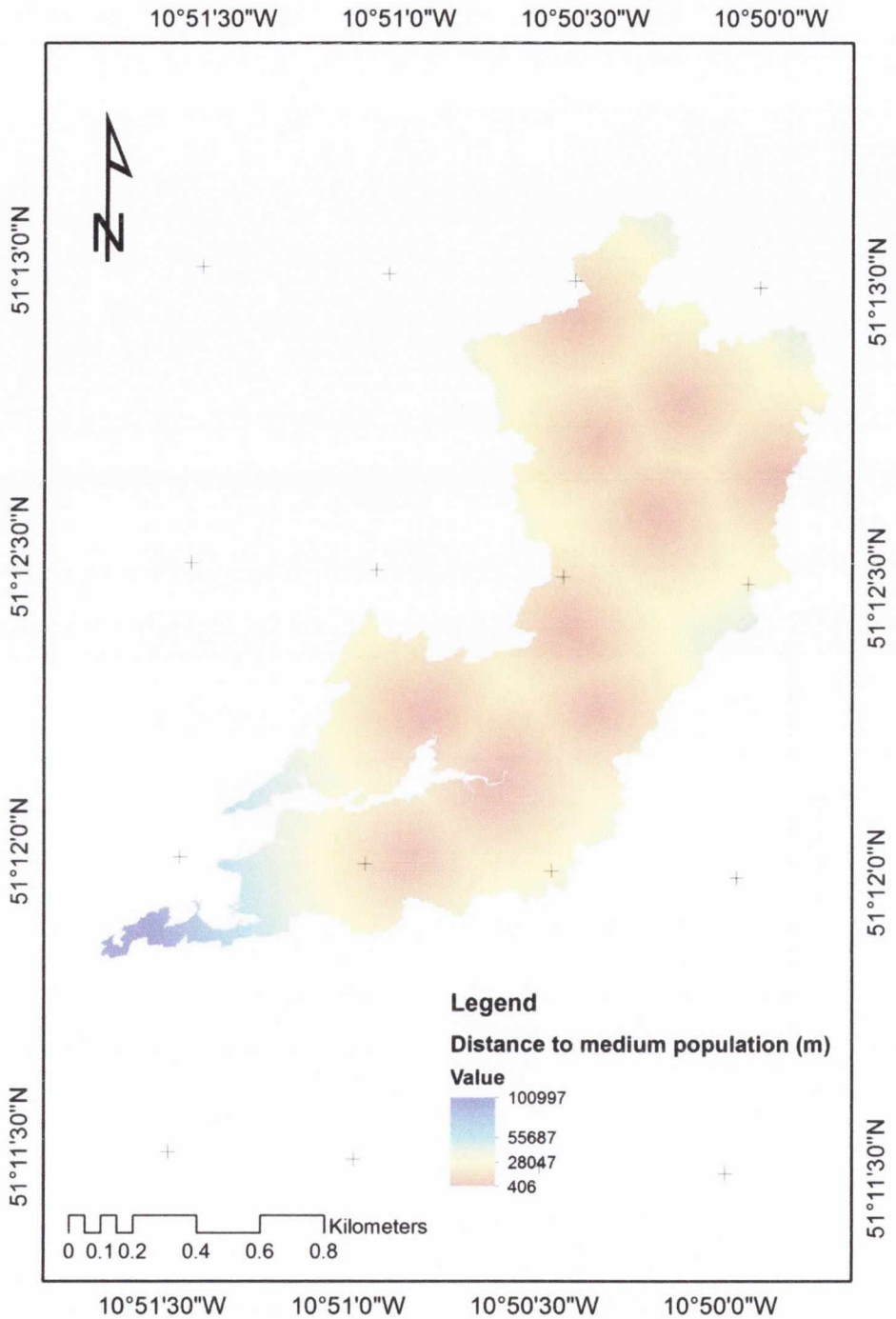

Figure 6.7: Distance to medium populated Electoral Divisions (m).

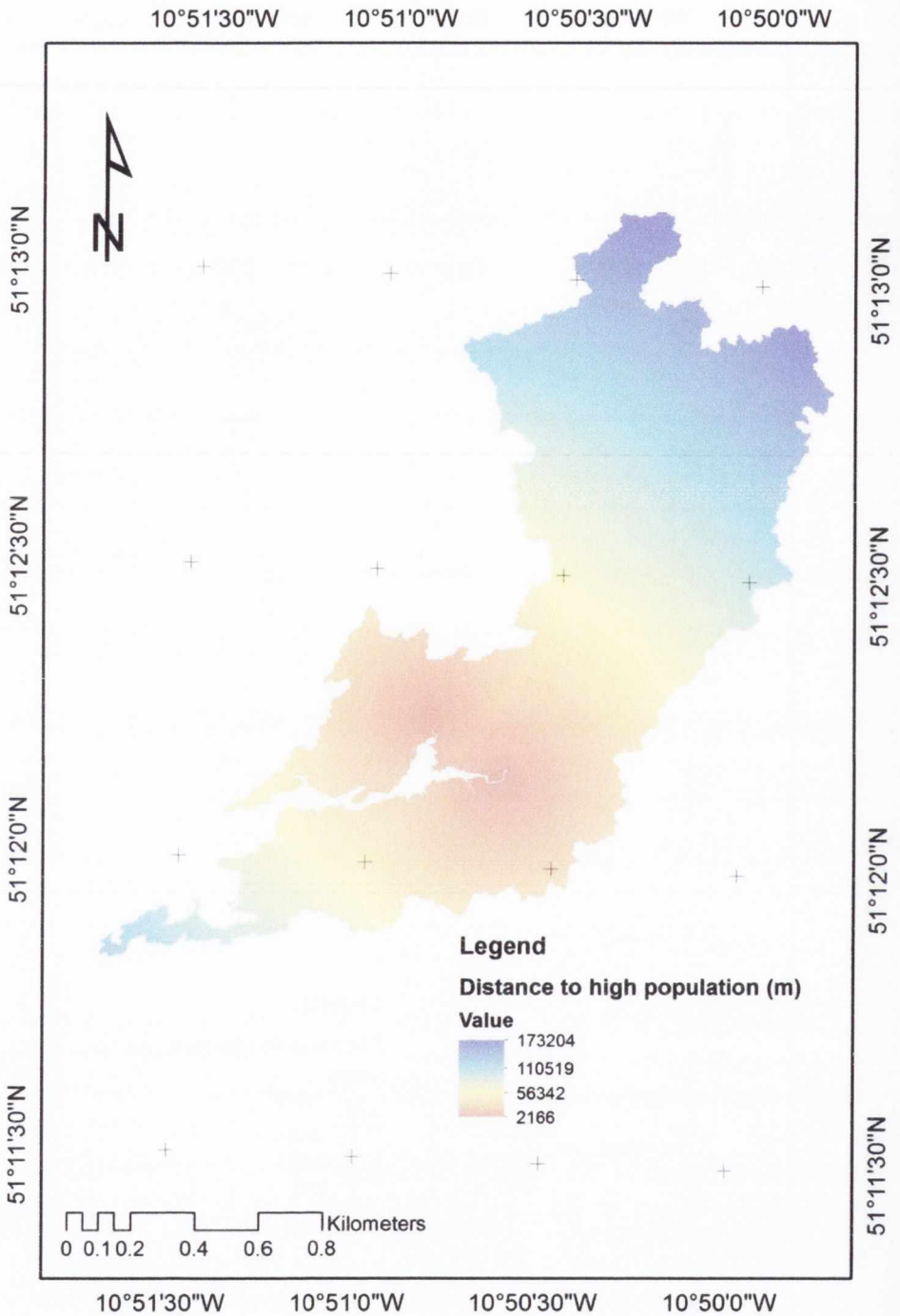

Figure 6.8: Distance to highly populated Electoral Divisions (m).

6.2.3.1.3 Distance to Towns/cities and existing communities

The influence of the socioeconomic conditions in the region can be best characterized by the access that a location has to socioeconomic centre, which has a significant effect on the urban growth pattern (Verburg et al., 2004, Li et al., 2013).

It is logical to think that new residential areas usually grow near or adjacent to existent residential areas - i.e. there is a high probability that the urban growth would expand closer to the town/cities centres or to the existing urban areas due to the neighborhood effect. These centres can reflect the accessibility effect on land use development at different levels.

Distance raster maps were prepared to the town/city centres to be input into the CA model. Figures 6.9 and 6.10 show the distance raster maps to the existing communities.

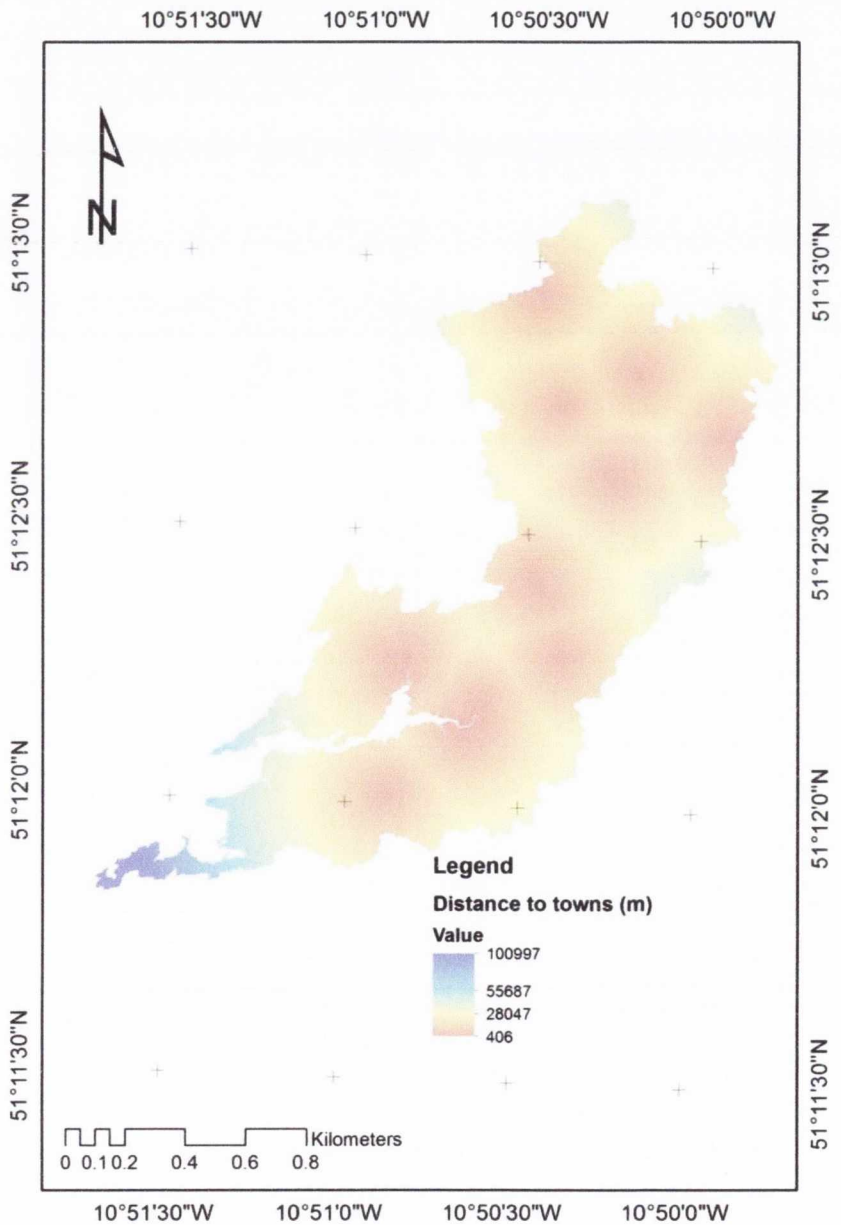

Figure 6.9: Distance to towns/cities raster map (m).

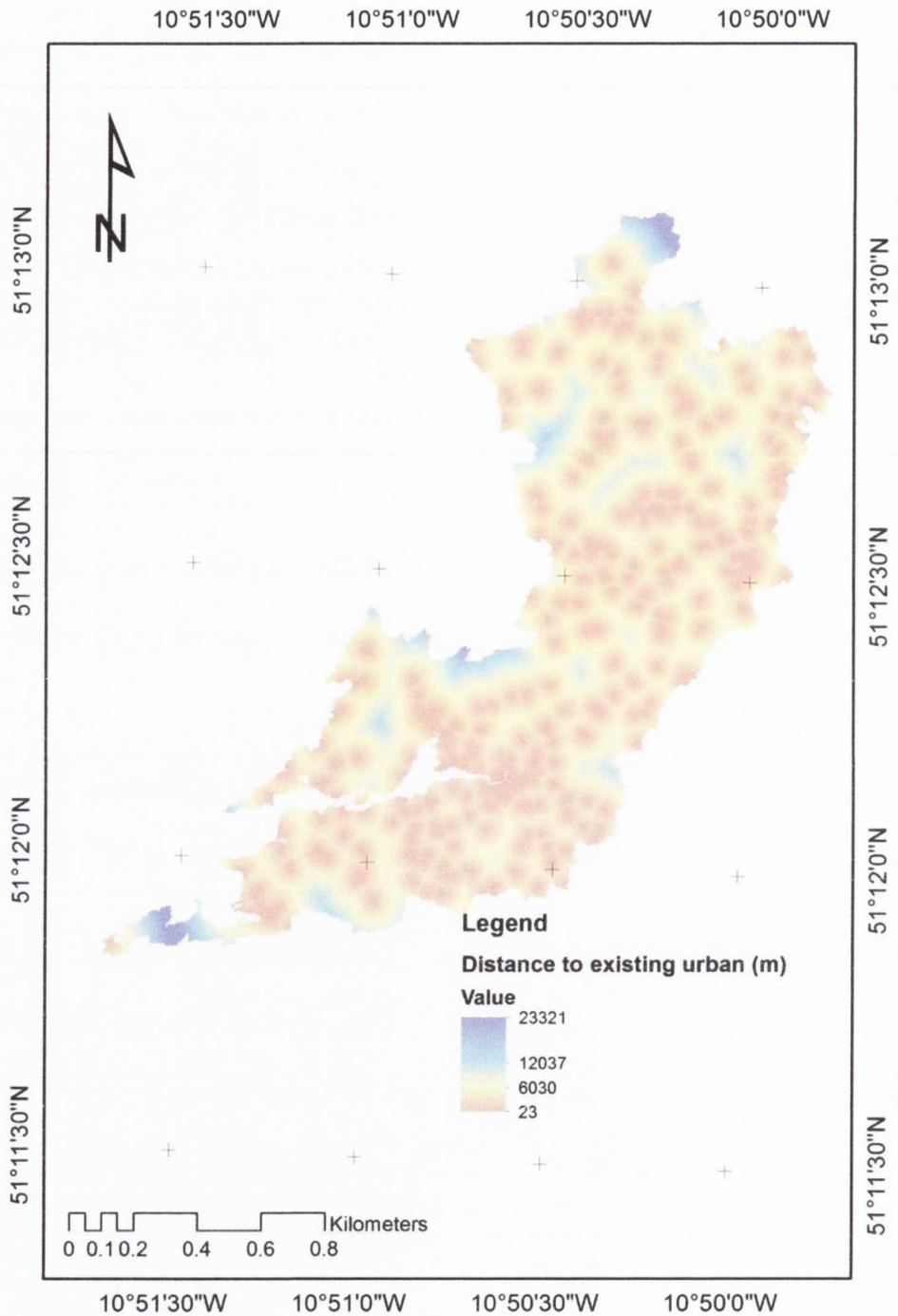

Figure 6.10: Distance to existing urban areas raster map (m).

6.2.3.1.4 Simulation constraint factors

6.2.3.1.4.1 Topographic Data

Suitability represents the degree of relevance of each cell to each land use type, according to a set of predefined criteria (Wu and Webster, 1998b, Rounsevell et al., 2006, Malczewski, 2004). Thus, land use suitability displays locations that fulfill suitability criteria defined for each land use class. Slope was used as one of the constraints to the River Shannon Basin Area development.

The Digital Elevation Map (DEM) obtained from EUROSTAT, was used to calculate the slope (in degrees) using the Spatial Analyst Tools.

After researching through the formal development policies in Ireland, it was found that there are no existing policies regarding slope ranges for development in the River Shannon Basin.

In the study of Shahumyan et al. (2009) to stimulate the future urban growth for the Greater Dublin Region, the values of the slope suitability were obtained from researchers at the Joint Research Centre. During the researching period, the EU Joint Research Centre was contacted in order to get the slope suitability values for the River Shannon Basin Area, but no response was received. Therefore, the same slope suitability values of the Greater Dublin Region were used, because the study is based in an Irish area and the topography might be similar.

The slope values were divided into two categories, suitable and non-suitable for the urban development. The CA understand these divisions in terms of 0 and 1: 0 means the land use is not suitable for development and 1 is suitable. The slope map used in the model was as follows 1= for the slope between 0° to 25°, and 0= for slope above 25°, i.e. the urban development is not possible above 25°. The slope map was initially converted into raster and then, using the reclassify tool in the spatial analyst toolbox in ArcGIS, divisions of 0 and 1 were created, as shown in Figure 6.11.

6.2.3.1.4.2 Zoning maps

Initial attempts were made to apply a direct translation of the development plans into zoning maps for the CA model. This process was, however, time consuming as the data is not avilable on digital format and needs to be collected from each city, twon and village council if its avilable and therefore an alternative approach was implemented to avoid this problem and to keep the same accuracy of the simulations, whereby zoning map was developed which included Special Areas of Conservation (SACs), protected as Special Protection Areas (SPAs) and Natural Heritage Areas (NHA). These areas were defined as constraints, where the development was limited. The three maps were converted into raster format and then using the reclassify tool in spatial analyst tools in ArcGIS the divisions of 0 and 1 was created. Where 0 represents all protected areas in which the development is restricted. The CA model used in this study accepts only one constraint map, therefore all the four maps, slope, Special Areas of Conservation (SACs), Special Protection Areas (SPAs) and Natural Heritage Areas (NHA) were combined into one constraint map using the raster calculator tool in spatial analyst tools in ArcGIS 10.1 (see Figure 6.11).

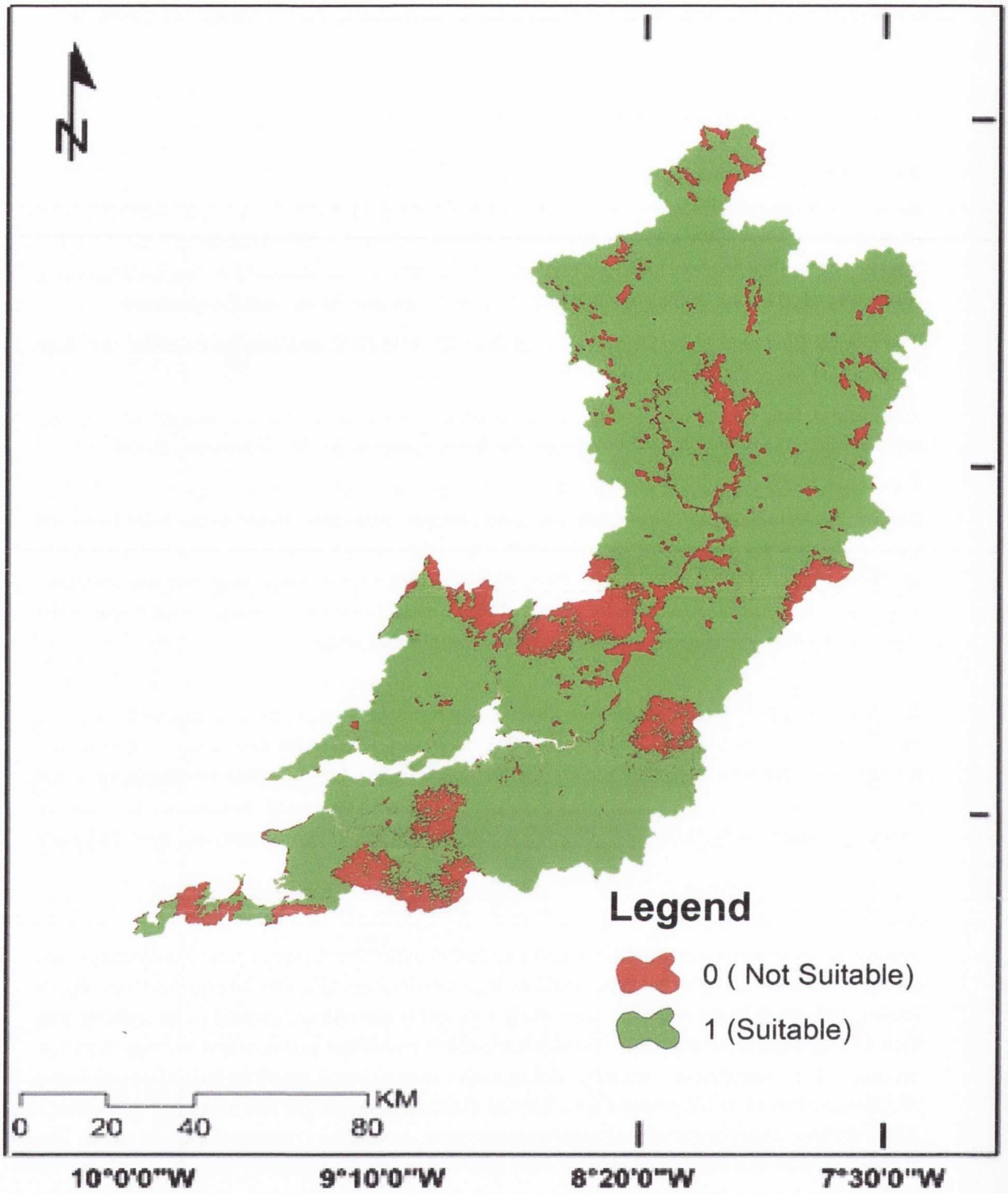

Figure 6.11: Constraint map for Shannon Basin.

6.2.3.2 Cellular Automata (CA) setup on GIS platform

Cellular automata models can be implemented within many types of software (Batty, 1997, Batty et al., 1999). For the urban development CA model, several programs have been implemented both inside and outside a GIS environment. These programs took advantage of the wide range of GIS spatial analysis functions, the graphic display and visualization capabilities. Moreover, as most applications of CA models need to consider the use of various data sources including historical land-use maps, census data, as well as satellite imagery, data processing and integration from different formats can be more easily implemented using an integrated CA and GIS software program (Liu, 2008).With these advantages, geographical models developed within a GIS environment are preferable in many applications.

In this study, a strong coupling approach was adopted to implement the CA model within a GIS environment. There are several reasons for using this approach, which is as follows:

(i) The main reason was that data were initially processed and stored in ArcGIS and then later converted into raster grid files.
(ii) The simulated outputs of the model were also stored as raster grid files in ArcGIS.
(iii) No data conversion was necessary between the GIS and the software model, which saved time on data communication. This feature was especially advantageous during the model calibration process when simulation results were compared and fitted with data illustrating actual Land Cover.
(iv) The spatial visualization capability was a very useful feature. As all input data and output, results were stored and processed within the same GIS environment.
(v) The results could be easily visualized spatially using the data display and visualization capabilities of ArcGIS.
(vi) The design of a friendly graphic user interface made it possible to modify and calibrate the model quickly.
(vii) The accuracy assessment calibration of the model was also carried out in ArcGIS by comparing the model's simulation outcomes with actual urban scenarios.

The digital space in the CA consists of a rectangular grid of square cells each representing a spatial scale chosen in this study of 100 m, i.e., an area of 100 m ×100 m on the ground. This is the same size as the minimum area mapped in urban areas in the land use datasets. All the data sets including the driving and constraints factors were also processed as regular spatial grids at a spatial scale of 100 m. These data sets are used to feed the model to simulate the urban growth in River Shannon Basin area.

Each cell is characterized by a vector of suitabilities, one suitability for each land use taking part in the dynamics, this vector includes the direction of the urbanization. The first suitability vector defined the weighted linear sum of a series of physical, environmental and institutional factors, characterizing each cell. They are normalized to values in the range of 0–1 (inclusive) using the fuzzy set memberships approach and represent the inherent capacity of a cell to support a particular activity or land use. Fuzzy logic allows the continuous analysis between "false" and "true" and bridges the gap between qualitative and quantitative modeling. Fuzzy logic is a generalization of the binary logic, when a fuzzy set is meant to manage quantitative (numerical) information, it is fully described by a membership function which returns a membership value (μ) within [0,1] for a given object in the fuzzy set.

The second suitability vector was associated with the accessibility factors for each cell. These factors represent the importance of access to transportation networks, closest towns, and existing urban areas, for various land uses for each cell. Finally, the third suitability vector for each cell was associated with a set of codes representing its zoning status for various land uses, and for various periods. Due to the combined effect of suitabilities, accessibilities, neighborhood effect, and zoning, every cell is essentially unique in its qualities with respect to possible land uses. It is in this highly differentiated digital space where the dynamics of the CA take place. The suitability map was kept constant during the simulation process unless the run was interrupted in order to edit the map manually.

The model used 5 cell states - wetlands, water bodies, urban areas, agricultural areas and forest - with urban area growth being the main focus of this study. Therefore, the classes that were considered as passive functions were: water bodies, wetlands, forest and agricultural. That is, functions that participate in the land use dynamics, but are not driven by an exogenous demand for land; they appear or disappear in response to land being taken or abandoned by the active functions. The active function class was the urban area which is forced by demands for land generated exogenously to the cellular automaton in response to the growth of the urban area. This included road and rail networks (and associated land), airports, mineral extraction sites, dumps, green urban areas, sport and leisure facilities, continuous urban fabric, discontinuous urban fabric, sea port, industrial and commercial and construction site.

During the modeling, the water bodies and wetlands features' growth were kept fixed; these features were assumed to be converted to another land use type but do not grow in the future. The main reason behind this assumption is that during the change detection pattern analyses, the reduction of wetlands and water bodies over the years was noticed, therefore, these two features could not be assumed growing in the future. However, they still had an effect on the dynamics of the active land uses, since in the neighborhood effect they may represent an attractive or repulsive effect.

With the concern that distortions may exist in a rectangular neighborhood-type configuration (Li and Yeh, 2002), a circular neighborhood was applied in this study. In the CA model, the neighborhood space was defined as a circular region around the central cell with a radius of eight cells. Consequently, the neighborhood contained 172 cells that were arranged in 30 discrete distance zones. The neighborhood radius represented 0.8 km; this distance delimits an area that can be defined as the influence area for urban land uses. That is similar to what residents of a town commonly identify to be their neighborhood, and thus should be sufficient to allow spatial processes to be captured in the CA transition rules.

In the urban CA, the neighborhood space effect was calculated for each of the 5 function states (passive and active) for each cell. Essentially, this effect defines the state to which the cell could be converted or remains in its original state. The effect represents the attraction (positive) and repulsion (negative) effects of the various land uses and land covers within the neighborhood of 172 cells in relation to the central cell. In general, cells that are more distant in the neighborhood will have a smaller effect in the evaluated central cell. However, a positive weight of a cell on itself (zero-distance weight) represents an inertia effect due to the implicit and monetary costs of changing from one land use to another. (Barredo et al., 2003).

Urban development is the result of both internal and external forces. Internally, an area tends to continue its development if it has started to develop from a rural to an urban state, especially if this natural tendency is supported by development from within its neighborhood. Externally,

factors such as the geographical conditions of the area, its socio-economic conditions, as well as institutional controls may also have an impact on the process of its development. Physical constraints such as water bodies and steep terrain may restrict or slow down the process of urban development, as do institutional controls that may accelerate or prohibit further urban growth. Socio-economic factors such as land availability and demands on available land, accessibility to nodes of employment and other services, and facilities such as schools, shops, public transport, and continuity to existing urban areas also play important roles in urban development (Liu, 2008). Using the CA model of urban development constructed in this study, the internal and external forces affecting the process of urban development in River Shannon Basin were simulated through the setting transition rules.

A vector of transition potential rules (one potential for each function) was calculated for each cell from transitional potential, dynamic constraints, elasticity of change and growth cells expectation, and the deterministic value was then given a stochastic perturbation using a modified extreme value distribution, such that most values are changed very little but a few are changed significantly:

$$t_{P_{k,x,y}}=(t_{T_{K,x,y}})(t_{C_{K,x,y}})(t_{E_{K,x,y}})(t_{G_{K,x,y}}) \quad \text{Eq 6.4}$$

- $t_{P_{K,x,y}}$ is the Cellular Automata transition rule of the cell (x,y) for land use K at time t.
- $t_{T_{K,x,y}}$ is the transitional potential of the cell (x,y) for land use K at time t, which basically had the suitability map for each land use that was generated by the mechanism overlaying the driving factor as well as several restrictions, such as zoning for protected areas and slope.
- $t_{C_{K,x,y}}$ is the change conversion elasticity probability value of the cell (x,y) for land use K at time t. the conversion probability for each simulated land use was used in order to convert land use under simulation process.
- $t_{E_{K,x,y}}$ is the dynamic constraint value of cell (x,y) for land use k at time t, which is basically the code of constraint land uses that certain land use is not allowed to change during the iteration processes.
- $t_{G_{K,x,y}}$ is the Growth cells estimated for (x,y) for land use K at time t.

Thus, the transition rule works to change each cell to the state for which it had the highest potential, subject to the constraint that the number of cells in each state must be equal to the number demanded in that iteration. Cell demands were generated outside the CA.

In every iteration, all cells were ranked by their highest potential and cell transitions begining with the highest ranked cell and proceeding downwards until a sufficient number of cells for a particular land use had been achieved. At each iteration, each cell was subject to this transition algorithm. However, most of the resulting transitions were back to the same state, as a result the cell remained in its current state. When a transition to another state occurred, the actual transition to the second state occurred after one iteration (1 year) delay; during this interval, the cell is assigned the state construction site.

It is important to mention the flexible way in which various factors that may impact the urban development in the Shannon River Basin could be introduced into the CA model through the transition rules. The total impact of the accelerating or constraining factors on the model's behavior are explained as follows:

If there is one accelerating/driving factor within the neighborhood of the cell in question, the speed of urban development of that cell will be upgraded one step higher in the "speed" fuzzy set, however, if there is one constraining factor within the neighborhood of the cell in question, the speed of urban development of the cell will be downgraded one step lower in the "speed" fuzzy set. If there is more than one such factor, the speed will be upgraded or downgraded two steps up or down. The existence of one accelerator and one constraint will cancel the effect of both factors; hence, the speed of development will stay unchanged.

The flexibility of the model enables it to function not only as an analytical tool to understand the forces driving the process of urban development but also as a planning tool to experiment with various planning proposals and generate different "what if" scenarios in the planning practice (Liu, 2008).

In order to input the transition rules into the CA model, the Fuzzy Set Memberships were used for all the driving factors maps, i.e. the values were converted to become real number format (0-1). The Fuzzy set memberships operation used in this study was monotonically decreasing. Monotonically decreasing represented the decay effect, i.e. the closer the distance the better, so the closer the cell to any of the driving factors, the higher probability for it to change into urban land. Weighted raster values were ascribed to each driving factor fuzzy map. The concept of Weighted Raster is overlaying equipped with each weight. This mechanism is intended to determine the influence by a factor towards a specific purpose of making a map of transitional potential units. The values of the weights were determined by studying the relative importance of each factor in driving the urban expansion and then an assumption has been made for each factor weight, as seen in Table 6.6.

Table 6-6: Raster weighted values used for the urban area land use class.

Fuzzy driving factors	Weighted raster values
Distance to Minor roads	0.12
Distance to major roads	0.12
Distance to town/cities	0.2
Distance to existing urban area	0.2
Distance to high population	0.15
Distance to medium population	0.11
Distance to small population	0.1

All driving-forces, after applying the weighted raster, were combined together with the slope and zoning of protecting area constraint map in order to generate the transitional potential map. Determination of Conversion Probability was generated by overlaying two land use maps (2000 to 2006 and 2006 to 2012) using ArcGIS overlaying tool, and the conversion rate value of a certain land use changing to another land use was obtained, see Table 6.7. Although the overlay method

may not capture the phenomena that might occur, the two periods conversion values were obtained and compared to reach an optimum conversion probability values. The growth of water bodies and wetlands were not considered in this study, but conversion probability was calculated for other classes when overlaying.

Table 6-7: Transition matrix for Shannon catchment based land cover data for 2006 and 2012, units in kilometer square.

Land Cover categories 2012	Land Cover categories 2006						
	Water bodies	Wetlands	Urban area	Agricultural	Forest	Total 2012	% 2012
Water bodies	406.62	5.24	0.83	22.5	4.47	439.66	2.39%
Wetlands	5.22	1637.13	0.86	112.73	54.36	1810.3	9.85%
Urban area	0.83	1.15	243.1	45.62	2.04	292.74	1.59%
Agricultural	22.37	114.29	39.46	13202.12	178.71	13556.95	73.79%
Forest	4.17	65.71	1.36	198.89	2001.48	2271.61	12.37%
Total 2006	439.21	1823.52	285.61	13581.86	2241.06	18371.26	100%
% 2006	2.39%	9.93%	1.55%	73.93%	12.20%	100%	

The determination of Growth Cell was obtained using the simple trend analysis based on the series of land use maps. The determination of the dynamic constraint was based on the logic probably occuring in the field. The only dynamic constraint used in this study was that an urban area would not be converted into water, wetlands, and forest.

For each land use function, a vector of transition potential was calculated by combining the transitional potential, dynamic constraints, the elasticity of change and growth cells as mentioned above. After preparing all the data, maps and weights, the CA LanduseSim extension for ArcMap was used to run the simulations (Pratomoatmojo, 2016, Ratriaga and Sardjito, 2016, Pratomoatmojo, 2012). LanduseSim is a GIS tool for land use/ land cover (LULC) modeling and simulation. LanduseSim is able to deal with land dynamic simulation and the general model framework is illustrated in Figure 6.12. LanduseSim in this project has been used as a processor for the CA simulations. All the input data that have been described earlier was pre-processed in ArcMap and then fed to LanduseSim to the outputs, then all the outputs were post-processed by ArcMap to get the future land cover projections.

Figure 6.12 shows the framework and the main simulation steps for the land cover simulation result from preparing the forcing factors for urban expansion then preparing the suitability map to the stage of running the CA to get the predictions.

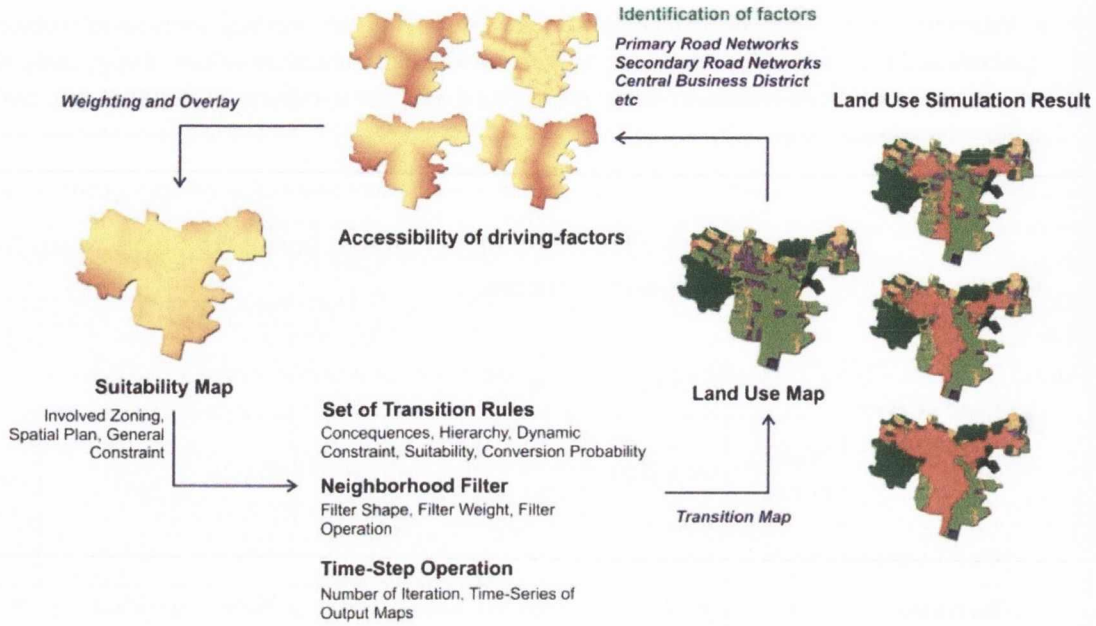

Figure 6.12: General model framework (Pratomoatmojo, 2016).

The fuzzy constrained CA model developed in this study was configured temporally when applying it to simulate the process of urban growth in River Shannon Basin. For the validation of the model, the start date was set to 2000, and the end date to 2006. Each temporal advance of the model represents one year in the urban growth context. Data illustrating the urban extent within the simulation period at every 6-year interval were used to calibrate the model temporally. The main reason for choosing the 6-year interval was the land cover maps used in the validation process were available in 6-year intervals, 2000, 2006 and 2012 from the Environmental Protection Agency (EPA).

6.3 Model validation and calibration

A land use simulation for the River Shannon Basin area was produced for the period 2000–2012 using the urban CA model. The simulation began using the historical datasets for the year 2000, in order to test in order to calibrate the model using the reference datasets for the year 2006. Afterwards, the model was simulated for the year 2012 and comparison with the actual land cover was also made for validation purposes.

The model was calibrated based on reproducing the weighting parameters and the conversion probability values for the input layers based on comparing the first run results for 2006 and the actual dataset for 2006.

Based on the configuration comprising a cell size of 100 m and a circular neighbourhood with a radius of two cells, the model of urban development of River Shannon Basin was first implemented with the primary transition rules that had the first weighting parameter assumption for the driving factors, the zoning protected areas constraints, the conversion probability values and the growth cells estimation obtained from the overlaying of the land cover maps.

Subsequently, the secondary transition rules were introduced into the model after changing the weighting parameters and conversion probability to calibrate the model and evaluate its simulation accuracies using the previous statistics of urban development from 2000 to 2006 and from 2000 to 2012 as references for validation.

The weighting parameters were calibrated in order to minimize the differences between the simulated land use map for 2006 and the actual land use map for that year.

The weighting assignment was done by verifying visually in the calibration process the spatial effects of the weights in the CA model. The simulations were produced in a few minutes using a good computer, which made it possible to modify the weight values until the results fit with the reference land use map.

Once all the functions had been calibrated, the model was re-run several times in order to verify if the land use transitions worked in a logical way. Another important factor for the calibration of the model was the conversion probability values. The values were obtained by overlaying the land cover maps for the periods 2000 to 2006, but after running the model simulation several times.

By varying the parameters of the transition rules within each iteration of the model and changing the balance between the rules, various simulation results were produced, and their accuracies against the land cover of the River Shannon Basin area at every 6-year interval were computed using the modified error matrix approach. Figure 6.13 shows the various simulation accuracies of the model under all transition rules over time, which can be illustrated by Table 6-8.

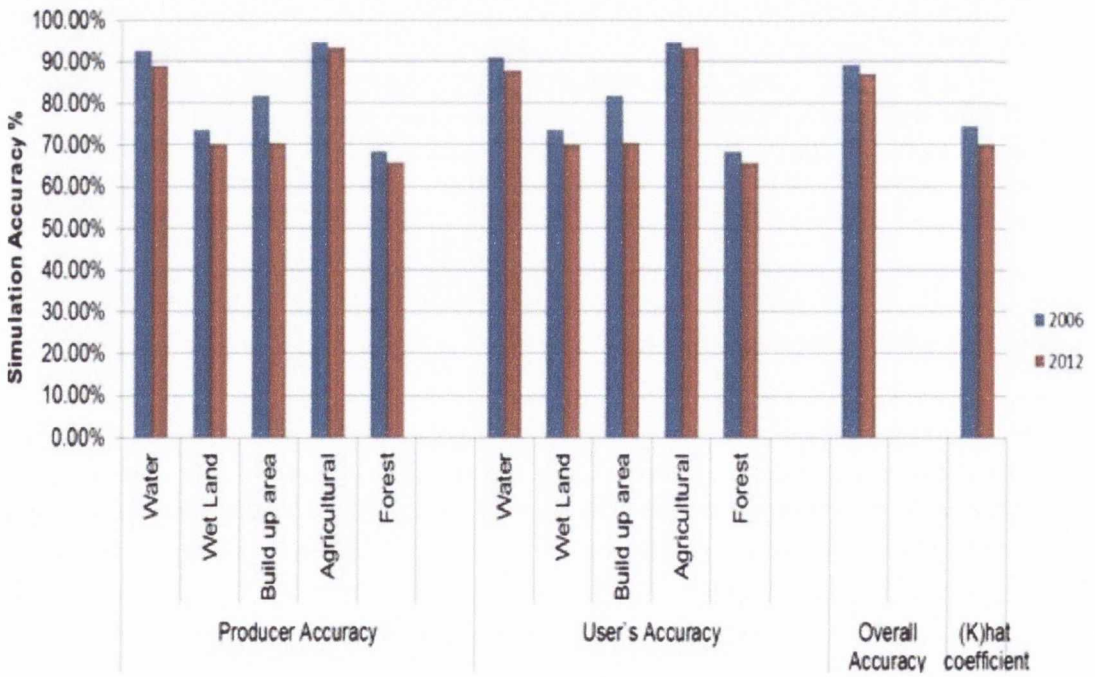

Figure 6.13: The model's simulation accuracies under all transition rules over time (2006-2012).

In general, results produced by the model matched well with the actual urban extent for the validation year 2012. The various types of simulation accuracies produced by the model for the land covers of 2006 and 2012 were very close. Based on the final validation process, the model had generated an overall accuracy of 89.0% and in 2012 an overall accuracy of 87.1%. The

simulated urban area for 2006 is 285.61 km^2 while the real mapped area is 278.2 km^2. The simulated urban area for 2012 is 292.73 km^2 while the real mapped area is 293.2 km^2. These results could be considered good or very good.

Table 6-8: Definitions of terms used in an error matrix and their computations.

Terms	Description	Computations
Producer`s accuracy	Probability of reference cells being correctly categorized in the classification data. This measure the omission error.	Number of cells on the major diagonal divided by the column total of each category
User`s accuracy	Probability that cells in the classification data actually, belongs to the same category as in the reference data. This measure the commission error	Number of cells on the major diagonal divided by the row total of each category
Omission error	Cells that are excluded (omitted) from the categories that they belong to in the reference data	Total of the off-diagonal column cells divided by the column total of each category
Commission error	Cells that are included (committed) in the categories that they do not belong to in the reference data	Total of the off-diagonal row cells divided by the row total of each category
Overall accuracy	A measurement of the overall proportion of correctly categorized cells in relation to the total number of cells under assessment	Total number of cells along the major diagonal of the matrix divided by the total number of all the cells

However, the producer's and user's accuracies (see Table 6.8 for the error terms), show that large discrepancies exist between the simulated results and the land cover in the forest category, resulting in lower accuracies from both the producer's and user's perspectives. For instance, the producer's and user's accuracies for the forest category in 2006 were only 68.3%. This means that 31.7% of the actual forest areas were omitted from being selected for development, and 32.7% of the simulated forest areas were committed to the category by the model incorrectly. In addition, for the same forest category, the producer's and user`s accuracy in 2012 were also low. This is also reflected in the model's results showing a lower percentage of 68.3% of forest areas in 2006 and 65.7% in 2012 compared to all other classes which are above 70%. This is largely due to the fact that the forest areas only consist of approximately 12% of the total area of the River Shannon Basin area; therefore, even a small amount of mismatched cells between the actual urban extent and the simulated results would result in a high percentage of discrepancy between the two datasets, and hence, lower the producer's and user's accuracies in this category.

For the fully urban area, because 1.36% of the River Shannon Basin area had already been fully urbanised at the start of the model in 2000, and these fully urban areas remain as urban during the whole simulation process, the actual composition of fully urban areas has only increased to 1.55% in 2006 and to 1.59% in 2012. The producer`s and user`s accuracy for the urban areas in 2006 was 81.8%. This means that 18.2% of the actual urban areas were omitted from being selected for development, and 18.2% of the simulated urban areas were committed to the category by the model incorrectly. In addition, for the same urban area category, the producer's and user`s accuracy in 2012 were 70.5%.

In 2006, in the urban area simulation class, 4462 cells were incorrectly assigned as agricultural areas. On the other hand, 604 cells were incorrectly assigned to the forest and 60 cells were incorrectly assigned by the simulation to water bodies. Also, 83 cells were incorrectly assigned to wetlands during the simulation. In 2012, 116 cells were incorrectly assigned as waters bodies and wetlands rather than urban areas. On the other hand, 7665 cells were incorrectly assigned to Agricultural and 740 cells were incorrectly assigned by the simulation to forest instead of urban areas.

Due to the transition rules of Cellular Automata model, such rules can, in effect, evenly locate new urban cells mainly in the city core and around the edge of initial urban areas. As a result, some of the simulated urban cells in the city core were located where no changes from non-urban to urban land uses took place. While some real developed cells were underestimated by models. The errors found in simulation results also reveal that some errors were caused by issues not related to the model, such as the complexity of urban growth. Urban expansion process usually has some unpredictable features because of the complexity of nature.

6.4 Results and discussions

Based on the discussed model accuracy, the combination of the different parameters and the calibrated model were used to produce a series of maps showing the future scenarios for the River Shannon Basin for the years 2020, 2050 and 2080 in order to use them later in water balance simulations.

The results of land cover conversions of the Shannon River Basin area in 2020 were compared to land cover in 2012, using GIS, producing matrices of land cover changes. The statistics generated in the matrices is "from-to" information for the study area, and it revealed a few insights into the question of where land cover changes will be occurring.

The results for the Shannon Basin indicate an increase of urban area from 1.59% in 2012 to 1.75% in 2020, which equates to a total of 28.5 km^2 of land will be converted into urban areas by 2020. That means the overall change percentage from 2012 to 2020 will be 9.75%. The majority of the urban area will come from the conversion of agricultural to urban areas; also, the small portion of the increase will be from converting wetlands and forest to urban area. That increase will depend on the economy growth of Ireland up to 2020. Rapid development requires more built-up land and industrial workers, which will also lead to relatively high urbanization speed. The incredible pressure of rapid urbanization on non-urban land will be reflected by the high loss of agricultural and forest land. Figure 6.14 shows the urban expansion will be mainly around Limerick city, Ennis, Mullingar, Athlone, Tralee, Cratloe, Clareabbey, Tullamore, Longford, and Roscommon rural, a map of the towns and cities in Shannon c in Figure 3.1.

Also, the model predicts an increase in forest land from 12.37% in 2012 to 12.75 in 2020, equating to 70.6 km^2, an overall change of 3.11%. The analysis showed that forest cover will increase at the expense of wetlands and agricultural areas mainly. Moreover, there will be a gradual increase in agricultural areas from 73.79% in 2012 to 74.40% in 2020, equating to 111.0 km^2 of land being converted into urban agricultural areas in 2020 (an overall change of 0.82%). The agricultural areas will increase at the expense of wetlands and forest cover mainly.

Due to the increase of urban areas, forest, and agricultural cover, there will be a reduction in wetlands and water bodies in 2020, with a decrease of 208.45 km^2 and 1.71 km^2 of wetlands and water bodies respectively. The wetlands will decrease from 9.85% in 2012 to 8.72% in 2020, an overall change of -11.51%. While the water bodies will decrease from 2.39% in 2012 to 2.38% in 2020 with an overall change of -0.39%. Figure 6.14 and Table 6.8 show the River Shannon Basin land cover predicated map and percentages in 2020.

The results of land cover conversion of the Shannon River Basin in 2050 were compared to land cover in 2012, producing matrices of land cover changes. The results for the Shannon Basin indicates an increase of urban area from 1.59% in 2012 to 2.34% in 2050, a total 136.38 km^2 of land converted into urban areas by 2050(an overall change percentage of 46.59%). Figure 6.15 shows the urban expansion will be mainly around Limerick city, Ballyvarra, Ballycummin, Patrickswell (in County Limerick), Mullingar, Athlone (County Westmeath), Tralee (County Kerry), Ennis Cratloe, Clareabbey, Ballyglass, Clenagh, Drumline, Newmarket, Urlan (in County Clare) Tullamore (County offaly), Longford (County Longford) and Roscommon rural (County Roscommon) and Nenagh (County Tipperary). A map of the towns and cities in the Shannon catchment can be seen in Figure 3.1.

Also, there will be an increase in forest land from 12.37% in 2012 to 14.18% in 2050, equating to 332.9 km^2, an overall change of 14.66%. The analysis showed that forest cover will increase at the expense of wetlands and agricultural areas mainly and a small portion of water bodies. Moreover, there will be a gradual increase in agricultural areas from 73.79% in 2012 to 76.81% in 2050, equating to a total of 553.6 km^2 of land will be converted into urban agricultural areas in 2050 (an overall change of 4.08%.) The agricultural areas will increase at the expense of wetlands and forest cover mainly and a small portion of water bodies.

Due to the increase of urban areas, forest, and agricultural cover, there will be a reduction in wetlands and water bodies in 2050, with a decrease of 941.21 km^2 and 81.7 km^2 of wetlands and water bodies respectively. The wetlands will decrease from 9.85% in 2012 to 4.73% in 2050 - an overall change of -51.99%. While the water bodies will decrease from 2.39% in 2012 to 1.95% in 2050 - an overall change of -18.58%. Figure 6.15 and Table 6.8 show the River Shannon Basin land cover predicted map and percentages in 2050.

The results of land cover conversions of the Shannon River Basin in 2080 were compared to land cover in 2012, producing matrices of land cover changes. The results for the Shannon Basin area indicate an increase of urban area from 1.59% in 2012 to 2.92% in 2080, equating to a total 244.05 km^2 of land converted into urban areas in 2080. (a change of 83.37%). Figure 6.16 shows the urban expansion will be mainly around Limerick city, Ballyvarra, Ballycummin, Patrickswell, Newcastle urban, Ranthkeale urban, Croom, Ballysimon, Ballynanty (Co. Limerick), Mullingar, Athlone (County Westmeath) Tralee (County Kerry), Ennis, Cratloe, Clareabbey, Ballyglass, Clenagh, Drumline, Newmarket, Urlan, Templemaley, Kilnamona (in County Clare) Tullamore (County Offaly), Longford (County Longford), Roscommon Rural (County Roscommon) and

Nenagh (County Tipperary). A map of the towns and cities in the Shannon catchment can be seen in Figure 3.1.

Also, there will be an increase in forest land from 12.37% in 2012 to 14.62 % in 2080, equating to 414.13 km^2, an overall change percentage of 18.23%. The analysis showed that forest cover will increase at the expense of wetlands and agricultural areas mainly and a small portion of water bodies. Moreover, there will be a gradual increase in agricultural areas from 73.79% in 2012 to 76.28% in 2050, a total of 456.42 km^2 of land converted into urban agricultural areas by 2080 (an overall change of 3.37%).

Due to the increase of urban areas, forest, and agricultural covers, there will be a reduction in wetlands and water bodies in 2080, with a decrease of 1024.49 km^2 and 90.11 km^2 of wetlands and water bodies respectively. The wetlands will decrease from 9.85% in 2012 to 4.28% in 2080, with an overall change of -56.59%. While the water bodies will decrease from 2.39% in 2012 to 1.90% in 2080 with an overall change of -20.50%. Figure 6.16 and Table 6.8 show the River Shannon Basin land cover predicted map and percentages in 2080.

Table 6-9: Land Cover transition matrix of River Shannon Basin area.

Land Cover Classes	km^2	percent
Change 2012 to 2020		
Water bodies	-1.71	-0.39%
Wetlands	-208.45	-11.51%
Urban area	28.53	9.75%
Agricultural	110.99	0.82%
Forest	70.64	3.11%
Change 2012 to 2050		
Water bodies	-81.7	-18.58%
Wetlands	-941.21	-51.99%
Urban area	136.38	46.59%
Agricultural	553.59	4.08%
Forest	332.94	14.66%
Change 2012 to 2080		
Water bodies	-90.11	-20.50%
Wetlands	-1024.5	-56.59%
Urban area	244.05	83.37%
Agricultural	456.42	3.37%
Forest	414.13	18.23%

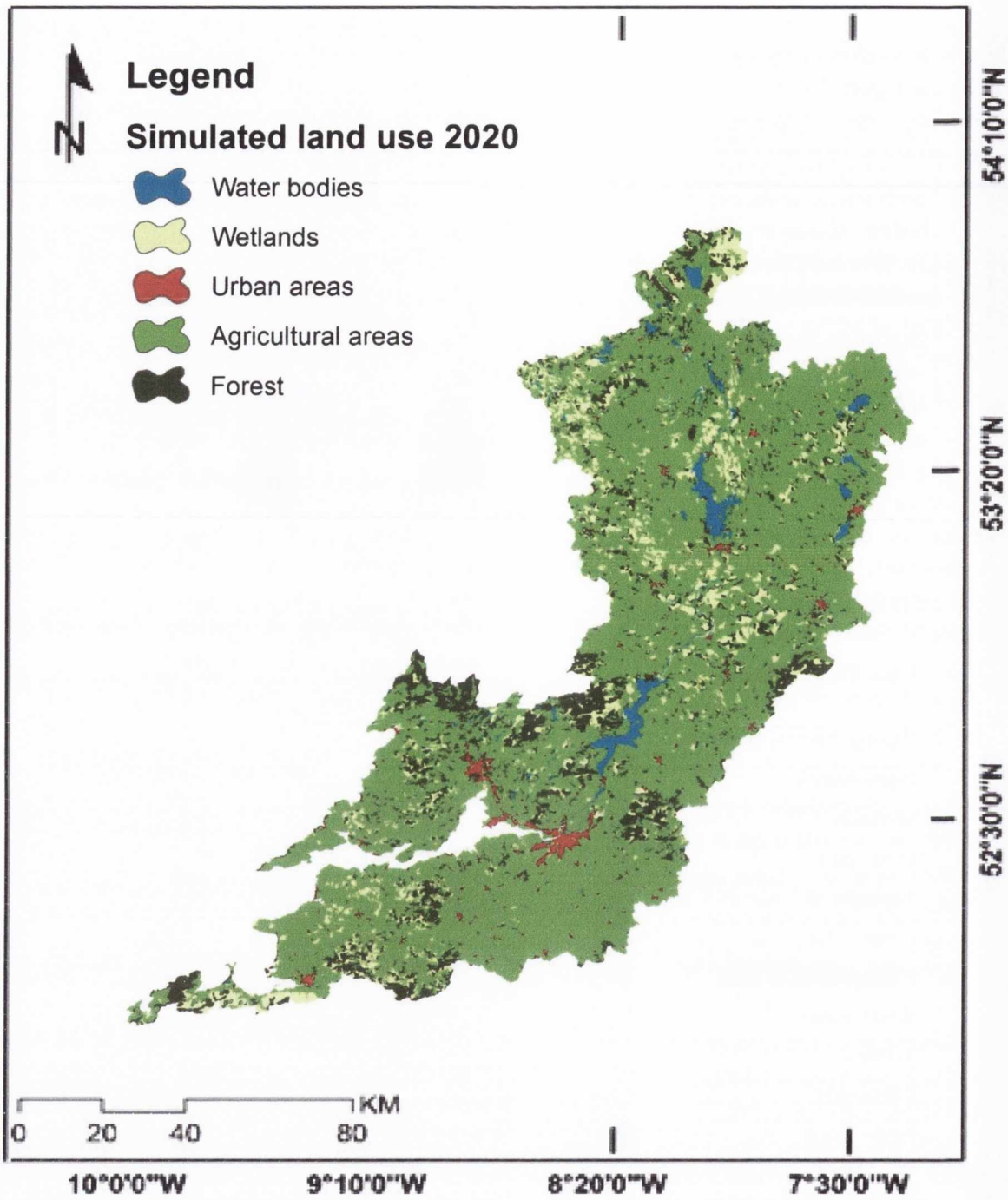

Figure 6.14: Cellular Automata (CA) predicted land cover for 2020.

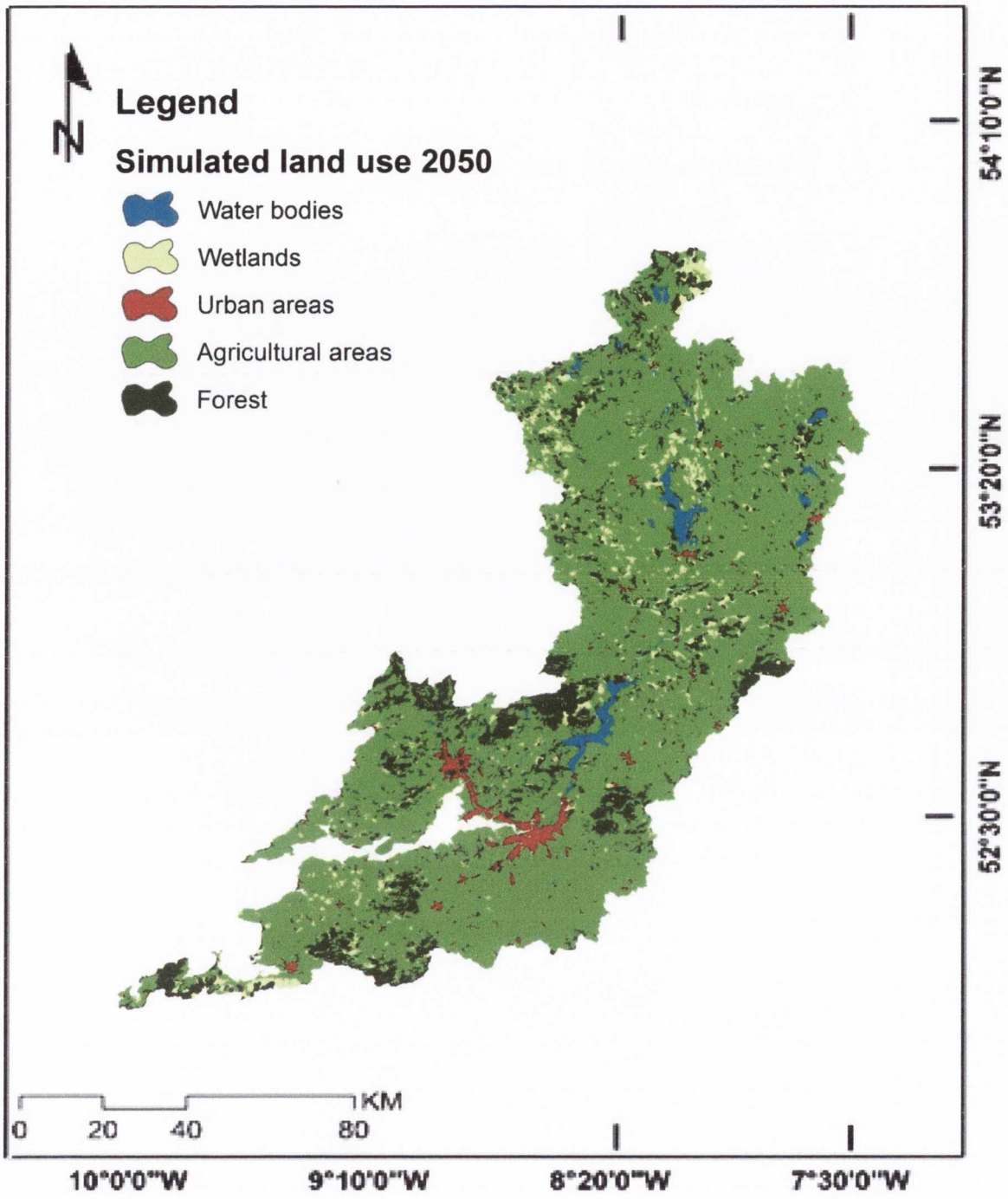

Figure 6.15: Cellular Automata (CA) predicted land cover for 2050.

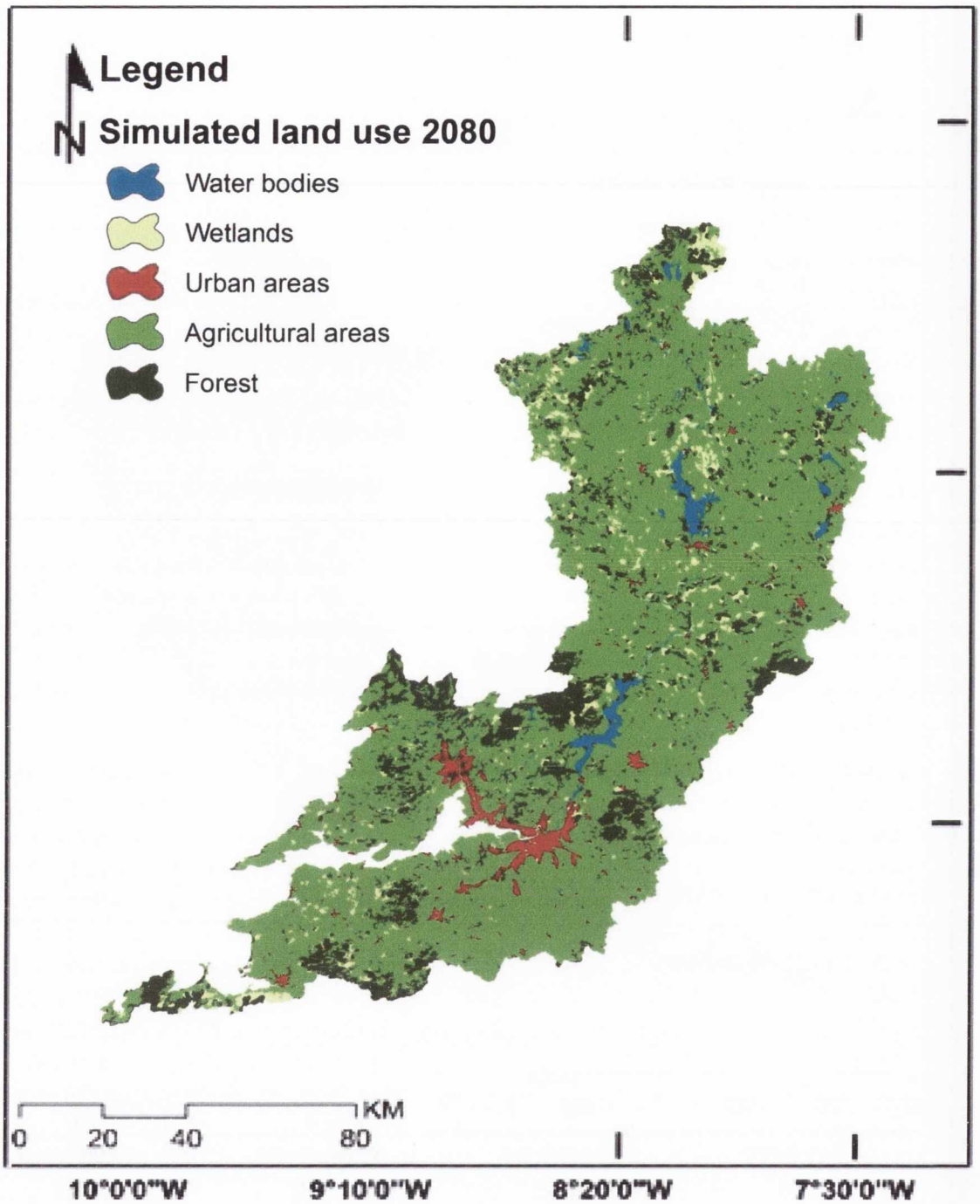

Figure 6.16: Cellular Automata (CA) predicted land cover for 2080.

6.5 Conclusions and limitations

This chapter presented a simulation model of urban development using the CA approach incorporating fuzzy set theories and spatial information technology. Through the development of the model, the study contributes to the integration of CA modeling and GIS for urban development research.

It has been concluded in this study that the weakness of the CA model was the assumption of spatial and temporal invariance for transition rules and the inability of CA to deal with stochastic behavior (Couclelis, 1985). The transition rules could not include conflict-resolving rules in the model (Jiao and Boerboom, 2006). Cellular Automata examines the synchronous dynamics of the urban environment, in essence, all cells update simultaneously at each iterative step, which means the cells were simply changed to the function to which they have the highest potential in terms of the factors modeled. But real cities are chaotic in their behavior, therefore other factors may contribute to deciding on the final locations of cells and simply changing cells to the highest potential may not be sufficient (Twumasi, 2008). So, based on this, a full socioeconomic profile for the city must be included in the simulation. Unlike many natural processes to which CA algorithms have been applied, land use does not mutate autonomously. The model itself had many limitations such as the complexity level when more land cover classes were included in the simulations, the increased simulations time when more accuracy were required. The model is very sensitive to the quality of the forcing factors parameters.

As part of this study the CA model got calibrated against 2006 land cover data set and got validated against 2012 data set and the overall accuracy in the validation process was around 85% which is to some extend enough to provide a good prediction for the future land cover.The prediction results for the Shannon Basin area indicate an increase of urban area from 1.59% in 2012 to 1.75% in 2020, equating to a total of 28.53 km^2 of land will be converted into urban areas in 2020 (an overall change of 9.75%). The results indicate an increase of urban area from 1.59% in 2012 to 2.34% in 2050, equating to 136.38 km^2 of land converted into urban areas in 2050. Finally, the results indicate an increase of urban area from 1.59% in 2012 to 2.92% in 2080, a total 244.05 km^2 of land converted into urban areas in 2080 (an overall change of 83.37%). The majority of the urban area will come from the conversion of agricultural to urban areas; also, the small portion of the increase will be from converting wetlands and forest to an urban area. The urban expansion will be mainly around Limerick city, Ennis, Mullingar, Athlone, and Tipperary. The quality of the predictions is very good and the resulted maps can be good estimations for the future land cover status. The results are very useful for many studies include study the impact of climate and land use change for the Shannon catchment.

Chapter 7. GIS algorithms for spatially distributed potential evapotranspiration modeling

7.1 Introduction

After precipitation, evapotranspiration is the largest component of the terrestrial hydrological budget and thus critical for water resources evaluation and sustainable water management policies (Liu and Phinn, 2003, Portugali et al., 1994, Wu, 2002).

Evapotranspiration (ET) is responsible for transferring moisture from the earth's surface to the atmosphere in vapor form. Due to complex interactions between meteorological and site-specific factors, ET is extremely difficult to quantify. Water balance modeling requires the spatial estimation of potential evapotranspiration (PET) throughout the catchment; that is the evapotranspiration, which would occur under optimal conditions.

Evapotranspiration includes two processes that occur simultaneously in the soil-plant-atmosphere system, direct evaporation of moisture from the Earth's surface, and the exchange of water vapor, which occurs within the leaves of plants (transpiration). (Swenson and Wahr, 2006, Wilson et al., 2001), and is the most important component of the Earth's environmental systems (Chuanyan et al., 2004, Mo et al., 2004). Evapotranspiration has long been recognized as a central process in the hydrological cycle (Penman, 1948, Rosenzweig, 1968, Holdridge, 1959, Gordon, 1998). The term potential evapotranspiration represents the ET, which would occur under optimal conditions where ET is not limited by factors such as soil moisture.

Evapotranspiration represents the most active of land-based hydrological processes, with approximately 65% of precipitation being evaporated and transpired (Kite and Droogers, 2000, Shukla and Mintz, 1982). Evapotranspiration fulfills numerous roles throughout its cycle. It accomplishes energy (heat) and mass (water vapor) transfer between the Earth's surface and atmosphere, and is the most active mechanism connecting the atmosphere, hydrosphsophere, lithosphere and biosphere (Zhao et al., 2004, Kite and Droogers, 2000, Zhang et al., 2001). Evapotranspiration is not only responsible for modulating atmospheric moisture but also temperature. Therefore, it can be seen that this process provides a vital link between the climatic, hydrological and ecological systems.

Potential evapotranspiration remains one of the least satisfactorily explained processes in the hydrological cycle, principally because of its spatial variability (Andréassian, 2004, Andréassian et al., 2004, Oudin et al., 2005).

Due to the complexity and difficulties faced in the measurement of PET, it is predominately estimated using formulae and observed meteorological data. There exists a vast number of models for estimating PET, which may be grouped into several categories such as radiation, water budget, mass transfer, temperature, and combination methods. These methods vary greatly in terms of complexity, data requirements, and reliability.

Met Éireann, the Irish National Meteorological Service, calculates daily estimates of PET at 25 synoptic weather stations throughout Ireland using the FAO Penman-Monteith method, 4 of which are located within the Shannon IRBD. As the catchment covers in excess of 18 000 km^2, it is evident that 4 point estimates are not sufficient for this research project. The Penman-Monteith method is widely considered as a standard method for the calculation of PET. However, its application, particularly for this project, is questionable due to the need for specific

data for a variety of parameters e.g. wind speed, relative humidity, solar radiation, dew point temperature, air temperature etc. which are only available from a limited number of locations and will result in interpolation of data from distant meteorological stations. As a result, less data intensive empirical models are often utilized which allows for data from a greater number of meteorological stations to be used thus resulting in more spatially representative estimates.

Developing a GIS tool for modeling spatially distributed PET from an undefined number of meteorological stations from monthly data of precipitation and temperature is the main objective of this chapter. This tool provides the user with the PET results on a seasonal and annual basis as well as an option to calculate values on a monthly frequency. The PET GIS tool is presented using many methods with the ability to calibrate and validate the results. This chapter presents the primary results of the calculated PET for both the baseline period and the future periods in addition to the validation process. Monthly raster maps depicting the PET within the Shannon RBD are calculated for each method, which was applied in this study for water balance modeling.

This tool used six methods for spatially distributed PET modeling as follow:

- Blaney-Criddle (Allen and Pruitt, 1986).
- Kharrufa (Kharrufa, 1985)
- Hargreaves and Samani (Hargreaves and Samani, 1982)
- Oudin (Oudin et al., 2010)
- Thornthwaite (Thornthwaite and Mather, 1957)
- Hamon (Hamon, 1961)

A comparison between monthly PET values for each model and those provided by MET Éireann for four synoptic weather stations in the Shannon RBD are made. This comparison determined the Hamon model to be the most appropriate to the Shannon RBD and was thus applied to the final stage of the study.

7.2 Materials and Methods

7.2.1 Evaluating and choosing models to quantify PET

The reliability of PET estimates depends upon the number of stations from which data is obtained and the number of years of available data (Chattopadhyay and Hulme, 1997). As a result, numerous authors such as Xu and Singh (2002), Fennessey and Vogel (1996), Chattopadhyay and Hulme (1997), Oudin et al. (2005) and Kite and Droogers (2000) among many others, recommend that more simplified methods be used when only a limited number of meteorological stations are available with the required data.

Studies have focused on developing methods to accurately estimate PET and improve on existing methods for over 70 years. In that time, numerous studies of varying scope have been completed to determine the most suitable model to be used to estimate PET for varying purposes. Jensen et al. (1990) evaluated 20 formulae for estimating PET versus lysimeter data from around the world. He concluded that the Penman-Monteith method was the best method, while the performance of the remainder varied depending on calibration and local conditions. As discussed previously, methods are most suited to the environment in which they were developed.

In evaluating models to estimate PET it is also necessary to consider what the requirements are for the calculated values. For instance, Oudin et al. (2005) compared the performance of 27 PET models over 308 catchments to find the most relevant for rainfall-runoff models. It was found that temperature and radiation based methods performed best and are as efficient as models that

are far more complex. Kay and Davies (2008) investigated the performance of a simple temperature based formula proposed by Oudin et al. (2005) compared to that of the Penman-Monteith method. PET estimates using both methods were compared to that of the UK meteorological office's PET values for a 30-year period 1961-1990. It was found that the much simpler temperature based method generally gave better estimates of PET than the Penman-Monteith method. This supports the opinion of many authors who consider more simple models, once locally calibrated, to be as effective as more complex models.

CGIAR-CSI (2007) spatially estimated PET using 4 temperature-based models (Droogers and Allen, 2002, Hargreaves and Samani, 1985, Holland, 1978, Thornthwaite, 1948). The results for each were compared to PET values at 2288 meteorological stations in South America and South Africa. Based on the results, the Hargreaves & Samani method was chosen as the most suitable to model PET globally. The Hargreaves model was found to perform almost as well the Penman-Monteith method but required far less parameterisation with significantly less sensitivity to error in climate inputs.

The most comprehensive research on available PET formulae has been completed by Xu and Singh who commenced a research program in 1996. Their first paper investigated thirteen equations based on the mass- transfer method; these equations were expressed in seven generalised equations (Singh and Xu, 1997). The seven generalized equations were then compared with pan evaporation results at four climatological stations in north-western Ontario, Canada. All of the formulae yielded satisfactory estimates for monthly PET. As discussed previously, model parameters were required to be calibrated using local meteorological variables.

Xu and Singh (2000) then evaluated five radiation based PET formulae (Abtew, Hargreaves, Makkink, Priestley-Taylor and Turc), which were compared with pan evaporation measured at Changing station in Switzerland (Turc, 1961, De Bruin, 1983, Makkink, 1957, Hargreaves and Samani, 1982, Abtew, 1996, Xu and Singh, 2000). The evaluation and comparison process was first completed using original empirical constants and then using recalibrated constant values. Using original values, the Abtew formula was found to give reasonable estimates of PET while the remainder demonstrated large errors. With recalibrated constants, a significant improvement was found in four out of the five methods. The Makkink and Priestley-Taylor formulae were concluded to be the best methods for use in the study region. Xu and Singh (2001) also evaluated and compared seven temperature-based formulae (Thornthwaite, Linacre, Blaney-Criddle, Hargreaves, Kharrufa, Hamon, Romanenko) with data from two climatological stations (Rawson Lake and Atikokan) in north-western Ontario, Canada. Similar to the foregoing study comparisons were made using both original and recalibrated constant values (Romanenko, 1973, Hamon, 1961, Kharrufa, 1985, Blaney and Criddle, 1964, Linacre, 1977, Xu and Singh, 2001, Hargreaves and Samani, 1982, Thornthwaite, 1948). Using original constants, the Blaney-Criddle equation resulted in mean seasonal evaporation values that agreed most closely with pan evaporation values, while the remainder demonstrated large errors. With recalibrated constant values, all seven methods provided reasonable results. With properly determined constant values, the Blaney–Criddle, Hargreaves and Thornthwaite methods were concluded to be the best temperature based methods for the study area. Based on the results of the foregoing studies Xu and Singh (2002) selected the best methods from each of the three categories: (i) mass-transfer based methods, (ii) radiation based methods, and (iii) temperature-based methods. A cross comparison of the best formulae selected from each category was made. Five PET formulae (Hargreaves and Blaney-Criddle (temperature-based), Makkink and Priestley-Taylor (radiation-based) and Rohwer (mass-transfer-based)) were evaluated and compared with PET values calculated using the Penman-Monteith method using daily meteorological data from the Changing

station in Switzerland for the 5-year period 1990-1994. The calculations of the Penman-Monteith equation followed the procedure recommended by FAO (Allen, 2000). Both original and recalibrated constant values were used. With original constant values, all except the Blaney-Criddle method returned reasonably similar results to the Penman-Monteith method. Significant improvement was achieved for the Blaney-Criddle method by recalibrating constants and adding a transition period in determining the parameter k. Constant values were also recalibrated for the remaining methods. It was concluded from the study that, using locally determined parameter values, all five empirical methods gave acceptable estimates of PET. The methods were ranked as follows:

1. Priestley-Taylor (Radiation-based).
2. Makkink (Radiation-based).
3. Hargreaves (temperature-based).
4. Blaney-Criddle (temperature-based).
5. Rohwer (Mass-transfer).
6. Penman-Monteith.

It was also concluded that the differences in performance between the best methods selected from each category are smaller than the differences between the different methods within each category as reported in earlier studies.

As mentioned, empirical PET formulae are typically developed using site-specific data and experiments, thus their performance will vary depending on location and local conditions. Although calibration of empirical constants with local data will maximize a given formula's performance for local conditions, the performance relative to other methods will continue to vary. Therefore, from the aforementioned comparative studies, all of which were completed outside of Ireland, it is not possible to identify the method most suited for use in Irish conditions. It is possible to identify the continuously best-performing methods and those which would be best suited for use in this project.

From a review of available literature, eight PET models were selected, as listed in Table 7.1. These methods were selected as they are the generally best performing methods and those which are most suited to spatially estimate PET within a GIS platform.

In order to further evaluate the chosen methods, four criteria were chosen by which to evaluate their suitability. Under each of the criteria, each method receives a rating between 1 and 3. The three methods with the lowest cumulative rating will be selected for further evaluation with local data and subject to the data availability.

The evaluation criteria were as follows:

A. The number of climatological datasets required e.g. Temperature, wind speed etc. Ratings for this criterion are as follows: 1 dataset = 1; 2 datasets = 2; 3+ datasets = 3.

B. The spatial availability of required data. Ratings for this criterion are as follows: temperature, precipitation = 1; wind speed = 2; Radiation, vapour pressure, atmospheric pressure = 3.

C. The number of computations required. The complexity of available empirical PET models varies greatly from relatively simple methods requiring an evaluation of a single formula to those, which would require an evaluation of several formulae prior to application of a formula to estimate PET. Ratings for this criterion are as follows: 1 computation = 1; 2 computations = 2; 3+ computations = 3.

D. Suitability for use within a GIS platform. Ratings for this criterion are as follows: Easily applied = 1; moderate = 2; difficult to apply = 3

Table 7-1: PET models.

Method	Category	A	B	C	D	Total
Priestley-Taylor	Radiation	3	3	2	3	11
Makkink	Radiation	3	3	1	3	10
Hargreaves & Samni	Temperature	1	1	2	1	5
Blaney Criddle	Temperature	1	1	1	1	4
Hargreaves	Temperature	1	1	2	1	5
Thornwhite	Temperature	1	1	3	2	7
Linacre	Temperature	1	1	1	1	4
Rohwer	Mass Transfer	3	3	1	1	8
Penman-Monteith	Mass Transfer	3	3	3	3	12

From the application of the rating procedure, four PET models were identified as being the most suitable (Hargreaves & Samani, Blaney-Criddle, Hargreaves, Linacre), which were taken to further assessment regarding the data availability and the suitability for the study area.

In order to run the PET simulation using the evaluated methods, it was the intention to use lysimeter data from a trusted device to calibrate the chosen empirical equations for local conditions. Whilst reviewing the data sources in Ireland, it was found that three lysimeters were operated by Met Éireann, as reported on Met Éireann's website. However, it transpired that only one lysimeter is maintained by Met Éireann, which is located on Valentia Island. Due to its location on a small island in the Atlantic Ocean data from the lysimeter would not be representative of the Shannon RBD. The remaining two locations were found to be operated by Teagasc, The Agriculture and Food Development Authority, and we could not access this data.

Because of the absence of reliable PET data with which those evaluated methods previously shortlisted may be calibrated it was not possible to calibrate nor identify the most appropriate

method for use within the Shannon RBD. As it was not possible to recalibrate the selected models for local conditions and thus identify the best performing model for application within the GIS, a number of models were selected for the application. In order to evaluate the performance of the model, short-term monthly data was sourced from Met Éireann. This data consisted of mean monthly values of PET for four synoptic weather stations within the Shannon, the PET values were calculated by Met Éireann by Penman-Monteith using the full range of required input data for the four point locations, this data was compared with the calculated results from PET models as an evaluation step.

As discussed previously, because of the absence of lysimeter PET data it was not possible to complete a comparative recalibration of the PET models shortlisted. This chapter aimed to produce a GIS tool to simulate PET using different simulation methods, this tool used six methods for spatially distributed PET modeling as follow:

- **Blaney-Criddle (Allen and Pruitt, 1986).**

The Blaney-Criddle (1950) method for estimating PET is most well known in the U.S.A, but it has been used extensively elsewhere. For example, the FAO temperature methodology recommended by Pruitt and Doorenbos (1977) is based on the Blaney-Criddle method. Although initially used for estimating the consumptive use of irrigated crops in the western United States, it is uniformly applicable for estimating PET in agricultural lands or catchments with reasonably uniform vegetation. The common form of the Blaney-Criddle equation is:

$$PET = Kp(0.46\,T_A + 8.13) \qquad \text{Eq 7.1}$$

where PET is ET in mm from a reference crop for the period in which p is expressed, T_a is the mean temperature in °C for the same period, p represents the percentage of total daytime hours for the period used (whether daily, weekly, monthly etc.) out of total daytime hours of the year, i.e. 365x12, and k is a monthly consumptive use coefficient (Pruitt and Doorenbos, 1977), depending on vegetation type, location and season.

Blaney-Criddle recognized that temperature has one of the greatest influences on ET rates and that records are far more uniformly available than other factors. Furthermore, sunshine hours were also identified as a noteworthy factor in the rate at which plants grow and consume water. However, sunshine records are not usually available thus Blaney-Criddle recommended the use of tables of theoretical sunshine hours for different latitudes in the absence of actual data.

- **Kharrufa (Kharrufa, 1985).**

Kharrufa (1985) derived a relatively simple equation similar to that of Blaney-Criddle described previously with which PET may be calculated. PET is calculated based on a relationship between temperature and sunshine duration and is given by:

$$PET = 0.34\,P\,T_A^{1.3} \qquad \text{Eq 7.2}$$

where PET is evapotranspiration in mm/month and p and T_a has the same definitions as that given previously.

- **Hargreaves and Samani (Hargreaves and Samani, 1982).**

Hargreaves (1975) published an empirical equation for estimating PET which was developed using data from a precision lysimeter and weather data for an 8-year period. It was found for a 5-day time step that 94% of the variance in measured versus modeled values was explained through average temperature and solar radiation. The portion of extra-terrestrial solar radiation which penetrates through clouds and reaches the earth's surface is the primary heat source for ET processes. Subsequent studies by Hargreaves and Samani (1982) showed solar radiation may be estimated from the difference between maximum and minimum temperature (Hargreaves and Samani, 1982). This is possible as under clear skies incoming solar radiation may pass freely through the atmosphere resulting in high temperatures while at night temperatures are low due to outgoing longwave radiation (Allen et al., 1998). Contrastingly under cloudy conditions a fraction of the incoming solar radiation is prevented from reaching earth thus resulting in lower temperatures, while at night temperatures are higher as cloud cover limits outgoing longwave radiation. As solar radiation data is frequently unavailable Hargreaves and Samani recommended estimating it from extra-terrestrial radiation and minimum and maximum temperature. Based on their previous studies Hargreaves and Samani (1985) presented a simplified equation, which requires only temperature, the day of the year and latitude.

$$PET=0.0135K_{RS}(RA/\lambda)\ (Tmax-Tmin)\text{^}0.5 * (TA + 17.8) \qquad \text{Eq 7.3}$$

where PET is the monthly evapotranspiration rate in mm, K_{Rs} is an empirical radiation adjustment coefficient, λ is the latent heat of vaporization in MJ/kg, for the mean air temperature commonly assumed to equal 2.45 MJ/kg, RA is the extra-terrestrial solar radiation in MJ/m^2/month. T_{MAX} and T_{MIN} are monthly maximum and minimum monthly temperature in °C, the constant 0.0135 is a factor to convert from empirical US units to the international system of metric units. T_A is the mean temperature in °C.

- **Oudin (Oudin et al., 2010).**

(Oudin et al., 2005) examined the efficiency of 27 PET models over a large sample of 308 catchments which were located in France, Australia, and the USA. It was found that models based upon temperature and solar radiation performed best. Oudin selected two of the best performing models (Jensen-Haise and McGuinness) both of which had the same generalized form (Parmele and McGuinness, 1974, McGuinness and Bordne, 1972). Oudin then calibrated his formula over the catchments and produced a common formula given by:

$$PET = \frac{RA}{\lambda\rho}\frac{Ta}{100} \qquad \text{Eq 7.4}$$

where PET is monthly potential evapotranspiration in mm and ρ is the relative density of water which = 1, λ is the latent heat of vaporization in MJ/kg, RA is the extra-terrestrial solar radiation in MJ/m^2/month, T_a is the mean temperature in °C.

The equation relies on expected solar radiation as calculated from Julian day and latitude and not actual measured data; thus, the only real independent variable is temperature. Therefore, the Oudin equation, similar to the Hargreaves and Samani method discussed previously, is referred to as a temperature based method although it has a strong dependency on solar radiation.

- **Thornthwaite (Thornthwaite and Mather, 1957)**

Thornthwaite (1948) developed a methodology to estimate ET for short vegetation. This is a widely used method which was derived by correlating values of mean monthly temperature with that of ET for valleys where sufficient soil moisture was always available to sustain active transpiration (Thornthwaite, 1948). The Thornthwaite method determines values of PET using values of observed air temperature and duration of sunlight data, the rationale being that air temperature acts as a proxy to net radiation. The determination of monthly PET involves a number of computational steps as follows:

$$PET' = C\ (\frac{10Ta}{I})^{a} \qquad \text{Eq 7.5}$$

where PET' is the unadjusted monthly potential evapotranspiration in mm, C is a constant = 16, I is the annual heat index given by equation 7.7, and a is an empirical exponent given by equation 7.8. The annual value of the heat index I is calculated by summing monthly indices over a 12-month period. The monthly indices are obtained from the equation:

$$i = \frac{Ta^{1.51}}{5} \qquad \text{Eq 7.6}$$

The yearly heat index in calculated by:

$$I = \sum_{1}^{12} i_j \qquad \text{Eq 7.7}$$

The exponent a is calculated by:

$$a = (67.5 \times 10^{-8}\ I^3) - (77.1 \times 10^{-6}\ I^2) + (0.0179\ I) + 0.492 \qquad \text{Eq 7.8}$$

PET' which is calculated using equation 7.5 is an unadjusted monthly value of PET for a standard month with 30 days with 12 hr/day of sunlight. These PET' values were adjusted depending on the number of days in a month and the duration of average monthly daylight which is a function of season and latitude. This process for any month is given by:

$$PET = PET' \frac{d}{12} \left(\frac{N}{30}\right) \qquad \text{Eq 7.9}$$

where PET is the adjusted monthly potential evapotranspiration in mm, d is the duration of average monthly daylight in hours, and N is the number of days in a given month (1 – 31 days).

- **Hamon (Hamon, 1961)**

Hamon (1961) formulated a simplified expression to estimate PET. The method proposed by Hamon is most commonly used for monthly, seasonally or yearly estimates of PET. The Hamon method estimates PET given mean air temperature and day length data. The Hamon method has been employed globally for hydrological studies where only temperature data is available (Hamon, 1961). The simplified equation proposed by Hamon is given by:

$$PET = 0.55\, D^2\, Pt \qquad \text{Eq 7.10}$$

where PET is the monthly potential evapotranspiration in mm, D is the hours of daylight for a given month in units of 12hr [hr/12hr] and Pt is a saturated water vapor density term calculated by:

$$PT = \frac{4.95\, e^{0062Ta}}{100} \qquad \text{Eq 7.11}$$

This method was developed based on the relationship between PET, maximum possible radiant energy and moisture-holding capacity of the air at the prevailing air temperature. Hamon determined the constant value of 0.55 through comparison of results from the far more complex Thornthwaite method discussed previously. Sunlight hours are used as a proxy for incoming radiant energy while Pt is used as a proxy for moisture-holding capacity of the air.

7.2.2 Data Setup

In this chapter, the required data is mainly climatological data for the baseline and three future scenarios. Multi-dimensional datasets for temperature, with minimum, mean and maximum values, which were processed and produced in Chapter 4, are required. Thus, a significant quantity of temperature data was required to produce long-term mean monthly estimates of PET within the Shannon RBD. The data source for all the baseline weather data was obtained from Met Éireann, the Irish National Meteorological Service (see Chapter 4).

Met Éireann is the leading provider of weather information and related services for Ireland. Observed daily data for temperature was obtained from all available stations (96 stations) in the Shannon RBD for the period 1961-2014. The majority of stations from which data was received can be considered low lying and of high quality. Baseline mean monthly temperature was calculated for the period 1961-2000, with the remainder reserved for calibration and evaluation processes. This data was processed within ArcGIS and a long-term mean monthly temperature raster was produced for each month. As discussed previously, throughout this study the Irish National Grid coordinate system and a 50 m^2 cell size were employed.

7.2.3 Design the PET GIS-based algorithms

The methodology mainly depended on the design of the PET GIS algorithms based on the methods illustrated in Section 7.3.1. A validation and performance evaluation process was then implemented to get the best-performing method in order to use it in the PET projection simulations, which were based on climate change scenarios.

As discussed in Section 7.2.1, six methods were used in PET modeling process using the designed flowcharts below, in some of these flowcharts the interpolation is used. As all the used methods are temperature based methods, and temperature as an atmospherically parameters is relatively smoothly spatially distributed parameter, and as the Shannon River catchment is relatively flat catchment without any really high mountains, so the Spline spatially interpolation method is used in all the methods.

- **Hargreaves and Samani**

The Hargreaves and Samani method was one of the most complex methods applied during this study. A flow chart of the methodology used in modeling PET using this method is shown in Figure 7.1, based on the spatially distributed calculation process for the previously discussed equations.

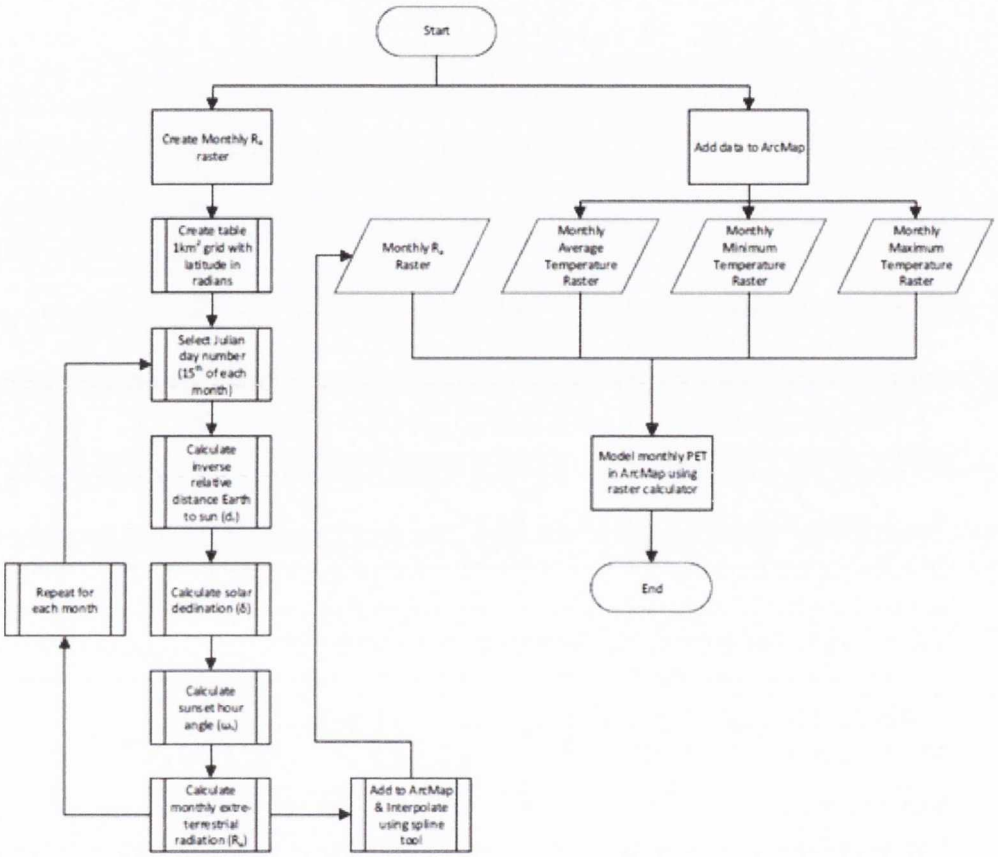

Figure 7.1: Hargreaves and Samani designed algorithm flowchart.

- **Thornthwaite**

The Thornthwaite method was completed using a similar methodology to the Hargreaves and Samani method using the designed algorithm flowchart illustrated in Figure 7.2. Monthly heat index values *I*, previously illustrated, were estimated from mean monthly temperatures. A raster file of *i* was created for each month, and then summed to produce a raster file of *I*. Once *I* had been calculated it was possible to create a raster of exponent *a*, then produce the PET monthly raster maps.

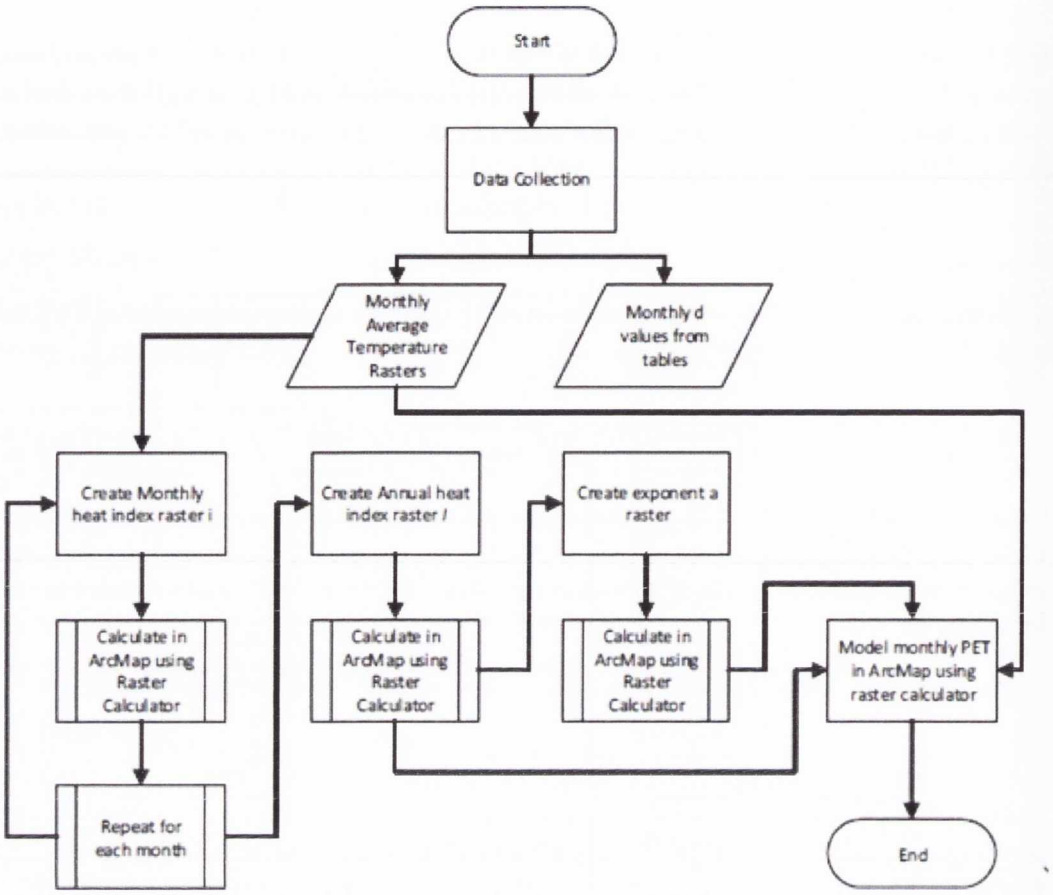

Figure 7.2: Thornthwaite designed algorithm flowchart.

- **Hamon**

Similar to the preceding methods, the Hamon method required pre-processing to create monthly raster files of variable Pt, which was previously illustrated in Section 7.2.1. The designed algorithm flowchart for this method illustrated in Figure 7.3.

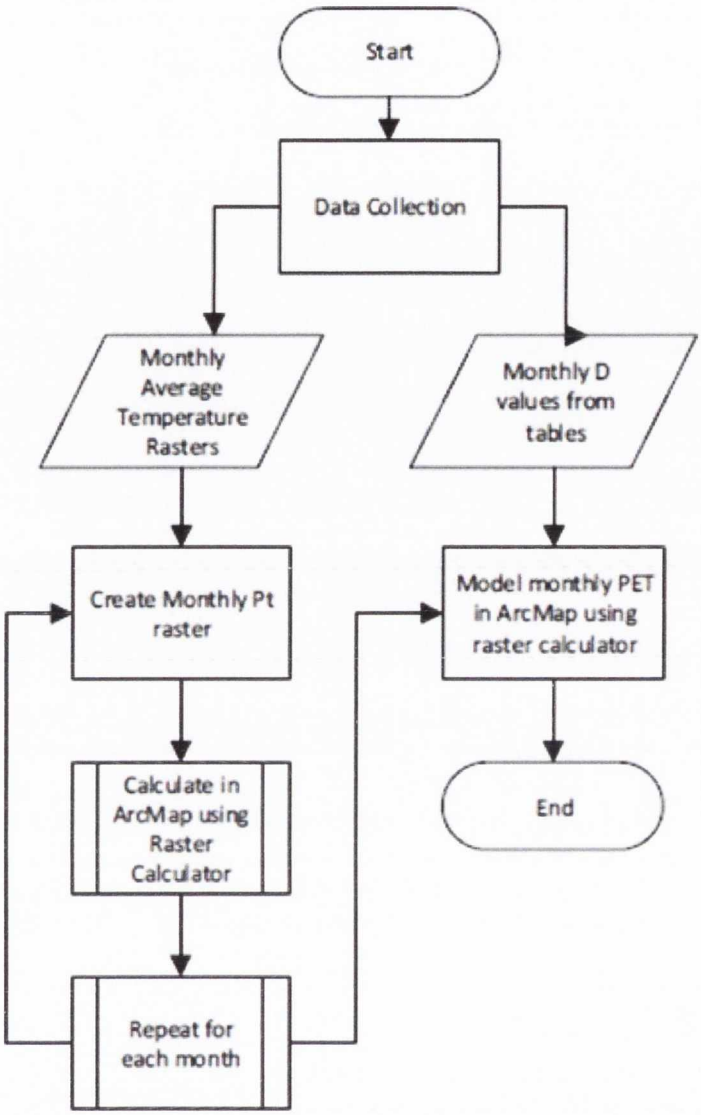

Figure 7.3: Hamon designed algorithm flowchart.

- **Blaney-Criddle and Kharrufa**

The Blaney-Criddle and Kharrufa methods were among the simplest methods applied within this study. Their application required mean monthly temperature rasters and monthly values for p, once retrieved the methods could be readily applied within the GIS. The designed algorithm flowchart for this method illustrated in Figure 7.4. The represented flow chart in the Figure 7.4 represents a practical simplification to the Eq 7.1, as the two input parameters in the equation are prepared in the raster data format then they used in the map algebra processor in the ArcMap to make the PET calculation according to the Eq 7.1.

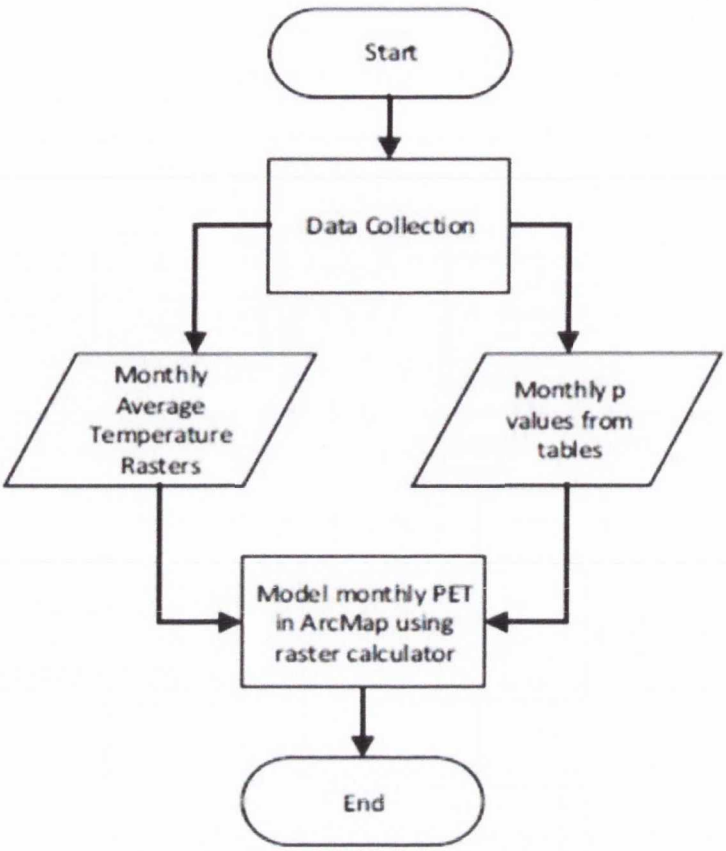

Figure 7.4: Blaney-Criddle and Kharrufa designed algorithm flowchart.

- **Oudin**

The Oudin method was similar in its application to the Hargreaves and Samani method described previously, requiring mean monthly temperature data and estimates of monthly extraterrestrial radiation as shown in Figure 7.5.

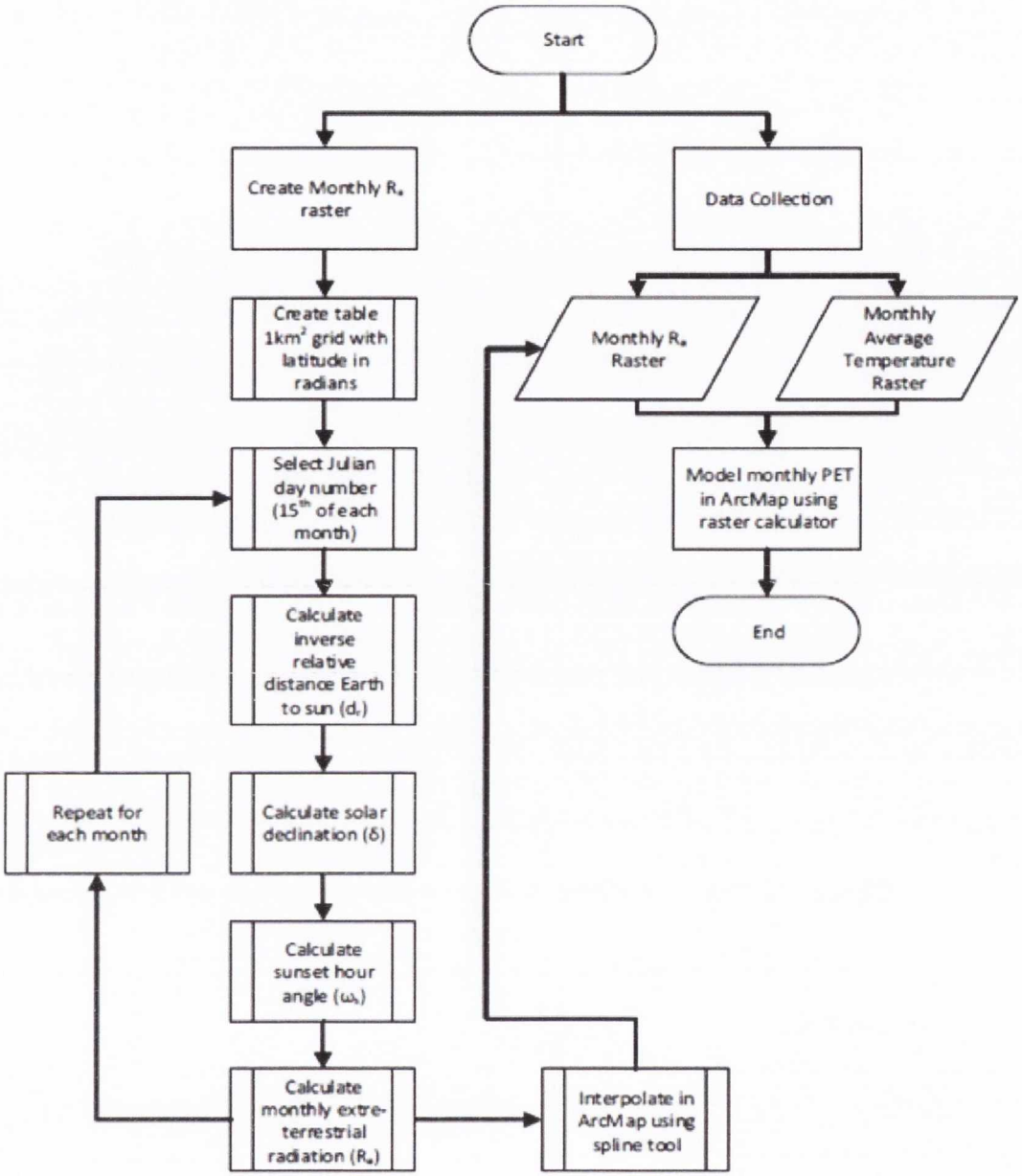

Figure 7.5: Oudin designed algorithm flowchart.

7.2.4 Validation and performance evaluation

Short-term (2012-2015) mean monthly PET rates for four synoptic weather stations within the Shannon RBD were obtained from Met Éireann. The four synoptic stations are listed in Table 7-2 with their respective coordinates. The resultant baseline mean monthly PET values at the same location as the synoptic meteorological stations from each of the six selected models were compared with that of the short-term mean monthly PET data from the Met Éireann stations (which are calculated by Penman-Monteith method). The evaluation of the performance of the PET models was completed on both a graphical and statistical basis. The modeled values were evaluated based on a number of statistical values. Firstly, the coefficient of determination (R^2) was determined for each data set, which is a statistical measure of how close the data are fitted

to the trusted data. Similarly, the root means square error (RMSE), which is a measure of the difference between modeled values and the trusted values was calculated. The mean absolute percentage error (MAPE), which is a measure of prediction error, in %, of the model was also calculated. Finally, the mean absolute deviation (MAD) was calculated, which measures the size of the error between the two sets of data.

Table 7-2: Synoptic meteorological stations within the Shannon RBD

Location	Easting	Northing
Mullingar	242335.8	254308.9
Mount Dillon	201314.2	275236
Gurteen College	199472	200233.7
Shannon Airport	137972.1	160256.2

7.2.5 Climate change effects on PET

Upon assessment, it was found that the results from the Hamon method best correlated with the data available from the synoptic stations. In that regard, the Hamon method was selected for modeling changes in future PET within the Shannon RBD as a consequence of climate change.

Climate change projections for the Shannon RBD were completed for several climate variables, including mean monthly temperature, from multi-GCM ensembles for three future time intervals (2020, 2050 and 2080) using a range of different Representative Concentration Pathways (RCPs). The climate change models were based upon two different RCPs; using a radiative forcing of 4.5 W/m^2 and 8.5 W/m^2 respectively, which were produced from 50% (median) and 75% (3rd quartile) multi-GCM ensembles simulation results, all of that was illustrated in Chapter 4.

The Hamon method was applied to three future time intervals each including four possible climate scenarios, each requiring PET to be estimated for twelve months; thus, it was required for the Hamon method to be applied for 144 monthly scenarios. A methodology flowchart for the algorithm created under the GIS environment is shown in Figure 7.6; where all processes encompassed in blue are applicable prior to all output rasters shown in green, simply Figure 7.6 can be described as a loop for the Figure 7.4 in order to get all the maps according to all the climate scenarios in monthly time step.

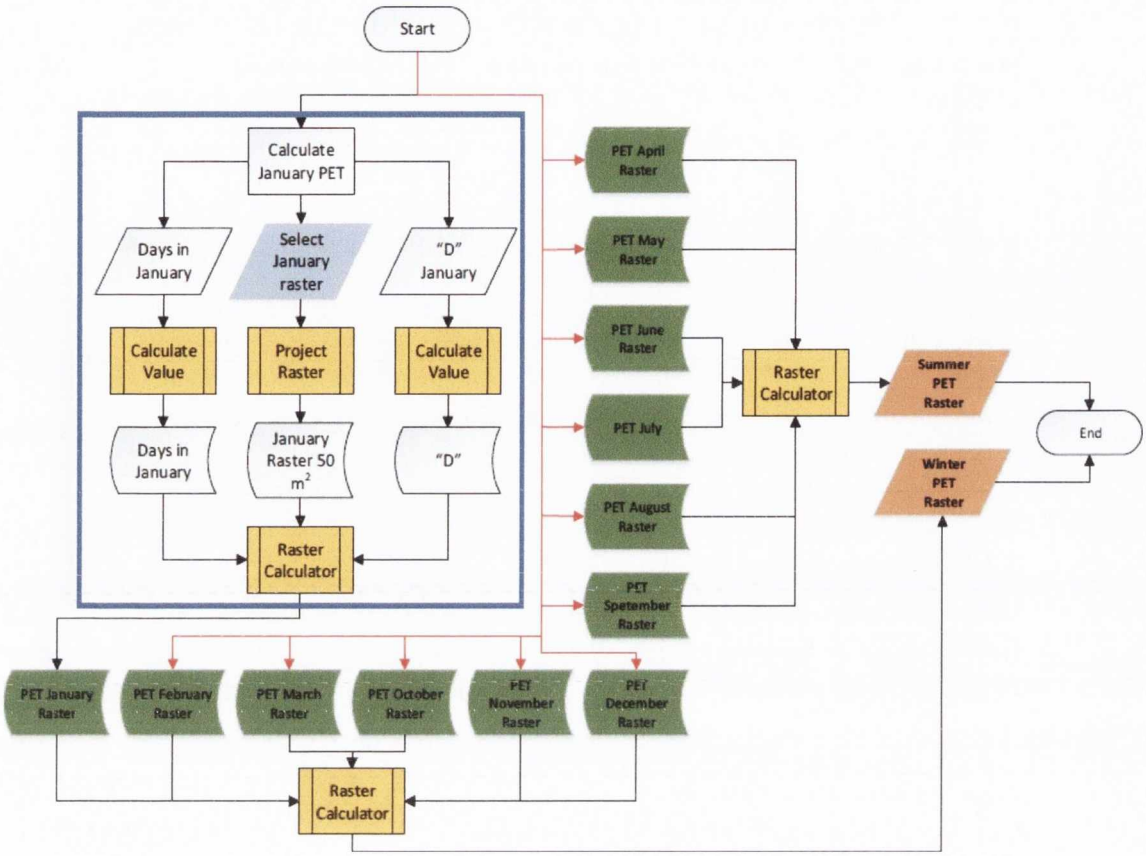

Figure 7.6: PET projection designed algorithm flowchart.

7.3 Results and Discussions

7.3.1 Baseline PET monthly simulation

The 6-selected empirical temperature based PET formulae were applied to long-term mean monthly temperature data for the Shannon RBD within a GIS. For each approach, a raster map of the Shannon RBD was created for each month of the year. These rasters depict the long-term mean monthly PET throughout the region in mm. The raster maps created are presented below.

- **Blaney-Criddle**

The Blaney-Criddle method estimates PET based on mean monthly temperature and sunshine hours; rasters created using this approach are shown in Figure 7.7. Figure 7.7 shows that in general a significant increase in the PET occurs in July. The simulated spatially distributed pattern of PET using Blaney-Criddle has a significant change over the different maps shown in Figure 7.7.

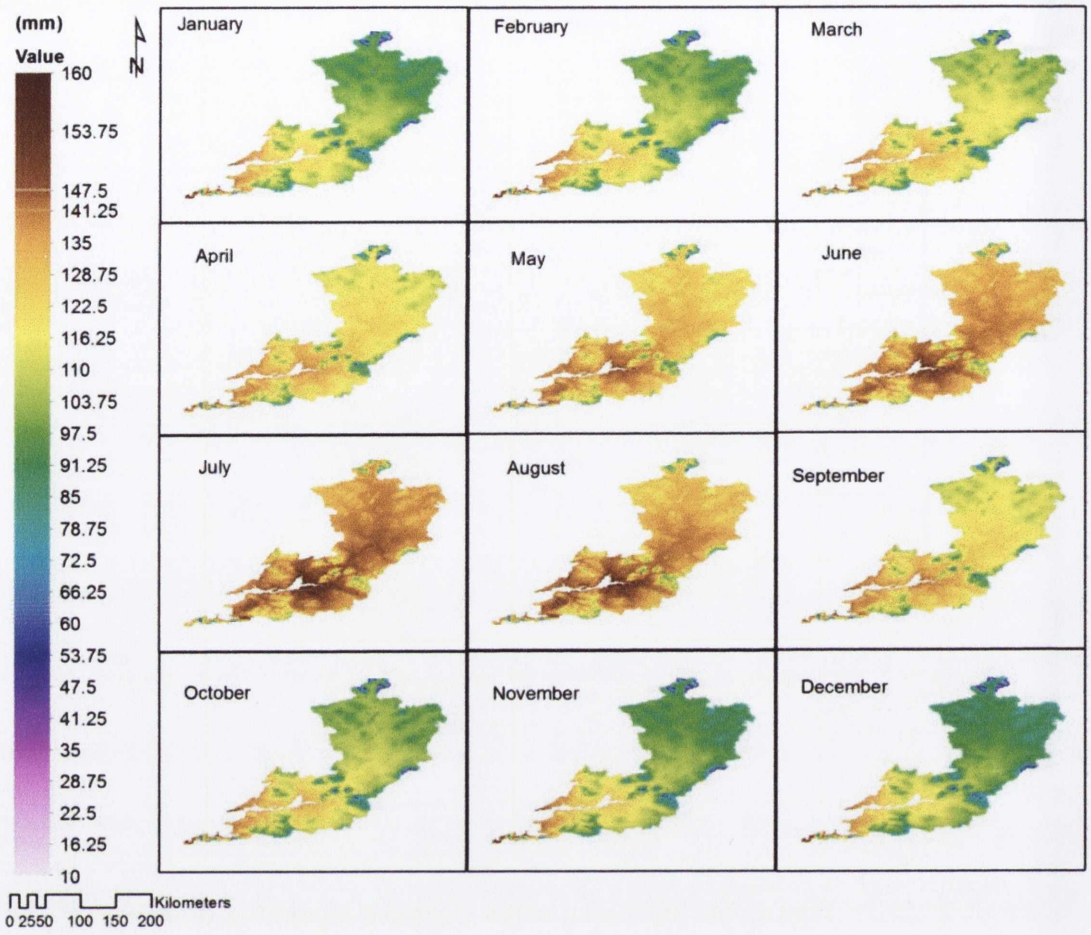

Figure 7.7: Blaney-Criddle baseline monthly PET raster maps

- **Kharrufa**

Similarly, to the Blaney-Criddle approach, the Kharrufa method uses mean monthly temperature and sunshine hours to estimate PET; raster maps created by means of this approach are presented in Figure 7.8. Figure 7.8 shows that Karrufa method produces almost the same spatially distributed patterns of PET using Blaney-Criddle over all the simulated months.

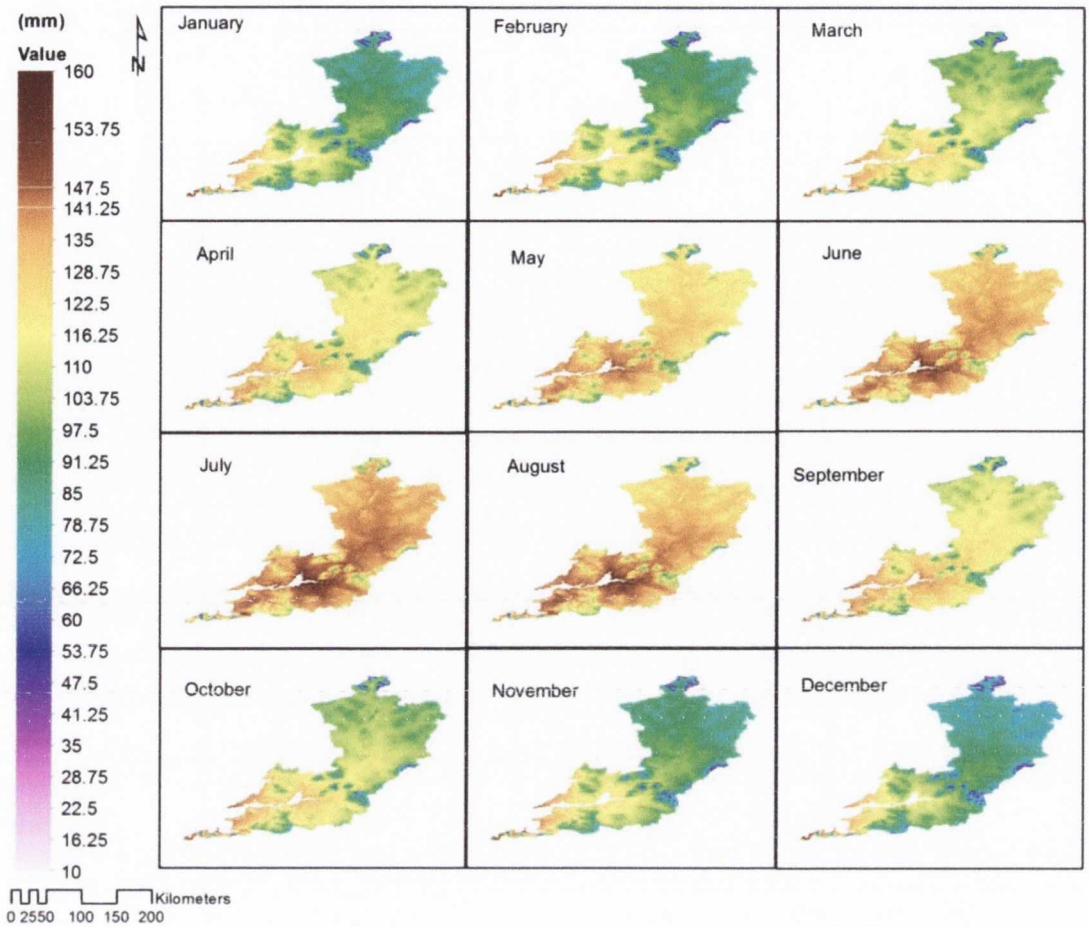

Figure 7.8: Kharrufa baseline monthly PET raster maps.

- **Hargreaves and Samani**

This approach represents one of the most complex applied during this study, requiring a minimum, maximum and mean temperature data as well as extra-terrestrial radiation. Raster map created using this approach are presented in Figure 7.9.

Figure 7.9 shows that Hargreaves and Samani method has almost the same spatially distributed patterns shown on all the simulated PET maps except for December, January and February, their spatially distributed patterns have significant differences from others.

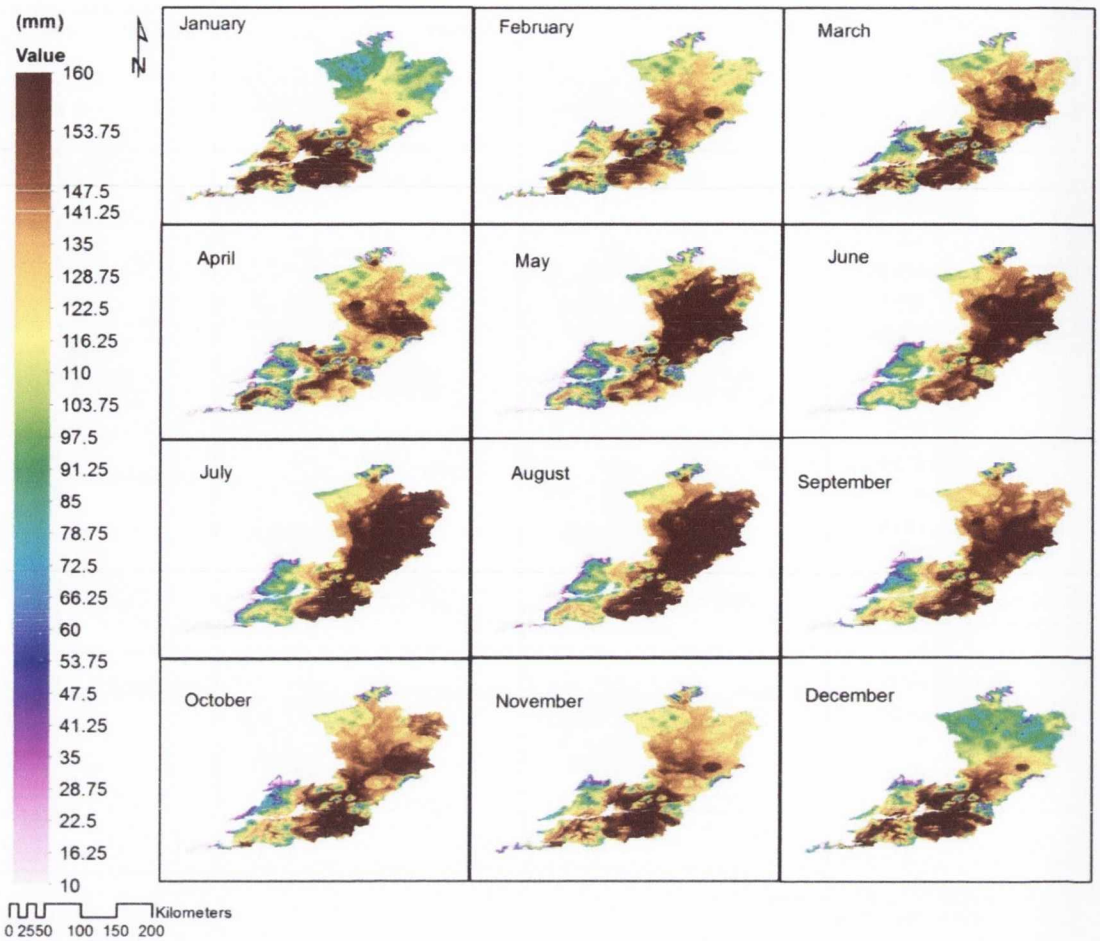

Figure 7.9: Hargreaves and Samani baseline monthly PET raster maps.

- **Oudin**

The equation presented by Oudin also requires extra-terrestrial radiation data, however unlike the Hargreaves and Samani only mean monthly temperature is required. Raster maps prepared using this method are shown in Figure 7.10.

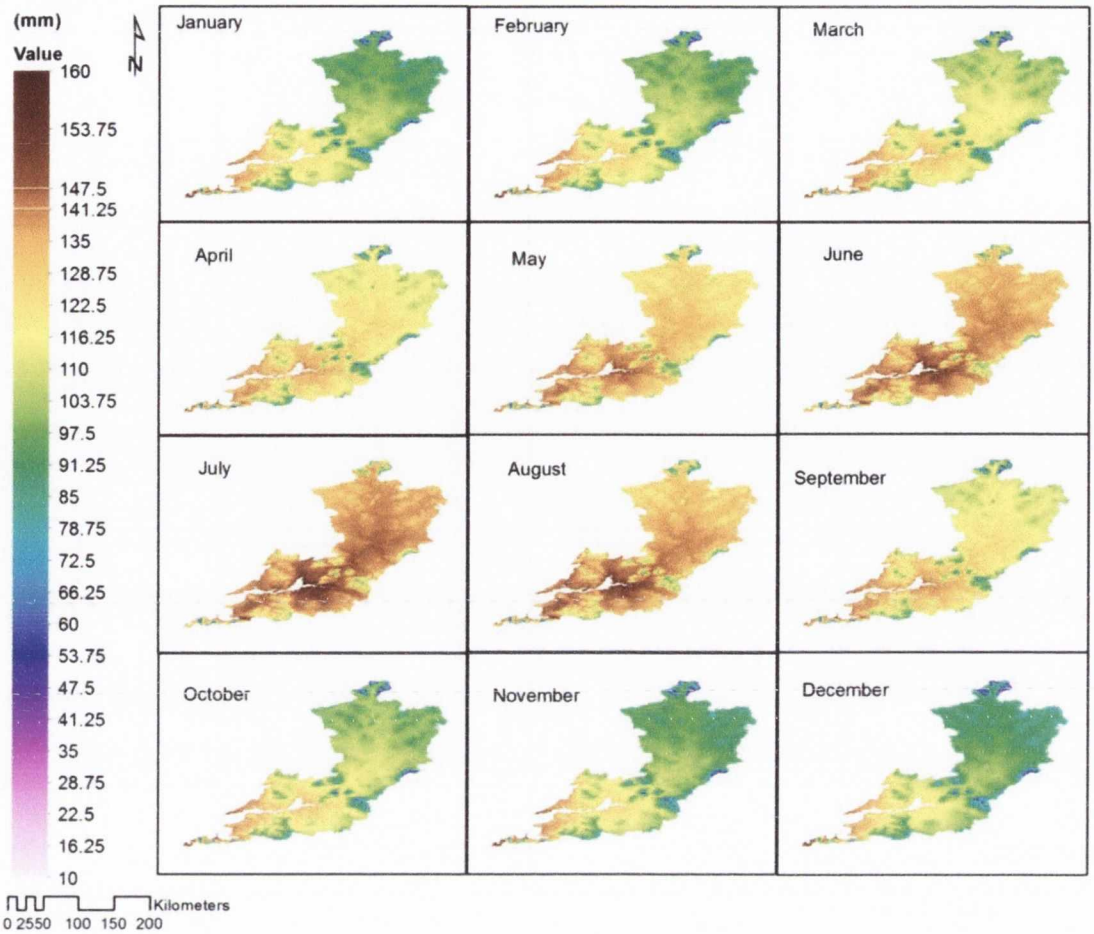

Figure 7.10: Oudin baseline monthly PET raster maps.

- **Thornthwaite**

The Thornthwaite method uses mean monthly temperature to estimate both a radiation term and PET; raster maps are presented in Figure 7.11. Thornthwaite method has the lowest simulated PET values for September, October and November with unique spatially distributed patterns for all of them compared with the other used methods, see figure 7.11.

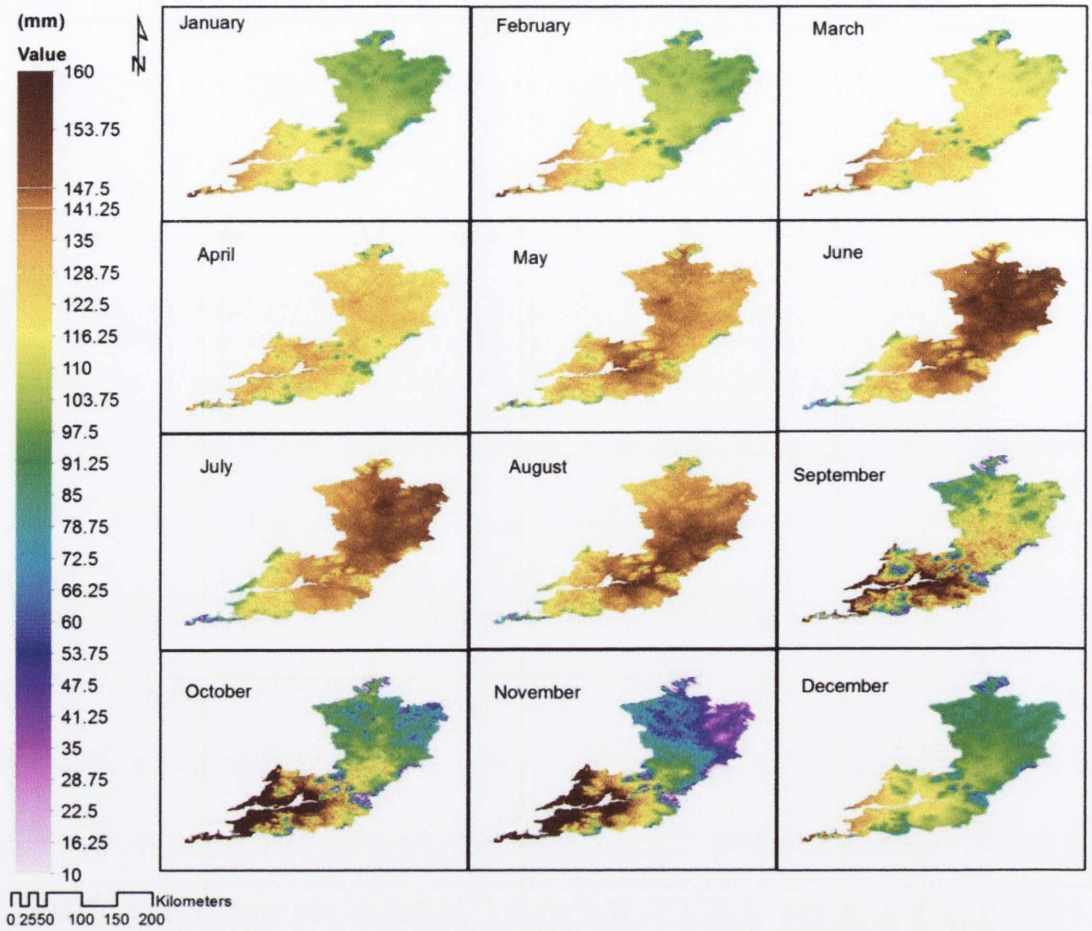

Figure 7.11: Thornthwaite baseline monthly PET raster maps.

- **Hamon**

PET is estimated based on mean temperature, which is used to calculate a vapor density term, and daylight hours; raster maps created are presented in Figure 7.12. Hamon method appears to be the most consistent method to simulate the PET between summer and winter. This method has almost one spatially distributed PET pattern for summer months and another different one for winter months.

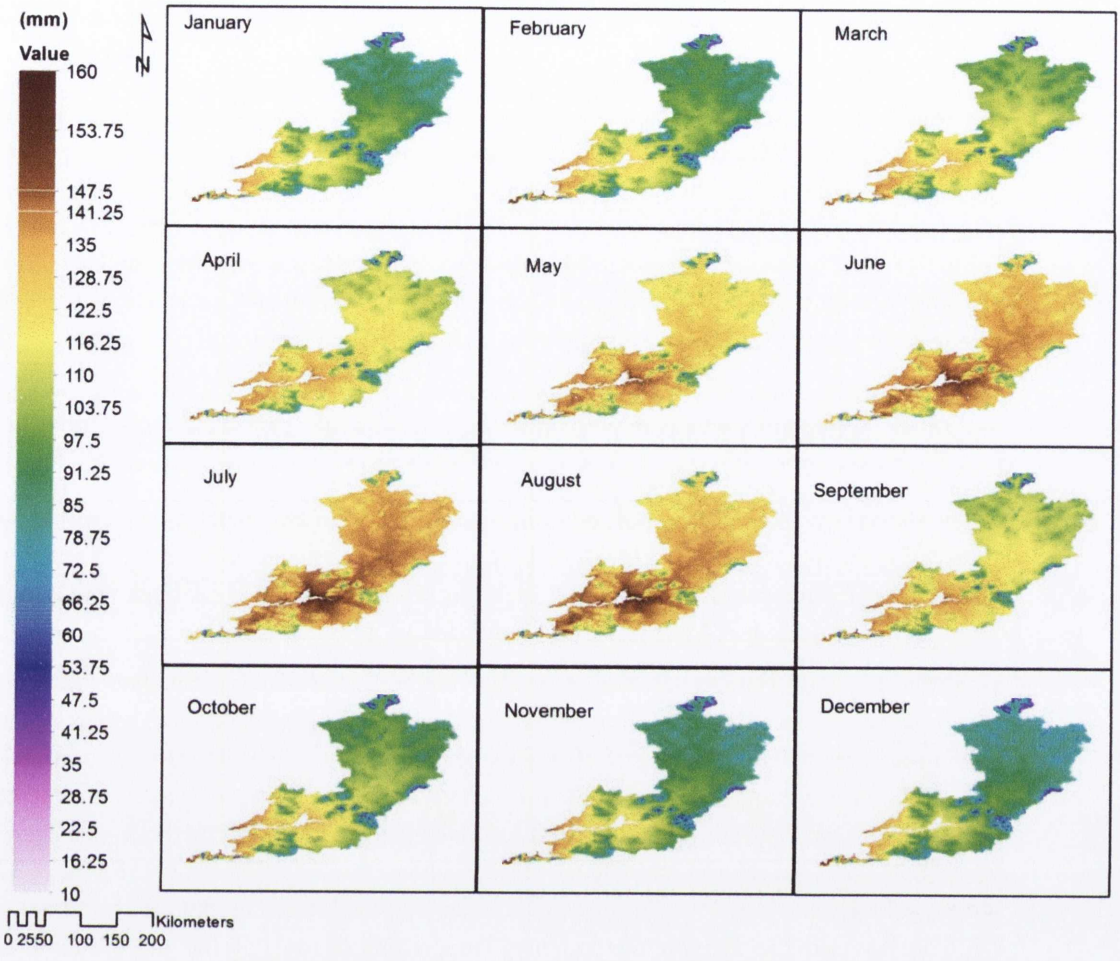

Figure 7.12: Hamon baseline monthly PET raster maps.

Each empirical method applied successfully produced a spatially distributed estimation of long-term mean monthly PET for the Shannon RBD. From initial inspection of the results, each method appears to produce reasonable estimates of PET throughout the region; with minimal PET rates during cold winter months and higher rates (up to 100+ mm per month) during summer months. In addition, a clear variation in PET is visible in coastal areas in the southwest of the region which would be expected. However, from inspecting the raster maps produced it was not possible to determine the most accurate method for use within the Shannon RBD. Thus, further evaluation of the methods was necessary and is discussed in the following section.

7.3.2 Validation and performance evaluation

The modeled values in this chapter were evaluated against the secured Penman-Monteith PET values of the four Met Éireann synoptic stations, based on a number of statistical values, as illustrated in Section 7.2.4, which are R^2, RMSE, MAPE and MAD. These statistical values were calculated for each of the four locations and a mean value was taken for each, which shown in Table 7.3. Evaluation of Blaney-Criddle modeled PET values is presented in Table 7.3 below. From the results, there is a clear disparity between the datasets at all four locations. This is further demonstrated by the low R^2 and high RMSE, MAPE and MAD values.

Similarly, results from the Kharrufa method are evaluated in Table 7.3 below. Although a more simplified approach the Kharrufa method returned somewhat more accurate results with a mean $R^2 = 0.652$, RMSE = 28.5 mm, MAPE = 51.5% and MAD = 20.9 mm.

Given the relative complexity of the Hargreaves and Samani method, one would have the expectation that the method would return somewhat accurate results. As it can be seen from Table 7.3 the modeled results are significantly more accurate the previous methods with a mean $R^2 = 0.774$, RMSE = 15.3 mm, MAPE = 24.8% and MAD = 11.8 mm.

Similarly to the Hargreaves and Samani method, the Oudin method also produced significantly improved estimates compared to the preceding methods as shown in Table 7.3, with a mean $R^2 = 0.860$, RMSE = 10.1 mm, MAPE = 18.6% and MAD = 7.7 mm. Similarly, given the relative complexity of the Thornthwaite method, one would have the expectation of more accurate estimates of PET compared to some of the most simple methods. As it can be seen from Table 7.3 it did return relatively accurate results with a mean $R^2 = 0.841$, RMSE = 12.7 mm, MAPE = 33.3% and MAD = 9.2 mm. Finally, results of the Hamon method are presented in Table 7.3. The fact that the Hamon method may be considered one of the more simple methods applied as part of this study it returned the best mean $R^2 = 0.888$, RMSE = 8.6 mm, MAPE = 16.5% and MAD = 6.5 mm. In order to more clearly delineate the deviance between modeled and Met Éireann values, monthly PET values were plotted for each location and are provided in Figure 7.13. From the figure, it is evident that, particularly during summer months (April-September), the PET models consistently overestimate PET. That might be because all the methods are not calibrated against the Irish summer long daytime and calibrating them was not possible due to the lack of observed evapotranspiration data. This overestimation is not really significant, so the validated methods can still be used in the Irish environment. During winter months (October-March) modeled results correspond more closely with the Met Éireann values, although it must also be considered that during this period PET rates are at their lowest. Through the evaluation of the statistical results presented previously and examination of Figure 7.13 the Hamon method was selected as the most appropriate method for application within the Shannon IRBD and thus was selected for application in the final stage of this study, the results of which are presented within the following section. It could be concluded that Hamon method was performing the best for the Shannon catchment because of the simple parameterization which includes two main factors, the daytime period and the temperature, with an exponential relation which is one of the main deference between Hamon and the other methods.

Table 7-3: Statistical parameters for performance evaluation process.

Methods	Stations	Statistical Parameters			
		R^2	RMSE (mm)	MAPE (%)	MAD (mm)
Blaney-Criddle	Mullingar	0.55	41.00	105.80	35.30
	Mount Dillon	0.54	41.80	101.80	35.80
	Gurteen College	0.56	40.00	81.90	33.70
	Shannon Airport	0.58	39.60	70.49	32.90
	Mean	0.56	40.60	90.00	34.43
Kharrufa	Mullingar	0.66	26.50	53.60	19.20
	Mount Dillon	0.64	28.30	55.80	20.90
	Gurteen College	0.65	28.40	47.50	20.90
	Shannon Airport	0.65	30.70	49.00	22.70
	Mean	0.65	28.48	51.48	20.93
Hargreaves and Samani	Mullingar	0.76	15.90	26.80	12.50
	Mount Dillon	0.73	18.50	31.50	14.40
	Gurteen College	0.76	16.90	24.00	12.50
	Shannon Airport	0.86	10.00	16.90	7.90
	Mean	0.77	15.33	24.80	11.83
Oudin	Mullingar	0.85	9.90	15.60	6.90
	Mount Dillon	0.84	10.80	20.50	8.30
	Gurteen College	0.87	9.50	18.20	7.70
	Shannon Airport	0.88	10.10	20.20	7.90
	Mean	0.86	10.08	18.63	7.70
Thornthwaite	Mullingar	0.82	13.90	41.20	10.80
	Mount Dillon	0.81	14.00	39.70	11.20
	Gurteen College	0.85	11.80	28.70	9.70
	Shannon Airport	0.89	11.00	23.70	9.20
	Mean	0.84	12.68	33.33	10.23
Hamon	Mullingar	0.88	8.40	20.00	6.30
	Mount Dillon	0.87	9.40	19.80	7.20
	Gurteen College	0.90	7.80	13.50	6.10
	Shannon Airport	0.90	8.70	12.50	6.30
	Mean	0.89	8.58	16.45	6.48

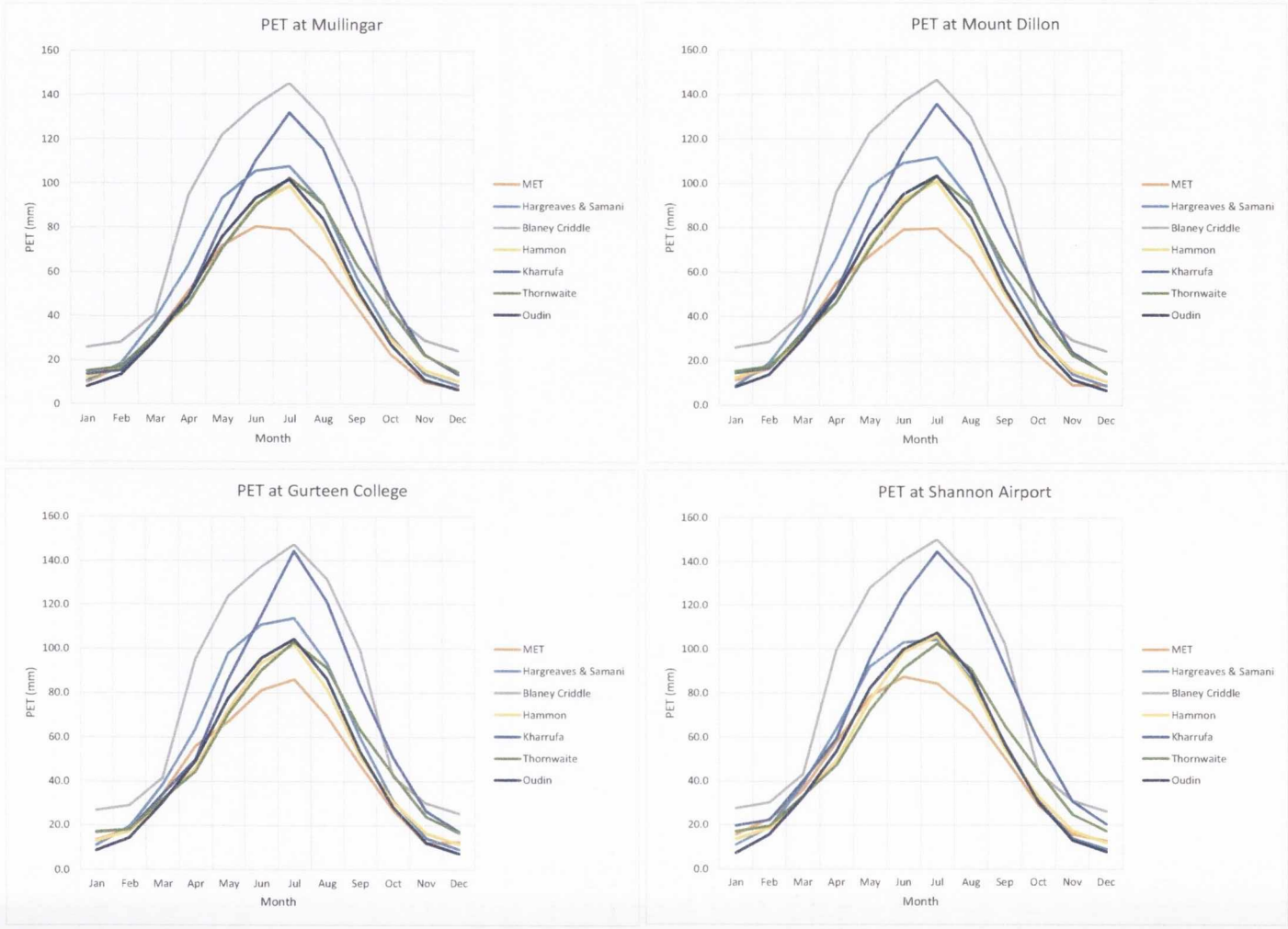

Figure 7.13: Met Éireann and modeled monthly PET at four synoptic stations located in the Shannon RBD.

7.3.3 Future PET simulations

The Hamon method was first applied to mean monthly temperature data from 2020 for the four modeled climate change scenarios. Given the uncertainty of future climate change, monthly PET raster maps were aggregated to represent growing (April to September) and non-growing (October to March) seasons, herein termed summer and winter respectively. Seasonal raster maps for baseline and 2020 PET projections are presented in Figure 7.14. As can be seen, a summer and winter raster map were created for each scenario. In order to evaluate the effect of climate change on PET under the scenarios considered, seasonal PET values at the same four locations as previously have been compared with baseline values as shown in Table 7.4.

Table 7-4: Seasonal PET Baseline and projections for 2020 at four synoptic stations located in the Shannon RBD.

	Baseline		50% Delta RCP4.5		50% Delta RCP8.5		75% Delta RCP4.5		75% Delta RCP8.5	
Location	**Winter**	**Summer**	**Winter**	**Summer**	**Winter**	**Summer**	**Winter**	**Summer**	**Winter**	**Summer**
Mullingar	116.5	434.7	117.6	439.0	117.8	439.8	117.8	439.0	118.1	440.6
Mount Dillon	118.6	442.1	119.6	446.0	119.8	446.7	119.8	446.0	120.0	447.8
Gurteen College	121.2	446.3	122.2	450.6	122.4	451.1	122.4	450.6	122.7	452.3
Shannon Airport	127.8	470.2	128.9	474.3	129.1	475.0	129.2	474.3	129.4	476.4
Mean	121.0	448.3	122.1	452.5	122.3	453.2	122.3	452.5	122.6	454.3
% Change			0.9	0.9	1.0	1.1	1.1	0.9	1.3	1.3

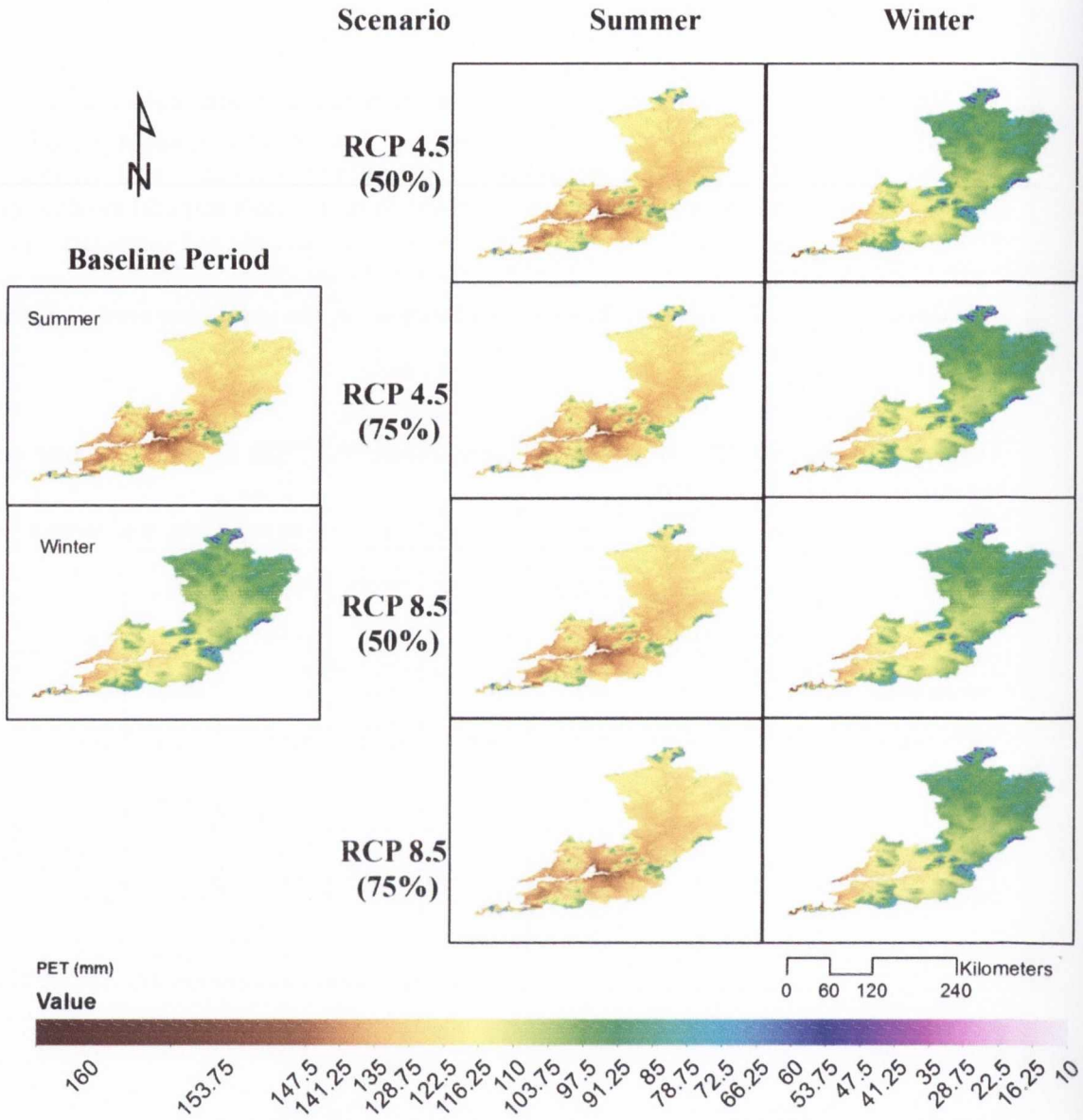

Figure 7.14: Seasonal PET baseline and projections for 2020 according to different Representative Concentration Pathways.

Similarly, to 2020, results for 2050 are shown in Figure 7.15 and Table 7.5.

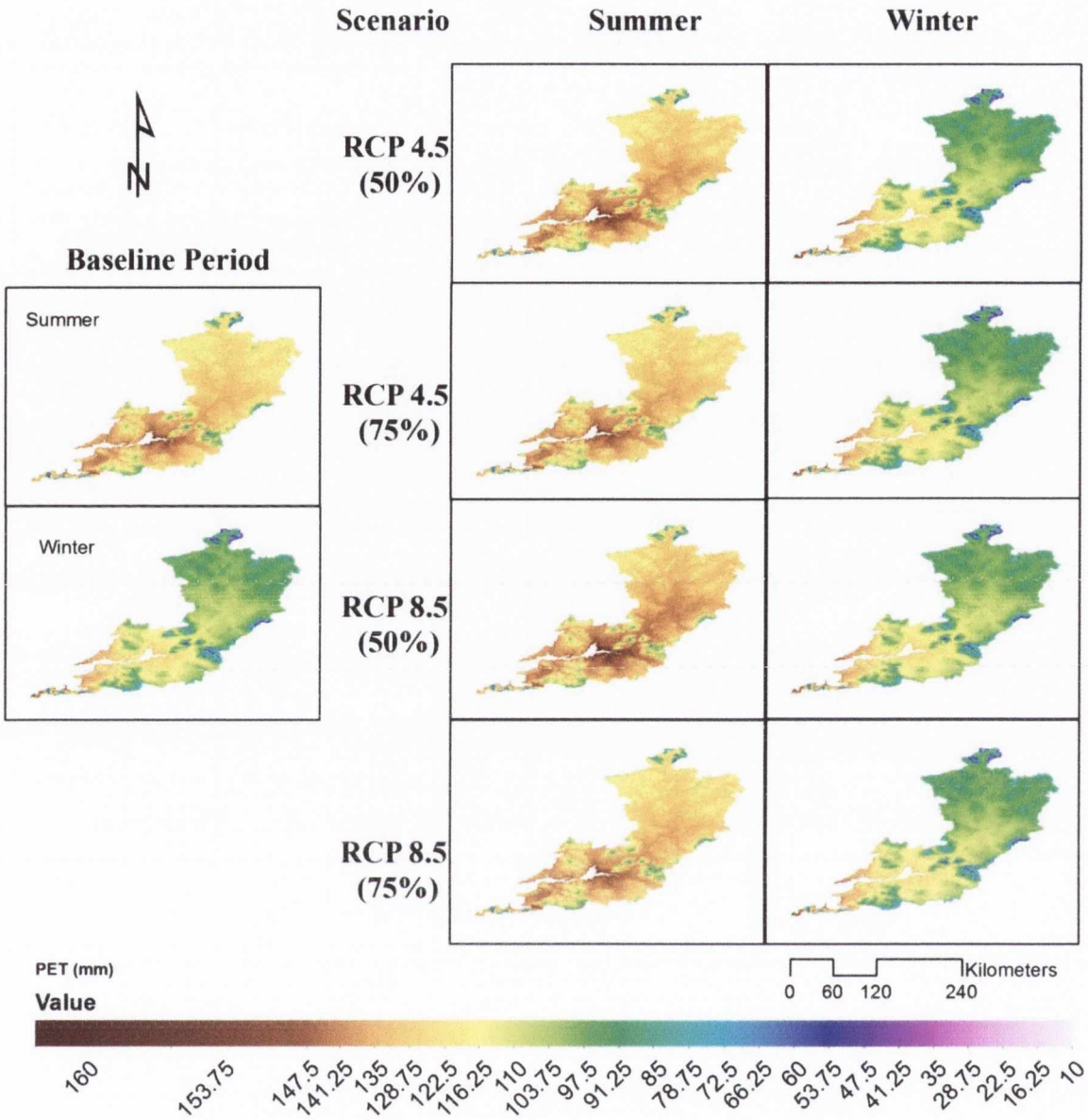

Figure 7.15: Seasonal PET baseline and projections for 2050 according to different Representative Concentration Pathways.

Table 7-5: Seasonal PET Baseline and projections for 2050 at four synoptic stations located in the Shannon RBD.

	Baseline		50% Delta RCP4.5		50% Delta RCP8.5		75% Delta RCP4.5		75% Delta RCP8	
Location	**Winter**	**Summer**	**Winter**	**Summer**	**Winter**	**Summer**	**Winter**	**Summer**	**Winter**	**Summe**
Mullingar	116.5	434.7	120.5	452.0	122.6	460.5	121.3	450.7	123.8	464.9
Mount Dillon	118.6	442.1	122.4	459.2	124.5	465.5	123.1	460.1	125.5	469.9
Gurteen College	121.2	446.3	125.3	467.9	127.6	472.6	126.2	470.0	128.9	478.0
Shannon Airport	127.8	470.2	132.0	474.8	134.3	494.2	132.9	486.8	135.6	496.0
Mean	121.0	448.3	125.1	463.5	127.3	473.2	125.9	466.9	128.5	477.2
% Change			3.3	3.4	5.1	5.5	4.0	4.1	6.1	6.4

Table 7-6: Seasonal PET Baseline and projections for 2080 at four synoptic stations located in the Shannon RBD.

	Baseline		50% Delta RCP4.5		50% Delta RCP8.5		75% Delta RCP4.5		75% Delta RCP8	
Location	**Winter**	**Summer**	**Winter**	**Summer**	**Winter**	**Summer**	**Winter**	**Summer**	**Winter**	**Summe**
Mullingar	116.5	434.7	122.3	458.4	129.0	458.4	123.4	456.5	131.4	497.0
Mount Dillon	118.6	442.1	124.2	463.5	130.7	463.5	125.2	466.0	132.9	500.9
Gurteen College	121.2	446.3	127.2	470.1	134.5	470.1	128.5	477.2	137.3	510.1
Shannon Airport	127.8	470.2	133.9	490.0	141.1	492.1	135.2	492.5	143.8	527.9
Mean	121.0	448.3	126.9	470.5	133.8	471.0	128.1	473.1	136.4	509.0
% Change			4.9	4.9	10.6	5.1	5.8	5.5	12.7	13.5

Finally, results for 2080 scenarios are presented in Figure 7.16 and Table 7.6.

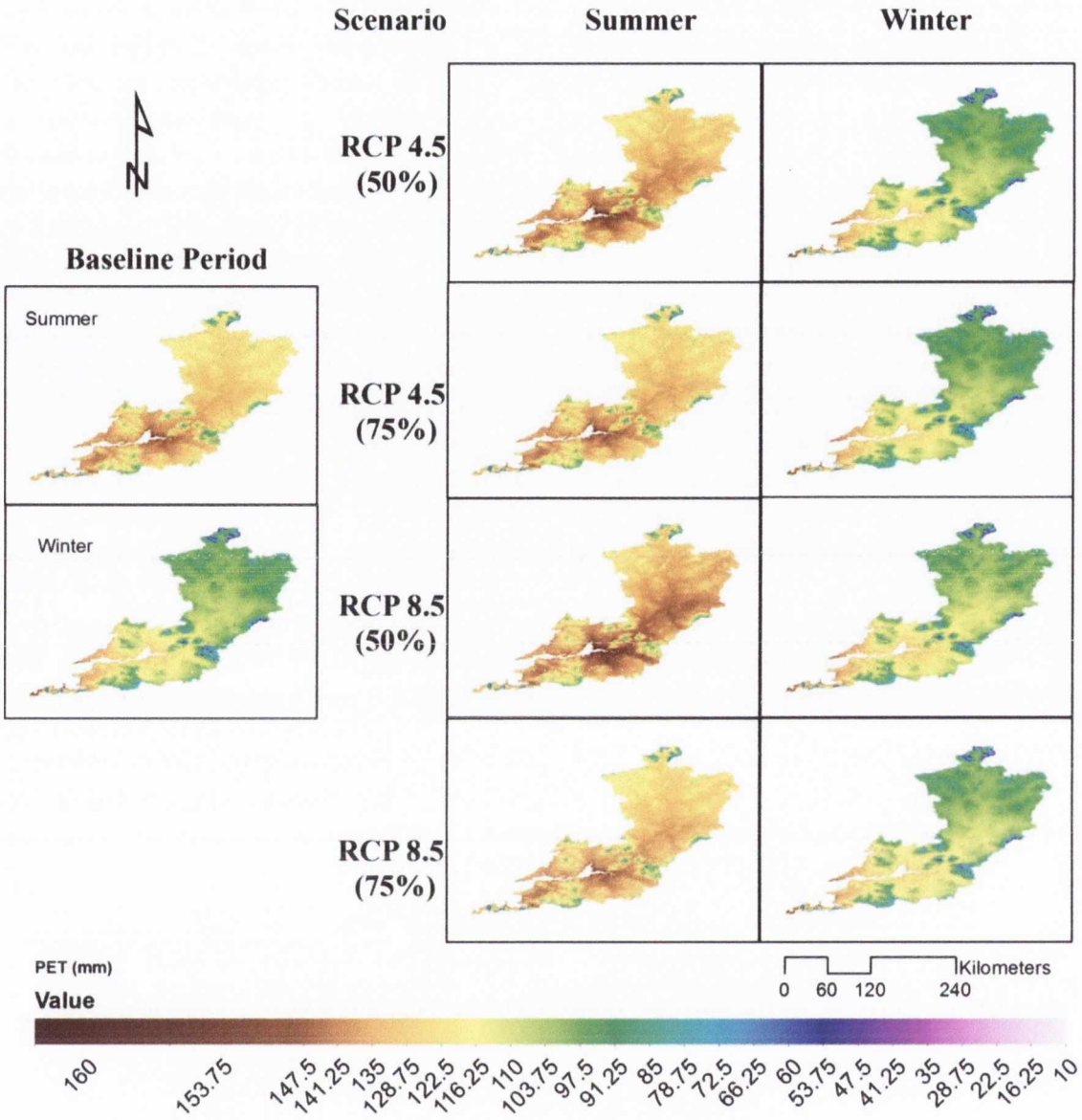

Figure 7.16: Seasonal PET baseline and projections for 2080 according to different Representative concentration pathways.

The results present evidence that the modeled climate change scenarios would have a significant impact on future PET rates within the Shannon IRBD. In all locations, all scenarios predicted an increase in PET for each future time interval.

7.3.4 Discussion

Empirical PET equations are most suited to the regions within which they are developed; consequently, one would expect disparity between results for different methods for given conditions. From the results, it can be seen that there exists significant deviation between modelled results of up to 61.9 mm per month (Blaney-Criddle/Hamon in July at Mount Dillon). Also it can be seen that the Blaney-Criddle, Kharrufa, and Hargreaves and Samani methods consistently overestimate PET and with their large mean RMSE values of 40.6 mm, 28.5 mm and 15.3 mm respectively, they were concluded as unsuitable for application within the Shannon RBD and excluded from further evaluation. As can be seen, the remaining three methods consistently returned relatively similar results and in addition, although the Penman-Monteith may be the most reliable method, the Met Éireann PET values are also subject to error making it difficult to ascertain the most accurate model. Yoder et al. (2005) compared lysimeter data with the Penman-Monteith method in a wet/humid region in the south-eastern United States similar to conditions prevailing in Ireland and found an R^2 of 0.91 with an error of 0.31 mm/day. Given this error it is possible to accumulate a total error of 9.3 mm in a 30 day period (Yoder et al., 2005). From Figure 7.13, it can be seen the presence of such an error could have a significant impact on the relative accuracy of the Oudin, Thornthwaite and Hamon Methods. As can be seen, there exists a substantial spatial variation in PET for a given period (in excess of 35 mm for July). Variations in excess of 20 mm exist between Oak Park Co. Carlow and Johnstown Castle Co. Wexford for July, which are sited approximately 70 km apart, see Figure 7.17. This represents approximately 33% of that measured at Oak Park. When Figure 7.18 is compared with Figure 7.13, it can be seen that values of PET calculated using the Hamon method for all locations correlate reasonably well with the trends of measured values. While this does not validate the application of the Hamon method, it does demonstrate the capacity of the formula to reasonably account for variations in PET within the Irish climate.

Figure 7.17: The six lysimeters locations, indicated with yellow stars.

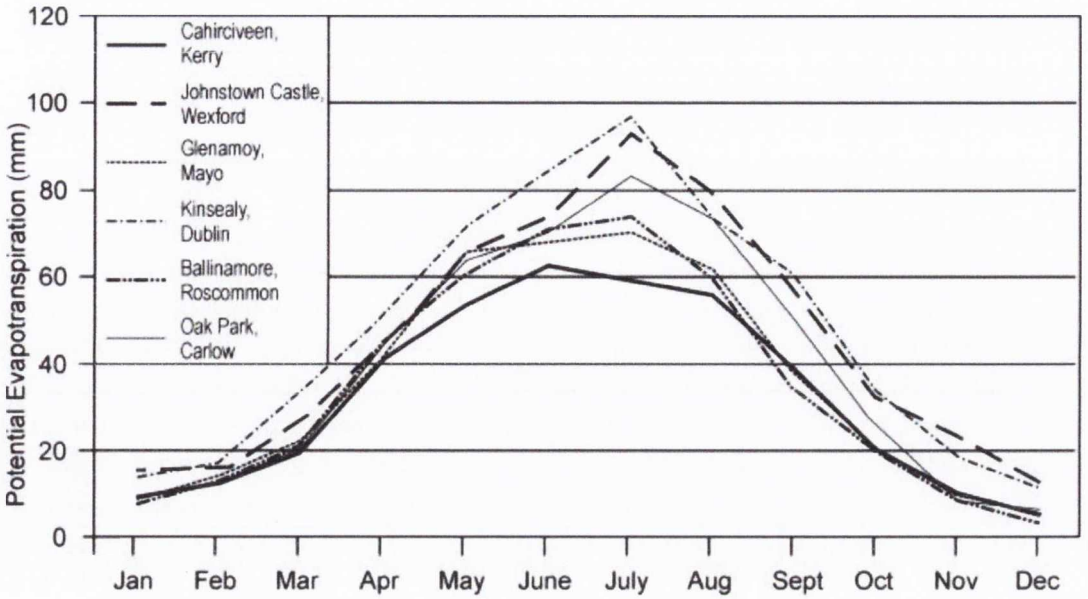

Figure 7.18: Average monthly evapotranspiration measured at six lysimeters over the period 1971-1990 (Mills, 2000).

Throughout the last 50 years, the global climate has been subjected to warming because of the continuous rise in the concentration of greenhouse gasses in the atmosphere, which can be largely attributed to human activities (Stocker et al., 2013b). Numerous studies of climate change have successfully revealed that the Earth's atmosphere is being altered by anthropogenic and biogenic emissions of carbon dioxide, other radioactively active gasses and aerosol precursors such as Sulphur dioxide (Chattopadhyay and Hulme, 1997). Global climate change is influencing the hydrological cycle by shifting rates of precipitation, recharge, discharge, and ET. To give an example of possible future scenarios; decreased precipitation during winter months to recharge groundwater storage within the Shannon RBD could exacerbate problems caused by reduced summer precipitation and increased ET rates. Consequently, reduced storage would result in less water being available during the drier summer months to sustain low flows and could result in water shortages. PET was spatially modeled within the Shannon RBD for three future time intervals (2020, 2050 and 2080) using the Hamon method. For each time interval, data from four climate change scenarios were modeled in an attempt to take consideration of the indefinite nature of future climate change. A clear trend is evident in the results, where PET is continuously increasing as a result of climate change from 0.9%-1.3% in 2020 up to 13.5% in 2080. A similar trend was discovered by (Scheff and Frierson, 2014), who modeled the effect of the warming of the earth's climate as a result of greenhouse gas pollution on PET over the 21st century and found that variations in annual- mean PET over the upcoming century are almost always positive. In order to better illustrate the fluctuations found in this study, Figure 7.19 displays the mean seasonal deviation of PET for each scenario considered. This figure further exhibits the increasing trend of PET in the future, which may significantly affect water resources and availability in the Shannon IRBD.

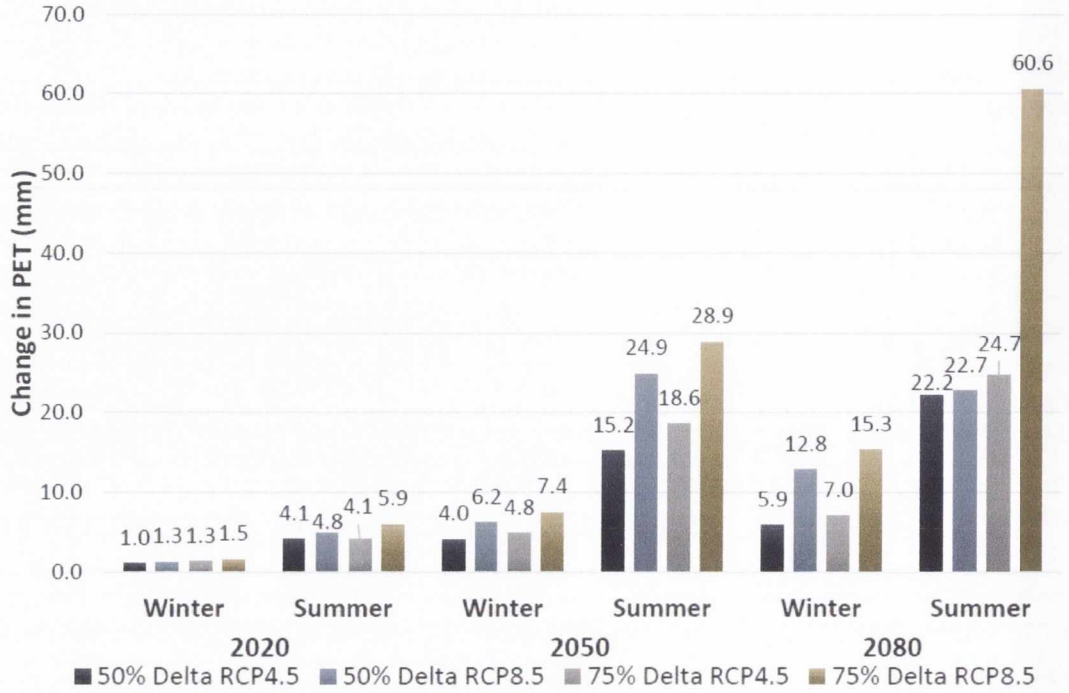

Figure 7.19: Mean deviation of future seasonal PET from baseline results for four climate change scenarios.

7.4 Conclusions

This chapter aimed to spatially estimate PET, a complex hydrological process, within Ireland's Shannon RBD using GIS-based algorithms. The ability to accurately determine PET is of critical importance in resource evaluation and sustainable water resource management policies as well as a host of hydrological and agricultural studies. Because of its complexity, and inherent spatial variability, PET is particularly difficult to determine for a given location. From the selection of possible approaches, the use of empirical PET formulae which integrate empirical constants and meteorological data were selected as the most appropriate method. Compared to more complex methods these relatively simple formulae require data which is monitored at a greater number of locations within the region, thus providing a more reliable spatial distribution of data. For example, temperature data which was used in this study was taken from 96 monitoring stations whereas more complex methods would require a host of variables some of which may only be measured at the four synoptic weather stations within the region or not at all. In this study, based on the availability of data, the complexity of formulae and their appropriateness for application within a GIS a number of methods were shortlisted.

Six temperature based methods were selected which would allow for the most appropriate to be identified. The 6 selected methods were applied within a GIS and each successfully produced long-term mean monthly PET raster maps of the region. Through comparison with the Met Éireann data, the Hamon method was found to produce the most precise results with an RMSE of 8.6 mm. Each method applied in its own produced spatially distributed estimates of PET. However, the Hamon method given its comparability to Met Éireann values and PET trends was determined to be the most appropriate of the models tested and concluded to produce reasonable estimates of PET within the Shannon RBD. It could be concluded that Hamon method was

performing the best for the Shannon catchment because of the simple parameterization which includes two main factors, the daytime period and the temperature, with an exponential relation which is one of the main deference between Hamon and the other methods.

The Hamon method was therefore applied for three future time intervals (2020, 2050 and 2080) to study the effects of climate change. Four possible climate change scenarios were considered and associated future temperature for these scenarios was available through the downscaling results from Chapter 4. It was found in the case of all scenarios that climate change would act to increase PET rates within the Shannon RBD. The scale of increases in PET was found to vary depending on climate change scenario and year. The maximum mean increase in PET was as a result of the 75% RCP 8.5 scenario in 2080 which returned an increase of 75.9 mm annually.

Chapter 8. GEO-CWB: GIS-based algorithms for parameterizing the responses of catchment dynamic water balance regarding climate and land use changes

8.1 Introduction

The effectiveness of water resources management and policies needs to consider the dynamic nature of any catchment's water balance, in order to develop innovative strategies for the future. Hence, future management planning scenarios and policies for a specific catchment have to integrate a dynamic water balance with future changes in climate variables and land use in a spatially distributed form. This integration allows decision makers and water resources modelers to predict climate change impacts and land use effects with more confidence in simulations for future scenarios or plans. A spatially distributed dynamic water balance across a catchment is defined as the mathematical simulation to track the changes in water budget spatially and temporally (Tekleab et al., 2011, Zhang et al., 2008).

Most studies on catchment water balances focus on the calculation of mean annual quantities as absolute values for the catchment without addressing the spatial variability of the dynamical water balance components (for example, Hickel and Zhang 2006, Potter and Zhang, 2009, Potter and Zhang, 2007, Zhang et al., 2008, Zhang et al., 2004a, Zhang et al., 2001, Milly, 1993). However, spatial and temporal variability can be significant factors in many catchments.

Although long-term dynamic water balance trends and variations estimations are required for sustainable water resource planning and management, mapping spatial variability of the dynamic water balance components are essential for the surface water and groundwater contaminant protection, in addition to planning the land-use allocation and development (Beigi and Tsai, 2014, Jyrkama and Sykes, 2007, Moiwo and Tao, 2014).

Land use, anthropogenic activities and climate change can significantly affect the dynamic catchment water balance. Irrigation, which is one of the major land use-related activities, is one of the main factors that affects the water balance across the globe (Gharbia et al., 2015e, Gharbia et al., 2015f, Junkermann et al., 2009, Yang and Tian, 2009, Fan et al., 2010). In order to study the dynamic water balance on catchment scale an integrated modelling framework needs to be designed which contains groundwater modelling, vegetation mapping, hydro-geochemical and climatic/land physiographic analysis in a GIS platform to take into account the multidimensional case of the dynamic water balance estimation process (Gharbia et al., 2015c, Gharbia et al., 2015a, Rodell et al., 2009, Moiwo et al., 2010, Woldeamlak et al., 2007, Moiwo and Tao, 2014).

This study aims to contribute to the understanding of the spatially distributed dynamic water balance calculation in response to climate and land use changes conditions over variable time scales by developing GEO-CWB as a user-friendly GIS algorithm. GEO-CWB could be considered as a holistic or systems approach to catchment dynamical water balance modeling. It enables the development of water balance models with consistency in process representation and parameterization, making them applicable for ungauged catchments and for predicting climate and land-use change impacts and responses.

GEO-CWB works on the integration of physical based models and formulas, statistics and computer learning techniques. This multi-stage and multi-scale system fills the gap in the current state of the art regarding combining several environmental systems effects such as climate and land use change on the hydrological systems.

This chapter describes and illustrates the developed catchment dynamic water balance model (GEO-CWB) in terms of the concept, the general framework, the physically basis and its integration with the GIS platform.

8.2 Conceptualization of GEO-CWB framework

The main idea behind GEO-CWB is to use different aspects of knowledge in order to simplify the simulation of such a complicated environmental problem. The model tries to simulate three different systems which are climate, land use and the hydrological system; these simulations need to capture the geographical changes in addition to temporal changes from climate and land use on the simulated hydrological system. The relationships between the three systems in the model need to be multidimensional as a flexible two-way simulation iterations process. This integration between all the multi-stage modelling process for the large catchment gives the GEO-CWB an advantage on the other available models, which are limited to small catchment system without the integration between all the modelling stages. In such models, due to computation and practical issues, it would be impossible to include all the known process in each system in the computation process. Also, it would be difficult to get the physical model or relationship behind each step in the simulation. This is the reason for the use of statistical based models and machine learning techniques in the design of the GEO-CWB.

In GEO-CWB, physical based models have been used in a very condensed way in the simulation of hydrological systems and the calculation of different components of the dynamic water balance such as runoff, subsurface water component, etc. The use of physical based relationships at this stage (see Figure 8.1) gives the ability to do the multi-iteration process in the simulation without checking the different assumptions inherent in other techniques (such as the assumption of normality for some statistical based models). Figure 8.1 shows the relationship between the main GEO-CWB simulation steps climate change, land use and water balance modelling. It shows how GEO-CWB deals with the spatial and temporal scales in the simulations and it illustrates that GEO-CWB applies the machine learning techniques in order to get the fine temporal scale outputs for the hydrological parameters. During the dynamical water balance stage in the GEO-CWB, the model work on a high spatial resolution and a fixed temporal scale, which is a monthly time step, after that the results from the water balance stage with the monthly time step are feed to the machine learning techniques in order to work on the finer temporal scale (daily). As illustrated in Figure 8.1, statistical based techniques have been used in the fine scale resolution downscaling for climate simulations. Statistically based models have been used widely in addressing complicated hydrological problems (Akgun and Erkan, 2016, Müller and Thompson, 2016, Daly et al., 2002, Legates and McCabe, 1999, Wood et al., 2004). In GEO-CWB, statistical based models and machine learning techniques play a crucial role in the parameter scaling process in both spatial and/or temporal dimensions. GEO-CWB provides the ability to use a series of produced land use/cover scenarios using the cellular automata method (Ku, 2016, Chen et al., 2016, Liao et al., 2016, Gharbia et al., 2016) and spatial regression models over a defined temporal scale, as discussed in Chapter 6. GIS is the platform used to run GEO-CWB (see Figure 8.2). This gives GEO-CWB three main advantages: (i) the ability to work with multidimensional files and phenomena, (ii) the ability to reuse the output from GEO-CWB as inputs for other impact models because of the flexibility with the file formats, (iii) providing a simple user-friendly interface for such a complicated tool, so the user does not need to use any coding to complete the simulation process.

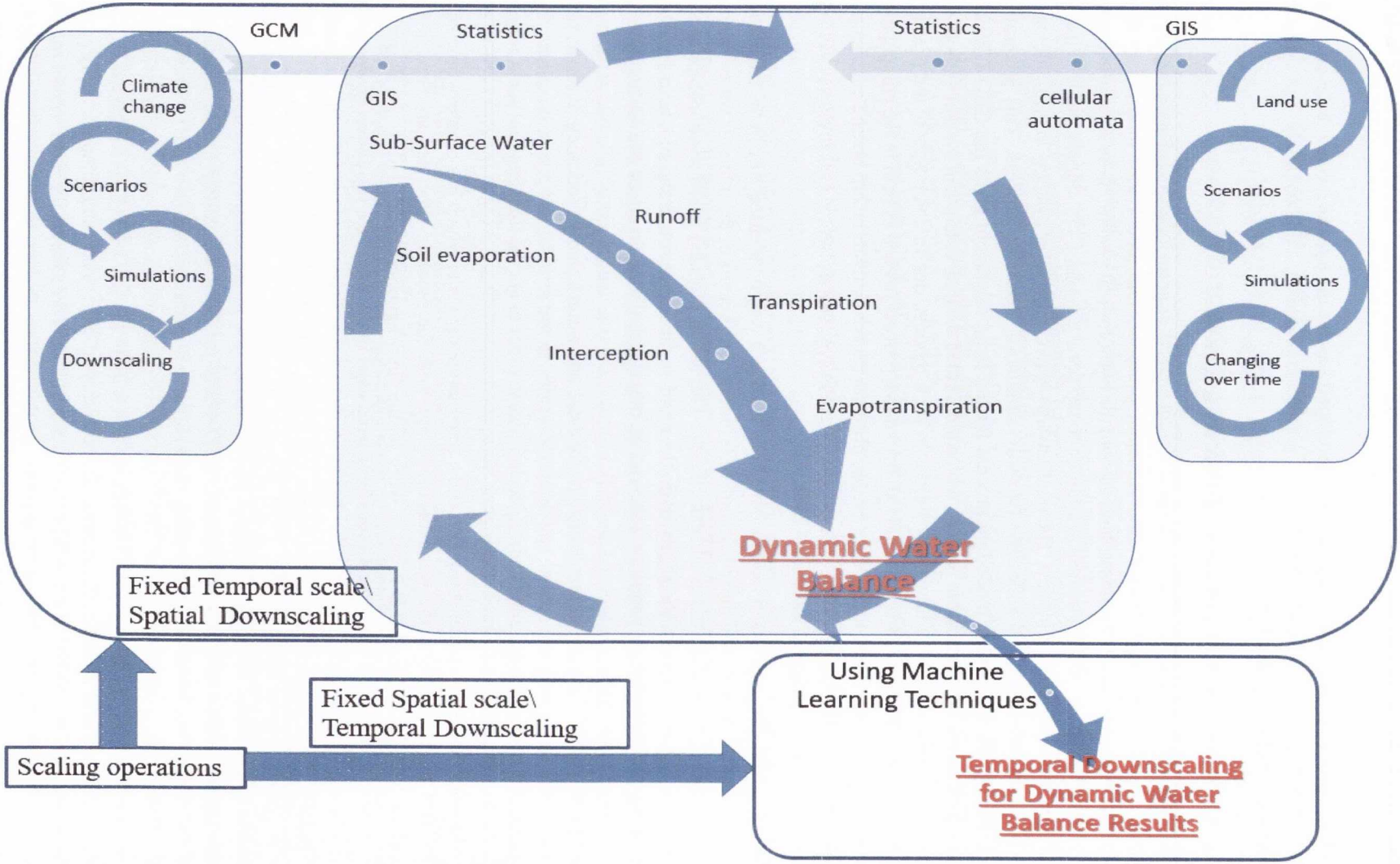

Figure 8.1: GEO-CWB general framework.

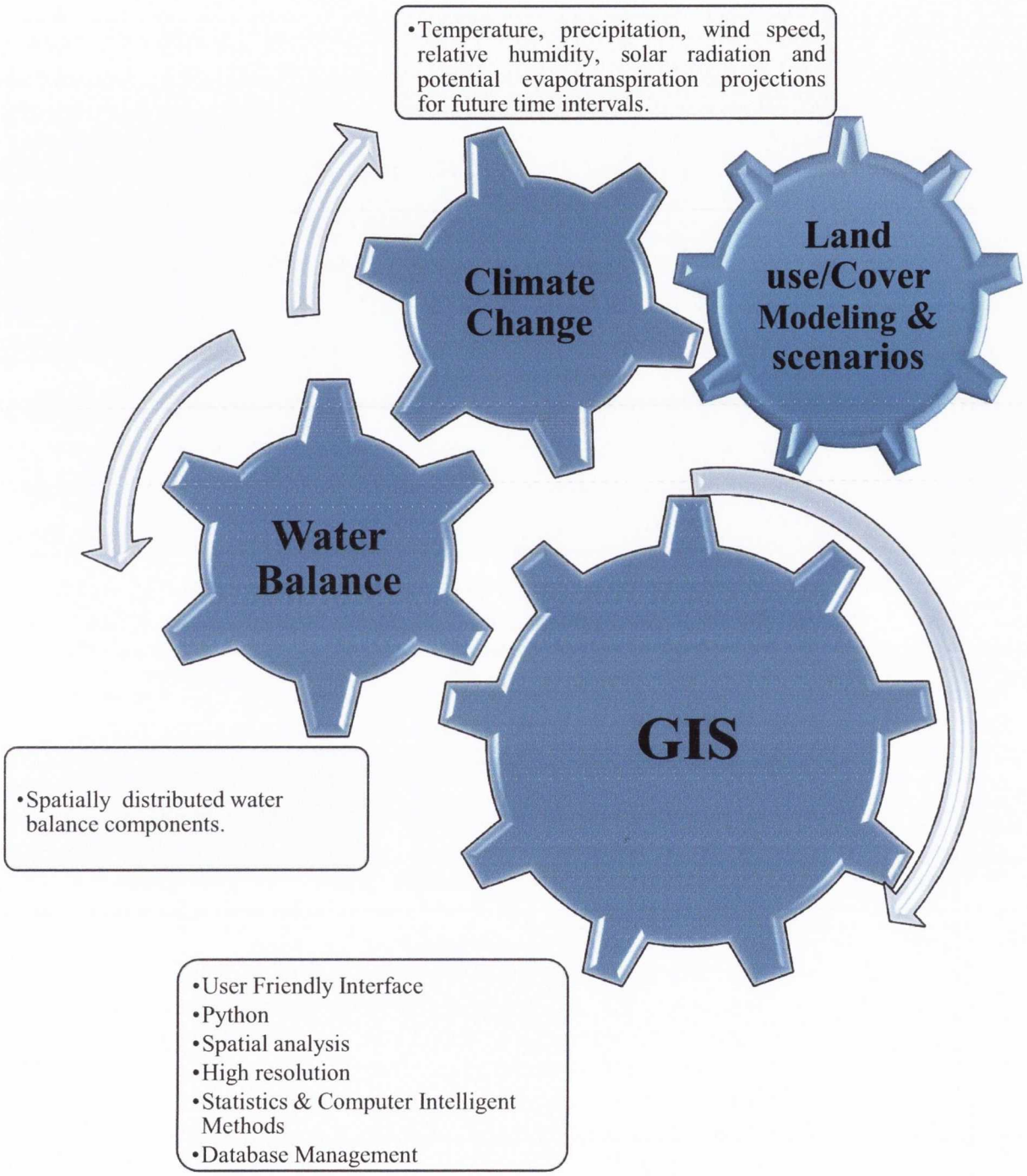

Figure 8.2: GEO-CWB general framework powered based on GIS platform.

8.3 GEO-CWB: The physical base and algorithm design

For the GEO-CWB design process, an integrated approach was adopted in order to combine all of the simulation processes. This approach, invented in this study, is named as the Pixelated Cubical Balance Approach (PCBA). The idea behind PCBA is to describe the model as a three-dimensional problem moving within a particular time scale, see Figure 8.3, which turns the problem to multidimensional problem, or a four-dimensional problem. Figure 8.3 shows an imaginary model extent; this extent can be divided into three dimensional cubes each cube can be assumed as a single isolated cell moving in time which can be solved against a certain phenomenon by applying it related baseline and boundary conditions. PCBA suggests dividing the model extent to small cubes, (the higher the number of cubes, the higher the accuracy), with each small cube having its own simulation process, which happens within the same time scale. The PCBA concept is applied in GEO-CWB in order to simplify the multidimensional scale complication problem and to allow the linkage between the physical and statistical based models.

Each single pixel in the domain in each time step runs through the GEO-CWB designed algorithm (Figure 8.5), using the input rasterized datasets, as following:

- Land cover, see chapter 6.
- Precipitation, see chapter 4.
- Potential evapotranspiration, see chapter 7.
- Wind speed, see chapter 4.
- Temperature, see chapter 4.
- Groundwater level from the Irish Environmental Protection Agency (EPA).
- Soil texture, see Appendix B.
- Slope, DEM raster, see chapter 6.
- Topography, DEM raster, see chapter 6.
- Average porosity (as a single value) or average porosity raster.

The model also uses parameters and properties tables related to the following:

- Soil parameters table: GEO-CWB assigns parameters for each pixel in the input soil layer from the soil parameters table. For each individual soil texture type the soil parameters table contains values for the Porosity, Wilting point, Field capacity, Residual water content, a soil empirical parameter for ET calculation, Plant Available Water, Tension saturated height and Soil evaporation depth.
- Land use parameters table: GEO-CWB assigns parameters for each pixel in the input land use layer from the land use parameters table. For each individual land use type the land use parameters table contains values for the Vegetation area fraction, Bare area fraction, Impervious area fraction, Open water area fraction, Rooting depth, Leaf Area Index, Minimal stomatal resistance, Interception percentage and Vegetation height.
- Runoff coefficients: this table contains the runoff coefficients for each single combination of soil, slope and land use types.

The use of these tables' parameters in GEO-CWB is illustrated in the subsections below.

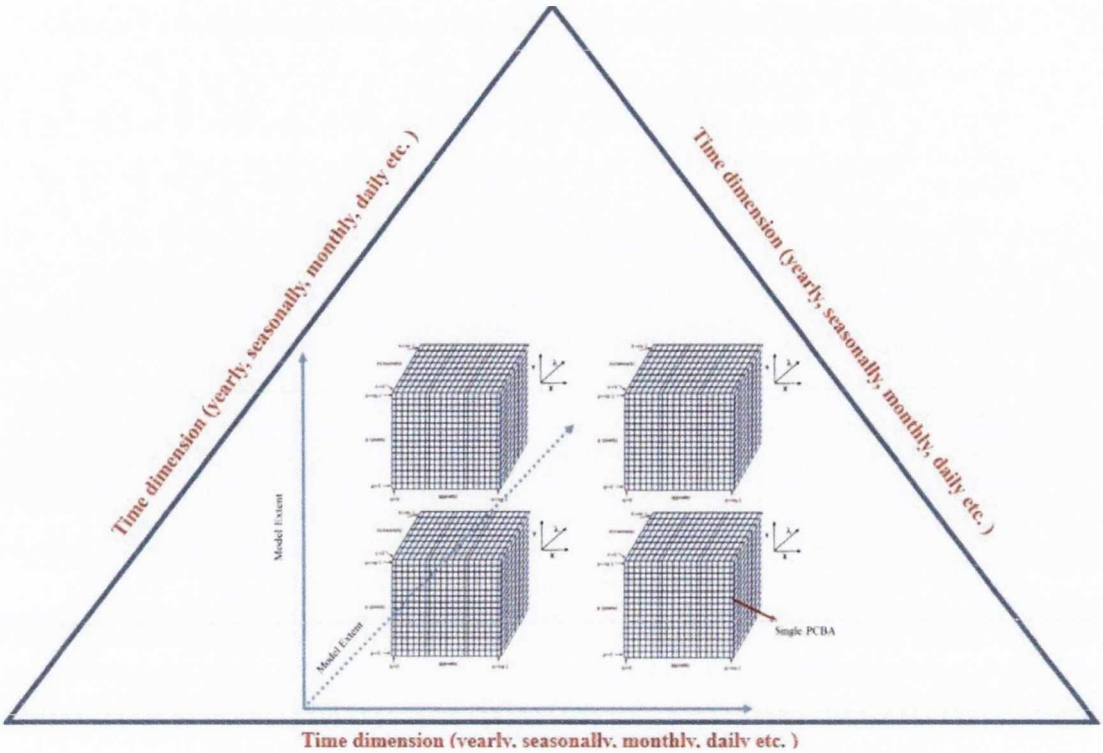

Figure 8.3: Pixelated Cubical Balance Approach (PCBA) simplified the structure for the model domain extent.

GEO-CWB has some assumptions/limitations behind it, these assumptions can be listed as follows:

1. GEO-CWB does not take into account the bedrock geologies of the catchment, so at the moment, it is not possible to get the absolute groundwater recharge value. Thus, it provides as one of the main outputs the sub-surface water component, which includes, aggregated together, mainly the subsurface water flow and the groundwater recharge. To get the recharge component in a large catchment like Shannon, the model needs to take into account the maximum capacity of the different aquifer types to take recharge (Misstear et al., 2009b), and this type of data and details are not available for the Shannon catchment. In Ireland, there are different recharge caps applied to different geological aquifers. So, the aquifer can only accept up to a maximum amount of water. Anything more than this leads to increase the subsurface flow/runoff via shallow subsoil pathways (O'Brien et al., 2013, Mockler and Bruen, 2013). These kinds of caps and levels have lots of variabilities and uncertainties in addition to the fact that they are not mapped or available for the Shannon catchment at both temporal and spatial scales. Based on that and according to data availability, at this stage, GEO-CWB calculates the subsurface water component which includes both the subsurface flow and the groundwater recharge. GEO-CWB has the framework set up to separate the two main components, subsurface flow and groundwater recharge, once the spatially distributed data for the recharge caps are available. For the Shannon catchment, GEO-CWB at this stage is not able to calculate the net groundwater recharge because of the lack of spatially distributed bedrock properties. Instead, it provides the total sub-surface water component, which includes both groundwater recharge and the sub-surface runoff.

2. The actual evapotranspiration, soil evaporation and transpiration components for the catchment are calculated based on the pre-calculated potential evapotranspiration in Chapter 7. As the actual evapotranspiration is the summation of some calculated sub-fractions of PET as illustrated in the equations of Section 8.3.1.1. Depending on which fraction of each cell is being modelled, the evapotranspiration could be equal to PET (open water fraction) or fraction of it (Bare soil or impervious surface fractions) or just equal to the simulated transpiration (vegetated fraction).
3. GEO-CWB calculates evapotranspiration and interception components individually which means that the total water loses from precipitation in the catchment is the summation of the two components.

8.3.1 GEO-CWB calculation stages

In order to parameterize the hydrological response of a catchment to the changes in climate and land use, GEO-CWB has a number simulation stages as follows:

8.3.1.1 GEO-CWB-Stage (1) - Dynamical Water Balance

As illustrated in the previous section, GEO-CWB uses the idea of dividing the model domain into pixels and then GEO-CWB runs the simulation for each pixel, so each calculation step has to be run for each single pixel. Figure 8.4 shows GEO-CWB single cell water balance components.

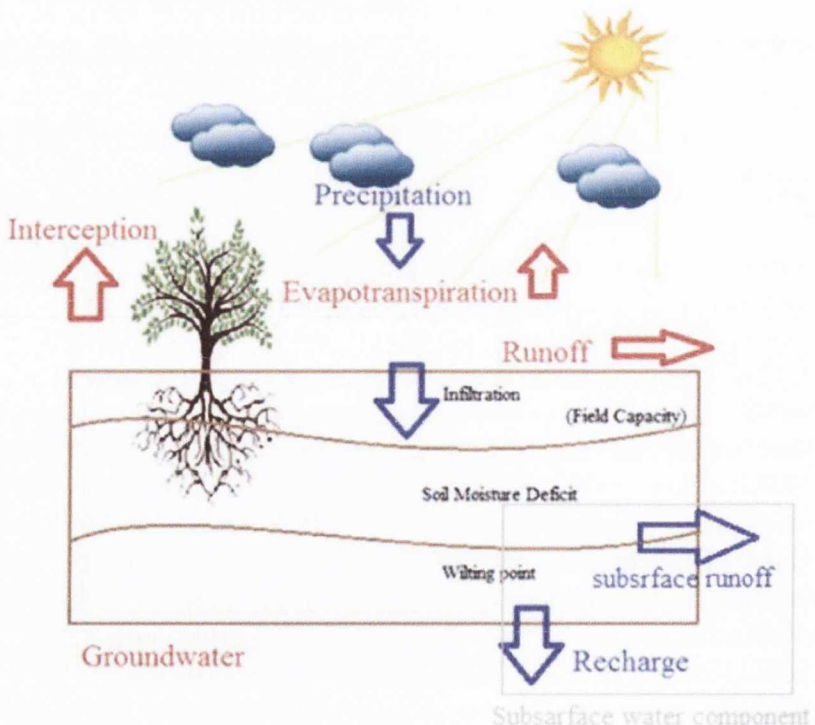

Figure 8.4: GEO-CWB single cell water balance components.

In this stage of GEO-CWB, individual dynamical pixel water balance is calculated by summing up the independent pixel's subdivision simulated water balance. Depending on the land use type assigned to each pixel, GEO-CWB divides the upper pixel's surface, into the vegetated area, bare soil area, open- water bodies, and impervious area.

The dynamic water balance parameters, which are used in the first stage of GEO-CWB, are listed with references to the equations and the input parameters in Table 8.1.

Table 8-1: References, comments and limitations behind physical and empirical methods that have been used in GEO-CWB.

Output Parameters	Comments	Physical and empirical methods behind the calculation
Surface Runoff	It represents the direct surface runoff and it does not include the subsurface runoff (subsurface flow via shallow subsoil pathways)	(Hernandez et al., 2000, Schumann et al., 2000, DE BOER, 1992, Arnold et al., 1993, Batelaan and De Smedt, 2001, Rushton et al., 2006, Batelaan and De Smedt, 2007)
Subsurface water	This includes many components mainly subsurface flow via shallow pathways and the groundwater recharge component.	(Rushton et al., 2006, Batelaan and De Smedt, 2007, Sophocleous, 1992, Jyrkama et al., 2002, Simmers, 2013, Walker et al., 1991)
Interception	Based on the vegetation type interception fraction represents a constant percentage of the annual precipitation value, which is a main part of the total water loss in the catchment.	(Dolman and Nonhebel, 1988, Batelaan and De Smedt, 2007, Batelaan and De Smedt, 2001, Van Dijk and Bruijnzeel, 2001, Calder et al., 1986, Gash et al., 1980, Calder and Newson, 1979, Calder, 1986)
Evapotranspiration	Depending on which fraction of each cell is being modelled, the evapotranspiration could be equal to PET (open water fraction) or fraction of it (Bare soil or impervious surface fractions) or just equal to the simulated transpiration (vegetated fraction).	(Vandewiele and Elias, 1995, Xu and Chen, 2005, Vandewiele et al., 1991, Mauser and Schädlich, 1998, Braud et al., 1995, Bradbury et al., 2002, Beven, 1979, Federer, 1979, Zhang et al., 2007, Zhang et al., 2004a, Zhang et al., 2004b, Zhang et al., 2001, Batelaan and De Smedt, 2007, Batelaan and De Smedt, 2001)
Soil evaporation	Based on the soil type, soil evaporation is a fraction of the PET.	(Vandewiele and Elias, 1995, Xu and Chen, 2005, Vandewiele et al., 1991, Mauser and Schädlich, 1998, Braud et al., 1995, Bradbury et al., 2002, Beven, 1979, Federer, 1979, Zhang et al., 2007, Zhang et al., 2004a, Zhang et al., 2004b, Zhang et al., 2001, Batelaan and De Smedt, 2007, Batelaan and De Smedt, 2001)
Transpiration	Based on the vegetation type, root depth, groundwater level, soil moisture, tension saturated height, temperature and many other factors, transpiration is calculated for the vegetated fraction of each cell.	(Vandewiele and Elias, 1995, Xu and Chen, 2005, Vandewiele et al., 1991, Mauser and Schädlich, 1998, Braud et al., 1995, Bradbury et al., 2002, Beven, 1979, Federer, 1979, Zhang et al., 2007, Zhang et al., 2004a, Zhang et al., 2004b, Zhang et al., 2001, Batelaan and De Smedt, 2007, Batelaan and De Smedt, 2001)

The water balance components of vegetated, bare-soil, open-water and impervious surfaces are used to calculate the total water balance of a raster cell. A precipitation event is taken as a starting point for the computation of the water balance of each of the above-mentioned components of a raster cell, the rest of the processes (runoff, interception, evapotranspiration, & recharge) follow in an orderly manner, see Eq8.35 - Eq8.38. This order becomes a prerequisite for the dynamical monthly time scale within which the processes will be quantified. Figure 8.5 shows the flowchart for the dynamic water balance simulation stage; the flowchart shows that for each single pixel in the model extent, GEO-CWB divides and carries out the pixel simulation, as defined in the following sections. The parameters used in the equations are defined below.

F_v: Vegetated fraction

F_{ow}: Open water

F_{bs}: bare soil fraction

F_{is}: Impervious surface fraction

P: Precipitation

I: Interception

S_v: Surface runoff in the vegetated fraction

T_v: Transpiration

T_{rv}: Reference transpiration

E_o: Seasonal potential evapotranspiration

S_r : Potential surface runoff

C: Vegetation coefficient

T: Temperature

H: Vegetation height

h_w : Wind measuring height

U: Wind speed (Km/hr)

Gwd: Groundwater depth

R_d: Rood depth

h_t: Tension saturated height

PWA: Plant available water content

a: Calibrated soil texture factor (Vandewiele et al., 1991)

Eps: Penman evaporation for wet soil

S_o: Runoff of open water fraction

R_o: subsurface water of open water fraction

Pet: Potential evapotranspiration

R_{cell}: The cell subsurface water component

As illustrated in the flowchart, Figure 8.5, GEO-CWB divides the model extent into pixels, and then it divides each pixel into fractions (vegetated, open water, bare soil and impervious surface) each fraction is moving in the time frame. Modelling the water balance using the baseline data and the boundary conditions for each single fraction can be done in a simple and fast way, so the idea in GEO-CWB is to solve each fraction separately and then companies all the fractions for a single pixel. After running all the fractions for all the pixels in the model extent using all the time steps, GEO-CWB can process the large catchment dynamical water balance.

8.3.1.1.1 Vegetation Fraction (Fv)

The water balance for a vegetated area depends on the mean seasonal precipitation, interception fraction, surface runoff, actual transpiration, and groundwater recharge.

Depending on the type of vegetation, the interception fraction represents a constant percentage of the annual precipitation value. Thus, the fraction decreases with an increase in an annual total rainfall amount (since the vegetation cover is assumed to be constant throughout the simulation period), see Eq. 8.1.

Surface runoff is calculated in relation to precipitation amount, precipitation intensity, interception and soil infiltration capacities, using the surface runoff coefficient for vegetated infiltration areas. The surface runoff coefficient is a function of vegetation type, soil type, and slope. Saturated surface runoff occurs in groundwater discharge areas giving rise to a very high surface runoff coefficient. This is due to the reduced dependency on soil, vegetation type and the vicinity of the area to the river, and is usually assumed to be constant. The actual surface runoff is calculated by considering the differences in precipitation intensities in relation to soil infiltration capacities. For example, the coefficient to calculate the actual surface runoff from the potential surface runoff for the groundwater discharge areas is equal to unity since all intensities of precipitation contribute to surface runoff. Only high-intensity storms can generate surface runoff in infiltration areas, see Eq. 8.2 and Eq. 8.3.

Evapotranspiration depends on which fraction of each cell is being modelled, the evapotranspiration could be equal to PET (open water fraction) or fraction of it (Bare soil or impervious surface fractions) or just equal to the simulated transpiration (vegetated fraction). The evapotranspiration calculation depends on the reference value of transpiration, which is obtained from open-water evaporation value and a vegetation coefficient as outlined in the Penman method (Penman, 1948). The vegetation coefficient can be calculated as the ratio of reference vegetation transpiration (Penman-Month) to the potential open-water evaporation (Penman). For vegetated groundwater discharge areas, the actual transpiration is equal to the reference transpiration as there is no soil or water availability limitation, see Eq8.4 - Eq8.14.

The last component, which is the subsurface water component, is then calculated as a residual term of the water balance. This component includes many components mainly subsurface flow component via shallow pathways and the groundwater recharge component. In general, if the catchment that is being modelled has a shallow sand/gravel aquifer this subsurface water component will be equal to the groundwater recharge. However, in Ireland a lot of the country is covered in so-called low productivity aquifers where they have an annual recharge cap and the spatially and temporally distributed data for these cap values for the Shannon catchment are not currently available. The spatially distributed subsurface water component is therefore estimated from the vegetation type, soil type, slope, groundwater depth, and climatic variables of precipitation, potential evapotranspiration, temperature, and wind speed. In addition, the subsurface water component will be associated with discharge areas owing to the concept that

there is a thin unsaturated zone present even in discharge areas, though this may not be the case in the summer season. In the summer season, there is a high potential transpiration due to vegetation and these results in negative subsurface water component values in discharge areas. In some cases, high winter subsurface water component will compensate the negative values, see Eq. 8.15.

There are two ways of incorporating the change in storage into the model on a seasonal basis. The first is by using different groundwater depth values for winter and summer, while in the second case, the plant available soil moisture reservoir in the winter is assumed to be filled up (i.e. at field capacity) but can be depleted in the summer. A similar procedure to that on vegetated surfaces is followed for the calculation of water balance for bare-soil, open-water, and impervious surfaces. The only difference is that there is no vegetation in these cases, and thus there are no interception and transpiration terms, see Eq.8.16 – Eq.8.34.

Interception= $F_{(\text{function of land use/cover})} * P$ Eq.8.1

Potential surface runoff ($Ro_{(PO)}$)= $F_{(vg,so,sl,wd)} * (p-I)$ Eq.8.2

Final surface runoff= $F_{(\text{Intensity, infiltration rate, wd})} * Ro_{(PO)}$ Eq.8.3

$R_a = Ln((hw-0.499H)/(0.123H))/(0.16\ U\ *0278)$ Eq.8.4

When $H_{(\text{vegetation height})} < 0.15m$, $LAI = 24*H$ Eq.8.5

When $H_{(\text{vegetation height})} > 0.15m$, $LAI = 1.5\ Ln\ (H) + 5.5$ Eq.8.6

$R_c = 100/(0.5*\ LAI)$ Eq.8.7

$\gamma/\Delta = 1.5411\ e\ ^\wedge\ (-0.057 * \text{Temperature})$ Eq.8.8

$C_{(\text{vegetation coefficient})} = (1+ \gamma/\Delta)\ /(1+\gamma/\Delta*(1+(Rc/Ra))$ Eq.8.9

$Trv_{(\text{reference transpiration})} = C * Pet$ Eq.8.10

When $Gwd > Rd + ht$, $W = P + n*(PAW)*Rd$ Eq.8.11

$F(PAW) = 1 - A^\wedge(W/T_{rv})$ Eq.8.12

Transpiration = $F\ (PAW)*T_{rv}$ Eq.8.13

When $Gwd < Rd + ht$,

Transpiration in vegetated groundwater discharge areas = Trv Eq.8.14

Subsurface water for vegetated fraction = P – Interception – Vegetated surface runoff – Transpiration Eq.8.15

8.3.1.1.2 Open Water Fraction (F_{ow})

Interception= $F_{(\text{function of land use/cover})} * P = 0$ Eq.8.16

Final surface runoff= 1* (P-I) Eq.8.17

$T_v = 0.00$ Eq.8.18

Open water evaporation = 1* Pet Eq.8.19

Open water subsurface water = $P - E_{ow} - S_{ow}$ Eq.8.20

8.3.1.1.3 Bare Soil Fraction (F_{bs})

Interception= $F_{(function\ of\ land\ use/cover\ and\ soil\ texture)} * P$ Eq.8.20

Potential surface runoff= $F_{(vg,so,sl,wd)} * (p - I)$ Eq.8.21

Final surface runoff= $F_{(Intensity,\ infiltration\ rate,\ wd)} * Ro_{(po)}$ Eq.8.22

Final surface runoff= $F_{(Intensity,\ infiltration\ rate,\ wd)} * Ro_{(po)}$ Eq.8.23

$W = P + n*(PAW)*Rd$ Eq.8.24

Eps (Penman evaporation rate for wet soil) = F (function of water content at field capacity and at root zoon, welting point) Eq.8.25

F (PAW) = 1 – A^ (W/Eps) Eq.8.26

Soil evaporation = F (PAW)* Pet Eq.8.27

Bare soil subsurface water = P – soil runoff – soil evaporation Eq8.28

8.3.1.1.4 Impervious surface fraction (F_{is})

Interception = $F_{(function\ of\ land\ use/cover)} * P$ Eq.8.29

Potential surface runoff = $F_{(lu,so,sl,wd)} * (p-I)$ Eq.8.30

Final surface runoff = $F_{(Intensity,\ infiltration\ rate,\ wd)} * Ro_{(po)}$ Eq.8.31

Fie = $F_{(Impervious\ surface\ evaporation\ fraction\ a\ function\ of\ land\ use\ type)}$ Eq.8.32

Impervious surface evaporation = Pet * Fie Eq.8.33

Impervious surface subsurface water component = P – Impervious surface evaporation – Impervious surface runoff Eq.8.34

8.3.1.1.5 Pixel/ Cell water balance

$Et_{cell} = (F_v * Et_v) + (F_{ow} * E_{ow}) + (F_{is} * E_i) + (F_{bs} * E_s)$ Eq.8.35

$S_{cell} = (F_v * S_v) + (F_{ow} * S_{ow}) + (F_{is} * S_i) + (F_{bs} * S_{bs})$ Eq.8.36

$R_{cell} = (F_v * R_v) + (R_{ow} * E_{ow}) + (F_{is} * R_i) + (F_{bs} * R_s)$ Eq.8.37

Cell Water Balance:

$P_{cell} = Et_{cell} + S_{cell} + R_{cell} + I_{cell}$ Eq.8.38

8.3.1.1.6 Error and the change in the storage in pixel water balance

The following equation quantifies the proportional error and the change in the storage per time step in the simulated water balance.

Error in Water Balance = $(P_{cell} – R_{cell} – Et_{cell} - S\ cell) / P_{cell}$ Eq.8.39

8.3.1.2 GEO-CWB-Stage (2) – Surface Runoff Iteration

The main aim of this stage is to recalculate the subsurface water component and surface runoff maps by iterating the groundwater depth variable.

The inputs in this stage will be the output from the first stage and the outputs will be the same variables but after the iteration, all the outputs will have the number 2 in the file name to indicate that this file is the final map for this parameter, which has resulted from the stage (2).

The main function of this stage is to recalculate the groundwater depth as a response to the simulated subsurface water component and runoff values, then reuse the new groundwater depth values to get the subsurface water component and runoff values; the process is an iteration loop, which stops when the last 10 iterations are equal.

8.3.1.3 GEO-CWB-Stage (3) – Climate and Land Use Vulnerability Parameters

This stage of GEO-CWB aims to calculate parameters using the outputs from all the previous stages to assess the vulnerability to climate and land use changes for each climatic period and land use scenario. The calculated parameters are as following:

- The accumulated runoff volume in the rainy season is an indication of how much runoff water could be harvested every year during the rainy season.

$$\text{Accumulated runoff } (m^3) = \int_A (Surface\ runoff) da \times 10^{-3} \qquad \text{Eq8.40}$$

- The safe yield groundwater abstraction rate expressed in (m^3/d/ha). GEO-CWB produces groundwater safe yield maps, which estimates how much groundwater can be pumped in a sustainable way without depleting the groundwater resources. Safe yield is usually expressed as a percentage of the groundwater recharge. Several authors from the least conservative 100% to a reasonably conservative 10% have suggested different values (Voudouris, 2006, Kalf and Woolley, 2005, Zhou, 2009). In general, sustainable yield should be considerably less than the groundwater recharge to sustain both the quantity and quality of streams, springs, wetlands and groundwater dependent ecosystems (Voudouris, 2006, Kalf and Woolley, 2005, Zhou, 2009). GEO-CWB adapts the 25% as a sustainable groundwater yield percentage from the calculated subsurface water component, Eq8.41. This is a simplistic formula for a country such as Ireland which has such differences in geology and aquifer types, so the results for Shannon is just a good indication for the decision makers.

$$\text{Safe yield } (m^3/day/ha) = 6.85 \times 10^{-3} \times Recharge\ (mm) \qquad \text{Eq8.41}$$

- The water deficit for ideal crop growth (WD) can be estimated as the difference between the crop water requirement and the actual evapotranspiration that is feasible only by rainfall. The crop water requirement can be defined as the amount of water needed to meet the water loss through evapotranspiration for optimal crop growth, which can be estimated as a crop coefficient time's reference evapotranspiration of well-watered grass (Vaux and Pruitt, 1983, Allen et al., 1998). Crop coefficients vary between 0.70 and 1.15 depending on crop type and growing stage. The crop coefficient can be assumed to be one and reference evaporation to equal PET, which allows an estimation of how much

water is needed for supplementary irrigation for optimal crop growth (Zhang et al., 2004b, Kendy et al., 2003). This calculation can be made on annual basis, but it is more interesting to do this separately for the summer season and the winter season, GEO-CWB uses Eq.8.42, where WD is the water deficit, PET is the potential evapotranspiration, ET is the actual evapotranspiration and Dn is the number of days in the season.

$$\text{WD } (m^3/day/ha) = \frac{10 \times (PET - ET)}{Dn} \quad \text{Eq8.42}$$

8.3.1.4 GEO-CWB-Stage (4) - Statistics Tables

This stage imports all the outputs from all the previous stages and runs spatial statistical algorithms to get the following statistical parameters for each resulted raster file. The results are exported as Excel tables, see Chapter 9.

1. The frequency
2. The summation of all the cells
3. The mean of all cells
4. The minimum value
5. The maximum value
6. The range
7. The standard deviation
8. The count of the cell numbers

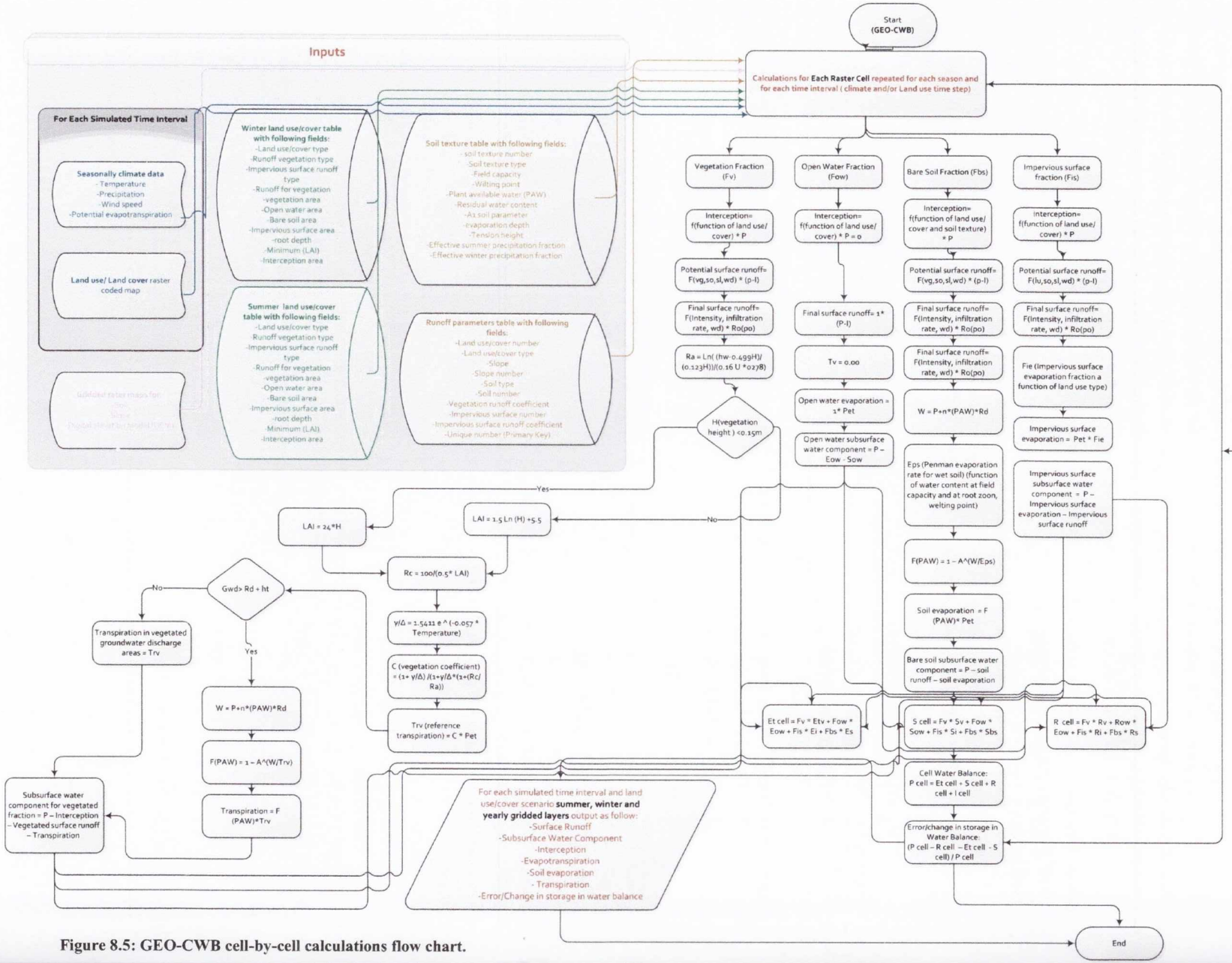

Figure 8.5: GEO-CWB cell-by-cell calculations flow chart.

8.4 GEO-CWB integration with GIS

GEO-CWB is fully integrated into the GIS platform; the model is a geospatial multi-dimensional model written in Python and uses ArcMap from ESRI as a running environment. GEO-CWB has a friendly interface integrated into the ArcMap toolbox, which means that the user does not need to use any coding to run the model, as shown in Figure 8.6. The user interfaces for GEO-CWB are presented in the appendix D.

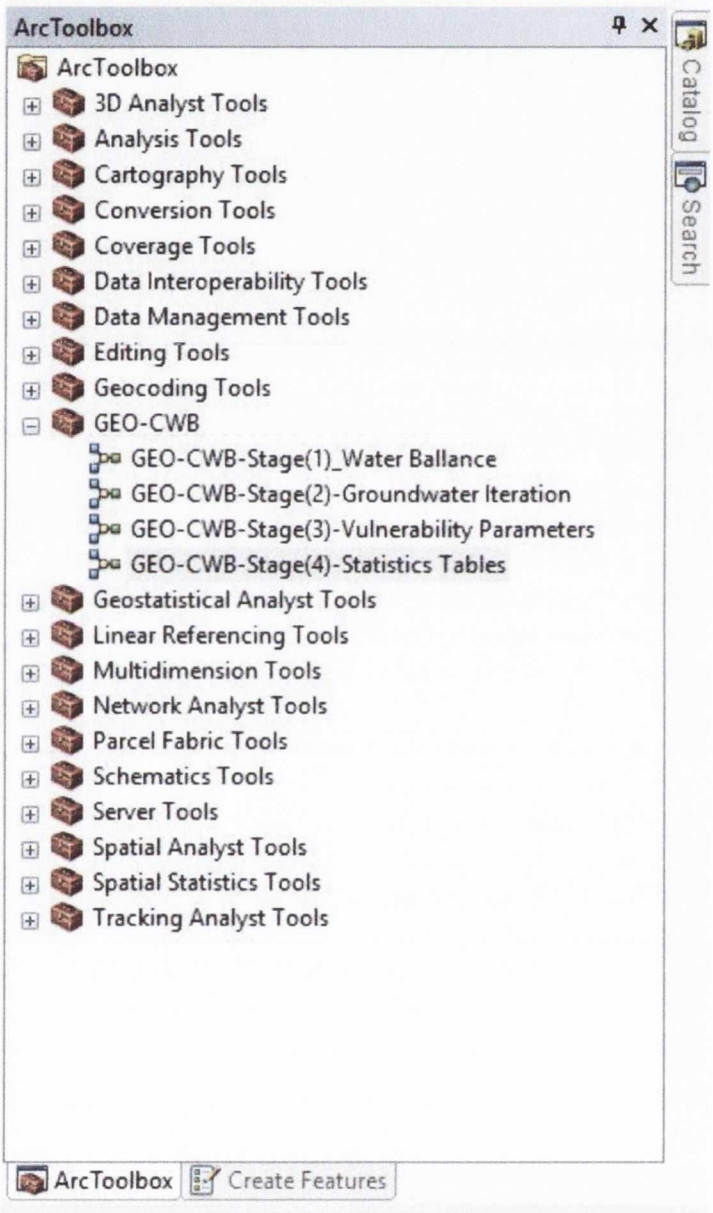

Figure 8.6: GEO-CWB as a tool in the ARC toolbox.

Chapter 9. GEO-CWB application: Climate and land use changes effects on the Shannon River catchment

This chapter applies GEO-CWB on the Shannon catchment in Ireland as an example of a large and complicated hydrological system. This application uses the output from all the previous chapters, i.e. climate and land use scenarios, as inputs in the GEO-CWB in order to get the results for the water balance components and the vulnerability parameters. The GEO-CWB inputs are listed in Section 8.4. This chapter shows the simulated and projected annual, winter and summer average raster maps for the GEO-CWB outputs for each land use and climate change scenario for the baseline period and the three projected periods 2020, 2050 and 2080. The first section of this chapter shows the validation process for the GEO-CWB simulations based on the Shannon River catchment simplified and structured hydrometric stations system, see Chapter 5.

9.1 GEO-CWB validation

After the calibration process of the GEO-CWB against the measured groundwater levels in the stage (2) by the iteration process for the surface runoff results, the results of the model need to be validated. The results of the GEO-CWB model are validated against river flow observations for the simplified and structured hydrometric station system for the Shannon River catchment (see Chapter 5). The river flow data was collected by the Irish EPA, OPW and ESB, data which are available as daily values covering the period from 1972 to 2014. Accumulated monthly river flows were calculated and accumulated to annual flows at the seven gauging stations to give the average daily, as shown in Table 9-1. In order to estimate the annual river discharge at the river gauging stations from the GEO-CWB results, surface runoff and subsurface water component, which includes subsurface water flow and groundwater recharge, are accumulated based on topography. Because surface runoff flows down gradient, it is possible to calculate the accumulated surface runoff at each point in the basin, using the standard hydrology GIS toolbox. The accumulated surface runoff represents the direct river flow. For the baseflow, it follows from the groundwater balance that long-term average drainage of groundwater should equal the groundwater recharge minus possible groundwater abstractions such as pumping wells. The groundwater abstraction can be ignored in the Shannon river catchment because most of the water consumption is taken from the surface water and any wells are only domestic with very small pumping rates compared to the total recharge.

The relationships between areas where groundwater recharge and discharge are occurring depend upon the groundwater flow system in the catchment, which is largely unknown and complicated in the Shannon River catchment. Groundwater flow systems are often strongly conditioned by topography (Gebreyohannes et al., 2013, Tóth, 2009, Haitjema and Mitchell-Bruker, 2005, Freeze and Cherry, 1979). As an approximation, it is assumed that the groundwater flow is also influenced by topography and river baseflow can be estimated by accumulating the GEO-CWB calculated subsurface water component, which includes subsurface flow and groundwater recharge, on the basis of topography as was done for surface runoff. The accumulated GEO-CWB surface runoff and subsurface water component at the locations of the hydrometric stations are calculated, then the average daily simulated water flow has been calculated and compared with the observed daily average flows in Table 9-1. The model results are close to the observations with an average percent of error around 5 % and the standard deviation for the validation is around

2.13 m^3/sec with an R^2 is 98.3%. The results of the validation process indicate that GEO-CWB simulates the water balance to a high level of accuracy.

Table 9-1: GEO-CWB evaluation table between the simulated average daily flow and the observed average daily flow for the simplified Shannon system.

Hydrometric Stations	Simulated average daily flow (m^3/s)	Observed average daily flow (m^3/s)	Difference (m^3/s)	Error %
Inny	16.90	15.51	1.39	8.99
Mid-Shannon	15.31	17.76	-2.45	-13.78
Suck	22.91	20.57	2.34	11.37
Brosna	12.96	14.94	-1.99	-13.30
Nenagh	9.15	6.83	2.31	33.88
Dead	14.26	12.89	1.37	10.60
Lower-Shannon	152.30	153.96	-1.66	-1.08

9.2 Water balance simulated parameters results

This section shows the simulated annual, summer and winter water balance variables and components for the Shannon River catchment by GEO-CWB model forced by the simulated climate change scenarios (Chapter 4), land use scenarios (Chapter 6) and the simulated PET scenarios (Chapter 7). Additional results from GEO-CWB for the Shannon catchment are presented in the appendix E.

9.2.1 Surface runoff

The annual average surface runoff maps simulated by GEO-CWB are shown in Figure 9.4. The runoff simulations and projections are presented for the baseline period and four climatic scenarios, which are RCP 4.5 50%, RCP 4.5 75% RCP 8.5 50% and RCP 8.5 75%, projected for three future time steps 2020, 2050 and 2080. The overall statistics for the surface runoff simulations are presented in Table 9-2, which show that, in general, the annual simulated surface runoff values vary through the climate change scenarios between the positive changes from the baseline and the negative changes from the baseline, as shown on Figure 9.1. Most of the changes in runoff are negative changes except for 2050 and 2080 of RCP 8.5 (75%) scenario, as the precipitation has a significant increase based on this climate scenario.

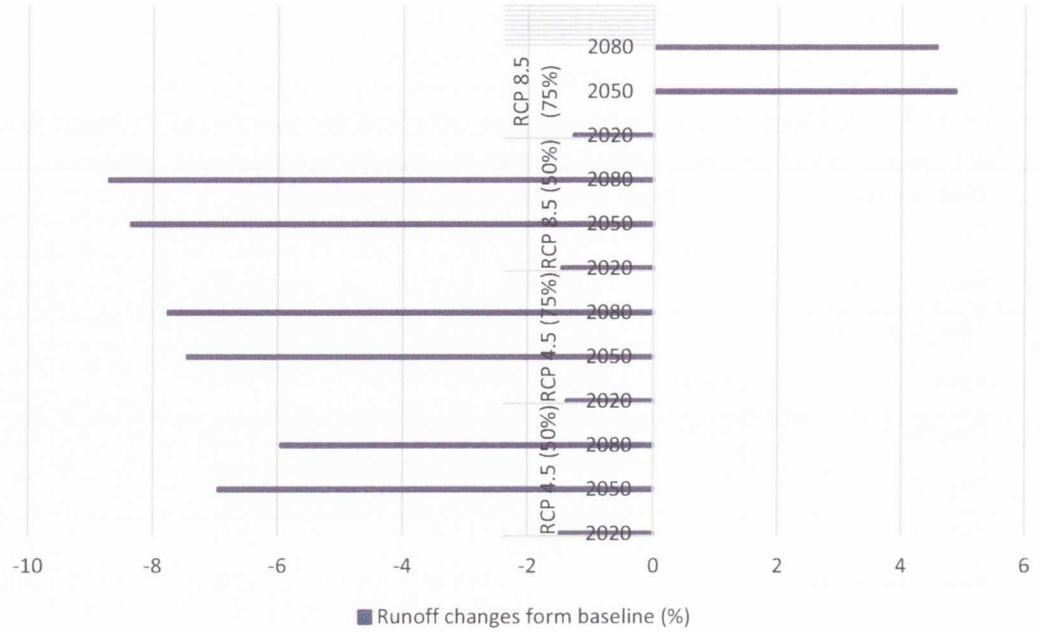

Figure 9.1: Simulated surface runoff changes percent for each climate change scenario from the baseline period.

Figures 9.2 and 9.3 give the mean winter and summer surface runoff for the combinations and interactions of land-use and soil classes. The largest surface runoff occurs on the rock soil group with wetlands, while the lowest values are for Luisol soil group with agricultural areas. The traceability of the soil type boundaries and the higher standard deviation values of the runoff for different soil groups indicate that surface runoff is more influenced by soil type than by land-use. Also, it is noticeable that both winter and summer runoff profiles in the Figures 9.2 and 9.3 are different.

Studying the different runoff values based on different soil profiles interactions with land use categories is very important in driving conclusions about which land use category combined by which soil group gives the lowest or the highest runoff values. That helps in the designing process of structures like rainwater collection basin, landfill or wastewater plants. Figures 9.2 and 9.3 show that urban areas seem to have lower runoff values for some of the soil groups except Groundwater Gley, Rendzina, Brown Earth and Rock. This is mainly because that most of the urban areas in the Shannon catchment are placed on top of relatively permeable soil groups which helps in increasing the infiltration process and that decrease the surface runoff. One can notice that there are wide variations of runoff values over the water bodies. These variations are mainly because of the different type of water body bed soil group and if there is any vegetation in it or not.

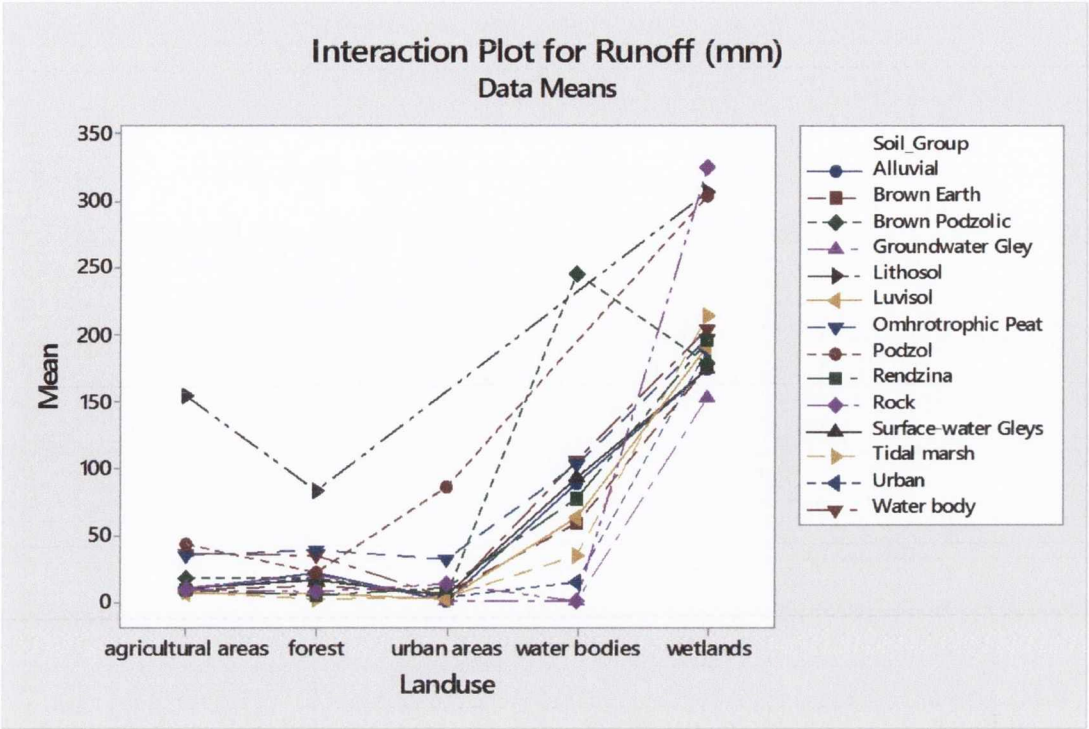

Figure 9.2: GEO-CWB winter surface runoff (mm), soil and land use categories interaction plot.

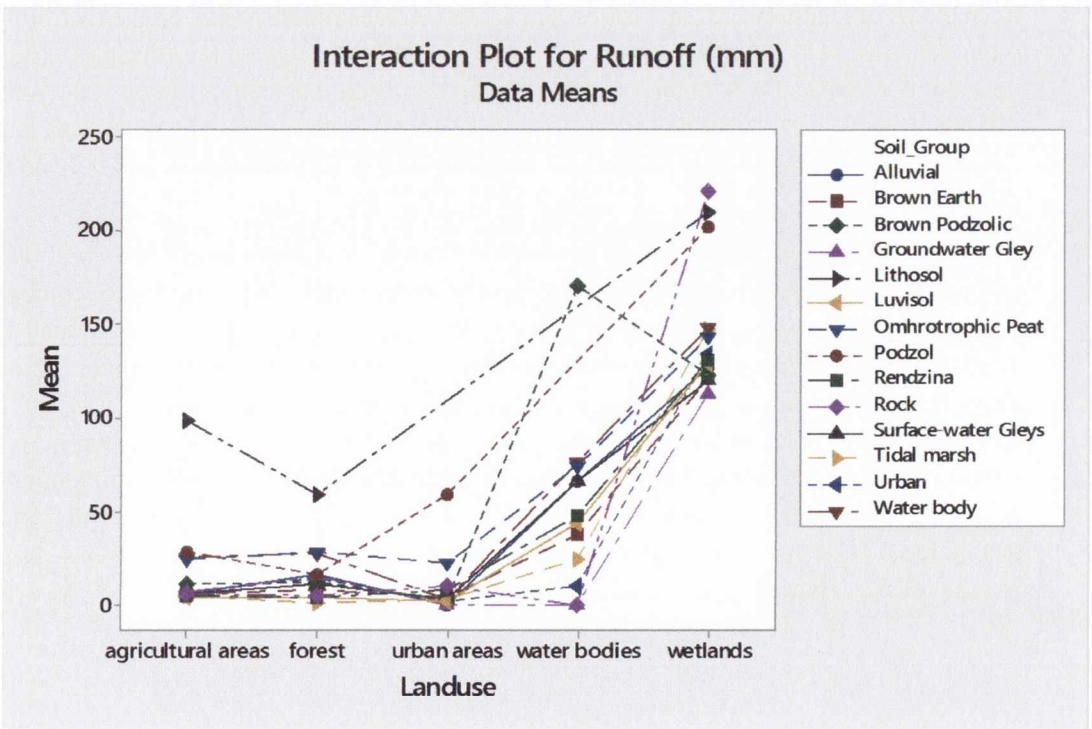

Figure 9.3: GEO-CWB summer surface runoff (mm), soil and land use categories interaction plot.

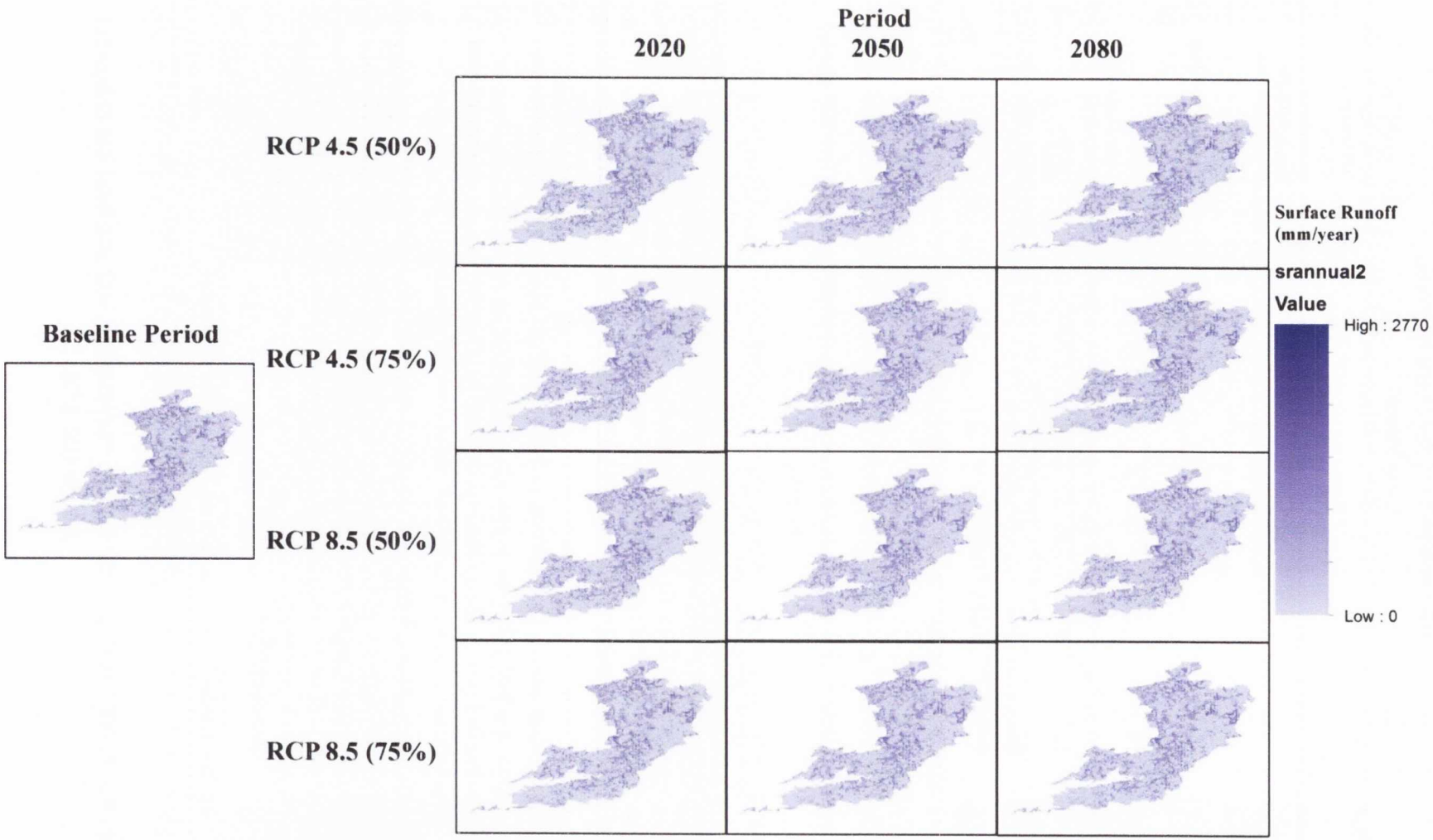

Figure 9.4: The average annual surface runoff for each climatic period and land use scenario simulated by GEO-CWB.

9.2.2 Subsurface water component

Based on the fact that, currently, GEO-CWB does not take into account the bedrock geologies of the catchment, it provides as one of the main outputs the sub-surface water component, which includes mainly the subsurface water flow and the groundwater recharge. To get the recharge component in a large catchment like the Shannon, the model needs to take into account the maximum capacity of the different aquifer types to take recharge (Misstear et al., 2009b), and this type of data and details are not available for the Shannon catchment. GEO-CWB has the framework setup to separate the two main components, subsurface flow and groundwater recharge, once the spatially distributed data for the recharge caps is available.

Groundwater recharge is concerned with the percolation of water through the soil, subsoil and down through the unsaturated zone to the water table (Misstear et al., 2009b). In general, groundwater recharge is estimated by first calculating the effective rainfall (defined as total rainfall minus actual evapotranspiration) through a soil moisture deficit method and then multiplying the calculated effective rainfall by a recharge coefficient (Misstear et al., 2009a, Misstear et al., 2008, Fitzsimons and Misstear, 2006, Misstear, 2000, Misstear et al., 2009b). The recharge coefficient is the percent of the effective rainfall that forms the groundwater recharge. The recharge coefficient depends mainly on the characteristics of the superficial deposits that overlie the aquifer. Where an aquifer is covered by thick glacial tills of low hydraulic conductivity, the recharge coefficient will be low, with most the effective rainfall being 'lost' to surface runoff or interflow. On the other hand, the recharge coefficient will be high where the overburden is thin, absent or has a high hydraulic conductivity (Fitzsimons and Misstear, 2006). Misstear et al. (2009a) states that there is a clear relationship between recharge coefficient and groundwater vulnerability, with high recharge coefficients expected in highly vulnerable aquifers and so on, based on that, Misstear et al. (2009a) has developed methodology for making initial estimates of groundwater recharge from groundwater vulnerability mapping. However, the developed methodology gives a good starting estimation but it is not enough to use its results for any management of modeling approach. GEO-CWB provides the framework of a cell by cell multidimensional dynamical groundwater recharge calculation for the catchment scale by applying the water balance calculation for each cell's subfraction, which provides a high accuracy simulation compared with the currently used approaches, when the spatially distributed recharge data is available.

Groundwater recharge in the Shannon River catchment basin, and anywhere else is promoted by low evapotranspiration and low surface runoff, e.g. typically for a flat topography and permeable soils. The annual averages of the spatially distributed subsurface water component, subsurface flow and groundwater recharge, maps for baseline period and the three projected periods, 2020, 2050 and 2080, forced by four different climatic scenarios are shown in Figure 9.8.

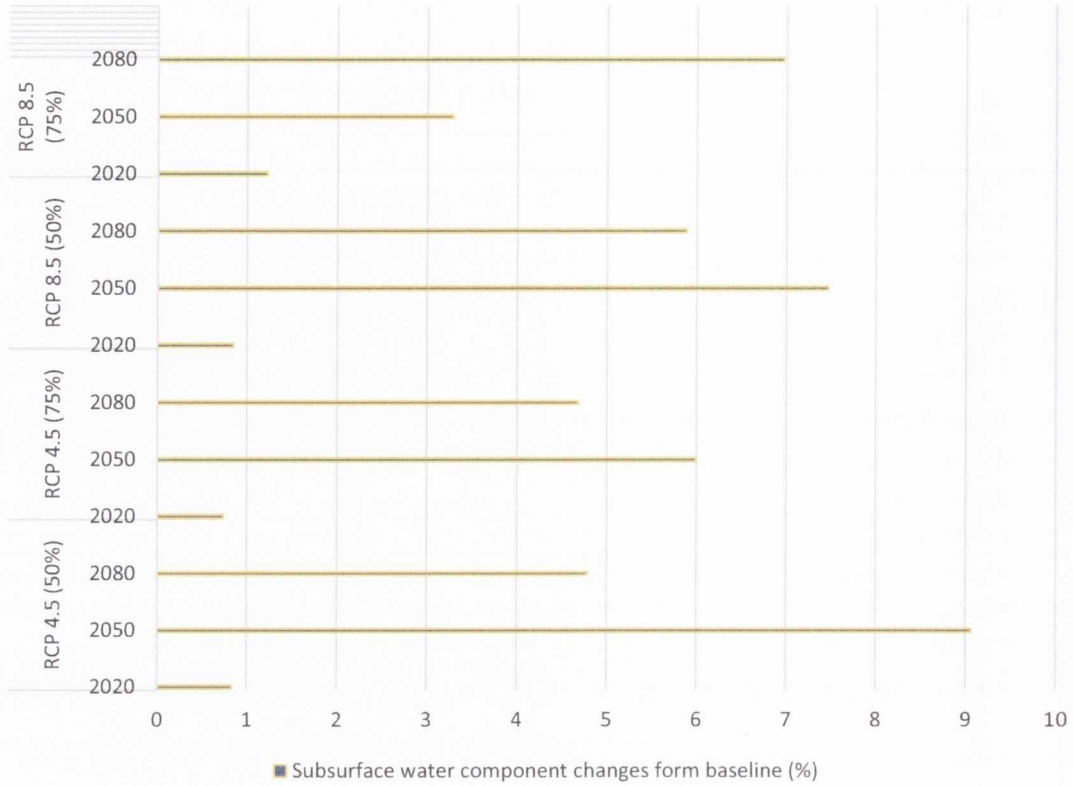

Figure 9.5: Simulated subsurface water component (groundwater recharge and subsurface runoff aggregated together) changes percent for each climate change scenario from the baseline period.

The simulated annual subsurface water component values vary through the climate change scenarios between 1% to 9% positive increasing changes from the baseline, this because the RCP models are predicting higher rainfall quantities which offset the ET (see Figure 9.5).

The annual subsurface water component in the Shannon River catchment is estimated as 40-55% of the total annual precipitation over the catchment. In general, around 84% of the contribution in the subsurface water component during the 6 months' rainy season in the winter while the remaining 16% occurs in the 6 months' summer season. Figures 9.6 and 9.7 give the mean annual subsurface water component values for different combinations and interactions of land use and soil classes. The largest subsurface water component is observed for the agricultural area on Podzol soil. This is basically because of the high permeability of these soils, but could partly also be due to lower evaporation rates and less runoff on the relatively gentler slopes of agricultural lands.

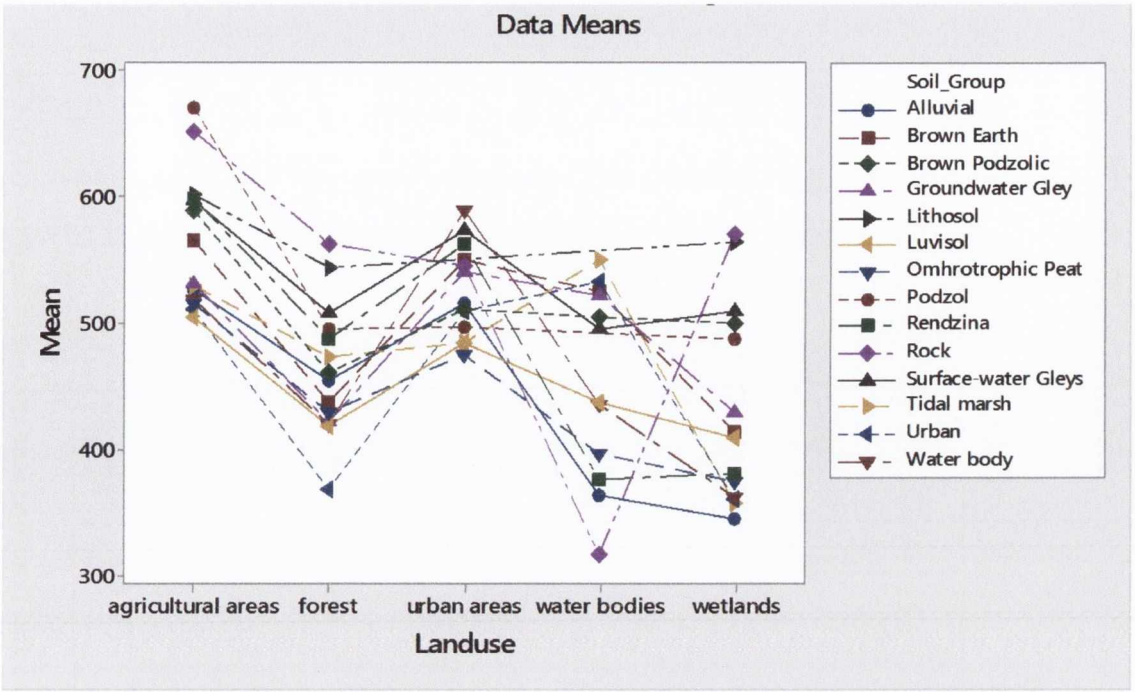

Figure 9.6: GEO-CWB winter subsurface water component (mm), soil and land use categories interaction plot.

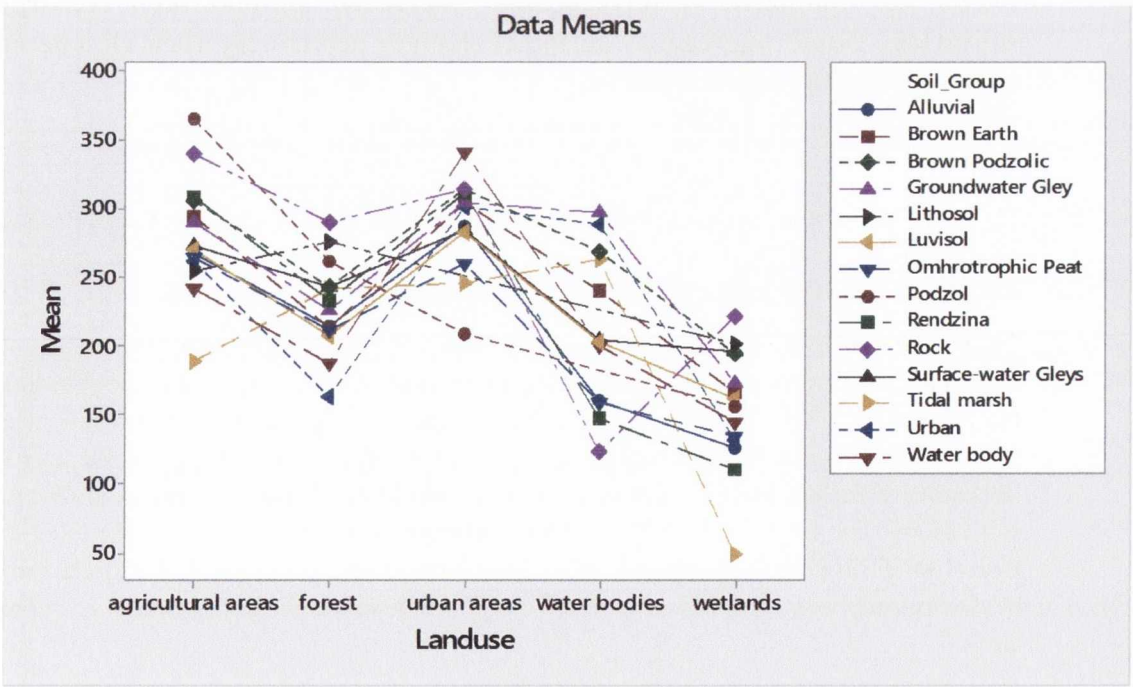

Figure 9.7GEO-CWB summer subsurface water component (mm), soil and land use categories interaction plot.

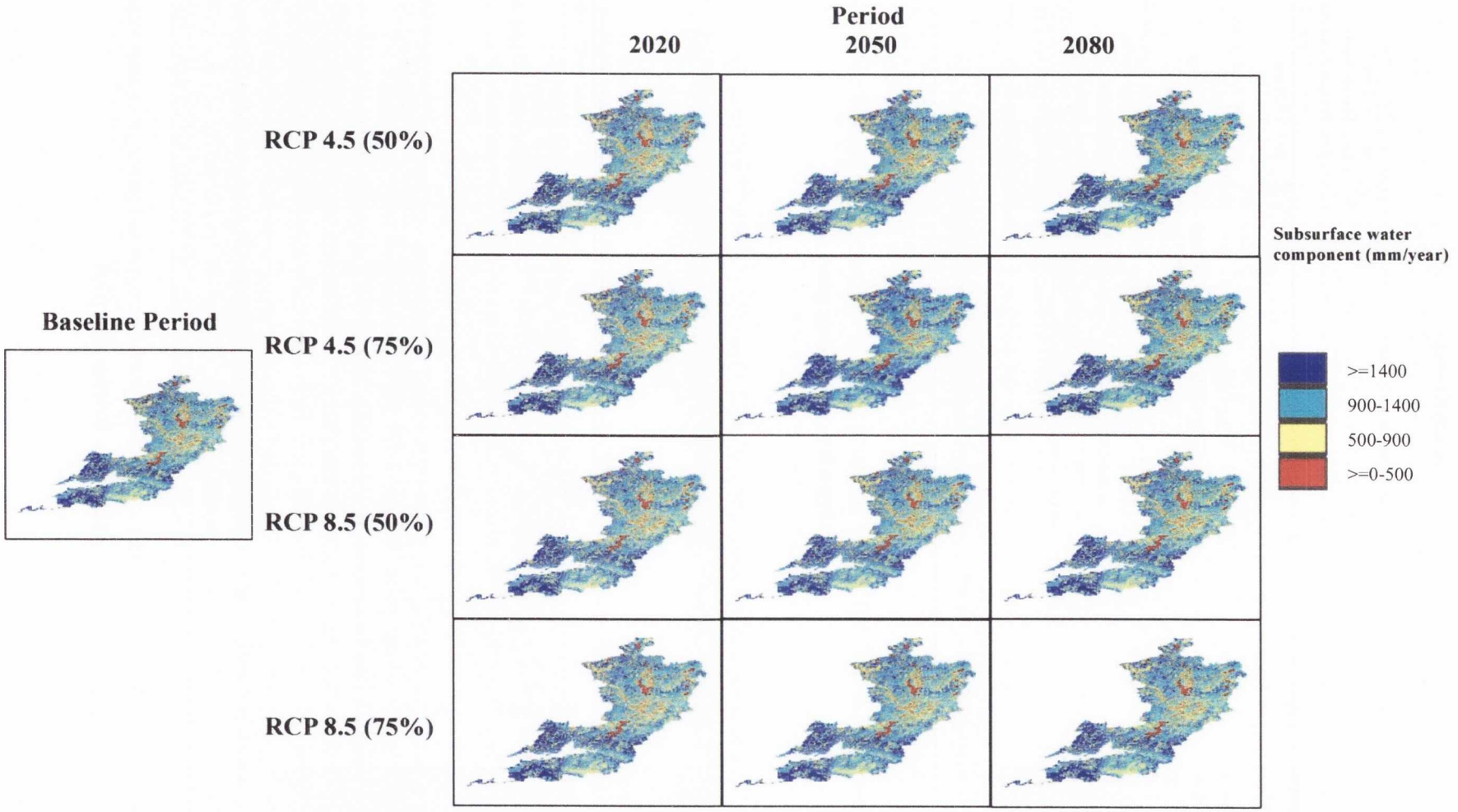

Figure 9.8: The average annual subsurface water component for each climatic period and land use scenario simulated by GEO-CWB.

9.2.3 Interception

Rainfall interception is the fraction of precipitation which falls onto vegetation but never reaches the ground, instead it evaporates from the wet canopy. The most direct way to measure rainfall interception evaporation is through the construction of weighing lysimeters, which is a major undertaking for forests (Dunin et al., 1988). Therefore interception loss (the amount of rainfall lost to wet canopy evaporation) has usually been derived as the residual between event gross precipitation measured above the canopy or in a nearby clearing, and net precipitation, the latter calculated as the sum of separately measured through fall and streamflow below the canopy (van Dijk et al., 2015). GEO-CWB calculates the interception as a direct fraction of precipitation, separated from the evapotranspiration, which means the total water loss from the precipitation in the catchment can be calculated by the summation of both evapotranspiration and interception. The annual spatially distributed interception maps for baseline period and the three projected periods, 2020, 2050 and 2080, forced by four different climatic scenarios are shown in Figure 9.12.

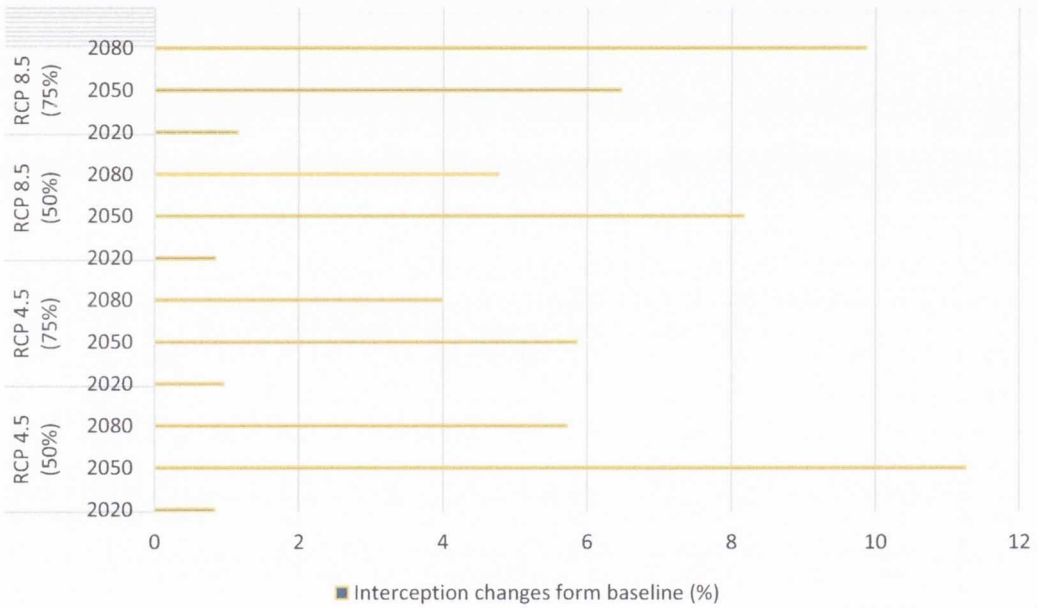

Figure 9.9: Simulated interception changes percent for each climate change scenario from the baseline period.

The simulated annual interception values vary through the climate change scenarios between 0.1% to 9% positive increasing changes from the baseline, Figure 9.9. The annual rainfall interception in the Shannon River catchment makes around 11% of the total annual precipitation over the catchment. In general, around 65% of the interception occurs during the 6 months' summer season while the remaining 35% occurs in the 6 months' winter season. Figures 9.10 and 9.11 give the mean annual interception values for different combinations and interactions of land use and soil classes, which show the different summer and winter interception interaction profiles.

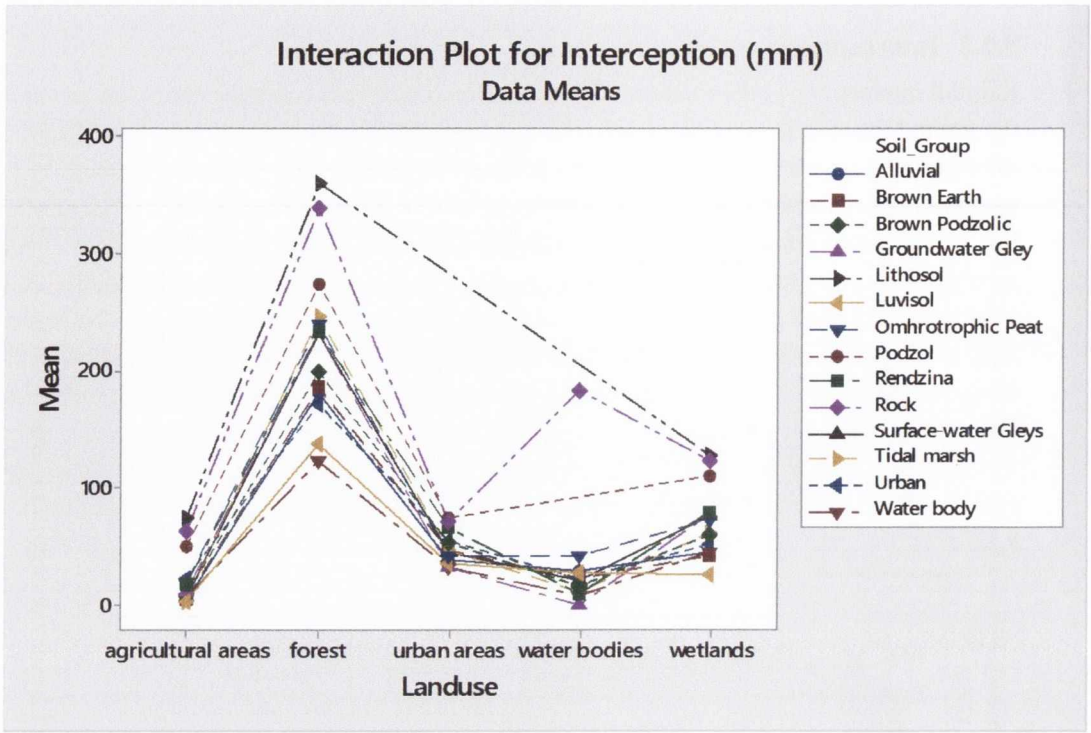

Figure 9.10: GEO-CWB winter interception (mm), soil, and land use categories interaction plot.

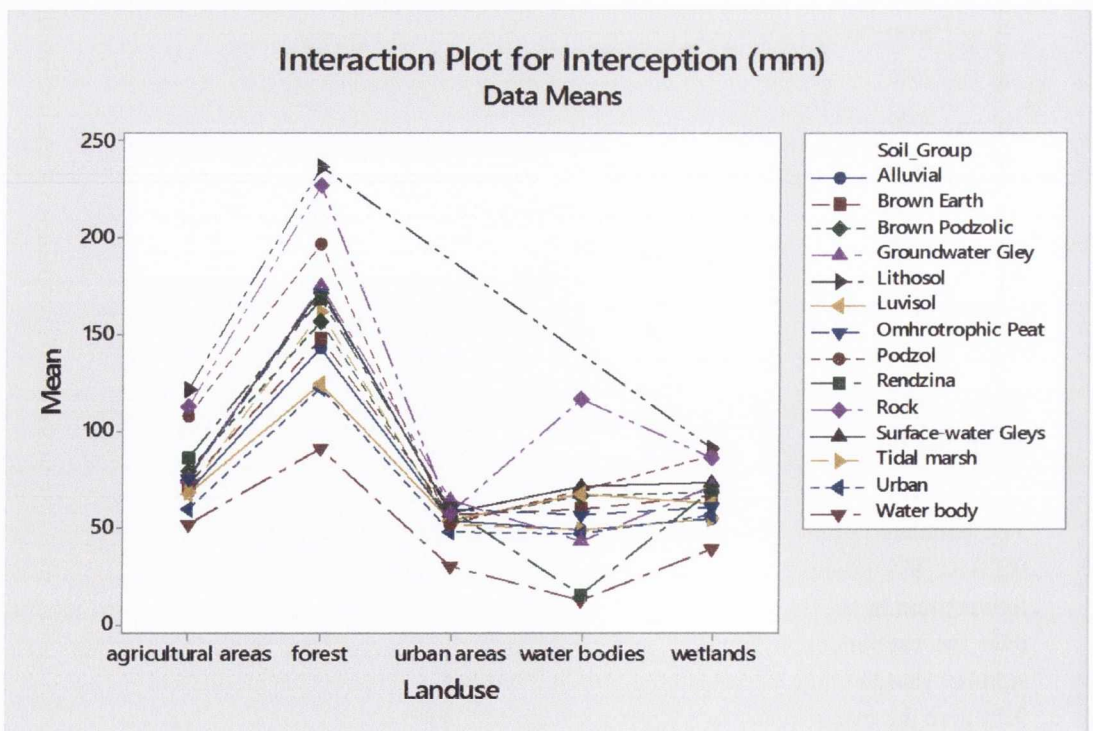

Figure 9.11: GEO-CWB summer interception (mm), soil and land use categories interaction plot.

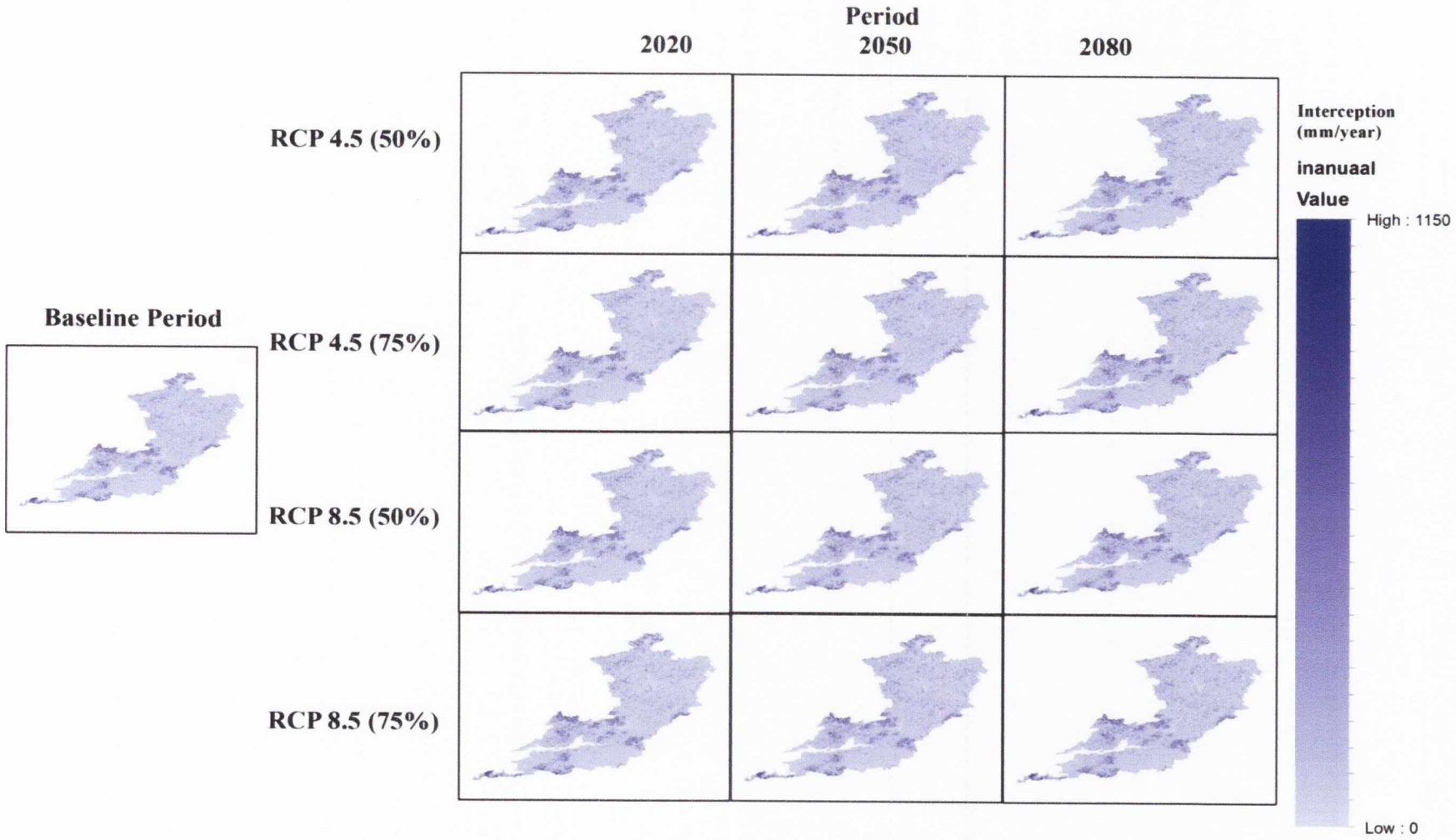

Figure 9.12: The average annual interception for each climatic period and land use scenario simulated by GEO-CWB.

9.2.4 Evapotranspiration

Evapotranspiration is calculated in the GEO-CWB as the sum of transpiration, and evaporation from open water bodies and soil. The actual evapotranspiration, soil evaporation and transpiration components for the catchment are calculated based on the pre-calculated potential evapotranspiration in Chapter 7. The actual evapotranspiration is a summation of some calculated sub-fractions of PET as illustrated in the equations of Section 8.3.1.1. Depending on which fraction of each cell is being modelled, the evapotranspiration could be equal to PET (open water fraction) or fraction of it (Bare soil or impervious surface fractions) or just equal to the simulated transpiration (vegetated fraction). GEO-CWB calculates evapotranspiration and interception components individually which means that the total water loses from precipitation in the catchment is the summation of the two components.

The annual averages spatially distributed evapotranspiration maps for baseline period and the three projected periods, 2020, 2050 and 2080, forced by the four different climatic scenarios are shown in Figure 9.17.

The maximum annual evapotranspiration in the catchment is obviously potential evapotranspiration from open water. Evapotranspiration and interception together are estimated to be around 30-40% of the annual precipitation in the Shannon River catchment. Around 76% of the evapotranspiration takes place during the summer season, while the remaining 24% takes place during the winter season, which is obviously due to the unequal temporal distribution of the temperature but also partly to the fact that the vegetation is less active in the winter season. The only available actual evapotranspiration map for Ireland is presented by Mills (2000) in the form of a percentage of the precipitation, Figure 9.14. However, this map is the only good estimate for the evapotranspiration. It is biased for overestimation with a very coarse scale (5 × 5 km) to be used for any hydrological application.

From Figures 9.15, 9.16 and 9.17, it can be concluded that evapotranspiration of the catchment is heavily influenced by soil type. The evapotranspiration maps areal statistics are presented in Table 9-2, which shows that, in general, the annual simulated evapotranspiration values vary through the climate change scenarios between the positive changes from the baseline and the negative changes from the baseline, (see Figure 9.13). Figures 9.15 and 9.16 give the mean seasonal evapotranspiration values for the combinations and interactions of land-use categories and soil groups. The mean annual evapotranspiration for different land uses categories shows that urban areas have the lowest values. While overall evapotranspiration is highly influenced by precipitation and to some extent by soil texture, the standard deviation values in Table 9-2 show that evapotranspiration in the Shannon River catchment is more variable within land-use categories than within soil group.

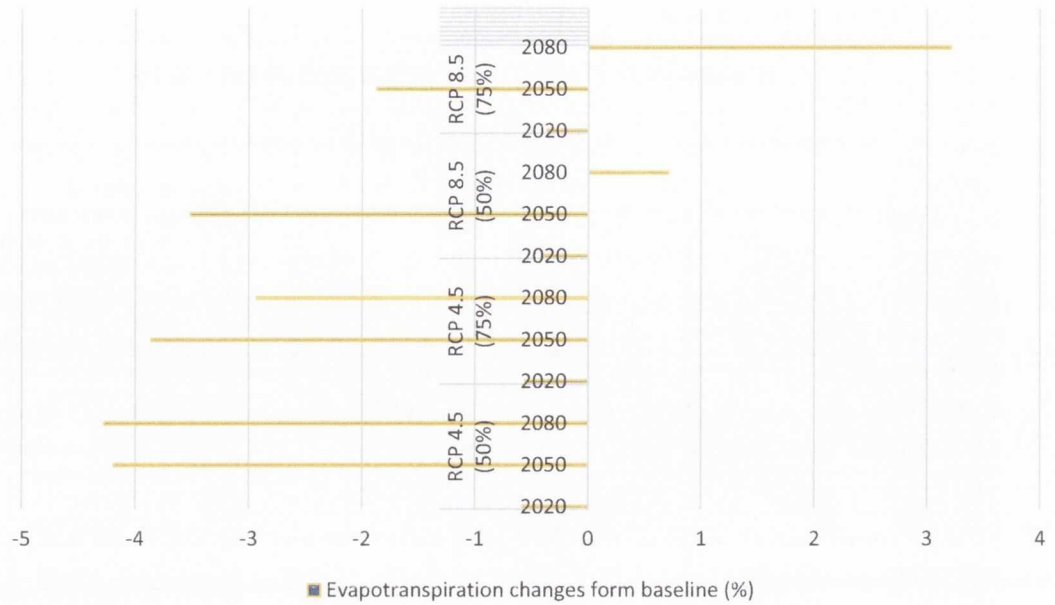

Figure 9.13: Simulated evapotranspiration changes percent for each climate change scenario from the baseline period.

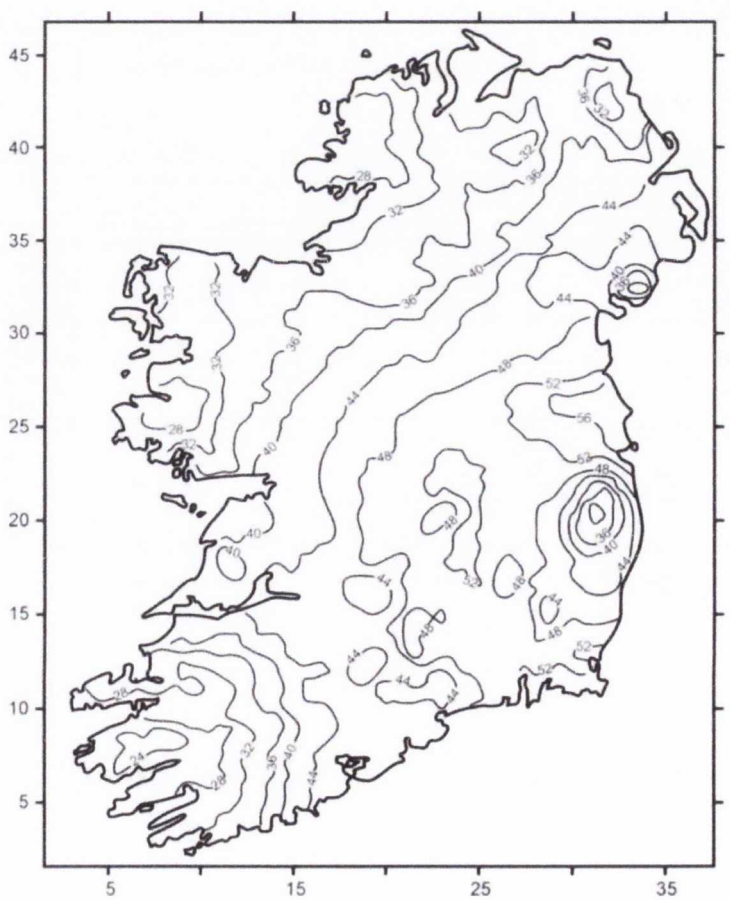

Figure 9.14: Average estimated actual evapotranspiration as percentage of annual precipitation (Mills, 2000).

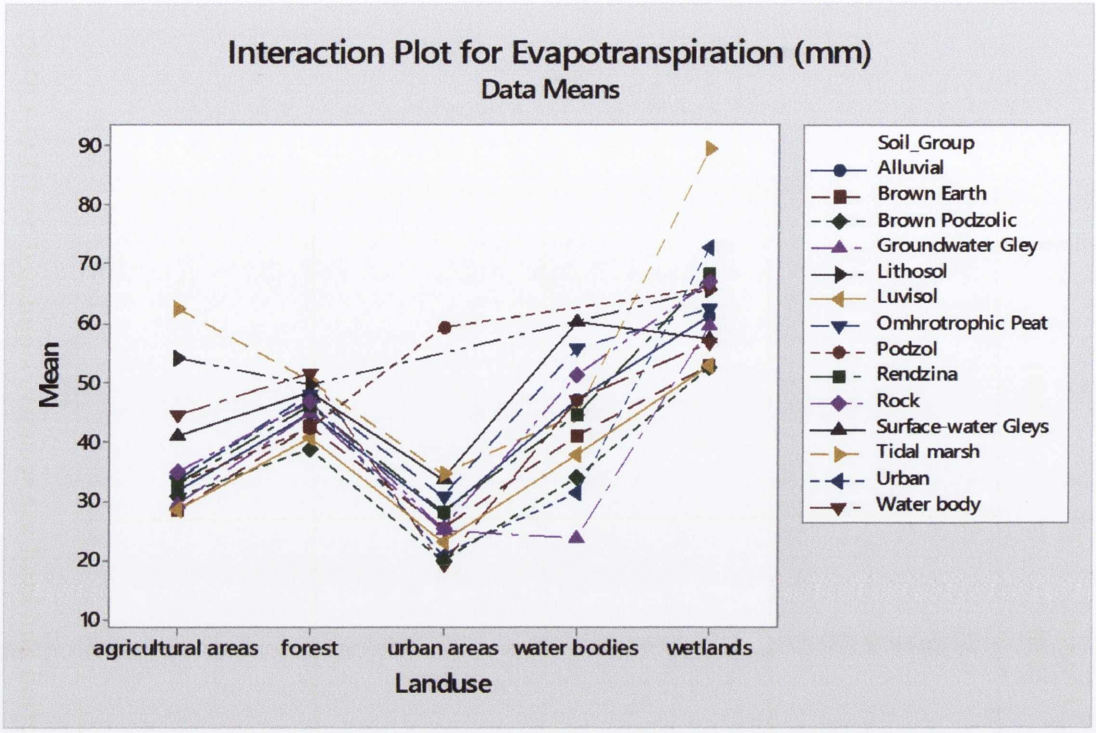

Figure 9.15: GEO-CWB winter evapotranspiration (mm), soil and land use categories interaction plot.

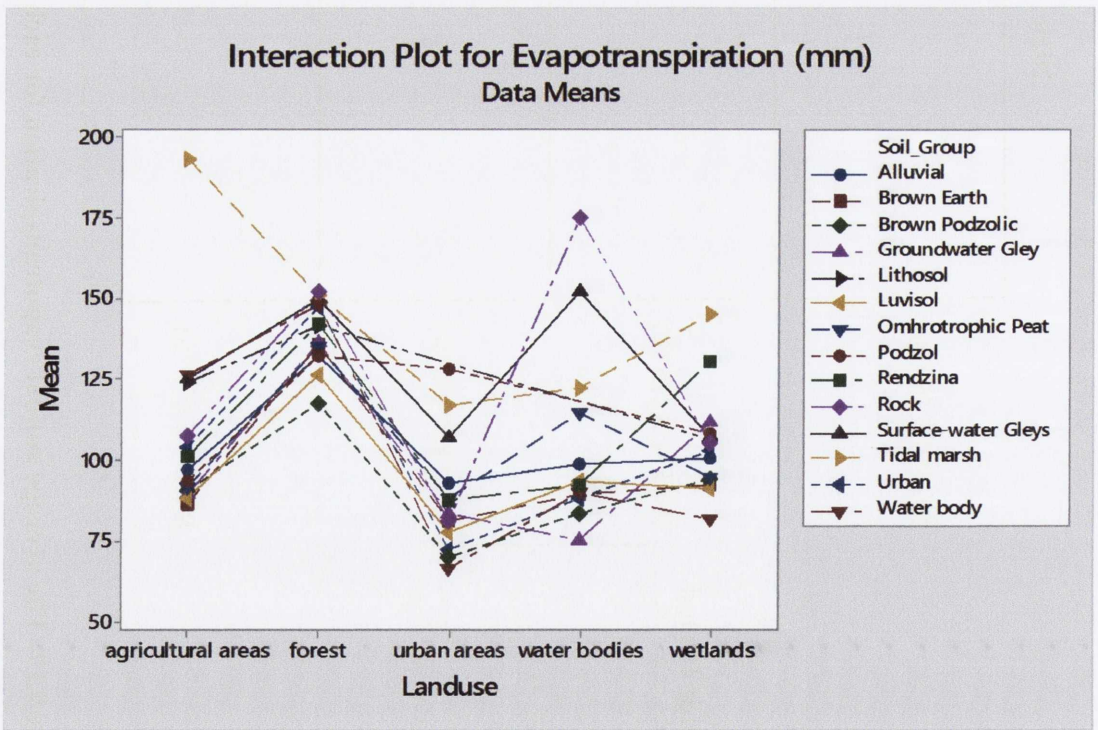

Figure 9.16: GEO-CWB summer evapotranspiration (mm), soil and land use categories interaction plot.

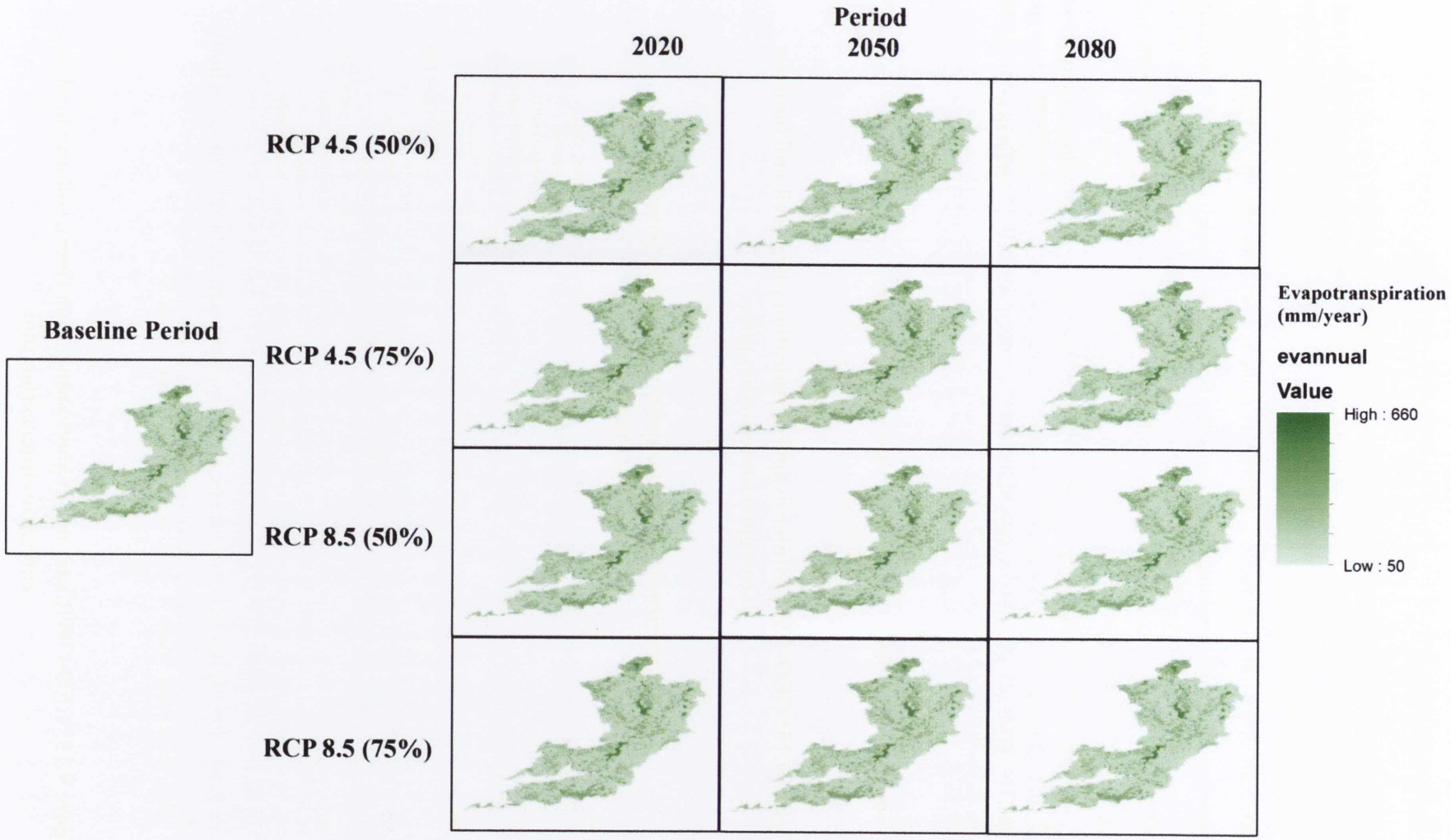

Figure 9.17: The average annual evapotranspiration for each climatic period and land use scenario simulated by GEO-CWB.

9.2.5 Soil evaporation

Soil evaporation is the evaporation from open soil area as a fraction of each simulated pixel and, as mentioned in Section 9.2.4, forms a part of the total evapotranspiration. The annual averages spatially distributed soil evaporation maps for the baseline period and the three projected periods, 2020, 2050 and 2080, forced by the four different climatic scenarios are shown in Figure 9.21.

The soil evaporation maps areal statistics are presented in Table 9-2, which show that, in general, the annual simulated soil evaporation has positive changes from the baseline (see Figure 9.18). Figures 9.19 and 9.20 give the mean seasonal soil evaporation values for the combinations and interactions of land-use categories and soil groups.

As the precipitation increases through all the climatic scenarios, the soil moisture increases as well, which means more water is available for the evaporation process and thus the temperature increases. This leads to a positive increase in the soil moisture among all the climatic periods and scenarios as shown in figure 9.18.

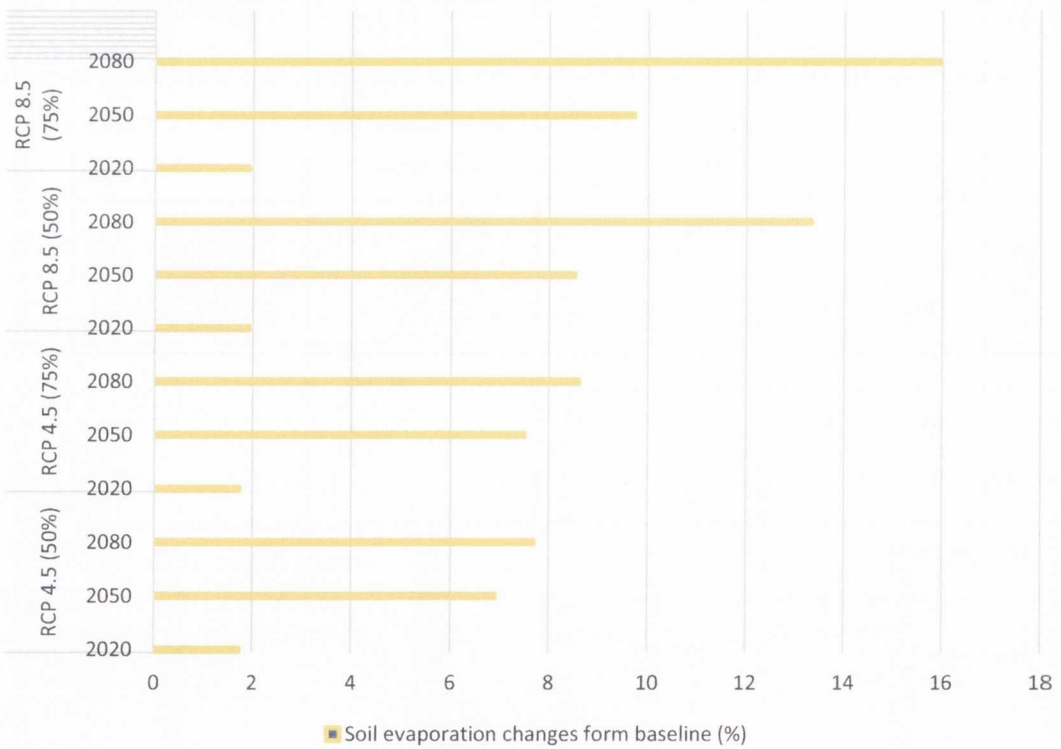

Figure 9.18: Simulated soil evaporation changes percent for each climate change scenario from the baseline period.

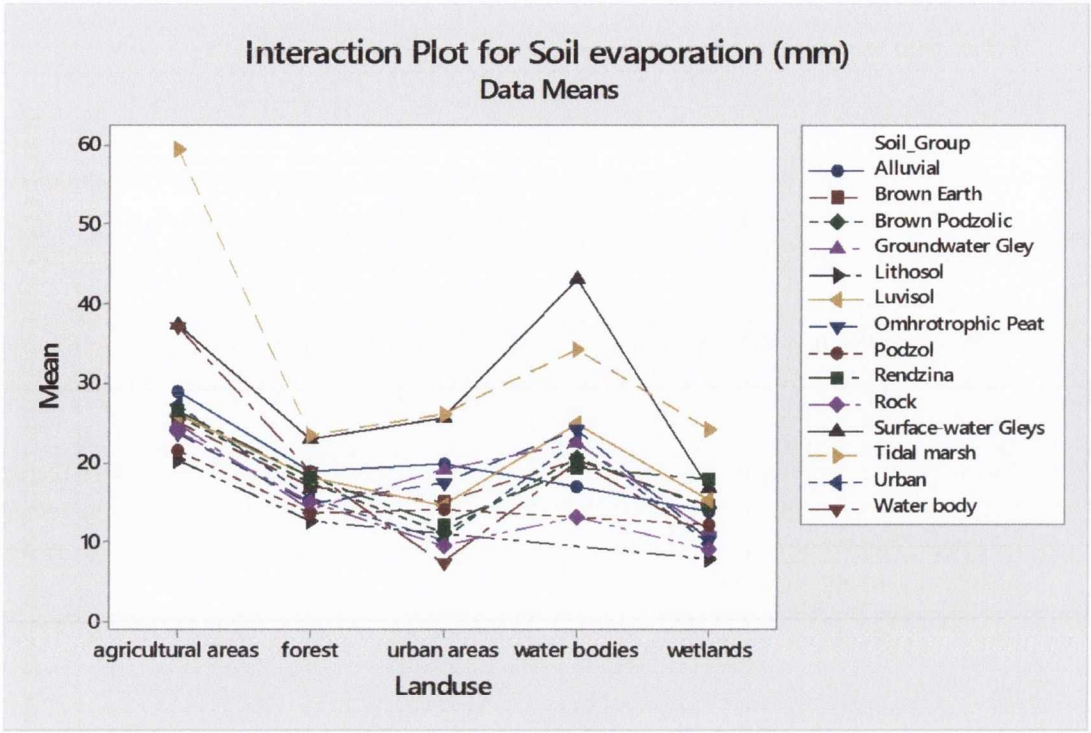

Figure 9.19: GEO-CWB winter soil evaporation (mm), soil and land use categories interaction plot.

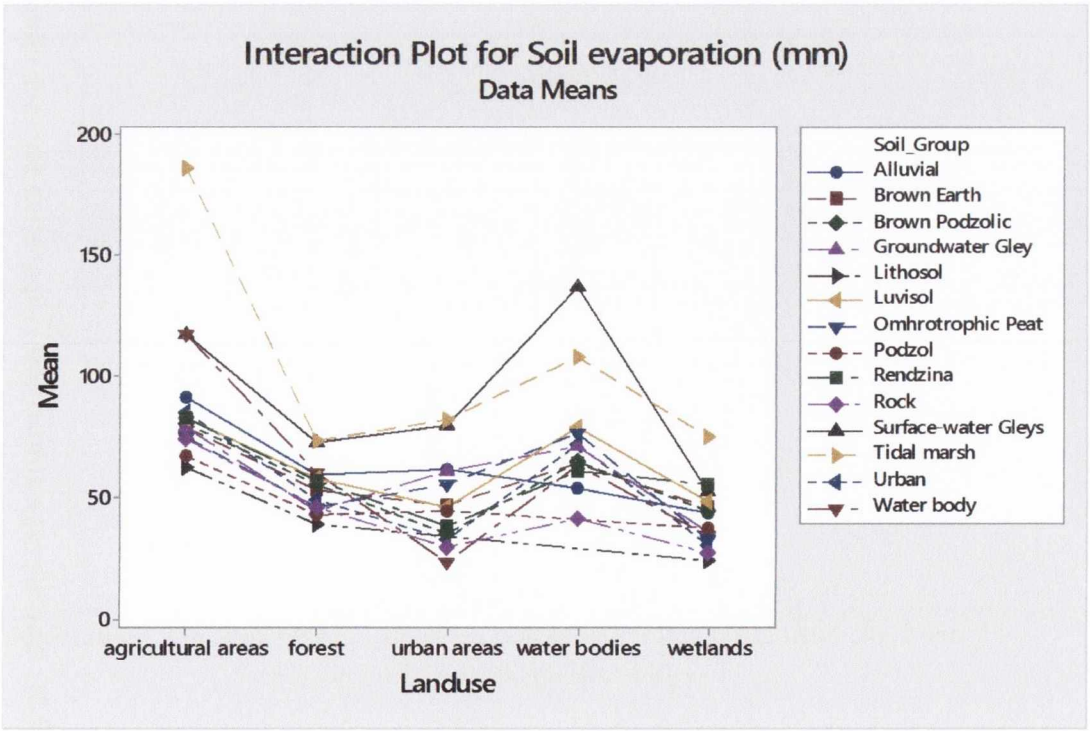

Figure 9.20: GEO-CWB summer soil evaporation (mm), soil and land use categories interaction plot.

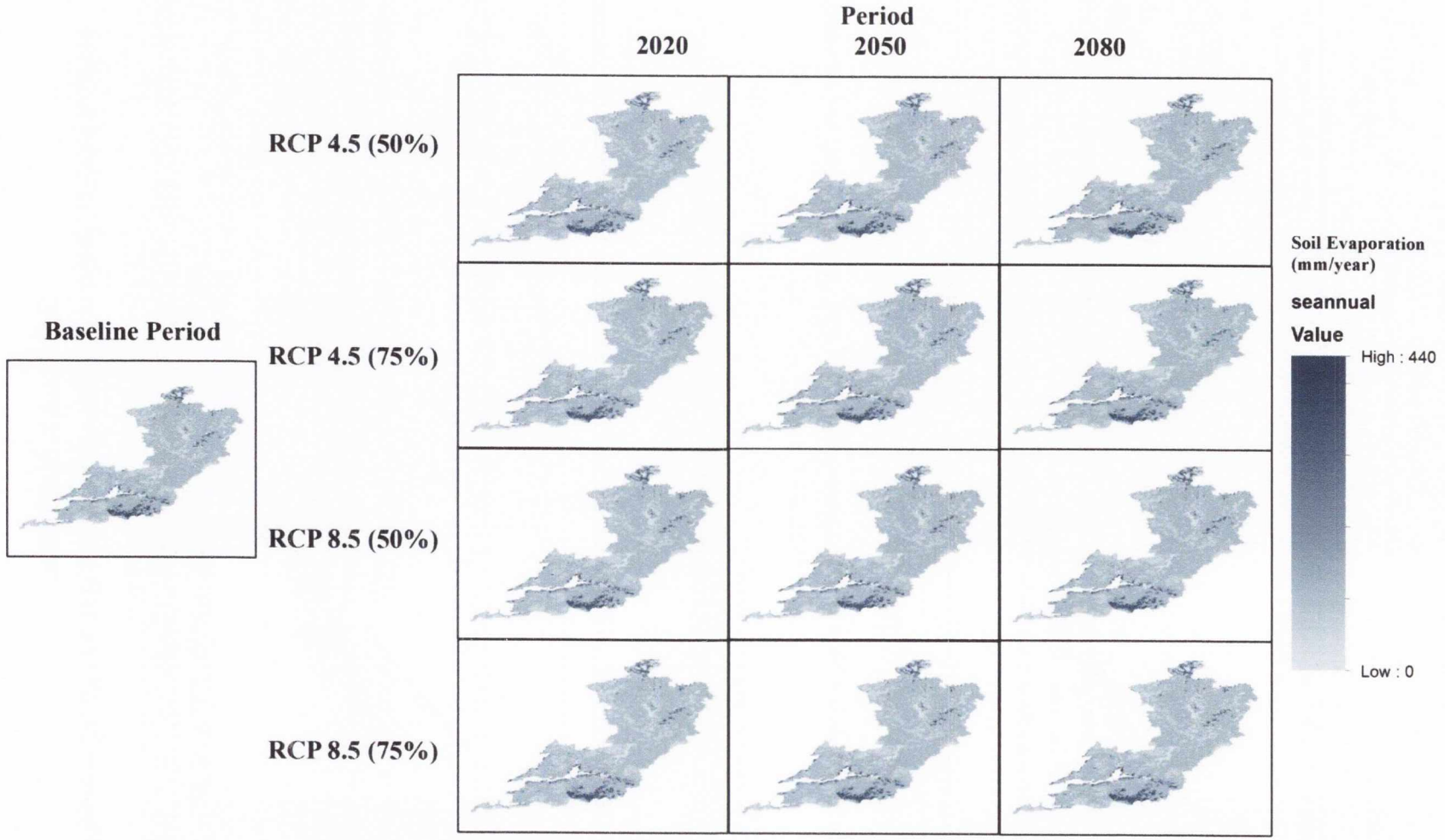

Figure 9.21: The average annual soil evaporation for each climatic period and land use scenario simulated by GEO-CWB.

9.2.6 Transpiration

Transpiration is the vaporization of water which is contained in plant tissues, that mainly occurs through the stem and leaf stomata. Transpiration, like direct evaporation, depends on factors such as radiation, air temperature, air humidity, and wind speed. In addition, the soil water content and the ability of the soil to conduct water upwards play a role. The length of the plant's root system also plays an important role in determining the transpiration rate, in addition to the vegetation type. The annual spatially distributed average transpiration maps for the baseline period and the three projected periods, 2020, 2050 and 2080, forced by the four different climatic scenarios are shown in Figure 9.25. The transpiration maps areal statistics are presented in Table 9-2, which show that, in general, the annual simulated transpiration varies between positive and negative changes from the baseline, based on the different simulated climatic scenarios (see Figure 9.22). Figures 9.23 and 9.24 give the mean seasonal transpiration values for the combinations and interactions of land-use categories and soil groups. As RCP8.5 (75%) has the highest increase in temperature and solar radiation, in addition to the predicted increase in the vegetation cover by 2080, the climatic period 2080 has the highest increase in transpiration as shown in figure 9.22. The average bassline transpiration is around 30 mm/year and the highest increase related to TCDP 8.5 (75%) is about 8.2% in 2080 which is equal to 2.5 mm/year, this amount of increase is very little in term of quantity.

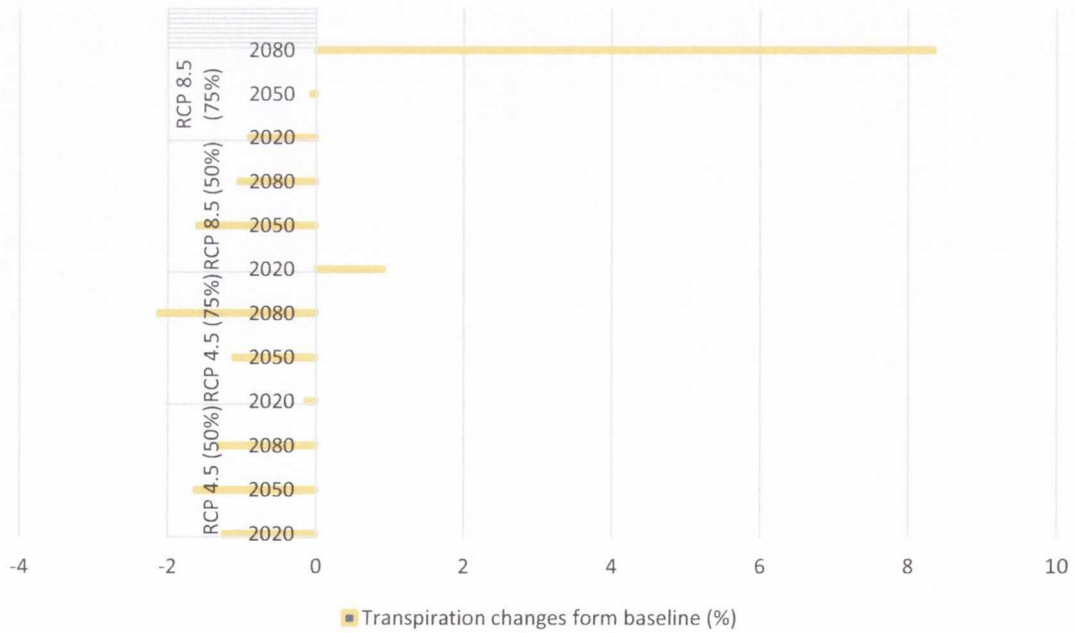

Figure 9.22: Simulated transpiration changes percent for each climate change scenario from the baseline period.

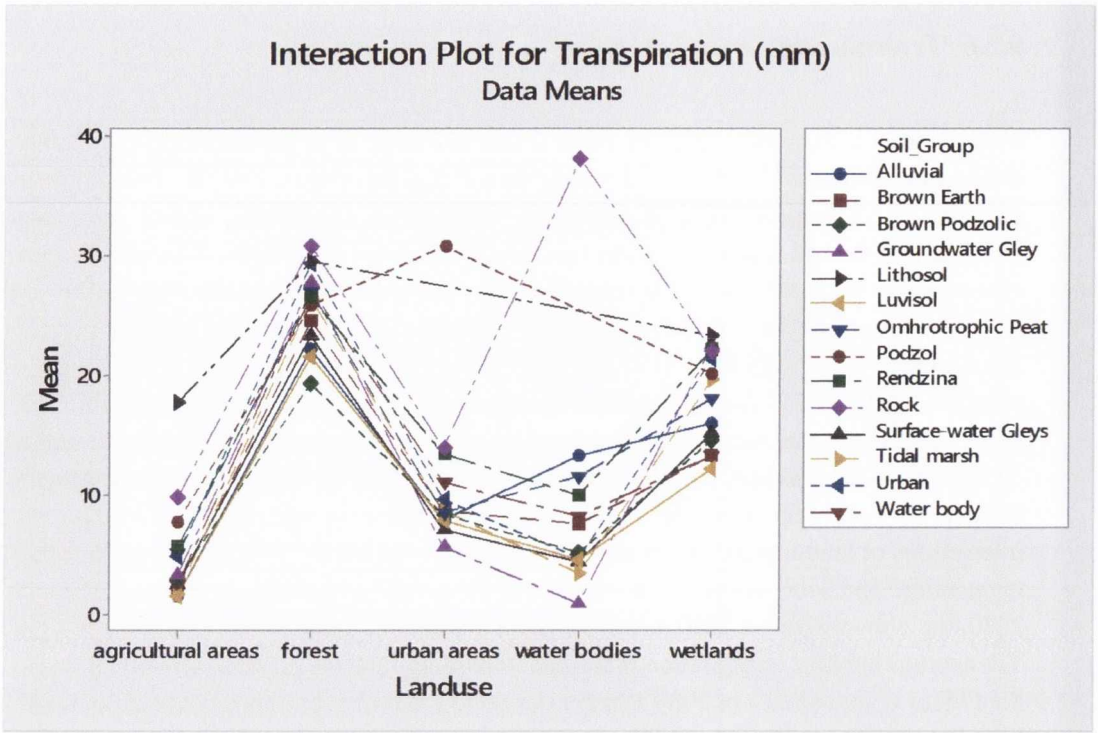

Figure 9.23: GEO-CWB winter transpiration (mm), soil and land use categories interaction plot.

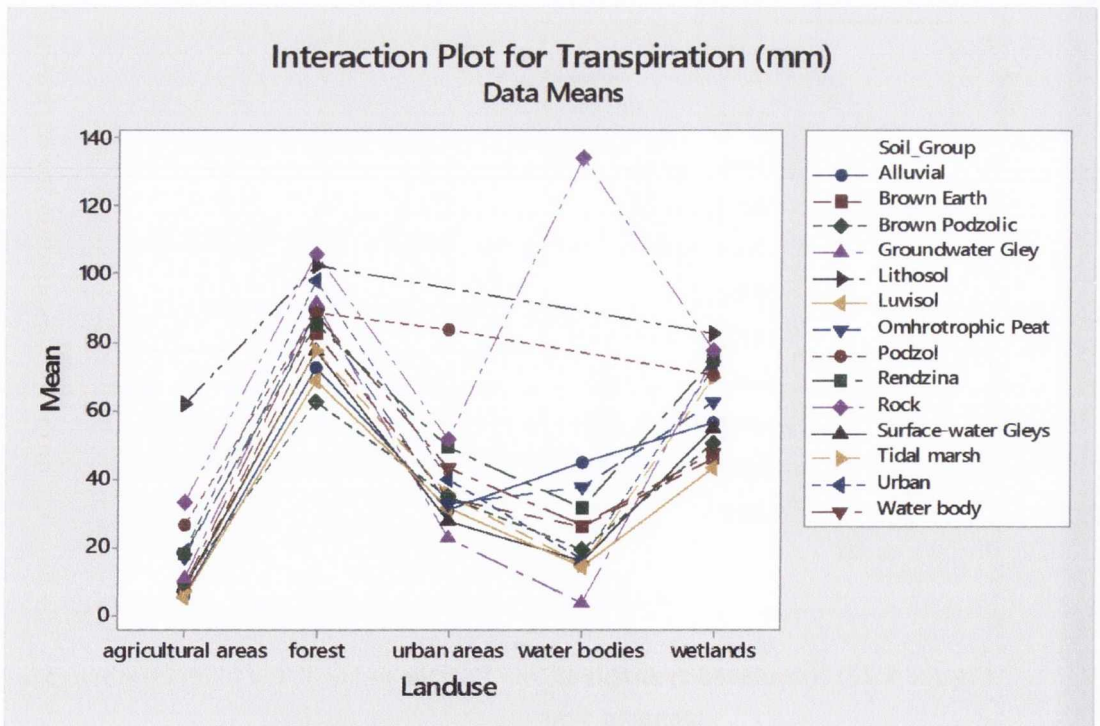

Figure 9.24: GEO-CWB summer transpiration (mm), soil and land use categories interaction plot.

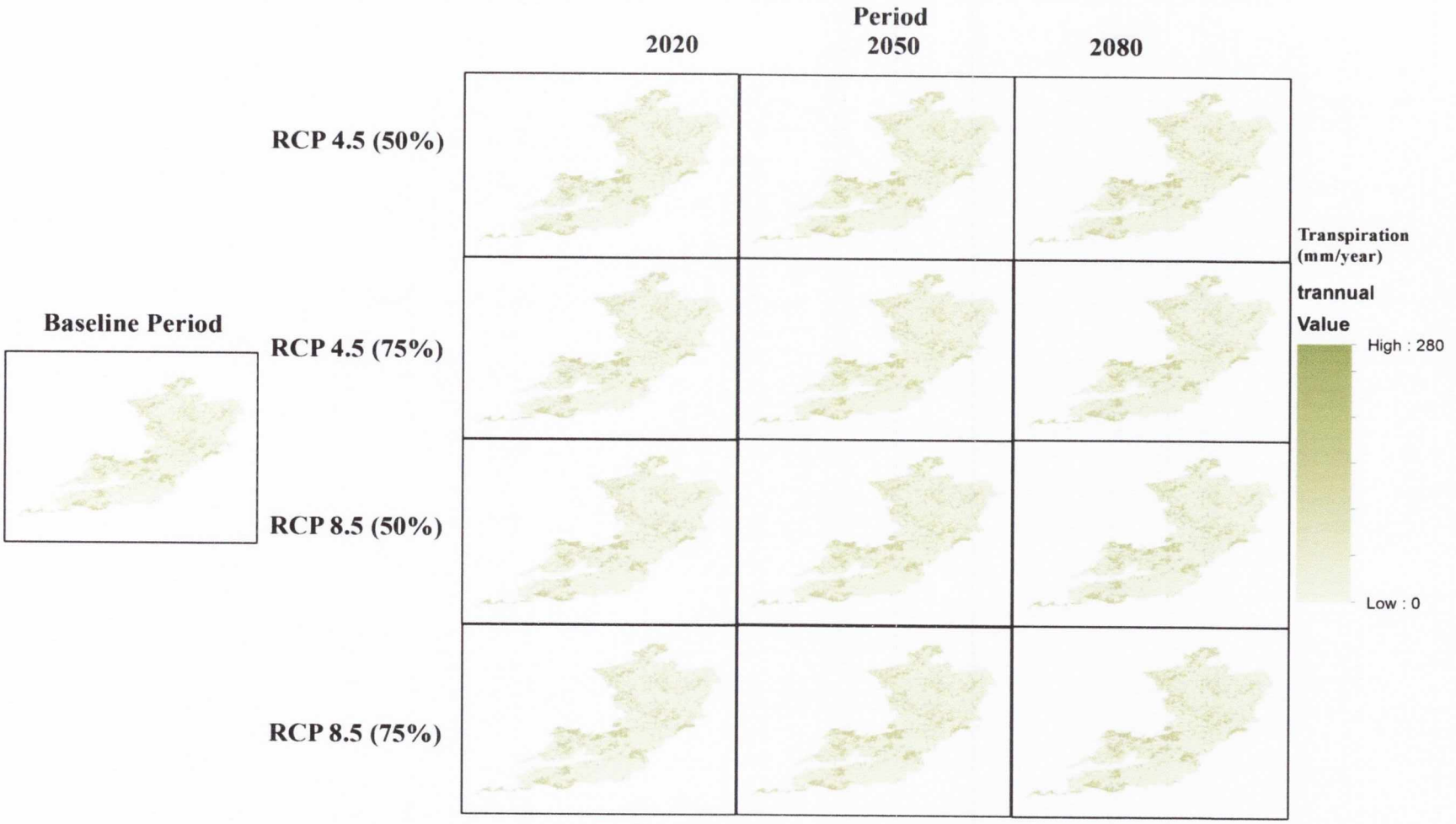

Figure 9.25: The average annual transpiration for each climatic period and land use scenario simulated by GEO-CWB.

Table 9-2: Annual, summer and winter rasters' areal statistics for all simulated water balance components by GEO-CWB for the baseline period and the projected periods with the calculated average values of the error in the simulated water balance.

Scenario	Period	Component	Annual-Mean	Annual-SD	Summer-Mean	Summer-SD	Winter-Mean	Winter-SD
Baseline Period	1961-2014	Runoff (Ro) mm	271.30	496.61	34.05	99.44	47.73	139.91
		Evapotranspiration (Et) mm	166.37	107.21	126.57	81.69	39.81	25.57
		Interception (In) mm	125.59	142.46	82.09	47.16	43.49	97.57
		Transpiration (Tr) mm	30.63	55.28	23.57	42.48	7.06	12.90
		Soil evaporation (Se) mm	102.29	70.58	77.57	53.48	24.72	17.10
		Subsurface water component (Re) mm	744.90	292.95	248.14	116.48	500.27	180.84
		Precipitation (P) mm	1136.27	224.02	486.22	83.58	650.04	143.10
		Water balance (WB) = P-Ro-Et-Re ; mm	-46.30	-	77.46	-	62.23	-
		Error in water balance (WB/ P; %)	-4.07	-	15.93	-	9.57	-
RCP 4.5 (50%)	2020	Runoff (Ro) mm	267.25	497.17	31.10	95.72	44.02	135.86
		Evapotranspiration (Et) mm	165.40	106.65	130.38	84.19	35.03	22.52
		Interception (In) mm	126.64	144.18	82.49	47.63	44.14	99.66
		Transpiration (Tr) mm	30.25	55.49	24.05	44.08	6.21	11.51
		Soil evaporation (Se) mm	104.06	71.11	81.81	55.85	22.24	15.27
		Subsurface water component (Re) mm	751.09	291.00	281.44	118.93	532.92	180.11
		Precipitation (P) mm	1137.67	223.67	484.31	83.02	653.37	143.43
		Water balance (WB) = P-Ro-Et-Re ; mm	-46.07	-	41.39	-	41.40	-
		Error in water balance (WB/ P; %)	-4.05	-	8.55	-	6.34	-
	2050	Runoff (Ro) mm	252.44	502.26	21.46	85.47	28.97	115.74
		Evapotranspiration (Et) mm	159.40	100.55	125.46	79.40	159.40	100.55
		Interception (In) mm	139.73	159.42	92.65	54.54	47.07	107.60
		Transpiration (Tr) mm	30.13	58.04	23.99	46.56	6.15	11.95
		Soil evaporation (Se) mm	109.36	71.99	86.04	56.56	23.32	11.43
		Subsurface water component (Re) mm	812.41	292.70	281.44	118.93	532.92	180.11
		Precipitation (P) mm	1193.54	239.25	525.06	96.41	668.48	144.61
		Water balance (WB) = P-Ro-Et-Re ; mm	-30.71	-	96.70	-	-52.81	-
		Error in water balance (WB/ P; %)	-2.57	-	18.42	-	-7.90	-

	2080	Runoff (Ro) mm	255.15	505.23	17.87	74.50	27.04	112.85
		Evapotranspiration (Et) mm	159.26	100.00	125.50	78.85	33.97	21.24
		Interception (In) mm	132.78	157.02	83.50	48.72	49.27	110.69
		Transpiration (Tr) mm	30.23	58.10	23.99	46.20	6.22	12.10
		Soil evaporation (Se) mm	110.17	72.58	86.64	57.00	23.53	15.59
		Subsurface water component (Re) mm	780.54	275.63	242.86	102.99	540.57	179.85
		Precipitation (P) mm	1174.86	221.16	470.30	78.75	677.55	145.37
		Water balance (WB) = P-Ro-Et-Re ; mm	-20.09	-	84.07	-	75.97	-
		Error in water balance (WB/ P; %)	-1.71	-	17.88	-	11.21	-
RCP 4.5 (75%)	2020	Runoff (Ro) mm	267.54	497.54	31.19	95.97	42.94	135.64
		Evapotranspiration (Et) mm	165.44	106.67	130.41	84.21	35.03	22.52
		Interception (In) mm	126.80	144.06	82.75	47.80	44.05	99.38
		Transpiration (Tr) mm	30.59	58.16	24.25	46.11	6.37	12.19
		Soil evaporation (Se) mm	104.06	71.11	81.81	55.85	22.24	15.27
		Subsurface water component (Re) mm	750.40	290.99	256.58	114.34	508.22	180.39
		Precipitation (P) mm	1137.08	223.94	485.67	83.51	651.41	143.17
		Water balance (WB) = P-Ro-Et-Re ; mm	-46.30	-	67.49	-	65.22	-
		Error in water balance (WB/ P; %)	-4.07	-	13.90	-	10.01	-
	2050	Runoff (Ro) mm	251.07	499.78	19.78	78.93	29.27	116.93
		Evapotranspiration (Et) mm	159.95	100.95	126.10	79.58	33.86	21.35
		Interception (In) mm	132.95	159.13	85.24	49.60	47.71	109.03
		Transpiration (Tr) mm	30.29	55.55	24.08	44.13	6.21	11.52
		Soil evaporation (Se) mm	109.97	72.42	86.51	56.90	23.47	15.53
		Subsurface water component (Re) mm	789.54	283.24	251.52	107.93	540.83	181.64
		Precipitation (P) mm	1160.53	226.42	483.15	83.18	677.38	145.71
		Water balance (WB) = P-Ro-Et-Re ; mm	-40.03	-	85.75	-	73.42	-
		Error in water balance (WB/ P; %)	-3.45	-	17.75	-	10.84	-
	2080	Runoff (Ro) mm	250.23	498.52	19.25	76.90	29.25	116.94
		Evapotranspiration (Et) mm	161.50	101.86	127.29	80.36	34.22	21.59
		Interception (In) mm	130.61	154.59	82.79	47.82	47.80	109.21
		Transpiration (Tr) mm	29.98	57.80	23.80	45.89	6.19	12.03

		Soil evaporation (Se) mm	111.09	73.13	87.39	57.45	23.70	15.68
		Subsurface water component (Re) mm	779.81	280.36	241.13	104.39	542.03	182.13
		Precipitation (P) mm	1173.33	229.49	481.63	82.99	691.69	149.02
		Water balance (WB) = P-Ro-Et-Re ; mm	-18.21	-	93.96	-	86.19	-
		Error in water balance (WB/ P; %)	-1.55	-	19.51	-	12.46	-
RCP 8.5 (50%)	2020	Runoff (Ro) mm	267.31	497.26	31.07	95.61	44.06	135.97
		Evapotranspiration (Et) mm	165.72	106.85	130.63	84.35	35.09	22.56
		Interception (In) mm	126.65	144.23	82.44	47.57	44.20	99.79
		Transpiration (Tr) mm	30.91	58.72	24.50	46.54	6.44	12.39
		Soil evaporation (Se) mm	104.25	71.25	81.97	55.96	22.28	15.30
		Subsurface water component (Re) mm	751.22	291.01	245.23	113.83	510.43	180.86
		Precipitation (P) mm	1148.40	221.01	469.49	78.51	678.90	145.49
		Water balance (WB) = P-Ro-Et-Re ; mm	-35.85	-	62.56	-	89.32	-
		Error in water balance (WB/ P; %)	-3.12	-	13.33	-	13.16	-
	2050	Runoff (Ro) mm	248.62	500.57	18.18	75.77	27.54	114.95
		Evapotranspiration (Et) mm	160.52	100.77	126.44	79.42	34.09	21.43
		Interception (In) mm	135.86	160.86	85.55	50.26	50.30	113.05
		Transpiration (Tr) mm	30.14	58.13	23.88	46.08	6.28	12.19
		Soil evaporation (Se) mm	111.00	73.17	87.26	57.44	23.74	15.73
		Subsurface water component (Re) mm	800.57	281.89	250.47	105.79	552.82	183.27
		Precipitation (P) mm	1137.92	223.58	483.88	82.79	654.09	143.43
		Water balance (WB) = P-Ro-Et-Re ; mm	-71.79	-	88.79	-	39.64	-
		Error in water balance (WB/ P; %)	-6.31	-	18.35	-	6.06	-
	2080	Runoff (Ro) mm	247.67	499.28	17.07	71.30	28.11	117.33
		Evapotranspiration (Et) mm	167.55	105.22	131.96	82.93	35.60	22.41
		Interception (In) mm	131.58	159.44	80.06	46.32	51.52	115.49
		Transpiration (Tr) mm	30.31	55.59	24.09	44.16	6.22	11.53
		Soil evaporation (Se) mm	115.92	79.37	91.20	59.95	24.73	16.00
		Subsurface water component (Re) mm	788.75	278.67	225.74	97.05	567.92	186.71
		Precipitation (P) mm	1161.69	218.05	451.37	73.34	710.32	148.23
		Water balance (WB) = P-Ro-Et-Re ; mm	-42.28	-	76.60	-	78.69	-

		Error in water balance (WB/ P; %)	-3.64	-	16.97	-	11.08	-
RCP 8.5 (75%)	2020	Runoff (Ro) mm	267.80	497.98	30.04	95.22	42.46	135.14
		Evapotranspiration (Et) mm	165.76	106.88	130.67	84.37	35.10	22.57
		Interception (In) mm	127.04	144.75	82.71	47.79	44.33	100.08
		Transpiration (Tr) mm	30.35	55.66	24.13	44.22	6.22	11.54
		Soil evaporation (Se) mm	104.25	71.25	81.97	55.96	22.28	15.30
		Subsurface water component (Re) mm	754.03	292.01	246.32	114.30	512.10	181.40
		Precipitation (P) mm	1141.70	224.82	485.55	83.49	656.15	140.97
		Water balance (WB) = P-Ro-Et-Re ; mm	-45.89	-	78.52	-	66.49	-
		Error in water balance (WB/ P; %)	-4.02	-	16.17	-	10.13	-
	2050	Runoff (Ro) mm	284.54	510.21	47.65	129.97	70.52	191.81
		Evapotranspiration (Et) mm	163.26	102.95	128.72	81.24	34.55	21.79
		Interception (In) mm	133.72	158.41	84.90	49.37	48.82	111.56
		Transpiration (Tr) mm	30.61	59.02	24.22	46.82	6.24	12.32
		Soil evaporation (Se) mm	112.23	73.93	88.31	58.09	23.92	15.84
		Subsurface water component (Re) mm	769.38	312.20	239.64	111.71	531.45	207.82
		Precipitation (P) mm	1175.13	229.75	481.39	82.96	693.73	149.32
		Water balance (WB) = P-Ro-Et-Re ; mm	-42.05	-	65.38	-	57.21	-
		Error in water balance (WB/ P; %)	-3.58	-	13.58	-	8.25	-
	2080	Runoff (Ro) mm	283.70	511.54	46.63	127.69	74.62	203.68
		Evapotranspiration (Et) mm	171.71	107.81	135.48	85.13	36.28	22.83
		Interception (In) mm	137.99	167.35	84.46	49.56	53.78	120.66
		Transpiration (Tr) mm	33.19	63.05	26.30	50.01	6.93	13.24
		Soil evaporation (Se) mm	118.60	78.23	93.41	61.52	25.20	16.71
		Subsurface water component (Re) mm	796.81	317.32	230.45	108.94	568.42	216.87
		Precipitation (P) mm	1216.77	235.33	475.93	82.05	741.29	156.21
		Water balance (WB) = P-Ro-Et-Re ; mm	-35.45	-	63.37	-	61.97	-
		Error in water balance (WB/ P; %)	-2.91	-	13.31	-	8.36	-

9.2.7 Error in water balance/change in storage

GEO-CWB calculates the error/change in storage fraction in each simulated cell water balance, which provides an error/change in storage in water balance map for each simulated time step in each simulated climatic scenario. The small error/change in storage in the water balance comes from the assumption that water bodies can always evaporate at the PET rate. Hence, this error should be subtracted from the runoff as open water bodies are supplied by runoff from surrounding areas, and it does not leave the basin as river flow but are evaporated instead. The annual spatially distributed average error in water balance maps for baseline period and the three projected periods, 2020, 2050 and 2080, forced by the four different climatic scenarios are shown in Figure 9.27. However, the average simulated error in water balance for each climatic period can be shown in Figure 9.26.

9.3 Simulated and projected water balance for Shannon catchment

The water balance simulation is based upon the continuity equation, i.e. inflow equals outflow plus the storage. Precipitation is the most significant inflow component. The most important outflow components of water balance are surface runoff, evapotranspiration, and subsurface water component, which includes groundwater recharge and subsurface runoff. Any simulated area that receives higher precipitation than the amount of water that it loses has water surplus. However, regions with a water deficit would get a smaller amount of rainfall than the amount that they lost through evapotranspiration.

Summaries of the numerical contributions to this net balance of the various components, which are discussed earlier in this chapter are presented in the Figures 9.28-9.32, based on the simulated climatic scenarios for each projected period. The overall summary of the water balance of the Shannon River catchment is given in Table 9.2.

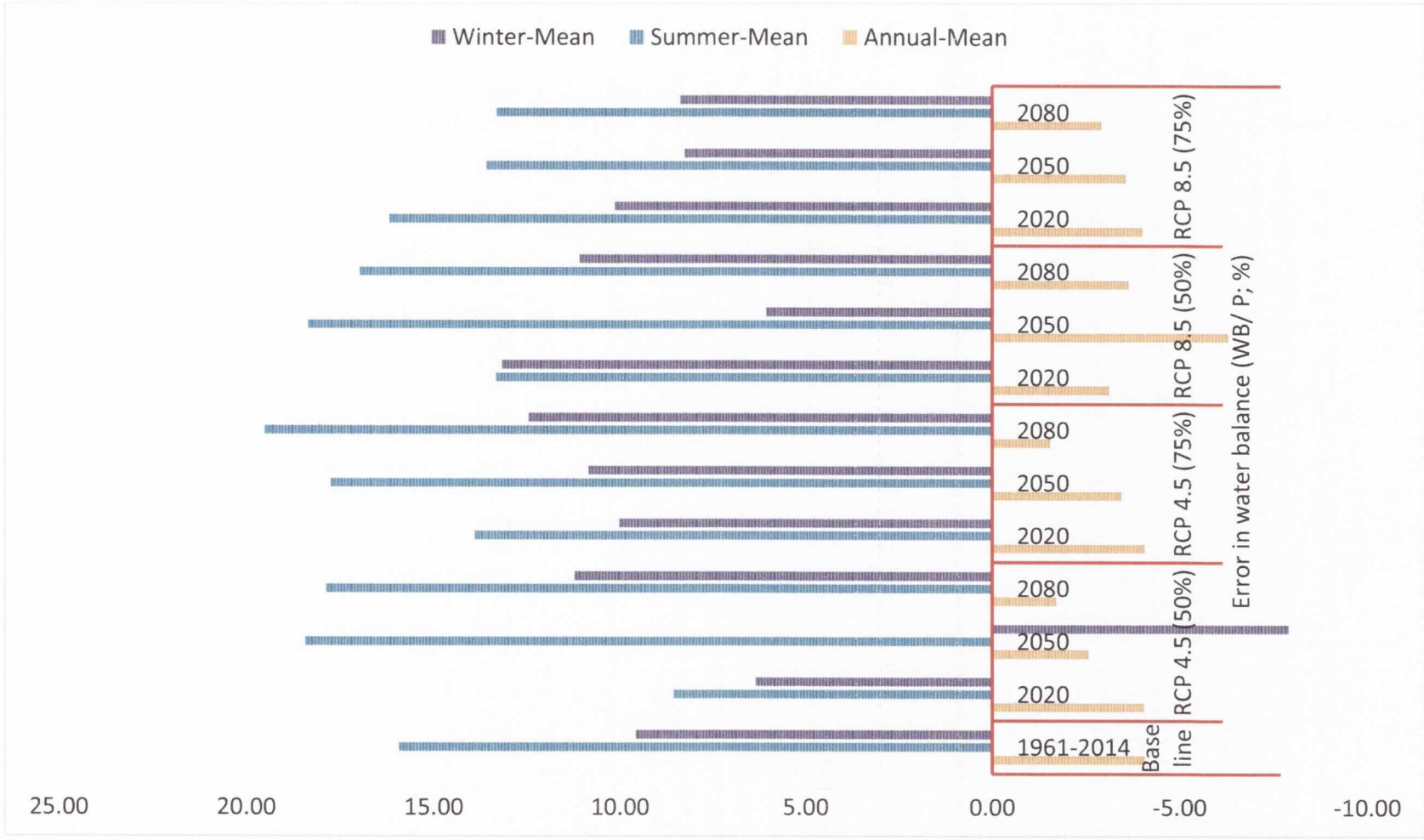

Figure 9.26: The average error/change in storage in water balance (%) for each climatic period and land use scenario simulated by GEO-CWB.

Figure 9.27: The spatially distributed average annual error/change in storage in water balance (mm/year) for each climatic period and land use scenario simulated by GEO-CWB.

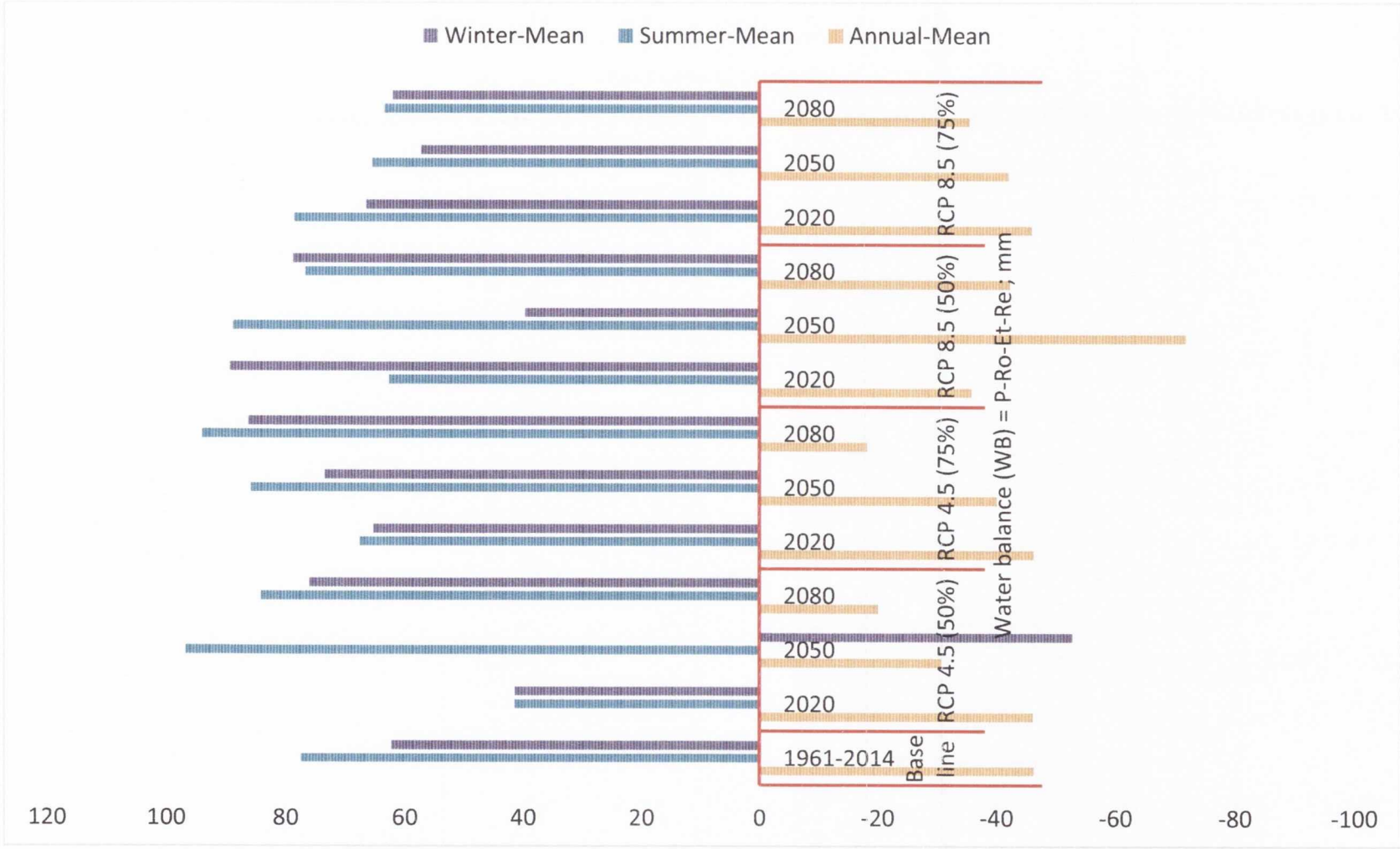

Figure 9.28: GEO-CEB simulated water balance (mm/year).

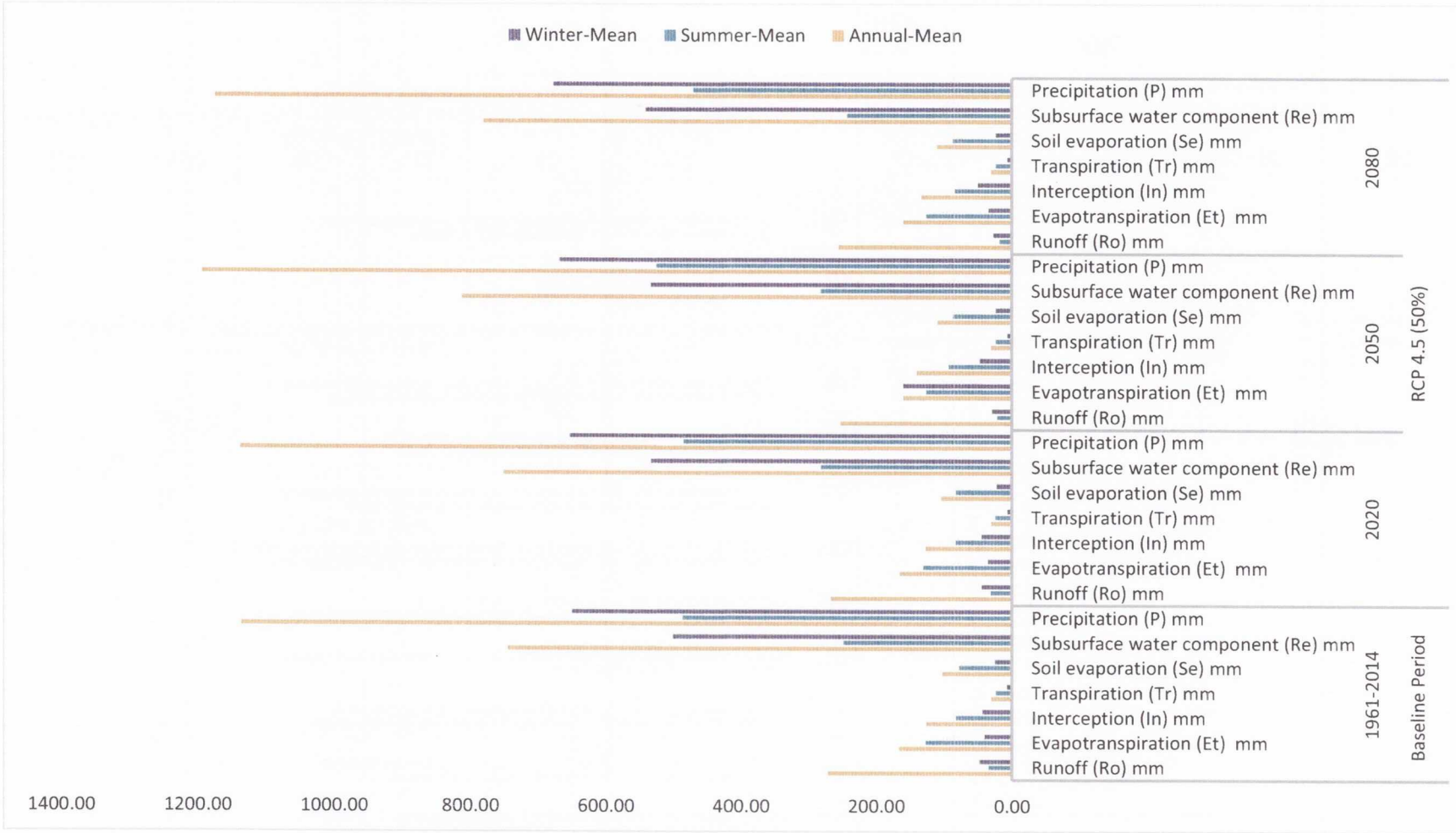

Figure 9.29: The GEO-CWB simulated water balance components for the baseline and the projected periods forced by RCP 4.5 (50%) climatic scenario.

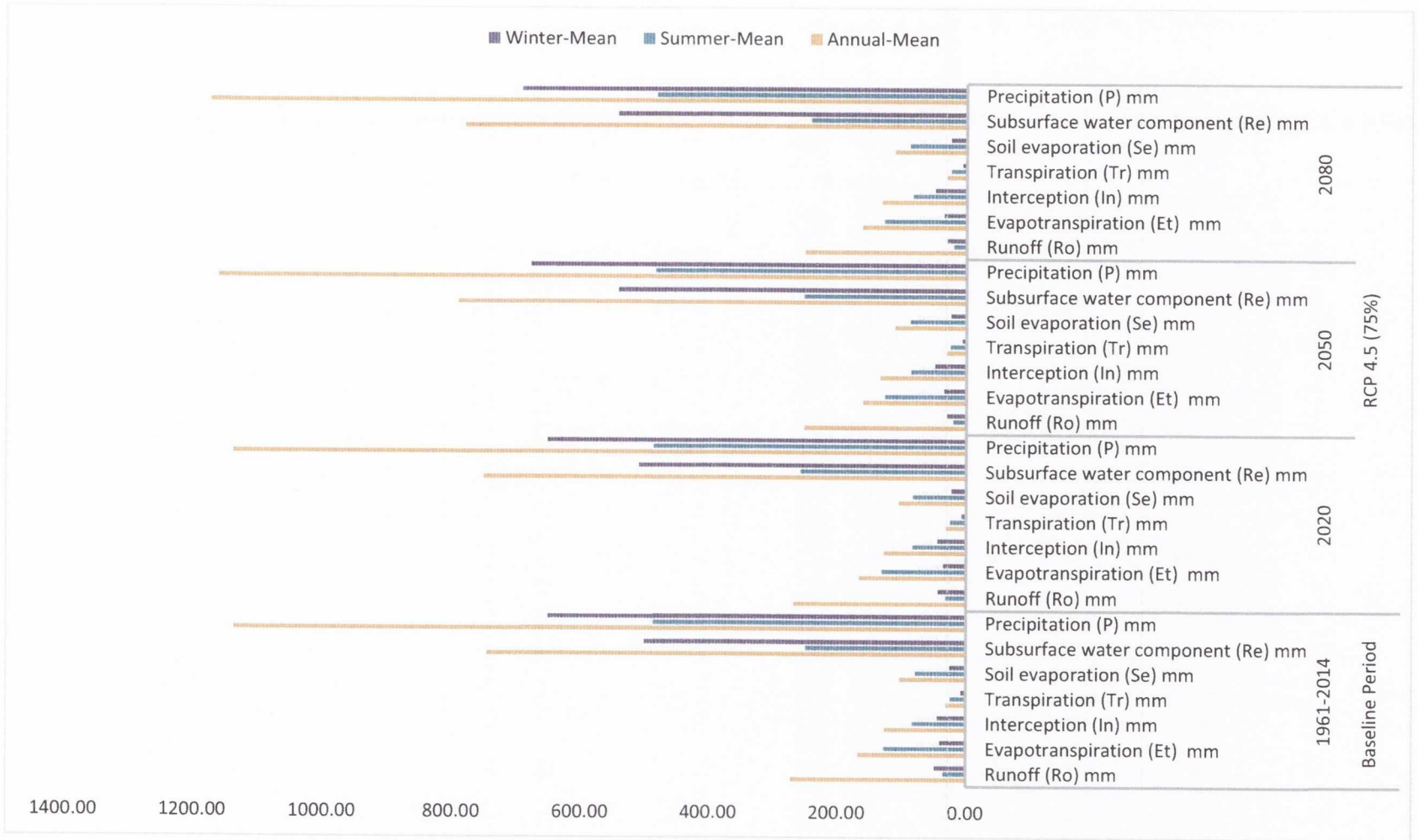

Figure 9.30: The GEO-CWB simulated water balance components for the baseline and the projected periods forced by RCP 4.5 (75%) climatic scenario.

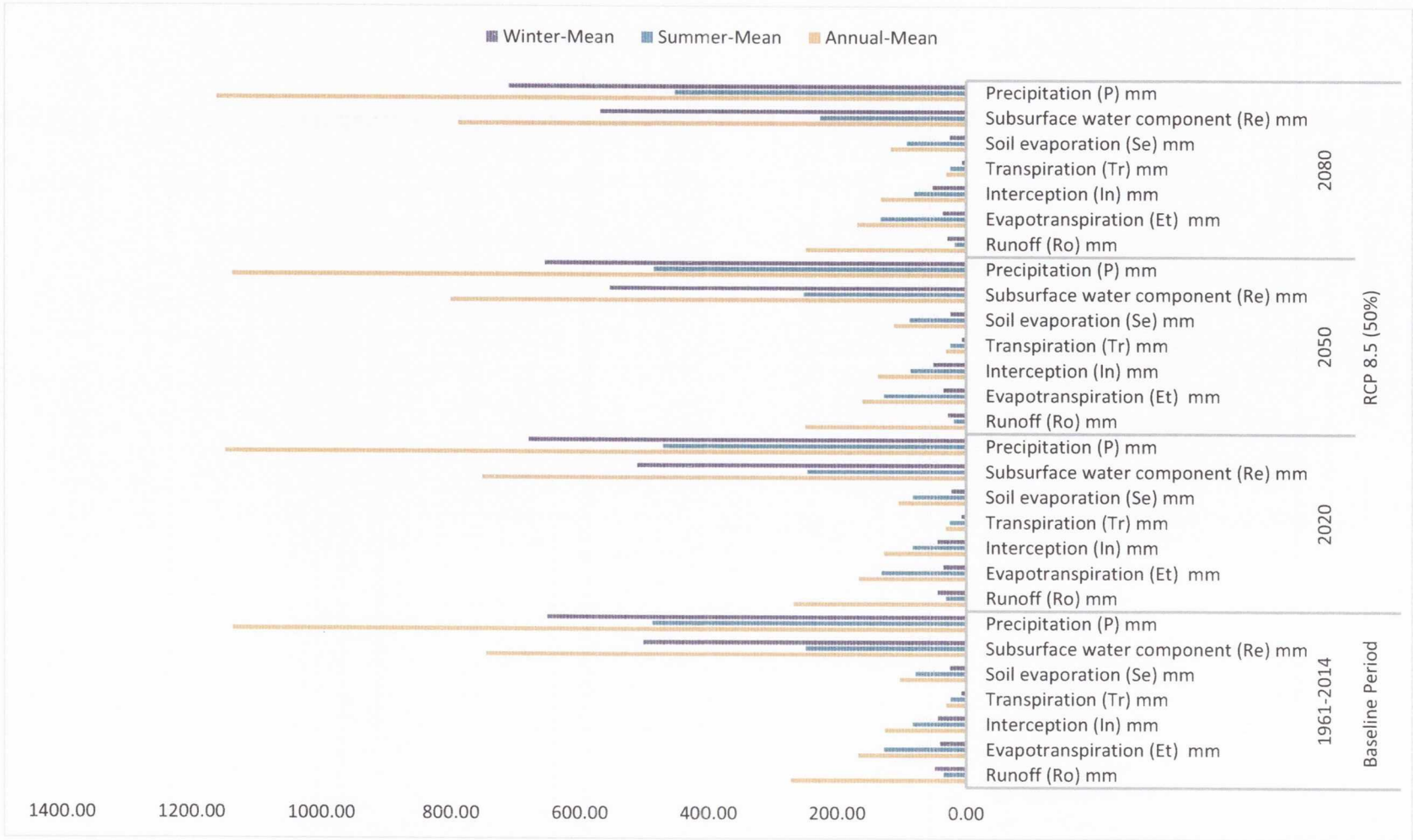

Figure 9.31: The GEO-CWB simulated water balance components for the baseline and the projected periods forced by RCP 8.5 (50%) climatic scenario.

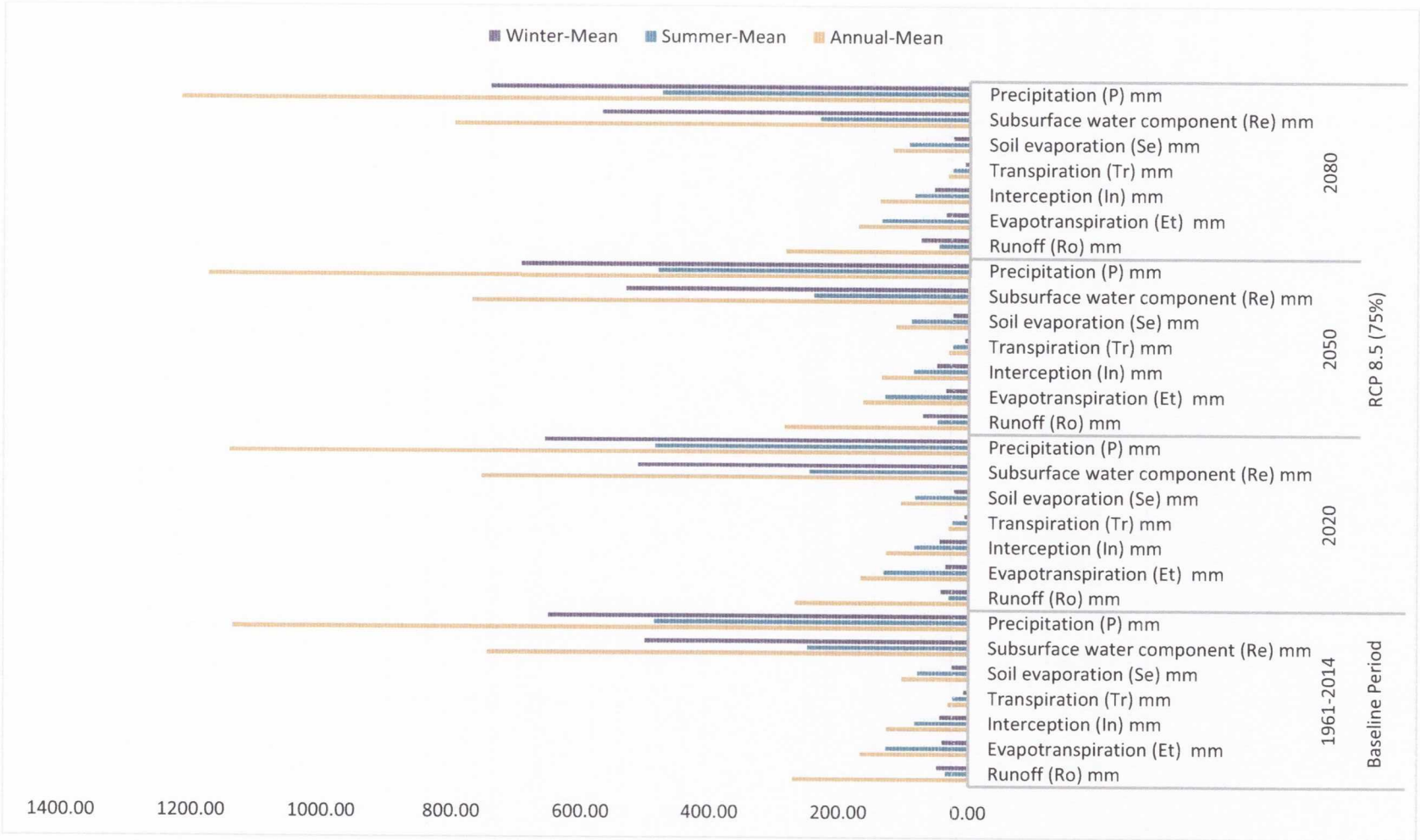

Figure 9.32: The GEO-CWB simulated water balance components for the baseline and the projected periods forced by RCP 8.5 (75%) climatic scenario.

9.4 Vulnerability parameters results

GEO-CWB produces some parameters from which an assessment can be made of the vulnerability to climate and land use changes for each climatic period and land use scenario, as follows.

9.4.1 Accumulated surface runoff volume

The accumulated runoff volume in the winter season is an indication of how much runoff water could be harvested every year during the winter. Figure 9.33 shows the calculated accumulated runoff volume as results to the different climate change conditions and land use scenarios. For the illustrated annual accumulated runoff, the baseline annual areal average accumulated runoff is 14.59×10^6 m^3 as an average for all cells in the simulation domain. However, the areal average value for the accumulated runoff for the climatic period the 2080s forced by RCP 8.5 (75%) climatic scenario is 15.48×10^6 m^3, which means the average increase in the accumulated runoff is around 6%. However, the areal accumulated runoff average for the whole catchment is increased but hotspot areas spatial distribution is changed as results of climate and land use changes.

9.4.2 The safe yield groundwater abstraction

The safe yield groundwater abstraction rates expressed in (m^3/d/ha) calculated by GEO-CWB are simplification values for such a large catchment like Shannon, which can only be used as an indication and a rough estimate for how much groundwater can be abstracted in a sustainable way without depleting the groundwater resources. Figure 9.34 show the annual and seasonal calculated safe yield ground water abstraction volume as results to the different climate change conditions and land use scenarios.

9.4.3 The water deficit for ideal crop

The water deficit for ideal crop growth, which can be estimated as the difference between the crop water requirement and the actual evapotranspiration. In the Shannon River catchment, most of the catchment is covered in grass (pasture) and there is hardly any deficit.

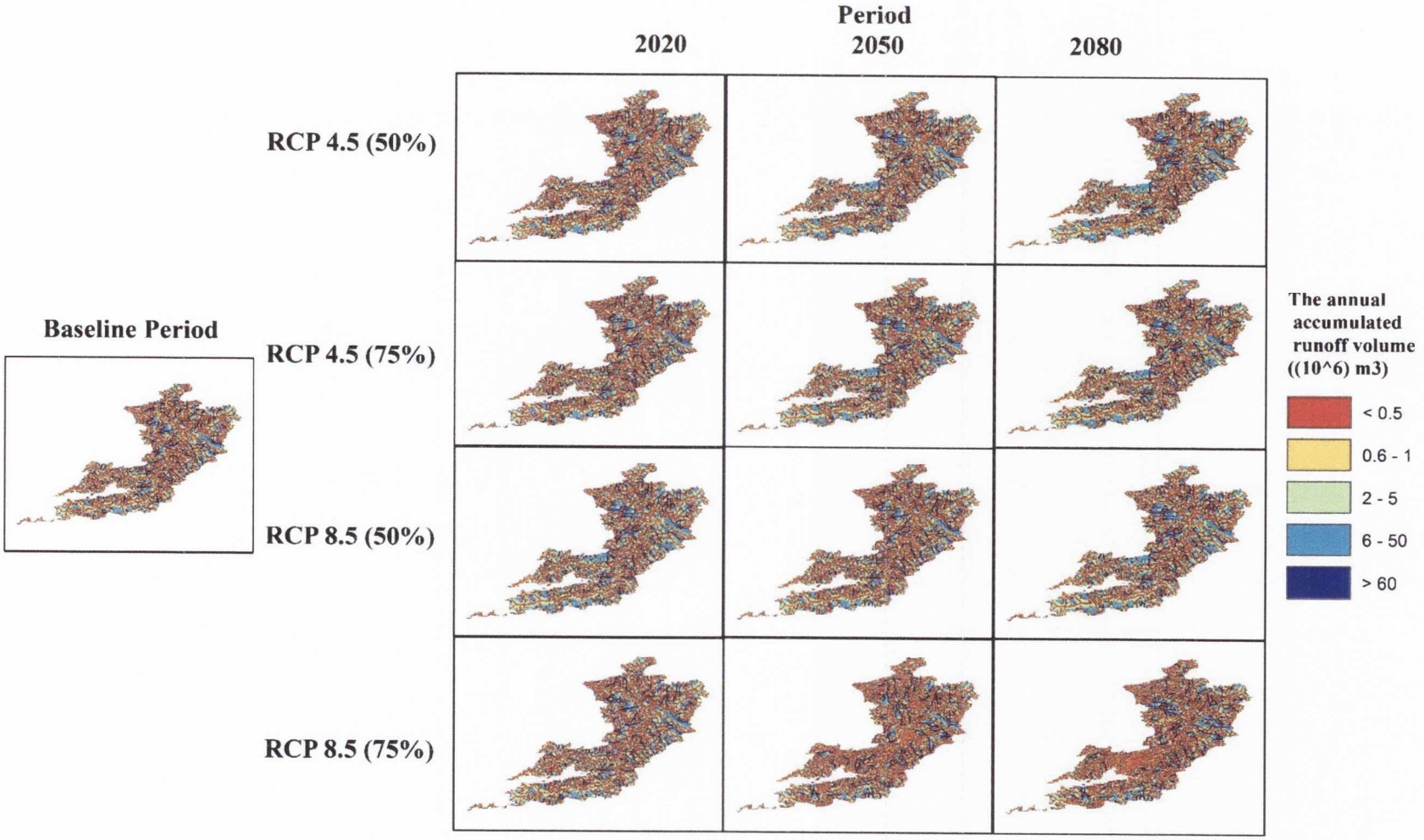

Figure 9.33: The accumulated surface runoff for each climatic period and land use scenario simulated by GEO-CWB.

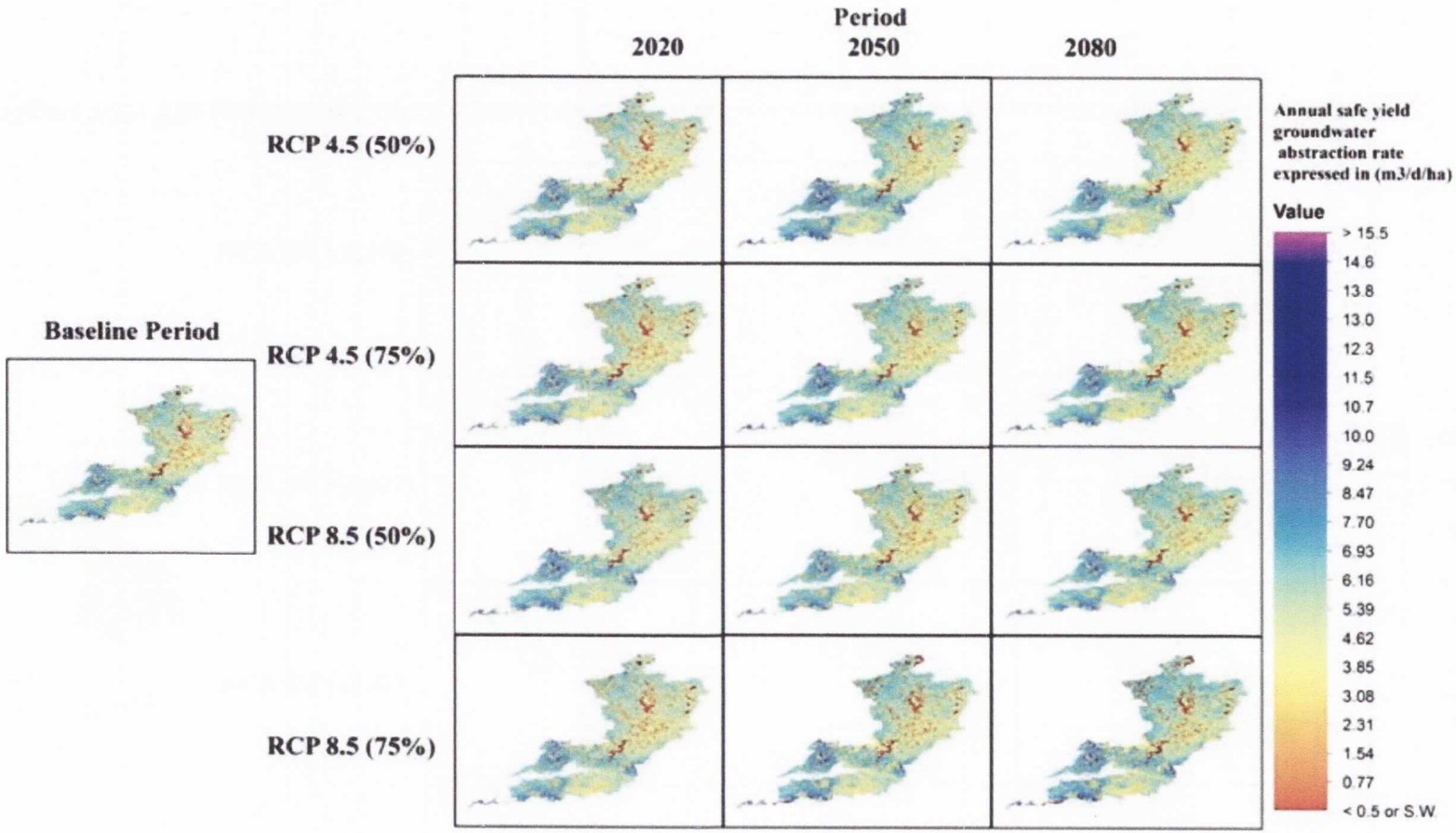

Figure 9.34: The average annual safe yield groundwater abstraction for each climatic period and land use scenario simulated by GEO-CWB.

Chapter 10. Hybrid data-driven models for hydrological parameters simulation and projection on the catchment scale

10.1 Introduction

Simulating and forecasting hydrological parameters at a daily time step, especially daily streamflow and water level, with high accuracy at a catchment scale is a key role in the management process of water resource systems. Reliable models and projections can be used as a tool by water authorities in the future allocation of the water resources among competing users such as agriculture, domestic and power stations. The performance of modeling and projection methods for any single hydrometric station will vary according to its catchment climatic zone and characteristics. Karran et al. (2014) state that methods that are proven as effective for modeling streamflow in water abundant regions might be unusable for the drier catchments, where water scarcity is a reality due to the intermittent nature of streams. Climate characteristics may severely affect the performance of different forecasting methods in different catchments and this area of research still requires much more exploration. The understanding of streamflow and water level dynamics is very important, which is described by various physical mechanisms occurring on a wide range of temporal and spatial scales (Sivakumar, 2003, Karran et al., 2014). Simulating these mechanisms and relations can be executed by physical, conceptual or data-driven models. Whilst physical and conceptual models are currently used to provide physical interpretations and illustrations of catchment-scale processes, they have been criticized for being difficult to implement for high-resolution time-scale prediction, as well as their requirements for many different types of data sets, which are usually very difficult to obtain. In general, physical and conceptual models are very difficult to run and the more resolution they have, the more data they need, which leads to the over-parameterization of complex models (Beven, 2006, Sivakumar, 2003, Karran et al., 2014). Machine learning techniques or data-driven models are described by the minimum information requirements, rapid development times, and accuracy in streamflow forecasting (Adamowski, 2008, Nalley et al., 2012). These data learning models have some limitations, which become increasingly obvious as the data become more complex (Karran et al., 2014). Usually, for machine learning models the data are nonlinear and non-stationary. Multiple linear regression (MLR) and autoregressive integrated moving average (ARIMA) models perform well for long-term variation analysis (see Chapter 5) and forecasts (Ghanbarpour et al., 2009, Magar and Jothiprakash, 2011, Adamowski et al., 2012), but both have the assumption of linearity in the data. Because of that, non-linear algorithms that use machine learning techniques as artificial neural networks (ANNs) and the more recent support vector machines (SVMs), have been applied in hydrologic modeling and forecasting.

ANNs have been used in hydrology in many applications such as stream flow modeling, water quality assessment and suspended sediment load predictions. The first uses for ANN in hydrology were introduced by two papers in the early 1990s (Kang et al., 1993, Daniell, 1991), which found the method useful for forecasting hydrological processes. The ANN then was used in many hydrological applications to confirm its usefulness and to model different hydrological parameters, such as stream flow. The multi-layer perceptron (MLP) ANN models seem to be the most used ANN algorithms, which are optimized with a back-propagation algorithm - these models improved the short-term hydrological forecasts. Examples of recent published applications for the use of ANN in hydrology can be listed as: Ebtehaj and Bonakdari (2013), Aziz et al. (2014), Kenabatho et al. (2015), Wu et al. (2014b), Aziz et al. (2013), Chen et al.

(2014), Kalteh (2013), Valipour et al. (2013), Chattopadhyay and Rangarajan (2014), Mekanik et al. (2013) and Shamseldin et al. (2007).

SVMs were introduced by Vapnik (2013) as machine learning systems that utilize a hypothesis space of linear relations in a high dimensional feature space, trained with optimization algorithms that implement a learning bias derived from statistical learning theory. This relatively new data-driven model was used as a hydrological application in 2006 by Khan and Coulibaly (2006), who stated that the SVR model out-performed the MLP ANNs in 3–12 month water levels predictions of a lake. The use of SVM in hydrology has then been promoted and recommended in many studies' conclusions from the use of flood stages, storm surge prediction, stream flow modeling to even daily evapotranspiration estimations. Deka (2014) published a review paper on the use of SVM in hydrological models. Examples of recent published applications for the use of SVM in hydrology can be listed as: Imani et al. (2014), Wu et al. (2014a), Kalra et al. (2013), Jajarmizadeh et al. (2015), Lin et al. (2013), Ghorbani et al. (2016a), Ghorbani et al. (2016b), Kalteh (2016) and Khlosi et al. (2016).

Machine learning techniques are not able to process the non-stationary data, data that does not have trend with time and its mean and variance changes with time, which leads to the recent development of hybrid models, where the input data are pre-processed for non-stationary characteristics first and then run through the post processing machine learning models to deal with the non-linearity issues. One promising data pre-processing methods is the use of the wavelet transformation, which decomposes the input time series into a comprehensible time-frequency representation at different scales, details, and approximations. Both discrete wavelet transform (DWT) and the continuous wavelet transform (CWT) are wavelet transforms, which have been used in a variety of ways in hydrology. Wavelet transforms can be used to analyze streamflow variability, frequency analysis on hydro-meteorological extremes or as a stand-alone technique for streamflow and flood forecasting, as well as groundwater-surface water interactions in karst systems (Wang et al., 2011, Dhanya and Nagesh Kumar, 2011, Labat, 2008, Adamowski et al., 2009, Nalley et al., 2012, Adamowski, 2008, Gill et al., 2013).

Wavelet transformation combined with machine learning models has been proven to give highly accurate and reliable short-term projections. The most popular hybrid model is the wavelet transform coupled with an artificial neural network (WANN). Kim and Valdés (2003) developed one of the first hydrological applications of the WANN model, which addressed the area of forecasting drought in the Conchos River Basin, Mexico. Since then many published studies have described applications of the WANN in streamflow forecasting and many research areas in hydrological modeling and prediction. In general, all the studies that have compared ANN and WANN conclude that the WANN models have outperformed the stand-alone ANNs. Examples of recently published applications for the use of WANN in hydrology can be listed as: Anctil and Tape (2004), Nourani et al. (2011), Nourani et al. (2009), Tiwari and Chatterjee (2010) and Kim and Valdés (2003).

Recently, wavelet transforms coupled with SVM/SVR (WSVM/WSVR) have been proposed for use in hydrology. To the author's best knowledge however, there has been very little research into the application of this hybrid model for streamflow forecasting and there is no application on water level forecasting. Karran et al. (2014) compares the use of four different models, namely artificial neural networks (ANNs), support vector regression (SVR), wavelet-ANN, and wavelet-SVR for one single station in each watershed of Mediterranean, Oceanic, and Hemiboreal watershed. The results show that SVR based models performed best overall, but no one model outperformed the others in more than one watershed, suggesting that some models may be more

suitable for certain types of data. Kisi and Cimen (2011) have applied the WSVR models with different methods to model monthly streamflow and find that the WSVR models outperformed the stand-alone SVR.

However, there has been no research that (i) explores the use of WSVR models for water level modeling and forecasting; and (ii) uses the data-driven models and the hybrid methods on multi-station large hydrological systems modeling and projection; and (iii) uses the WSVR method and other hybrid methods for long-term projections based on different climatic scenarios; (iv) uses temperature as an input variable for the prediction in order to teach the model the long-term climate variation in the data; (v) uses machine learning techniques as a transfer function for the output of the empirical hydrological model in order to model the water flow and water level, (vi) explores the most suitable input variables' lag value for the machine learning models in order to get the best models for the catchment. This chapter aims to address the previous gaps in the literature through comparing four different models, namely artificial neural networks (ANNs), support vector machine (SVM), wavelet-ANN, and wavelet-SVM as transfer models for the results from GEO-CWB to simulate the long-term water level and water flow in the Shannon River hydrological system based on the structured simplified system.

10.2 Materials and methods

10.2.1 Data setup and hydrometric stations

The four data-driven models/machine learning techniques were fed with three types of 30-year daily time series data sets (1983-2013), which can be divided between observed data sets (maximum temperature (Tmax) (°C), minimum temperature (Tmin) (°C), water level (WL) (m) and water flow (Q)(m^3/s)) and simulated data set runoff (mm) by GEO-CWB. GEO-CWB provides monthly simulated runoff values, which is downscaled to daily time scale using the observed daily precipitation data through the developed GIS-based downscaling algorithm, as described in Chapter 4. All the data sets are related to the five main hydrometric stations in the simplified and structured hydrometric system for the Shannon River catchment, which is presented in Chapter 5. Table 10-1 shows the descriptive statistics for the input data sets related to each hydrometric station.

10.2.2 Workflow and framework

Four different types of models are developed in this study: ANNs, WANNs, SVRs, and WSVRs. For each of the five daily time series variables discussed in the previous section (maximum temperature, minimum temperature, water level, water flow and runoff), two sets of inputs were created: the variables themselves delayed by 1 (t-1), 2 (t-2), 3 (t-3), 4 (t-4) days and so on until 15 (t-15) days; the same delayed variables were then decomposed by wavelet transformation into their respective high- and low-frequency components (details and approximations). The delayed variables become the inputs for the ANNs and SVRs, whereas, the delayed wavelet sub-time series are the inputs for the WANNs and WSVRs. Figure 10.1 shows the data and simulation flowchart and structure. In this chapter, a combination of off-the-shelf software, packages and self-coded algorithms has been used to run the simulations. RapidMiner has been used as a processor to run and optimise the ANN and the SVM models. A Python package has been used to run the Wavelet transforms and self-developed algorithms have been used to connect all the steps together to work as one algorithm in an optimise and repetitive way. The use of these packages and software is illustrated in the next sections.

Table 10-1: Descriptive statistics for the variables' training and testing data sets.

Station	Parameters	Datasets	Mean	SEMean	StDev	Variance	Q1	Median	Q3	IQR	TRMean	Min.	Max.	Range	Skewness	Kurtosis	MSSD	N
Inny	Daily average Tmax (C Degrees)	Training	13.895	0.058	5.108	26.090	10.200	13.500	17.600	7.400	13.843	-1.500	30.600	32.100	0.159	-0.391	2.488	7697
		Testing	14.212	0.120	5.246	27.523	10.700	14.500	18.500	7.800	14.366	-6.500	28.000	34.500	-0.420	-0.041	2.432	1925
	Daily average Tmin (C Degrees)	Training	5.525	0.058	5.082	25.829	1.700	5.700	9.500	7.800	5.579	-8.900	18.300	27.200	-0.145	-0.666	6.974	7697
		Testing	5.313	0.126	5.513	30.389	1.000	6.000	9.900	8.900	5.447	-14.000	17.100	31.100	-0.324	-0.572	7.594	1925
	Daily average simulated runoff (mm)	Training	2.547	0.051	4.490	20.163	0.000	0.600	3.200	3.200	1.874	0.000	65.000	65.000	3.538	20.781	16.360	7697
		Testing	2.765	0.113	4.939	24.396	0.000	0.600	3.600	3.600	1.993	0.000	40.500	40.500	3.257	14.115	19.530	1925
	Daily average water level (mm)	Training	45.471	0.004	0.372	0.138	45.140	45.398	45.716	0.576	45.450	44.923	47.124	2.201	0.786	-0.015	0.002	7697
		Testing	45.531	0.010	0.453	0.205	45.140	45.357	45.802	0.662	45.503	44.996	47.294	2.298	0.925	-0.286	0.002	1925
	Daily flow volume (m3/s)	Training	16.988	0.165	14.479	209.644	5.070	12.341	24.476	19.406	15.661	1.656	104.231	102.575	1.355	1.951	3.542	7697
		Testing	18.453	0.391	17.154	294.249	5.070	10.911	25.745	20.675	17.044	2.543	105.846	103.303	1.302	0.839	3.400	1925
Suck	Daily average Tmax (C Degrees)	Training	14.173	0.058	4.983	24.827	10.500	14.000	18.000	7.500	14.139	-3.000	30.300	33.300	0.102	-0.430	2.467	7303
		Testing	13.922	0.129	5.520	30.467	10.200	14.000	18.200	8.000	14.014	-6.500	29.200	35.700	-0.236	-0.192	2.573	1826
	Daily average Tmin (C Degrees)	Training	5.723	0.059	5.014	25.136	2.000	6.000	9.700	7.700	5.789	-8.600	18.300	26.900	-0.179	-0.668	7.118	7303
		Testing	5.252	0.133	5.673	32.178	0.900	5.850	9.900	9.000	5.369	-14.000	17.500	31.500	-0.285	-0.621	7.152	1826
	Daily average simulated runoff (mm)	Training	2.752	0.055	4.698	22.069	0.000	0.600	3.700	3.700	2.053	0.000	61.800	61.800	3.057	14.385	17.800	7303
		Testing	3.053	0.126	5.397	29.130	0.000	0.500	4.000	4.000	2.230	0.000	49.400	49.400	3.172	14.133	22.321	1826
	Daily average water level (mm)	Training	41.201	0.006	0.513	0.263	40.855	40.946	41.519	0.664	41.163	40.540	42.782	2.242	1.092	0.010	0.004	7303
		Testing	41.409	0.016	0.673	0.453	40.855	41.095	41.841	0.986	41.385	40.544	43.279	2.735	0.683	-0.944	0.004	1826
	Daily flow volume (m3/s)	Training	20.867	0.253	21.613	467.104	5.589	10.763	30.382	24.793	18.522	1.140	123.518	122.378	1.542	1.762	7.313	7303
		Testing	32.055	0.773	33.032	1091.110	6.101	15.960	42.920	36.819	29.744	1.493	221.214	219.721	1.360	1.788	8.952	1826
Brosna	Daily average Tmax (C Degrees)	Training	13.746	0.074	5.179	26.824	10.000	13.500	17.500	7.500	13.714	-3.000	30.600	33.600	0.089	-0.367	2.590	4844
		Testing	13.872	0.142	4.927	24.275	10.300	13.600	17.600	7.300	13.875	-1.500	29.200	30.700	0.028	-0.470	2.422	1211
	Daily average Tmin (C Degrees)	Training	5.482	0.074	5.130	26.322	1.600	5.600	9.500	7.900	5.543	-9.000	18.000	27.000	-0.156	-0.672	7.101	4844
		Testing	5.459	0.145	5.030	25.304	1.600	5.600	9.400	7.800	5.519	-7.800	17.000	24.800	-0.148	-0.644	6.503	1211
	Daily average simulated runoff (mm)	Training	2.499	0.067	4.664	21.754	0.000	0.300	3.000	3.000	1.777	0.000	57.000	57.000	3.488	18.270	18.106	4844
		Testing	2.369	0.121	4.216	17.771	0.000	0.400	3.200	3.200	1.731	0.000	38.100	38.100	3.248	15.421	15.976	1211
	Daily average water level (mm)	Training	40.375	0.136	9.472	89.712	42.155	42.433	42.806	0.651	42.423	0.000	45.056	45.056	-4.018	14.204	9.010	4844
		Testing	42.574	0.015	0.527	0.278	42.186	42.398	42.748	0.562	42.522	41.941	44.662	2.721	1.423	1.690	0.009	1211
	Daily flow volume (m3/s)	Training	17.972	0.220	15.341	235.349	7.149	13.031	23.520	16.371	16.378	1.141	112.674	111.533	1.718	3.575	13.693	4844
		Testing	17.339	0.398	13.861	192.140	8.325	12.935	21.164	12.839	15.601	1.846	91.496	89.650	2.125	5.453	10.953	1211

Nenagh	Daily average Tmax (C Degrees)	Training	14.198	0.060	5.083	25.837	10.500	14.000	18.000	7.500	14.173	-1.500	30.600	32.100	0.086	-0.397	2.508	7278
		Testing	14.026	0.129	5.506	30.312	10.425	14.300	18.300	7.875	14.132	-6.500	29.200	35.700	-0.283	-0.159	2.550	1820
	Daily average Tmin (C Degrees)	Training	5.668	0.060	5.085	25.859	1.800	6.000	9.700	7.900	5.732	-9.000	18.300	27.300	-0.174	-0.684	7.134	7278
		Testing	5.363	0.133	5.676	32.217	1.000	6.000	10.000	9.000	5.491	-14.000	17.500	31.500	-0.311	-0.598	7.221	1820
	Daily average simulated runoff (mm)	Training	2.619	0.055	4.730	22.369	0.000	0.500	3.300	3.300	1.890	0.000	55.200	55.200	3.329	16.389	16.659	7278
		Testing	2.740	0.120	5.131	26.323	0.000	0.500	3.400	3.400	1.944	0.000	59.800	59.800	3.796	22.195	20.356	1820
	Daily average water level (mm)	Training	0.484	0.003	0.226	0.051	0.384	0.405	0.524	0.140	0.458	0.139	2.597	2.458	2.710	11.208	0.005	7278
		Testing	0.669	0.008	0.343	0.118	0.430	0.534	0.767	0.337	0.649	0.230	2.475	2.245	1.259	1.051	0.005	1820
	Daily flow volume (m3/s)	Training	5.701	0.074	6.279	39.422	2.821	2.964	6.161	3.340	4.822	0.221	70.948	70.727	3.131	13.730	4.273	7278
		Testing	10.508	0.231	9.846	96.952	3.444	5.848	14.037	10.593	9.821	0.748	66.395	65.648	1.342	1.330	4.007	1820
Lower-Shannon	Daily average Tmax (C Degrees)	Training	14.087	0.062	4.965	24.655	10.500	13.800	18.000	7.500	14.054	-3.000	30.600	33.600	0.106	-0.399	2.744	6494
		Testing	14.338	0.138	5.563	30.943	10.500	14.850	18.500	8.000	14.473	-6.500	29.200	35.700	-0.360	-0.074	2.548	1624
	Daily average Tmin (C Degrees)	Training	5.603	0.062	5.030	25.299	1.800	5.800	9.500	7.700	5.665	-9.400	18.300	27.700	-0.165	-0.696	7.417	6494
		Testing	5.592	0.143	5.744	32.990	1.000	6.100	10.100	9.100	5.745	-14.000	17.500	31.500	-0.382	-0.562	7.279	1624
	Daily average simulated runoff (mm)	Training	3.077	0.062	5.007	25.074	0.000	0.700	4.200	4.200	2.344	0.000	44.100	44.100	2.692	9.640	19.984	6494
		Testing	3.017	0.123	4.945	24.448	0.000	0.700	4.200	4.200	2.321	0.000	52.500	52.500	3.033	14.490	19.669	1624
	Daily average water level (mm)	Training	33.233	0.002	0.153	0.023	33.160	33.300	33.300	0.140	33.244	32.640	33.950	1.310	-1.242	1.700	0.003	6494
		Testing	33.210	0.004	0.163	0.027	33.050	33.250	33.320	0.270	33.219	32.090	33.530	1.440	-0.945	1.553	0.002	1624
	Daily flow volume (m3/s)	Training	151.754	1.780	143.425	20570.800	37.890	91.050	239.053	201.163	138.929	10.000	741.700	731.700	1.177	0.577	758.298	6494
		Testing	218.997	4.133	166.565	27743.900	85.690	163.875	390.830	305.140	211.779	10.500	842.320	831.820	0.702	-0.312	354.854	1624

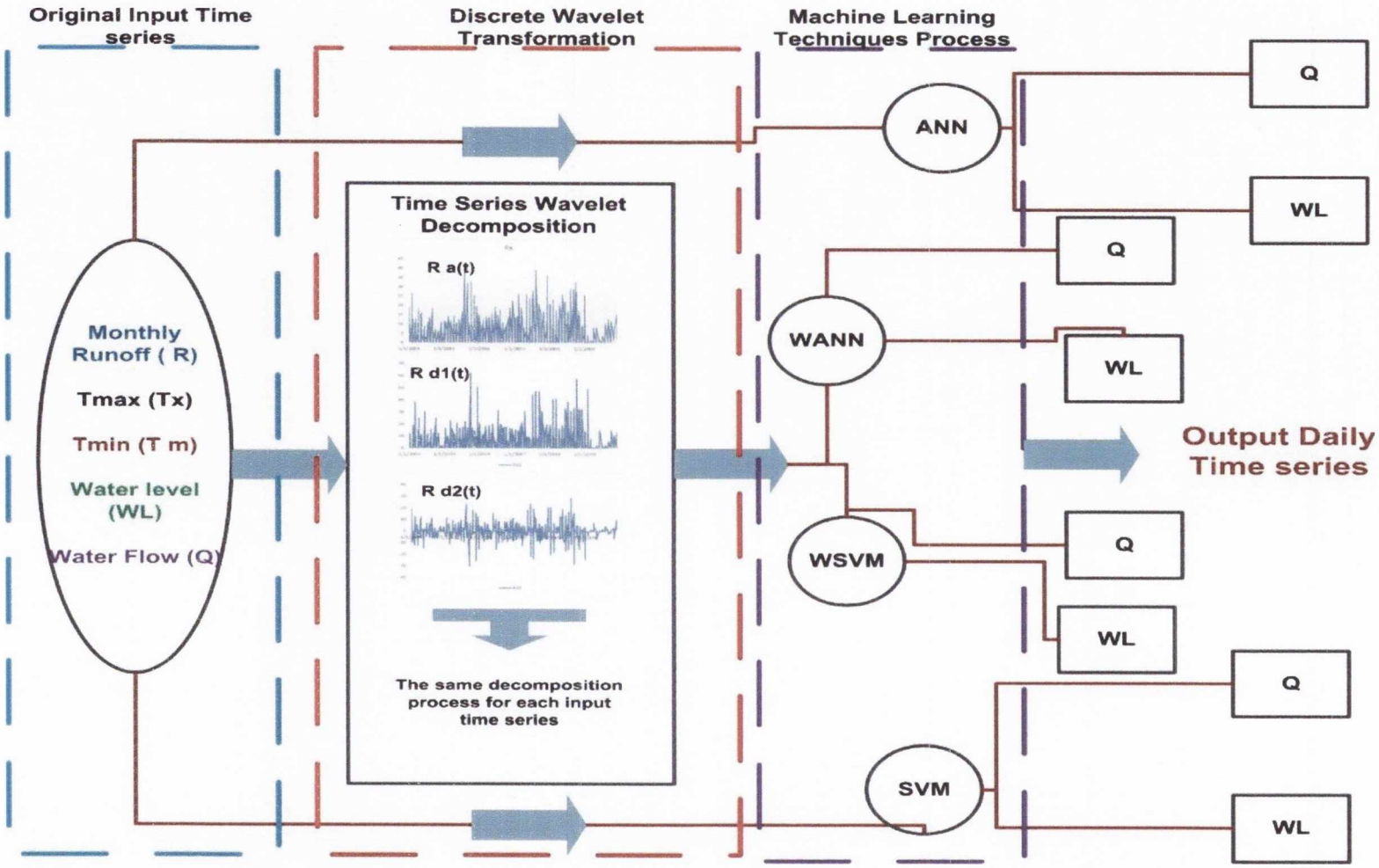

Figure 10.1: The structure and framework of the proposed hybrid combination models.

10.2.3 Artificial Neural Network (ANN)

Masters (1993) provides an extensive literature review for the ANN approach and equations. A three layer feed forward neural network with backpropagation algorithm (Network, 1999, Masters, 1993) which contains one input layer, one hidden layer, and one output layer was applied in this application. The Nodes activation function is a very important aspect in the ANN models, which are bounded, continuous, and not constant functions. The most frequently employed function is the Sigmoid function. This function is differentiable, continuous, and monotonically increasing in its domain. Schmitz et al. (2006) used sigmoid functions as activation functions in hidden and output layers' nodes. The application of ANN for predicting water level and water flow consists of two steps. The first step is training the ANN models and the second one is testing the models. In ANN modeling, two important items should be considered: the ANN structure and the training iteration number (epoch). Appropriate selection of two mentioned items can progress the model efficiency in both steps of calibration and verification, which helps to prevent over-trained models. In this research, it was concluded that 500 epochs satisfy the training network considering a learning rate of 0.1 with momentum of 0.1. In ANN models, another critical point is determining the number of neurons in input and hidden layers to provide the best training results. An automated RapidMiner algorithm (Hofmann and Klinkenberg, 2013) is assigned to determine and optimize the number of required neurons in hidden layer for simulating functions. Once the training stage was completed, the testing stage begins using the optimum values found for the number of neurons in each input layer and hidden layer. For the ANN models, there is a maximum of 16 inputs for each ANN model. The data are divided into 80% training, 20% validation, and testing.

10.2.4 Support Vector Machine (SVM)

The aim of SVMs is to define a functional dependency $f(x_1,x_2, \ldots. x_n)$ between the input variables $x_1, x_2, \ldots. x_n$ and the target values $y_1,y_2, \ldots. y_n$, where n is the total number of training samples. This functional dependency has several dimensions in the feature space, that has a prescribed maximum deviation and, at the same time, remains as flat as possible. For a theoretical review on SVM and its applications the following papers can be recommended: (Schölkopf et al., 2000, Smola and Schölkopf, 2004, Schölkopf et al., 1997, Suykens and Vandewalle, 1999, Hsu et al., 2003).

RapidMiner is a visual workflow designer and processor for data science. The RapidMiner platform has been used as the machine learning processor, so all the data got processed by Python and then fed to the RapidMiner platform to run the ANN and SVR to save the time of the simulation. Similar to the ANN models, there is a maximum of 16 inputs for each SVR model. The data are divided into 80% training, 20% validation, and testing.

The non-linear dot kernel is selected for this research, which requires that two parameters are selected by the user, namely: cost (C), and epsilon (ε). The C value was set to the value of 0.0001 and the ε value was set to the value of 0.001. The selected combination of variables is adjusted with more precision through a trial and error process for a more localized optimization of the model parameters.

10.2.5 Wavelet transformation

Discrete wavelet transforms (DWTs) are applied to decompose the original time series into a time-frequency representation at different scales (wavelet sub-times series). Over the past two decades, wavelet transforms have been used and developed a lot (see, (Shensa, 1992, Burrus et al., 1997). In this research, the level of decomposition is set to be 3, two levels of details and one level of approximations. The signals were decomposed using the redundant à trous algorithm (Murtagh et al., 2004) in conjunction with the non-symmetric db1 wavelet as the mother function. Three sets of wavelet sub-time series were created, including a low-frequency component (Approximation) that uncovers the signal's trend, and two sets of high-frequency components (Details). The using of the à trous algorithm with the db1 wavelet mother function is a result of the optimizing Python Wavelet tool (Wasilewski, 2010). Simply, the original signal is always recreated by simply summing the details with the smoothest approximation of the signal. All the input time series are gone through the designed wavelet transform and the resulted sub data sets have been used in the two hybrid models WANN and WSVM.

10.2.6 Hybrid models

10.2.6.1 Wavelet-ANN

In the WANN models, the decomposed time series are fed to the ANN for prediction of water level and water flow one day ahead (see Figure 10.1). The WANN model employs a discrete wavelet transform, as illustrated in the previous subsection, to overcome the difficulties associated with the conventional ANN model, as the wavelet transform can overcome the non-stationary properties of time series. In this chapter, not only the sensitivity of the pre-processing to the wavelet type and decomposition level is investigated, but also the effect of a number of inputs is examined as a multivariate simulation.

10.2.6.2 Wavelet-SVM

The WSVR models are built in the same way as the WANN models. Significant sets of wavelet sub-time series are fed as inputs for the SVR models and the training and validation data sets proceed as shown in Figure 10.1.

10.2.7 Validation and performance evaluation

Legates and McCabe (1999) confirmed that the correlation coefficient (R) is unsuitable for the evaluation of machine learning models. Instead, it has been suggested that a perfect evaluation of model performance should include one 'goodness-of-fit' or relative error measure and one absolute error measure. In this chapter, the ANN, WANN, SVM and WSVM model performances have been evaluated using the coefficient of determination (R^2), root means square error (RMSE) and mean absolute error (MAE). In brief, the models' predictions are optimum if R^2, MAE, and RMSE are close to 1, 0, and 0, respectively.

10.2.8 Lag value

According to the GIS, spatial analysis for the travel time of the water between the sub-catchments in the Shannon River catchment, reveals the shortest and the longest traveling times to be from the Suck sub-catchment and Lower-Shannon sub-catchment, respectively. Both sub-catchments Suck and Lower-Shannon are used in the analysis process to choose the best day lag values for the input parameters. The four models ANN, SVM, WANN, and WSVM are run for the both sub-catchments using 15 different lag values as presented in the Tables 10.1 and 10.2. The evaluation process is performed to choose the best lag value for both water flow and water level parameters.

10.2.8.1 Water flow models lag value

It can be seen from Table 10.2 and Figures 10.2 and 10.3 that all the water flow models perform the best with a lag value of 3 for the input parameters. Lag value 2 or 1 have not been used as using any of them caused the models' overfitting problem.

Figure 10.2: Water flow mean R-squared interaction diagram with the simulated lag values and the four different models for the Suck station.

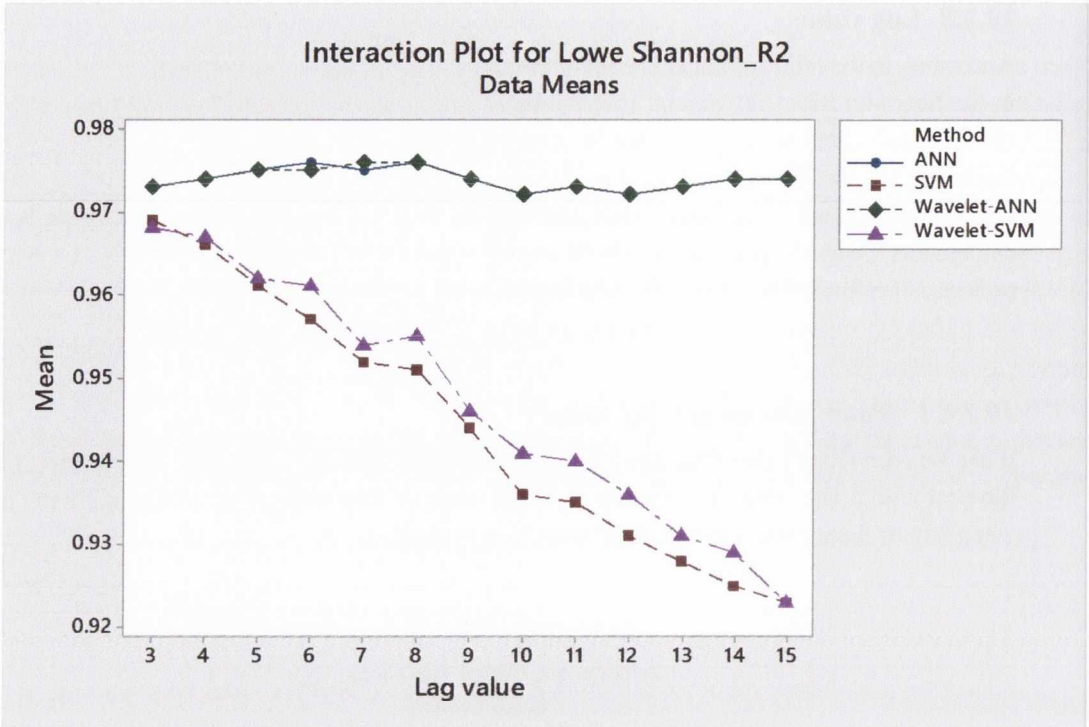

Figure 10.3: Water flow mean R-squared interaction diagram with the simulated lag values and the four different models for the lower-Shannon station.

Table 10-2: Different lag values evaluation among the different four machine learning techniques water flow models.

Water Flow (Q) m^3

Station	lag value	Suck			Lower-Shannon		
Method	(days)	RMSE	MAE	R(Square)	RMSE	MAE	R(Square)
ANN	3	4.145	2.085	0.986	27.249	16.645	0.973
	4	4.111	2.09	0.986	27.391	16.827	0.974
	5	4.101	2.124	0.986	27.114	16.842	0.975
	6	4.109	2.135	0.986	26.918	17.125	0.976
	7	4.13	2.217	0.986	27.38	17.645	0.975
	8	4.122	2.22	0.986	26.935	17.447	0.976
	9	4.038	2.153	0.986	26.809	17.1	0.974
	10	4.171	2.263	0.986	27.369	17.73	0.972
	11	4.192	2.247	0.986	26.9	17.264	0.973
	12	4.278	2.327	0.985	27.162	17.408	0.972
	13	4.362	2.432	0.985	26.784	17.091	0.973
	14	4.314	2.366	0.985	26.581	16.844	0.974
	15	4.299	2.341	0.985	26.697	16.99	0.974
SVM	3	3.831	1.783	0.987	29.782	18.191	0.969
	4	3.983	1.939	0.987	31.83	19.736	0.966
	5	4.136	2.059	0.986	34.751	22.274	0.961
	6	4.269	2.15	0.985	36.915	24.174	0.957
	7	4.429	2.271	0.984	39.569	26.244	0.952
	8	4.592	2.41	0.983	40.254	27.146	0.951

	9	4.709	2.464	0.983	40.727	27.775	0.944
	10	4.842	2.55	0.982	43.105	29.739	0.936
	11	4.986	2.631	0.981	44.354	30.758	0.935
	12	5.121	2.718	0.981	45.906	31.881	0.931
	13	5.226	2.773	0.98	47.71	33.456	0.928
	14	5.311	2.824	0.979	49.316	34.83	0.925
	15	5.412	2.896	0.979	50.925	36.143	0.923
Wavelet-ANN	3	4.373	2.01	0.984	27.398	16.696	0.973
	4	4.396	2.073	0.984	27.242	16.483	0.974
	5	4.222	1.971	0.985	27.173	16.882	0.975
	6	4.238	2.003	0.985	27.303	17.019	0.975
	7	4.21	2.063	0.985	27.184	17.24	0.976
	8	4.396	2.08	0.984	26.863	17.074	0.976
	9	4.299	2.08	0.985	26.908	17.031	0.974
	10	4.409	2.107	0.984	27.02	16.959	0.972
	11	4.257	2.052	0.985	26.844	17.034	0.973
	12	4.379	2.087	0.984	27.18	17.275	0.972
	13	4.309	2.018	0.985	26.646	16.672	0.973
	14	4.32	2.078	0.985	26.502	16.507	0.974
	15	4.363	2.08	0.984	26.623	16.71	0.974
Wavelet-SVM	3	4.076	1.469	0.985	30.715	19.89	0.968
	4	4.162	1.541	0.985	32.622	22.14	0.967
	5	4.348	1.606	0.983	35.886	24.724	0.962
	6	4.407	1.636	0.983	37.706	26.697	0.961
	7	4.507	1.682	0.982	40.553	28.669	0.954
	8	4.59	1.744	0.982	40.994	29.541	0.955
	9	4.688	1.805	0.981	42.131	30.602	0.946
	10	4.77	1.871	0.98	44.82	33.058	0.941
	11	4.86	1.921	0.98	46.581	34.25	0.94
	12	4.943	1.992	0.979	48.838	36.101	0.936
	13	5.019	2.04	0.979	50.707	37.381	0.931
	14	5.083	2.093	0.978	52.751	39.24	0.929
	15	5.141	2.142	0.978	55.401	41.331	0.923

10.2.8.2 Water level models lag value

It can be seen from Table 10.3 and Figures 10.4 and 10.5 that all the water level models perform the best with lag value 3 for the input parameters. Lag value 2 or 1 have not been used as using any of them caused the models' overfitting problem. In figure 10.4, all the models got to perform all most the same for the first 7 lag values and that due to the actual absolute water level values of Suck station do not change significantly over a short period of time, so the models' sensitivity to changes can be very slow. In Figure 10.5, some of the models got to perform at lag value 8 better than lag value 3, but the deference in the R^2 is 0.003 which is negligible in addition to the risk of missing the first 8 records of each run rather than just 2 records, so lag value 3 was chosen to be used in this research.

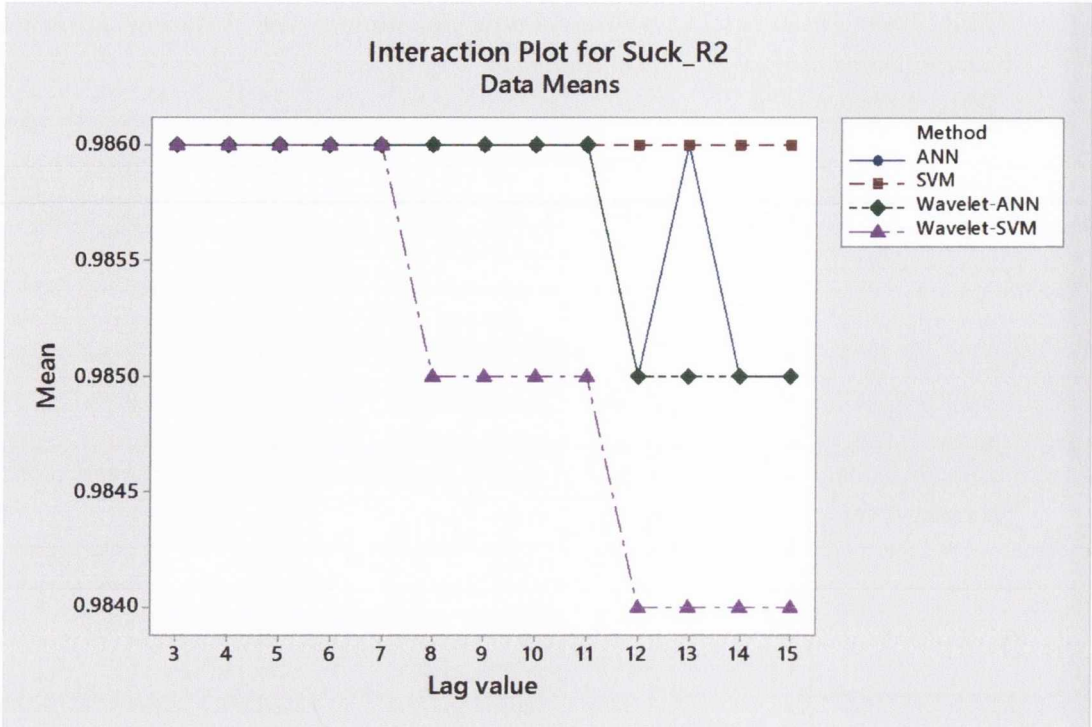

Figure 10.4: Water level mean R-squared interaction diagram with the simulated lag values and the four different models for the Suck station.

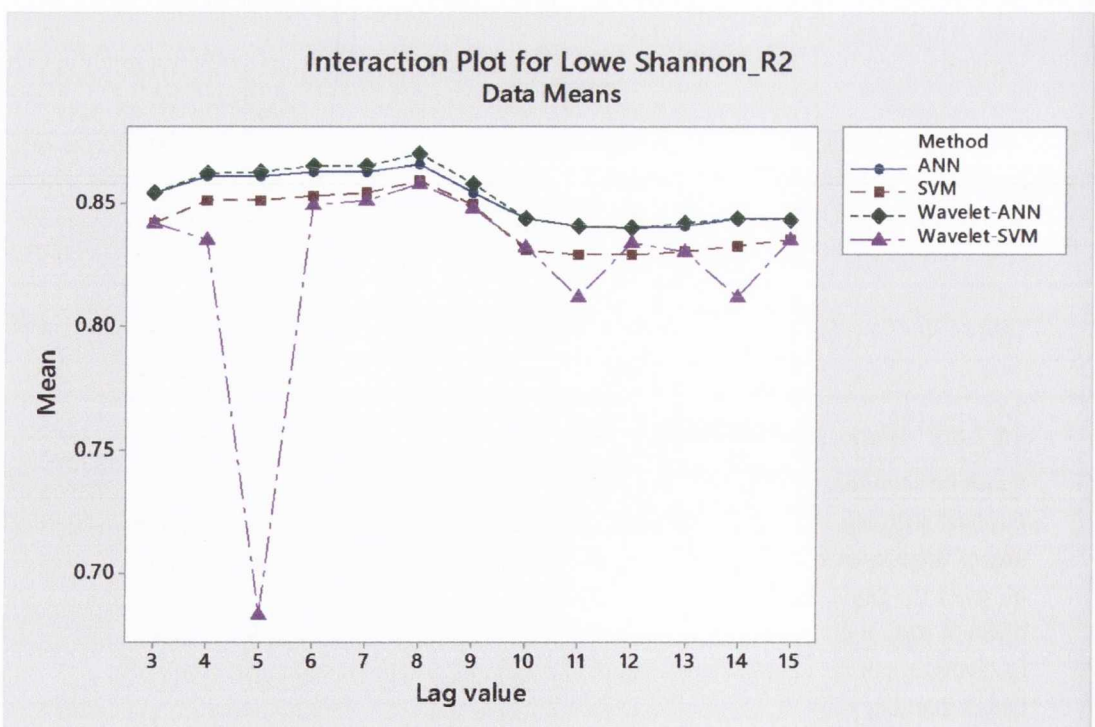

Figure 10.5: Water level mean R-squared interaction diagram with the simulated lag values and the four different models for the lower-Shannon station.

Table 10-3: Different lag values evaluation among the different four machine learning techniques water level models.

Water Level (WL) m

Station	lag value	Suck			Lower-Shannon		
Method	(days)	RMSE	MAE	R(Square)	RMSE	MAE	R(Square)
	3	0.08	0.042	0.986	0.063	0.039	0.854
	4	0.079	0.041	0.986	0.062	0.038	0.861
	5	0.079	0.042	0.986	0.064	0.039	0.861
	6	0.08	0.043	0.986	0.064	0.038	0.863
	7	0.08	0.042	0.986	0.064	0.039	0.863
	8	0.081	0.044	0.986	0.063	0.038	0.866
ANN	9	0.081	0.044	0.986	0.064	0.038	0.854
	10	0.081	0.044	0.986	0.062	0.037	0.844
	11	0.082	0.045	0.986	0.062	0.037	0.841
	12	0.084	0.047	0.985	0.062	0.037	0.84
	13	0.082	0.045	0.986	0.062	0.037	0.841
	14	0.085	0.048	0.985	0.062	0.036	0.844
	15	0.085	0.048	0.985	0.062	0.037	0.844
	3	0.079	0.031	0.986	0.066	0.037	0.842
	4	0.08	0.031	0.986	0.065	0.035	0.851
	5	0.081	0.033	0.986	0.066	0.036	0.851
	6	0.081	0.033	0.986	0.066	0.035	0.853
	7	0.08	0.03	0.986	0.066	0.035	0.854
	8	0.081	0.03	0.986	0.065	0.034	0.859
SVM	9	0.082	0.033	0.986	0.065	0.034	0.849
	10	0.082	0.032	0.986	0.065	0.034	0.831
	11	0.082	0.033	0.986	0.065	0.034	0.829
	12	0.083	0.033	0.986	0.065	0.034	0.829
	13	0.082	0.031	0.986	0.065	0.033	0.83
	14	0.083	0.034	0.986	0.064	0.033	0.833
	15	0.082	0.033	0.986	0.064	0.033	0.835
	3	0.079	0.039	0.986	0.063	0.039	0.854
	4	0.08	0.04	0.986	0.062	0.038	0.862
	5	0.079	0.039	0.986	0.063	0.038	0.863
	6	0.08	0.039	0.986	0.063	0.038	0.865
	7	0.08	0.038	0.986	0.064	0.038	0.865
	8	0.081	0.04	0.986	0.062	0.037	0.87
Wavelet-ANN	9	0.081	0.038	0.986	0.063	0.037	0.858
	10	0.081	0.039	0.986	0.062	0.037	0.844
	11	0.082	0.039	0.986	0.062	0.036	0.841
	12	0.084	0.041	0.985	0.062	0.037	0.84
	13	0.083	0.041	0.985	0.062	0.037	0.842
	14	0.083	0.04	0.985	0.062	0.036	0.844
	15	0.084	0.041	0.985	0.062	0.037	0.843
	3	0.08	0.031	0.986	0.066	0.036	0.842
Wavelet-SVM	4	0.08	0.03	0.986	0.069	0.044	0.835
	5	0.081	0.03	0.986	0.102	0.082	0.684

6	0.082	0.03	0.986	0.067	0.038	0.849
7	0.082	0.03	0.986	0.067	0.038	0.851
8	0.083	0.031	0.985	0.065	0.036	0.858
9	0.084	0.03	0.985	0.065	0.035	0.848
10	0.085	0.031	0.985	0.065	0.034	0.832
11	0.085	0.031	0.985	0.069	0.045	0.812
12	0.086	0.031	0.984	0.067	0.041	0.834
13	0.086	0.032	0.984	0.065	0.033	0.83
14	0.086	0.031	0.984	0.068	0.045	0.812
15	0.087	0.032	0.984	0.064	0.033	0.835

10.3 Models application and evaluation

10.3.1 Flow evaluation

Although all the simulated flow models performed very well, as presented in the Table 10.4, SVR performed the best overall, as confirmed by Figure 10.6 which shows the visual R^2 distribution. The mean absolute error (MAE) depends on the absolute value of the water flow, thus MAE values for the Lower-Shannon are high, as the water flow rate in the Lower-Shannon is the highest. The average water flow rate in the Lower-Shannon is around 150 m^3/s, however the Suck station, which comes in the second order of water flow rate after Lower-Shannon, water flow rate is around 20 m^3/s.

Table 10-4: R2, MAE, and RMSE values for flow (m^3/s) by ANN, SVM, WANN and WSVM models in the testing period.

Water Flow (Q) m^3

Method	Station	RMSE	MAE	R(Square)
ANN	**Brosna**	4.378	2.339	0.902
	Inny	2.721	1.249	0.977
	Lower-Shannon	27.1	16.665	0.974
	Nenagh	3.183	1.723	0.899
	Suck	4.25	2.09	0.985
SVR	**Brosna**	4.257	1.975	0.912
	Inny	2.712	0.956	0.977
	Lower-Shannon	29.782	18.191	0.969
	Nenagh	3.039	1.414	0.919
	Suck	3.831	1.783	0.987
WANN	**Brosna**	4.39	2.368	0.901
	Inny	2.785	1.389	0.977
	Lower-Shannon	27.335	16.622	0.973
	Nenagh	3.197	1.738	0.899
	Suck	4.252	1.954	0.985
WSVR	**Brosna**	4.192	1.903	0.912
	Inny	2.673	0.933	0.978
	Lower-Shannon	30.715	19.89	0.968
	Nenagh	3.039	1.383	0.918
	Suck	4.075	1.469	0.985

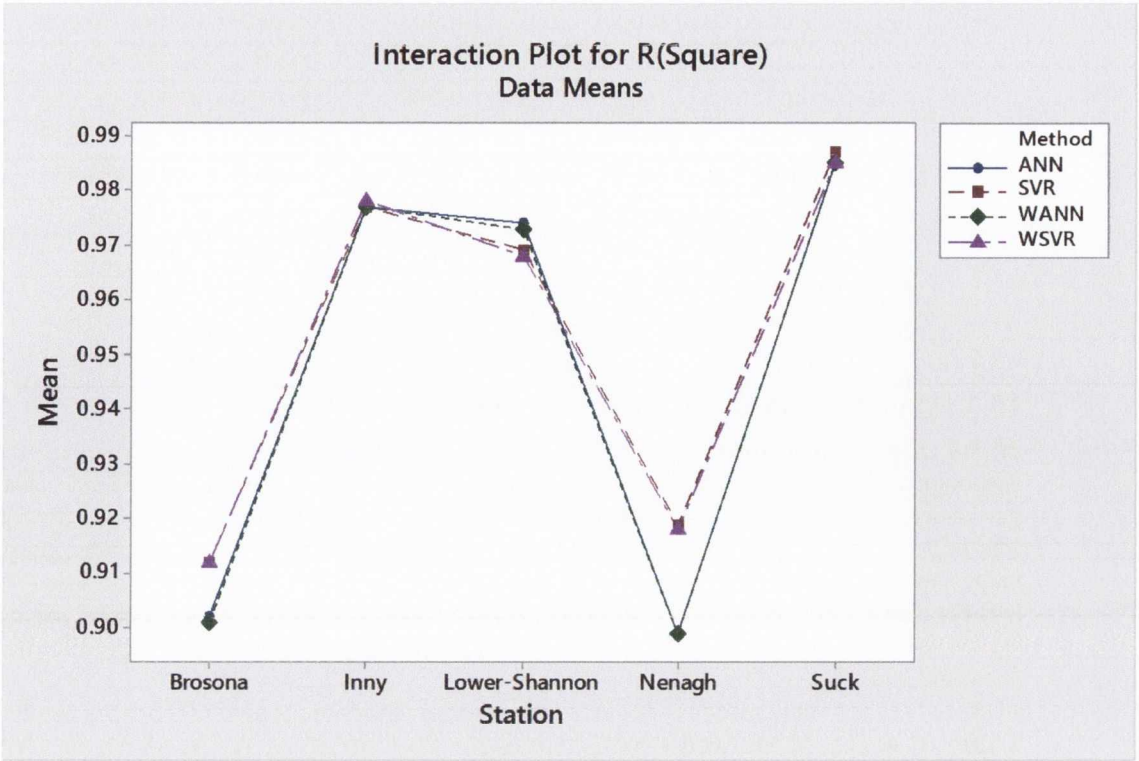

Figure 10.6: Interaction flow validation R^2 diagram for the models and stations.

10.3.2 Water level evaluation

All the simulated water level models performed very well, as presented in the Table 10.5. However, the hybrid WANN model performed the best of all the models, as it is the only model that succeeds in modeling the water levels for Brosna hydrometric station. Figure 10.7 shows the visual R^2 distribution, which confirms that WANN is the best water level model.

Table 10-5: R2, MAE, and RMSE values for the water level (m) by ANN, SVM, WANN and WSVM models in the testing period.

Water Level (WL) m

Method	Station	RMSE	MAE	R(Square)
ANN	Brosna	0.34	0.259	0.762
	Inny	0.061	0.025	0.982
	Lower-Shannon	0.063	0.039	0.853
	Nenagh	0.108	0.06	0.905
	Suck	0.08	0.042	0.986
SVR	Brosna	10.978	8.138	0
	Inny	0.06	0.022	0.983
	Lower-Shannon	0.066	0.037	0.842
	Nenagh	0.104	0.05	0.922
	Suck	0.079	0.031	0.986
WANN	Brosna	0.348	0.27	0.788
	Inny	0.061	0.026	0.982

	Lower-Shannon	0.063	0.038	0.854
	Nenagh	0.108	0.061	0.906
	Suck	0.079	0.039	0.986
WSVR	**Brosna**	6.92	5.22	0
	Inny	0.06	0.023	0.983
	Lower-Shannon	0.065	0.036	0.842
	Nenagh	0.103	0.048	0.921
	Suck	0.08	0.031	0.986

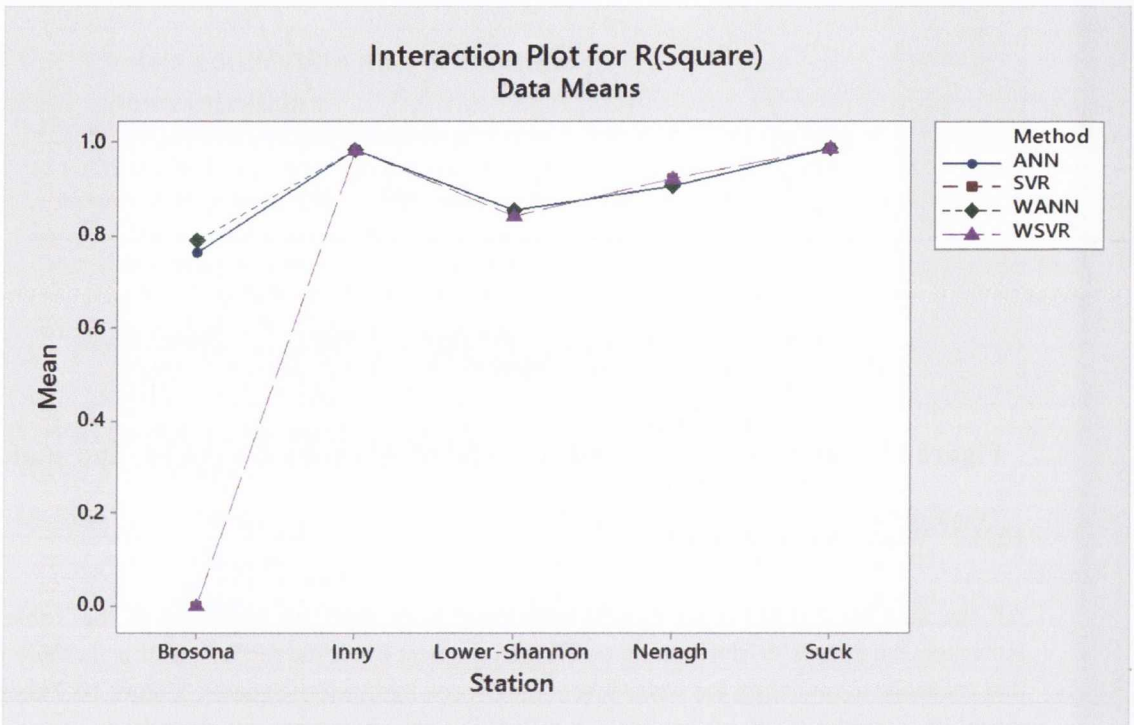

Figure 10.7: Interaction water level validation R^2 diagram for the models and stations.

10.4 Results and discussion

10.4.1 Flow simulation results

The flow models performance statistics for the Shannon River Catchment are presented here. The SVR model has the highest R^2 and overall performs better than the two simulated hybrid models. Figures 10.8-10.9 show the comparison of observed versus forecasted water flow values for the ANN, SVR, WANN and WSVR models for Suck and Lower-Shannon hydrometric stations in the structured system for the Shannon catchment. Figures 10.10-11 show the residual of the SVR water flow model for Suck and Lower-Shannon hydrometric stations. In general, the models are able to simulate and predict the water flow, capturing the regular and no flow periods and to some extent some peaks. However, the models did not capture the very high flow peaks very accurately. Additional results are presented in the appendix F.

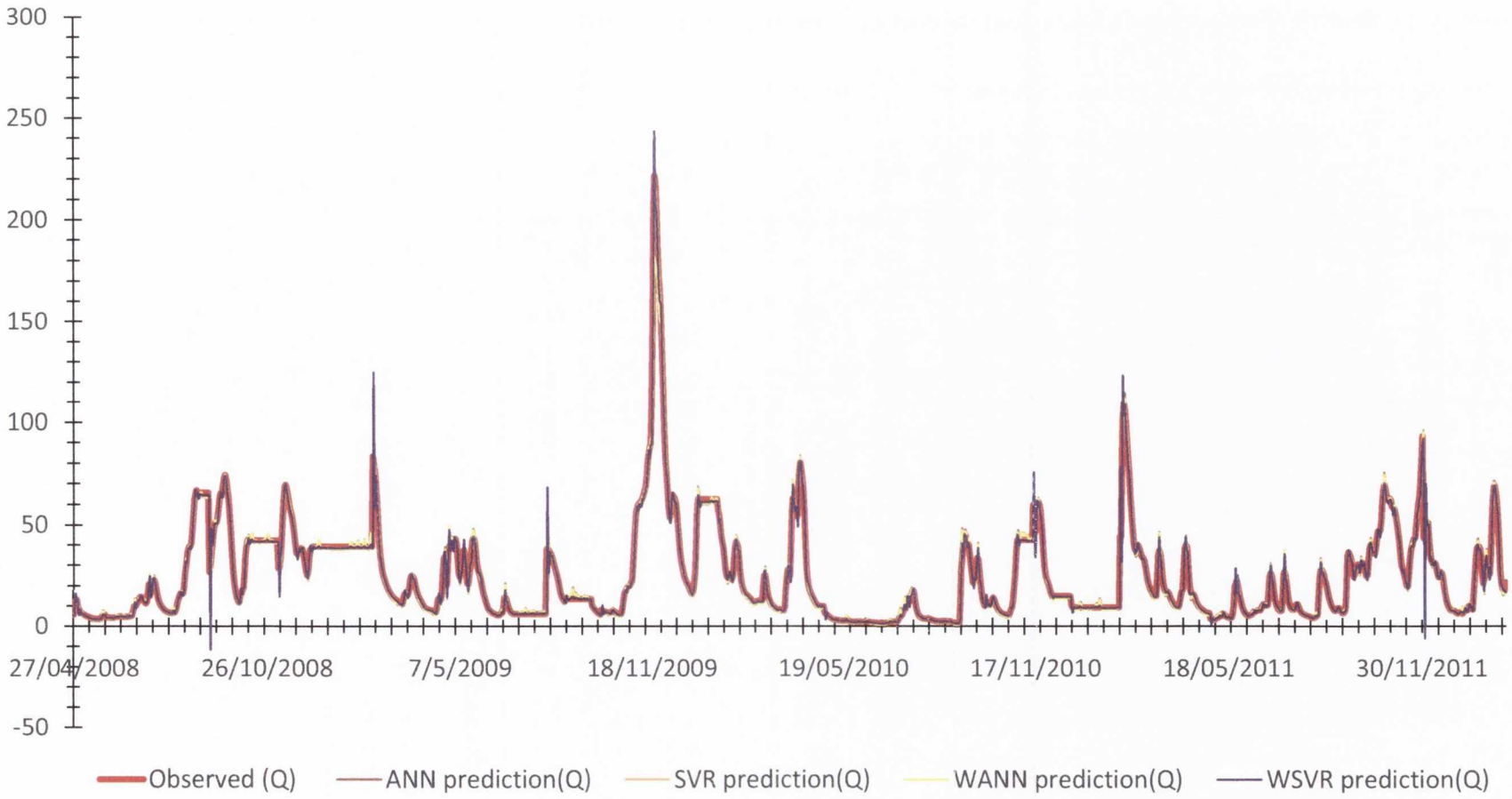

Figure 10.8: Comparisons between the measured and predicted flow (m^3/s) based on the testing data for Suck hydrometric station.

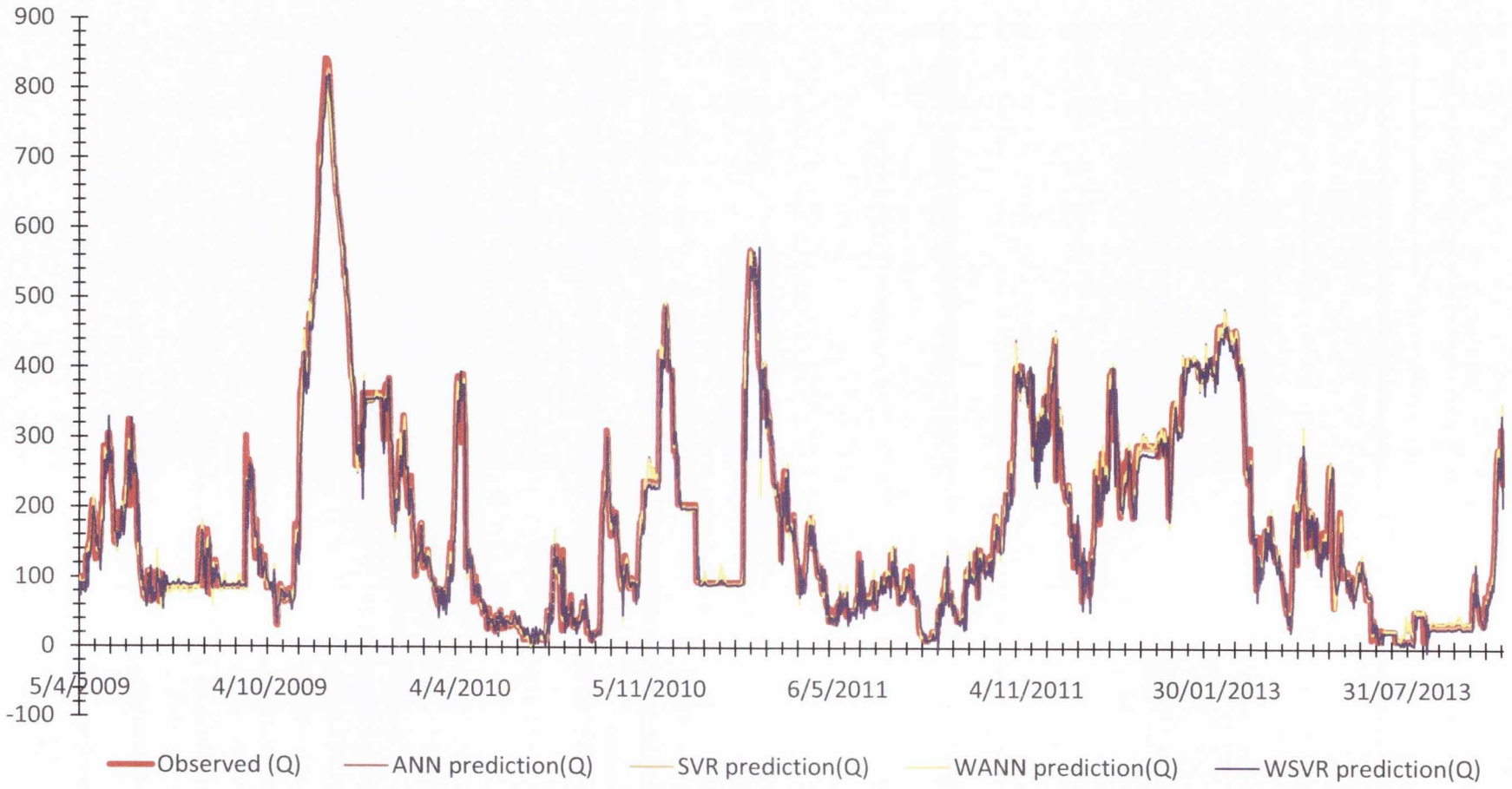

Figure 10.9: Comparisons between the measured and predicted flow (m^3/s) based on the testing data for Lower-Shannon hydrometric station.

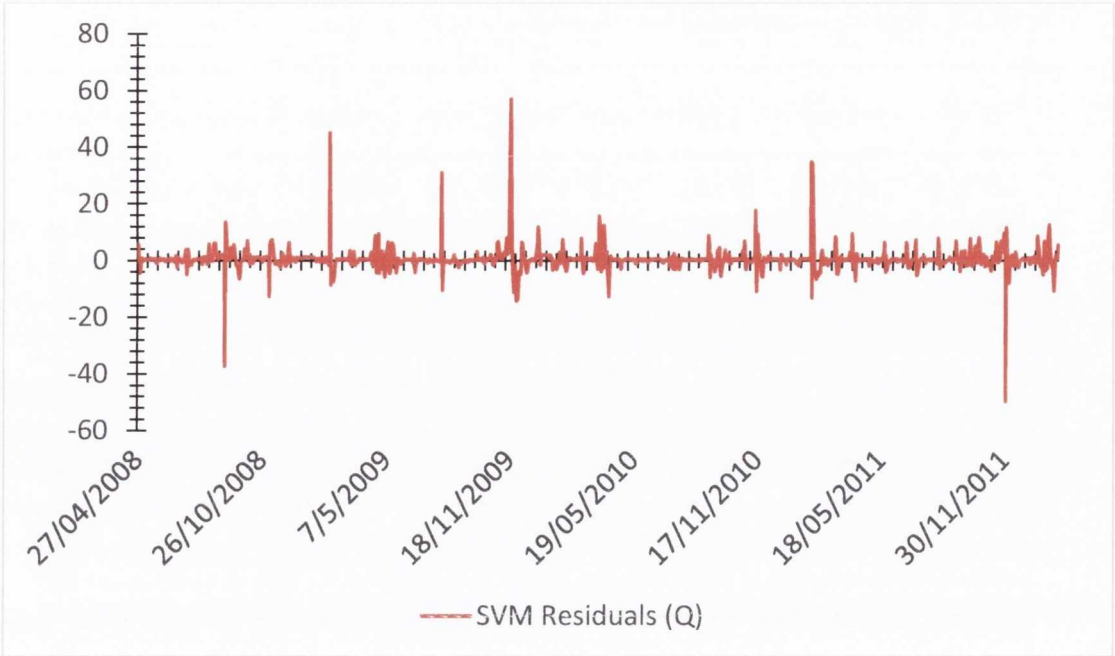

Figure 10.10: Residuals of best performing flow SVM model for Suck.

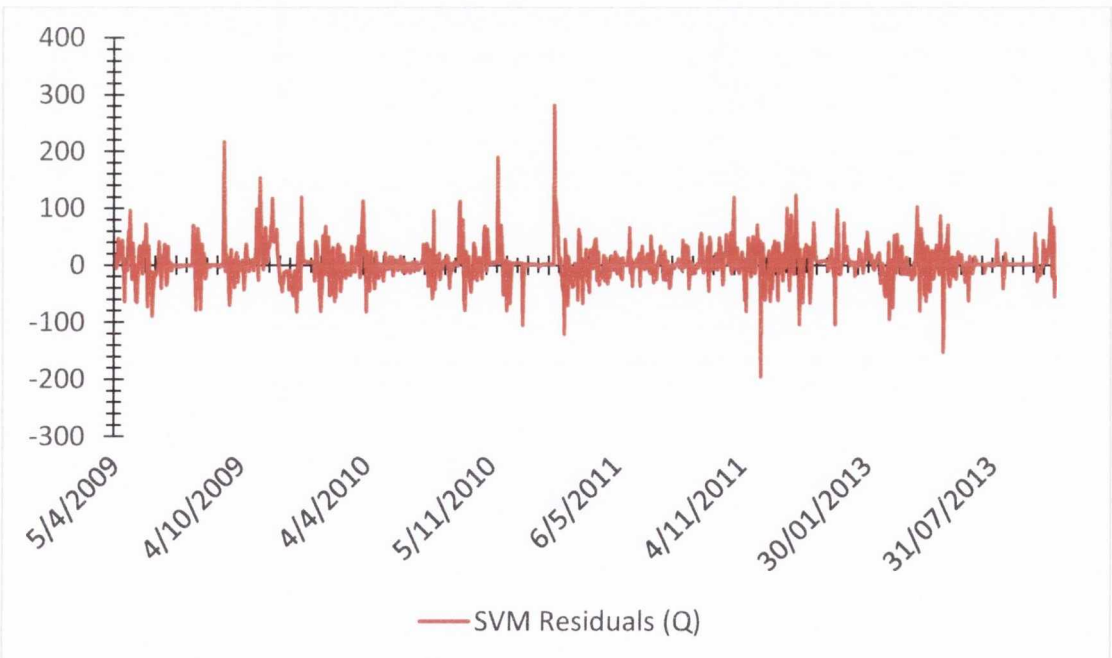

Figure 10.11: Residuals of best performing water flow SVM model for Lower-Shannon.

10.4.2 Water level simulation results

The water level models' performance statistics for the Shannon River Catchment are presented here. The hybrid WANN model has the highest testing R^2 and overall, WANN performs better than WSVM hybrid model, as coupling the ANN with wavelet transformed data improved model performance; however, it decreased the model performance of the SVR models, which might be because regression based models are not as able as the ANN models to create a function with wavelet transformed data. It should be noted that a similar conclusion was reached for the flow parameter as reported by Karran et al. (2014).

Figures 10.12-10.14 show the comparison of observed versus forecasted water level values for the ANN, SVR, WANN and WSVR models for selected hydrometric stations in the structured system for the Shannon catchment. Figures 10.15-17 show the residual of the WANN water level model among the selected hydrometric stations. Again, in general the models are able to simulate and predict the water level and they do capture regular and no flow periods and to some extent the peaks. However, the models did not capture the very high flow peaks very accurately.

For Brosna hydrometric station, Figure 10.14, all the models produced noise except WANN it was the only model that captured the signal, that was due to the fact Brosna is a very small flashy sub-catchment with non-stationary data set and as described before this hybrid WANN can be the solution to model such a case as can be seen in Figure 10.17. Additional results are presented in the appendix F.

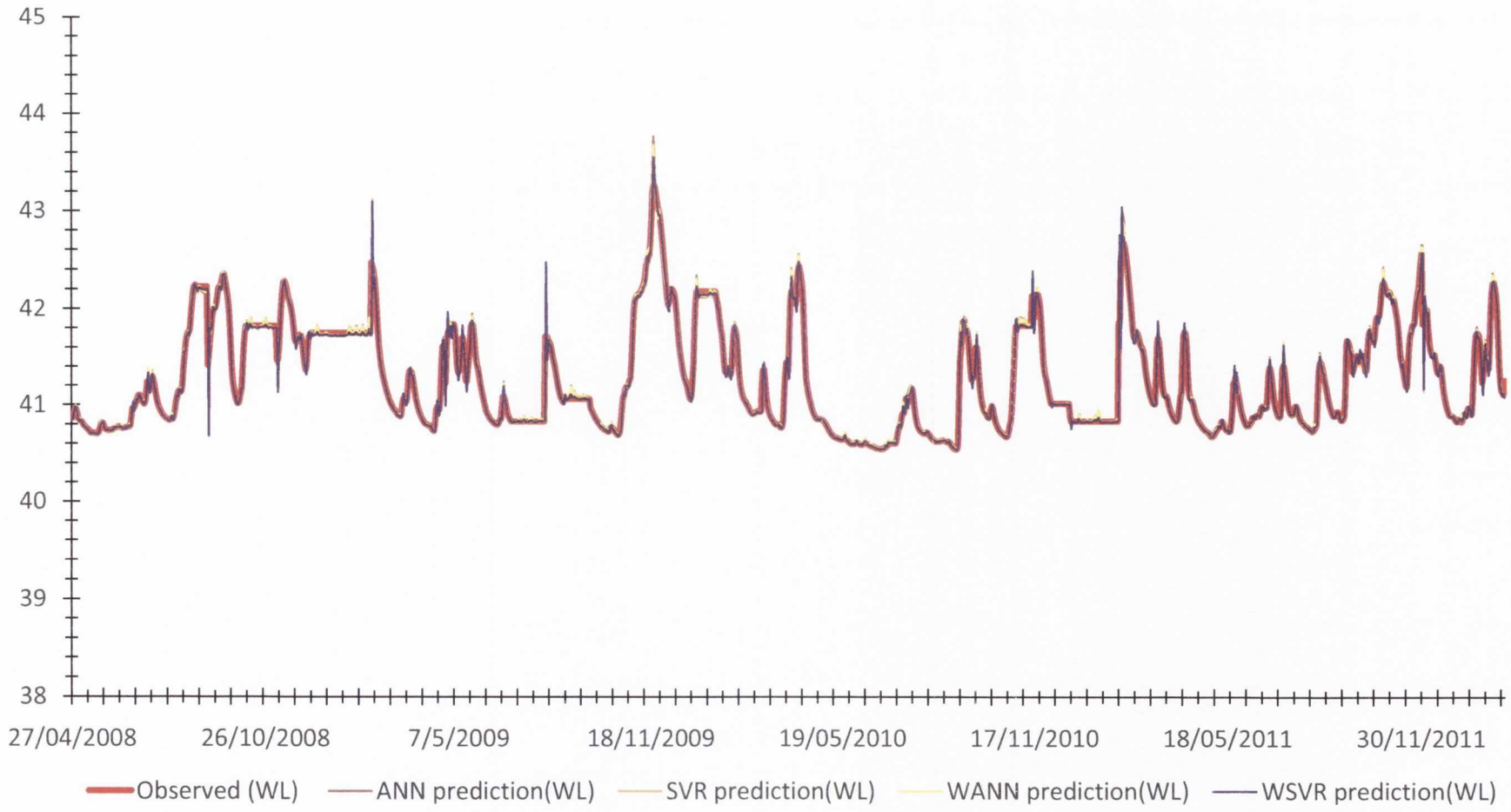

Figure 10.12: Comparisons between the measured and predicted water level (m) based on the testing data for Suck hydrometric station.

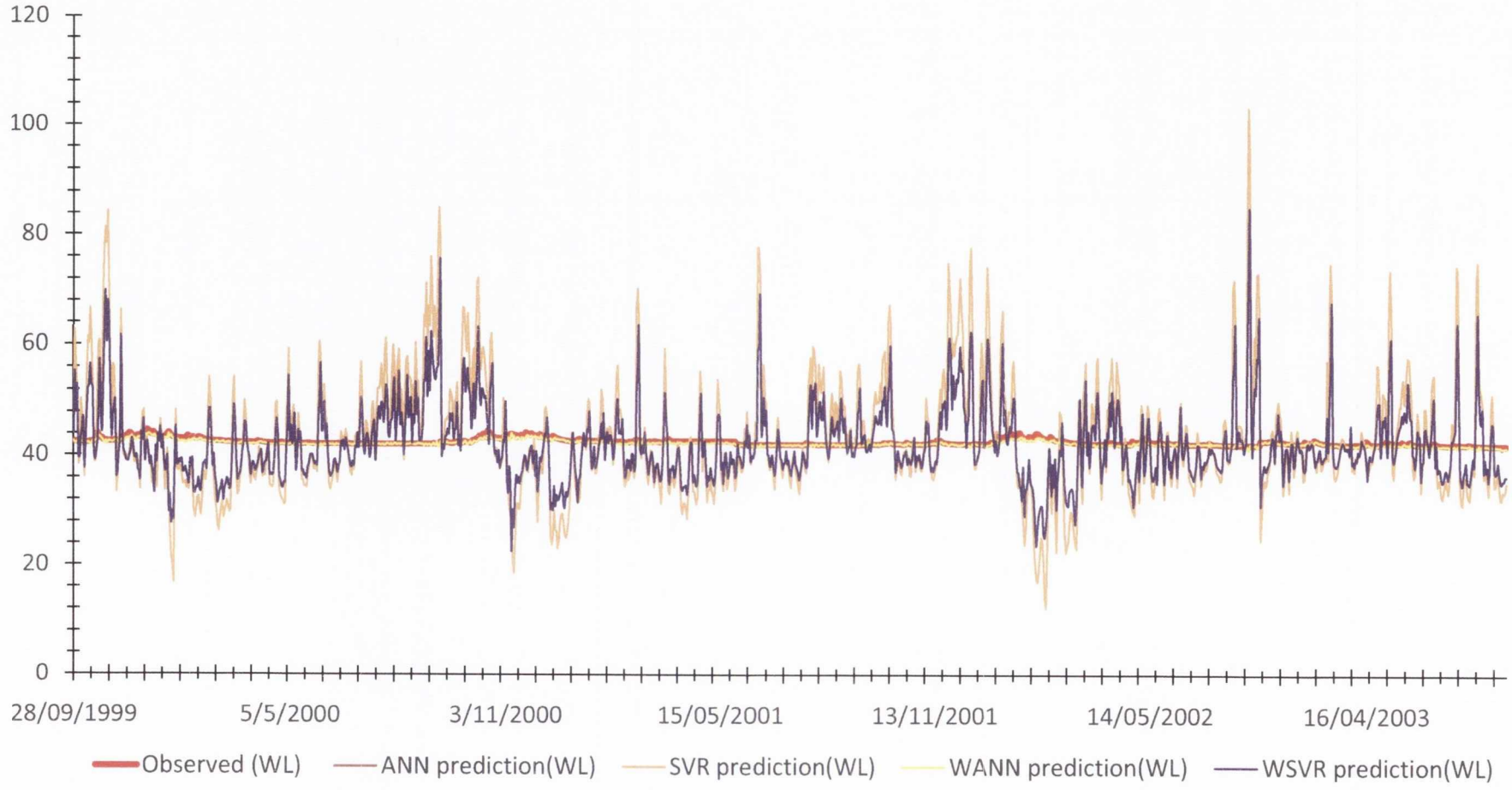

Figure 10.13: Comparisons between the measured and predicted water level (m) based on the testing data for Brosna hydrometric station.

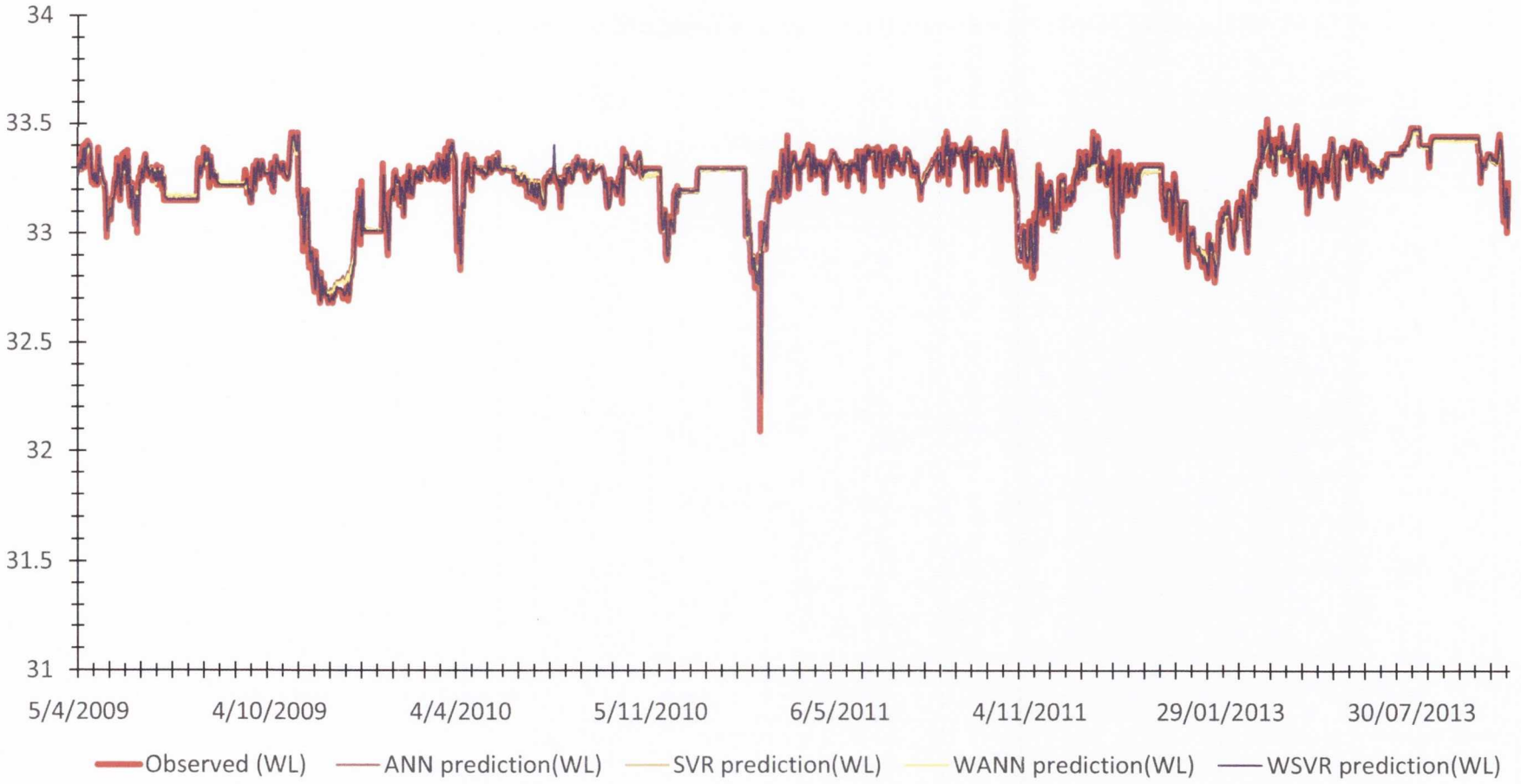

Figure 10.14: Comparisons between the measured and predicted water level (m) based on the testing data for Lower-Shannon hydrometric station.

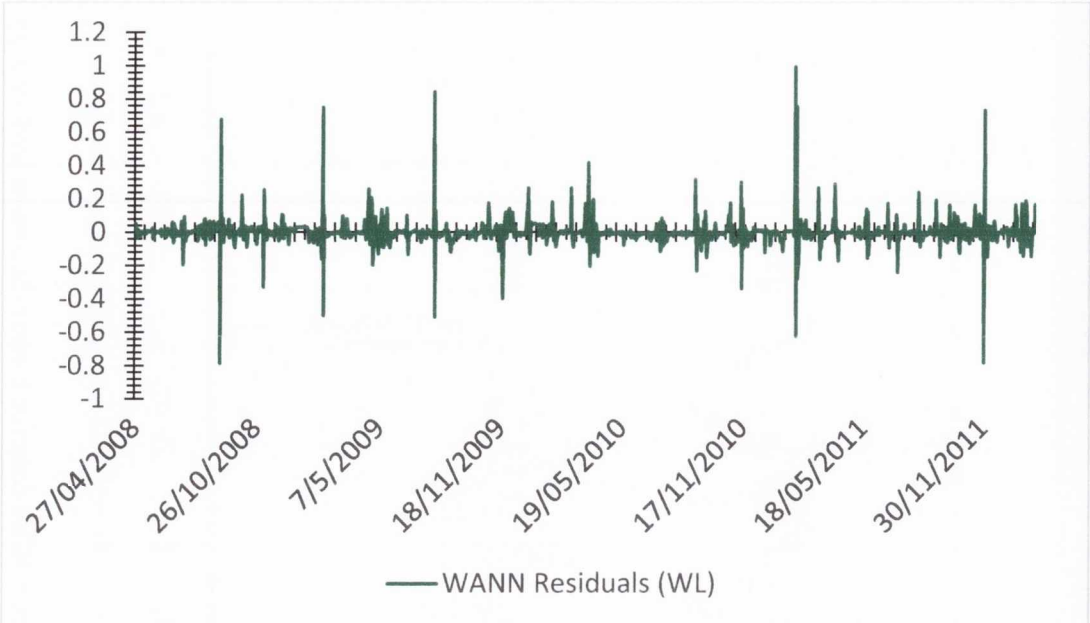

Figure 10.15: Residuals of best performing water level WANN model for Suck.

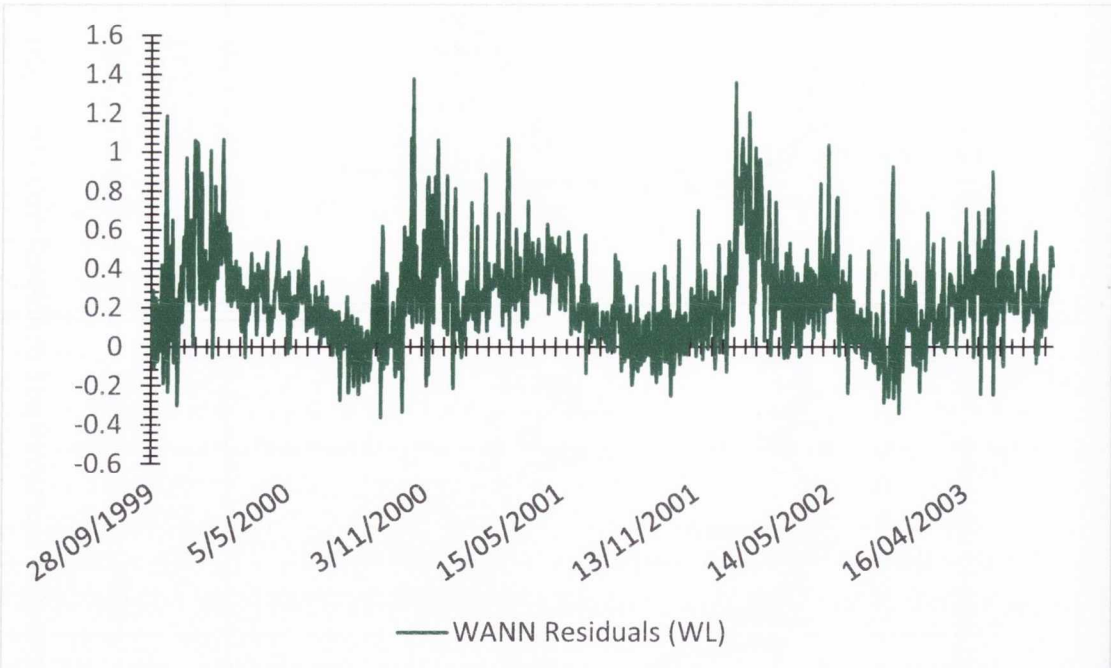

Figure 10.16: Residuals of best performing water level WANN model for Brosna.

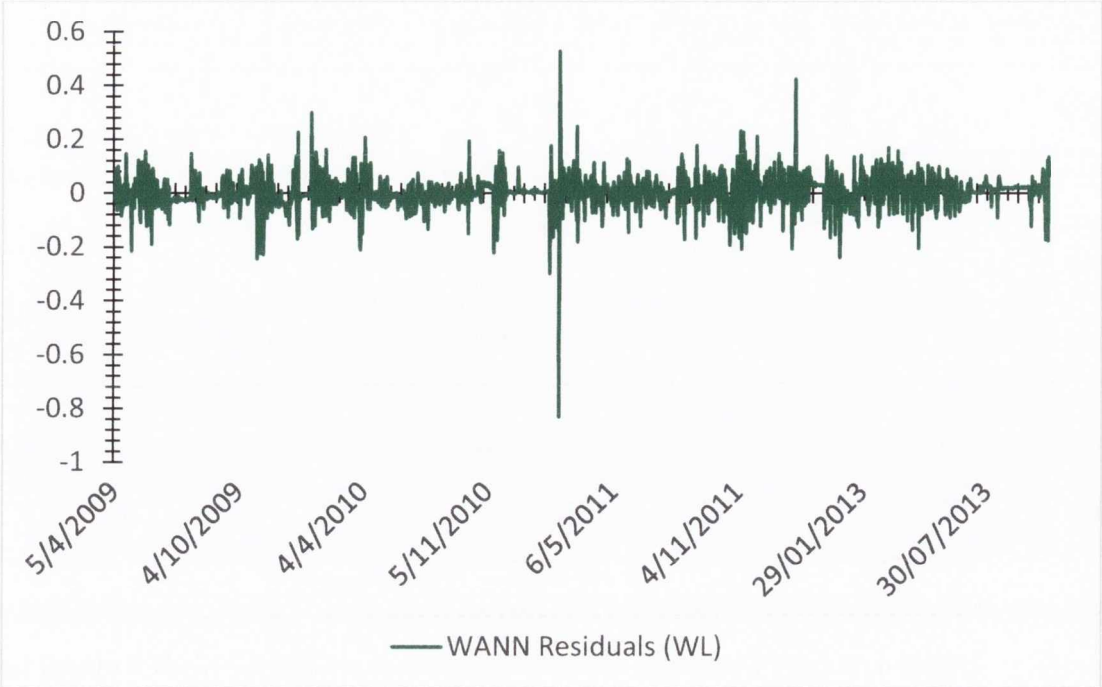

Figure 10.17: Residuals of best performing water level WANN model for Lower-Shannon.

10.4.3 Projections based on climate change scenarios

This chapter used long-term data sets to train the data-driven models (1983-2013) and the models have been validated against 4 years observed data on the catchment scale. The resultant SVR flow model and WANN level model have then been used to predict the long-term future daily water levels and flows for the Lower-Shannon hydrometric station for the period (2014-2080), based on the simulated climatic scenarios as described in Chapter 4.

Tables 10-6 and 10.7 represent the descriptive statistics for the predicted river's flow and levels, respectively. Figures 10.18 and 10.19 show the predicted flow and level time series based on the different scenarios. The two climatic scenarios relating to the RCP 8.5 provide the highest increase in water level trends, however, RCP4.5 (75%) and RCP 8.5 (75%) provide the highest increase in water flow trends. Both scenarios, RCP 4.5 75% and RCP 8.5 75%, have significant standard variations with the temporal scale. From Table 10-6, the flow sum for all scenarios from RCP 4.5 50% to RCP 8.5 75%, respectively, show significant increases in the total amount of flow in the catchment due to climate change. The average increase in the water flow among all the simulated scenarios is around 2-4% from the baseline.

Based on the two scenarios RCP 4.5 75% and RCP 8.5 75%, it has been concluded that for both variables, water level and flow, there are increases in the predicted data skewness with time. Skewness is a measure of the asymmetry of the probability distribution about the mean value, which means that water level and flow predictions gradually depart away more from normality, which means that ordinary statistical time series models cannot be used for predicting water level and flow and using data driven models such as this study is a must.

Table 10-6: Lower-Shannon water flow (m^3/s) daily projections (2014-2080) statistics based on the different four climatic scenarios using the developed SVM model.

Parameters	Climatic Scenario (Q(m3)) Prediction			
	RCP4.5 50%(Q)	RCP4.5 75%(Q)	RCP8.5 50%(Q)	RCP8.5 75%(Q)
Mean	89.57	90.94	88.92	91.04
SEMean	0.200	0.209	0.203	0.217
StDev	31.12	32.46	31.48	33.67
Variance	968.93	1054.24	991.52	1133.68
CVariation	34.75	35.70	35.41	36.98
Q1	69.04	69.58	68.12	68.92
Median	83.14	84.06	82.48	83.87
Q3	103.22	104.82	102.65	105.25
IQR	34.18	35.23	34.52	36.32
TRMean	86.97	88.16	86.29	88.12
Sum	$21.91x10^5$	$21.92 x10^5$	$21.43 x10^5$	$21.94 x10^5$
Minimum	37.10	36.82	35.01	34.43
Maximum	327.60	336.59	328.44	344.93
Range	290.50	299.76	293.42	310.49
SSQ	$21.67 x10^7$	$22.47 x10^7$	$21.45 x10^7$	$22.71 x10^7$
Skewness	1.78	1.81	1.77	1.81
Kurtosis	6.11	6.10	5.97	5.99
MSSD	59.25	63.09	59.97	66.10

Table 10-7: Lower-Shannon water level (m) daily projections (2014-2080) statistics based on the different four climatic scenarios using the developed WANN model.

Parameters	Climatic Scenario (WL(m)) Prediction			
	RCP4.5 50%(WL)	RCP4.5 75%(WL)	RCP8.5 50%(WL)	RCP8.5 75%(WL)
Mean	33.278	33.277	33.281	33.280
SEMean	0.000	0.000	0.000	0.000
StDev	0.036	0.038	0.037	0.039
Variance	0.001	0.001	0.001	0.002
CVariation	0.109	0.113	0.112	0.118
Q1	33.259	33.258	33.261	33.260
Median	33.281	33.281	33.283	33.283
Q3	33.305	33.305	33.308	33.309
IQR	0.046	0.047	0.048	0.049
TRMean	33.280	33.279	33.283	33.282
Minimum	33.127	33.123	33.129	33.120
Maximum	33.381	33.383	33.388	33.392
Range	0.253	0.260	0.259	0.272
Skewness	-0.775	-0.810	-0.753	-0.806
Kurtosis	0.672	0.759	0.604	0.733
MSSD	0.000	0.000	0.000	0.000

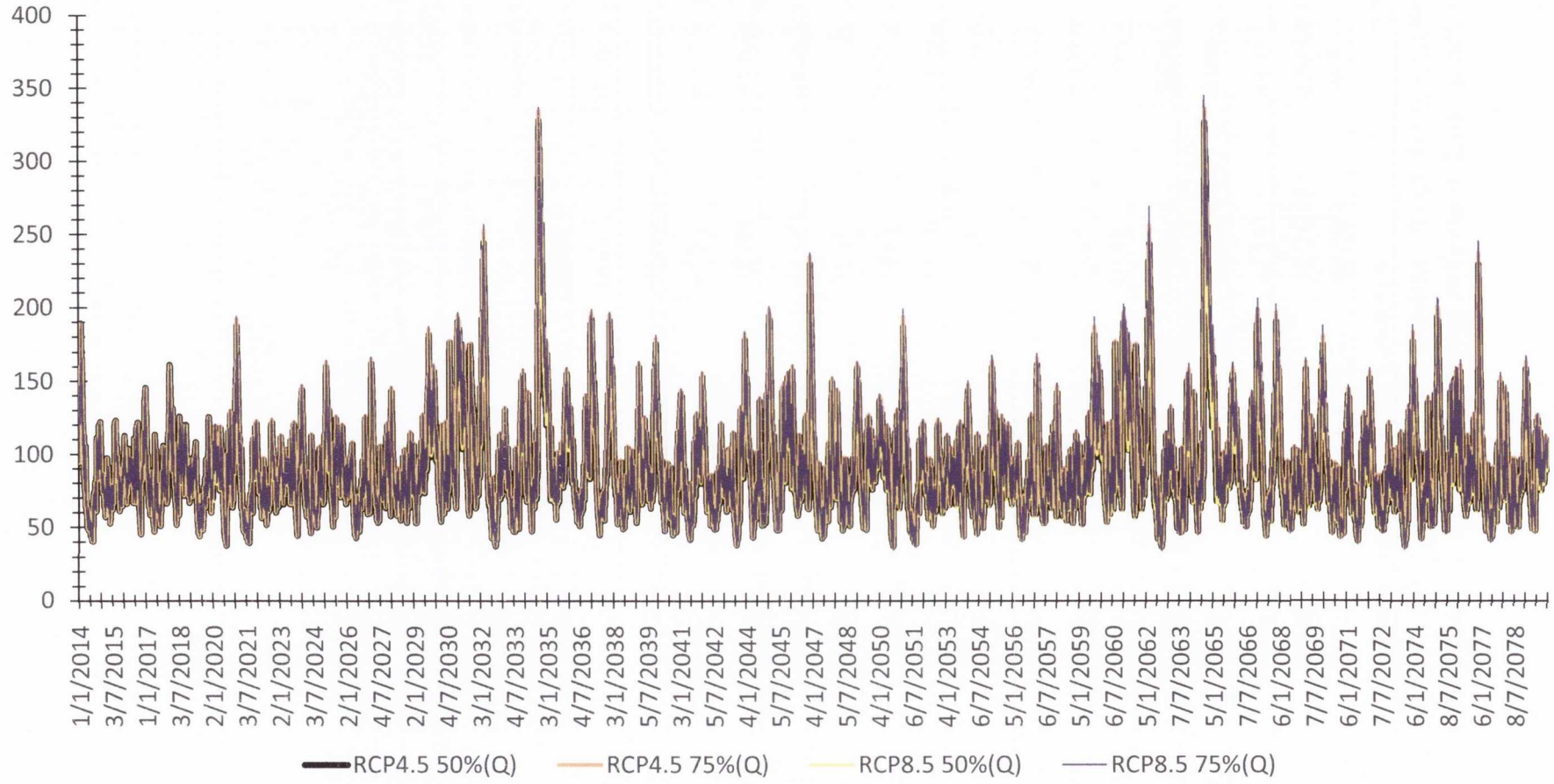

Figure 10.18: Lower-Shannon water flow (m^3/s) daily projections (2014-2080) for the different four climatic scenarios using the developed SVM model.

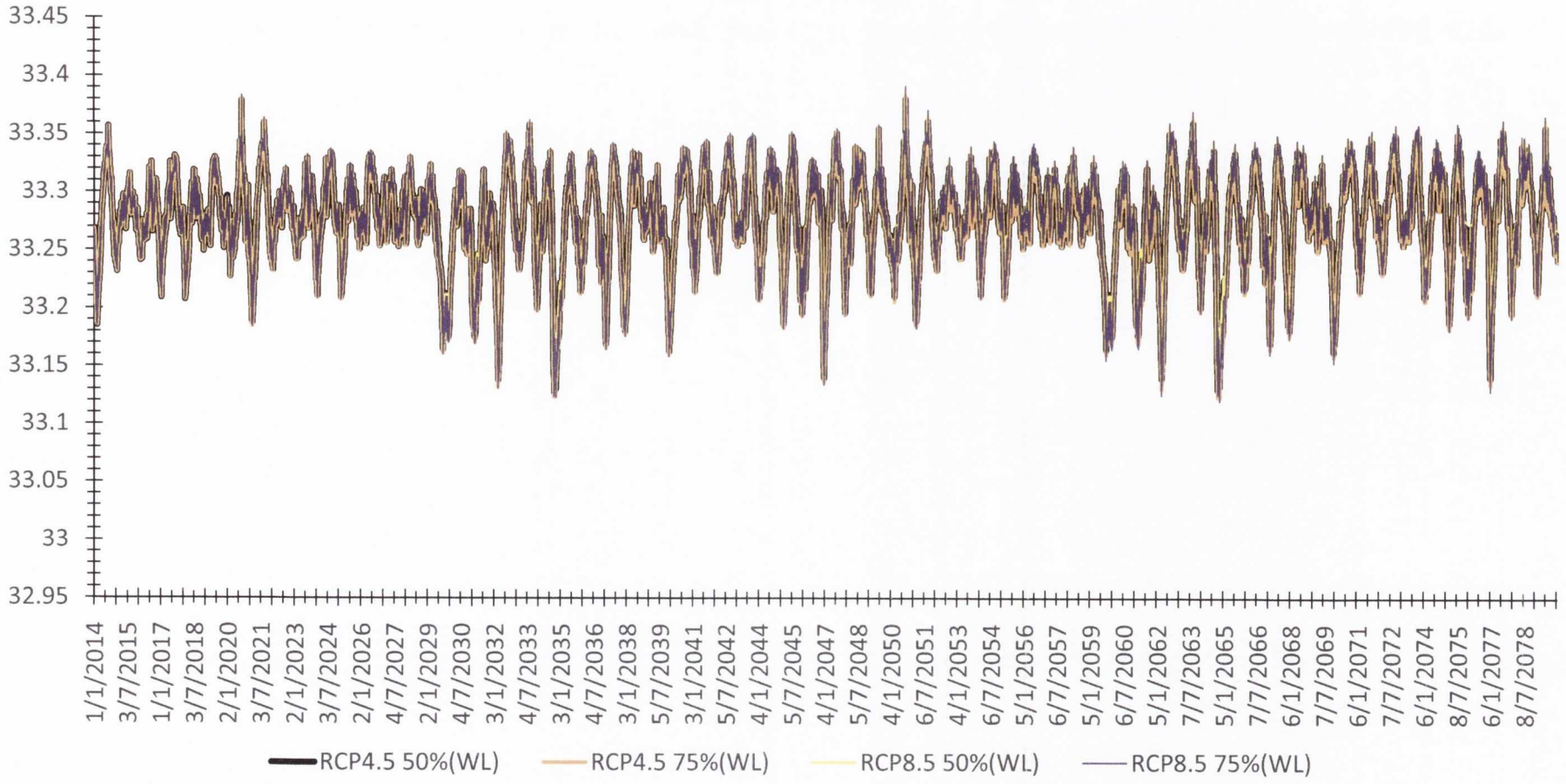

Figure 10.19: Lower-Shannon water level (m) daily projections (2014-2080) for the different four climatic scenarios using the developed WANN model.

10.5 Conclusions

This chapter presents the application of new data-driven methods for modeling and predicting daily streamflow and water level at a catchment scale. The chapter compares the use of four different models, namely artificial neural networks (ANNs), support vector machine (SVM), wavelet-ANN, and wavelet-SVM as transfer models for the results from GEO-CWB to simulate the long-term water level and flow in the Shannon River hydrological system based on the structured simplified system.

The inputs to the ANN and SVM models consist of a combination of 30-year daily time series data sets (1983-2013), which can be divided between observed data sets (maximum temperature (Tmax) (°C), minimum temperature (Tmin) (°C), water level (WL) (m) and water flow (Q)(m^3/s)) and simulated data set runoff (mm) by GEO-CWB, in addition to the 15 different lag values for each data set. The inputs for the WANN and WSVR models consist of the same data sets decomposed by wavelet transformation into their corresponding wavelet sub-time series. The models' performances are tested for the 15 different lag values and the results show that lag value of 3 performed the best.

For simulating the flow parameter on the catchment hydrological system, SVM-based transfer functions perform best overall. Regarding modeling the water level parameter on the catchment scale, the hybrid model wavelet-ANN performs the best among all the constructed models. The validated two transfer models, SVM for water flow and wavelet-ANN for water level, were then used for long-term daily simulations in the Shannon catchment system based on the different climate change scenarios.

From this chapter, it has been concluded that the hybrid WANN models perform better than the hybrid WSVM models for both water level and flow modeling and forecasting. It has been proven that data-driven models could be used as long-term multi-station large hydrological systems modeling and projection transfer functions on a catchment scale. The use of temperature as an input variable for the prediction helped in the capture of the climate effect signal into the model.

Chapter 11. Conclusions and recommendations

11.1 Conclusions

This work presents GEO-CWB as an innovative and integrated environmental modeling framework and set of tools by applying the empirical hydrological model, statistics and Machine Learning Techniques/data mining methods to a Geographic Information System. The main objective of this research is to develop a framework and a model which can be used to predict climate and land use change impacts on very large river catchments. The developed tool allows the scientific community, modelers, planners and decision makers to study the impact of climate and land use changes on water resources. The main simulation steps for this framework are (i) Climate change modeling and projection. (ii) Land use scenarios modeling and projection. (iii) Hydrological system simplifying algorithm and long-term variation analysis for historical data such as water level and streamflow. (iv) Future dynamical spatially distributed water balance projection. (v) Using Machine Learning Techniques to model and predict water level and streamflow regime.

The model uses a mixture of algorithms developed as part of this research project, commercial software and open source software. ArcMap software from ESRI was used as a platform to run all the developed algorithms and the used software. Python is the language that was used to develop all the algorithms, and it was used to connect all the simulation process together as well. RapidMiner software was connected to the developed framework by Python to act as the processor for all the machine learning techniques simulations. LanduseSim software was connected to the developed platform to be used as the CA processor for all the land cover simulations. R software was used to run all the statistical analysis that is presented in this thesis. All the climate downscaling algorithms, hydrological system simplifying algorithms, land cover CA forcing factors algorithms, PET algorithms and the dynamical water balance algorithms are developed as part of this project and written using Python language.

As GEO-CWB is a multi-stage modelling approach and each stage presents one of the main modelling steps, listed in section 1.2.2, the conclusions are presented for each step as follows:

- **Step (1): Develop a GIS algorithm to evaluate and downscale climate changes from multi GCMs ensembles and apply this algorithm to the River Shannon catchment.**

In this research, a GIS-based statistical downscaling algorithm has been developed, evaluated and used to present the significant changes in temperature, precipitation, wind speed, solar radiation, and relative humidity, which are projected for three future time intervals 2020, 2050 and 2080 using a multi-model ensemble approach. This research presents the GIS platform as a downscaling environment through a designed algorithm, which applies statistical downscaling models to multidimensional GCM-Ensembles simulations. Applying such an algorithm on a GIS platform provides a wide range of output formats for the datasets, which can be used in most of the impact models without any extra effort in formatting the output datasets. The use of a GIS platform with raster data is a powerful multidimensional downscaling tool, which gives the ability to spatially link all the variables that participated in the downscaling process. The GIS platform also allows for the control of these links through the geostatistical processors, to derive very fine scale data for future projected changes in climate. The ability to use geostatistical processors in a GIS

platform is of crucial importance for the assessment process in complex hydrological systems (such as large catchments) to estimate how much confidence can be achieved in climate change projections and subsequent impact assessments. The study shows that the differences between climate ensembles mainly depend on the original GCMs that were used in the ensembles. In this study, the comparisons between ensembles forced by two different RCPs show that there are some agreements in the climate change signal simulation in the study area. However, it is not easy to locate the changes with spatial precision and accuracy especially for precipitation, which makes the use of such results for decision-making by relevant stakeholders and practitioners problematic. The study shows that downscaling is a sensitive step when only one climate model is used for climate change simulations because of the wide uncertainty related to the choice of GCM. This study suggests that multi-climate models should be applied as an ensemble under the GIS environment for climate change simulations, especially for hydrological impact studies, as the output results in formats from the GIS platform can be used directly in the hydrological models, as raster or vector data formats.

Using a GIS platform as a downscaling environment gives the ability to capture different seasonality and spatial patterns within climate variables. For example, the study of temperature in this study shows that there are important differences between the ensembles results, especially in summer months. These differences are of interest because of how they affect the accuracy of simulations of hydrological models. It can be concluded that the uncertainty related to the downscaling process is lower than the uncertainty related to the RCP selection. Further work is still needed in the area of climate projections using a GIS platform, especially in the context of linking climate change simulations with hydrological physical-based models.

- **Step (2): Model and evaluate the long-term urban and land cover expansions and changes under GIS environment and provide the results to the River Shannon catchment scale.**

This research project presents a simulation model of urban development using the cellular automata approach incorporating fuzzy set theories and spatial information technology. Through the development of the model, the study contributes to the integration of cellular automata modeling and GIS for urban development research. It has been concluded at this stage of the study that the weakness of the Cellular Automata (CA) model is the assumption of spatial and temporal invariance for transition rules and the inability of CA to deal with stochastic behavior.

The prediction results from this stage for the Shannon Basin area indicate an increase of urban area from 1.59% in 2012 to 1.75% in 2020, which is a total of 28.53 km^2 of land which will be converted into urban areas in 2020. That means the overall change percentage from 2012 to 2020 will be 9.75%. The results for the Shannon Basin area indicate an increase of urban area from 1.59% in 2012 to 2.34% in 2050, which is a total 136.38 km^2 of land will be converted into urban areas in 2050. Also, the results indicate an increase of urban area from 1.59% in 2012 to 2.92% in 2080, which is a total 244.05 km^2 of land will be converted into urban areas in 2080. That means the overall change percentage from 2012 to 2080 will be 83.37%. Most of the urban area will come from the conversion of agricultural to urban areas; also, the small portion of the increase will be from converting wetlands and forest to an urban area. The urban expansion will be mainly around Limerick city, Ennis, Mullingar, Athlone, and Tipperary.

Using the CA within the GIS environment has a very good potential. However, this area of research needs a lot more investigations in order to make it able to accommodate the full range of

land cover class, as currently the more class the model has, the more complex and processing time-consuming it gets.

- **Step (3): Investigate the long-term variation in observed hydrological data for a simplified hydrological system using a designed GIS algorithm for the Shannon River catchment.**

In this study, a new advanced analytical approach to investigate the long-term variations and trends of a large hydrological system taking into account the spatial and the temporal variations has been developed. An integrated GIS-based algorithm has been used to simplify the large hydrological system to a structured system, which can be used for the long-term trend and variation analysis. The long-term change analysis includes a study of the changes in water level and flow hydrological variables for the Shannon River catchment. Before conducting the long-term change analyses, the data is tested with the assumption of independence, normality, and homogeneity tests using some data transformation methods to get the normality assumption valid. The analysis shows changes in the flow over the study period (1976-2015). This step of the research combines the GIS geospatial algorithms and the time series statistical decomposition functions to analyse and evaluate the spatial and temporal variations of the Shannon river catchment in Ireland.

From this step of the research, the conclusions are drawn as follows.

- The designed GIS-based algorithm for simplifying the large and complicated hydrological system is an efficient algorithm which can capture the spatial variation of the large system.
- The long-term trend analysis showed a significant increase (at the 95% confidence level) of streamflow in the Shannon river for the period of 1976–2015. Seasonal and annual streamflow analyses showed consistency with the increasing trends.

Based on this developed algorithm, a similar framework needs to be investigated and developed to the ungauged large catchments which are the catchments that do not have water level and water flow observation systems, as currently, this area of research has a huge need.

- **Step (4): Develop a GIS-based tool to calculate potential evapotranspiration depending on different methods and time scales and apply it to the River Shannon catchment.**

This work presents GIS-based algorithms to spatially estimate potential evapotranspiration (PET) within the Shannon River catchment. The ability to accurately determine PET is of decisive importance in water resource evaluation and sustainable water resource management policies as well as a host of hydrological and agricultural studies. Because of its complexity, the inherent spatial variability of PET is particularly difficult to determine for a given location. From the selection of possible approaches the use of empirical PET formulas which integrate empirical constants and meteorological data are selected as the most appropriate methods. Compared to more complex methods these relatively simple formulas require data which are monitored at a greater number of locations within the region, thus providing a more reliable spatial distribution of data. For example, temperature data, which is used in this study is taken from 96 monitoring stations whereas more complex methods would require a host of variables some of which may only be measured at four synoptic weather stations within the region or not at all.

According to the availability of data, the complexity of formulae and their appropriateness for application within a GIS, a number of methods are shortlisted. Six temperature based methods were selected which would allow for the most appropriate one to be identified. The six selected methods are applied within a GIS, and each successfully produced long-term mean monthly PET raster maps of the region. Through comparison with the Met Éireann data (based on the Penman-Monteith method), the Hamon method was found to produce the most precise results with an RMSE of 8.6 mm. The Hamon method is therefore applied for the three future time intervals (2020, 2050 and 2080) to study the effects of climate change, using the simulated four climate change scenarios, which are available through the downscaling results as derived in Chapter 4. It is found in the case of all scenarios that climate change would act to increase PET rates within the Shannon RBD. The scale of increases in PET is found to vary depending on climate change scenario and year. The maximum mean increase in PET is as a result of the 75% RCP 8.5 scenario in 2080 which returned an increase of 75.9 mm annually.

Although the developed tool provided good estimates for the PET, in my opinion, there is a need to develop an Irish PET calibrated formula based on real evapotranspiration measurements.

- **Step (5): Develop a transferable GIS framework and algorithm for dynamical water balance determination taking into account the projected climate and land use changes and apply it to the River Shannon catchment.**

Parameterizing the spatially distributed dynamic catchment water balance is a key factor in studying the hydrological system responses to climate and land use changes. This research project presents a developed GIS-based algorithm, which is designed based on integrated physical, statistical and computer learning technics algorithms.

GEO-CWB has been applied on the Shannon catchment in Ireland as an example of a large and complicated hydrological system. This application uses the output from all of the previous stages, i.e. climate and land use scenarios, as inputs in the GEO-CWB to get the results for the water balance components and the vulnerability parameters. The results of the GEO-CWB model are validated against river flow observations for the simplified and structured hydrometric station system for the Shannon River catchment. The model results are close to the observations with an average percent of error around 5 %, and the standard deviation for the validation is around 2.13 m^3/sec and the R^2 is 98.3%. The results of the validation process indicate that GEO-CWB simulates the water balance with high accuracy. This study shows the simulated annual, summer and winter water balance variables and components for the Shannon River catchment by the GEO-CWB model forced by the simulated climate change scenarios, land use scenarios and the simulated PET scenarios. The water balance simulations and projections are presented for the baseline period and four climatic scenarios, which are RCP 4.5 50%, RCP 4.5 75% RCP 8.5 50% and RCP 8.5 75%, projected for three future time steps 2020, 2050 and 2080. The results show that the largest surface runoff occurs on the rock soil group with wetlands, while the lowest values are for Luisol soil group with agricultural areas and the traceability of the soil type boundaries and the higher standard deviation values of the runoff for different soil groups indicate that Shannon's surface runoff is more influenced by soil type than by land-use. GEO-CWB provides cell by cell multidimensional dynamic subsurface water component values, which include groundwater recharge and subsurface runoff, for the catchment scale by applying the water balance calculation for each cell's subfraction, which provides a high accuracy simulation compared with the currently used approaches. The simulated annual subsurface water component

values vary through the climate change scenarios between 1% to 9% positive increasing changes from the baseline. In general, around 84% of the subsurface water component contribution occurs during the 6 months of winter season while the remaining 16% occurs in the 6 months' summer season. The largest subsurface water component is observed for the agricultural area on Podzol soils. This is attributed to the high permeability of these soils, but could partly also be due to lower evaporation rates and less runoff on the relatively gentler slopes of agricultural lands. The simulated annual interception values vary through the climate change scenarios between 0.1% to 9% positive increasing changes from the baseline. The annual rainfall interception in the Shannon River catchment makes around 11% of the total annual precipitation over the catchment. In general, around 65% of the interception occurs during the 6 months' winter season while the remaining 35% occurs in the 6 months' summer season. The maximum annual evapotranspiration in the catchment is potential evapotranspiration from open water. Evapotranspiration and interception together can be estimated to around 30-40% of the annual precipitation in the Shannon River catchment. Around 76% of the evapotranspiration takes place during the summer season, while the remaining 24% takes place during the winter season, which is obviously due to the unequal temporal distribution of the temperature but also partly to the fact that the vegetation is less active in the winter season. In general, the annual simulated evapotranspiration values vary through the climate change scenarios between the positive changes from the baseline and the negative changes from the baseline. The mean annual evapotranspiration for different land uses categories shows that urban areas have the lowest values. While overall evapotranspiration is highly influenced by precipitation and to some extent by soil texture, the standard deviation values show that evapotranspiration in the Shannon River catchment is more variable within land-use categories than within soil group. GEO-CWB produces some calculated parameters to assess the vulnerability to climate and land use changes for each climatic period and land use scenario. These parameters are the accumulated surface runoff volume, the safe yield groundwater abstraction rate and the water deficit for ideal crop growth. For example, the baseline annual areal average accumulated runoff is 14.59×10^6 m^3 as an average for all cells in the simulation domain, however, the areal average value for the accumulated runoff for the climatic period the 2080s forced by RCP 8.5 (75%) climatic scenario is 15.48×10^6 m^3, which means the average increase in the accumulated runoff is around 6%. However, the areal accumulated runoff average for the whole catchment is increased but hotspot areas spatial distribution is changed as a result of climate and land use changes.

GWO-CWB has some critical assumptions and limitations. GEO-CWB does not take into account the bedrock geologies of the catchment. Thus it provides as one of the main outputs the sub-surface water component, which includes mainly the subsurface water flow and the groundwater recharge.

Estimating the groundwater recharge is very important for the hydrological studies. Thus a very important future research activity is to expand GEO-CWB to estimate the groundwater recharge.

Also, GEO-CWB does not use the physical basis for the routing process in order to calculate the water flow. It has the unique application of using the machine learning techniques to estimate the flows, so there is potential to develop a technique with integrates the physics and the machine learning techniques to calculate flows as part of GEO-CWB.

The application of the GEO-CWB has shown good results for the simulated parameters, but the model needs further work on parameter calibration. More parameters have to be taken into account to obtain better results and surface storage is one of the main settings that need to be taken into account in the calibration process.

- **Step (6): Investigate and evaluate the integration of Machine Learning Techniques and physically based modelling under GIS environment on the hydrological modelling process of the Shannon River catchment.**

The last stage of this research project presents the application of new data-driven methods for modeling and predicting daily streamflow and water level on the catchment scale for the Shannon river catchment. The chapter compares the use of four different models, namely artificial neural networks (ANNs), support vector machine (SVM), wavelet-ANN, and wavelet-SVM as transfer models for the results from GEO-CWB to simulate the long-term water level and water flow in the Shannon River hydrological system based on the structured, simplified system. The inputs to the ANN and SVM models consist of a combination of 30-year daily time series data sets (1983-2013), which can be divided between observed data sets (maximum temperature (Tmax) (°C), minimum temperature (Tmin) (°C), water level (WL) (m) and water flow (Q)(m^3/s)) and simulated data set runoff (mm) by GEO-CWB, in addition to the 15 different lag values for each data set. The inputs for the WANN and WSVR models consist of the same data sets decomposed by wavelet transformation into their corresponding wavelet sub-time series. The models' performance was tested for the 15 different lag values, and the results show that a lag value of 3 performed the best. For simulating flow on the catchment hydrological system, SVM-based transfer functions perform best overall. Regarding modeling the water level on the catchment scale, the hybrid model wavelet-ANN performs the best among all the constructed models. The two validated transfer models, SVM for water flow and wavelet-ANN for water level, are used for long-term daily simulations in the Shannon catchment system based on the different climate change scenarios. It has been concluded that the hybrid WANN models are performing better than the hybrid WSVM models for both water level and water flow modeling and forecasting. It has been proven that data-driven models could be used as long-term multi-station large hydrological systems modeling and projection transfer functions on a catchment scale. The use of temperature as an input variable for the prediction helped in capture the climate effect signal into the model.

Using the machine learning techniques provide very good estimates for the water flow and levels. However, all the machine learning techniques are black-box modelling techniques, which are heavily depending on the data they are driven with. Using such black-box modelling techniques in hydrology provides another aspect of uncertainty. More research is needed to quantify and correct the uncertainty related to using these techniques in hydrology.

11.2 Contribution to Knowledge

As stated above, this research is concerned with addressing gaps in the state of knowledge regarding the modelling and prediction of climate and land use changes and their impacts on water resources. The main contribution of this research is a model which can be used to predict climate change in very large river catchments because existing models can only deal with small catchments.

The following key contributions to knowledge are made:

- A comprehensive literature review has been carried out to outline the state of knowledge concerning climate and land use change effects on water resources as well as the use of machine learning techniques in water resources modelling. This has identified several areas where further research is required.
- The use of GIS-Based Algorithms for GCMs' Performance Evaluation and design algorithms for statistical downscaling using GIS platform.
- Providing a GIS-based frame work for the long-term prediction of urban and land use expansion and changes under different planning scenarios for water resources modelling.
- Providing a statistical method for the long-term variation analysis of hydrological observations.
- Providing a design method and GIS-based algorithm for simplifying large and complicated hydrological systems
- Providing a GIS-based algorithm, which uses several integrated empirical methods calibrated against each other, to calculate potential evapotranspiration using meteorological data.
- The creation of an innovative and integrated environmental modelling tool (GEO-CWB) by applying Machine Learning Techniques and physically based models to a Geographic Information system (GIS) to model the spatially distributed water balance on the catchment scale based on the effects of future climate and land use changes.
- The use of integrated physical Computer Learning Techniques to model the complicated hydrological systems.
- Providing an integrated study of the impacts of climate and land-use changes on Shannon catchment as a case study, which is the most important catchment in the island of Ireland.

11.3 Published papers from this research

- **Gharbia Salem S.**, Gabor Makrai, Laurence Gill, Paul Johnston, and Francesco Pilla. "Integrated machine learning techniques, time series statistics and GIS systematic algorithms for long-term hydrological parameters modelling and prediction" (Journal paper to be submitted)

- **Gharbia Salem S.**, Laurence Gill, Paul Johnston, and Francesco Pilla. " GEO-CWB: GIS-based algorithms for parameterizing the responses of catchment dynamic water balance regarding climate and land use changes" (Journal paper to be submitted)

- **Gharbia Salem S.**, Trevor Smullen, Laurence Gill, Paul Johnston, and Francesco Pilla. "GIS algorithms based on physical and empirical formulas for spatially distributed potential evapotranspiration modelling and projection." (Journal paper to be submitted)

- **Gharbia Salem S.**, Laurence Gill, Paul Johnston, Francesco Pilla. "Future water vulnerability in Ireland: an integrated water resources, climate and land use changes model", *National Hydrology Conference, Athlone, Co. Westmeath, Ireland,* 2016. (Published)

- **Gharbia Salem S.**, Sara Abd Alfatah, Laurence Gill, Paul Johnston, and Francesco Pilla. "Land use scenarios and projections simulation using an integrated GIS cellular automata algorithms." *Modeling Earth Systems and Environment* 2, no. 3 (2016): 151. (Published)

- **Gharbia Salem S.**, Laurence Gill, Paul Johnston, Francesco Pilla. "Multi-GCM ensembles performance for climate projection on a GIS platform for the Shannon Catchment, Ireland", *Modelling Earth System and Environment,* 2016. (Published)

- **Gharbia Salem S.**, Laurence Gill, Paul Johnston, Francesco Pilla. "Using GIS-Based Algorithms for GCMs' Performance Evaluation", *IEEE*, 2016. (Published)

- **Gharbia Salem S.**, Laurence Gill, Paul Johnston, Francesco Pilla. "Trans-boundary European River's Long-term Changes Analysis for Water Level and Streamflow Regime", *42nd IAH Congress (AQUA2015), Rome, Italy*, 2015. (Published)

- **Gharbia Salem S.**, Laurence Gill, Paul Johnston, Francesco Pilla. "GEO-CWB: a Dynamic Water Balance Tool for Catchment Water Management", *5th International Multidisciplinary Conference on Hydrology and Ecology (HydroEco2015), Vienna, Austria*, 2015. (Published)

11.4 Recommendations for future research

Based on this research, future research topics and areas can be recommended as following:

- Develop a nested RCM-statistical climate model ensembles GIS-based downscaling algorithm. By this integration between the dynamical and statistical downscaling techniques, the physics behind the climate models can be introduced and transferred to the GIS downscaling process.

- Integrate the bedrock geology of the catchment in the GEO-CWB in order to simulate the groundwater recharge caps so that the subsurface flow can be separated from the groundwater recharge in the GEO-CWB simulated subsurface water component. At the current situation, GEO-CWB does not take into account the bedrock geology of the catchment, which means that it is not able to simulate the net groundwater recharge. Instead, it provides the subsurface water component which contains both ground water recharge and sub-surface runoff.

- Quantitative assessment of uncertainty for each stage in the GEO-CWB is one of the future issues to be considered. From the analysis in this study, it was difficult to choose among the available downscaling methods, GCMs, climate scenarios, land cover modelling techniques and the assumptions behind the simulations as most choices are subjective. For example, the climate scenarios data are based on sets of assumptions on geopolitics, economic and population growth rate and technical development as well. These assumptions are dependent on local dynamics of the system which cannot be provided in a quantitative term like many other climate change impact assessments. The present study has considered the soil characteristics remains the same in the future, which is not realistic but the only way to do it. There is hope from the next IPCC assessment

report to come up with the evaluation process of such changes in impact assessment, which will help in developing more accurate results from GEO-CWB.

- The GEO-CWB uncertainty space related to hydrological model structure uncertainty is not being addressed in this study. A future application of this modelling framework should include hydrological model uncertainty as an additional source of uncertainty by incorporating a multi-model approach.

- GEO-CWB can be developed to expand its applications to include:
  1. Flood warning tool based on weather forecasts.
  2. Drought analysis and predictions.
  3. Hydraulic structures management.

- Develop a GIS modeling and simplifying algorithm for the groundwater fracture system to include such a system in the water balance calculations for the large catchments.

- In the future, GEO-CWB should make use of the remotely sensed data as it is a very important source of information for the large catchment systems.

- Future application of GEO-CWB should include the water supply and irrigation system to the flow exchanges between the sub-catchments.

- Upgrade GEO-CWB to be able to use a Graphics Processing Unit (GPU) for computation, or in general try to apply this technique to the water resources modeling process, in order to be able to model very fine scale models with hundreds of parameters for the large catchments, as that will save a massive amount of model running time.

- Machine learning techniques are described as black-box modelling techniques. More investigation of machine learning techniques in the cell by cell spatially distributed water resources modeling is needed, as this area of research has a very good potential to integrate the physics behind the water balance modeling in the machine learning techniques parameterizations to develop a sort of semi-black-box technique to be used in hydrology.

References

2012. *Environmental Protection Agency (EPA)* [Online]. Available: http://www.epa.ie/soilandbiodiversity/soils/land/corine/#.VbjfhflViko [Accessed 15 February 2015].

ABAURREA, J. & ASÍN, J. 2005. Forecasting local daily precipitation patterns in a climate change scenario. *Climate Research,* 28**,** 183-197.

ABBOTT, M., BATHURST, J., CUNGE, J., O'CONNELL, P. & RASMUSSEN, J. 1986a. An introduction to the European Hydrological System—Systeme Hydrologique Europeen,"SHE", 2: Structure of a physically-based, distributed modelling system. *Journal of hydrology,* 87**,** 61-77.

ABBOTT, M. B., BATHURST, J. C., CUNGE, J. A., O'CONNELL, P. E. & RASMUSSEN, J. 1986b. An introduction to the European Hydrological System—Systeme Hydrologique Europeen,"SHE", 1: History and philosophy of a physically-based, distributed modelling system. *Journal of hydrology,* 87**,** 45-59.

ABDULLAH, J., MUHAMMAD, N. S. & JULIEN, P. Y. 2015. Hydrological Modeling in Malaysia. *ISFRAM 2014.* Springer.

ABTEW, W. 1996. Evapotranspiration measurements and modeling for three wetland systems in south florida1. Wiley Online Library.

ADAMOWSKI, J., FUNG CHAN, H., PRASHER, S. O., OZGA-ZIELINSKI, B. & SLIUSARIEVA, A. 2012. Comparison of multiple linear and nonlinear regression, autoregressive integrated moving average, artificial neural network, and wavelet artificial neural network methods for urban water demand forecasting in Montreal, Canada. *Water Resources Research,* 48.

ADAMOWSKI, J. F. 2008. Development of a short-term river flood forecasting method for snowmelt driven floods based on wavelet and cross-wavelet analysis. *Journal of Hydrology,* 353**,** 247-266.

ADAMOWSKI, K., PROKOPH, A. & ADAMOWSKI, J. 2009. Development of a new method of wavelet aided trend detection and estimation. *Hydrological Processes,* 23**,** 2686-2696.

AGUILERA, F., VALENZUELA, L. M. & BOTEQUILHA-LEITÃO, A. 2011. Landscape metrics in the analysis of urban land use patterns: A case study in a Spanish metropolitan area. *Landscape and Urban Planning,* 99**,** 226-238.

AJAMI, N. K., GUPTA, H., WAGENER, T. & SOROOSHIAN, S. 2004. Calibration of a semi-distributed hydrologic model for streamflow estimation along a river system. *Journal of Hydrology,* 298**,** 112-135.

AKGUN, A. & ERKAN, O. 2016. Landslide susceptibility mapping by geographical information system-based multivariate statistical and deterministic models: in an artificial reservoir area at Northern Turkey. *Arabian Journal of Geosciences,* 9**,** 1-15.

AKHTAR, M., AHMAD, N. & BOOIJ, M. 2008. The impact of climate change on the water resources of Hindukush–Karakorum–Himalaya region under different glacier coverage scenarios. *Journal of hydrology,* 355, 148-163.

ALFATAH, S. A. 2015. *Modelling urban expansion for Shannon River Basin area.* Master Thesis Trinity College Dublin

ALLEN, R. G. 2000. Using the FAO-56 dual crop coefficient method over an irrigated region as part of an evapotranspiration intercomparison study. *Journal of Hydrology,* 229, 27-41.

ALLEN, R. G., PEREIRA, L. S., RAES, D. & SMITH, M. 1998. Crop evapotranspiration-Guidelines for computing crop water requirements-FAO Irrigation and drainage paper 56. *FAO, Rome,* 300, D05109.

ALLEN, R. G. & PRUITT, W. O. 1986. Rational use of the FAO Blaney-Criddle formula. *Journal of Irrigation and Drainage Engineering,* 112, 139-155.

ALMEIDA, C., GLERIANI, J., CASTEJON, E. F. & SOARES-FILHO, B. 2008. Using neural networks and cellular automata for modelling intra-urban land-use dynamics. *International Journal of Geographical Information Science,* 22, 943-963.

ANCTIL, F. & TAPE, D. G. 2004. An exploration of artificial neural network rainfall-runoff forecasting combined with wavelet decomposition. *Journal of Environmental Engineering and Science,* 3, S121-S128.

ANDRÉASSIAN, V. 2004. Waters and forests: from historical controversy to scientific debate. *Journal of Hydrology,* 291, 1-27.

ANDRÉASSIAN, V., PERRIN, C. & MICHEL, C. 2004. Impact of imperfect potential evapotranspiration knowledge on the efficiency and parameters of watershed models. *Journal of Hydrology,* 286, 19-35.

ANDRÉASSON, J., LINDSTRÖM, G., GRAHN, G. & JOHANSSON, B. Runoff in Sweden: mapping of climate change impacts on hydrology. XXIII Nordic Hydrological Conference Tallinn, Estonia, 2004.

ARAÚJO, M. B., WHITTAKER, R. J., LADLE, R. J. & ERHARD, M. 2005. Reducing uncertainty in projections of extinction risk from climate change. *Global Ecology and Biogeography,* 14, 529-538.

ARNELL, N. W. & GOSLING, S. N. 2013. The impacts of climate change on river flow regimes at the global scale. *Journal of Hydrology,* 486, 351-364.

ARNOLD, J. G., ALLEN, P. M. & BERNHARDT, G. 1993. A comprehensive surface-groundwater flow model. *Journal of hydrology,* 142, 47-69.

ARNOLD, J. G., SRINIVASAN, R., MUTTIAH, R. S. & WILLIAMS, J. R. 1998. Large area hydrologic modeling and assessment part I: Model development1. Wiley Online Library.

ARSANJANI, J. J., HELBICH, M., KAINZ, W. & BOLOORANI, A. D. 2013. Integration of logistic regression, Markov chain and cellular automata models to simulate urban expansion. *International Journal of Applied Earth Observation and Geoinformation,* 21, 265-275.

ASSESSMENT, S. C.-B. F. R. 2013. Hydrology Report Unit of Management 25/26 Draft Report.

AZIZ, K., RAHMAN, A., FANG, G. & SHRESTHA, S. 2014. Application of artificial neural networks in regional flood frequency analysis: a case study for Australia. *Stochastic environmental research and risk assessment,* 28, 541-554.

AZIZ, K., RAHMAN, A., SHAMSELDIN, A. & SHOAIB, M. Regional flood estimation in Australia: Application of gene expression programming and artificial neural network techniques. Proceedings of 20th International Congress on Modelling and Simulation, Adelaide, 2013.

BAE, D.-H., JUNG, I. W. & CHANG, H. 2008. Potential changes in Korean water resources estimated by high-resolution climate simulation. *Climate Research,* 35, 213-226.

BAI, S., LÜ, G., WANG, J., ZHOU, P. & DING, L. 2011. GIS-based rare events logistic regression for landslide-susceptibility mapping of Lianyungang, China. *Environmental Earth Sciences,* 62, 139-149.

BALZTER, H., BRAUN, P. W. & KÖHLER, W. 1998. Cellular automata models for vegetation dynamics. *Ecological Modelling,* 107, 113-125.

BARON, J. S., POFF, N. L., ANGERMEIER, P. L., DAHM, C. N., GLEICK, P. H., HAIRSTON JR, N. G., JACKSON, R. B., JOHNSTON, C. A., RICHTER, B. D. & STEINMAN, A. D. 2002. Meeting ecological and societal needs for freshwater. *Ecological Applications,* 12, 1247-1260.

BARREDO, J. I. & DEMICHELI, L. 2003. Urban sustainability in developing countries' megacities: modelling and predicting future urban growth in Lagos. *Cities,* 20, 297-310.

BARREDO, J. I., KASANKO, M., MCCORMICK, N. & LAVALLE, C. 2003. Modelling dynamic spatial processes: simulation of urban future scenarios through cellular automata. *Landscape and Urban Planning,* 64, 145-160.

BASTOLA, S., MURPHY, C. & SWEENEY, J. 2011. The role of hydrological modelling uncertainties in climate change impact assessments of Irish river catchments. *Advances in Water Resources,* 34, 562-576.

BATELAAN, O. & DE SMEDT, F. 2001. WetSpass: a flexible, GIS based, distributed recharge methodology for regional groundwater modelling. *IAHS PUBLICATION*, 11-18.

BATELAAN, O. & DE SMEDT, F. 2007. GIS-based recharge estimation by coupling surface–subsurface water balances. *Journal of hydrology,* 337, 337-355.

BATTY, M. 1997. Cellular Automata and Urban Form: A Primer. *Journal of the American Planning Association,* 63, 266-274.

BATTY, M. 1998. Urban evolution on the desktop: simulation with the use of extended cellular automata. *Environment and Planning A,* 30, 1943-1967.

BATTY, M. 2007. *Cities and complexity: understanding cities with cellular automata, agent-based models, and fractals*, The MIT press.

BATTY, M. 2009. Urban modeling. *International Encyclopedia of Human Geography. Oxford, UK: Elsevier.*

BATTY, M., XIE, Y. & SUN, Z. 1999. Modeling urban dynamics through GIS-based cellular automata. *Computers, environment and urban systems,* 23, 205-233.

BEIGI, E. & TSAI, F. T.-C. 2014. GIS-based water budget framework for high-resolution groundwater recharge estimation of large-scale humid regions. *Journal of Hydrologic Engineering*.

BERGKAMP, G. J. J., ORLANDO, B. & BURTON, I. 2003. *Change: adaptation of water resources management to climate change*, IUCN.

BERGSTRÖM, S. & FORSMAN, A. 1973. Development of a conceptual deterministic rainfall-runoff model. *Hydrology Research,* 4, 147-170.

BERKHOUT, F., HERTIN, J. & JORDAN, A. 2002. Socio-economic futures in climate change impact assessment: using scenarios as 'learning machines'. *Global Environmental Change,* 12, 83-95.

BERLING-WOLFF, S. & WU, J. 2004. Modeling urban landscape dynamics: A review. *Ecological Research,* 19, 119-129.

BERRY, P., DAWSON, T., HARRISON, P. & PEARSON, R. 2002. Modelling potential impacts of climate change on the bioclimatic envelope of species in Britain and Ireland. *Global Ecology and Biogeography,* 11, 453-462.

BEVEN, K. 1979. A sensitivity analysis of the Penman-Monteith actual evapotranspiration estimates. *Journal of hydrology,* 44, 169-190.

BEVEN, K. 1996. The limits of splitting: Hydrology. *Science of the Total Environment,* 183, 89-97.

BEVEN, K. 2001. How far can we go in distributed hydrological modelling? *Hydrology and Earth System Sciences Discussions,* 5, 1-12.

BEVEN, K. & KIRKBY, M. J. 1979. A physically based, variable contributing area model of basin hydrology/Un modèle à base physique de zone d'appel variable de l'hydrologie du bassin versant. *Hydrological Sciences Journal,* 24, 43-69.

BEVEN, K. J. 2006. *Streamflow generation processes*, IAHS Press.

BHADURI, B., HARBOR, J., ENGEL, B. & GROVE, M. 2000. Assessing watershed-scale, long-term hydrologic impacts of land-use change using a GIS-NPS model. *Environmental Management,* 26, 643-658.

BLANEY, H. F. & CRIDDLE, W. D. 1964. Determining water requirements for settling water disputes. *Nat. Resources J.,* 4, 29.

BOÉ, J., TERRAY, L., HABETS, F. & MARTIN, E. 2007. Statistical and dynamical downscaling of the Seine basin climate for hydro-meteorological studies. *International Journal of Climatology,* 27, 1643-1655.

Bohr, J., 2014. Public views on the dangers and importance of climate change: predicting climate change beliefs in the United States through income moderated by party identification. Climatic change, 126(1-2), pp.217-227.

BOOTH, B. 2000. *Using ArcGIS 3D analyst: GIS by ESRI*, Esri Press.

BOURNE, L. S. 1982. *Internal structure of the city: readings on urban form, growth, and policy*, Oxford University Press.

BOWERMAN, B. L. & O'CONNELL, R. T. 1993. Forecasting and time series: An applied approach. 3rd.

BOX, G. E., JENKINS, G. M., REINSEL, G. C. & LJUNG, G. M. 2015. *Time series analysis: forecasting and control*, John Wiley & Sons.

BOX, G. E. & PIERCE, D. A. 1970. Distribution of residual autocorrelations in autoregressive-integrated moving average time series models. *Journal of the American Statistical Association,* 65, 1509-1526.

BRADBURY, J. A., DINGMAN, S. L. & KEIM, B. D. 2002. New England Drought and Relations with Large Scale Atmospheric Circulation Patterns1. Wiley Online Library.

BRAUD, I., DANTAS-ANTONINO, A., VAUCLIN, M., THONY, J. & RUELLE, P. 1995. A simple soil-plant-atmosphere transfer model (SiSPAT) development and field verification. *Journal of hydrology,* 166, 213-250.

BROWN, D. G., RIOLO, R., ROBINSON, D. T., NORTH, M. & RAND, W. 2005. Spatial process and data models: Toward integration of agent-based models and GIS. *Journal of Geographical Systems,* 7, 25-47.

BROWN, D. G. & ROBINSON, D. T. 2006. Effects of heterogeneity in residential preferences on an agent-based model of urban sprawl. *Ecology and society,* 11, 46.

BURRUS, C. S., GOPINATH, R. A. & GUO, H. 1997. Introduction to wavelets and wavelet transforms: a primer.

BUSS, T. F. 2001. The effect of state tax incentives on economic growth and firm location decisions: An overview of the literature. *Economic Development Quarterly,* 15, 90-105.

CALDER, I. & NEWSON, M. D. 1979. LAND-USE AND UPLAND WATER RESOURCES IN BRITAIN-A STRATEGIC LOOK1. *JAWRA Journal of the American Water Resources Association,* 15, 1628-1639.

CALDER, I., WRIGHT, I. & MURDIYARSO, D. 1986. A study of evaporation from tropical rain forest—West Java. *Journal of hydrology,* 89, 13-31.

CALDER, I. R. 1986. A stochastic model of rainfall interception. *Journal of hydrology,* 89, 65-71.

CAMPBELL, D. J., LUSCH, D. P., SMUCKER, T. A. & WANGUI, E. E. 2005. Multiple methods in the study of driving forces of land use and land cover change: a case study of SE Kajiado District, Kenya. *Human Ecology,* 33, 763-794.

CARUSO, G., ROUNSEVELL, M. & COJOCARU, G. 2005. Exploring a spatio-dynamic neighbourhood-based model of residential behaviour in the Brussels periurban area. *International Journal of Geographical Information Science,* 19, 103-123.

CHANGE, C. 2007. IPCC Fourth Assessment Report. *The Physical Science Basis*.

CHANGE, I. C. 2013. The physical science basis. Contribution of working group I to the fifth assessment report of the intergovernmental panel on climate change. *K., Tignor, M., Allen, SK, Boschung, J., Nauels, A., Xia, Y., Bex, V., Midgley, PM, Eds*, 1535.

CHANGE, I. P. O. C. 2007c. Climate change 2007: The physical science basis. *Agenda,* 6, 333.

CHARLTON, R., FEALY, R., MOORE, S., SWEENEY, J. & MURPHY, C. 2006. Assessing the impact of climate change on water supply and flood hazard in Ireland using statistical downscaling and hydrological modelling techniques. *Climatic change,* 74, 475-491.

CHATTOPADHYAY, N. & HULME, M. 1997. Evaporation and potential evapotranspiration in India under conditions of recent and future climate change. *Agricultural and Forest Meteorology,* 87, 55-73.

CHATTOPADHYAY, P. B. & RANGARAJAN, R. 2014. Application of ANN in sketching spatial nonlinearity of unconfined aquifer in agricultural basin. *Agricultural Water Management,* 133, 81-91.

CHEN, C.-W., WEI, C.-C., LIU, H.-J. & HSU, N.-S. 2014. Application of neural networks and optimization model in conjunctive use of surface water and groundwater. *Water resources management,* 28, 2813-2832.

CHEN, D., ACHBERGER, C., RÄISÄNEN, J. & HELLSTRÖM, C. 2006. Using statistical downscaling to quantify the GCM-related uncertainty in regional climate change scenarios: A case study of Swedish precipitation. *Advances in Atmospheric Sciences,* 23, 54-60.

CHEN, J., BRISSETTE, F. P. & LECONTE, R. 2011. Uncertainty of downscaling method in quantifying the impact of climate change on hydrology. *Journal of Hydrology,* 401, 190-202.

CHEN, M., LU, D. & ZHA, L. 2010. The comprehensive evaluation of China's urbanization and effects on resources and environment. *Journal of Geographical Sciences,* 20, 17-30.

CHEN, Q. & MYNETT, A. E. 2003. Effects of cell size and configuration in cellular automata based prey–predator modelling. *Simulation Modelling Practice and Theory,* 11, 609-625.

CHEN, Y., LI, X., LIU, X., AI, B. & LI, S. 2016. Capturing the varying effects of driving forces over time for the simulation of urban growth by using survival analysis and cellular automata. *Landscape and Urban Planning,* 152, 59-71.

CHEN, Z., CHEN, Y. & LI, B. 2013. Quantifying the effects of climate variability and human activities on runoff for Kaidu River Basin in arid region of northwest China. *Theoretical and Applied Climatology,* 111, 537-545.

CHENG, C., CHAU, K., SUN, Y. & LIN, J. Long-term prediction of discharges in Manwan Reservoir using artificial neural network models. International Symposium on Neural Networks, 2005. Springer, 1040-1045.

CHENG, J. & MASSER, I. 2003. Urban growth pattern modeling: a case study of Wuhan city, PR China. *Landscape and urban planning,* 62, 199-217.

CHIANG, W.-Y. K., ZHANG, D. & ZHOU, L. 2006. Predicting and explaining patronage behavior toward web and traditional stores using neural networks: a comparative analysis with logistic regression. *Decision Support Systems,* 41, 514-531.

CHIEW, F., HARROLD, T., SIRIWARDENENA, L., JONES, R. & SRIKANTHAN, R. Simulation of climate change impact on runoff using rainfall scenarios that

consider daily patterns of change from GCMs. MODSIM 2003: International Congress on Modelling and Simulation: Proceedings, 2003. Modelling and Simulation Society of Australia and New Zealand, Canberra ACT, Townsville, 154-159.

CHO, H. & SWARTZLANDER, E. E. 2007. Adder designs and analyses for quantum-dot cellular automata. *Nanotechnology, IEEE Transactions on,* 6, 374-383.

CHOAT, B., JANSEN, S., BRODRIBB, T. J., COCHARD, H., DELZON, S., BHASKAR, R., BUCCI, S. J., FEILD, T. S., GLEASON, S. M. & HACKE, U. G. 2012. Global convergence in the vulnerability of forests to drought. *Nature,* 491, 752-755.

CHOI, W. & DEAL, B. M. 2008. Assessing hydrological impact of potential land use change through hydrological and land use change modeling for the Kishwaukee River basin (USA). *Journal of Environmental Management,* 88, 1119-1130.

CHUANYAN, Z., ZHONGREN, N. & ZHAODONG, F. 2004. GIS-assisted spatially distributed modeling of the potential evapotranspiration in semi-arid climate of the Chinese Loess Plateau. *Journal of Arid Environments,* 58, 387-403.

CLARKE, K. C. & GAYDOS, L. J. 1998. Loose-coupling a cellular automaton model and GIS: long-term urban growth prediction for San Francisco and Washington/Baltimore. *International Journal of Geographical Information Science,* 12, 699-714.

CLARKE, K. C., HOPPEN, S. & GAYDOS, L. 1997. A self-modifying cellular automaton model of historical urbanization in the San Francisco Bay area. *Environment and Planning B: Planning and Design,* 24, 247-261.

CLARKE, L., EDMONDS, J., JACOBY, H., PITCHER, H., REILLY, J. & RICHELS, R. 2007. Scenarios of greenhouse gas emissions and atmospheric concentrations. *US Department of Energy Publications*, 6.

COHEN, B. 2004. Urban growth in developing countries: a review of current trends and a caution regarding existing forecasts. *World development,* 32, 23-51.

COPPIN, P., JONCKHEERE, I., NACKAERTS, K., MUYS, B. & LAMBIN, E. 2004. Review ArticleDigital change detection methods in ecosystem monitoring: a review. *International Journal of Remote Sensing,* 25, 1565-1596.

COPPOLA JR, E., SZIDAROVSZKY, F., POULTON, M. & CHARLES, E. 2003. Artificial neural network approach for predicting transient water levels in a multilayered groundwater system under variable state, pumping, and climate conditions. *Journal of Hydrologic Engineering,* 8, 348-360.

COUCLELIS, H. 1985. Cellular worlds: a framework for modeling micro - macro dynamics. *Environment and Planning A,* 17, 585-596.

COUCLELIS, H. 1988. Of mice and men: what rodent populations can teach us about complex spatial dynamics. *Environment and Planning A,* 20, 99-109.

COUCLELIS, H. 1997. *Environment and Planning B: Planning and Design,* 24, 165.

COUCLELIS, H. 2000. From sustainable transportation to sustainable accessibility: can we avoid a new tragedy of the commons? *Information, Place, and Cyberspace.* Springer.

COULIBALY, P. & BALDWIN, C. K. 2005. Nonstationary hydrological time series forecasting using nonlinear dynamic methods. *Journal of Hydrology,* 307, 164-174.

CRANE, R. G. & HEWITSON, B. C. 1998. Doubled CO2 precipitation changes for the Susquehanna Basin: Down-scaling from the Genesis general circulation model. *International Journal of Climatology,* 18, 65-76.

CRAWFORD, N. H. & LINSLEY, R. K. 1966. Digital Simulation in Hydrology'Stanford Watershed Model 4.

CROSBIE, R. S., DAWES, W. R., CHARLES, S. P., MPELASOKA, F. S., ARYAL, S., BARRON, O. & SUMMERELL, G. K. 2011. Differences in future recharge estimates due to GCMs, downscaling methods and hydrological models. *Geophysical Research Letters,* 38.

DALY, C., GIBSON, W. P., TAYLOR, G. H., JOHNSON, G. L. & PASTERIS, P. 2002. A knowledge-based approach to the statistical mapping of climate. *Climate research,* 22, 99-113.

DANIELL, T. Neural networks. Applications in hydrology and water resources engineering. National Conference Publication- Institute of Engineers. Australia, 1991.

DE BOER, D. H. 1992. Constraints on spatial transference of rainfall-runoff relationships in semiarid basins drained by ephemeral streams. *Hydrological sciences journal,* 37, 491-504.

DE BRUIN, H. 1983. A model for the Priestley-Taylor parameter α. *Journal of climate and applied meteorology,* 22, 572-578.

DE ROO, A., SCHMUCK, G., PERDIGAO, V. & THIELEN, J. 2003. The influence of historic land use changes and future planned land use scenarios on floods in the Oder catchment. *Physics and Chemistry of the Earth, Parts A/B/C,* 28, 1291-1300.

DEFRIES, R. & ESHLEMAN, K. N. 2004. Land-use change and hydrologic processes: A major focus for the future. *Hydrological processes,* 18, 2183-2186.

DEFRIES, R. S., RUDEL, T., URIARTE, M. & HANSEN, M. 2010. Deforestation driven by urban population growth and agricultural trade in the twenty-first century. *Nature Geoscience,* 3, 178-181.

DEKA, P. C. 2014. Support vector machine applications in the field of hydrology: a review. *Applied soft computing,* 19, 372-386.

DENG, J. S., WANG, K., HONG, Y. & QI, J. G. 2009. Spatio-temporal dynamics and evolution of land use change and landscape pattern in response to rapid urbanization. *Landscape and Urban Planning,* 92, 187-198.

DEUTSCH, A. & DORMANN, S. 2007. *Cellular automaton modeling of biological pattern formation: characterization, applications, and analysis*, Springer Science & Business Media.

DEWAN, A. & YAMAGUCHI, Y. 2009. Using remote sensing and GIS to detect and monitor land use and land cover change in Dhaka Metropolitan of Bangladesh during 1960–2005. *Environmental Monitoring and Assessment,* 150, 237-249.

DHANYA, C. & NAGESH KUMAR, D. 2011. Predictive uncertainty of chaotic daily streamflow using ensemble wavelet networks approach. *Water Resources Research,* 47.

DIAZ-NIETO, J. & WILBY, R. L. 2005. A comparison of statistical downscaling and climate change factor methods: impacts on low flows in the River Thames, United Kingdom. *Climatic change,* 69, 245-268.

DIBIKE, Y. B. & COULIBALY, P. 2005. Hydrologic impact of climate change in the Saguenay watershed: comparison of downscaling methods and hydrologic models. *Journal of hydrology,* 307, 145-163.

DIBIKE, Y. B., VELICKOV, S., SOLOMATINE, D. & ABBOTT, M. B. 2001. Model induction with support vector machines: introduction and applications. *Journal of Computing in Civil Engineering*.

DIRECTIVE, W. F. 2000. EU Water framework directive. Directive 2000/60/EC.

DOLMAN, A. & NONHEBEL, S. 1988. Modelling forest water consumption in The Netherlands. *Agricultural water management,* 14, 413-422.

DROOGERS, P. & ALLEN, R. G. 2002. Estimating reference evapotranspiration under inaccurate data conditions. *Irrigation and drainage systems,* 16, 33-45.

DU, H. & MULLEY, C. 2006. Relationship between transport accessibility and land value: Local model approach with geographically weighted regression. *Transportation Research Record: Journal of the Transportation Research Board,* 197-205.

DUFRESNE, J.-L., FOUJOLS, M.-A., DENVIL, S., CAUBEL, A., MARTI, O., AUMONT, O., BALKANSKI, Y., BEKKI, S., BELLENGER, H. & BENSHILA, R. 2013. Climate change projections using the IPSL-CM5 Earth System Model: from CMIP3 to CMIP5. *Climate Dynamics,* 40, 2123-2165.

DUNIN, F., O'LOUGHLIN, E. & REYENGA, W. 1988. Interception loss from eucalypt forest: lysimeter determination of hourly rates for long term evaluation. *Hydrological processes,* 2, 315-329.

DUNNE, T. & LEOPOLD, L. B. 1978. *Water in environmental planning*, Macmillan.

DUPONT, A. 2008. The strategic implications of climate change. *Survival,* 50, 29-54.

EBTEHAJ, I. & BONAKDARI, H. 2013. Evaluation of sediment transport in sewer using artificial neural network. *Engineering Applications of Computational Fluid Mechanics,* 7, 382-392.

ELLIS, C. J., COPPINS, B. J., DAWSON, T. P. & SEAWARD, M. R. 2007. Response of British lichens to climate change scenarios: trends and uncertainties in the projected impact for contrasting biogeographic groups. *Biological Conservation,* 140, 217-235.

ENGLER, S. & WERNER, J. P. 2015. Processes Prior and during the Early 18th Century Irish Famines—Weather Extremes and Migration. *Climate,* 3, 1035-1056.

EPA. 2012. *Environmental Protection Agency (EPA)* [Online]. Available: http://www.epa.ie/soilandbiodiversity/soils/land/corine/#.VbjfhflViko [Accessed 15 February 2015].

EPA. 2015. *Corine Land Cover Mapping, EPA* [Online]. Environmental Agency Protection (EPA)
Available: http://www.epa.ie/soilandbiodiversity/soils/land/corine/#.Vbo-2_lViko [Accessed 20 June 2015].

ESPANA, S., ALCALA, F. J., VALLEJOS, A. & PULIDO-BOSCH, A. 2011. ArcE: A GIS tool for modelling actual evapotranspiration. *Computers & geosciences,* 37, 1468-1475.

ESPER, J., FRANK, D., BÜNTGEN, U., VERSTEGE, A., LUTERBACHER, J. & XOPLAKI, E. 2007. Long-term drought severity variations in Morocco. *Geophysical Research Letters,* 34.

EVANS, D. The habitats of the European Union habitats directive. Biology and Environment: Proceedings of the Royal Irish Academy, 2006. JSTOR, 167-173.

FAN, J., TIAN, F., YANG, Y., HAN, S. & QIU, G. 2010. Quantifying the magnitude of climate and human effect on runoff decline in Mian River Basin via SWAT model. *Water Science and Technology—Water Supply,* 62, 783-791.

FEALY, R. & SWEENEY, J. 2008. Statistical downscaling of temperature, radiation and potential evapotranspiration to produce a multiple GCM ensemble mean for a selection of sites in Ireland. *Irish Geography,* 41, 1-27.

FEDERER, C. 1979. A soil-plant-atmosphere model for transpiration and availability of soil water. *Water Resources Research,* 15, 555-562.

FEDERER, C., VÖRÖSMARTY, C. & FEKETE, B. 1996. Intercomparison of methods for calculating potential evaporation in regional and global water balance models. *Water Resources Research,* 32, 2315-2321.

FENNESSEY, N. M. & VOGEL, R. M. 1996. Regional models of potential evaporation and reference evapotranspiration for the northeast USA. *Journal of Hydrology,* 184, 337-354.

FITZSIMONS, V. P. & MISSTEAR, B. D. 2006. Estimating groundwater recharge through tills: a sensitivity analysis of soil moisture budgets and till properties in Ireland. *Hydrogeology Journal,* 14, 548-561.

FLACHE, A. & HEGSELMANN, R. 2001. Do irregular grids make a difference? Relaxing the spatial regularity assumption in cellular models of social dynamics. *Journal of Artificial Societies and Social Simulation,* 4.

FOLEY, J. A., DEFRIES, R., ASNER, G. P., BARFORD, C., BONAN, G., CARPENTER, S. R., CHAPIN, F. S., COE, M. T., DAILY, G. C., GIBBS, H. K., HELKOWSKI, J. H., HOLLOWAY, T., HOWARD, E. A., KUCHARIK, C. J., MONFREDA, C., PATZ, J. A., PRENTICE, I. C., RAMANKUTTY, N. & SNYDER, P. K. 2005. Global Consequences of Land Use. *Science,* 309, 570-574.

FOOD AND AGRICULTURE ORGANIZATION , F. 1995. Planning for sustainable use of land resources. *FAO LAND AND WATER BULLETIN 2,* Land and Water Development Division.

FOODY, G. M. 2002. Status of land cover classification accuracy assessment. *Remote Sensing of Environment,* 80, 185-201.

FOWLER, H., BLENKINSOP, S. & TEBALDI, C. 2007. Linking climate change modelling to impacts studies: recent advances in downscaling techniques for hydrological modelling. *International journal of climatology,* 27, 1547-1578.

FREEZE, R. A. & HARLAN, R. 1969. Blueprint for a physically-based, digitally-simulated hydrologic response model. *Journal of Hydrology,* 9, 237-258.

FREI, A., ARMSTRONG, R. L., CLARK, M. P. & SERREZE, M. C. 2002. Catskill Mountain water resources: vulnerability, hydroclimatology, and climate-change sensitivity. *Annals of the Association of American Geographers,* 92, 203-224.

FUJIHARA, Y., TANAKA, K., WATANABE, T., NAGANO, T. & KOJIRI, T. 2008. Assessing the impacts of climate change on the water resources of the Seyhan River Basin in Turkey: Use of dynamically downscaled data for hydrologic simulations. *Journal of Hydrology,* 353, 33-48.

GARBRECHT, J. D. & PIECHOTA, T. C. 2006. *Climate variations, climate change, and water resources engineering*, American Society of Civil Engineers.

GASH, J., WRIGHT, I. & LLOYD, C. R. 1980. Comparative estimates of interception loss from three coniferous forests in Great Britain. *Journal of hydrology,* 48, 89-105.

GAUTAM, M. & ACHARYA, K. 2012. Streamflow trends in Nepal. *Hydrological sciences journal,* 57, 344-357.

GEBREYOHANNES, T., DE SMEDT, F., WALRAEVENS, K., GEBRESILASSIE, S., HUSSIEN, A., HAGOS, M., AMARE, K., DECKERS, J. & GEBREHIWOT, K. 2013. Application of a spatially distributed water balance model for assessing surface water and groundwater resources in the Geba basin, Tigray, Ethiopia. *Journal of hydrology,* 499, 110-123.

GEERTMAN, S., HAGOORT, M. & OTTENS, H. 2007. Spatial-temporal specific neighbourhood rules for cellular automata land-use modelling. *International Journal of Geographical Information Science,* 21, 547-568.

GEURS, K. T. & VAN WEE, B. 2004. Accessibility evaluation of land-use and transport strategies: review and research directions. *Journal of Transport geography,* 12, 127-140.

GHANBARPOUR, M. R., ABBASPOUR, K. C. & HIPEL, K. W. 2009. A comparative study in long-term river flow forecasting models. *International Journal of River Basin Management,* 7, 403-413.

GHARBIA, S. S., AISH, A. & PILLA, F. 2015a. Impacts of Climate Change on a Spatially Distributed Water Balance in the Gaza Strip, Palestine. *Journal of Environment and Earth Science,* 5, 76-91.

GHARBIA, S. S., AISH, A. & PILLA, F. 2015c. Modelling Potential Impacts of Climate Change on Groundwater of the Gaza Coastal Aquifer from Ensemble of Global Climate Model Projections. *Civil and Environmental Research,* 7, 44-60.

GHARBIA, S. S., AISH, A., PILLA, F. & GHARBIA, A. S. 2015e. Potential Effects of Climate Change on Groundwater Recharge-a Case Study of the Gaza Strip, Palestine.

GHARBIA, S. S., ALFATAH, S. A., GILL, L., JOHNSTON, P. & PILLA, F. 2016a. Land use scenarios and projections simulation using an integrated GIS cellular automata algorithms. *Modeling Earth Systems and Environment,* 2, 151.

GHARBIA, S. S., GILL, L., JOHNSTON, P. & PILLA, F. GEO-CWB: a Dynamic Water Balance Tool for Catchment Water Management. 5th International Multidisciplinary Conference on Hydrology and Ecology (HydroEco2015), At Vienna, Austria, 2015f.

GHARBIA, S. S., GILL, L., JOHNSTON, P. & PILLA, F. 2016b. Using GIS Based Algorithms for GCMs' Performance Evaluation. *18th IEEE Mediterranean Electrotechnical Conference MELECON 2016.* Cyprus: IEEE.

GHORBANI, M. A., KHATIBI, R., GOEL, A., FAZELIFARD, M. H. & AZANI, A. 2016a. Modeling river discharge time series using support vector machine and artificial neural networks. *Environmental Earth Sciences,* 75, 1-13.

GHORBANI, M. A., ZADEH, H. A., ISAZADEH, M. & TERZI, O. 2016b. A comparative study of artificial neural network (MLP, RBF) and support vector machine models for river flow prediction. *Environmental Earth Sciences,* 75, 1-14.

GILL, L., NAUGHTON, O., JOHNSTON, P., BASU, B. & GHOSH, B. 2013. Characterisation of hydrogeological connections in a lowland karst network using time series analysis of water levels in ephemeral groundwater-fed lakes (turloughs). *Journal of Hydrology,* 499, 289-302.

GIORGI, F., CHRISTENSEN, J., HULME, M., VON STORCH, H., WHETTON, P., JONES, R., MEARNS, L., FU, C., ARRITT, R. & BATES, B. 2001. Regional climate information-evaluation and projections. *Climate Change 2001: The Scientific Basis. Contribution of Working Group to the Third Assessment Report of the Intergouvernmental Panel on Climate Change [Houghton, JT et al.(eds)]. Cambridge University Press, Cambridge, United Kongdom and New York, US.*

GIUDICI, M. 2002. Development, calibration, and validation of physical models. *Clarke, K.C., Parks, B.O., & Crane, M.P. (Eds.),* Geographic Information Systems and Environmental Modeling.

GORDON, D. R. 1998. Effects of invasive, non-indigenous plant species on ecosystem processes: lessons from Florida. *Ecological Applications,* 8, 975-989.

GOSLING, S. N., ZAHERPOUR, J., MOUNT, N. J., HATTERMANN, F. F., DANKERS, R., ARHEIMER, B., BREUER, L., DING, J., HADDELAND, I. & KUMAR, R. 2016. A comparison of changes in river runoff from multiple global and catchment-scale hydrological models under global warming scenarios of 1° C, 2° C and 3° C. *Climatic Change,* 1-19.

GRAHAM, L. P., ANDRÉASSON, J. & CARLSSON, B. 2007. Assessing climate change impacts on hydrology from an ensemble of regional climate models, model scales and linking methods–a case study on the Lule River basin. *Climatic Change,* 81, 293-307.

GRANGER, R. 1989. A complementary relationship approach for evaporation from nonsaturated surfaces. *Journal of Hydrology,* 111, 31-38.

GRAYSON, R. B., MOORE, I. D. & MCMAHON, T. A. 1992. Physically based hydrologic modeling: 1. A terrain-based model for investigative purposes. *Water resources research,* 28, 2639-2658.

GRIMM, N. B., GROVE, J. G., PICKETT, S. T. & REDMAN, C. L. 2000. Integrated Approaches to Long-Term Studies of Urban Ecological Systems Urban ecological systems present multiple challenges to ecologists—pervasive human impact and extreme heterogeneity of cities, and the need to integrate social and ecological approaches, concepts, and theory. *BioScience,* 50, 571-584.

GROTCH, S. L. & MACCRACKEN, M. C. 1991. The use of general circulation models to predict regional climatic change. *Journal of Climate,* 4, 286-303.

HAITJEMA, H. M. & MITCHELL-BRUKER, S. 2005. Are water tables a subdued replica of the topography? *Ground water,* 43, 781-786.

HAMON, W. R. 1961. Estimating potential evapotranspiration. *Journal of the Hydraulics Division,* 87, 107-120.

HARGREAVES, G. H. & SAMANI, Z. A. 1982. Estimating potential evapotranspiration. *Journal of the Irrigation and Drainage Division,* 108, 225-230.

HARGREAVES, G. H. & SAMANI, Z. A. 1985. Reference crop evapotranspiration from temperature. *Applied engineering in agriculture,* 1, 96-99.

HATCH, C. E., FISHER, A. T., REVENAUGH, J. S., CONSTANTZ, J. & RUEHL, C. 2006. Quantifying surface water–groundwater interactions using time series analysis of streambed thermal records: Method development. *Water Resources Research,* 42.

HAY, L. E. & CLARK, M. 2003. Use of statistically and dynamically downscaled atmospheric model output for hydrologic simulations in three mountainous basins in the western United States. *Journal of hydrology,* 282, 56-75.

HAY, L. E., WILBY, R. L. & LEAVESLEY, G. H. 2000. A comparison of delta change and downscaled GCM scenarios for three mounfainous basins in THE UNITED STATES1. Wiley Online Library.

HE, C., OKADA, N., ZHANG, Q., SHI, P. & LI, J. 2008. Modelling dynamic urban expansion processes incorporating a potential model with cellular automata. *Landscape and urban planning,* 86, 79-91.

HE, C., OKADA, N., ZHANG, Q., SHI, P. & ZHANG, J. 2006. Modeling urban expansion scenarios by coupling cellular automata model and system dynamic model in Beijing, China. *Applied Geography,* 26, 323-345.

HEPPENSTALL, A. J., CROOKS, A. T., SEE, L. M. & BATTY, M. 2011. *Agent-based models of geographical systems*, Springer Science & Business Media.

HERNANDEZ, M., MILLER, S. N., GOODRICH, D. C., GOFF, B. F., KEPNER, W. G., EDMONDS, C. M. & JONES, K. B. 2000. Modeling runoff response to land cover and rainfall spatial variability in semi-arid watersheds. *Monitoring Ecological Condition in the Western United States.* Springer.

HEROLD, M., COUCLELIS, H. & CLARKE, K. C. 2005. The role of spatial metrics in the analysis and modeling of urban land use change. *Computers, Environment and Urban Systems,* 29, 369-399.

HEROLD, M., GOLDSTEIN, N. C. & CLARKE, K. C. 2003. The spatiotemporal form of urban growth: measurement, analysis and modeling. *Remote Sensing of Environment,* 86, 286-302.

HEWITSON, B. & CRANE, R. 2006. Consensus between GCM climate change projections with empirical downscaling: precipitation downscaling over South Africa. *International Journal of Climatology,* 26, 1315-1337.

HICKEL, K. & ZHANG, L. 2006. Estimating the impact of rainfall seasonality on mean annual water balance using a top-down approach. *Journal of Hydrology,* 331, 409-424.

HIPEL, K. W. & MCLEOD, A. I. 1994. *Time series modelling of water resources and environmental systems*, Elsevier.

HOFMANN, M. & KLINKENBERG, R. 2013. *RapidMiner: Data mining use cases and business analytics applications*, CRC Press.

HOLDRIDGE, L. R. 1959. Simple method for determining potential evapotranspiration from temperature data. *Science,* 130, 572-572.

HOLLAND, W. R. 1978. The role of mesoscale eddies in the general circulation of the ocean-numerical experiments using a wind-driven quasi-geostrophic model. *Journal of Physical Oceanography,* 8, 363-392.

HOLMES, M., YOUNG, A., GUSTARD, A. & GREW, R. 2002. A region of influence approach to predicting flow duration curves within ungauged catchments. *Hydrology and Earth System Sciences Discussions,* 6, 721-731.

HOUGHTON, J. T., MEIRA FILHO, L., LIM, B., TREANTON, K. & MAMATY, I. 1997. Revised 1996 IPCC guidelines for national greenhouse gas inventories. v. 1: Greenhouse gas inventory reporting instructions.-v. 2: Greenhouse gas inventory workbook.-v. 3: Greenhouse gas inventory reference manual.

HSU, C.-W., CHANG, C.-C. & LIN, C.-J. 2003. A practical guide to support vector classification.

HULME, M. & CARTER, T. R. Representing uncertainty in climate change scenarios and impact studies. Representing uncertainty in climate change scenarios and impact studies (Proc. ECLAT-2 Helsinki Workshop, 14-16 April, 1999 (Eds. T. Carter, M. Hulme and D. Viner). 128pp Climatic Research Unit, Norwich, UK, 1999. 11-37.

IMANI, M., YOU, R.-J. & KUO, C.-Y. 2014. Forecasting Caspian Sea level changes using satellite altimetry data (June 1992–December 2013) based on evolutionary support vector regression algorithms and gene expression programming. *Global and Planetary Change,* 121, 53-63.

IOVINE, G., D'AMBROSIO, D. & DI GREGORIO, S. 2005. Applying genetic algorithms for calibrating a hexagonal cellular automata model for the simulation of debris flows characterised by strong inertial effects. *Geomorphology,* 66, 287-303.

IRMAK, S. & HAMAN, D. Z. 2003. Evapotranspiration: potential or reference. *IFAS Extension, ABE,* 343.

ITAMI, R. M. 1994. *Landscape and Urban Planning,* 30, 24.

JACKSON, R. D., IDSO, S., REGINATO, R. & PINTER, P. 1981. Canopy temperature as a crop water stress indicator. *Water resources research,* 17, 1133-1138.

JAIN, A. & KUMAR, A. M. 2007. Hybrid neural network models for hydrologic time series forecasting. *Applied Soft Computing,* 7, 585-592.

JAJARMIZADEH, M., LAFDANI, E. K., HARUN, S. & AHMADI, A. 2015. Application of SVM and SWAT models for monthly streamflow prediction, a case study in South of Iran. *KSCE Journal of Civil Engineering,* 19, 345-357.

JANTZ, C. A., GOETZ, S. J. & SHELLEY, M. K. 2004. Using the SLEUTH urban growth model to simulate the impacts of future policy scenarios on urban land use in the Baltimore-Washington metropolitan area. *Environment and Planning B: Planning and Design,* 31, 251-271.

JAT, M. K., GARG, P. K. & KHARE, D. 2008. Monitoring and modelling of urban sprawl using remote sensing and GIS techniques. *International journal of Applied earth Observation and Geoinformation,* 10, 26-43.

JAYAWARDENA, A. & LAI, F. 1994. Analysis and prediction of chaos in rainfall and stream flow time series. *Journal of Hydrology,* 153, 23-52.

JAYAWARDENA, A., LI, W. & XU, P. 2002. Neighbourhood selection for local modelling and prediction of hydrological time series. *Journal of Hydrology,* 258, 40-57.

JENERETTE, G. D. & WU, J. 2001. Analysis and simulation of land-use change in the central Arizona – Phoenix region, USA. *Landscape Ecology,* 16, 611-626.

JENSEN, M. E., BURMAN, R. D. & ALLEN, R. G. Evapotranspiration and irrigation water requirements. 1990. ASCE.

JHA, M., ARNOLD, J. G., GASSMAN, P. W., GIORGI, F. & GU, R. R. 2006. CLIMATE CHHANGE SENSITIVITY ASSESSMENT ON UPPER MISSISSIPPI RIVER BASIN STREAMFLOWS USING SWAT1. Wiley Online Library.

JIAO, J. & BOERBOOM, L. 2006. Transition Rule Elicitation Methods for Urban Cellular Automata Models. *In:* VAN LEEUWEN, J. & TIMMERMANS, H. P. (eds.) *Innovations in Design & Decision Support Systems in Architecture and Urban Planning.* Springer Netherlands.

JOKAR ARSANJANI, J., HELBICH, M., KAINZ, W. & DARVISHI BOLOORANI, A. 2013. Integration of logistic regression, Markov chain and cellular automata models to simulate urban expansion. *International Journal of Applied Earth Observation and Geoinformation,* 21, 265-275.

JOUBERT, A. & HEWITSON, B. 1997. Simulating present and future climates of southern Africa using general circulation models. *Progress in Physical Geography,* 21, 51-78.

JUNKERMANN, W., HACKER, J., LYONS, T. & NAIR, U. 2009. Land use change suppresses precipitation. *Atmospheric Chemistry and Physics,* 9, 6531-6539.

JYRKAMA, M. I. & SYKES, J. F. 2007. The impact of climate change on spatially varying groundwater recharge in the grand river watershed (Ontario). *Journal of hydrology,* 338, 237-250.

JYRKAMA, M. I., SYKES, J. F. & NORMANI, S. D. 2002. Recharge estimation for transient ground water modeling. *Groundwater,* 40, 638-648.

KALF, F. R. & WOOLLEY, D. R. 2005. Applicability and methodology of determining sustainable yield in groundwater systems. *Hydrogeology Journal,* 13, 295-312.

KALRA, A., MILLER, W. P., LAMB, K. W., AHMAD, S. & PIECHOTA, T. 2013. Using large-scale climatic patterns for improving long lead time streamflow forecasts for Gunnison and San Juan River Basins. *Hydrological Processes,* 27, 1543-1559.

KALTEH, A. M. 2013. Monthly river flow forecasting using artificial neural network and support vector regression models coupled with wavelet transform. *Computers & Geosciences,* 54, 1-8.

KALTEH, A. M. 2016. Improving Forecasting Accuracy of Streamflow Time Series Using Least Squares Support Vector Machine Coupled with Data-Preprocessing Techniques. *Water Resources Management,* 30, 747-766.

KANG, K., KIM, J., PARK, C. & HAM, K. Evaluation of hydrologic forecasting system based on neural network model. PROCEEDINGS OF THE CONGRESS-INTERNATIONAL ASSOCIATION FOR HYDRAULIC RESEARCH, 1993. LOCAL ORGANIZING COMMITTEE OF THE XXV CONGRESS, 257-257.

KARRAN, D. J., MORIN, E. & ADAMOWSKI, J. 2014. Multi-step streamflow forecasting using data-driven non-linear methods in contrasting climate regimes. *Journal of Hydroinformatics,* 16, 671-689.

KATTENBERG, A., GIORGI, F., GRASSL, H., MEEHL, G., MITCHELL, J., STOUFFER, R., TOKIOKA, T., WEAVER, A. & WIGLEY, T. 1996. Climate models—projections of future climate. *Climate Change 1995: The Science of Climate Change. Contribution of Working Group I to the Second Assessment Report of the Intergovernmental Panel on Climate Change*, 285-357.

KAY, A. & DAVIES, H. 2008. Calculating potential evaporation from climate model data: a source of uncertainty for hydrological climate change impacts. *Journal of Hydrology,* 358, 221-239.

KAY, A., DAVIES, H., BELL, V. & JONES, R. 2009. Comparison of uncertainty sources for climate change impacts: flood frequency in England. *Climatic Change,* 92, 41-63.

KENABATHO, P., PARIDA, B., MOALAFHI, D. & SEGOSEBE, T. 2015. Analysis of rainfall and large-scale predictors using a stochastic model and artificial neural network for hydrological applications in southern Africa. *Hydrological Sciences Journal,* 60, 1943-1955.

KENDY, E., GÉRARD-MARCHANT, P., TODD WALTER, M., ZHANG, Y., LIU, C. & STEENHUIS, T. S. 2003. A soil-water-balance approach to quantify groundwater recharge from irrigated cropland in the North China Plain. *Hydrological processes,* 17, 2011-2031.

KHALIQ, M., OUARDA, T. B., GACHON, P., SUSHAMA, L. & ST-HILAIRE, A. 2009. Identification of hydrological trends in the presence of serial and cross

correlations: A review of selected methods and their application to annual flow regimes of Canadian rivers. *Journal of Hydrology,* 368, 117-130.

KHAN, M. S. & COULIBALY, P. 2006. Application of support vector machine in lake water level prediction. *Journal of Hydrologic Engineering,* 11, 199-205.

KHARRUFA, N. 1985. Simplified equation for evapotranspiration in arid regions. *Beiträge zur Hydrologie,* 5, 39-47.

KHLOSI, M., ALHAMDOOSH, M., DOUAIK, A., GABRIELS, D. & CORNELIS, W. 2016. Enhanced pedotransfer functions with support vector machines to predict water retention of calcareous soil. *European Journal of Soil Science,* 67, 276-284.

KIELY, G. 1999. Climate change in Ireland from precipitation and streamflow observations. *Advances in Water Resources,* 23, 141-151.

KIM, T.-W. & VALDÉS, J. B. 2003. Nonlinear model for drought forecasting based on a conjunction of wavelet transforms and neural networks. *Journal of Hydrologic Engineering,* 8, 319-328.

KISI, O. & CIMEN, M. 2011. A wavelet-support vector machine conjunction model for monthly streamflow forecasting. *Journal of Hydrology,* 399, 132-140.

KITE, G. W. & DROOGERS, P. 2000. Comparing evapotranspiration estimates from satellites, hydrological models and field data. *Journal of Hydrology,* 229, 3-18.

KROEZE, C., MOSIER, A. & BOUWMAN, L. 1999. Closing the global N2O budget: a retrospective analysis 1500–1994. *Global Biogeochemical Cycles,* 13, 1-8.

KU, C.-A. 2016. Incorporating spatial regression model into cellular automata for simulating land use change. *Applied Geography,* 69, 1-9.

KUEPPERS, L., BAER, P., HARTE, J., HAYA, B., KOTEEN, L. & SMITH, M. 2004. A Decision Matrix Approach to Evaluating the Impacts of Land-Use Activities Undertaken to Mitigate Climate Change. *Climatic change,* 63, 247-257.

KULKARNI, P., BARON, P. A. & WILLEKE, K. 2011. *Aerosol measurement: principles, techniques, and applications*, John Wiley & Sons.

KUMAR, M., RAGHUWANSHI, N., SINGH, R., WALLENDER, W. & PRUITT, W. 2002. Estimating evapotranspiration using artificial neural network. *Journal of Irrigation and Drainage Engineering,* 128, 224-233.

KUROSAWA, A. 2004. Multigas reduction strategy under climate stabilization target. *Contributed Paper,* 181.

LABAT, D. 2008. Wavelet analysis of the annual discharge records of the world's largest rivers. *Advances in Water Resources,* 31, 109-117.

LAMBIN, E. F. 1997. Modelling and monitoring land-cover change processes in tropical regions. *Progress in physical geography,* 21, 375-393.

LAMBIN, E. F., GEIST, H. J. & LEPERS, E. 2003. Dynamics of land-use and land-cover change in tropical regions. *Annual Review of Environment and Resources,* 28, 205-241.

LAU, K. H. & KAM, B. H. 2005. A cellular automata model for urban land-use simulation. *Environment and Planning B: Planning and Design,* 32, 247-263.

LEAVESLEY, G. H. 1994. Modeling the effects of climate change on water resources-a review. *Climatic change,* 28, 159-177.

LEE, D. S., FAHEY, D. W., FORSTER, P. M., NEWTON, P. J., WIT, R. C., LIM, L. L., OWEN, B. & SAUSEN, R. 2009. Aviation and global climate change in the 21st century. *Atmospheric Environment,* 43, 3520-3537.

LEES, M. J. 2000. Data-based mechanistic modelling and forecasting of hydrological systems. *Journal of Hydroinformatics,* 2, 15-34.

LEGATES, D. R. & MCCABE, G. J. 1999. Evaluating the use of "goodness-of-fit" measures in hydrologic and hydroclimatic model validation. *Water resources research,* 35, 233-241.

LI, C. 2014. *Monitoring and analysis of urban growth process using Remote Sensing, GIS and Cellular Automata modeling: A case study of Xuzhou city, China.* TU Dortmund University.

LI, M., XU, K., WATANABE, M. & CHEN, Z. 2007. Long-term variations in dissolved silicate, nitrogen, and phosphorus flux from the Yangtze River into the East China Sea and impacts on estuarine ecosystem. *Estuarine, Coastal and Shelf Science,* 71, 3-12.

LI, W., PACKARD, N. H. & LANGTON, C. G. 1990. Transition phenomena in cellular automata rule space. *Physica D: Nonlinear Phenomena,* 45, 77-94.

LI, X. & YEH, A. G.-O. 2000. Modelling sustainable urban development by the integration of constrained cellular automata and GIS. *International Journal of Geographical Information Science,* 14, 131-152.

LI, X. & YEH, G.-O. 2002. Integration of principal components analysis and cellular automata for spatial decisionmaking and urban simulation. *Science in China Series D: Earth Sciences,* 45, 521-529.

LI, X., ZHOU, W. & OUYANG, Z. 2013. Forty years of urban expansion in Beijing: What is the relative importance of physical, socioeconomic, and neighborhood factors? *Applied Geography,* 38, 1-10.

LIAO, J., TANG, L., SHAO, G., SU, X., CHEN, D. & XU, T. 2016. Incorporation of extended neighborhood mechanisms and its impact on urban land-use cellular automata simulations. *Environmental Modelling & Software,* 75, 163-175.

LIN, G.-F., CHOU, Y.-C. & WU, M.-C. 2013. Typhoon flood forecasting using integrated two-stage support vector machine approach. *Journal of Hydrology,* 486, 334-342.

LINACRE, E. T. 1977. A simple formula for estimating evaporation rates in various climates, using temperature data alone. *Agricultural meteorology,* 18, 409-424.

LINDNER, M., MAROSCHEK, M., NETHERER, S., KREMER, A., BARBATI, A., GARCIA-GONZALO, J., SEIDL, R., DELZON, S., CORONA, P. & KOLSTRÖM, M. 2010. Climate change impacts, adaptive capacity, and vulnerability of European forest ecosystems. *Forest Ecology and Management,* 259, 698-709.

LIU, J., KUANG, W., ZHANG, Z., XU, X., QIN, Y., NING, J., ZHOU, W., ZHANG, S., LI, R. & YAN, C. 2014. Spatiotemporal characteristics, patterns, and causes of land-use changes in China since the late 1980s. *Journal of Geographical Sciences,* 24, 195-210.

LIU, J., ZHAN, J. & DENG, X. 2005. Spatio-temporal patterns and driving forces of urban land expansion in China during the economic reform era. *AMBIO: a journal of the human environment,* 34, 450-455.

LIU, J., ZHANG, Z., XU, X., KUANG, W., ZHOU, W., ZHANG, S., LI, R., YAN, C., YU, D. & WU, S. 2010. Spatial patterns and driving forces of land use change in China during the early 21st century. *Journal of Geographical Sciences,* 20, 483-494.

LIU, X., LI, X., LIU, L., HE, J. & AI, B. 2008. A bottom-up approach to discover transition rules of cellular automata using ant intelligence. *International Journal of Geographical Information Science,* 22, 1247-1269.

LIU, Y. 2008. *Modelling urban development with geographical information systems and cellular automata*, CRC Press (Taylor & Francis Group).

LIU, Y. & DE SMEDT, F. 2004. WetSpa extension, a GIS-based hydrologic model for flood prediction and watershed management. *Vrije Universiteit Brussel, Belgium,* 1-108.

LIU, Y. & HE, J. Developing a web-based cellular automata model for urban growth simulation. International Symposium on Spatial Analysis, Spatial-temporal Data Modeling, and Data Mining, 2009. International Society for Optics and Photonics, 74925C-74925C-8.

LIU, Y. & PHINN, S. R. 2003. Modelling urban development with cellular automata incorporating fuzzy-set approaches. *Computers, Environment and Urban Systems,* 27, 637-658.

LOUKAS, A., VASILIADES, L. & DALEZIOS, N. R. 2002. Potential climate change impacts on flood producing mechanisms in southern British Columbia, Canada using the CGCMA1 simulation results. *Journal of Hydrology,* 259, 163-188.

LU, D. & WENG, Q. 2004. Spectral Mixture Analysis of the Urban Landscape in Indianapolis with Landsat ETM+ Imagery. *Photogrammetric Engineering & Remote Sensing,* 70, 1053-1062.

MNARD, A. & MARCEAU, D. J. 2005. Exploration of spatial scale sensitivity in geographic cellular automata. *Environment and Planning B: Planning and Design,* 32, 693-714.

MACHIWAL, D. & JHA, M. K. 2016. Evaluating persistence and identifying trends and abrupt changes in monthly and annual rainfalls of a semi-arid region in Western India. *Theoretical and Applied Climatology*, 1-20.

MAGAR, R. B. & JOTHIPRAKASH, V. 2011. Intermittent reservoir daily-inflow prediction using lumped and distributed data multi-linear regression models. *Journal of earth system science,* 120, 1067-1084.

MAKKINK, G. 1957. Testing the Penman formula by means of lysimeters. *J. Inst. Water Eng,* 11, 277-288.

MALCZEWSKI, J. 2004. GIS-based land-use suitability analysis: a critical overview. *Progress in planning,* 62, 3-65.

MANTON, M., DELLA-MARTA, P., HAYLOCK, M., HENNESSY, K., NICHOLLS, N., CHAMBERS, L., COLLINS, D., DAW, G., FINET, A. & GUNAWAN, D.

2001. Trends in extreme daily rainfall and temperature in Southeast Asia and the South Pacific: 1961–1998. *International Journal of Climatology,* 21, 269-284.

MARÉCHAL, D. 2004. A soil-based approach to rainfall-runoff modelling in ungauged catchments for England and Wales.

MAS, J.-F., PUIG, H., PALACIO, J. L. & SOSA-LÓPEZ, A. 2004. Modelling deforestation using GIS and artificial neural networks. *Environmental Modelling & Software,* 19, 461-471.

MASTERS, T. 1993. *Practical neural network recipes in C++*, Morgan Kaufmann.

MATILAINEN, A., GJESSING, E. T., LAHTINEN, T., HED, L., BHATNAGAR, A. & SILLANPÄÄ, M. 2011. An overview of the methods used in the characterisation of natural organic matter (NOM) in relation to drinking water treatment. *Chemosphere,* 83, 1431-1442.

MATTHEWS, R. B., GILBERT, N. G., ROACH, A., POLHILL, J. G. & GOTTS, N. M. 2007. Agent-based land-use models: a review of applications. *Landscape Ecology,* 22, 1447-1459.

MAURER, E. & HIDALGO, H. 2008. Utility of daily vs. monthly large-scale climate data: an intercomparison of two statistical downscaling methods. *Hydrology and Earth System Sciences,* 12, 551-563.

MAUSER, W. & SCHÄDLICH, S. 1998. Modelling the spatial distribution of evapotranspiration on different scales using remote sensing data. *Journal of hydrology,* 212, 250-267.

MAY, R. M. 1976. Simple mathematical models with very complicated dynamics. *Nature,* 261, 459-467.

MC CUMISKEY, L. The Shannon as a water resource. Symposium on Management of the River Shannon, Athlone, 1976.

MCCARTHY, T., FRANKIEWICZ, P., CULLEN, P., BLASZKOWSKI, M., O'CONNOR, W. & DOHERTY, D. 2008. Long-term effects of hydropower installations and associated river regulation on River Shannon eel populations: mitigation and management. *Hydrobiologia,* 609, 109-124.

MCCOY, J., JOHNSTON, K. & INSTITUTE, E. S. R. 2001. *Using ArcGIS spatial analyst: GIS by ESRI*, Environmental Systems Research Institute.

MCGUINNESS, J. L. & BORDNE, E. F. 1972. *A comparison of lysimeter-derived potential evapotranspiration with computed values*, US Dept. of Agriculture.

MEINSHAUSEN, M., SMITH, S. J., CALVIN, K., DANIEL, J. S., KAINUMA, M., LAMARQUE, J., MATSUMOTO, K., MONTZKA, S., RAPER, S. & RIAHI, K. 2011. The RCP greenhouse gas concentrations and their extensions from 1765 to 2300. *Climatic change,* 109, 213-241.

MEKANIK, F., IMTEAZ, M., GATO-TRINIDAD, S. & ELMAHDI, A. 2013. Multiple regression and Artificial Neural Network for long-term rainfall forecasting using large scale climate modes. *Journal of Hydrology,* 503, 11-21.

MELILLO, J. M., MCGUIRE, A. D., KICKLIGHTER, D. W., MOORE, B., VOROSMARTY, C. J. & SCHLOSS, A. L. 1993. Global climate change and terrestrial net primary production. *Nature,* 363, 234-240.

MEYER, W. B. & TURNER, B. L. 1992. Human population growth and global land-use/cover change. *Annual review of ecology and systematics,* 23, 39-61.

MEYER, W. B. & TURNER II, B. 1996. Land-use/land-cover change: challenges for geographers. *GeoJournal,* 39, 237-240.

MILLER, H. J. 1999. Measuring space-time accessibility benefits within transportation networks: basic theory and computational procedures. *Geographical Analysis,* 31, 1-26.

MILLER, J. D., KIM, H., KJELDSEN, T. R., PACKMAN, J., GREBBY, S. & DEARDEN, R. 2014. Assessing the impact of urbanization on storm runoff in a peri-urban catchment using historical change in impervious cover. *Journal of Hydrology,* 515, 59-70.

MILLS, G. 2000. Modelling the water budget of Ireland—evapotranspiration and soil moisture. *Irish Geography,* 33, 99-116.

MILLY, P. 1993. An analytic solution of the stochastic storage problem applicable to soil water. *Water Resources Research,* 29, 3755-3758.

MINAMI, M. ESRI (2000) Using ArcMap: GIS. *Redlands, California.*

MIRZAEI, P. A. & HAGHIGHAT, F. 2010. Approaches to study Urban Heat Island - Abilities and limitations. *Building and Environment,* 45, 2192-2201.

MISSTEAR, B., BROWN, L. & DALY, D. 2009a. A methodology for making initial estimates of groundwater recharge from groundwater vulnerability mapping. *Hydrogeology Journal,* 17, 275-285.

MISSTEAR, B., BROWN, L. & JOHNSTON, P. 2009b. Estimation of groundwater recharge in a major sand and gravel aquifer in Ireland using multiple approaches. *Hydrogeology Journal,* 17, 693-706.

MISSTEAR, B., BROWN, L. & WILLIAMS, N. H. 2008. Groundwater recharge to a fractured limestone aquifer overlain by glacial till in County Monaghan, Ireland. *Quarterly Journal of Engineering Geology and Hydrogeology,* 41, 465-476.

MISSTEAR, B. D. Groundwater recharge assessment: a key component of river basin management. River basin management, Proceedings, National Hydrology Seminar, Tullamore, 2000. Citeseer, 52-59.

MITCHELL, T. & OSBORN, T. 2005. ClimGen: a flexible tool for generating monthly climate data sets and scenarios. *Tyndall Centre for Climate Change Research Working Paper.*

MO, X., LIU, S., LIN, Z. & ZHAO, W. 2004. Simulating temporal and spatial variation of evapotranspiration over the Lushi basin. *Journal of Hydrology,* 285, 125-142.

MOCKLER, E. & BRUEN, M. 2013. Parameterizing dynamic water quality models in ungauged basins: issues and solutions. *Understanding Freshwater Quality Problems in a Changing World,* 361, 235-242.

MOIWO, J. P., LU, W., ZHAO, Y., YANG, Y. & YANG, Y. 2010. Impact of land use on distributed hydrological processes in the semi-arid wetland ecosystem of Western Jilin. *Hydrological processes,* 24, 492-503.

MOIWO, J. P. & TAO, F. 2014. Groundwater recharge and discharge analysis for land use conditions suitable for the hydrology and ecology of semiarid regions.

MOSS, R. H., BABIKER, M., BRINKMAN, S., CALVO, E., CARTER, T., EDMONDS, J. A., ELGIZOULI, I., EMORI, S., LIN, E. & HIBBARD, K. 2008. Towards new scenarios for analysis of emissions, climate change, impacts, and response strategies.

MOSS, R. H., EDMONDS, J. A., HIBBARD, K. A., MANNING, M. R., ROSE, S. K., VAN VUUREN, D. P., CARTER, T. R., EMORI, S., KAINUMA, M. & KRAM, T. 2010. The next generation of scenarios for climate change research and assessment. *Nature,* 463, 747-756.

MÜLLER, M. & THOMPSON, S. 2016. Comparing statistical and process-based flow duration curve models in ungauged basins and changing rain regimes. *Hydrology and Earth System Sciences,* 20, 669-683.

MUNSHI, T., ZUIDGEEST, M., BRUSSEL, M. & VAN MAARSEVEEN, M. 2014. Logistic regression and cellular automata-based modelling of retail, commercial and residential development in the city of Ahmedabad, India. *Cities,* 39, 68-86.

MURTAGH, F., STARCK, J.-L. & RENAUD, O. 2004. On neuro-wavelet modeling. *Decision Support Systems,* 37, 475-484.

NALLEY, D., ADAMOWSKI, J. & KHALIL, B. 2012. Using discrete wavelet transforms to analyze trends in streamflow and precipitation in Quebec and Ontario (1954–2008). *Journal of Hydrology,* 475, 204-228.

NAYAK, P. C., SUDHEER, K., RANGAN, D. & RAMASASTRI, K. 2004. A neuro-fuzzy computing technique for modeling hydrological time series. *Journal of Hydrology,* 291, 52-66.

NELSON, G. C., ROSEGRANT, M. W., KOO, J., ROBERTSON, R., SULSER, T., ZHU, T., RINGLER, C., MSANGI, S., PALAZZO, A. & BATKA, M. 2009. *Climate change: Impact on agriculture and costs of adaptation*, Intl Food Policy Res Inst.

NETWORK, N. 1999. A Comprehensive Foundation. *Prentice-Hall, Inc., Upper Saddle River, New Jersey,* 7458.

NEW, M. & HULME, M. 2000. Representing uncertainty in climate change scenarios: a Monte-Carlo approach. *Integrated assessment,* 1, 203-213.

NIEHOFF, D., FRITSCH, U. & BRONSTERT, A. 2002. Land-use impacts on storm-runoff generation: scenarios of land-use change and simulation of hydrological response in a meso-scale catchment in SW-Germany. *Journal of Hydrology,* 267, 80-93.

NIRUPAMA, N. & SIMONOVIC, S. P. 2007. Increase of flood risk due to urbanisation: A canadian example. *Natural Hazards,* 40, 25-41.

NOURANI, V., BAGHANAM, A. H., ADAMOWSKI, J. & KISI, O. 2014. Applications of hybrid wavelet–Artificial Intelligence models in hydrology: A review. *Journal of Hydrology,* 514, 358-377.

NOURANI, V., KOMASI, M. & ALAMI, M. T. 2011. Hybrid wavelet–genetic programming approach to optimize ANN modeling of rainfall–runoff Process. *Journal of Hydrologic Engineering,* 17, 724-741.

NOURANI, V., KOMASI, M. & MANO, A. 2009. A multivariate ANN-wavelet approach for rainfall–runoff modeling. *Water resources management,* 23, 2877-2894.

NPWS. 2015. *The National Parks and Wildlife Service (NPWS)* [Online]. Available: http://www.npws.ie/.

O'BRIEN, R. J., MISSTEAR, B. D., GILL, L. W., DEAKIN, J. L. & FLYNN, R. 2013. Developing an integrated hydrograph separation and lumped modelling approach to quantifying hydrological pathways in Irish river catchments. *Journal of Hydrology,* 486, 259-270.

OFFICE, C. S. 2011. *Central Statistics Office, Census of Population* [Online]. Available: http://www.cso.ie/ [Accessed 20 February 2015].

OFFICE OF PUBLIC WORKS, J. E. 2011. Technical Assessment - River Shannon Level Operation Review - Shannon CFRAM Study Office of Public Works.

OPITZ-STAPLETON, S. & GANGOPADHYAY, S. 2011. A non-parametric, statistical downscaling algorithm applied to the Rohini River Basin, Nepal. *Theoretical and Applied Climatology,* 103, 375-386.

OPW 2007. Shannon International River Basin District Booklet. 6.

OPW 2015a. Shannon CFRAM Study.

OPW. 2015b. *Shannon River Basin District Project* [Online]. Available: http://www.shannonrbd.com/ [Accessed 20 June 2015].

OUDIN, L., HERVIEU, F., MICHEL, C., PERRIN, C., ANDRÉASSIAN, V., ANCTIL, F. & LOUMAGNE, C. 2005. Which potential evapotranspiration input for a lumped rainfall–runoff model?: Part 2—Towards a simple and efficient potential evapotranspiration model for rainfall–runoff modelling. *Journal of Hydrology,* 303, 290-306.

OUDIN, L., MOULIN, L., BENDJOUDI, H. & RIBSTEIN, P. 2010. Estimating potential evapotranspiration without continuous daily data: possible errors and impact on water balance simulations. *Hydrological Sciences Journal–Journal des Sciences Hydrologiques,* 55, 209-222.

PACHAURI, R. & REISINGER, A. 2007a. IPCC fourth assessment report. *IPCC, Geneva,* 2007.

PARKER, D. C., MANSON, S. M., JANSSEN, M. A., HOFFMANN, M. J. & DEADMAN, P. 2003. Multi-Agent Systems for the Simulation of Land-Use and Land-Cover Change: A Review. *Annals of the Association of American Geographers,* 93, 314-337.

PARMELE, L. & MCGUINNESS, J. 1974. Comparisons of measured and estimated daily potential evapotranspiration in a humid region. *Journal of Hydrology,* 22, 239-251.

PARTAL, T. & KÜÇÜK, M. 2006. Long-term trend analysis using discrete wavelet components of annual precipitations measurements in Marmara region (Turkey). *Physics and Chemistry of the Earth, Parts A/B/C,* 31, 1189-1200.

PECHLIVANIDIS, I., JACKSON, B., MCINTYRE, N. & WHEATER, H. 2011. Catchment scale hydrological modelling: a review of model types, calibration

approaches and uncertainty analysis methods in the context of recent developments in technology and applications. *Global NEST Journal,* 13, 193-214.

PECHLIVANIDIS, I., MCINTYRE, N. & WHEATER, H. 2010. Calibration of the semi-distributed PDM rainfall–runoff model in the Upper Lee catchment, UK. *Journal of Hydrology,* 386, 198-209.

PENMAN, H. L. Natural evaporation from open water, bare soil and grass. Proceedings of the Royal Society of London A: Mathematical, Physical and Engineering Sciences, 1948. The Royal Society, 120-145.

PERRIN, C., MICHEL, C. & ANDRÉASSIAN, V. 2001. Does a large number of parameters enhance model performance? Comparative assessment of common catchment model structures on 429 catchments. *Journal of Hydrology,* 242, 275-301.

PIJANOWSKI, B., TAYYEBI, A., DELAVAR, M. & YAZDANPANAH, M. 2010. Urban expansion simulation using geospatial information system and artificial neural networks. *International Journal of Environmental Research,* 3, 493-502.

PIJANOWSKI, B. C., BROWN, D. G., SHELLITO, B. A. & MANIK, G. A. 2002. Using neural networks and GIS to forecast land use changes: a land transformation model. *Computers, environment and urban systems,* 26, 553-575.

POELMANS, L. & VAN ROMPAEY, A. 2010. Complexity and performance of urban expansion models. *Computers, Environment and Urban Systems,* 34, 17-27.

POELMANS, L., VAN ROMPAEY, A. & BATELAAN, O. 2010. Coupling urban expansion models and hydrological models: How important are spatial patterns? *Land Use Policy,* 27, 965-975.

PORTUGALI, J. & BENENSON, I. 1995. Artificial planning experience by means of a heuristic cell-space model: simulating international migration in the urban process. *Environment and Planning A,* 27, 1647-1665.

PORTUGALI, J., IZAK, B. & IZAK, O. 1994. *Geographical Analysis,* 26, 321.

POTTER, N. & ZHANG, L. 2007. Water balance variability at the interstorm timescale. *Water Resources Research,* 43.

POTTER, N. J. & ZHANG, L. 2009. Interannual variability of catchment water balance in Australia. *Journal of Hydrology,* 369, 120-129.

PRASKIEVICZ, S. & CHANG, H. 2009. A review of hydrological modelling of basin-scale climate change and urban development impacts. *Progress in Physical Geography,* 33, 650-671.

PRATOMOATMOJO, N. A. 2012. *Land use change modelling under tidal flood scenario by means of markov-cellular automata in pekalongan municipal.* Universitas Gadjah Mada.

PRATOMOATMOJO, N. A. 2016. LanduseSimPractice : Spatial Modeling of Settlement and Industrial Growth by means of Cellular Automataand Geographic Information System. Urban and Regional Planning Department, Sepuluh Nopember Institute of Technolog.

PRESS, S. J. & WILSON, S. 1978. Choosing between logistic regression and discriminant analysis. *Journal of the American Statistical Association,* 73, 699-705.

PRESTON, S. H. 1979. Urban growth in developing countries: A demographic reappraisal. *Population and Development Review*, 195-215.

PRUDHOMME, C., JAKOB, D. & SVENSSON, C. 2003. Uncertainty and climate change impact on the flood regime of small UK catchments. *Journal of hydrology,* 277, 1-23.

PRUDHOMME, C., REYNARD, N. & CROOKS, S. 2002. Downscaling of global climate models for flood frequency analysis: where are we now? *Hydrological processes,* 16, 1137-1150.

PRUITT, W. & DOORENBOS, J. 1977. *Empirical Calibration: A Requisite for Evapotranspiration Formulae Based on Daily Or Longer Mean Climate Data?*, The Committee.

QASSIM, A. & ASHCROFT, B. 2002. Estimating vegetable crop water use with moisture-accounting method# AG1192, DPI Victoria. Retrieved October.

QUILBÉ, R., ROUSSEAU, A., MOQUET, J.-S., SAVARY, S., RICARD, S. & GARBOUJ, M. 2008. Hydrological responses of a watershed to historical land use evolution and future land use scenarios under climate change conditions. *Hydrology and Earth System Sciences Discussions,* 12, 101-110.

QUINTANA SEGUI, P., RIBES, A., MARTIN, E., HABETS, F. & BOÉ, J. 2010. Comparison of three downscaling methods in simulating the impact of climate change on the hydrology of Mediterranean basins. *Journal of hydrology,* 383, 111-124.

RAMANKUTTY, N. & FOLEY, J. A. 1999. Estimating historical changes in land cover:North American croplands from 1850 to 1992. *Global Ecology and Biogeography,* 8, 381-396.

RAMIREZ, J. & JARVIS, A. 2008. High resolution statistically downscaled future climate surfaces. *International Center for Tropical Agriculture (CIAT).*

RATRIAGA, A. R. N. & SARDJITO, S. 2016. Penentuan Rute Angkutan Umum Optimal Dengan Transport Network Simulator (TRANETSIM) di Kota Tuban. *Jurnal Teknik ITS,* 4, C87-C91.

RATTO, M., YOUNG, P., ROMANOWICZ, R., PAPPENBERGER, F., SALTELLI, A. & PAGANO, A. 2007. Uncertainty, sensitivity analysis and the role of data based mechanistic modeling in hydrology. *Hydrology and Earth System Sciences Discussions,* 11, 1249-1266.

REILLY, M. K., O'MARA, M. P. & SETO, K. C. 2009. From Bangalore to the Bay Area: Comparing transportation and activity accessibility as drivers of urban growth. *Landscape and Urban Planning,* 92, 24-33.

REINAU, K. H. Cellular Automata and Urban Development. Nordic GIS Conference, 2006. 75-80.

RIAHI, K., GRÜBLER, A. & NAKICENOVIC, N. 2007. Scenarios of long-term socio-economic and environmental development under climate stabilization. *Technological Forecasting and Social Change,* 74, 887-935.

RIAHI, K., RAO, S., KREY, V., CHO, C., CHIRKOV, V., FISCHER, G., KINDERMANN, G., NAKICENOVIC, N. & RAFAJ, P. 2011. RCP 8.5—A scenario of comparatively high greenhouse gas emissions. *Climatic change,* 109, 33-57.

RIETVELD, P. & BRUINSMA, F. 2012. *Is transport infrastructure effective?: transport infrastructure and accessibility: impacts on the space economy*, Springer Science & Business Media.

RODELL, M., VELICOGNA, I. & FAMIGLIETTI, J. S. 2009. Satellite-based estimates of groundwater depletion in India. *Nature,* 460, 999-1002.

ROGERS, C., BEVEN, K., MORRIS, E. & ANDERSON, M. 1985. Sensitivity analysis, calibration and predictive uncertainty of the Institute of Hydrology Distributed Model. *Journal of hydrology,* 81, 179-191.

ROMANENKO, P. 1973. Effect of a Transverse Mass Flow on Heat Transfer and Dynamics of a Turbulent Hot Air Flow in Axi Symmetric Diffusor with a Permeable Wall. DTIC Document.

ROSENZWEIG, M. L. 1968. Net primary productivity of terrestrial communities: prediction from climatological data. *American Naturalist*, 67-74.

ROUNSEVELL, M., REGINSTER, I., ARAÚJO, M. B., CARTER, T., DENDONCKER, N., EWERT, F., HOUSE, J., KANKAANPÄÄ, S., LEEMANS, R. & METZGER, M. 2006. A coherent set of future land use change scenarios for Europe. *Agriculture, Ecosystems & Environment,* 114, 57-68.

RUSHTON, K., EILERS, V. & CARTER, R. 2006. Improved soil moisture balance methodology for recharge estimation. *Journal of hydrology,* 318, 379-399.

RYDELLU, L. E. 1956. RIVER SHANNON FLOOD PROBLEM. Corps of Engineers US. Army.

SAFARI, A., DE SMEDT, F. & MOREDA, F. 2012. WetSpa model application in the distributed model intercomparison project (DMIP2). *Journal of Hydrology,* 418, 78-89.

SAID, S. E. & DICKEY, D. A. 1984. Testing for unit roots in autoregressive-moving average models of unknown order. *Biometrika,* 71, 599-607.

SALATHE, E. P., MOTE, P. W. & WILEY, M. W. 2007. Review of scenario selection and downscaling methods for the assessment of climate change impacts on hydrology in the United States Pacific Northwest. *International Journal of Climatology,* 27, 1611-1621.

SALVADORE, E., BRONDERS, J. & BATELAAN, O. 2015. Hydrological modelling of urbanized catchments: A review and future directions. *Journal of Hydrology,* 529, 62-81.

SANTÉ, I., GARCÍA, A. M., MIRANDA, D. & CRECENTE, R. 2010. Cellular automata models for the simulation of real-world urban processes: A review and analysis. *Landscape and Urban Planning,* 96, 108-122.

SCHEFF, J. & FRIERSON, D. M. 2014. Scaling potential evapotranspiration with greenhouse warming. *Journal of Climate,* 27, 1539-1558.

SCHMITZ, J. E., ZEMP, R. J. & MENDES, M. J. 2006. Artificial neural networks for the solution of the phase stability problem. *Fluid Phase Equilibria,* 245, 83-87.

SCHÖLKOPF, B., SIMARD, P., VAPNIK, V. & SMOLA, A. 1997. Improving the accuracy and speed of support vector machines. *Advances in neural information processing systems,* 9, 375-381.

SCHÖLKOPF, B., SMOLA, A. J., WILLIAMSON, R. C. & BARTLETT, P. L. 2000. New support vector algorithms. *Neural computation,* 12, 1207-1245.

SCHUMANN, A., FUNKE, R. & SCHULTZ, G. 2000. Application of a geographic information system for conceptual rainfall–runoff modeling. *Journal of hydrology,* 240, 45-61.

SCIBEK, J., ALLEN, D. M., CANNON, A. J. & WHITFIELD, P. H. 2007. Groundwater–surface water interaction under scenarios of climate change using a high-resolution transient groundwater model. *Journal of Hydrology,* 333, 165-181.

SEGUÍ, P. Q., RIBES, A., MARTIN, E., HABETS, F. & BOÉ, J. 2010. Comparison of three downscaling methods in simulating the impact of climate change on the hydrology of Mediterranean basins. *Journal of Hydrology,* 383, 111-124.

SERNEELS, S. & LAMBIN, E. F. 2001a. Impact of land-use changes on the wildebeest migration in the northern part of the Serengeti-Mara ecosystem. *Journal of Biogeography,* 28, 391.

SERNEELS, S. & LAMBIN, E. F. 2001b. Proximate causes of land-use change in Narok District, Kenya: a spatial statistical model. *Agriculture, Ecosystems & Environment,* 85, 65-81.

SETO, K. C. & FRAGKIAS, M. 2005. Quantifying Spatiotemporal Patterns of Urban Land-use Change in Four Cities of China with Time Series Landscape Metrics. *Landscape Ecology,* 20, 871-888.

SEYAM, M. & OTHMAN, F. 2015. Long-term variation analysis of a tropical river's annual streamflow regime over a 50-year period. *Theoretical and Applied Climatology,* 121, 71-85.

SHAHUMYAN, H., TWUMASI, B. O., CONVERY, S., FOLEY, R., VAUGHAN , E., CASEY, E., CARTY , J., WALSH, C. & BRENNAN, M. 2009. Data Preparation for the MOLAND Model Application for the Greater Dublin Region. *UCD Urban Institute Ireland,* Working Paper Series.

SHAMSELDIN, A. Y., O'CONNOR, K. M. & NASR, A. E. 2007. A comparative study of three neural network forecast combination methods for simulated river flows of different rainfall—runoff models. *Hydrological Sciences Journal,* 52, 896-916.

SHENSA, M. J. 1992. The discrete wavelet transform: wedding the a trous and Mallat algorithms. *IEEE Transactions on signal processing,* 40, 2464-2482.

SHERMAN, L. K. 1932. Streamflow from rainfall by the unit-graph method. *Eng. News Record,* 108, 501-505.

SHI, W. & PANG, M. Y. C. 2000. Development of Voronoi-based cellular automata -an integrated dynamic model for Geographical Information Systems. *International Journal of Geographical Information Science,* 14, 455-474.

SHUKLA, J. & MINTZ, Y. 1982. Influence of land-surface evapotranspiration on the earth's climate. *Science,* 215, 1498-1501.

SILVER, C. S. & DEFRIES, R. S. 1992. *One Earth, One Future:: Our Changing Global Environment*, National Academies Press.

SIM, L. K. & BALAMURUGAN, G. 1991. Urbanization and urban water problems in Southeast Asia a case of unsustainable development. *Journal of Environmental Management,* 32, 195-209.

SIMMERS, I. 2013. *Estimation of natural groundwater recharge*, Springer Science & Business Media.

SIMMIE, J. & MARTIN, R. 2010. The economic resilience of regions: towards an evolutionary approach. *Cambridge journal of regions, economy and society,* 3, 27-43.

SINGH, A. 1989. Review Article Digital change detection techniques using remotely-sensed data. *International Journal of Remote Sensing,* 10, 989-1003.

SINGH, V. & XU, C. 1997. Evaluation and generalization of 13 mass-transfer equations for determining free water evaporation. *Hydrological processes,* 11, 311-323.

SINGH, V. P. & WOOLHISER, D. A. 2002. Mathematical modeling of watershed hydrology. *Journal of hydrologic engineering,* 7, 270-292.

SIVAKUMAR, B. 2003. Forecasting monthly streamflow dynamics in the western United States: a nonlinear dynamical approach. *Environmental Modelling & Software,* 18, 721-728.

SIVAPALAN, M., BLÖSCHL, G., ZHANG, L. & VERTESSY, R. 2003. Downward approach to hydrological prediction. *Hydrological processes,* 17, 2101-2111.

SMITH, S. J. & WIGLEY, T. 2006. Multi-gas forcing stabilization with MiniCAM. *The Energy Journal*, 373-391.

SMOLA, A. J. & SCHÖLKOPF, B. 2004. A tutorial on support vector regression. *Statistics and computing,* 14, 199-222.

SOLOMON, S. 2007. *Climate change 2007-the physical science basis: Working group I contribution to the fourth assessment report of the IPCC*, Cambridge University Press.

SOPHOCLEOUS, M. 1992. Groundwater recharge estimation and regionalization: the Great Bend Prairie of central Kansas and its recharge statistics. *Journal of hydrology,* 137, 113-140.

STEELE-DUNNE, S., LYNCH, P., MCGRATH, R., SEMMLER, T., WANG, S., HANAFIN, J. & NOLAN, P. 2008. The impacts of climate change on hydrology in Ireland. *Journal of hydrology,* 356, 28-45.

STEVENS, D., DRAGICEVIC, S. & ROTHLEY, K. 2007. iCity: A GIS–CA modelling tool for urban planning and decision making. *Environmental Modelling & Software,* 22, 761-773.

STOCKER, T. F., QIN, D., PLATTNER, G.-K., TIGNOR, M., ALLEN, S. K., BOSCHUNG, J., NAUELS, A., XIA, Y., BEX, V. & MIDGLEY, P. M. 2013a. Climate change 2013: The physical science basis. *Intergovernmental Panel on Climate Change, Working Group I Contribution to the IPCC Fifth Assessment Report (AR5)(Cambridge Univ Press, New York)*.

STOCKER, T. F., QIN, D., PLATTNER, G., TIGNOR, M., ALLEN, S., BOSCHUNG, J., NAUELS, A., XIA, Y., BEX, V. & MIDGLEY, P. 2013b. Climate change 2013: the physical science basis. Intergovernmental panel on climate change, working group I contribution to the IPCC fifth assessment report (AR5). New York: Cambridge University Press.

SUYKENS, J. A. & VANDEWALLE, J. 1999. Least squares support vector machine classifiers. *Neural processing letters,* 9, 293-300.

SWEENEY, J., BRERETON, T., BYRNE, C., CHARLTON, R., EMBLOW, C., FEALY, R., HOLDEN, N., JONES, M., DONNELLY, A. & MOORE, S. 2003. Climate Change: Scenarios & Impacts for Ireland (2000-LS-5.2. 1-M1) ISBN: 1-84095-115-X.

SWENSON, S. & WAHR, J. 2006. Estimating large-scale precipitation minus evapotranspiration from GRACE satellite gravity measurements. *Journal of Hydrometeorology,* 7, 252-270.

TAGUE, C., GRANT, G., FARRELL, M., CHOATE, J. & JEFFERSON, A. 2008. Deep groundwater mediates streamflow response to climate warming in the Oregon Cascades. *Climatic Change,* 86, 189-210.

TAKEYAMA, M. & COUCLELIS, H. 1997. Map dynamics: integrating cellular automata and GIS through Geo-Algebra. *International Journal of Geographical Information Science,* 11, 73-91.

TALLAKSEN, L. M. & VAN LANEN, H. A. 2004. *Hydrological drought: processes and estimation methods for streamflow and groundwater*, Elsevier.

TAYLOR, K. E. 2001. Summarizing multiple aspects of model performance in a single diagram. *Journal of Geophysical Research: Atmospheres (1984–2012),* 106, 7183-7192.

TAYLOR, K. E., STOUFFER, R. J. & MEEHL, G. A. 2009. A summary of the CMIP5 experiment design. *PCDMI Rep,* 33.

TAYLOR, K. E., STOUFFER, R. J. & MEEHL, G. A. 2012. An overview of CMIP5 and the experiment design. *Bulletin of the American Meteorological Society,* 93, 485-498.

TEKLEAB, S., UHLENBROOK, S., MOHAMED, Y., SAVENIJE, H., TEMESGEN, M. & WENNINGER, J. 2011. Water balance modeling of Upper Blue Nile catchments using a top-down approach. *Hydrology and Earth System Sciences, 15,(7)*.

THEILER, J., EUBANK, S., LONGTIN, A., GALDRIKIAN, B. & FARMER, J. D. 1992. Testing for nonlinearity in time series: the method of surrogate data. *Physica D: Nonlinear Phenomena,* 58, 77-94.

THODSEN, H. 2007. The influence of climate change on stream flow in Danish rivers. *Journal of Hydrology,* 333, 226-238.

THORNTHWAITE, C. W. 1948. An approach toward a rational classification of climate. *Geographical review,* 38, 55-94.

THORNTHWAITE, C. W. & MATHER, J. R. 1957. Instructions and tables for computing potential evapotranspiration and the water balance.

TIWARI, M. K. & CHATTERJEE, C. 2010. Development of an accurate and reliable hourly flood forecasting model using wavelet–bootstrap–ANN (WBANN) hybrid approach. *Journal of Hydrology,* 394, 458-470.

TOBLER, W., GALE, S. & OLSSON, G. 1979. *Philosophy in Geography.*

TOBLER, W. R. 1970. A Computer Movie Simulating Urban Growth in the Detroit Region. *Economic Geography,* 46, 234-240.

TODINI, E. 1988. Rainfall-runoff modeling—Past, present and future. *Journal of Hydrology,* 100, 341-352.

TORRENS, P. M. 2000. How cellular models of urban systems work (1. theory). *CASA Working Papers 28.*

TÓTH, J. 2009. *Gravitational systems of groundwater flow: theory, evaluation, utilization*, Cambridge University Press.

TRIANTAKONSTANTIS, D. & MOUNTRAKIS, G. 2012. Urban growth prediction: A review of computational models and human perceptions.

TRIPATHI, S., SRINIVAS, V. & NANJUNDIAH, R. S. 2006. Downscaling of precipitation for climate change scenarios: a support vector machine approach. *Journal of hydrology,* 330, 621-640.

TRZASKA, S. & SCHNARR, E. 2014. A review of downscaling methods for climate change projections. *United States Agency for International Development by Tetra Tech ARD*, 1-42.

TUCKER, G. E. & SLINGERLAND, R. 1997. Drainage basin responses to climate change. *Water Resources Research,* 33, 2031-2047.

TURC, L. 1961. Estimation of irrigation water requirements, potential evapotranspiration: a simple climatic formula evolved up to date. *Ann Agron,* 12, 13-49.

TURNER II, B. L., KASPERSON, R. E., MEYER, W. B., DOW, K. M., GOLDING, D., KASPERSON, J. X., MITCHELL, R. C. & RATICK, S. J. 1990. Two types of global environmental change: Definitional and spatial-scale issues in their human dimensions. *Global Environmental Change,* 1, 14-22.

TURNER, M. G. 1989. Landscape ecology: the effect of pattern on process. *Annual review of ecology and systematics*, 171-197.

TWUMASI, B. O. 2008. Recommendations for Further Improvement to the MOLAND Model. *Urban Institute Ireland Working Paper Series.*

UNITED NATIONS, U. 2012. *World Urbanization Prospects: The 2011 Revision* [Online]. Population Division, Department of Economic and Social Affairs, UN. Available: http://esa.un.org/unpd/wpp/ [Accessed June 30 2015].

VALIPOUR, M., BANIHABIB, M. E. & BEHBAHANI, S. M. R. 2013. Comparison of the ARMA, ARIMA, and the autoregressive artificial neural network models in forecasting the monthly inflow of Dez dam reservoir. *Journal of hydrology,* 476, 433-441.

VAN DIJK, A. & BRUIJNZEEL, L. 2001. Modelling rainfall interception by vegetation of variable density using an adapted analytical model. Part 1. Model description. *Journal of hydrology,* 247, 230-238.

VAN DIJK, A. I., GASH, J. H., VAN GORSEL, E., BLANKEN, P. D., CESCATTI, A., EMMEL, C., GIELEN, B., HARMAN, I. N., KIELY, G. & MERBOLD, L. 2015. Rainfall interception and the coupled surface water and energy balance. *Agricultural and Forest Meteorology,* 214, 402-415.

VAN VUUREN, D. P., DEN ELZEN, M. G., LUCAS, P. L., EICKHOUT, B., STRENGERS, B. J., VAN RUIJVEN, B., WONINK, S. & VAN HOUDT, R. 2007. Stabilizing greenhouse gas concentrations at low levels: an assessment of reduction strategies and costs. *Climatic change,* 81, 119-159.

VAN VUUREN, D. P., EDMONDS, J., KAINUMA, M., RIAHI, K., THOMSON, A., HIBBARD, K., HURTT, G. C., KRAM, T., KREY, V. & LAMARQUE, J.-F. 2011a. The representative concentration pathways: an overview. *Climatic change,* 109, 5-31.

VAN VUUREN, D. P., EDMONDS, J. A., KAINUMA, M., RIAHI, K. & WEYANT, J. 2011b. A special issue on the RCPs. *Climatic change,* 109, 1-4.

VANDEWIELE, G. & ELIAS, A. 1995. Monthly water balance of ungauged catchments obtained by geographical regionalization. *Journal of hydrology,* 170, 277-291.

VANDEWIELE, G., XU, C.-Y. & HUYBRECHTS, W. 1991. Regionalisation of physically-based water balance models in Belgium. Application to ungauged catchments. *Water Resources Management,* 5, 199-208.

VAPNIK, V. 2013. *The nature of statistical learning theory*, Springer Science & Business Media.

VAUX, H. & PRUITT, W. O. 1983. Crop-water production functions. *Advances in irrigation,* 2, 61-95.

VELÁZQUEZ, J., SCHMID, J., RICARD, S., MUERTH, M., GAUVIN ST-DENIS, B., MINVILLE, M., CHAUMONT, D., CAYA, D., LUDWIG, R. & TURCOTTE, R. 2013. An ensemble approach to assess hydrological models' contribution to uncertainties in the analysis of climate change impact on water resources. *Hydrology and Earth System Sciences,* 17, 565-578.

VERBURG, P. H., DE NIJS, T. C. M., RITSEMA VAN ECK, J., VISSER, H. & DE JONG, K. 2004. A method to analyse neighbourhood characteristics of land use patterns. *Computers, Environment and Urban Systems,* 28, 667-690.

VEZHNEVETS, V. & KONOUCHINE, V. GrowCut: Interactive multi-label ND image segmentation by cellular automata. proc. of Graphicon, 2005. Citeseer, 150-156.

VLIET, J. V., WHITE, R. & DRAGICEVIC, S. 2009. Modeling urban growth using a variable grid cellular automaton. *Computers, Environment and Urban Systems,* 33, 35-43.

VON STORCH, H., ZORITA, E. & CUBASCH, U. 1993. Downscaling of global climate change estimates to regional scales: an application to Iberian rainfall in wintertime. *Journal of Climate,* 6, 1161-1171.

VOUDOURIS, K. 2006. Groundwater Balance and Safe Yield of the coastal aquifer system in NEastern Korinthia, Greece. *Applied Geography,* 26, 291-311.

WAGENER, T., SIVAPALAN, M., TROCH, P. & WOODS, R. 2007. Catchment classification and hydrologic similarity. *Geography Compass,* 1, 901-931.

WAGENER, T., WHEATER, H. & GUPTA, H. V. 2004. *Rainfall-runoff modelling in gauged and ungauged catchments*, World Scientific.

WAGNER, D. F. 1997. Cellular automata and geographic information systems. *Environment and Planning B: Planning and Design,* 24, 219-234.

WALKER, G. R., JOLLY, I. D. & COOK, P. G. 1991. A new chloride leaching approach to the estimation of diffuse recharge following a change in land use. *Journal of hydrology,* 128, 49-67.

WANG, S., MCGRATH, R., SEMMLER, T., SWEENEY, C. & NOLAN, P. 2006. The impact of the climate change on discharge of Suir River Catchment (Ireland) under different climate scenarios. *Natural Hazards and Earth System Science,* 6, 387-395.

WANG, W.-C., CHAU, K.-W., CHENG, C.-T. & QIU, L. 2009. A comparison of performance of several artificial intelligence methods for forecasting monthly discharge time series. *Journal of Hydrology,* 374, 294-306.

WANG, W., HU, S. & LI, Y. 2011. Wavelet transform method for synthetic generation of daily streamflow. *Water resources management,* 25, 41-57.

WANG, X., HAO, G., YANG, Z., LIANG, P., CAI, Y., LI, C., SUN, L. & ZHU, J. 2015. Variation analysis of streamflow and ecological flow for the twin rivers of the Miyun Reservoir Basin in northern China from 1963 to 2011. *Science of the Total Environment,* 536, 739-749.

WANG, Z.-M., BATELAAN, O. & DE SMEDT, F. 1996. A distributed model for water and energy transfer between soil, plants and atmosphere (WetSpa). *Physics and Chemistry of the Earth,* 21, 189-193.

WASILEWSKI, F. 2010. Pywavelets: Discrete wavelet transform in Python. *Availabl e:* http://www. *pybytes. com/pywavelets.*

WESSELUNG, C. G., KARSSENBERG, D. J., BURROUGH, P. A. & DEURSEN, W. 1996. Integrating dynamic environmental models in GIS: the development of a Dynamic Modelling language. *Transactions in GIS,* 1, 40-48.

WHEATER, H., JAKEMAN, A. & BEVEN, K. 1993. Progress and directions in rainfall-runoff modelling.

WHETTON, P., MCINNES, K., JONES, R., HENNESSY, K., SUPPIAH, R., PAGE, C., BATHOLS, J. & DURACK, P. 2006. *Australian climate change projections for impact assessment and policy application: a review*, CSIRO Marine and Atmospheric Research.

WHITE, A. F. & BLUM, A. E. 1995. Effects of climate on chemical_ weathering in watersheds. *Geochimica et Cosmochimica Acta,* 59, 1729-1747.

WHITE, R. 1998. Cities and cellular automata. *Discrete Dynamics in Nature and Society,* 2, 111-125.

WHITE, R. & ENGELEN, G. 1993. Cellular automata and fractal urban form: a cellular modelling approach to the evolution of urban land-use patterns. *Environment and planning A,* 25, 1175-1199.

WHITE, R. & ENGELEN, G. 1997. Cellular automata as the basis of integrated dynamic regional modelling. *Environment and Planning B: Planning and Design,* 24, 235-246.

WHITE, R. & ENGELEN, G. 2000. High-resolution integrated modelling of the spatial dynamics of urban and regional systems. *Computers, environment and urban systems,* 24, 383-400.

WHITE, R., ENGELEN, G. & ULJEE, I. 1997. The use of constrained cellular automata for high-resolution modelling of urban land-use dynamics. *Environment and Planning B: Planning and Design,* 24, 323-343.

WHITE, R., ENGELEN, G., ULJEE, I., LAVALLE, C. & ENRLICH, D. 1999. Developing an urban land use simulator for European cities. *Proceedings of the 5th EC-GIS Workshop.* Stresa, Italy.

WILBY, R., WHITEHEAD, P., WADE, A., BUTTERFIELD, D., DAVIS, R. & WATTS, G. 2006. Integrated modelling of climate change impacts on water resources and quality in a lowland catchment: River Kennet, UK. *Journal of hydrology,* 330, 204-220.

WILBY, R. L. & HARRIS, I. 2006. A framework for assessing uncertainties in climate change impacts: Low-flow scenarios for the River Thames, UK. *Water Resources Research,* 42.

WILBY, R. L. & WIGLEY, T. 1997. Downscaling general circulation model output: a review of methods and limitations. *Progress in Physical Geography,* 21, 530-548.

WILLEMS, P. & VRAC, M. 2011. Statistical precipitation downscaling for small-scale hydrological impact investigations of climate change. *Journal of hydrology,* 402, 193-205.

WILSON, K. B., HANSON, P. J., MULHOLLAND, P. J., BALDOCCHI, D. D. & WULLSCHLEGER, S. D. 2001. A comparison of methods for determining forest evapotranspiration and its components: sap-flow, soil water budget, eddy covariance and catchment water balance. *Agricultural and forest Meteorology,* 106, 153-168.

WINCHELL, M., SRINIVASAN, R., DI LUZIO, M. & ARNOLD, J. 2007. ArcSWAT interface for SWAT2005 User's guide. *Texas Agricultural Experiment Station and United States Department of Agriculture, Temple, TX.*

WOLDEAMLAK, S., BATELAAN, O. & DE SMEDT, F. 2007. Effects of climate change on the groundwater system in the Grote-Nete catchment, Belgium. *Hydrogeology Journal,* 15, 891-901.

WOLFRAM, S. 1983. Statistical mechanics of cellular automata. *Reviews of modern physics,* 55, 601.

WOLFRAM, S. 1984. Universality and complexity in cellular automata. *Physica D: Nonlinear Phenomena,* 10, 1-35.

WOOD, A. W., LEUNG, L. R., SRIDHAR, V. & LETTENMAIER, D. 2004. Hydrologic implications of dynamical and statistical approaches to downscaling climate model outputs. *Climatic change,* 62, 189-216.

WORRALL, F. & BURT, T. 2004. Time series analysis of long-term river dissolved organic carbon records. *Hydrological processes,* 18, 893-911.

WU, F. 1998. SimLand: a prototype to simulate land conversion through the integrated GIS and CA with AHP-derived transition rules. *International Journal of Geographical Information Science,* 12, 63-82.

WU, F. 2002. Calibration of stochastic cellular automata: the application to rural-urban land conversions. *International Journal of Geographical Information Science,* 16, 795-818.

WU, F. & WEBSTER, C. J. 1998a. *Environment and Planning B,* 25, 103.

WU, F. & WEBSTER, C. J. 1998b. Simulation of land development through the integration of cellular automata and multicriteria evaluation. *Environment and Planning B: Planning and Design,* 25, 103-126.

WU, M. C., LIN, G. F. & LIN, H. Y. 2014a. Improving the forecasts of extreme streamflow by support vector regression with the data extracted by self-organizing map. *Hydrological Processes,* 28, 386-397.

WU, W., DANDY, G. C. & MAIER, H. R. 2014b. Protocol for developing ANN models and its application to the assessment of the quality of the ANN model development process in drinking water quality modelling. *Environmental Modelling & Software,* 54, 108-127.

XIAN, G. & CRANE, M. 2005. Assessments of urban growth in the Tampa Bay watershed using remote sensing data. *Remote Sensing of Environment,* 97, 203-215.

XIAOGE, X., LI, Z., JIE, Z., TONGWEN, W. & YONGJIE, F. 2013. Climate change projections over East Asia with BCC_CSM1. 1 climate model under RCP scenarios. *気象集誌. 第 2 輯,* 91, 413-429.

XU, C.-Y. & CHEN, D. 2005. Comparison of seven models for estimation of evapotranspiration and groundwater recharge using lysimeter measurement data in Germany. *Hydrological processes,* 19, 3717-3734.

XU, C.-Y., GONG, L., JIANG, T., CHEN, D. & SINGH, V. 2006. Analysis of spatial distribution and temporal trend of reference evapotranspiration and pan evaporation in Changjiang (Yangtze River) catchment. *Journal of Hydrology,* 327, 81-93.

XU, C.-Y. & SINGH, V. 2002. Cross comparison of empirical equations for calculating potential evapotranspiration with data from Switzerland. *Water Resources Management,* 16, 197-219.

XU, C. & SINGH, V. 2000. Evaluation and generalization of radiation-based methods for calculating evaporation. *Hydrological processes,* 14, 339-349.

XU, C. Y. & SINGH, V. 2001. Evaluation and generalization of temperature-based methods for calculating evaporation. *Hydrological processes,* 15, 305-319.

YANG, X., ZHENG, X.-Q. & LV, L.-N. 2012. A spatiotemporal model of land use change based on ant colony optimization, Markov chain and cellular automata. *Ecological Modelling,* 233, 11-19.

YANG, Y. & TIAN, F. 2009. Abrupt change of runoff and its major driving factors in Haihe River Catchment, China. *Journal of Hydrology,* 374, 373-383.

YODER, R., ODHIAMBO, L. & WRIGHT, W. 2005. Evaluation of methods for estimating daily reference crop evapotranspiration at a site in the humid southeast United States. *Applied engineering in agriculture,* 21, 197-202.

YOUNG, P. 2003. Top-down and data-based mechanistic modelling of rainfall–flow dynamics at the catchment scale. *Hydrological processes,* 17, 2195-2217.

YOUNG, P. C. 2002. Advances in real–time flood forecasting. *Philosophical Transactions of the Royal Society of London A: Mathematical, Physical and Engineering Sciences,* 360, 1433-1450.

YOUNG, P. C. & BEVEN, K. J. 1994. Data-based mechanistic modelling and the rainfall-flow non-linearity. *Environmetrics,* 5, 335-363.

YUAN, F., SAWAYA, K. E., LOEFFELHOLZ, B. C. & BAUER, M. E. 2005. Land cover classification and change analysis of the Twin Cities (Minnesota) Metropolitan Area by multitemporal Landsat remote sensing. *Remote Sensing of Environment,* 98, 317-328.

ZHANG, L., DAWES, W. & WALKER, G. 2001. Response of mean annual evapotranspiration to vegetation changes at catchment scale. *Water Resources Research,* 37, 701-708.

ZHANG, L., HICKEL, K., DAWES, W., CHIEW, F. H., WESTERN, A. & BRIGGS, P. 2004a. A rational function approach for estimating mean annual evapotranspiration. *Water Resources Research,* 40.

ZHANG, L., POTTER, N., HICKEL, K., ZHANG, Y. & SHAO, Q. 2008. Water balance modeling over variable time scales based on the Budyko framework–Model development and testing. *Journal of Hydrology,* 360, 117-131.

ZHANG, R. & ZHU, D. 2011. Study of land cover classification based on knowledge rules using high-resolution remote sensing images. *Expert Systems with Applications,* 38, 3647-3652.

ZHANG, Y., KENDY, E., QIANG, Y., CHANGMING, L., YANJUN, S. & HONGYONG, S. 2004b. Effect of soil water deficit on evapotranspiration, crop yield, and water use efficiency in the North China Plain. *Agricultural water management,* 64, 107-122.

ZHANG, Y., LIU, C., TANG, Y. & YANG, Y. 2007. Trends in pan evaporation and reference and actual evapotranspiration across the Tibetan Plateau. *Journal of Geophysical Research: Atmospheres (1984–2012),* 112.

ZHAO, C., FENG, Z. & CHEN, G. 2004. Soil water balance simulation of alfalfa (Medicago sativa L.) in the semiarid Chinese Loess Plateau. *Agricultural water management,* 69, 101-114.

ZHOU, F., XU, Y., CHEN, Y., XU, C.-Y., GAO, Y. & DU, J. 2013. Hydrological response to urbanization at different spatio-temporal scales simulated by coupling of CLUE-S and the SWAT model in the Yangtze River Delta region. *Journal of Hydrology,* 485, 113-125.

ZHOU, Y. 2009. A critical review of groundwater budget myth, safe yield and sustainability. *Journal of hydrology,* 370, 207-213.

ZORITA, E. & VON STORCH, H. 1999. The analog method as a simple statistical downscaling technique: comparison with more complicated methods. *Journal of Climate,* 12, 2474-2489.

Appendices

Appendix A: Key studies

This Appendix presents some key studies, see Table A-1, that demonstrate the effects of the geography of the catchments on the climate change impact studies.

Table A-1: Key hydrological impact studies.

Authors	Objectives	Results/main conclusion
Arnell and Gosling (2013)	The paper presented an assessment of the impacts of climate change on a series of indicators of hydrological regimes across the global domain, using a global hydrological model run with climate scenarios constructed using pattern-scaling from 21 CMIP3 (Coupled Model Intercomparison Project Phase 3) climate models.	The results provided a considerable variability between regions, depending largely on projected changes in precipitation. Uncertainty in projected river flow regimes was dominated by variation in the spatial patterns of climate change between climate models (hydrological model uncertainty was not included). There was, however, a strong degree of consistency in the overall magnitude and direction of change. More than two-thirds of climate models project a significant increase in average annual runoff across almost a quarter of the land surface, and a significant decrease over 14%, with considerably higher degrees of consistency in some regions. Most climate models project increased runoff in Canada and high-latitude eastern Europe and Siberia, and decreased runoff in central Europe, around the Mediterranean, the Mashriq, central America and Brazil.
Velázquez et al. (2013)	The study investigates two humid, mid-latitude catchments with natural flow conditions; one located in Southern Quebec (Canada) and one in Southern Bavaria (Germany). ´ Daily flow is simulated with four different hydrological models, forced by outputs from regional climate models driven by global climate models over a reference (1971–2000) and a future (2041–2070) period.	The results show that for the hydrological model ensemble, the choice of model strongly affects the climate change response of selected hydrological indicators, especially those related to low flows. Indicators related to high flows seem less sensitive to the choice of the hydrological model.

Gosling et al. (2016)	This paper presented one of the first climate change impact assessments on river runoff that utilized an ensemble of global hydrological models (Glob-HMs) and an ensemble of catchment-scale hydrological models (Cat-HMs), across multiple catchments: the upper Amazon, Darling, Ganges, Lena, upper Mississippi, upper Niger, Rhine, and Tagus.	The simulation results highlighted that for The Rhine, Tagus and Lena catchments, in particular, global climate change mitigation, which limits global-mean temperature rise to below 2 °C above pre-industrial levels, could avoid some of the hydrological hazards that could be seen with higher magnitudes of global warming.
Jha et al. (2006)	This paper used downscaled GCM output to run the Soil and Water Assessment Tool (SWAT) in order to project impacts of climate change through the 2040s on the hydrology of the Upper Mississippi River catchment.	The results included a 51% increase in annual streamflow, a 43% increase in groundwater recharge, and a 50% increase in total water yield.
Thodsen (2007)	The paper used the lumped conceptual hydrological model NAM, driven by an RCM, to simulate impacts of climate change on runoff in five Danish catchments.	The simulation found that mean annual runoff will increase by 12% by the end of the twenty-first century.
Andréasson et al. (2004)	The paper investigated potential impacts of climate change on water resources in six Swedish catchments.	The Results differed according to the latitude of the catchments, with southern Sweden mostly predicted to experience decreases in annual runoff and northern Sweden to experience increases, particularly in autumn.
Bae et al. (2008)	The paper assessed potential impacts of climate change on runoff amount and timing in South Korea's 139 drainage catchment. The paper used scenarios from two GCMs, downscaled through a stochastic weather generator, to run the hydrological model Precipitation Runoff Modelling System (PRMS).	The results suggest that the changes in the runoff will vary seasonally and regionally within the nation, with increases in the north and decreases in the south.
Fujihara et al. (2008)	The paper modeled the hydrological impacts of climate change in Turkey's Seyhan River catchment, using the Hydrological River Basin Environmental Assessment Model (Hydro-BEAM) driven by two GCMs.	The results included a decrease in annual runoff of 52–61%. In addition, this showed the differing hydrological response as to whether the catchment was in a relatively humid or arid region.

Appendix B: Soil data

This appendix presents the soil data for Ireland, including the matching between the soil groups and texture types which is shown in Figure B.1 and Tables B-1 and B-2.

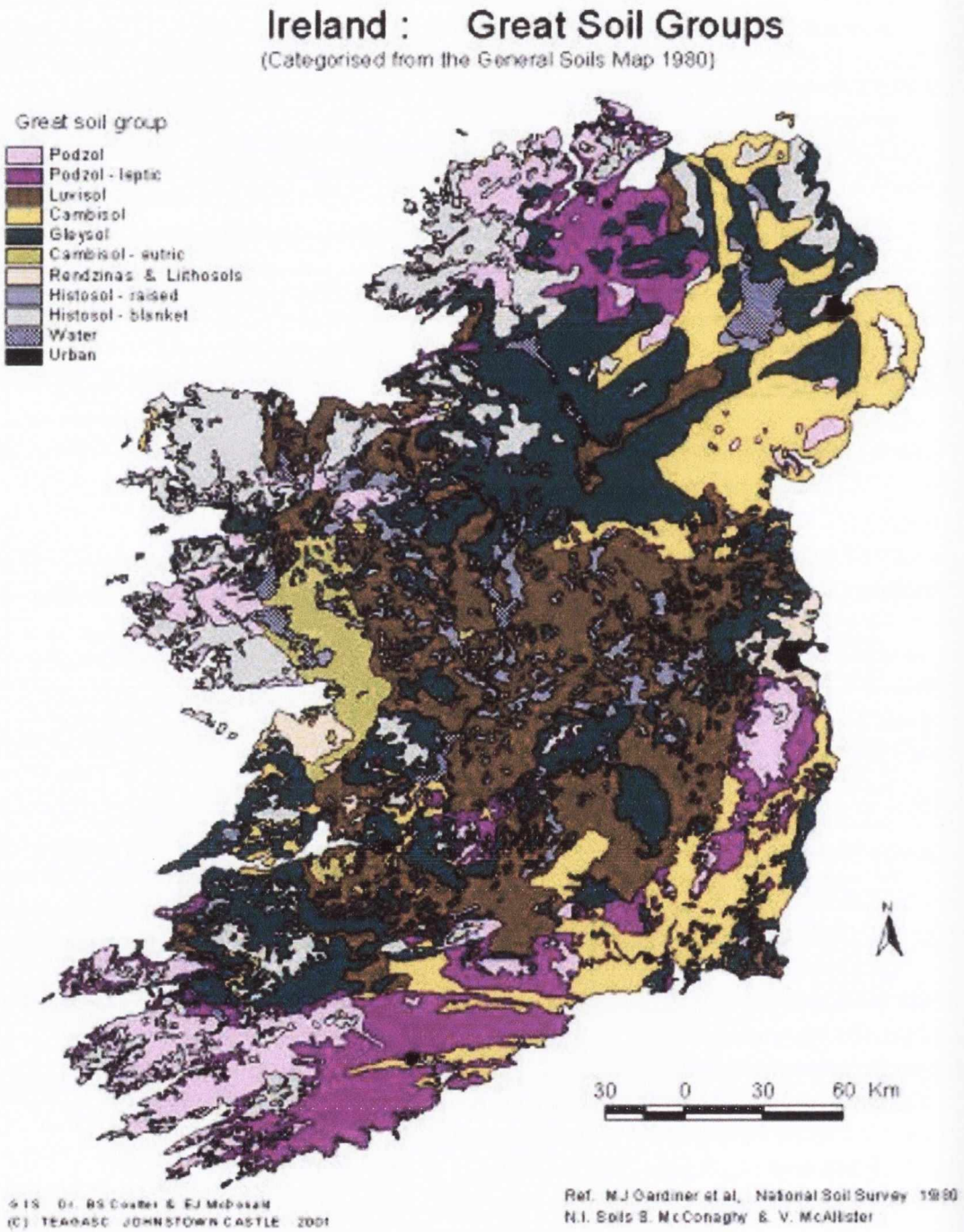

Figure B.0.1: Irish soil classification (Source: FAO).

Table B-1: Soil classification scheme used in Ireland and the equivalent FAO classification.

Great Soil Group

USDA	FAO	Occurrence %
Podzols	Podzol	10.1
Brown Podzolics	Leptic Podzol	11.7
Grey Brown Podzolics	Cambisol	19.7
Brown Earths	Luvisol	13.6
Gleys	Gleysol	25
Rendzinas	Rendzina	2.7
Lithosols	Lithosols	1.4
Regosols	Regosols	.1
Basin Peats	Raised Histosol	5.0

Table B-2: Irish soil classification and description.

Soil Association	Series leader	Description	Grate soil Groups	Texture
1xx			Ombrotrophic Peat	Loamy
0300a	Seafield	Podzols, Brown Podzolics and Groundwater Gleys with sandy textures associated with stoneless drift	Rendzina	Sandy
0360a	Burren	Rendzinas and decalcified Lithosols on outcropping limestone, Luvisols and Brown earth associated with limestone bedrock and Peat	Rendzina	Fine-loamy
0360c	Crush	Rendzinas and Calcareous Brown Earth on calcareous gravels and limestone bedrock, with inclusions of Luvisols and Brown Earth on drift with limestones	Rendzina	Coarse-loamy
0410a	Carrigvahanagh	Peat associated with Lithosols, Brown Podzolics, Podzols and Brown Earth over igneous and metamorphic stones, with inclusions of Groundwater Gleys	Lithosol	Loamy
0410b	Bantry	Peat associated with Lithosols on sandstones and shale bedrock with inclusions of Podzols and Brown Podzolics on sandstones and shale bedrock	Lithosol	Loamy
05LAK	Gurteen	Alluvial and drained alluvial soils of fine textures and base rich.	Alluvial	Loamy
05MAR	Wexford Slob	Alluvial and drained alluvial soils on reclaimed coastal flats	Alluvial	Silty

05RIV	Boyne	Alluvial and drained alluvial soils on river floodplain with base rich and medium to coarse textures	Alluvial	Silty
0600a	Kilpierce	Poorly drained soils composed of Groundwater Gleys, Luvisols and Brown Earths soils, which are restricted to depressions and the less favorable slopes on drift with siliceous stones.	Groundwater Gley	Fine-loamy
0650a	Mylerstown	Poorly drained soils consisting of Calcareous and Humic Calcareous Groundwater Gleys and Luvisols on drift with limestones	Groundwater Gley	Loamy
0660c	Package	Poorly drained soils composed by Humic Groundwater Gleys, Surface-water Gleys, on drift with siliceous stones and Peat, with inclusions of Humic Lithosols and Humic Brown Podzolics on drift with siliceous stones	Groundwater Gley	Coarse-loamy
0660d	Package	Poorly drained soils located in the uplands composed by Humic Groundwater Gleys, Podzols and Brown Podzolics on drift with siliceous stones and Peat	Groundwater Gley	Coarse-loamy
0660e	Ballywilliam	Poorly drained soils located in the uplands composed by Humic Groundwater Gleys, Brown Earths and Lithosols on drift with igneous and metamorphic stones with some inclusions of Brown Podzolics and Surface-water Gleys.	Groundwater Gley	Coarse-loamy
0700a	Macamore	Surface-water Gleys in clayey marine drift; well drained sandy Brown Podzolics on outwash sands and gravels	Surface-water Gleys	Fine-loamy
0700b	Kilrush	Surface-water Gleys, Brown Earths and Brown Podzolics on drift with siliceous stones, and inclusions of Groundwater Gleys	Surface-water Gleys	Fine-loamy
0700c	Drumkeeran	"Heavy" soils with clayey and fine textures. Association composed commonly of Surface-water Gleys and in lesser proportions, Luvisols, with inclusions of Brown Earths.	Surface-water Gleys	Clayey
0700d	Straffan	Surface water and Luvisols commonly associated with fluvioglacial outwash gravels and Calcareous Brown Earth on lower slopes over limestones bedrock	Surface-water Gleys	Fine-loamy
0700f	Newport	Surface-water Gleys on lower slopes and Humic Brown Podzolics and Podzols in upper altitude, all on drift with siliceous stones	Surface-water Gleys	Coarse-loamy
0700h	Kilrush	Surface-water Gleys associated with Luvisols, on drift with siliceous stones and Basin Peat	Surface-water Gleys	Fine-loamy

0760a	Gortaclareen	Mostly Surface-water Gleys associated with Brown Earths, over shale and slate bedrock and on drift with siliceous stones	Surface-water Gleys	Fine-loamy
0760c	Howardstown	Surface-water Gley and Luvisols in Clayey lowlands on drift with limestones with inclusions of Calcareous Brown Earth	Surface-water Gleys	Clayey
0760e	Ballinamore	Humic Surface-water Gleys and Humic Groundwater Gleys, on drift with limestones, and Peat	Surface-water Gleys	Fine-loamy
0760f	Driminidy	Humic Surface-water Gleys and Humic Brown Earths on moderate slopes; upland with Blanket Peat with extensive bedrock with Historic Lithosols and Podzols.	Surface-water Gleys	Coarse-loamy
0800a	Black Rock Mountain	Podzols on drift with igneous and metamorphic stones in uplands and Peat; and Lithosols over gneiss and schist on slopes	Podzol	Sandy
0800c	Ballycondon	Podzols and Brown Podzolics on drift with siliceous stones and sandstone bedrock and Peat	Podzol	Loamy
0843b	Knockastanna	Podzols and Brown Podzolics over shale and slate bedrock and Peat, with inclusions of Humic Rendzinas and Brown Earth on bedrock	Podzol	Loamy
0843e	Plenary	Podzols and Brown Podzolics on drift with siliceous stones and Peat	Podzol	Sandy
0843f	Plenary	Blanket Peat and Podzols in Mountainous areas, with outcropping rock and Humic Lithosols (on sandstones bedrock); interspersed with Stagno-Podzols and Surface-water Gleys, on drift with siliceous stones.	Podzol	Loamy
0900a	Cooga	Brown Podzolic soils with Groundwater Gleys on drift with siliceous stones an inclusions of Podzols and Brown Earth	Brown Podzolic	Loamy
0900b	Kiltealy	Brown Podzolics and Brown Earth predominate with altitudinal sequence of upland Peat, Lithosols and Podzols on drift with igneous and metamorphic stones	Brown Podzolic	Sandy
0900e	Ross Carbery	Brown Podzolics and Brown Earths mainly on drift with siliceous stones, Surface-water Gleys and Groundwater Gleys in lowland areas	Brown Podzolic	Coarse-loamy
0900f	Clonin	Shallow Peat soils beside Lithosols, Podzols over sandstone bedrock and Brown Podzolics in upland on drift with siliceous stones	Brown Podzolic	Loamy
0900g	Cupidstownhill	Brown Ppodzolics and Brown earth on undulating shale/slate bedrock and on drift with siliceous stone	Brown Podzolic	Fine-loamy

0900h	NBP4	Predominantly Brown Podzolic and Brown Earths and Rendzinas on gneiss and shist bedrock and on drift with igneous and metamorphic stones, with inclusions of Surface-water Gleys and Groundwater Gleys	Brown Podzolic	Fine-loamy
0920a	Clonegall	Gleyic Brown Podzolics, Podzols and Brown Earth on drift with siliceous stones and inclusions of Groundwater Gleys	Brown Podzolic	Coarse-loamy
0960c	Borrisoleigh	Humic Brown Podzolics, gleyic, and humic Brown Earth on a wet undulating on shale bedrock and on drifting siliceous with inclusions of Groundwater Gleys and Humic Lithosols	Brown Podzolic	Fine-loamy
0960d	Knockaceol	Altitudinal sequence of Humic Brown Podzolics, Podzols on sandstone bedrock and on drift siliceous and Peat with inclusions of Surface-water Gleys and Rendzinas	Brown Podzolic	Coarse-loamy
0960e	Knockboy	Brown Podzolics with Podzols on upper slopes and Surface- water Gleys in depressions, on drifting with siliceous stones	Brown Podzolic	Coarse-loamy
1000a	Elton	Luvisols associated with Surface-water Gleys, Stagnic Brown Earths, and Calcareous Brown Earths, on drift with limestones	Luvisols	Fine-loamy
1000x			Luvisol	Fine-loamy
1000c	Elton	Luvisols associated to historic and humic Groundwater Gleys and Calcareous Brown Earths, on drift with limestones and Basin Peat	Luvisol	Fine-loamy
1000g	Elton	Heavier textures in the soils of this association. Association with Luvisols, Groundwater Gleys, and Calcareous Brown Earths, on drift with limestones	Luvisol	Fine-loamy
1000x	Elton	Luvisols and Surface water Gleys on drift with mixed of limestones and siliceous stones	Luvisol	Fine-loamy
1030a	Crosstown	Luvisols, Surface-water Gleys, and Stagnic Brown Earths on drift with siliceous stones, with inclusions of Groundwater Gleys	Luvisol	Fine-loamy
1030b	Rathowen	Luvisols, Surface-water Gleys, Groundwater Gleys on drift with limestones and Peat	Luvisol	Fine-loamy
1100a	Clonroche	Well drained Brown Earth on drift with siliceous stones in an undulating land with some Brown Podzolics on upper slopes. Surface-water Gleys and Groundwater Gleys found in depressions	Brown Earth	Fine-loamy

1100c	Clashmore	Brown Earths and Luvisols on upper slopes; Surface-water Gleys and Groundwater Gleys in depressions	Brown Earth	Fine-loamy
1100d	Ballyvorheen	Brown Earths, Brown Podzolics and Podzols, soils related to coarse textures on drift with siliceous stones	Brown Earth	Sandy
1100e	Ballylanders	Brown Earth on lower slopes, Podzols on steeper slopes, Luvisols and Surface-water Gleys in depressions, related to fine soil textures on shale bedrock and on drift with siliceous stones.	Brown Earth	Fine-loamy
1100h	Borris	Brown Earths and Brown Podzolics on slope on drift with igneous and metamorphic stones, inclusions of Surface-water Gleys	Brown Earth	Coarse-loamy
1100l	Kennycourt	Brown Earths, Luvisols and Groundwater Gleys on drift with limestones	Brown Earth	Fine-loamy
1100m	Kill	Brown Earths, Brown Podzolics and Podzols on an undulating land with igneous and metamorphic stones, inclusions of Surface-water Gleys in depressions.	Brown Earth	Fine-loamy
1100n	Clashmore	Brown Earths, Luvisols and Surface-water Gleys on drift with siliceous stones	Brown Earth	Coarse-loamy
1100q	Mullabane	Mostly Brown Earth and Calcareous Brown Eaths on drift with limestones, associated with Luvisols and some inclusions of Rendzinas and Peat	Brown Earth	Fine-loamy
1100s	Broomhill	Brown Earths and Brown Podzolics mainly on sandstones bedrock and some occurs on drift with siliceous stones, with inclusions of Podzols and Surface-water Gleys	Brown Earth	Fine-loamy
1130a	Moord	Brown Earths and Surface-water Gleys associated to humic and gleyic diagnostic features on drift with siliceous stones and inclusions of Luvisols in a drumlin area.	Brown Earth	Fine-loamy
1130b	Duarrigle	Brown Earths, Surface-water Gleys, and Lithosols on shale/sandstone bedrock in an undulating area	Brown Earth	Fine-loamy
1150a	Baggotstown	Calcareous Brown Eaths, Brown Earths and Luvisols on calcareous gravels and on drift limestones, inclusions of Rendzinas	Brown Earth	Coarse-loamy
1150b	Ballincurra	Calcareous Brown Earths and Luvisols associated with Rendzinas and decalcified Lithosols, on limestones bedrock	Brown Earth	Fine-loamy

1150c	Faoldroim	Calcareous Brown Eaths, Brown Earths and Luvisols on drift with limestones, associated with Rendzinas and decalcified Lithosols on limestones bedrock and Peat	Brown Earth	Fine-loamy
1160a	Ashgrove	Humic and gleyic Brown Earths and Surface-water Gleys, on drift with siliceous stones	Brown Earth	Fine-loamy
1160c	Schull	Brown Earth, Brown Podzolics, Podzols and Surface-water Gleys associated to humic and gleyic diagnostic features on drift with siliceous stones	Brown Earth	Coarse-loamy

Appendix C: Additional climate downscaling results

This appendix presents the seasonal summer and winter projected raster maps statistics based on different periods and different climate scenarios for both precipitation and temperature.

Table C-1: Raster maps statistics for baseline and projected seasonal summer precipitation according to different Representative Concentration Pathways.

Period															
Baseline				2020					2050				2080			
Min. (mm/y)	Max. (mm/y)	Mean (mm/y)	Standard Deviation (mm/y)	Scenarios	Min. (mm/y)	Max. (mm/y)	Mean (mm/y)	Standard Deviation (mm/y)	Min. (mm/y)	Max. (mm/y)	Mean (mm/y)	Standard Deviation (mm/y)	Min. (mm/y)	Max. (mm/y)	Mean (mm/y)	Standard Deviation (mm/y)
353.29	1181.31	486.22	83.58	RCP 4.5 (50%)	351.37	1173.48	484.30	82.99	388.40	1288.02	525.06	96.41	337.34	1116.43	470.30	78.75
				RCP 4.5 (75%)	352.74	1180.37	485.67	83.51	350.24	1176.11	483.15	83.18	348.73	1173.55	481.63	82.99
				RCP 8.5 (50%)	350.95	1171.77	483.88	82.86	336.53	1113.13	469.49	78.51	318.79	1040.09	451.37	73.34
				RCP 8.5 (75%)	352.62	1180.16	485.55	83.96	348.50	1173.13	481.39	82.96	343.33	1161.76	475.93	82.05

Table C-2: Raster maps statistics for baseline and projected seasonal winter precipitation according to different Representative Concentration Pathways.

Period																
Baseline					2020				2050				2080			
Min. (mm/y)	Max. (mm/y)	Mean (mm/y)	Standard Deviation (mm/y)	Scenarios	Min. (mm/y)	Max. (mm/y)	Mean (mm/y)	Standard Deviation (mm/y)	Min. (mm/y)	Max. (mm/y)	Mean (mm/y)	Standard Deviation (mm/y)	Min. (mm/y)	Max. (mm/y)	Mean (mm/y)	Standard Deviation (mm/y)
441.39	1832.21	650.04	143.10	RCP 4.5 (50%)	443.97	1836.85	653.36	143.37	455.77	1858.17	668.48	144.61	462.85	1876.72	677.55	145.37
				RCP 4.5 (75%)	441.12	1824.24	651.41	143.17	465.08	1887.94	677.38	145.71	473.36	1923.53	691.69	149.02
				RCP 8.5 (50%)	444.56	1837.63	654.09	143.43	463.96	1872.61	678.90	145.49	488.41	1916.59	710.32	148.23
				RCP 8.5 (75%)	446.08	1845.61	656.15	143.97	474.92	1928.01	693.73	149.32	511.42	2032.31	741.29	156.21

Table C-3: Raster maps statistics for baseline and projected seasonal summer temperature according to different representative concentration pathways.

Period																
Baseline					2020				2050				2080			
Min. (°c)	Max. (°c)	Mean (°c)	Standard Deviation (°c)	Scenarios	Min. (°c)	Max. (°c)	Mean (°c)	Standard Deviation (°c)	Min. (°c)	Max. (°c)	Mean (°c)	Standard Deviation (°c)	Min. (°c)	Max. (°c)	Mean (°c)	Standard Deviation (°c)
7.72	14.10	12.73	0.80	RCP 4.5 (50%)	7.78	14.22	12.86	0.5	7.98	14.59	13.27	0.51	8.06	17.74	13.45	0.52
				RCP 4.5 (75%)	7.81	14.28	12.90	0.504	8.09	14.81	13.41	0.52	13.25	14.36	13.83	0.32
				RCP 8.5 (50%)	8.07	14.76	13.50	0.522	7.79	14.24	12.88	0.50	8.07	14.76	13.50	0.522
				RCP 8.5 (75%)	8.44	15.44	14.24	0.55	8.27	15.15	13.7	0.53	8.826	16.2	14.67	0.56

Table C-4: Raster maps statistics for baseline and projected seasonal winter temperature according to different Representative Concentration Pathways.

Period																
Baseline					2020				2050				2080			
Min. (°c)	Max. (°c)	Mean (°c)	Standard Deviation (°c)	Scenarios	Min. (°c)	Max. (°c)	Mean (°c)	Standard Deviation (°c)	Min. (°c)	Max. (°c)	Mean (°c)	Standard Deviation (°c)	Min. (°c)	Max. (°c)	Mean (°c)	Standard Deviation (°c)
2.41	8.91	6.57	0.63	RCP 4.5 (50%)	2.46	9.04	6.70	0.64	2.60	9.41	7.06	0.65	2.68	9.63	7.28	0.65
				RCP 4.5 (75%)	2.46	9.07	6.72	0.64	2.62	9.52	7.14	0.66	2.72	9.80	7.40	0.67
				RCP 8.5 (50%)	2.47	9.07	6.72	0.64	2.70	9.67	7.32	0.65	2.99	10.46	8.07	0.68
				RCP 8.5 (75%)	2.48	9.10	6.75	0.64	2.73	9.85	7.44	0.67	3.06	10.81	8.32	0.71

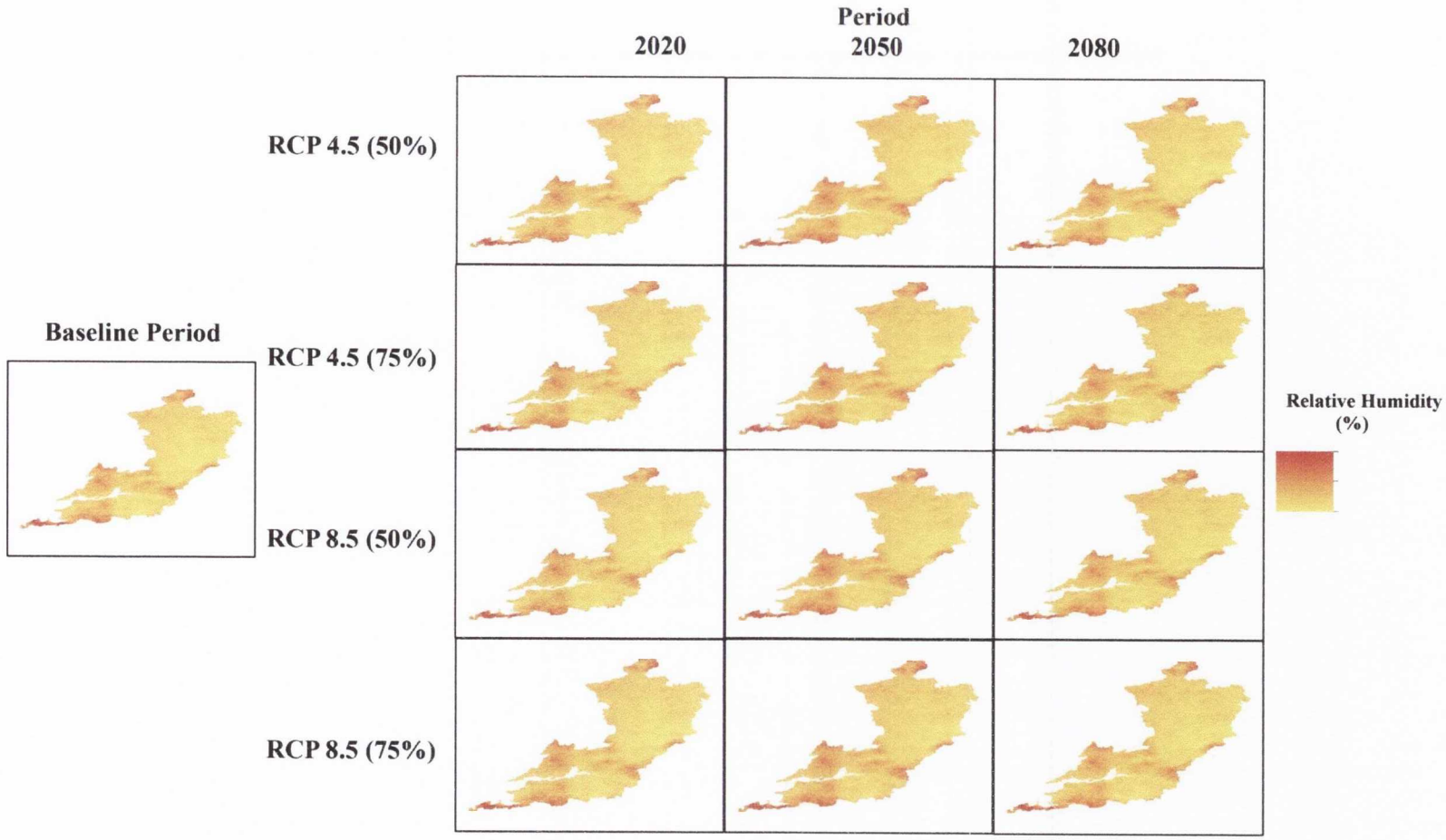

Figure C.1: Relative humidity long-term average for baseline and projection periods according to different Representative Concentration Pathways.

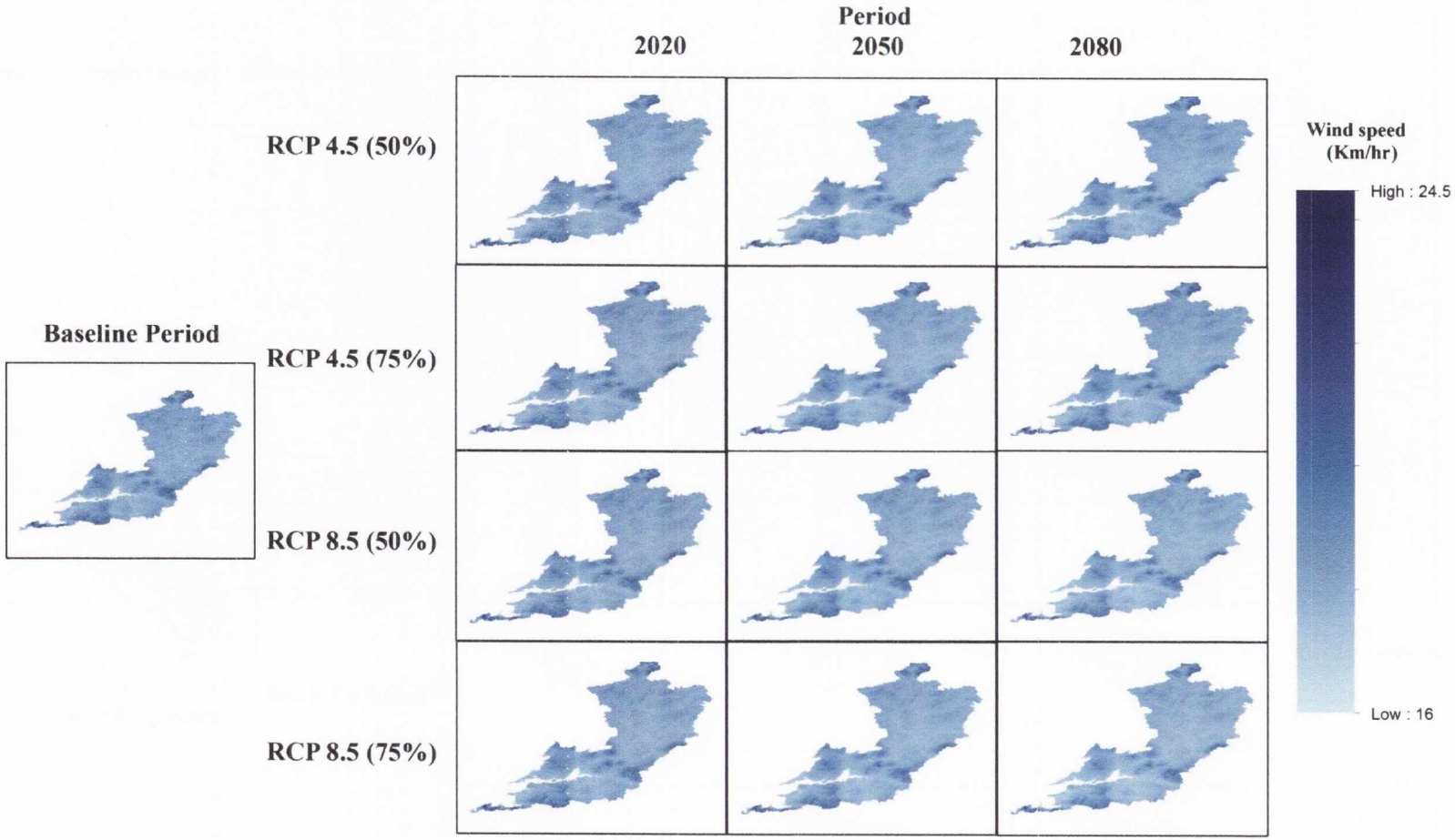

Figure 0.2: Wind speed long-term average for baseline and projection periods according to different Representative Concentration Pathways.

Appendix D: GEO-CWB user interfaces

This Appendix presents the designed user interfaces for the different stages of GEO-CWB.

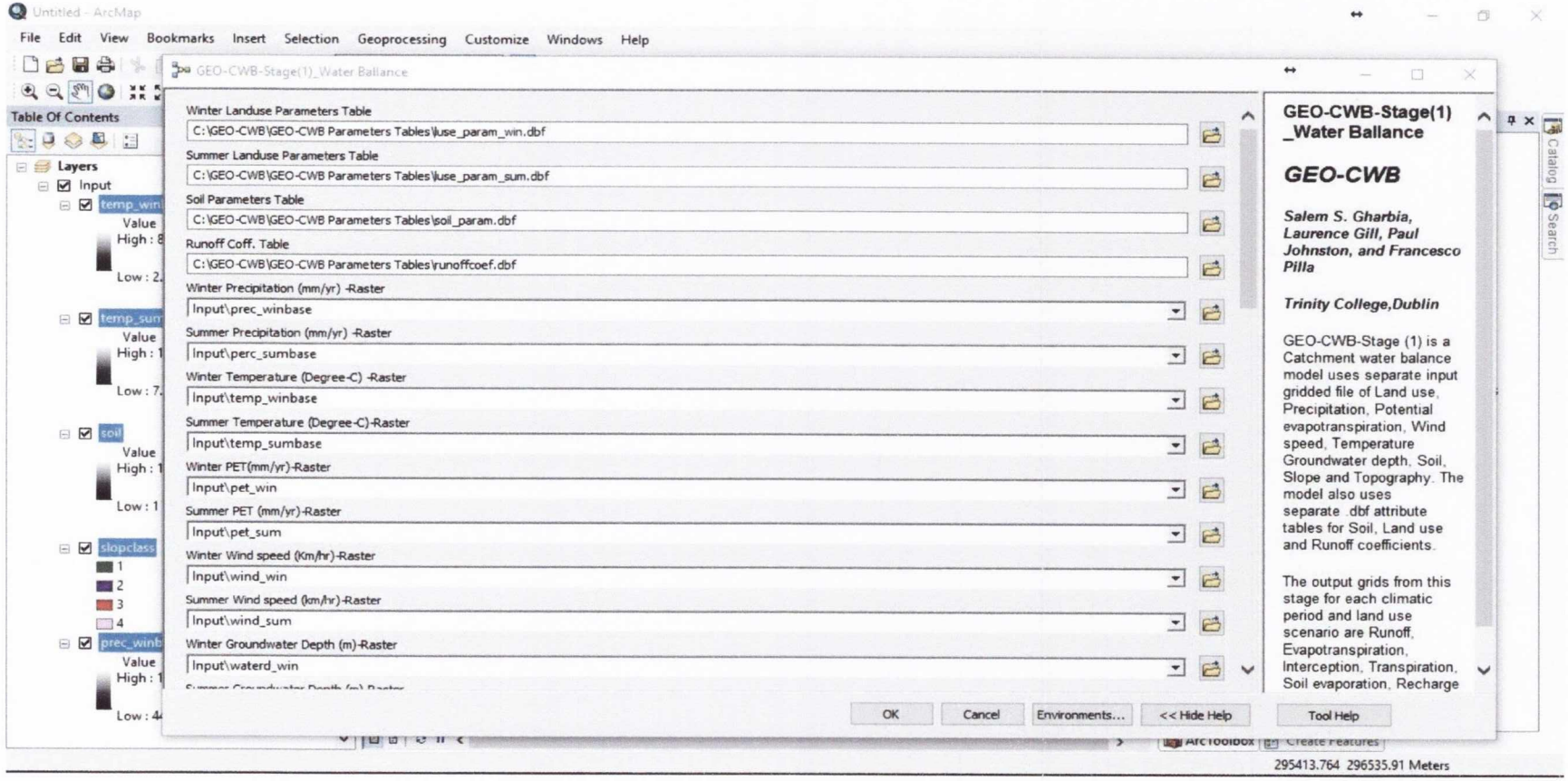

Figure D.1: GEO-CWB stage (1) interface.

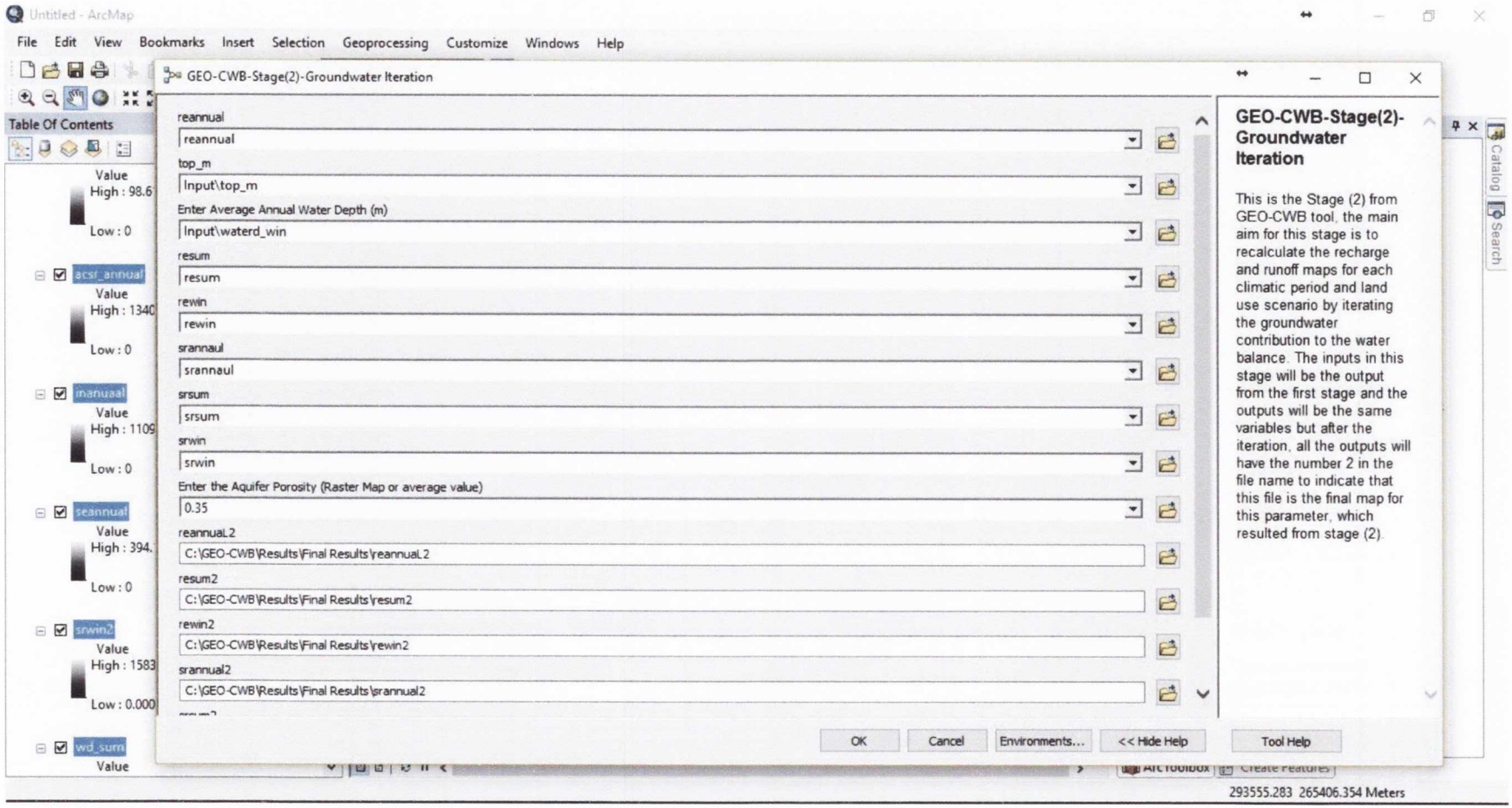

Figure D.2: GEO-CWB stage (2) interface.

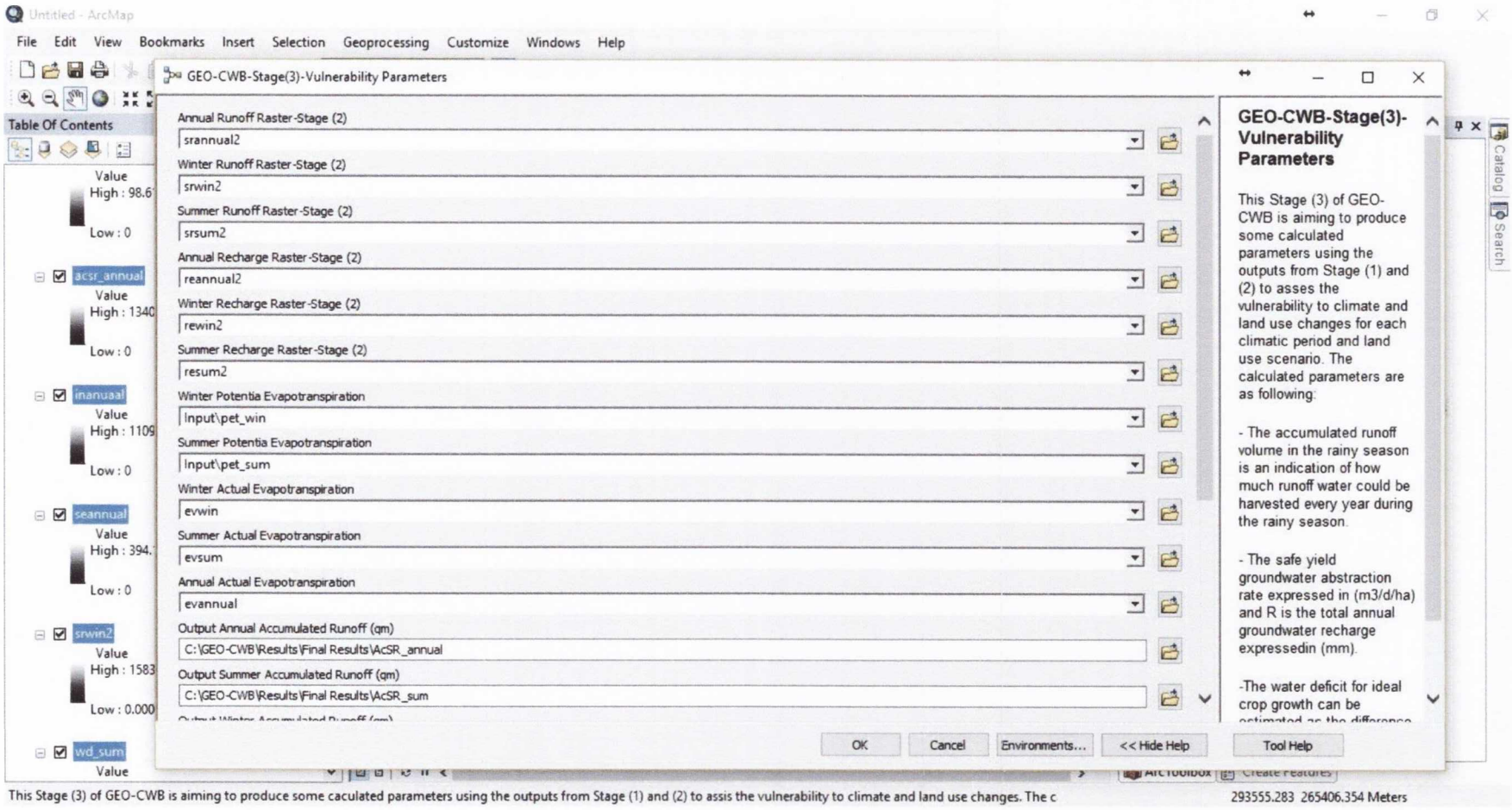

Figure D.3: GEO-CWB stage (3) interface.

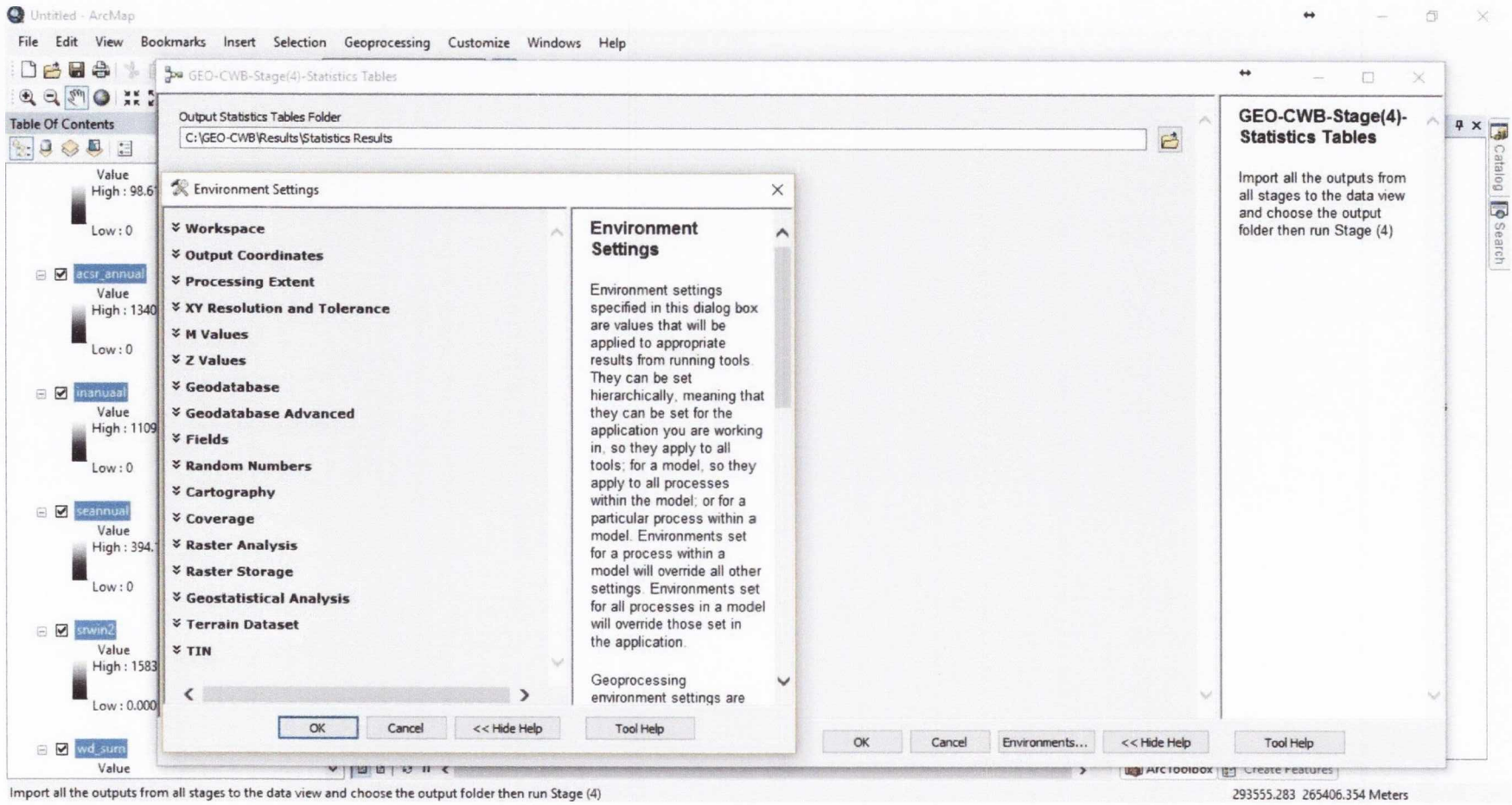

Figure D.4: GEO-CWB stage (4) interface.

Appendix E: Additional GEO-CWB results

This appendix shows the seasonal summer and winter raster maps results from GEO-CWB for runoff, sub-surface water components, transpiration, evapotranspiration, soil evaporation, change in the storage and safe yield ground water abstraction based on different simulated climate scenarios.

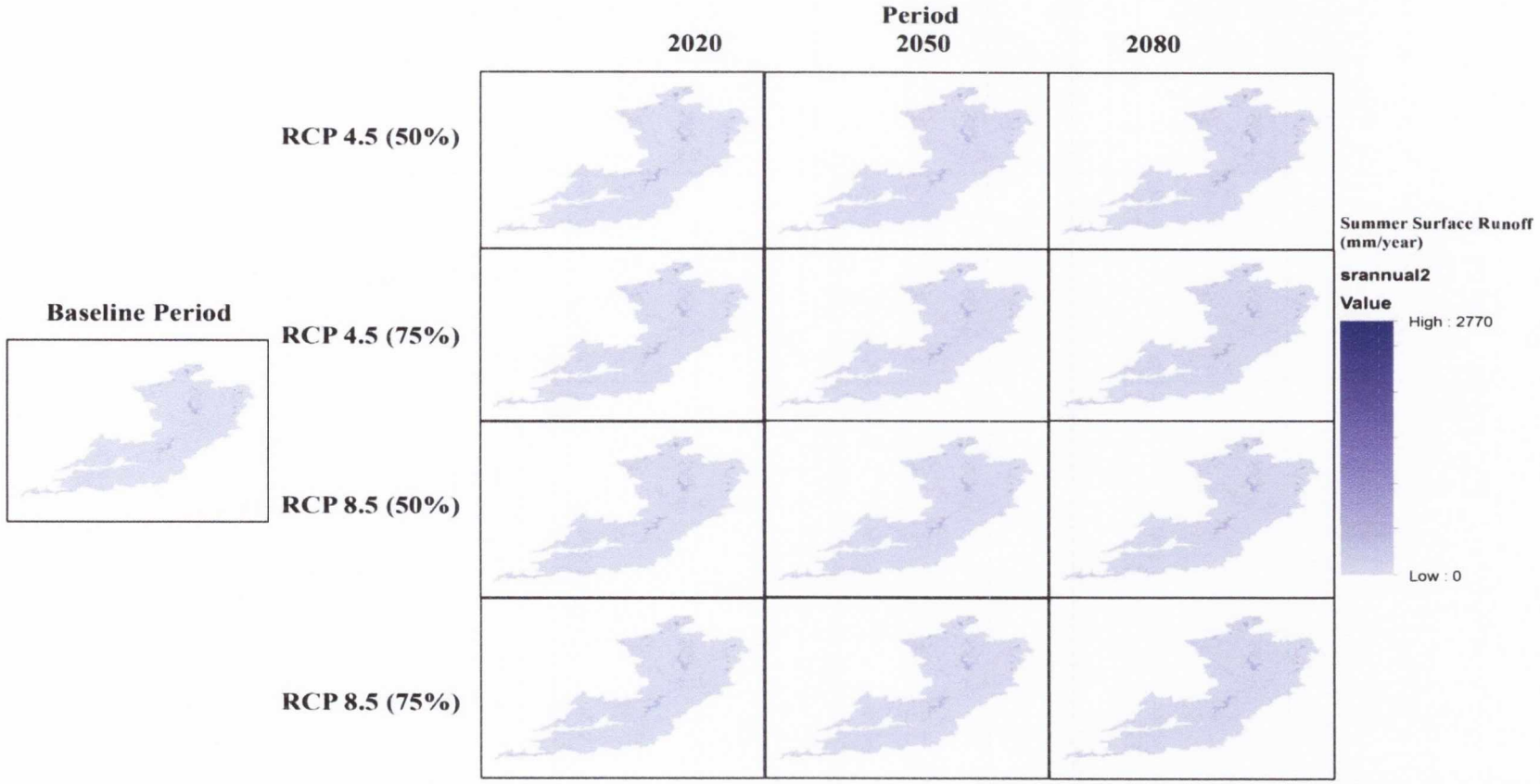

Figure E.1: The average summer surface runoff for each climatic period and land use scenario simulated by GEO-CWB.

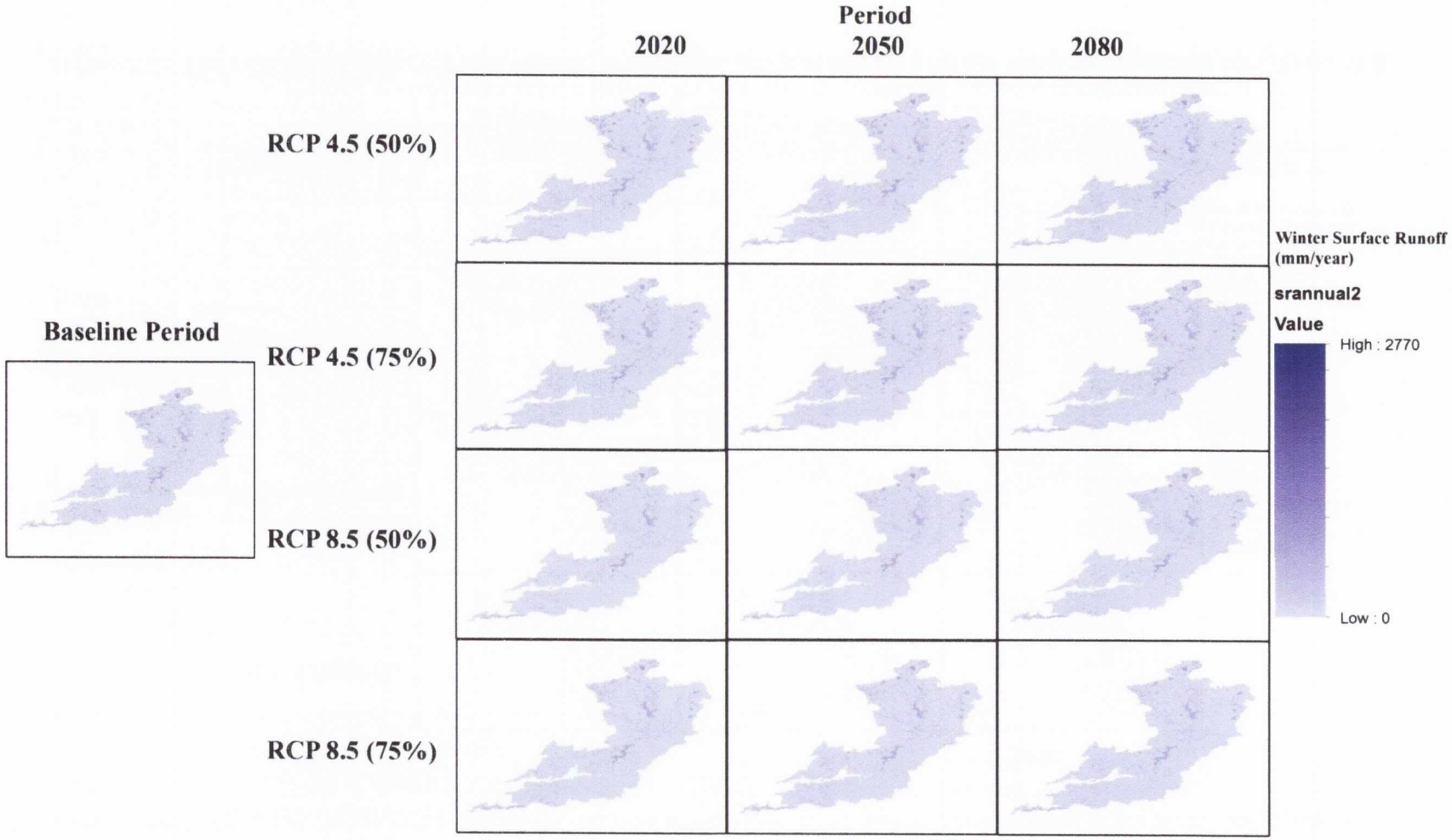

Figure E.2: The average winter surface runoff for each climatic period and land use scenario simulated by GEO-CWB.

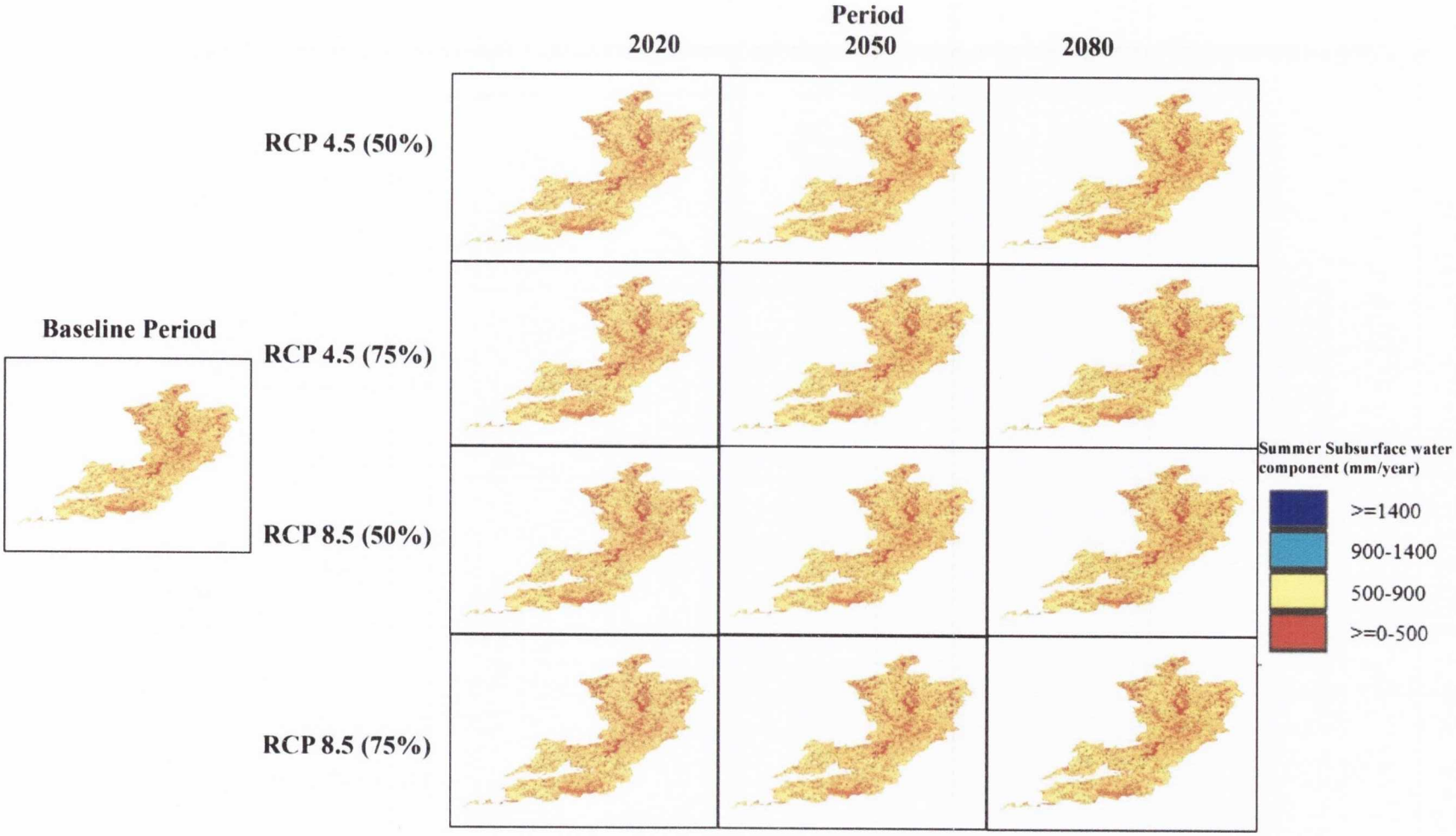

Figure E.3: The average summer subsurface water component for each climatic period and land use scenario simulated by GEO-CWB.

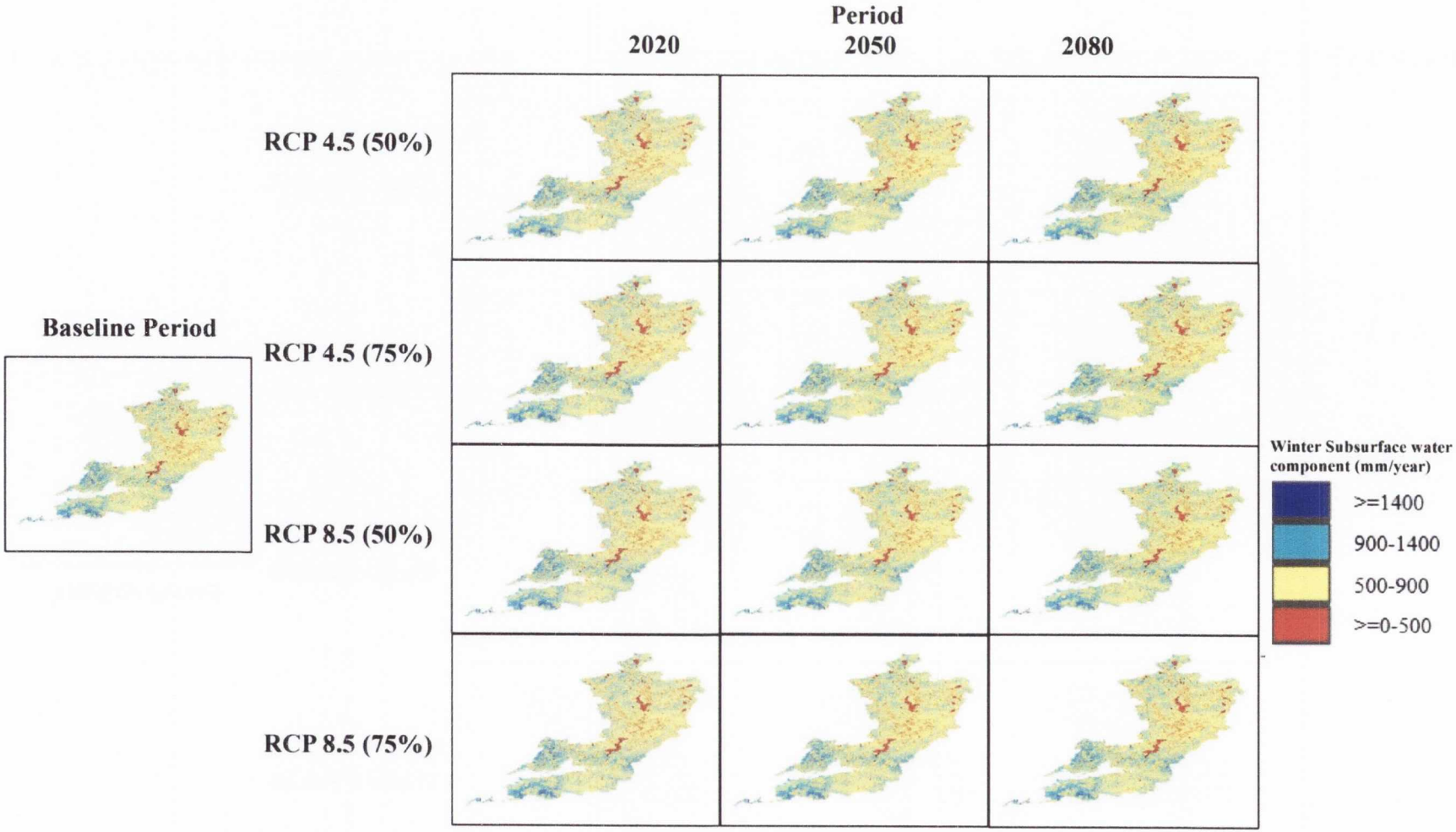

Figure E.4: The average winter subsurface water component for each climatic period and land use scenario simulated by GEO-CWB.

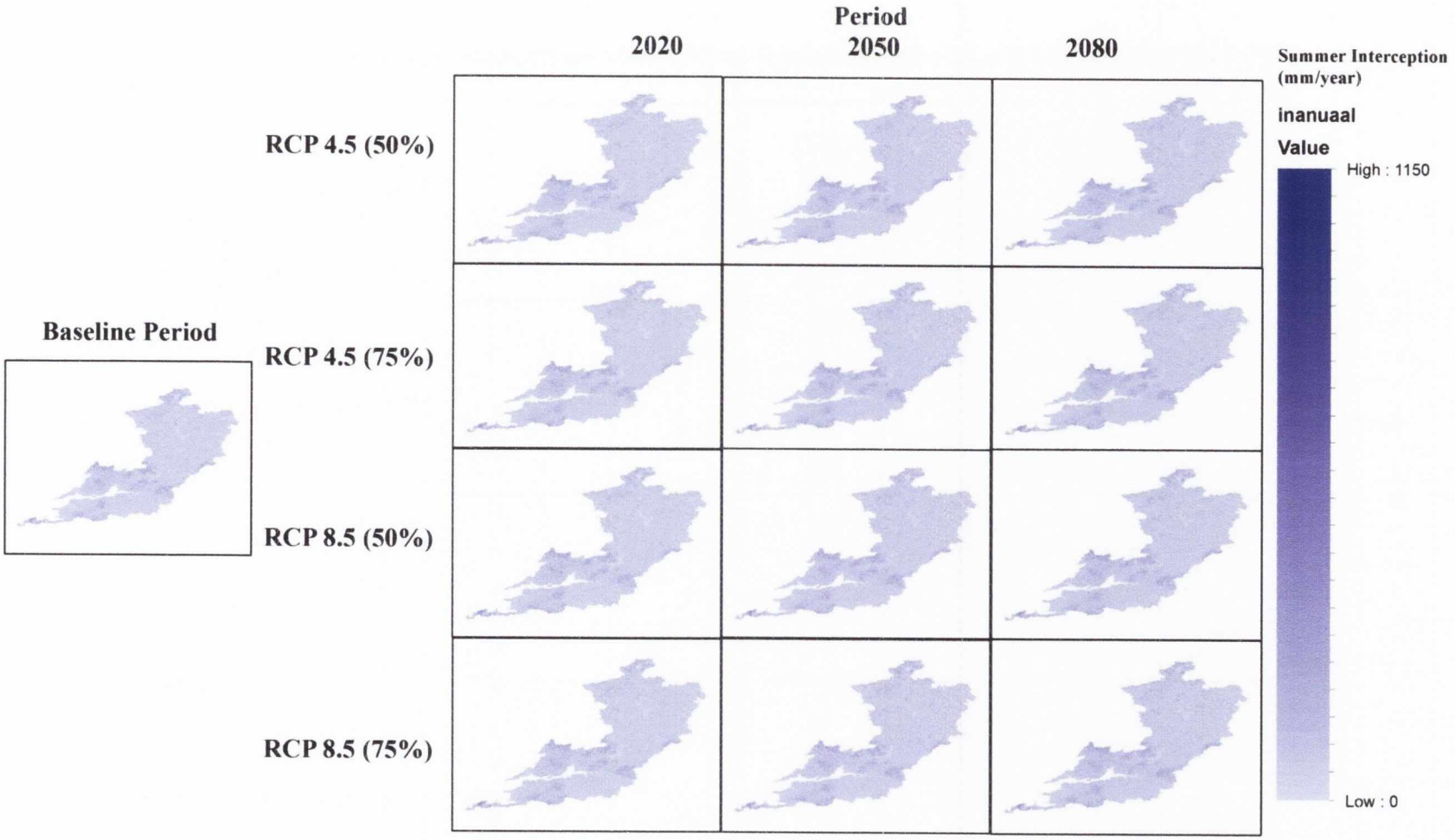

Figure E.5: The average summer interception for each climatic period and land use scenario simulated by GEO-CWB.

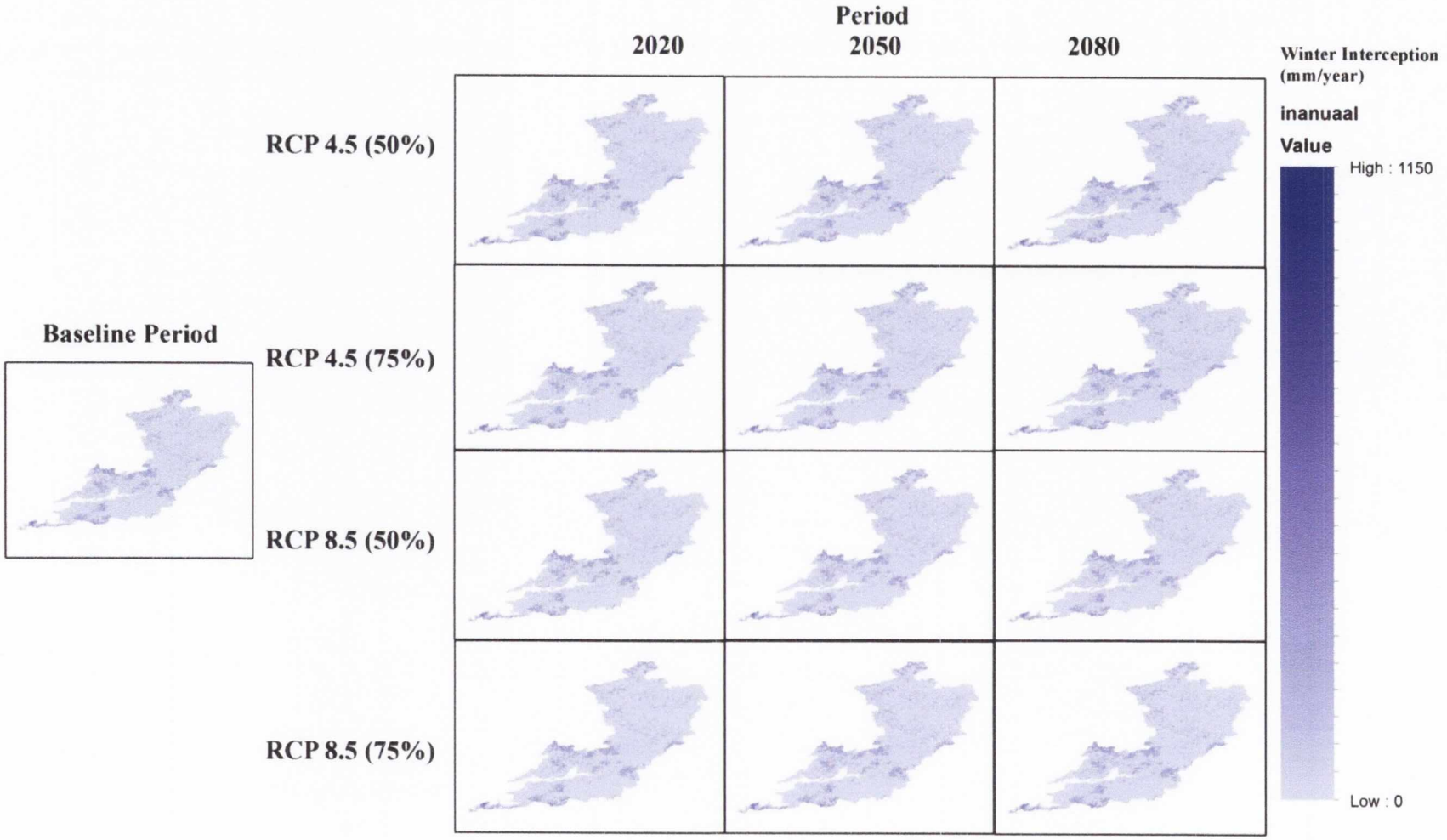

Figure E.7: The average winter interception for each climatic period and land use scenario simulated by GEO-CWB.

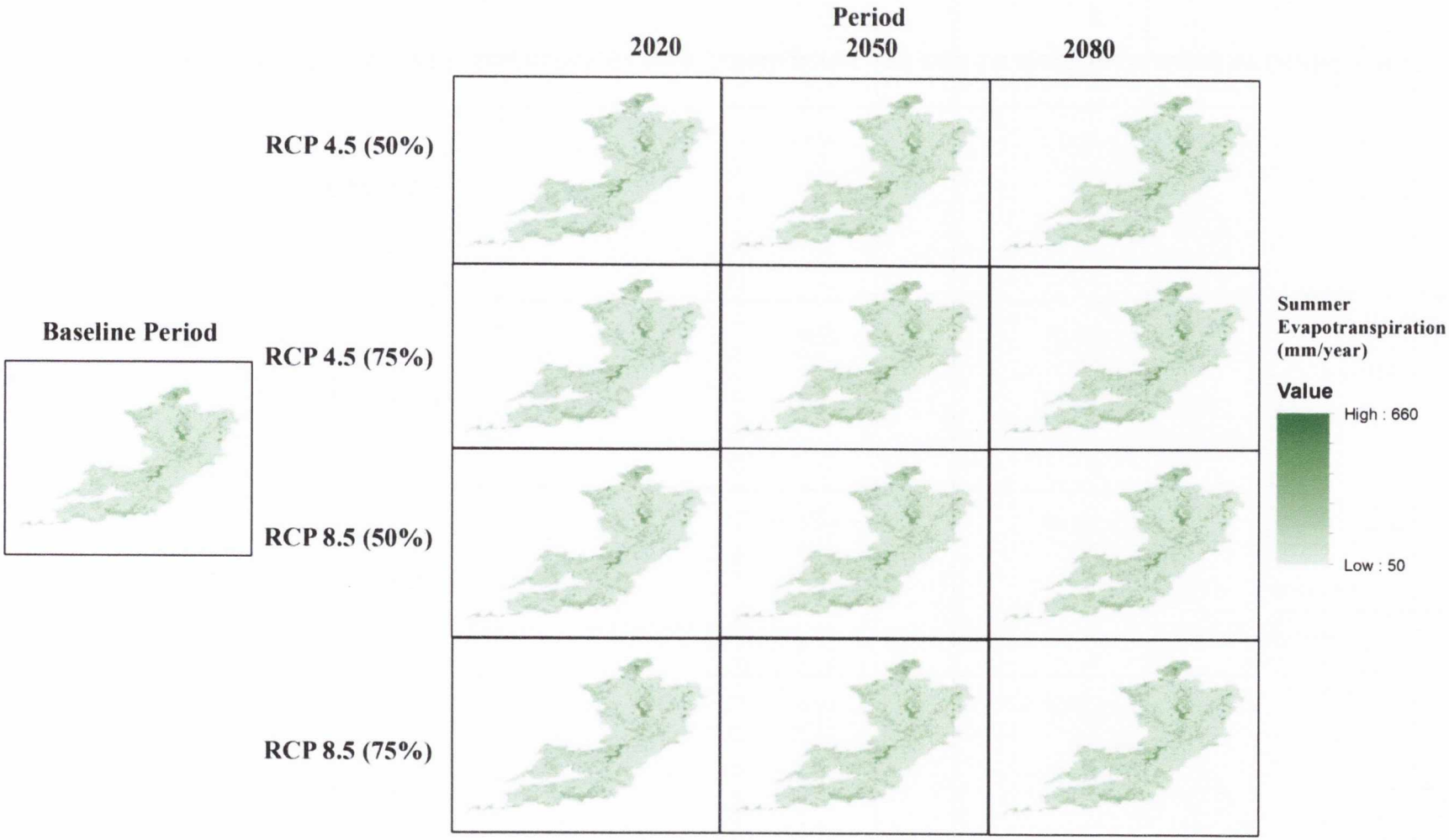

Figure E.7: The average summer evapotranspiration for each climatic period and land use scenario simulated by GEO-CWB.

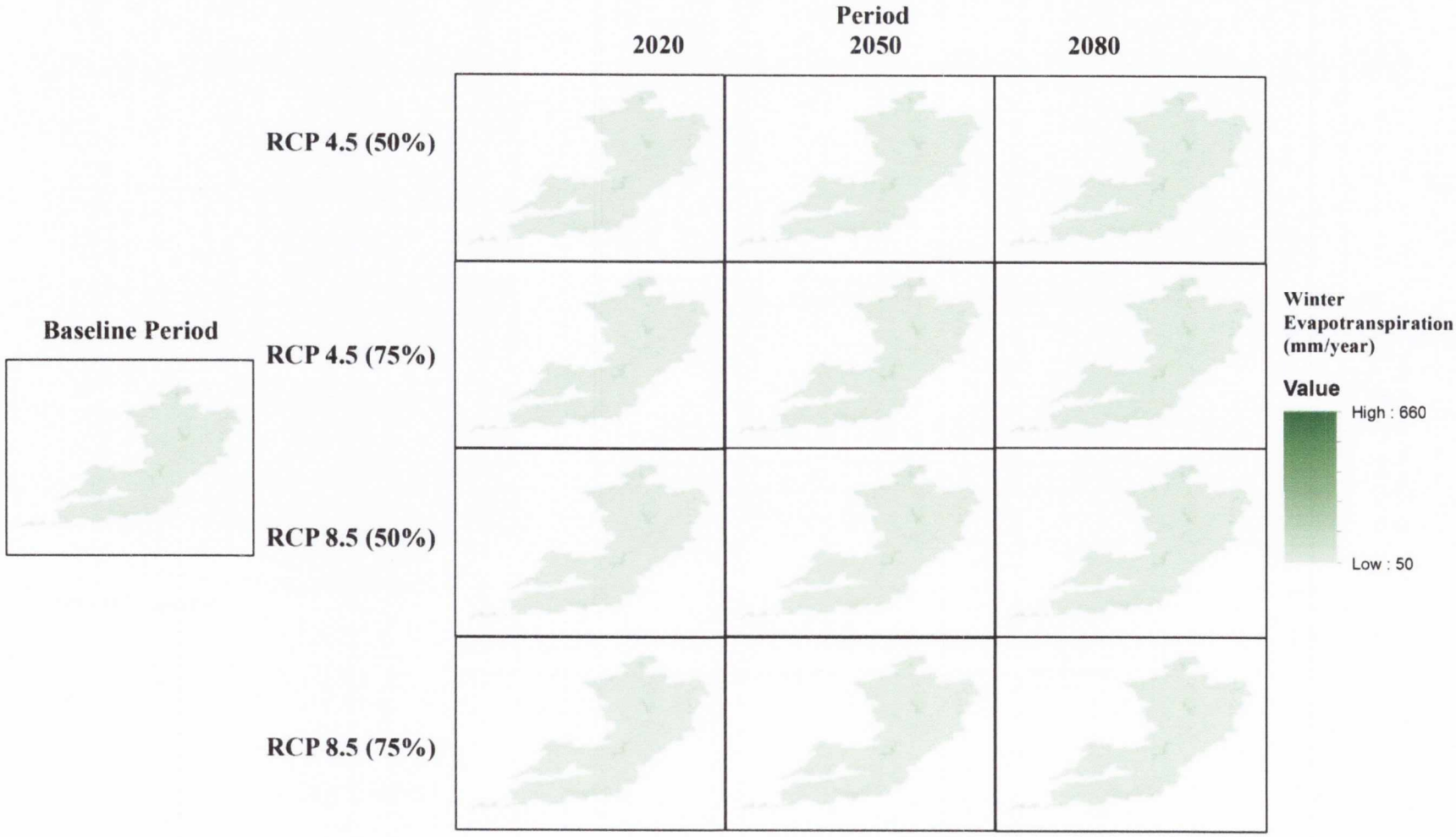

Figure E.9: The average winter evapotranspiration for each climatic period and land use scenario simulated by GEO-CWB.

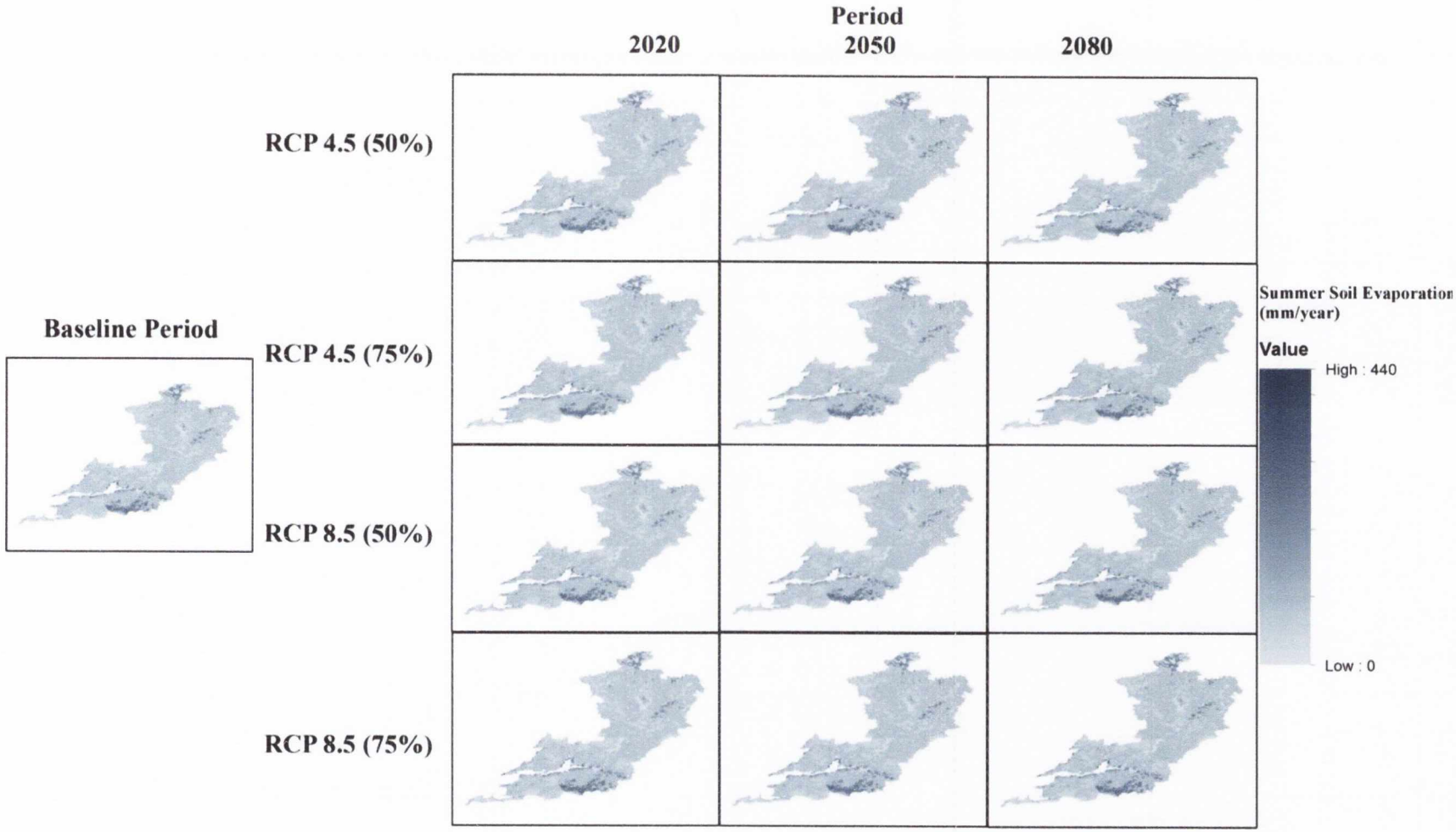

Figure E.10: The average summer soil evaporation for each climatic period and land use scenario simulated by GEO-CWB.

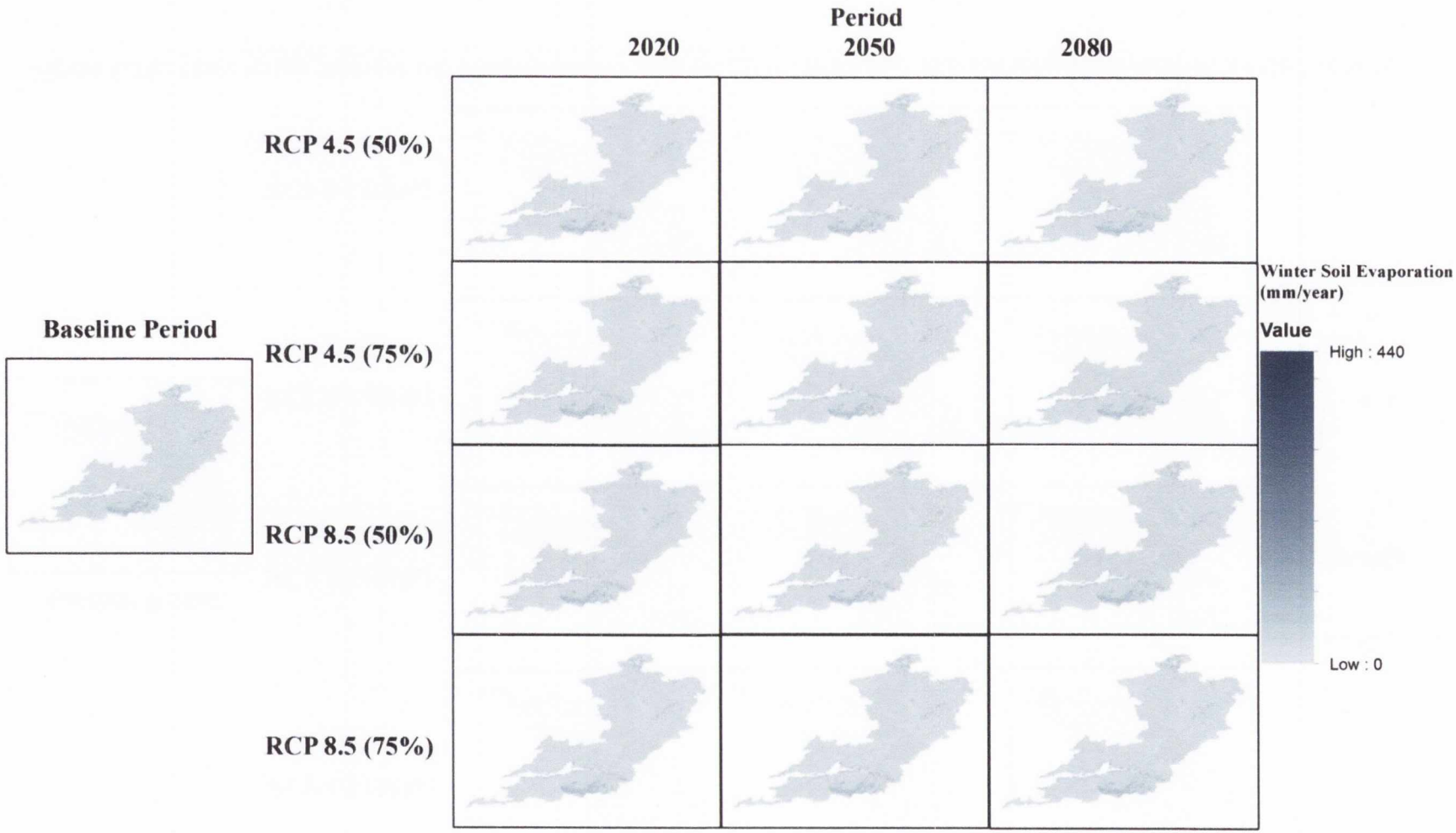

Figure E.11: The average winter soil evaporation for each climatic period and land use scenario simulated by GEO-CWB.

Figure E.12: The average summer transpiration for each climatic period and land use scenario simulated by GEO-CWB.

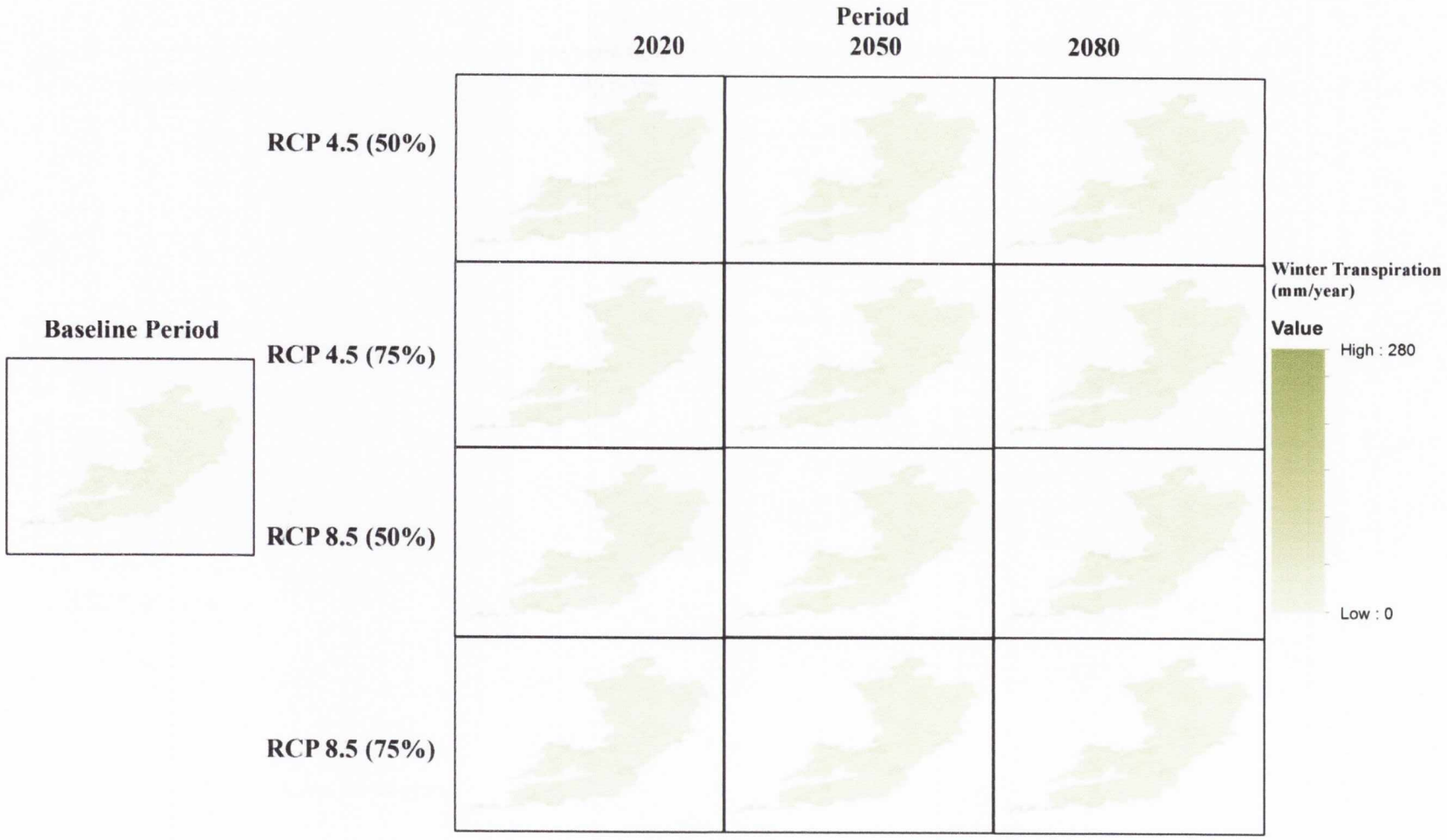

Figure E.13: The average winter transpiration for each climatic period and land use scenario simulated by GEO-CWB.

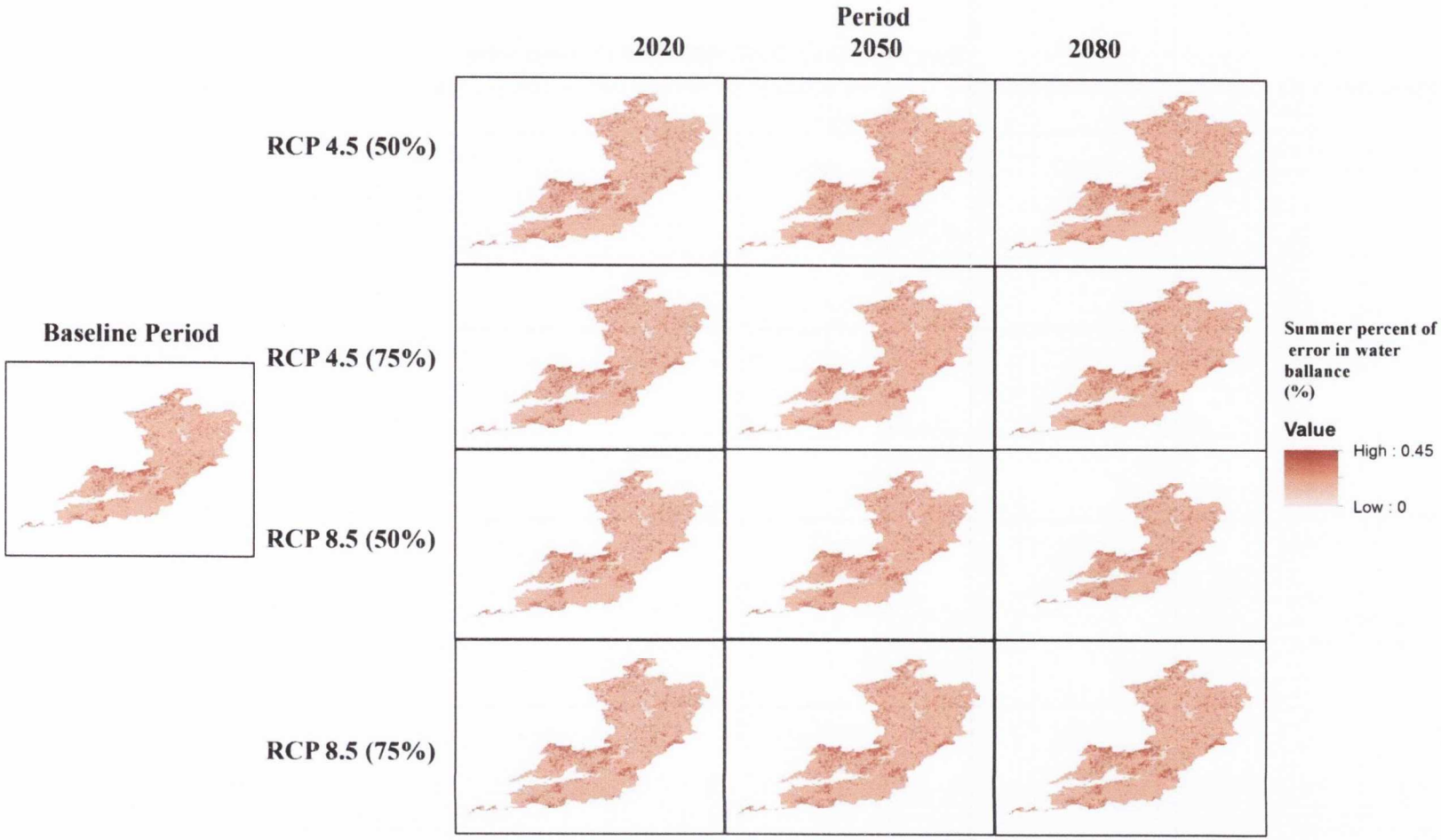

Figure E.14: The spatially distributed average summer error/change in storage in water balance (mm/year) for each climatic period and land use scenario simulated by GEO-CWB.

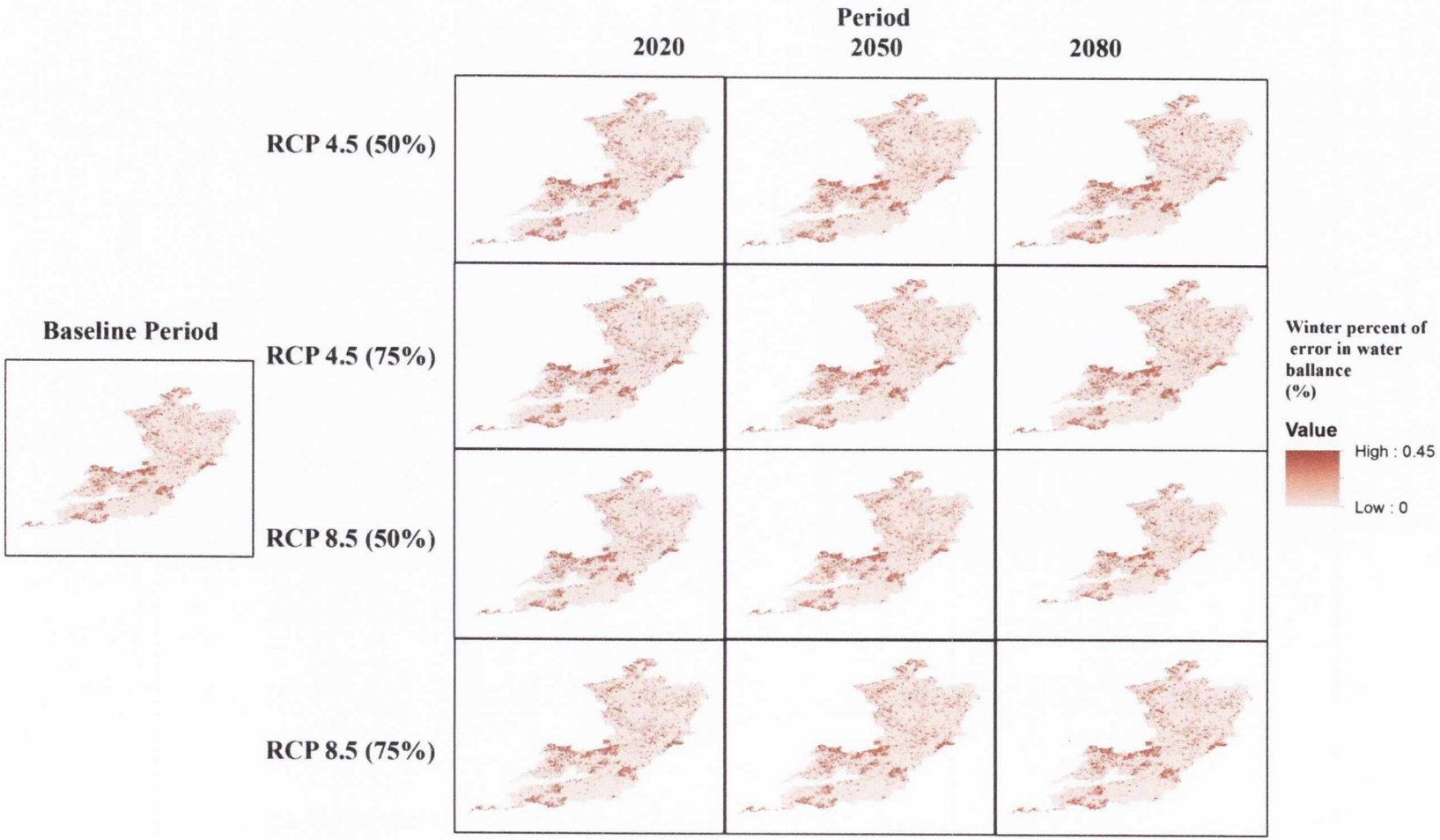

Figure E.15: The spatially distributed average winter error/change in storage in water balance (mm/year) for each climatic period and land use scenario simulated by GEO-CWB.

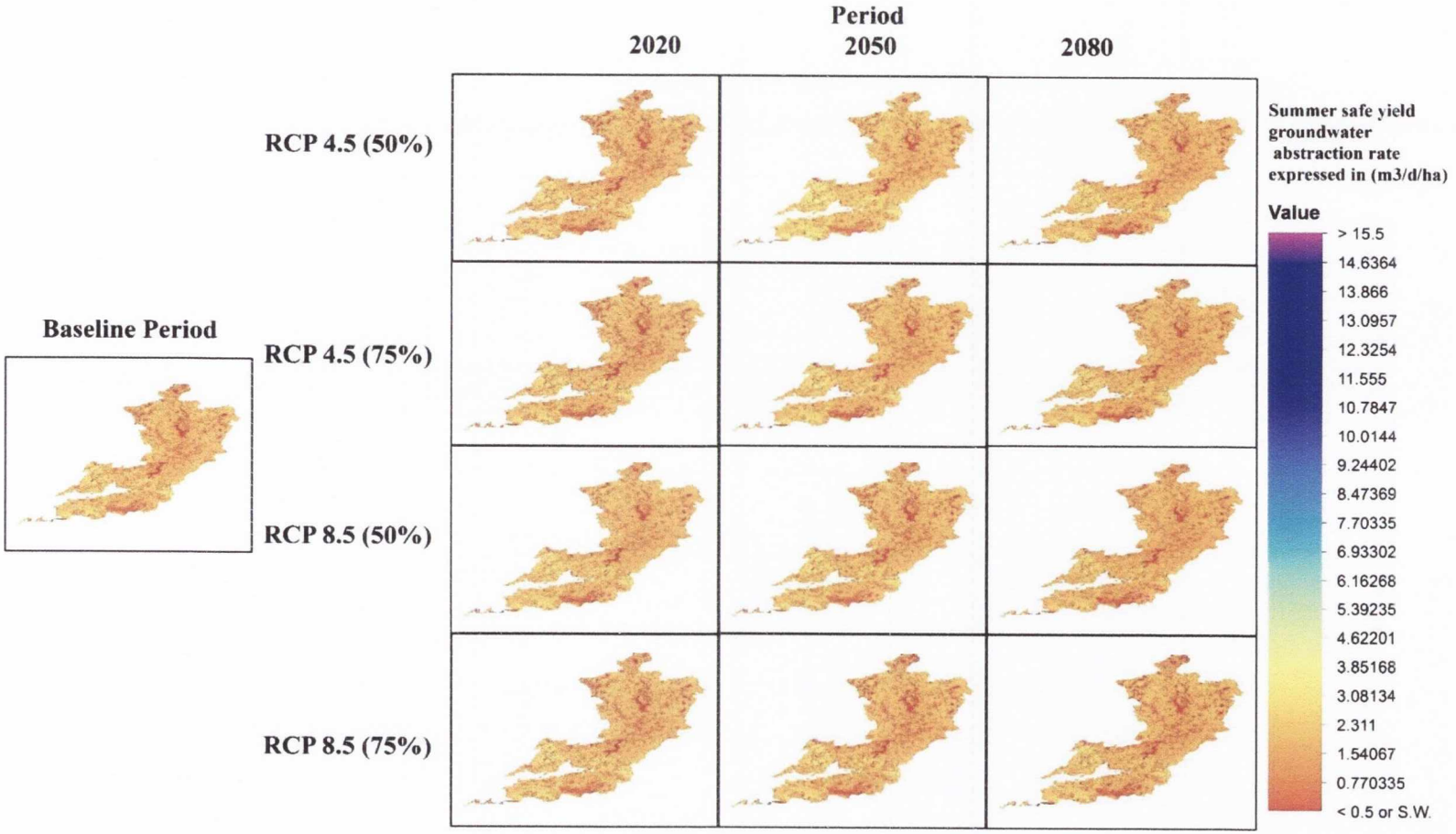

Figure E.16: The average summer safe yield groundwater abstraction for each climatic period and land use scenario simulated by GEO-CWB.

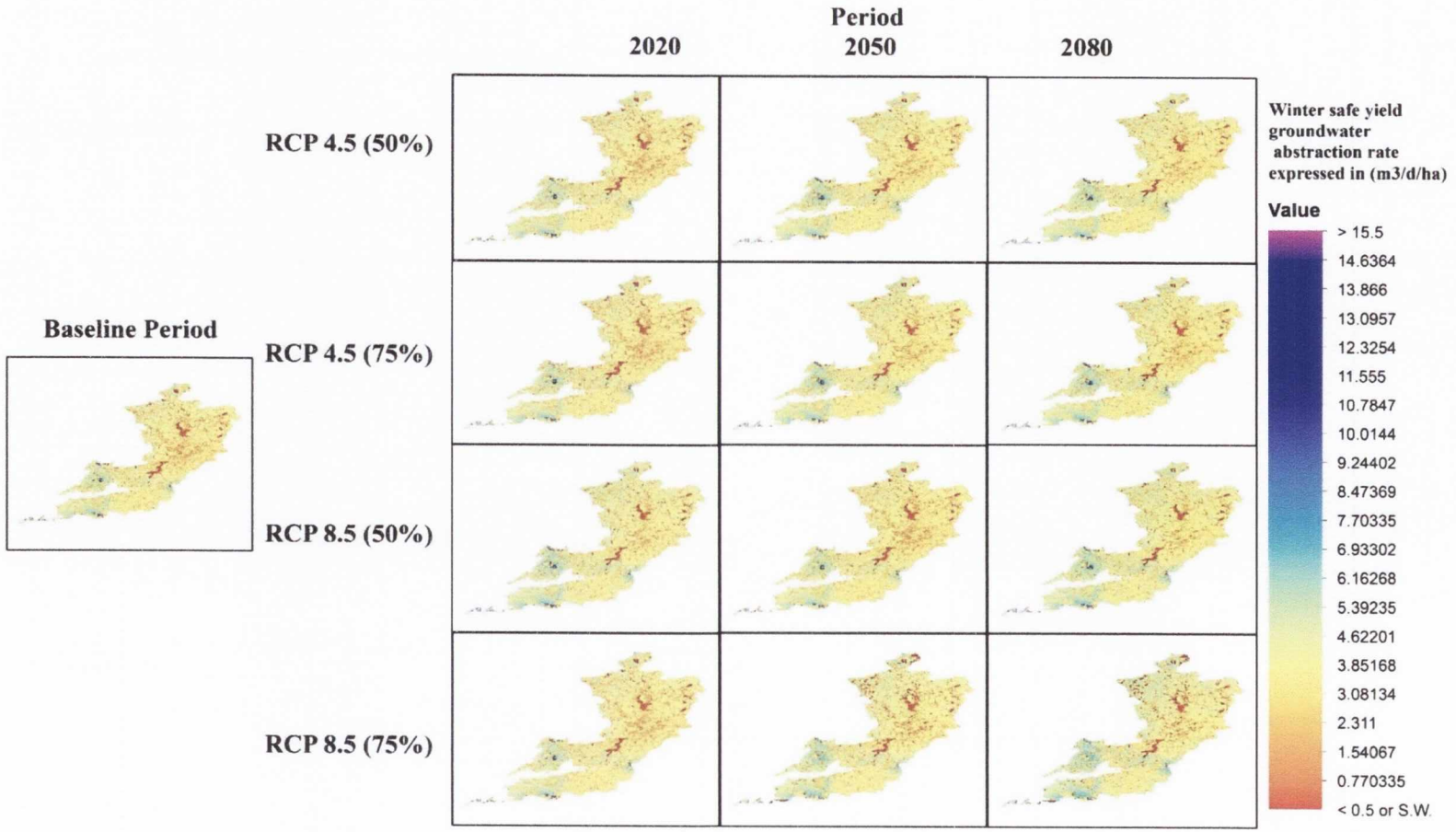

Figure E.17: The average winter safe yield groundwater abstraction for each climatic period and land use scenario simulated by GEO-CWB.

Appendix F: Additional machine learning techniques results

This appendix shows additional results from the performed machine learning techniques runs as part of this project for water level and water flow parameters. Two types of information are presented here for a number of hydrometric stations, the validation diagrams and the residuals diagrams. The validation diagrams present a comparison between the observed data and the simulated data for both water level and water flow parameters.

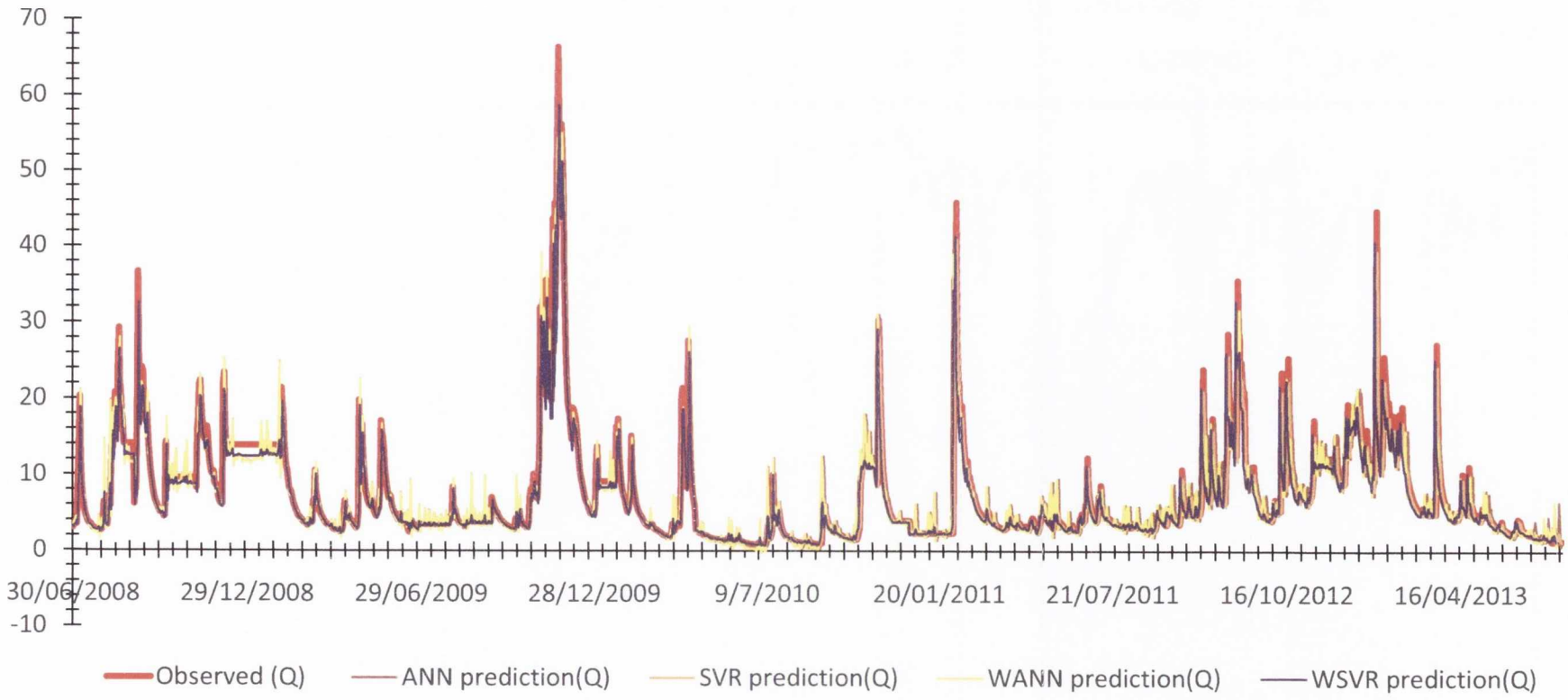

Figure F.1: Comparisons between the measured and predicted flow (m^3/s) based on the testing data for Nenagh hydrometric station.

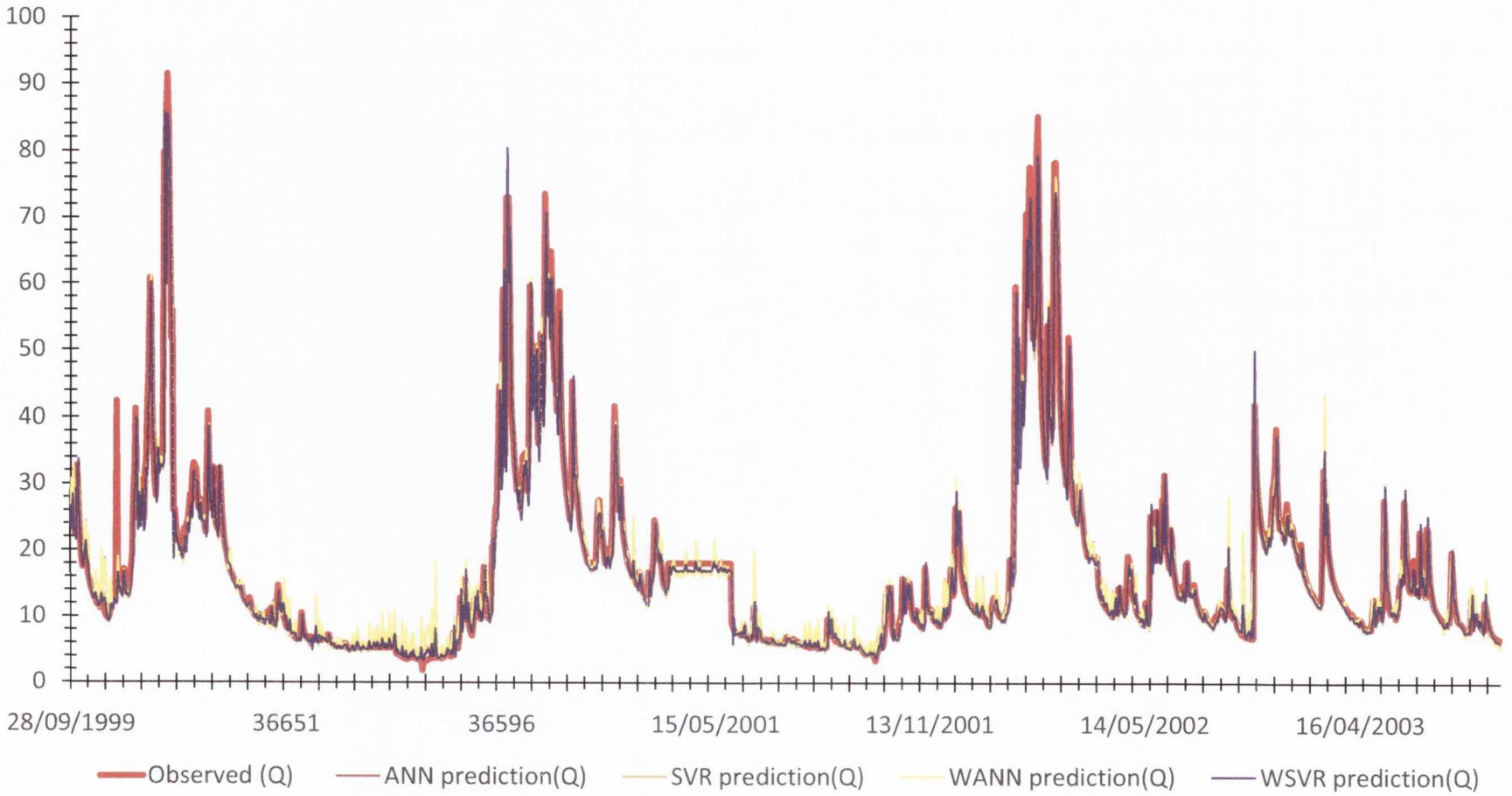

Figure F.2: Comparisons between the measured and predicted flow (m^3/s) based on the testing data for Brosna hydrometric station.

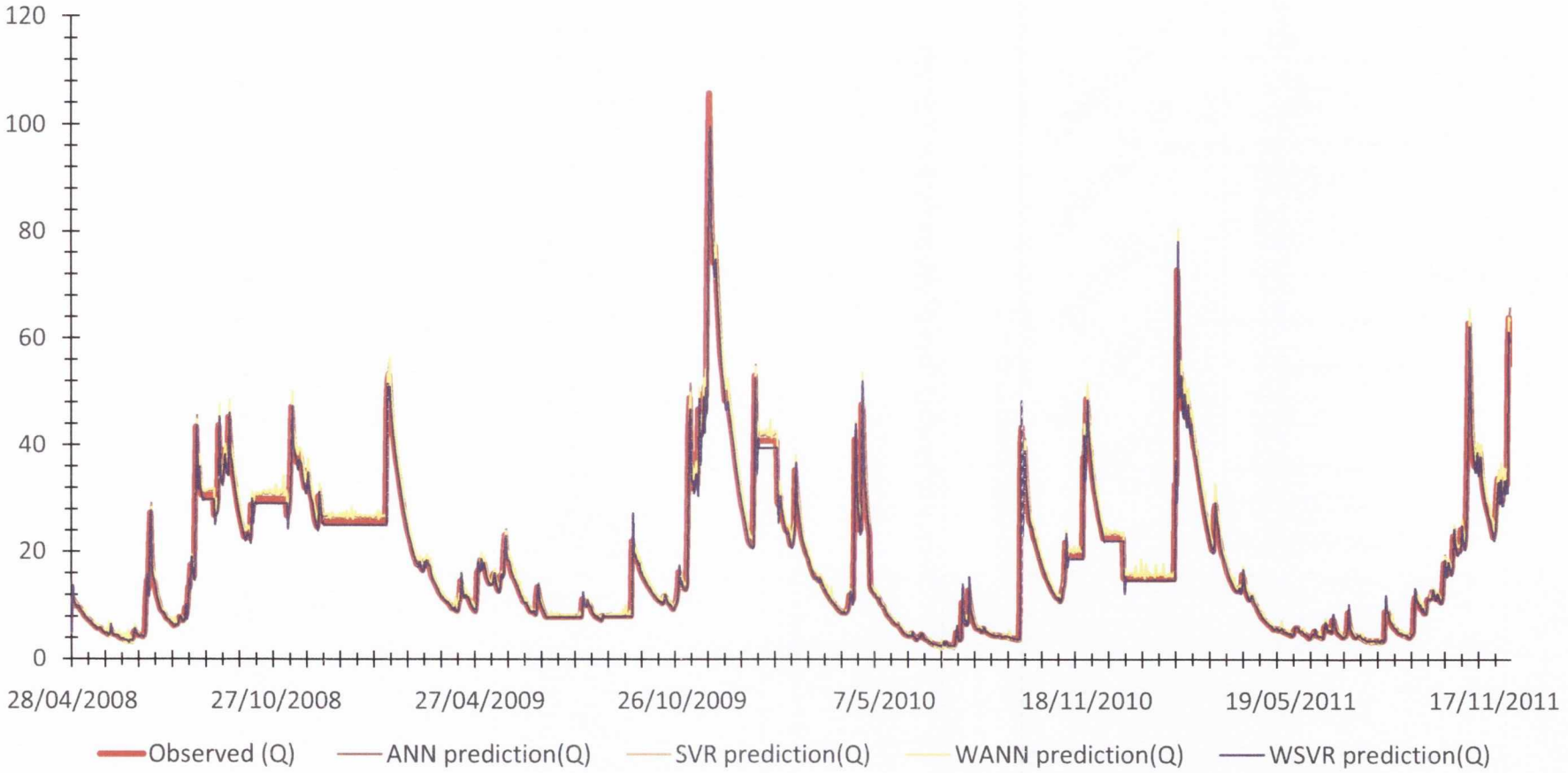

Figure F.3: Comparisons between the measured and predicted flow (m^3/s) based on the testing data for Inny hydrometric station.

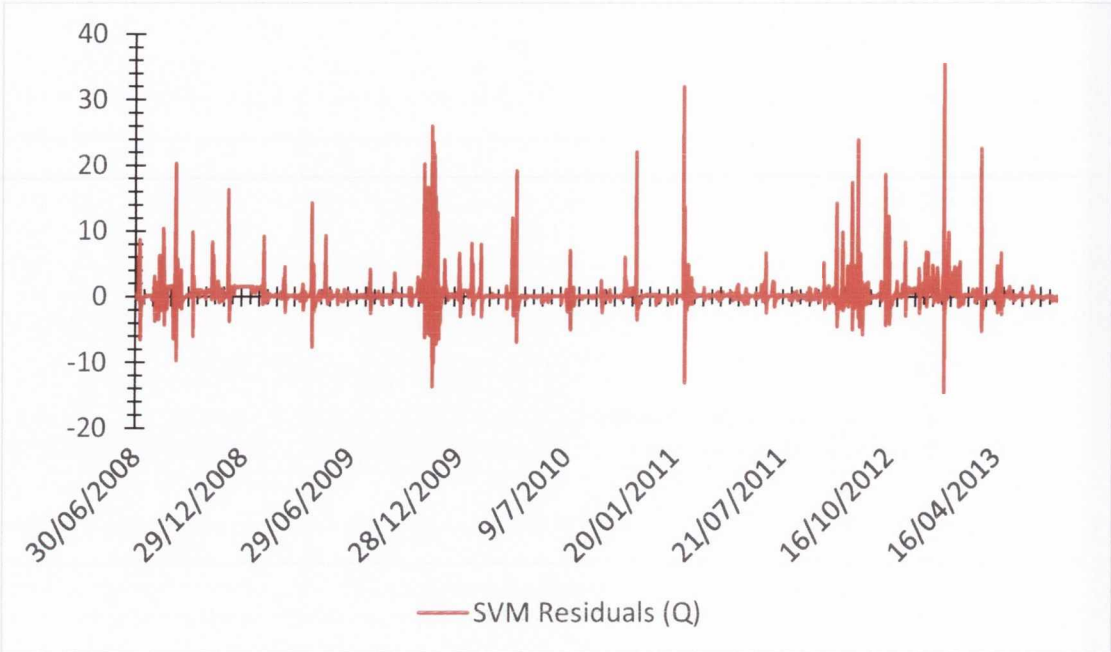

Figure F.4: Residuals of best performing flow SVM model for Nenagh.

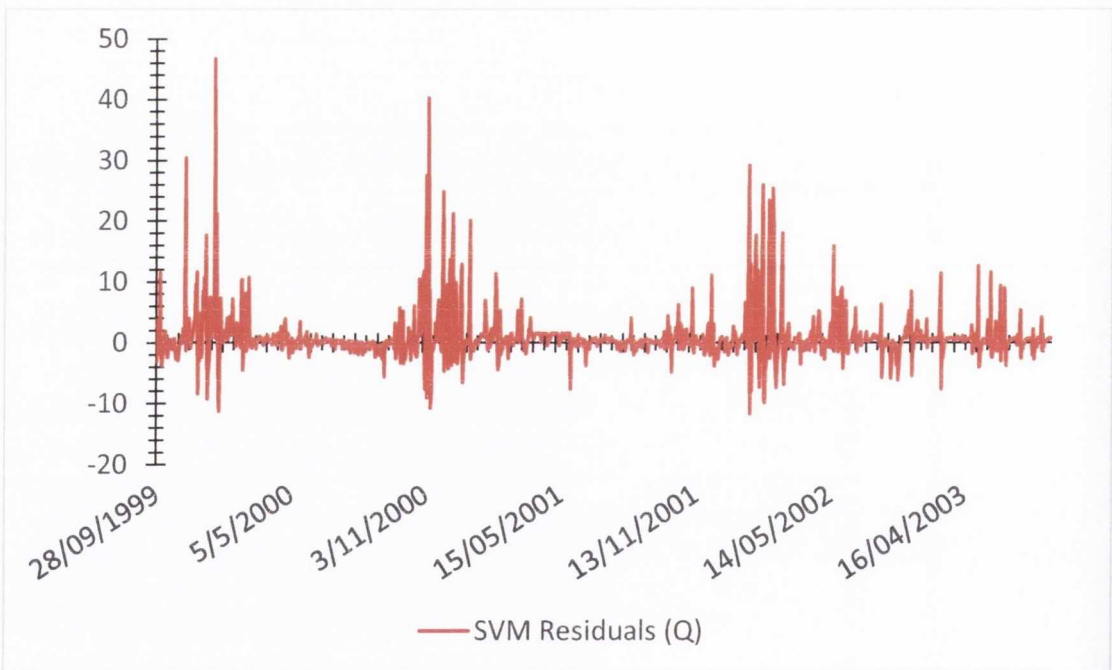

Figure F.5: Residuals of best performing flow SVM model for Brosna.

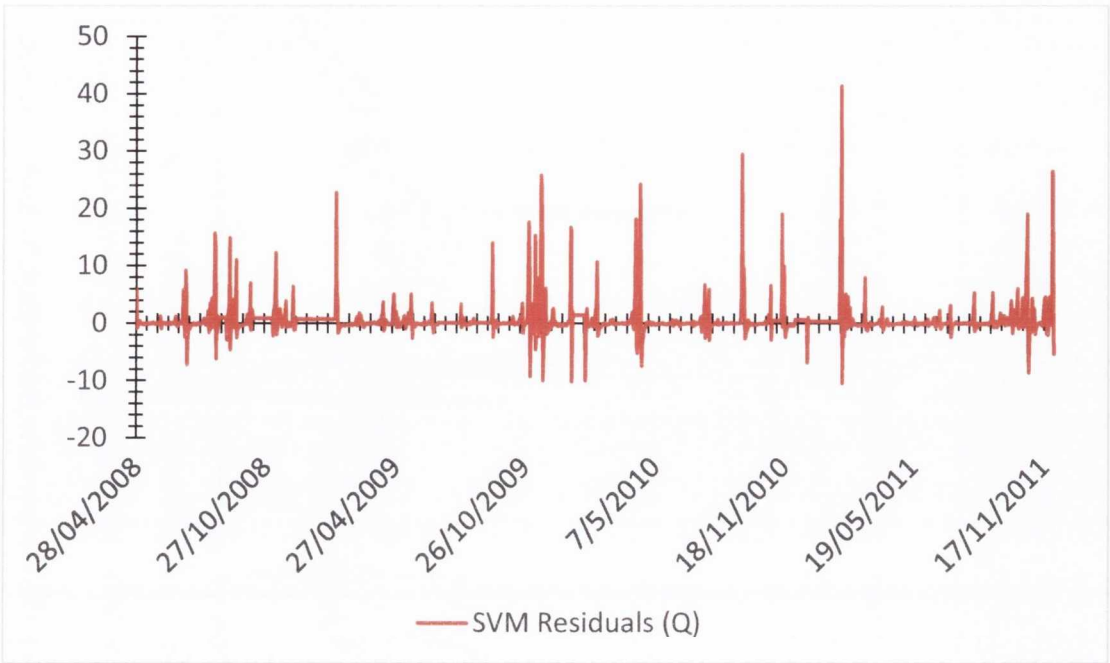

Figure F.6: Residuals of best performing water flow SVM model for Inny.

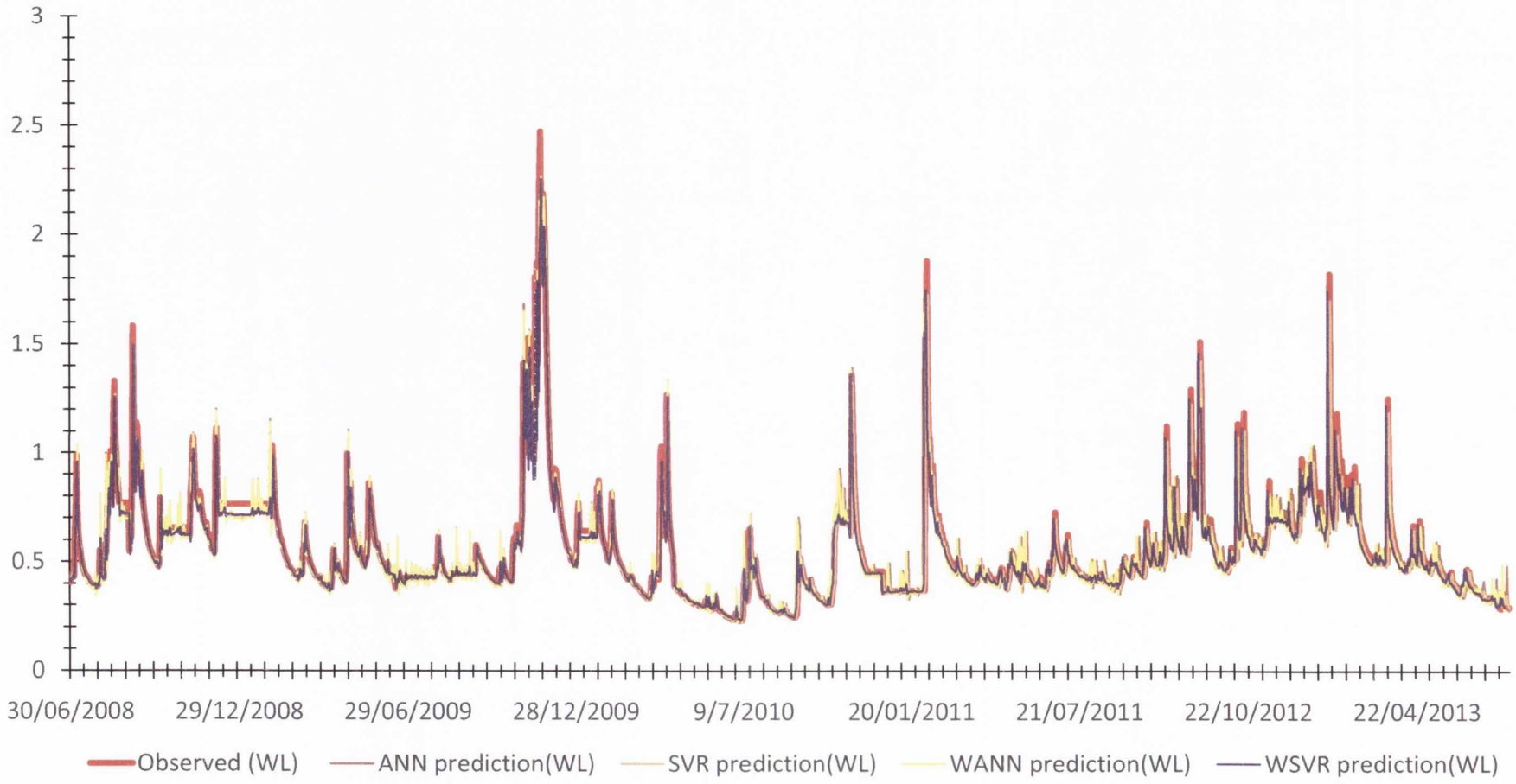

Figure F.7: Comparisons between the measured and predicted water level (m) based on the testing data for Nenagh hydrometric station.

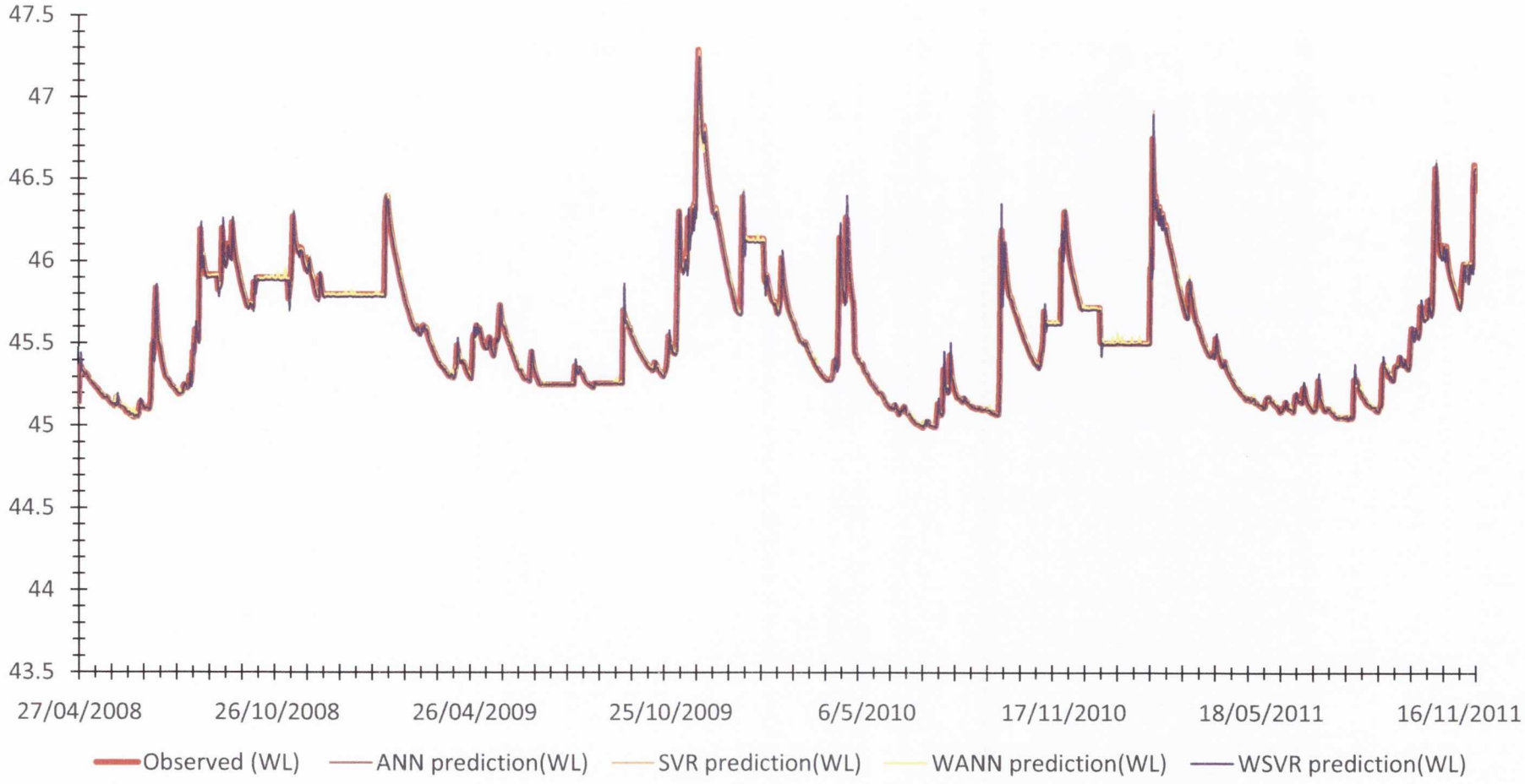

Figure F.8: Comparisons between the measured and predicted water level (m) based on the testing data for Inny hydrometric station.

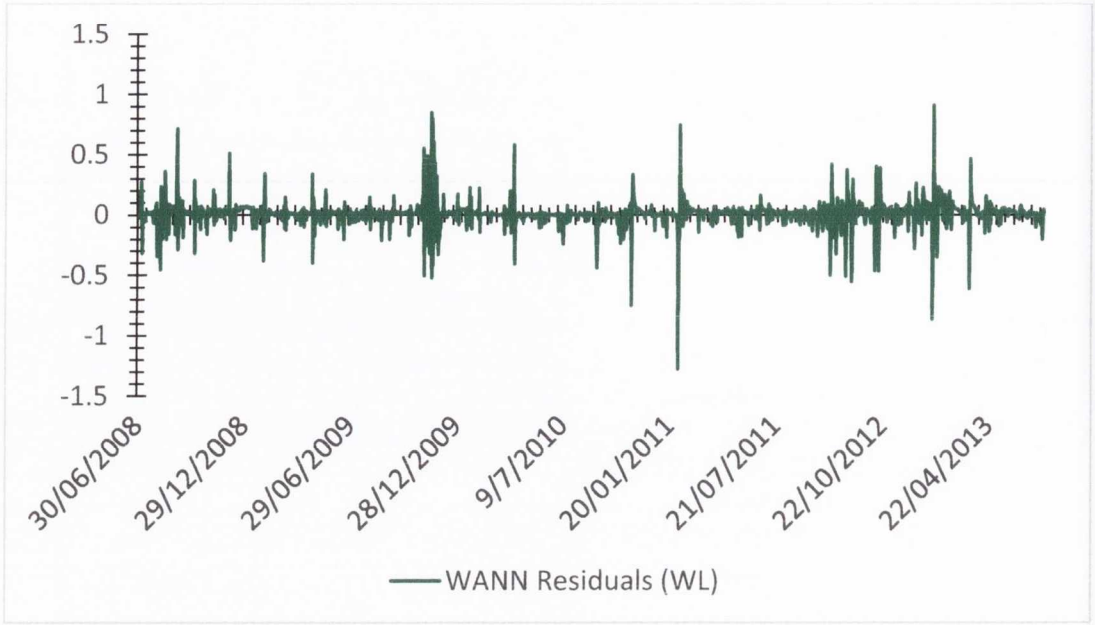

Figure F.9: Residuals of best performing water level WANN model for Nenagh.

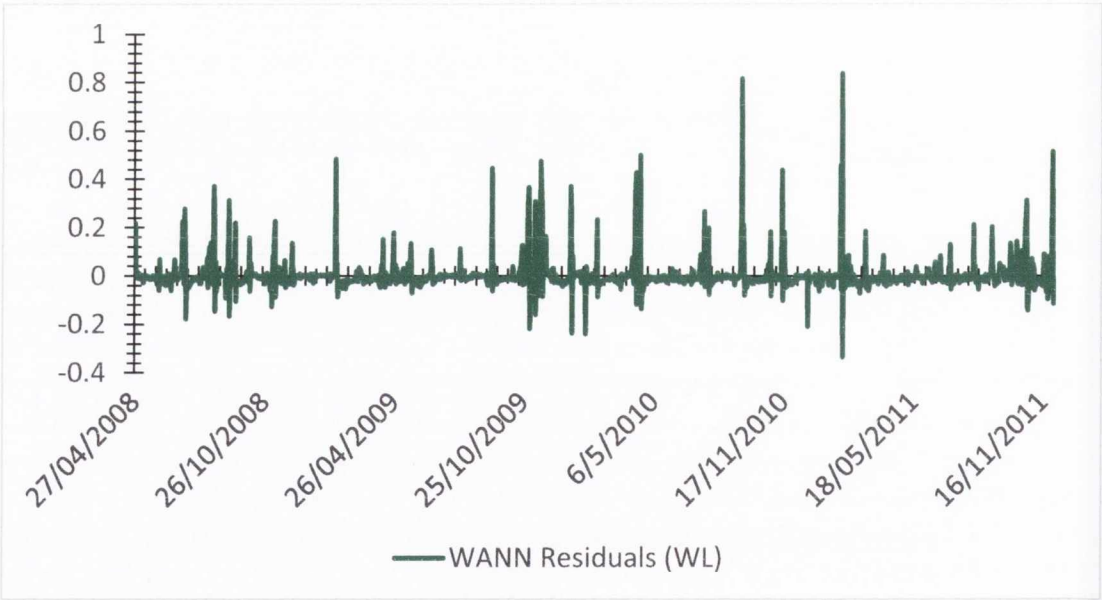

Figure F.10: Residuals of best performing water level WANN model for Inny.

Appendix G: List of publications

This appendix presents the full list of publications for the author.

- **Gharbia Salem S.**, Laurence Gill, Paul Johnston, Francesco Pilla. "Future water vulnerability in Ireland: an integrated water resources, climate and land use changes model", *National Hydrology Conference, Athlone, Co. Westmeath, Ireland,* 2016. (Published)

- **Gharbia Salem S.**, Sara Abd Alfatah, Laurence Gill, Paul Johnston, and Francesco Pilla. "Land use scenarios and projections simulation using an integrated GIS cellular automata algorithms." *Modeling Earth Systems and Environment* 2, no. 3 (2016): 151.

- **Gharbia Salem S**, Adnan Aish ,Thaer Abushbak, Ghassan Qishawi, Izz Al- Shawa, Abdalkarim Gharbia, Martina Zelenakova, Laurence Gill, Francesco Pilla. "Evaluation of wastewater post-treatment options for reuse purposes in the agricultural sector under rural development conditions", *Journal of Water Process Engineering*, 02/2016; 214:1-12. DOI:10.1016/j.jwpe.2015.12.003.

- **Gharbia, Salem S.**, Laurence Gill, Paul Johnston, and Francesco Pilla. "Multi-GCM ensembles performance for climate projection on a GIS platform." *Modeling Earth Systems and Environment* 2, no. 2 (2016): 1-21.

- **Gharbia Salem S**, Owen Naughton, Vincent Farrelly, Ronan Lyons, Francesco Pilla. "Attitudes to systemic risk: the impact of flood risk on the housing market in Dublin", *IEEE*, 2016.

- Gharbia, Abdalkarim S., **Salem S. Gharbia**, Thaer Abushbak, Hisham Wafi, Adnan Aish, Martina Zelenakova, and Francesco Pilla. "Groundwater Quality Evaluation Using GIS Based Geostatistical Algorithms." *Journal of Geoscience and Environment Protection* 4, no. 02 (2016): 89.

- **Gharbia Salem S**, Laurence Gill, Paul Johnston, Francesco Pilla. "Using GIS Based Algorithms for GCMs' Performance Evaluation", *IEEE*, 2016.

- **Gharbia Salem S**, Laurence Gill, Paul Johnston, Francesco Pilla. "Trans-boundary European River's Long-term Changes Analysis for Water Level and Streamflow Regime", *42nd IAH Congress (*AQUA2015*), Rome, Italy*, 2015.

- **Gharbia Salem S.**, Laurence Gill, Paul Johnston, Francesco Pilla. "GEO-CWB: a Dynamic Water Balance Tool for Catchment Water Management", *5th International Multidisciplinary Conference on Hydrology and Ecology (HydroEco2015), Vienna, Austria*, 2015.

- **Gharbia Salem S.**, Adnan Aish, Francesco Pilla, Modelling Potential Impacts of Climate Change on Groundwater of the Gaza Coastal Aquifer from Ensemble of Global Climate Model Projections, *Civil and Environmental Research, 7, (2), 2015.*

- **Gharbia Salem S.**, Adnan Aish, Francesco Pilla, Impacts of Climate Change on a Spatially Distributed Water Balance in the Gaza Strip, Palestine, *Journal of Environment and Earth Science, 5, (4),* 2015.

- **Gharbia Salem S.**, Adnan Aish, Francesco Pilla, Abdalkarim S. Gharbia, Projection of Future Climate by Multi-Model Median Approach under GIS Environment along the Gaza Strip, Palestine, *Journal of Environment and Earth Science*, 5, (3), 2015.

- **Gharbia Salem S.**, Francesco Pilla, Abdalkarim S. Gharbia. "Correlating Biochemical and Chemical Oxygen Demand of Influents And Effluents - a Case Study of Selected Wastewater Treatment Plants in the Gaza Strip, Palestine", *Conference paper in XVth IWRA World Water Congress, Edinburgh, Scotland,* 2015.

- **Gharbia Salem S.**, Francesco Pilla, Abdalkarim S. Gharbia. "Potential Effects of Climate Change on Groundwater Recharge - a Case Study of the Gaza Strip, Palestine", *Conference paper in XVth IWRA World Water Congress, Edinburgh, Scotland,* 2015.

- **Gharbia Salem S.**, Adnan Aish. "Future Changes in Climate Projected by a Multi-Model Ensemble Over The Gaza Strip, Palestine", *Palestinian Conference on Graduate Student Research in Natural and Applied Sciences at Birzeit University, Palestine*, 2014.

- **Gharbia Salem S.**, Adnan Aish. Impacts of Climate Change on Groundwater of the Gaza Coastal Aquifer Using GIS and MODFLOW. *LAP LAMBERT Academic Publishing, Germany,* 2013.

- **Gharbia Salem S.**, Adnan Aish. Climate Changes projection for the Gaza Strip Using GIS., International Conference: *GIS software locally and globally at University of Applied Sciences, Palestine*, 2013.

Appendix H: Datasets and algorithms

Due to the data size, the following list of datasets, tables, raster maps and coded algorithms are available in digital formats upon request. This includes the full digital raster maps resulted from the climate change projection process, potential evapotranspiration process and the Shannon water balance simulations, all in gridded formats. In addition to the GEO-CWB model and its Python code.

I **The climate change results and tables.**

II **Hydrometric station tables and observed data.**

III **Land use forcing factors raster maps, tables and the resulted maps.**

IV **Potential evapotranspiration resulted maps.**

V **GEO-CWB model and the Python code.**

VI **Shannon catchment water balance maps.**

VII **The resulted tables for chapter 10.**